Journal of Heat Transfer

Published Bimonthly by ASME

VOLUME 126 • NUMBER 4 • AUGUST 2004

HEAT TRANSFER PHOTOGALLERY

493 **Introduction**
Kenneth D. Kihm

494 **Natural Heat Transfer Phenomena**
Jack Howell

Two-Phase Flow Phenomena

495 **Visualization of Flow Boiling in Narrow Rectangular Channels**
Gopinath R. Warrier and Vijay K. Dhir

496 **Single and Dual Bubble Behavior Under the Influence of Electric Fields**
C. Herman, D. Mewes, Z. Liu, J. Radke, and I. Yoo

497 **Nucleation and Growth of Vapor Bubbles in a Heated Silicon Microchannel**
Evelyn N. Wang, Shankar Devasenathipathy, Juan G. Santiago, Kenneth E. Goodson, and Thomas W. Kenny

498 **Visualization of Wettability Effects on Microchannel Two-Phase Flow Resistance**
Sang Young Son and Jeffrey S. Allen

499 **Droplet Impact on a Heated Stainless Steel Surface: Influence of Camera Framing Rate**
Samuel L. Manzello and Jiann C. Yang

Forced Convection

500 **Steady Recirculation and Laminar Forced Convection in a Sinusoidal Wavy Channel**
Saurabh Vyas, Jiehai Zhang, and Raj M. Manglik

501 **Adiabatic Effectiveness of Film Cooling With Compound Angle Holes—The Effect of Blowing Ratio and Freestream Turbulence**
James E. Mayhew, James W. Baughn, and Aaron R. Byerley

502 **Surface Flow Visualization Using Encapsulated Thermal Tufts for Steady Flow and a Dynamic Heat Transfer Measurement Technique for Unsteady Flows**
James W. Baughn, A. David Ochoa, Jason S. Smith, and Aaron R. Byerley

503 **Temperature Measurements Using Thermochromic Liquid Crystals**
Roland Wiberg and Noam Lior

Nano-Scale Transport

504 **Nanoparticle Tracking Using CLSM and OSSM Imaging**
J. S. Park, C. K. Choi, and K. D. Kihm

505 **Three-Dimensional Tracking of Nanoparticles Using R-TIRFM Technique**
A. Banerjee and K. D. Kihm

506 **Evaporative Transport of Aqueous Liquid in a Closed Carbon Nanotube: A Nano Heat Pipe?**
Almila G. Yazicioglu, Constantine M. Megaridis, and Yury Gogotsi

(Contents continued on inside back cover)

Transactions of the ASME, Journal of Heat Transfer (ISSN 0022-1481) is published bi-monthly (Feb., Apr., June, Aug., Oct., Dec.) by The American Society of Mechanical Engineers, Three Park Avenue, New York, NY 10016. Periodicals postage paid at New York, NY and additional mailing offices. POSTMASTER: Send address changes to Transactions of the ASME, Journal of Heat Transfer, c/o THE AMERICAN SOCIETY OF MECHANICAL ENGINEERS, 22 Law Drive, Box 2300, Fairfield, NJ 07007-2300.
CHANGES OF ADDRESS must be received at Society headquarters seven weeks before they are to be effective. Please send old label and new address.
STATEMENT from By-Laws. The Society shall not be responsible for statements or opinions advanced in papers or ... printed in its publications (B7.1, Para. 3), **COPYRIGHT**

Journal of Heat Transfer Volume 126, Number 4 AUGUST 2004

RESEARCH PAPERS

Evaporation, Boiling, and Condensation

507 A New Model for the Effect of Calcium Sulfate Scale Formation on Pool Boiling Heat Transfer
M. Jamialahmadi and H. Müller-Steinhagen

518 An Experimental Investigation of Flow Boiling Characteristics of Water in Parallel Microchannels
Mark E. Steinke and Satish G. Kandlikar

527 The Condensation of Ammonia-Water Mixtures in a Horizontal Shell and Tube Condenser
Chris Philpott and Joe Deans

Experimental Techniques

535 A Dual-Scale Computational Method for Correcting Surface Temperature Measurement Errors
T. C. Tszeng and G. F. Zhou

Forced Convection

540 Experimental Investigation of the Potential of Metallic Porous Inserts in Enhancing Forced Convective Heat Transfer
Bogdan I. Pavel and Abdulmajeed A. Mohamad

546 Effect of Squealer Geometry on Tip Flow and Heat Transfer for a Turbine Blade in a Low Speed Cascade
Vikrant Saxena and Srinath V. Ekkad

Jets, Wakes, and Impingement Cooling

554 The Effects of Nozzle Diameter on Impinging Jet Heat Transfer and Fluid Flow
Dae Hee Lee, Jeonghoon Song, and Myeong Chan Jo

Melting and Solidification

558 Melting Heat Transfer Characteristics of Microencapsulated Phase Change Material Slurries With Plural Microcapsules Having Different Diameters
Hideo Inaba, Myoung-Jun Kim, and Akihiko Horibe

Micro/Nanoscale Heat Transfer

566 Nano-Scale Machining Via Electron Beam and Laser Processing
Basil T. Wong, M. Pinar Mengüç, and R. Ryan Vallance

577 Finite Size Effects in Determination of Thermal Conductivities: Comparing Molecular Dynamics Results With Simple Models
Patrice Chantrenne and Jean-Louis Barrat

Natural and Mixed Convection

586 Three-Dimensional Instabilities of Natural Convection Flow in a Vertical Cylinder With Partially Heated Sidewall
A. Rubinov, V. Erenburg, A. Yu. Gelfgat, E. Kit, P. Z. Bar-Yoseph, and A. Solan

600 Numerical Analysis of Natural Convection and Mixing in Two-Fluid Stratified Pools With Internal Heat Sources
A. A. Gubaidullin and B. R. Sehgal

Radiative Heat Transfer

611 A Computational Study on Flame-Solid Radiative Interaction in Flame Spread Over Thin Solid-Fuel
Amit Kumar, Kevin Tolejko, and James S. T'ien

621 Reverse Monte Carlo Method for Transient Radiative Transfer in Participating Media
Xiaodong Lu and Pei-feng Hsu

Thermal Systems

628 A Two-Temperature Model for the Analysis of Passive Thermal Control Systems
Shankar Krishnan, Jayathi Y. Murthy, and Suresh V. Garimella

TECHNICAL NOTES

638 Local Pool Boiling Coefficients on the Inside Surface of a Horizontal Tube
Myeong-Gie Kang

642 Three-Dimensional Conjugate Heat Transfer in a Horizontal Channel With Discrete Heating
Qinghua Wang and Yogesh Jaluria

648 Use of Wavelets for Analyzing Transient Radiative Heat Transfer in an Inhomogeneous Medium
Oguzhan Guven and Yildiz Bayazitoglu

652 The Thermal Constriction Resistance for an Eccentric Spot on a Circular Heat Flux Tube
A. Baïri and N. Laraqi

656 Entropy Generation Minimization of Fully Developed Internal Flow With Constant Heat Flux
Eric B. Ratts and Atul G. Raut

Journal of Heat Transfer Volume 126, Number 4 AUGUST 2004

DISCUSSIONS AND CLOSURE

660 Discussion: "Self-Organization and Self-Similarity in Boiling Systems" [L. H. Chai and M. Shoji, ASME J. Heat Transfer, 124(3), pp. 507–515 (2002)]

660 E. Yantovski

660 Allan D. Kraus

660 José Viriato Coelho Vargas

661 Gianfranco Guerreri

661 Tanmay Basak

662 Signe Kjelstrup and Dick Bedeaux

662 Jaime Cervantes de Gortari

663 Closure to "Discussion of 'Self-Organization and Self-Similarity in Boiling Systems' [ASME J. Heat Transfer 124(3), pp. 507–515 (2002)]"
L. H. Chai and M. Shoji

ERRATUM

666 Erratum: "Investigation of Steady-State Drawing Force and Heat Transfer in Polymer Optical Fiber Manufacturing" [Journal of Heat Transfer, 2004, 126(2), pp. 236–243]
H. M. Reeve, A. M. Mescher, and A. F. Emery

ANNOUNCEMENT

667 Call for Photographs

The ASME Journal of Heat Transfer is abstracted and indexed in the following:

Applied Science and Technology Index, AMR Abstracts Database, Chemical Abstracts, Chemical Engineering and Biotechnology Abstracts (Electronic equivalent of Process and Chemical Engineering), Civil Engineering Abstracts, Compendex (The electronic equivalent of Engineering Index), Corrosion Abstracts, Current Contents, E & P Health, Safety, and Environment, Ei EncompassLit, Engineered Materials Abstracts, Engineering Index, Enviroline (The electronic equivalent of Environment Abstracts), Environment Abstracts, Environmental Engineering Abstracts, Environmental Science and Pollution Management, Fluidex, Fuel and Energy Abstracts, Index to Scientific Reviews, INSPEC, International Building Services Abstracts, Mechanical & Transportation Engineering Abstracts, Mechanical Engineering Abstracts, METADEX (The electronic equivalent of Metals Abstracts and Alloys Index), Petroleum Abstracts, Process and Chemical Engineering, Referativnyi Zhurnal, Science Citation Index, SciSearch (The electronic equivalent of Science Citation Index), Theoretical Chemical Engineering

Journal of Heat Transfer

Heat Transfer Photogallery

The eighth ''Heat Transfer Photogallery'' was sponsored by the K-22 Heat Transfer Visualization Committee for the 2003 International Mechanical Engineering Congress and Exhibition (IMECE) held in Washington, D.C., on November 16–21, 2003. Out of the total 18 submitted entries, the peer-reviewed selection process identified the top thirteen entrees for publication in the ASME Journal of Heat Transfer August issue of 2004. Ballots to mark for acceptance for publication for each entry were solicited from those who participated and visited the Photogallery session at 2003 IMECE.

The purpose of publishing these photographs is to draw attention to the innovative features of optical diagnostic techniques and aesthetic qualities of thermal processes. To focus on visualization, the text is kept to a minimum and further details should be found directly from the authors. My wish is that the journal readers enjoy viewing these collections, acquire knowledge of the state-of-the-art features potentially applicable for their own research, and also promote their participation in the 2004-IMECE [http://www.asmeconferences.org/congress04] Photogallery session presentation (refer to the **Call for Photogallery for 2004-IMECE** announced in this volume).

The present Photogallery boasts its fanfare with ''Natural Heat Transfer Phenomena,'' presented by Jack Howell of University of Texas-Austin, former Editor of Journal of Heat Transfer. The remaining twelve entries are organized in three different groups, based on their technical topics. Brief overviews for individual entries are summarized:

(A) Two-Phase Flow Phenomena

- Boiling phenomena in narrow rectangular channels [G. R. Warrier and V. K. Dhir, UCLA]
- Behavior of boiling bubbles of a few millimeter dimensions [C. Herman et al., Johns Hopkins University]
- Growth of boiling bubbles in a microchannel of 270×95 μm [E. N. Wang et al., Stanford University]
- Wettability of two-phase flow in a 330 μm microchannel [S. Y. Son and J. S. Allen, NASA/NCMR]
- Droplet impact on a heated surface [S. L. Manzello and J. C. Yang, NIST]

(B) Forced Convection

- Sinusoidal wavy channel flows [S. Vyas et al., University of Cincinnati]
- Film cooling from angle holes [J. E. Mayhew et al., Rose-Hulman Institute, UC-Davis, USAF-Academy]
- Steady and unsteady flows through protruding cylinders [J. W. Baughn et al., UC-Davis, USAF-Academy]
- Flow over a cylinder and a steel gear [R. Wiberg, KTH, and N. Lior, Univ. of Pennsylvania]

(C) Nano-Scale Transport

- Nanoparticle tracking in micrometer resolution [J. S. Park et al., Texas A&M University]
- Nanoparticle tracking in nanometer resolution [A. Banerjee and K. D. Kihm, Texas A&M University]
- Evaporative transport inside a carbon nanotube [A. G. Yazicioglu et al., UIC, Drexel University]

Kenneth D. Kihm
Department of Mechanical, Aerospace
and Biomedical Engineering,
University of Tennessee,
Knoxville, TN 37996-2210

NATURAL HEAT TRANSFER PHENOMENA

Jack Howell, Department of Mechanical Engineering
The University of Texas at Austin

Chimera's Burial

This mountain in Turkey has a methane flame that is continuously burning. Legend has it that the fire-breathing dragon Chimera was captured by Belaraphon riding his winged horse Pegasus, and was buried in the mountain. He still breathes forth flames, as clearly demonstrated by the photo. Chimera had the body of a goat, the head of a lion and the tail of a serpent and maybe looked a lot like this:

The presence of soot in the methane diffusion flame causes it to become luminous as the carbon particles become incandescent.. The luminous character here indicates that the flame is burning fuel-rich or there are higher hydrocarbons present, as methane flames normally are transparent or blue.

Lava

The Big Island of Hawaii has extinct and active volcanoes that have covered much of the island with spectacular lava flows. Two types of lava are found. One type is called Pāhoehoe lava; it cools into a smooth surface with spectacular patterns.

Pāhoehoe lava

The second form is called A'ā lava, and its fractured form results from trapped gas exploding outward as the lava reaches the surface and the lower pressure causes massive effusion of the trapped gases. Local lore says that the name comes from native Hawai'ians expressing pain as they walked barefoot across the hot lava.

A'ā lava

The Kiluea volcano on the Big Island has been active for many years, and molten lava still flows to the sea. You can hike to active flows in Volcanoes National Park, and see a view like the bottom one taken at night

Molten lava flow at night

The Giant's Causeway

On the Northern coast of Ireland, an ancient lava flow apparently slowly cooled by natural convection, forming the usual hexagonal Bénard cells while cooling. When the lava hardened and geological upheavals occurred, the lava fractured at the cell boundaries, forming acres of hexagonal cells constructing a spectacular structure called The Giant's Causeway. The picture at the left shows a small segment of the cell structure.

Bénard cells

All photos except for the statue of Chimera are by the author. Chimera photo from Ugo Bardi, Univerity of Firenze

1

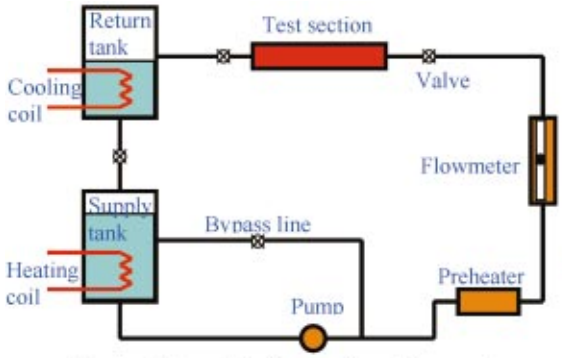

Fig. 1 Schematic of experimental apparatus.

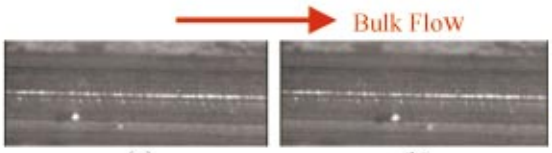

Fig. 2 Bubble nucleation and departure.

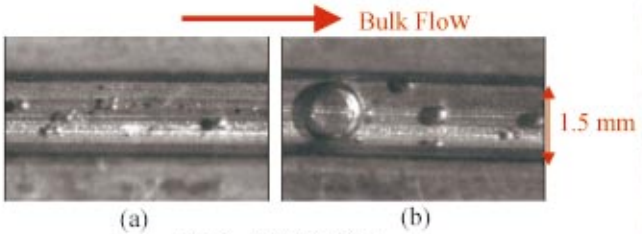

Fig. 3 Bubbly flow.

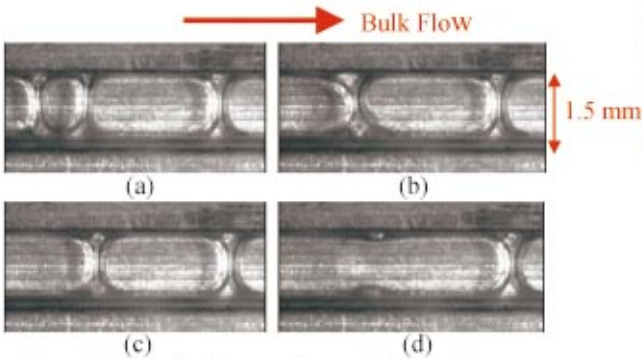

Fig. 4 Merger of vapor slugs.

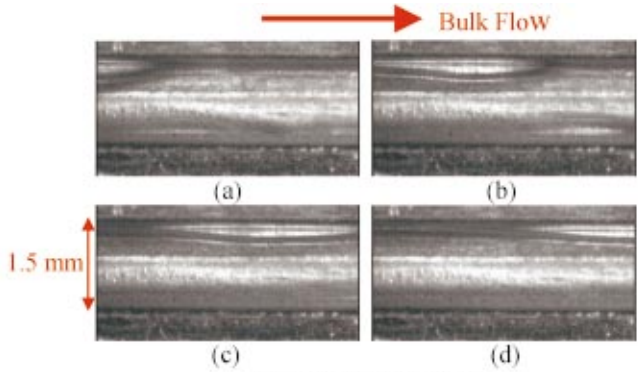

Fig. 5 Annular flow.

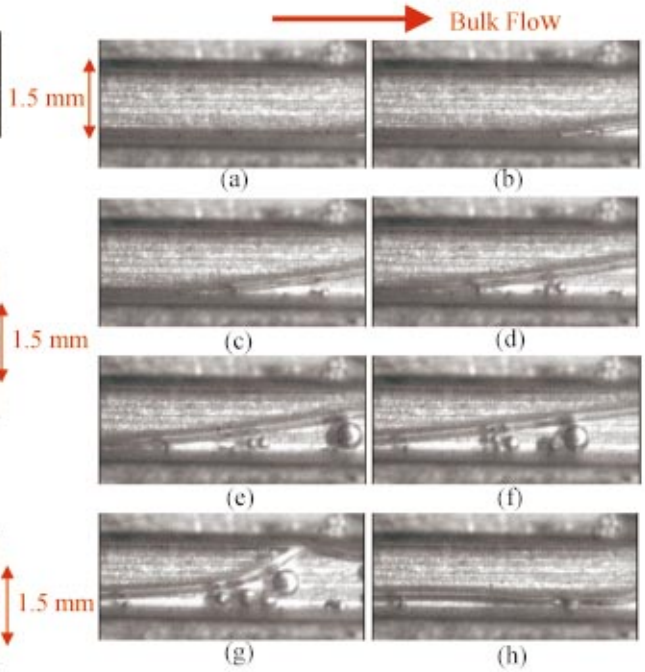

Fig. 6 Annular flow with flow reversal.

VISUALIZATION OF FLOW BOILING IN NARROW RECTANGULAR CHANNELS

Gopinath R. Warrier and Vijay K. Dhir
University of California, Los Angeles, CA, USA

The schematic of the flow boiling test loop is shown in Fig. 1. The test section consists of five parallel channels each with a hydraulic diameter of 0.75 mm (1.5 mm width, 0.50 mm height) and 325 mm long. The water flow rate was maintained at 2.15 g/s, while the inlet subcooling and exit pressure were maintained at 20 °C and 1.05 bar., respectively. The heat flux was varied in the range 2.21 to 8.85 W/cm^2. Figure 2 shows nucleation of a bubble and its subsequent departure from its site of origin. At higher heat fluxes, bubbly flow is observed as shown in Fig. 3. Figure 4 shows the merger of vapor slugs to form larger slugs. Annular flow with a thin liquid layer at the walls is shown is Fig. 5. Figure 6 is a sequence of photographs showing flow reversal during annular flow. Bubble nucleation occurs inside the liquid layer during the flow reversal process. As the liquid flows back, it begins to fill the entire channel. Once the liquid completely fills the channel, it is immediately washed away and the flow reverts back to annular flow. The sequence of the photographs is from left to right and from top to bottom.

Test cell

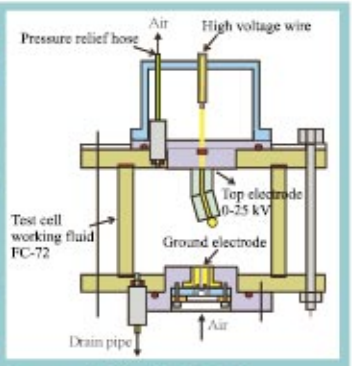

- Air bubble was injected into the test cell filled with FC-72.
- Static electric field (0-25 kV) formed between the bottom copper cylinder electrode (electrically grounded) and a spherical top electrode, spaced 11.6 mm apart.

Electric field

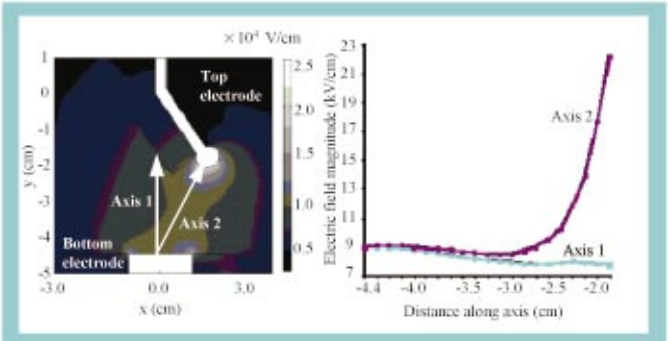

Spherical off-axis top electrode Along axis 1, axis 2

- Initial electric field distribution in the test cell : Top electrode: U=25kV; Bottom electrode: U=0V.

Selected results

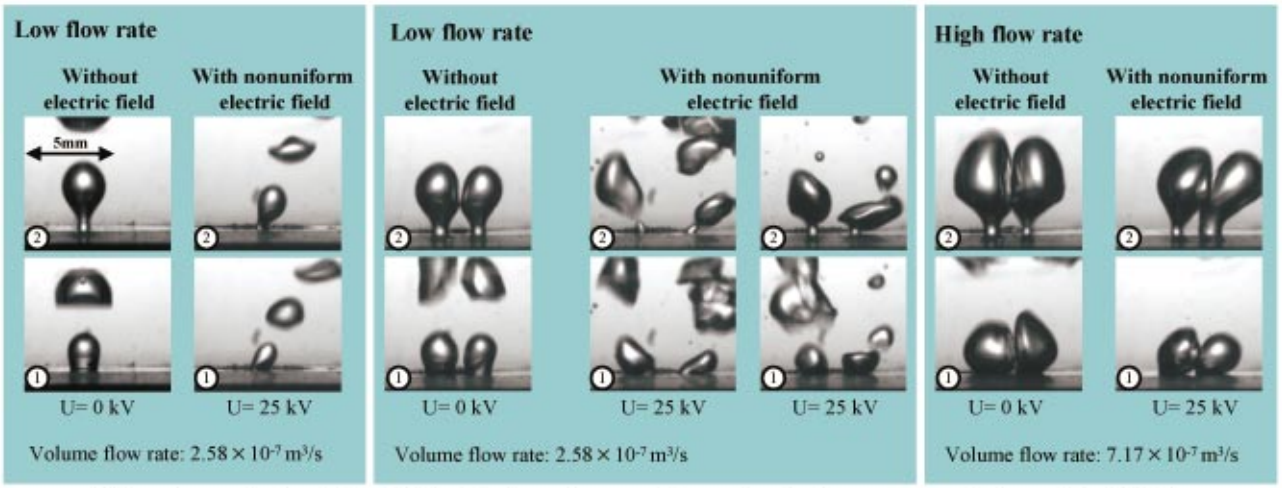

Single and dual bubble behavior under the influence of electric fields

C. Herman[1]*, D. Mewes[2], Z. Liu[1], J. Radke[2], I. Yoo[1]

[1]Department of Mechanical Engineering, The Johns Hopkins University, 3400 North Charles Street, Baltimore, Maryland 21218, U.S.A.,* herman@titan.me.jhu.edu

[2]Institut für Verfahrenstechnik, Universität Hannover, Callinstr. 36, 30167 Hannover, Germany

Bubble coalescence has a strong impact on the performance of two-phase flow systems. In order to understand and control the EHD enhanced heat transfer in boiling processes, experimental investigation of bubble formation and coalescence were studied with and without electric fields to identify specific behavior patterns. The results of experimental visualization clearly indicate the significant differences in bubble shape, size and trajectory due to the effects of electric fields. In single bubble experiments the bubble can be deformed towards or away from the upper electrode. Although the direction of the tilt can alternate (even in a single experiment), in the majority of the cases it is towards the electrode. In dual bubble experiments the bubbles behave similar to the single bubble case at large volume flow rates. In low volume-flow-rate experiments the bubble pair can repell each other in the opposite direction. Furthermore, the detachment volume of the bubble decreases under the influence of electric fields, which leads to a higher detachment frequency. The long-term goal of this research is to explore the possibility to enhance boiling heat transfer in the low gravity environment by substituting the buoyancy force with a force induced by the electric field.

Acknowledgements

This research was supported by NASA, NSF and DAAD.

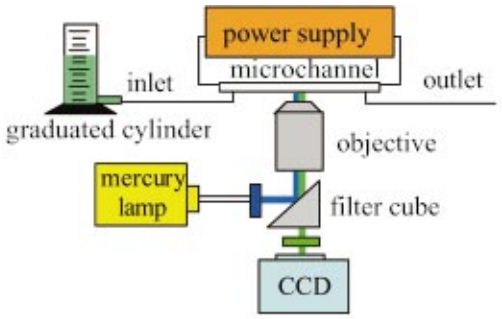

(a) Experimental setup

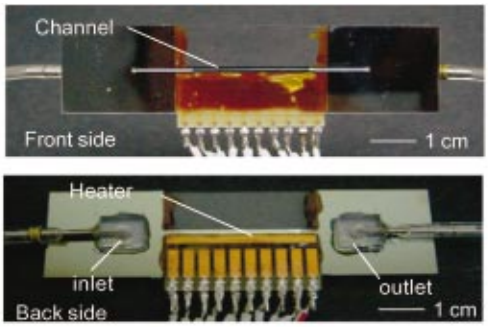

(b) Microchannel with integrated heater

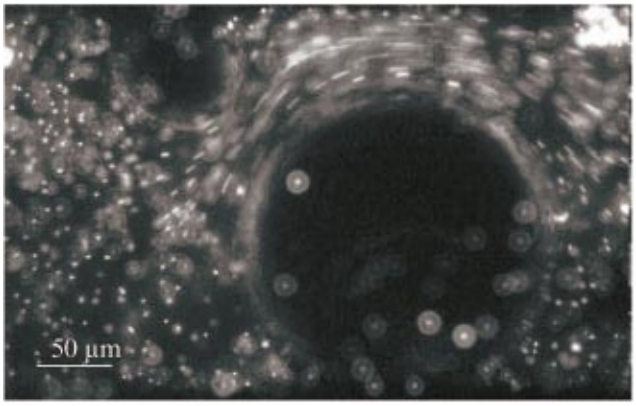

(c) P = 1.2 W

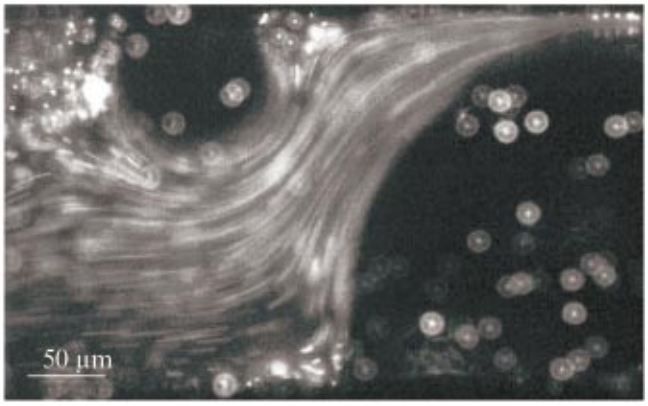

(d) P = 1.4 W, 56 ms later

Nucleation and Growth of Vapor Bubbles in a Heated Silicon Microchannel

Evelyn N. Wang, Shankar Devasenathipathy, Juan G. Santiago, Kenneth E. Goodson, Thomas W. Kenny
Mechanical Engineering Department, Stanford University

Flow visualizations of boiling in a heated 270 µm wide by 95 µm deep microchannel are presented. The inlet liquid flowrate is 0.2 µl/min, and the fluorescent seed particles are 700 nm diameter polystyrene spheres. The schematic of the experimental rig is shown in (a), which includes an epi-fluorescent microscope, a 20 X objective (0.75 numerical aperture), and a 12-bit resolution interline CCD camera. An anodically bonded glass cover slide provides optical access to the microchannel shown in (b). Aluminum heaters are sputtered onto the back side of the silicon chip. Two nucleated vapor bubbles on the side walls are captured in (c) and (d) with 1 ms exposure times. Power is increased from 1.2 to 1.4 W, increasing the vapor volume and consequently accelerating the liquid in (d). The images show particle pathlines between the two bubbles. The image focal plane is approximately 20 µm from the inner surface of the glass cover slide. Some particles adsorb onto the walls at the onset of partial dry-out.

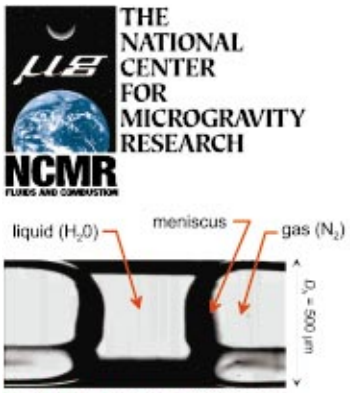

Fig. 4. Slug flow in an hydrophilic (uncoated) square microchannel.

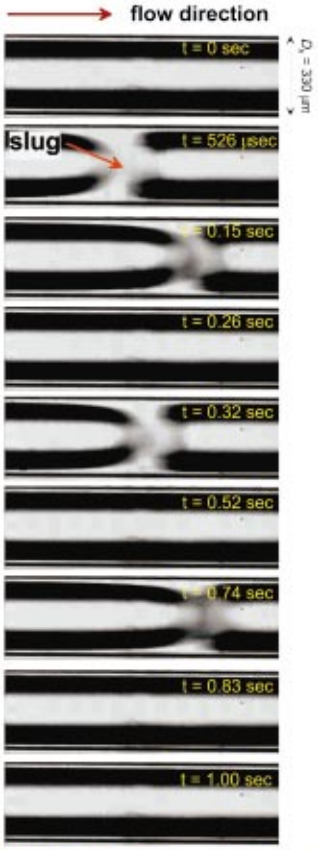

Fig. 6. Slug flow in hydrophilic circular microchannel.

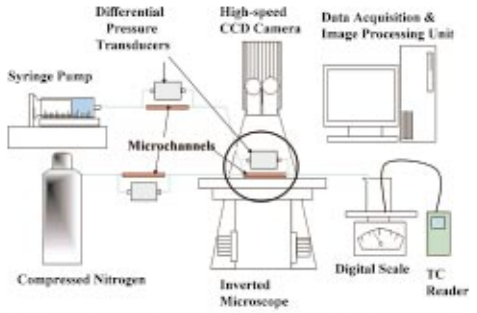

Fig. 1. Single and two-phase flow rates measurement setup

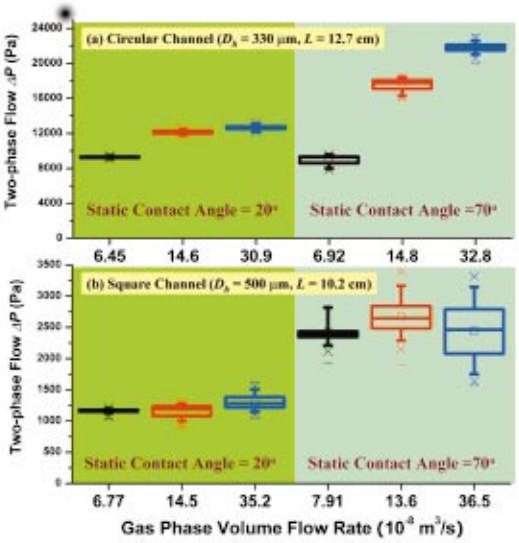

Fig. 2. Two-phase flow pressure drop vs. variable gas (N_2) volume flow rate with a fixed liquid volume flow rate (5.8x10^{-8} m^3/s).

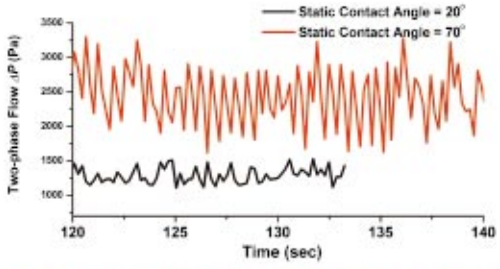

Fig. 3. Temporal two-phase flow pressure drop variations in square microchannels having different wettability conditions.

Fig. 5. Droplet formation from two-phase flow in hydrophobic (coated) square microchannel.

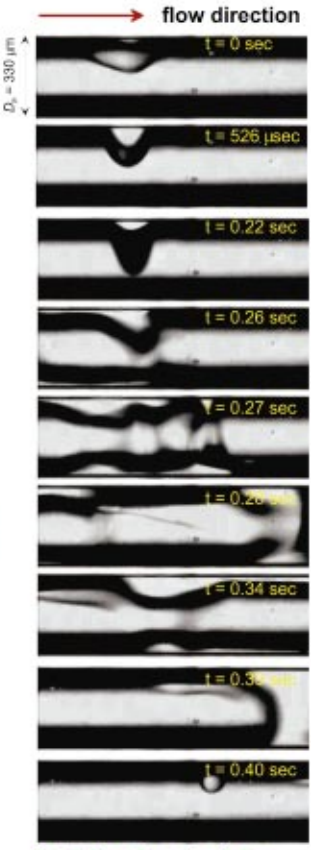

Fig. 7. Drop formation & flow instability in hydrophobic circular microchannel.

Visualization of Wettability Effects on Microchannel Two-Phase Flow Resistance

Sang Young Son and Jeffrey S. Allen

National Center for Microgravity Research
NASA Glenn Research Center, Cleveland, OH

The effect of surface wettability on two-phase flow (water and nitrogen) in microscale channels has been experimentally investigated using high speed microscopy (Fig. 1). Images taken at 1900 frames per second combined with precise differential pressure measurements in circular and square microchannels show that wetting conditions play a significant role in the flow resistance. Two channel cross-sections, 330 μm diameter circular and 500 μm square, were tested for various gas-liquid flow rates. In addition, two surface energies, or static contact angles, were tested. The two contact angles were less than 20 ° for uncoated microchannels and approximately 70° for coated microchannels. The coating is a commercial polymer (RainX®) which forms a teflon-like layer on the glass surface. The hydrophobic (coated) microchannels exhibit a much higher and less stable two-phase pressure drop (Figs. 2 and 3) as compared to the hydrophilic (uncoated) microchannels under identical flow conditions. The uncoated channels show stable flow with high velocity liquid slugs translating on an annular liquid film (Figs. 4 and 6). High speed microscopy confirms the less stable flow in the coated channels which exhibits droplet formation and contact line drag (Figs. 5and 7).

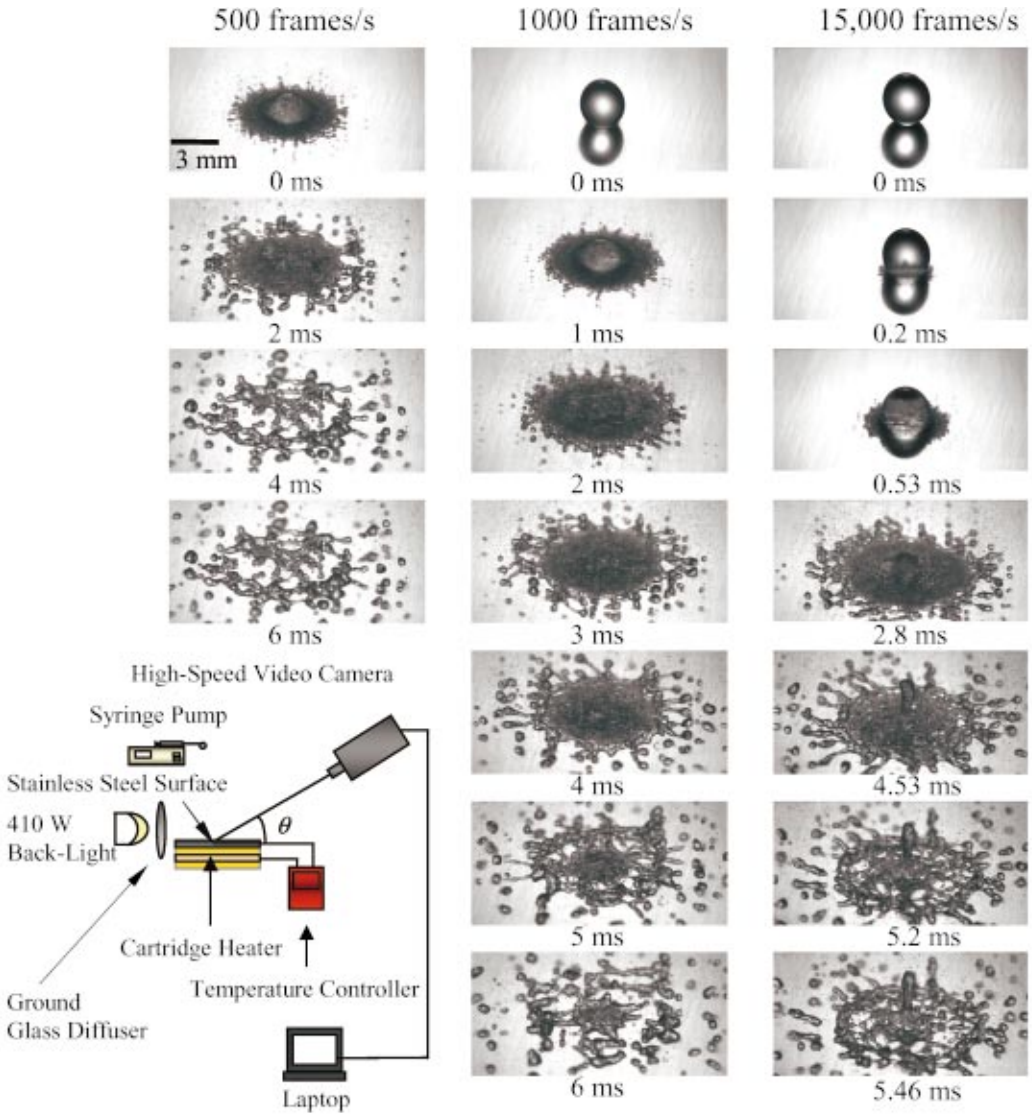

Droplet Impact on a Heated Stainless Steel Surface: Influence of Camera Framing Rate

Samuel L. Manzello and Jiann C. Yang
Building and Fire Research Laboratory (BFRL)
National Institute of Standards and Technology (NIST)
Gaithersburg, MD 20899-8662 USA

The impact of a single water droplet upon a polished stainless steel surface was imaged using a Digital High Speed Camera at 500, 1000, and 15,000 frames per second with shutter speed set to 50 μs. The camera was fitted with a 60 mm micro lens to obtain the required spatial resolution to capture droplet impingement. The camera was aligned at an angle $\theta = 33\,^{\circ}$ with respect to the horizontal. Surface heating was accomplished using a copper block with two miniature cartridge heaters embedded within it. The surface temperature was controlled within $\pm$ 1 °C using a temperature controller. The surface temperature and impact Weber number ($We = \rho D V^2/\sigma$, where D is droplet diameter, V is impact velocity, ρ is density, σ is surface tension) were fixed for each framing rate at T_s = 345 °C and We = 165, respectively. At 15,000 frames per second, jetting was observed during breakup of the liquid film.

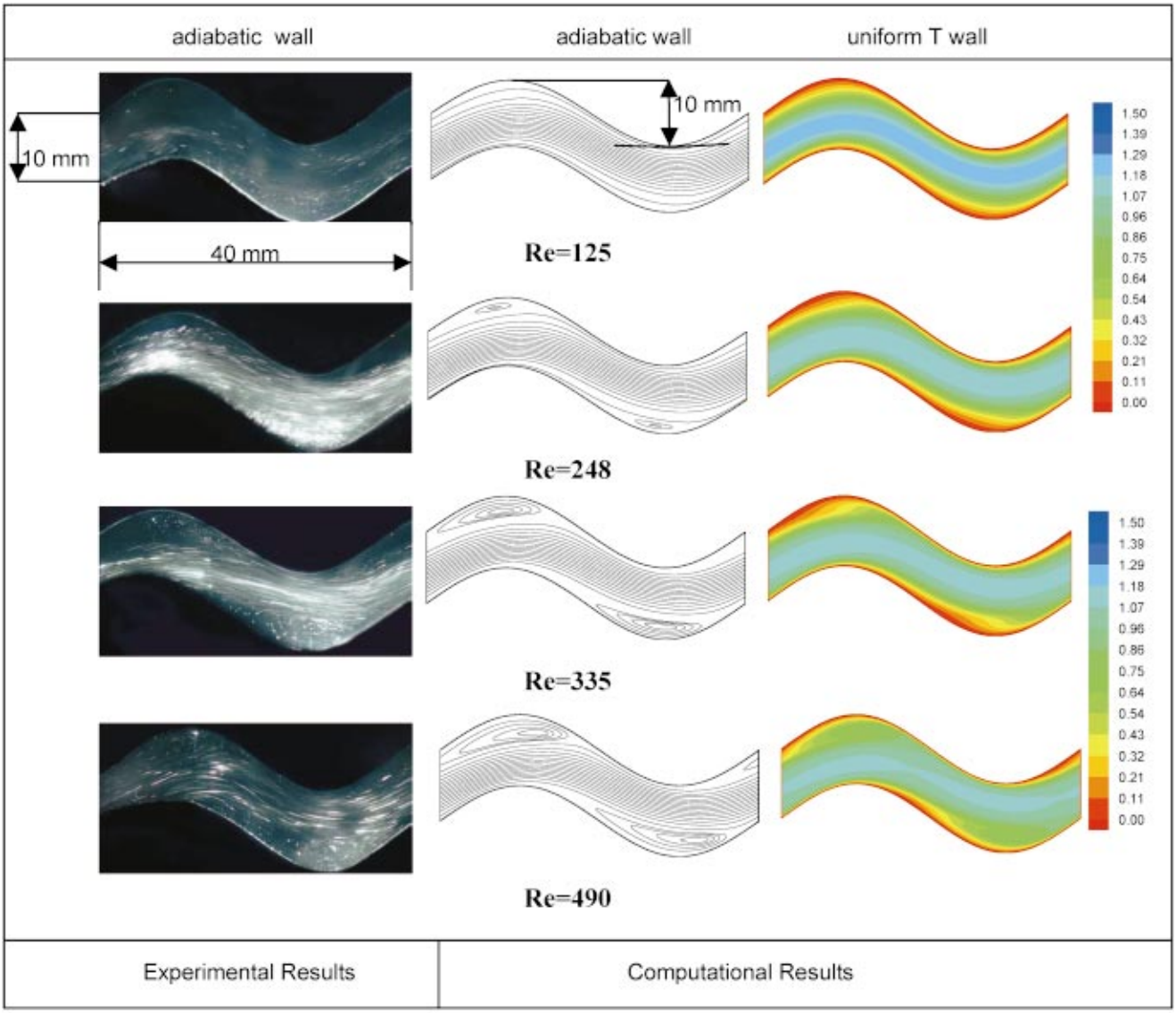

Axial flow and temperature distributions in a wavy plate channel at different Reynolds number

Steady Recirculation and Laminar Forced Convection in a Sinusoidal Wavy Channel

Saurabh Vyas, Jiehai Zhang and Raj M. Manglik
Thermal-Fluids & Thermal Processing Laboratory
University of Cincinnati, Cincinnati, OH

Experimental and computational characterization of swirl flow and heat transfer in a nominally two-dimensional (plate separation-to-width = 0.067), sinusoidal wavy channel with an aspect ratio (2 × amplitude/wavelength) of 0.25 and the spacing ratio (plate spacing / 2 × amplitude) of 1.0 is presented. The computational work is carried out using finite-volume techniques with a non-orthogonal, non staggered grid. In the experimental visualization, flow pattern photographs are obtained by injecting very fine aluminum dust (63 μm) in the flow field, illuminating it with a high-luminosity light sheet and capturing the image on a digital camera with a shutter speed of 1/8th second. The experimentally visualized flow fields amply validate the computational stream function simulations. At low Re (< 200) the flow is essentially streamline and contoured to the wall waviness. With increasing Re (> 200), lateral re-circulation, induced by the wall curvature, sets in the trough regions of the wavy channel. The swirl strength and spatial flow coverage increases with Re to produce temperature fields that have sharper gradients at the wall, with considerable thinning of the boundary layer, and enhanced heat transfer.

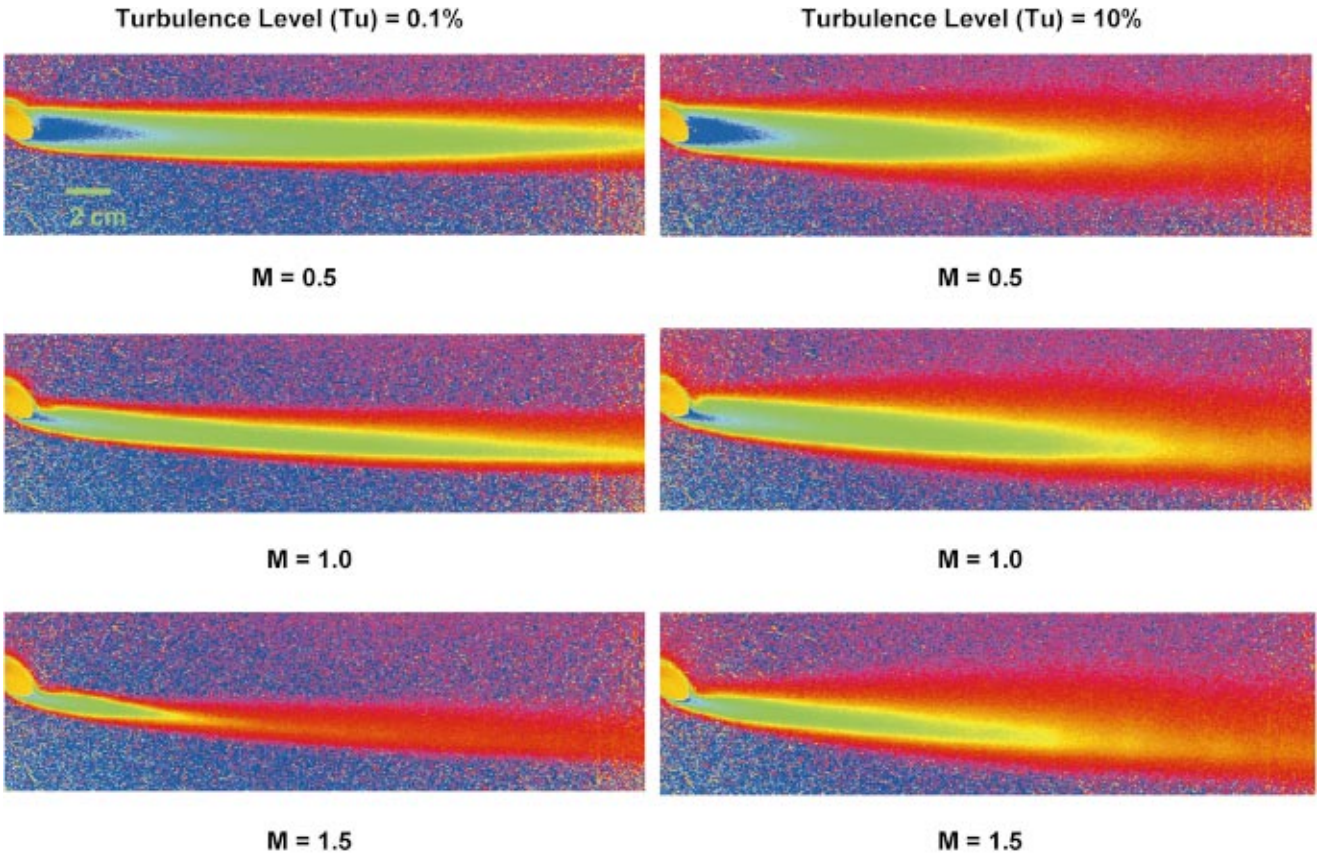

ADIABATIC EFFECTIVENESS OF FILM COOLING WITH COMPOUND ANGLE HOLES – THE EFFECT OF BLOWING RATIO AND FREESTREAM TURBULENCE

James E. Mayhew
Rose-Hulman Institute of Technology

James W. Baughn
University of California, Davis

Aaron R. Byerley
United States Air Force Academy

These photographs show the strong effects of blowing ratio and freestream turbulence on the adiabatic effectiveness of film cooling with compound angle holes. The photographs on the left are for three different blowing ratios (M = 0.5, 1.0 and 1.5 respectively) with low freestream turbulence levels (Tu = 0.1%) and those on the right are for the same blowing ratios with high freestream turbulence levels (Tu = 10%).

The surface in these photographs is insulated (Styrofoam) and is airbrushed with black paint and microencapsulated thermochromic liquid crystals (TLCs). The hole is oriented with a compound angle of 45° and with an injection angle of 30° from the flat plate surface.

The colors are the hue values for the TLCs and are calibrated against temperature, thus the photographs represent the surface temperature distribution. When slightly corrected for radiation and a small amount of conduction, this is the adiabatic wall temperature. The jet is heated above the freestream temperature. The adiabatic effectiveness is defined as the ratio of the difference between the adiabatic wall temperature and the freestream temperature to the difference between the jet temperature and the freestream temperature. Thus the colors (hues) in these photographs represent the adiabatic effectiveness directly. Adiabatic effectiveness is important in determining the total heat transfer for film cooling.

These photographs show that both blowing ratio and freestream turbulence have significant effects on the adiabatic effectiveness. Increased blowing ratio decreases the area over which cooling occurs, while freestream turbulence increases this area.

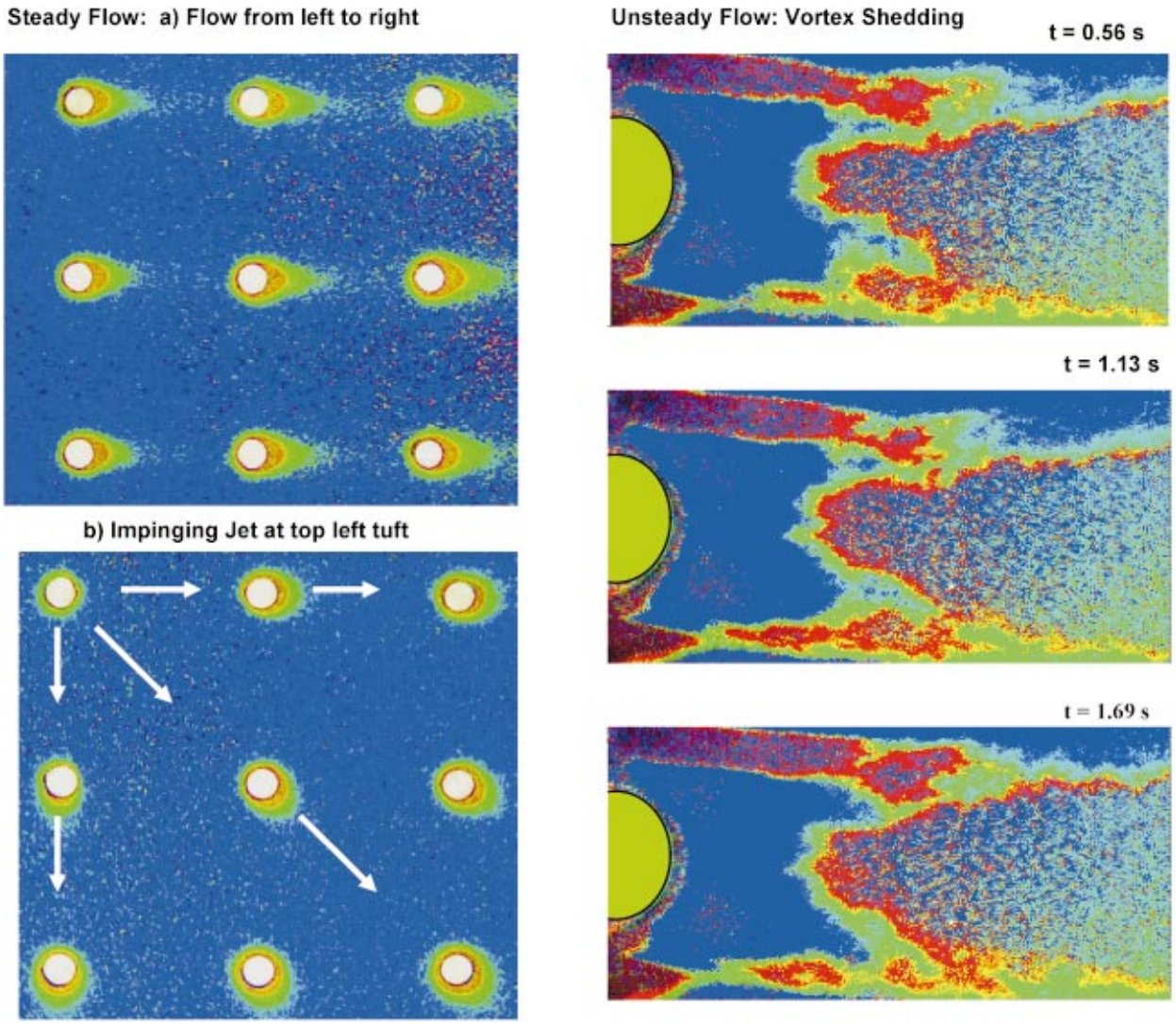

SURFACE FLOW VISUALIZATION USING ENCAPSULATED THERMAL TUFTS FOR STEADY FLOW AND A DYNAMIC HEAT TRANSFER MEASUREMENT TECHNIQUE FOR UNSTEADY FLOWS

James W. Baughn, A. David Ochoa, and Jason S. Smith
University of California, Davis, California

Aaron R. Byerley
United States Air Force Academy, Colorado

The photographs above show the flow direction on a surface using thermal tufts produced with embedded capsules. The capsules are short copper cylinders (3 mm diameter) containing a phase change material (water). The wall is made of a poor conductor air brushed with microencapsulated thermochromic liquid crystals. For these pictures a color play temperature of 12°C with a 6°C band was chosen. The model is cooled until the water freezes. When exposed to flow the surface approaches ambient temperature while the embedded capsules thaw to the phase change temperature and then remain isothermal. The thermal tuft appears on the surface downstream of the capsules pointing in the direction of the surface flow. If it is desired to initially heat the model, other phase change materials can be used above the ambient temperature reversing the process. The thermal tufts produced by this new surface flow visualization method are similar to those produced by the "laser thermal tuft".

The sequence of photographs above show the time-dependent heat transfer coefficient distribution on a wall downstream of a protruding cylinder with vortex shedding, providing dynamic heat transfer measurements and dynamic surface flow visualization. The experimental technique uses a low thermal mass substrate (thin tissue paper) for the surface which is embedded with microencapsulated thermochromic liquid crystals and heated uniformly with infrared radiation. The hue is temperature-dependent and thus each hue represents a specific surface temperature and corresponding heat transfer coefficient (h). The frequency response is dependent on the value of h, its fluctuation, the color play temperatures, and the thermal mass of the substrate. For air, it is estimated that fluctuations in the range of 10-100 Hz can be observed. Observation of the flow fluctuations in these photographs is limited by the video frame rate of 30 fps.

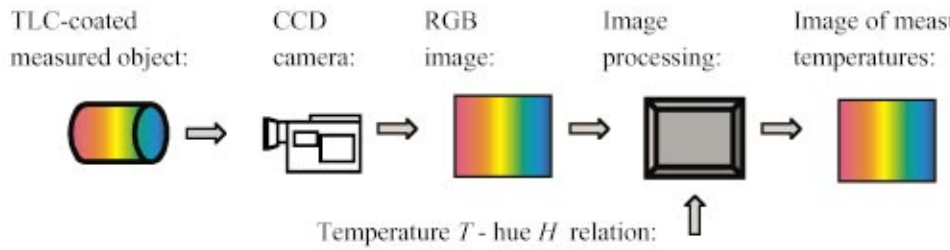

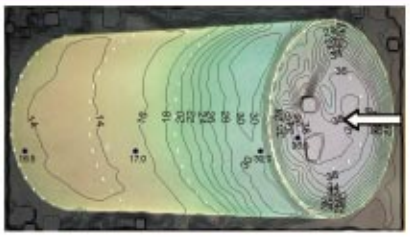

a.

b.

a. TLC measured temperatures on a cylinder, heated electrically by a thin foil on its surface, in 63m/s axial air flow. b. The rear part.

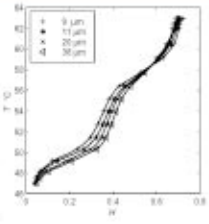

c.

c. Temperature - hue relations.

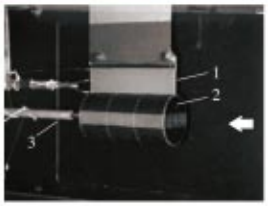

d.

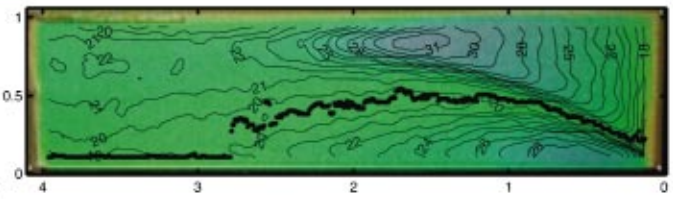

e.

d. The cylinder (2), and a TLC-coated and electrically-heated thin plate (1). e. The isotherms on the thin plate (1 in Fig. d) indicate the separated flow.

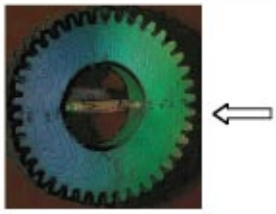

f.

f. Isotherms on a steel gear D= 100 mm cooled from 115°C by 30 m/s 20°C air crossflow.

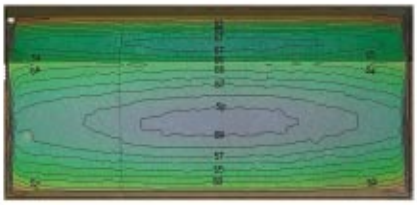

g.

g. Surface isotherms (°C) on a steel prism, in 20 m/s 20°C air crossflow from below.

Temperature measurements using thermochromic liquid crystals

Roland Wiberg
Dept. of Mechanics, KTH, Stockholm, Sweden.
Email: roland@mech.kth.se

Noam Lior
Dept. of Mechanical Engng. and Appl. Mechanics, Univ. of Pennsylvania, Philadelphia

Thermochromic liquid crystals (TLC), change their reflected colors with their temperature, and are, with digital image processing, used for wireless temperature field measurements. The temperatures and the applied surface heat flux can also be used to determine convective heat transfer coefficients.

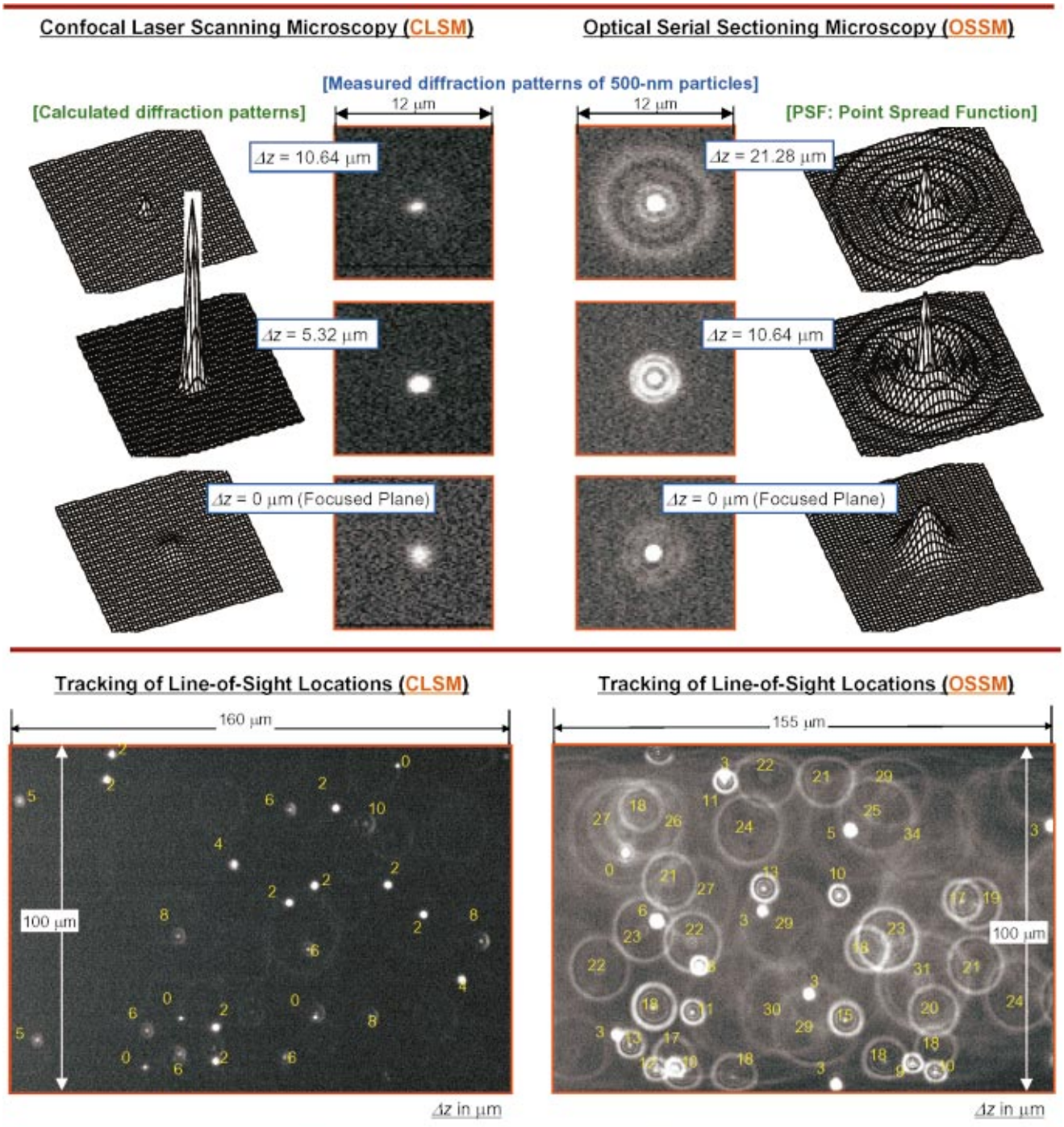

Nanoparticle Tracking Using CLSM* & OSSM** Imaging

J.S. Park, C.K. Choi and K.D. Kihm
Micro/Nano-Scale Fluidics and Heat Transport Laboratory [http://go.to/microlab]
Texas A&M University, College station, Texas

The Confocal Laser Scanning Microscopy* (CLSM) and Optical Serial Sectioning Microscopy** (OSSM) enable nano-particle tracking to locate their axial locations with a micrometer resolution. The three-dimensional diffraction patterns, so-called Point Spread Function (PSF), are theoretically predicted and experimentally validated so that the defocus distance (Δz) can be determined from the comparison of the two. A plan-fluorite objective (40X, NA 0.75) are used to detect the diffraction patterns of 500-nm fluorescence-coated polystyrene spheres suspended in the 170-μm deep micro-layer of water.

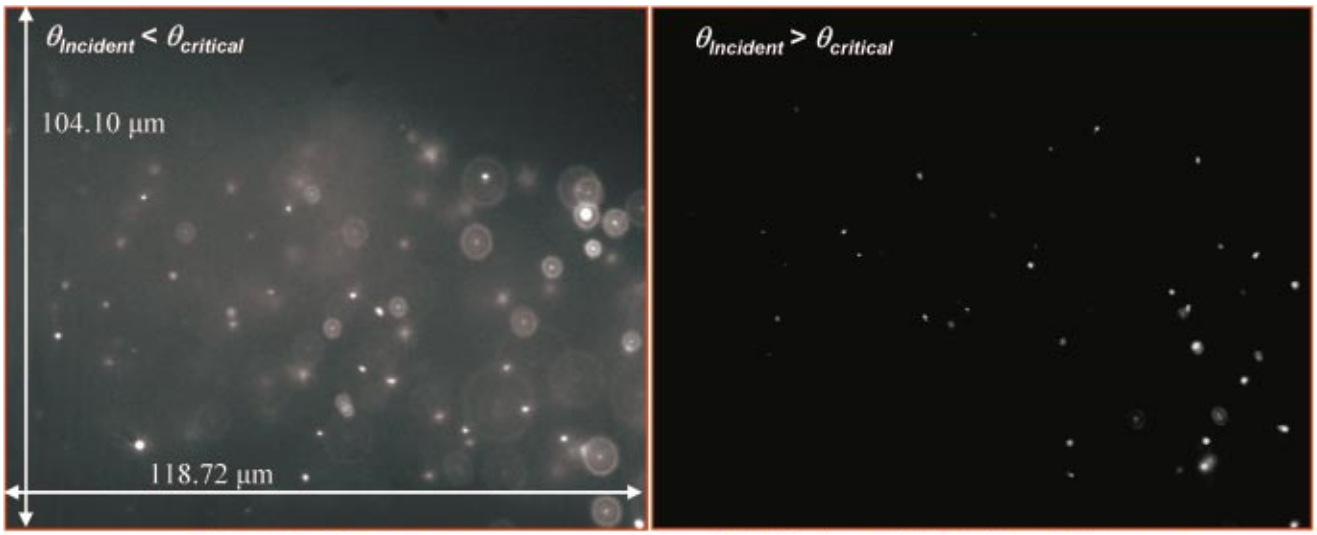

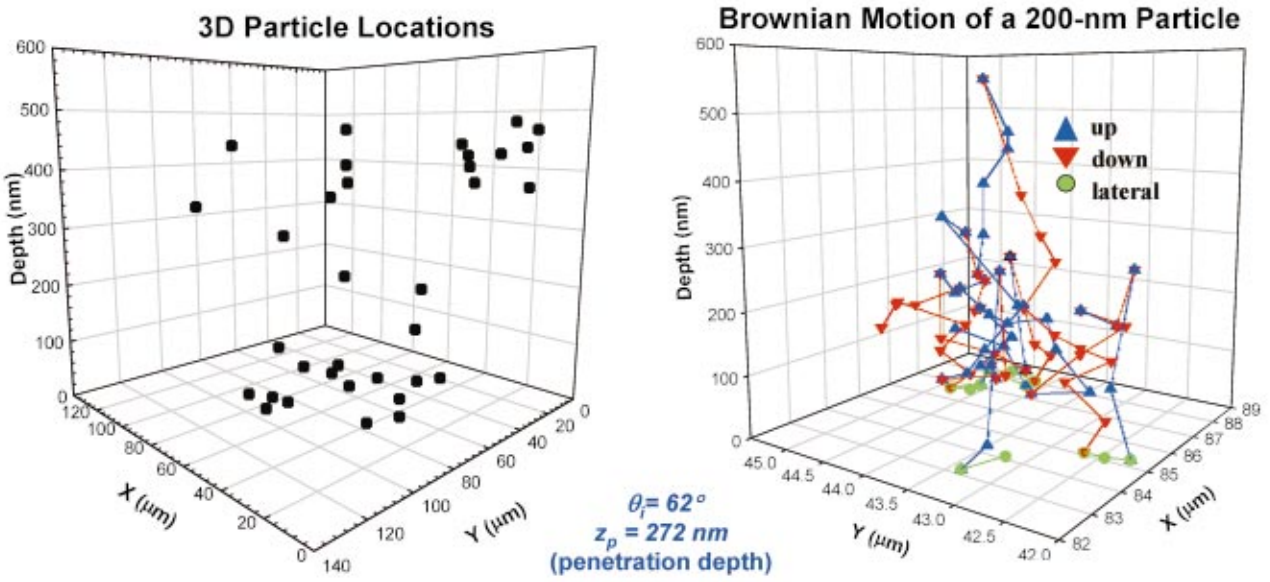

Three-Dimensional Tracking of Nanoparticles Using R-TIRFM* Technique

A. Banerjee and K. D. Kihm
Micro/Nano-Scale Fluidics and Heat Transport Laboratory [http://go.to/microlab]
Texas A&M University, College Station, Texas

The novel Ratiometric-Total Internal Reflection Fluorescence Microscope* (R-TIRFM) imaging technique enables nano-particle tracking in the line-of-sight (z) direction with a nanometer spatial resolution. The digital tracking of the particle image centers on the x-y plane provides its lateral locations with the spatial resolution equivalent to the CCD pixel dimensions. An oil immersed TIRF lens (60X, NA=1.45) is used to track 200-nm fluorescent micro-sphere tracers illuminated by an argon-ion blue laser. The technique is the first of its kind to tag and track nano-particles with nanometer spatial resolutions in a full three-dimensional way. This work was partially sponsored by the NASA-Fluid Physics Program Grant No. 3-2712 and partially by the USDOE/Argonne National Laboratory Grant No. DE-FG02-04ER46101.

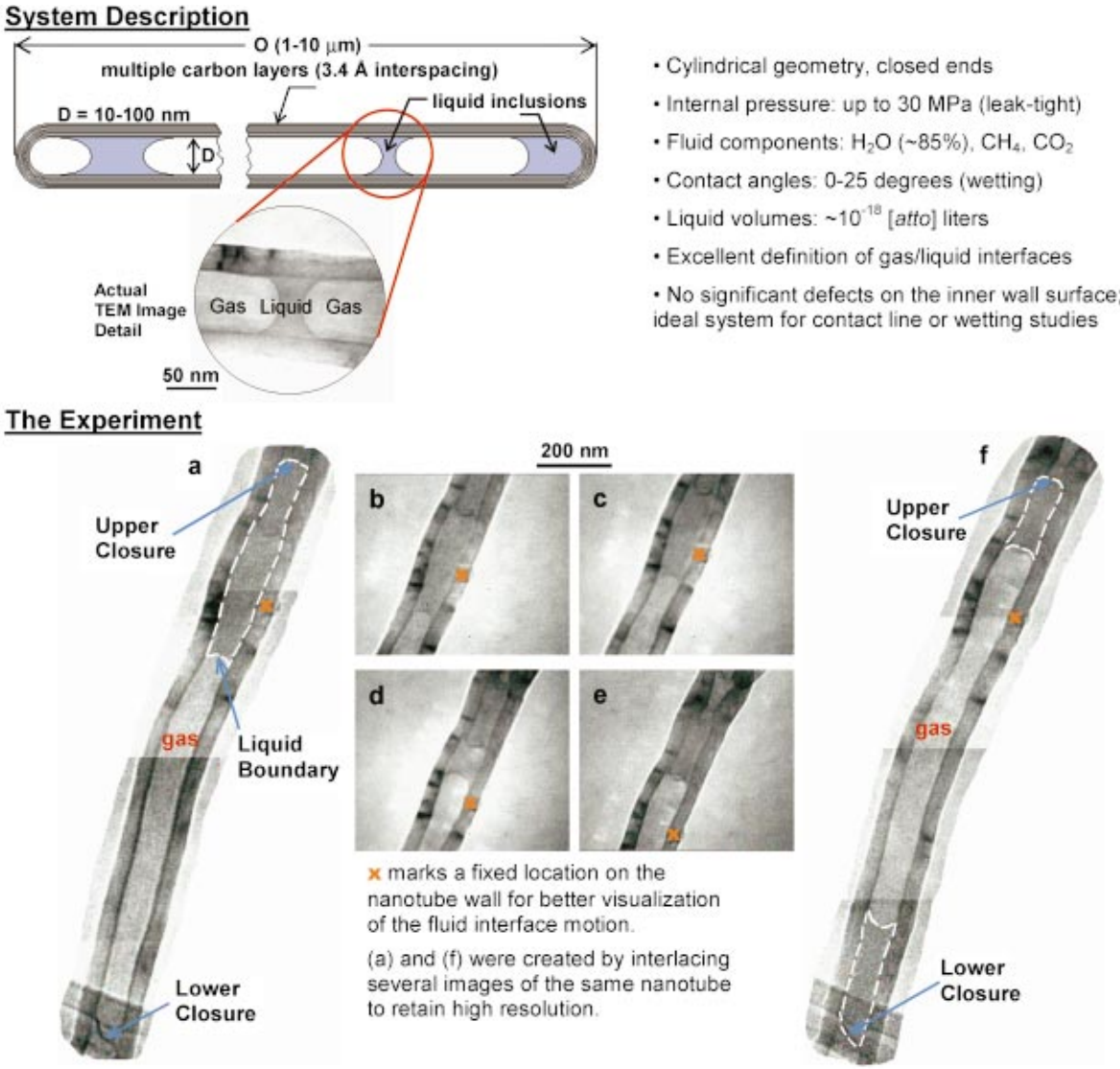

EVAPORATIVE TRANSPORT OF AQUEOUS LIQUID IN A CLOSED CARBON NANOTUBE: A NANO HEAT PIPE?

Almila G. Yazicioglu, Constantine M. Megaridis
University of Illinois at Chicago, Chicago, IL

Yury Gogotsi
Drexel University, Philadelphia, PA

Evaporative transport of liquid from one end of a carbon nanotube compartment, about 1μm long, to the other end was achieved using a hydrothermally-produced multiwall nanotube and the beam of a transmission electron microscope (TEM, JEOL JEM-3010, 300 keV) as the heat source. The inner diameter of the tube shown above is 70 nm. Initially, the liquid inclusion (marked by the white dashed outline) was constrained between an internal closure and a long gas bubble (frame a). The field of view of the TEM was moved to the top area of the shown nanotube (b), where the liquid was initially located, and this area was heated slowly by focusing the electron beam. As the beam was contracted, the liquid gradually evaporated due to the induced heating (c,d). When the heating was ceased, approximately 65% of the liquid had evaporated from this area (e). The TEM field of view was subsequently moved to the other (lower) end of the nanotube, which was relatively cool during the heating of the top area, to reveal that the liquid had condensed there (f). The entire sequence (a-f) lasted for about 20 seconds.

This sequence demonstrates the ability to transfer energy between the two ends of the nanotube. Assuming the liquid is pure water, the energy transported in this process is approximately 2 nJ. This energy, if delivered in its entirety, could raise the temperature of a 5 μm biological cell by ~0.01 K. Supported by NSF NIRT grant CTS-0210579.

A New Model for the Effect of Calcium Sulfate Scale Formation on Pool Boiling Heat Transfer

M. Jamialahmadi
The University of Petroleum Industry,
Ahwaz,
Iran

H. Müller-Steinhagen
Institute for Thermodynamics and Thermal Engineering,
University of Stuttgart,
Institute of Technical Thermodynamics,
German Aerospace Centre (DLR),
Germany

Scale deposition on the heat transfer surfaces from water containing dissolved salts considerably reduces fuel economy and performance of heat transfer equipment. This problem is more serious during nucleate boiling due to the mechanisms of bubble formation and detachment. Using a precision pool boiling test apparatus, the effects of heat flux and calcium sulfate concentration on heat transfer coefficient and formation and growth of deposits are investigated. The transient change in heat transfer is closely related to wick boiling, and the associated changes in bubble departure diameter and bubble site density. A physically sound prediction model was developed for the prediction of heat transfer coefficients as a function of time during deposition processes. Based on comparison with experimental data over a wide range of foulant concentrations and heat fluxes, the model is considered to be sufficiently accurate for practical application.
[DOI: 10.1115/1.1777579]

Keywords: Boiling, Bubble Growth, Crystal Growth, Fouling, Heat Transfer, Modeling, Scaling

Introduction

Heat transfer to hard waters is an essential operation in most concentration, crystallization and evaporation processes. In costal desalination plants for the production of fresh water, seawater with high dissolved salt content is evaporated. In these processes, various salts will precipitate and cause fouling of the heat transfer surfaces in a certain order depending on operating conditions, especially temperature and concentration of foulants in the solution. The solubility of most salts increases with increasing temperature, and as a rule, these salts do not crystallize on heated surfaces unless their concentrations are extremely high. Fouling of heat transfer surfaces is caused by those salts whose solubility is generally limited and in most instances decreases with increasing temperature. The principal constituents that cause problems in seawater and most industrial evaporators are calcium sulfate and calcium carbonate. Theoretically, maintaining a slightly acidic pH can control the deposition of calcium carbonate. Calcium sulfate, however, is not significantly affected by pH and tends to precipitate on the heat transfer surfaces once the water becomes supersaturated. The major limiting economic factor in evaporation processes is the degree to which industrial fluids can be concentrated before calcium sulfate scale occurs. For example, seawater becomes saturated with respect to calcium sulfate anhydrite when it is evaporated at 100°C to two-third of its original volume [1]. Deposits pose a barrier to heat transfer, which means additional energy is required to maintain the desired process conditions. They can typically degrade the performance of heat transfer surfaces by as much as 80 percent and can sometimes cause complete failure [2]. Eventually, operation must be curtailed to remove these deposits, which results in high heat exchanger cleaning and downtime costs. One of the major restrictions to economic operation of industrial boilers is the problem of fouling of the heat transfer surfaces. Even though the problems associated with scale formation have been known since the beginning of the industrial revolution, they have rarely been a cause of much concern as long as reasonably good water quality control was maintained. More recently, there has been an intensification of activities to reduce the energy requirements in response to environmental concerns and the high prices for energy.

Heat recovery, which is an important aspect of any energy management, depends on the effective operation of heat exchangers. Cleaning schedules in processes such as the live steam heater in the Bayer process for the production of alumina or in phosphoric acid evaporators in the dihydrate process may be required every two weeks, which is a major drawback in any energy saving scheme [3,4]. The fouling problems can even be more serious if, for example, the evaporators are incorrectly designed or operated.

Fouling is a function of time, starting from zero and proceeding according to some pseudo-asymptotic or linear relationship. Using a constant value for the fouling resistance at the design stage, which is common practice in designing heat exchangers, can thus predict what will happen to the heat exchanger performance but not when it will happen [5]. It is, hence, likely that the equipment will have to be taken out of service for cleaning at an inconvenient and economically undesirable time. Advanced design procedures for heat exchangers subject to fouling should allow not only the forecasting of whether fouling deposits will build-up, but also the time and the extent to which this will happen [6].

A review of the existing literature on scale formation during pool boiling of salt solutions reveals that there have been few serious attempts to understand the effects of boiling mechanisms on the formation of scale. The results of experimental and theoretical investigations on this subject have been reviewed by Jamialahmadi and Müller-Steinhagen [7] and Bott [8]. Most of this work has been done at heat fluxes well below 100 kW/m^2. Additional experimental studies are needed at higher heat fluxes. While the understanding of the mechanisms of scale formation under pool boiling conditions has improved, sound modeling of boiling heat transfer in the presence of deposits is not possible yet. One of the impediments to developing a prediction model for the deposition process is the complexity of the basic mechanisms of scale formation and the interaction between deposition and bubble growth, nucleation site density and detachment phenomena.

The reliable prediction of clean (i.e., initial) heat transfer coefficients of salts with negative solubility is also of major importance for optimum and economical overall plant design and a prerequisite for any in-depth study on fouling in these processes.

Contributed by the Heat Transfer Division for publication in the JOURNAL OF HEAT TRANSFER. Manuscript received by the Heat Transfer Division October 31, 2003; revision received April 30, 2004. Associate Editor: M. K. Jensen.

Boiling heat transfer coefficients for salt solutions will be different from those for pure water because of the widely different surface tension, wetting characteristics and bubble coalescence behavior. A main objective of the present investigation was, hence, to study systematically clean heat transfer to calcium sulfate solutions by measuring heat transfer coefficients over a wide range of heat fluxes and concentrations. A unified model was developed to predict the clean pool boiling heat transfer coefficients of salts with negative solubility.

The fouling mechanisms of calcium sulfate under pool boiling conditions have then been obtained by measuring heat transfer coefficient, bubble size, bubble shape, bubble frequency and nucleation site distribution during the fouling period. After clarification of the mechanisms of fouling and the effects of various parameters on the fouling process, a predictive model for calcium sulfate fouling rates under pool boiling conditions has been developed.

Experimental Equipment and Procedure

Pool Boiling Apparatus. The complete pool boiling apparatus used in this investigation is shown in Fig. 1. The boiling rig consists of a boiling section, a closed loop containing condensing and preheating sections, heaters with power control units, and instrumentation to both provide local indication and data acquisition input. The boiling section is a 40 liter capacity, thick-walled cylindrical stainless steel vessel, with glass view ports at both sides. An electric resistance band heater controlled by a variable a.c. power supply heats the vessel externally. Output from a thermocouple fitted inside the vessel is used to trip the variac unit if the solution temperature exceeds a set limit. The test heater is mounted horizontally within the tank and can be observed and photographed through the observation glasses. Heaters are manufactured by Ashland Chemical Company according to an HTRI design. Four E-type thermocouples are embedded inside the heater as shown in Fig. 2. Three of the thermocouples are used for data acquisition and the forth is used as a trip input for the test heater's variac power supply, should the internal temperature of the heater exceed a defined limit. A safety relief valve is fitted at the top of the flow circuit to relieve the pressure in the event of a pressure excursion due to failure in cooling or failure of the variac controllers. The condenser is a co-current two-stage single tube heat exchanger that can be configured to include one or both condensing sections. Cooling is effected by domestic water regulated by means of a rotameter and a manual flow control valve. Following condensation the water is heated just prior to returning to the boiling tank by an electric resistance pre-heater manually controlled by a variac power supply. Boiling tank, condenser, preheater and pipe-work are heavily insulated to reduce heat losses to the ambient air. Pipe-work is stainless steel tubing connected by

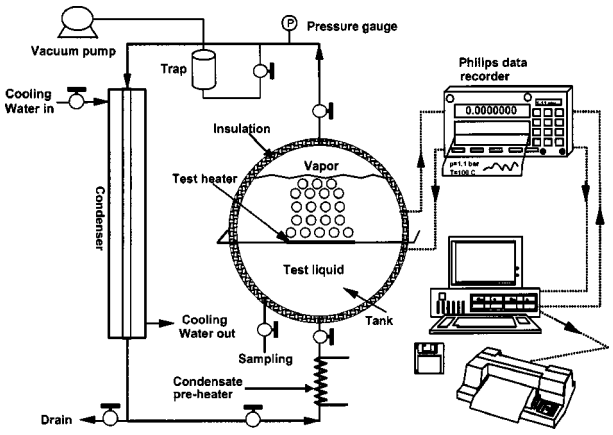

Fig. 1 Pool boiling apparatus

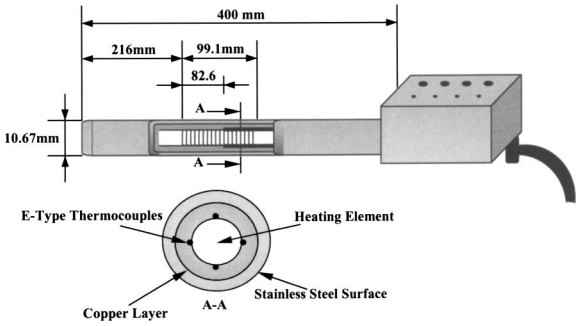

Fig. 2 Schematic diagram of the test heater

type 316 stainless steel Swagelok tube fittings. Vacuum is drawn in the system using a vacuum pump connected to the rig through a water trap.

Data Acquisition and Data Reduction. An OMEGA microcomputer-controlled data acquisition system was used to measure temperatures and pressure continuously at given time intervals. The power supplied to the test heater could be calculated from the measured current and voltage drop. The average of ten voltage readings was used to determine the difference between the wall and bulk temperature for each thermocouple. The average temperature difference was the arithmetic average for four thermocouple locations. The temperature drop between the location of the wall thermocouples and the heat transfer surface was deducted from the measured temperature difference according to

$$T_s - T_b = (T_{th} - T_b) - \frac{s}{\lambda}\dot{q} \tag{1}$$

In this equation, s is the distance between the thermocouple location and the heat transfer surface and λ is the thermal conductivity of the tube material. The heat transfer coefficient α is calculated from

$$\alpha = \frac{\dot{q}}{T_s - T_b} \tag{2}$$

At regular time intervals, pictures of the heat transfer surface were taken with a microprocessor-controlled camera. In addition, video equipment was used to record the formation and growth of bubbles at the heat transfer surface. These recordings were then used to determine the bubble departure diameter, active nucleation site density and bubble frequency as a function of time.

Error Analysis. The experimental error for the measured heat transfer coefficients may be due to errors in the measurement of heat flux, bulk and heat transfer surface temperature. As all test heaters were sanded with grade 240 emery paper, it was postulated that in all experiments the heat transfer surfaces were comparable with respect to surface roughness. By repeating some fouling runs, almost the same fouling curves were obtained, which confirms the above assumption. The error of the adjusted heat flux is due to errors in the measurements of electrical current and voltage. It was observed that the power delivered by the heater box showed small fluctuations depending on the time of the day. During the night and the weekends, a higher heat flux than during working days was observed. For example, it was intended to run the test with a heat flux of 301.2 kW/m^2. The average of heat flux was 304.5 kW/m^2. This magnitude corresponds to a deviation of 1.1 percent of the target value. It is accepted that this phenomenon has some minor effect on the values of heat transfer coefficients. The liquid and vapor temperatures were measured with K-type thermocouples located in the bulk of the solution. These thermocouples were initially calibrated against a quartz thermometer with an accuracy of about 0.02 K. The inaccuracy in temperature

measurements due to calibration errors of the thermocouples may lead to a deviation of approximately ± 0.2 K. The pressure of the system was measured with strain-gauge sensors having a factory calibrated accuracy of about 0.5 percent of the operating range, which was adequate for the fouling experiments.

Experimental Procedure

The solubility of calcium sulfate has been studied in detail by Marshal and Slusher [9]. Najibi [10], by nonlinear regression analysis of these data, developed the following correlation for the prediction of the saturation concentration of calcium sulfate as a function of ionic strength of solution and temperature

$$C^* = 10^{a+bZ} \tag{3}$$

where the parameters a, b, and Z are given by

$$a = 2.047 - 0.01136T$$

$$b = -6.5832 + 0.0226T \tag{4}$$

$$Z = \frac{\sqrt{I}}{1 + 1.5\sqrt{I}}$$

At temperatures higher than 40°C, the solubility of calcium sulfate decreases with increasing temperature for the ordinary solid phases. Under normal operating conditions, the hottest portion of water is the layer next to the surface of the heating element. If there is calcium sulfate in the water, its point of lowest solubility is at the surface of the heating element. Any precipitation is, therefore, expected to take place there.

The calcium sulfate solution was prepared for each run by dissolving reagent grade calcium sulfate hemi-hydrate in demineralized distilled water, and allowing it to stand for more than 24 hours. For the present investigation, the calcium sulfate concentration was in the range 0.8 to 2 kg/m^3, which provided a supersaturated solution in the vicinity of the test heater. All runs were performed under pool boiling conditions and at a pressure of 1.1 bar, according to the following procedure:

Prior to commencing a test run the test heater was cleaned to remove scale from previous test runs and then abraded using 240 grade wet and dry sand paper. The direction of abrasion was along the heater to give a longitudinal pattern of shallow grooves on the heater surface. This practice was similar to that of Wenzel [11], who reported a mean roughness average value R_a of 0.407 μm and an integral roughness value R_p of 1.01 μm. Following abrasion the test heater was washed with distilled water to remove all abraded and abrasive material, dried with clean paper towels and finally cleaned with acetone prior to installation in the test apparatus. The glass observation windows were closed, and the system connected to the vacuum pump. Once the pressure of the system reached approximately 0.1 bar, the salt solution, which was prepared and filtered 24 hours earlier, was introduced to the boiling vessel through a 6 mm (0.25 in.) sample line. Following this, the tank heater and condenser pre-heater were switched on and the temperature of the system was allowed to rise to the saturation temperature. Meanwhile, the system was deaerated several times and then left at saturation temperature and 1.1 bar pressure for about 10 hours to obtain a homogeneous condition throughout. Then, the power was supplied to the test heater and kept at a pre-determined value. Data acquisition system, microprocessor-controlled camera and video equipment were simultaneously switched on to record temperatures, pressure, heat flux and visual information. Samples were taken from the solution during the experiments and analyzed by atomic absorption and spectrophotometry. Immediately after the run, the solution was drained and the test heater allowed to cool and dry. It was then removed from the system, the deposit weighed and a sample taken for electron scanning microscopy.

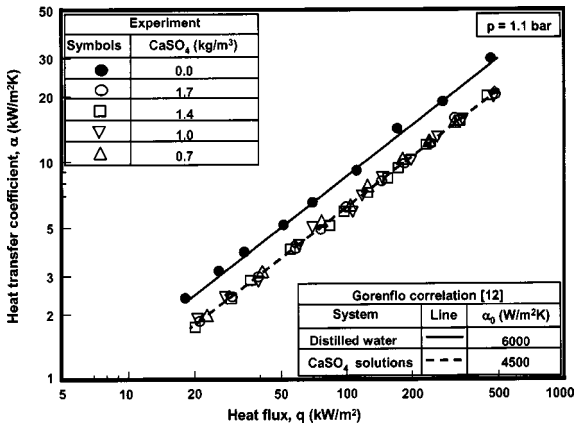

Fig. 3 Heat transfer coefficients for pool boiling of water and calcium sulfate solutions

Results and Discussion

Clean Heat Transfer Coefficient. Figure 3 shows heat transfer coefficients as a function of heat flux for calcium sulfate solutions with various concentrations. The results are compared with those obtained for de-mineralized water under identical operating conditions. The experimental data for de-mineralized water are also compared with the prediction of the correlation suggested by Gorenflo [12]

$$\frac{\alpha}{\alpha_{\text{ref}}} = F_q \cdot F_p \cdot F_{WR} \cdot F_{WM} \tag{5}$$

where

$$F_q = \left(\frac{\dot{q}}{q_o}\right)^{0.9-0.3p_r^{0.15}}, \quad F_p = 1.2p_r^{0.27} + 2.05p_r + \frac{p_r}{1-p_r} \tag{6}$$

$$F_{WR} = \left(\frac{R_a}{R_{a,\text{ref}}}\right)^{0.133}, \quad \text{F}_{\text{WM}} = \left(\frac{\rho c_p \lambda}{(\rho c_p \lambda)_{ref}}\right)^{0.25} \tag{7}$$

For de-mineralized water the reference heat transfer coefficient α_{ref} for a reference heat flux of 20 kW/m^2 and a reference-reduced pressure of 0.1 is 6 kW/m^2 K [12]. The agreement between experimental data for de-mineralized water and predicted values is very good. The heat transfer coefficient drops rapidly when a small amount of calcium sulfate salt is added to the demineralized water. However, the results show that the actual salt concentration has only a negligible effect on the deterioration of the heat transfer coefficients. The degradation of the boiling heat transfer coefficients is attributed to several phenomena, which occur simultaneously in the vicinity of the vapor bubbles on the heat transfer surface [13,14]. When calcium sulfate solution is vaporized, the concentration of water at the vapor-liquid interface is lower than its concentration in the bulk. As a consequence, there is back-diffusion of calcium sulfate molecules away from the interface into the bulk of the solution, leading to a dynamic equilibrium as long as the interface concentration remains below the saturation concentration. Schlünder [15] and Schmitt [16] have shown that the vaporization process can be divided into two consecutive stages. In the first stage, nucleate boiling occurs with bubble growth at the heat transfer surface. Heat flows through the liquid layer, from the heating surface to the bubble interface. Preferential evaporation of water at this stage raises the local bubble point temperature from T_b to T_i, which reduces the superheat driving the evaporation process. In the second stage, the bubbles detach from the heat transfer surface and rise to the surface of the liquid, where their temperature falls from T_i to T_b. Schlünder [15] assumed that this process takes place adiabatically. In addition to the latent heat of vaporization, which is required to form the bubbles,

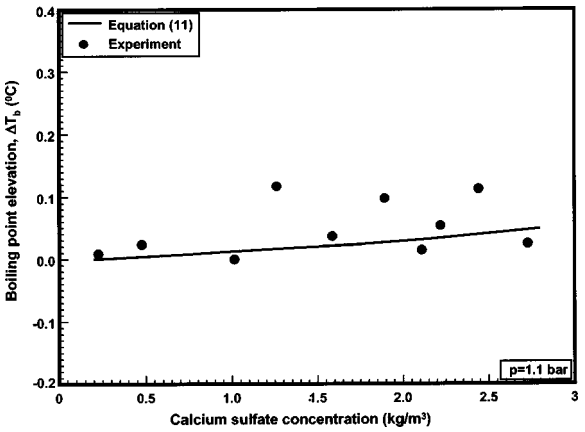

Fig. 4 Effect of calcium sulfate concentration on the boiling point elevation of solution

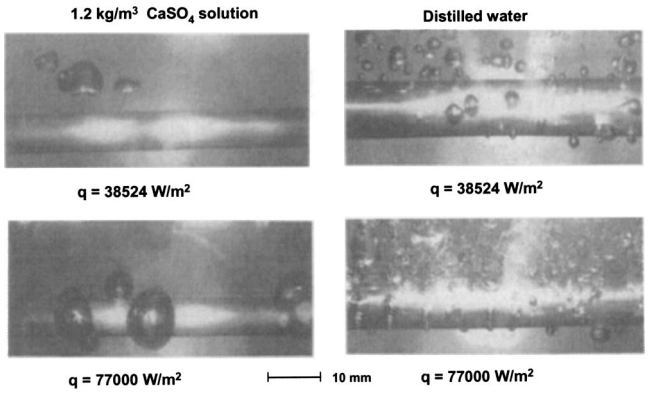

Fig. 5 Comparison of bubble departure diameter and nucleation site density during boiling of a calcium sulfate solution with those in distilled water

a certain proportion of the total heat supplied is generally transferred directly by convection to the boiling liquid. The heat transfer coefficient in the first stage may be defined as

$$\dot{q} = \alpha_i (T_s - T_i) \tag{8}$$

For practical purposes, the pool boiling heat transfer coefficients are generally defined according to the difference between heat transfer surface temperature and bulk temperature

$$\dot{q} = \alpha (T_s - T_b) \tag{9}$$

Combining Eqs. (8) and (9) yields

$$\frac{1}{\alpha} = \frac{1}{\alpha_i} + \frac{T_i - T_b}{\dot{q}} = \frac{1}{\alpha_i} + \frac{\Delta T_b}{\dot{q}} \tag{10}$$

In terms of thermal resistances, the first term on the right hand side presents the interfacial heat transfer resistance and the second term presents the additional resistance caused by the mass transfer. The general approach for the calculation of the second term is to obtain the interfacial composition from mass transfer principles and then to estimate the interfacial temperature from boiling point data. This approach has been used with some success for modeling of boiling heat transfer to solutions with high dissolved salt concentration by Wadekar et al. [17] and by the present authors [18].

Boiling point elevation is related to vapor pressure lowering, and, hence, to molar concentration. It can be expressed by the following simple relationship [19]:

$$\Delta T_b = i m K_b \tag{11}$$

The parameter **i** is the van't Hoff factor which takes into consideration the effect of ionization of solute molecules, m is the molarity of the solution, and K_b is the molar boiling point elevation constant. For calcium sulfate solutions, $i=2$ and $K_b=0.512$ [19]. Salts with negative solubility are sparingly soluble in water; therefore, according to Eq. (11) their boiling point elevation is much less than for salt solutions with positive solubility. The solubility of calcium sulfate in water is limited to about 2 kg/m^3 at its normal boiling point. Hence, when calcium sulfate salt is added to water it has only a negligible effect with respect to boiling point elevation. The measured boiling point elevation of calcium sulfate solutions is given in Fig. 4 as a function of concentration. The experimental data are also compared with the prediction of Eq. (11). The results illustrate that the boiling point elevation of calcium sulfate solutions is almost independent of concentration. Hence, for this case

$$\Delta T_b \approx 0 \tag{12}$$

and Eq. (10) reduces to

$$\alpha = \alpha_i \tag{13}$$

Hence boiling point elevation can not explain the observation that heat transfer coefficients for calcium sulfate solutions are significantly different from those of pure water. Figure 5 compares bubble growth on the heat transfer surface for a calcium sulfate solution and for pure water under otherwise identical operating conditions. It is apparent that the number of nucleation sites is decreased, while the bubble departure diameter is increased due to the presence of the salt. The general approach for the calculation of $\boldsymbol{\alpha_i}$ is to use a pure fluid boiling correlation with physical properties of the mixture [18]. The reference heat transfer coefficient, α_0 in the Gorenflo correlation (Eqs. (5)–(7)) can be calculated using the correlation suggested by Stephan and Preusser [20,21]. For the calcium sulfate solutions a reference heat transfer coefficient of 4500 W/m^2 K is obtained for a reference heat flux of 20 kW/m^2 and a reference reduced pressure of 0.1. The predicted clean heat transfer coefficients for calcium sulfate solutions based on these reference conditions show good agreement with the experimental results, see Fig. 3.

Change in Heat Transfer Coefficient With Time Due to Scale Formation. Formation of deposits on the heat transfer surface further reduces the heat transfer coefficient. Figures 6(a) to 6(g) show heat transfer coefficients as a function of time for heat fluxes ranging from 35,000 to 480,000 W/m^2. The general shape of the heat transfer coefficient versus time curves is characterized by a sharp decrease to a minimum (region 1), followed by an increase to a maximum (region 2) and a subsequent gradual decrease towards an asymptotic value (region 3). The extent of the variations in heat transfer coefficient with time is strongly affected by the adjusted heat flux and foulant concentration. With increasing heat flux, the operation time between regions 1 and 2 decreases and heat transfer decreases faster and to a larger extent than for low heat fluxes. The appearance of the heating element, bubble size and nucleation site density during a run at 38,522 W/m^2 is shown in Fig. 7. It is obvious that the presence of the deposit sharply increased the number of the active sites in region 2 as compared to region 1. In region 3, the number of nucleation sites decreased again. Figure 8 shows the variation of active nucleation sites with time for a heat flux of 38,524 W/m^2. The number of active nucleation sites rises towards a maximum, after which it falls back to a value close to that at the beginning of the experiment. Between the two data sets was a region with very high nucleation site density, for which individual bubbles could not be counted, anymore. Comparing these results with those shown in Fig. 6(a), consistent trends are found. In region 1, only a few nucleation sites are present on the heat transfer surface. In region 2, the number of active nucleation sites increases sharply with time, owing to the formation of additional sites by the de-

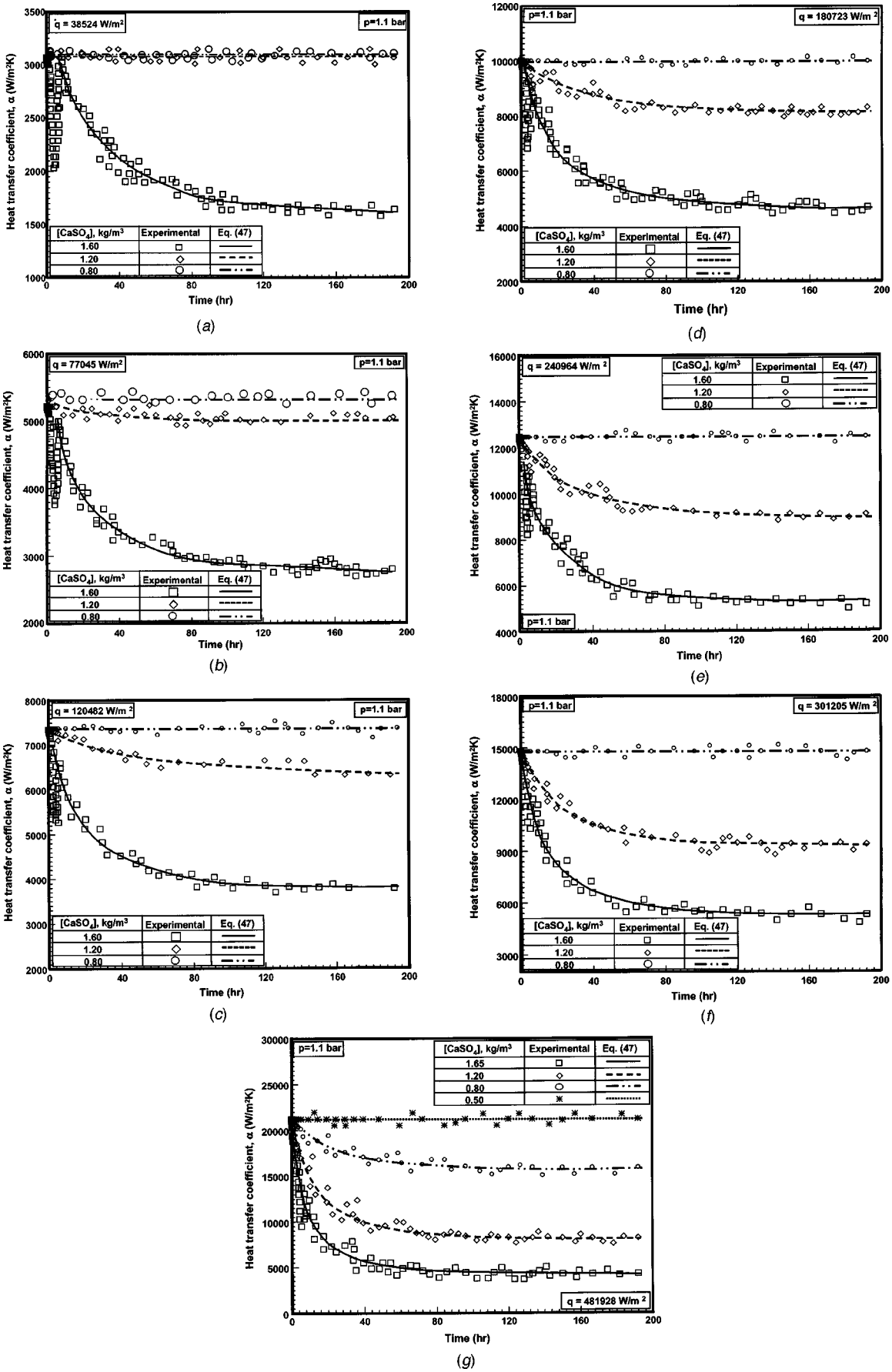

Fig. 6 (a–g) **Heat transfer coefficient as a function of time for various heat fluxes**

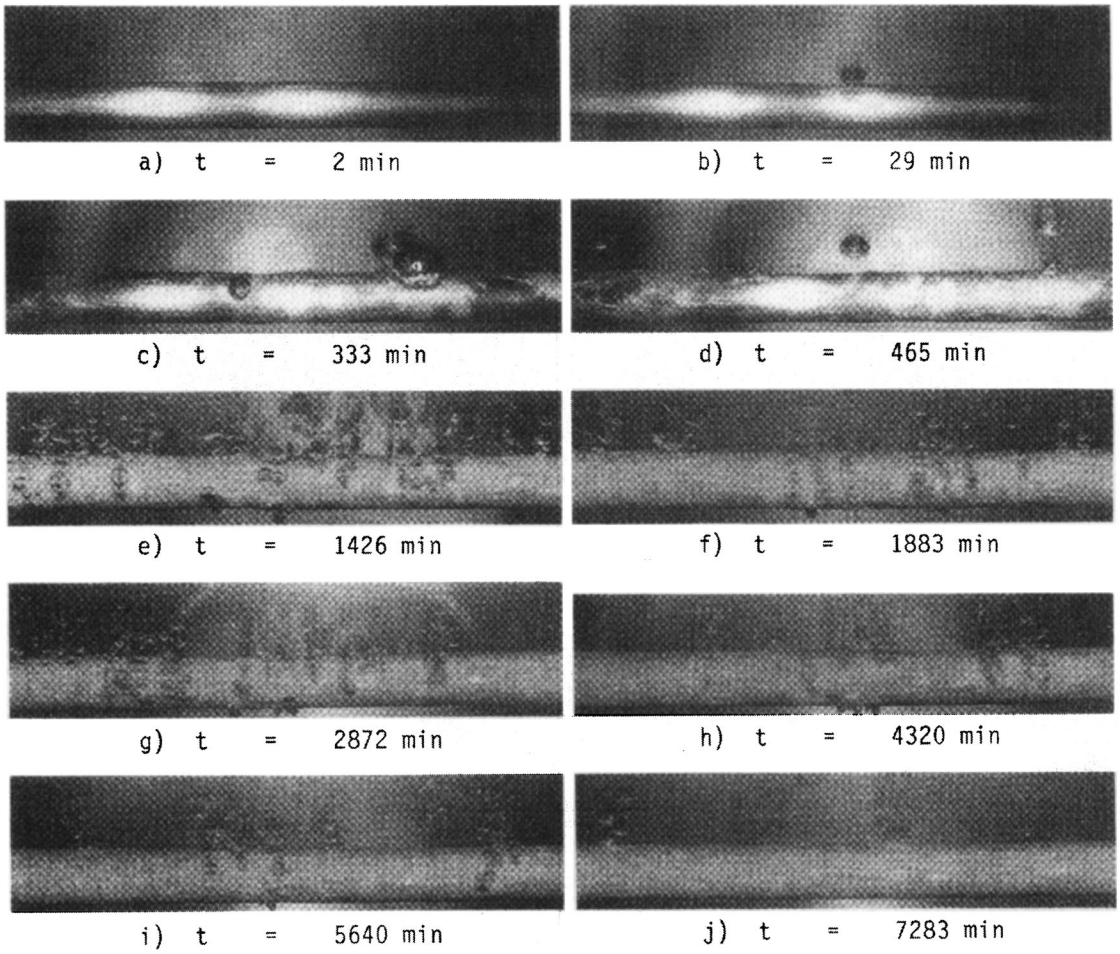

Fig. 7 Appearance of heating element during a fouling run at 38,522 W/m^2

posit. The number of these sites gradually decreases throughout region 3. The bubbles in region 1 are hemispherical with large contacting area with average diameters between 10 to 25 mm and a detachment frequency of about 7 bubbles per second. In regions 2 and 3, only spherical bubbles are observed, with an almost uniform diameter of about 2 mm. The observed changes in bubble formation due to the growth of deposit on the heat transfer surface are explained in detail, elsewhere [22].

Kinetics of Deposition Process and Nature of Deposit

The deposition of calcium sulfate scale on heat transfer surfaces can be expressed by the following reaction

$$Ca^{2+} + SO_4^{2-} \rightarrow CaSO_4\uparrow \tag{14}$$

Almost all investigators confirmed experimentally that the crystal-

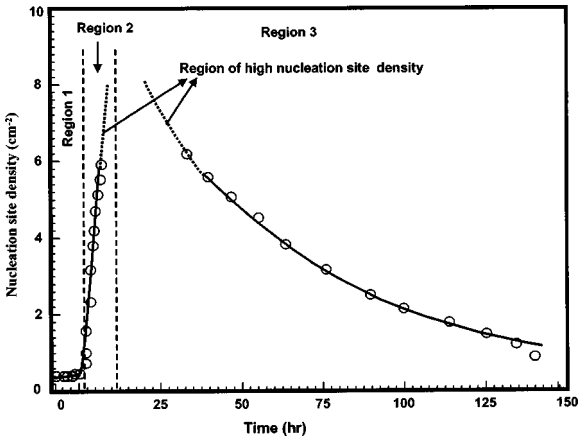

Fig. 8 Active nucleation site density as a function of time

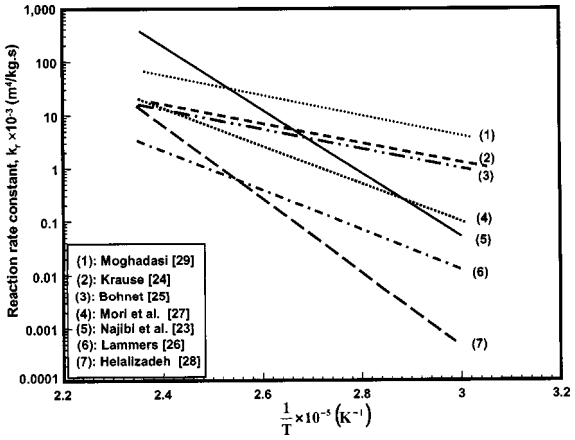

Fig. 9 Comparison of the rate constant of calcium sulfate deposition suggested by various investigator

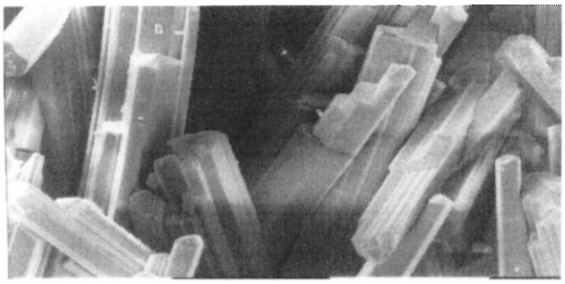

(*a*)

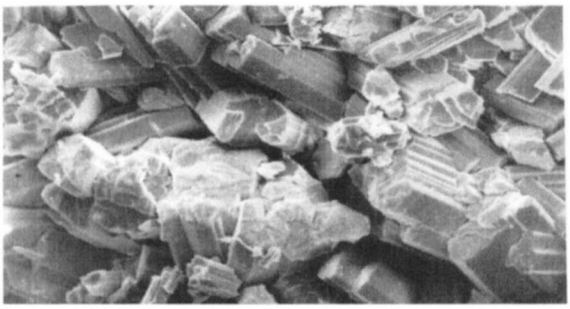

(*b*)

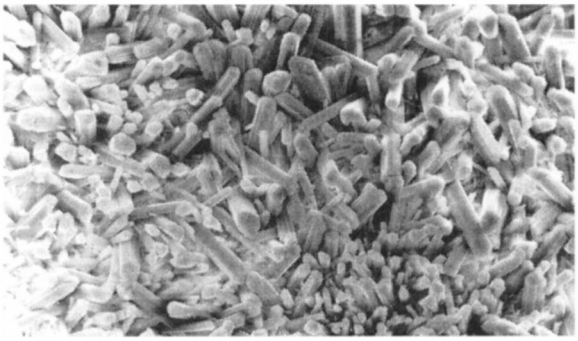

(*c*)

Fig. 10 Deposits observed at different heat fluxes (width=0.32 mm): (*a*) $q=28{,}892\ W/m^2$; (*b*) $q=120{,}482\ W/m^2$; and (*c*) $q=301{,}205\ W/m^2$

lization of calcium sulfate is an elementary reaction. Hence, the rate of formation of calcium sulfate deposit can be written as

$$\dot{m}_d = -\frac{V}{A}\frac{dC}{dt} = k_r[Ca^{2+}][SO_4^{2-}] = k_r[CaSO_4]^2 = k_r(C_s^i - C^*)^2 \tag{15}$$

The kinetic constant of calcium sulfate deposition follows an Arrhenius type equation

$$k_r = k_o e^{-E/RT} \tag{16}$$

The Arrhenius constant k_o and the activation energy E are generally obtained from nonlinear regression analysis of the experimental data. A range of values for these two parameters is available in the literature [23–29]. Reaction rate constants calculated from these values are compared in Fig. 9. While all models predict a considerable increase in reaction rate constant with temperature, the variation between the various models is extremely high.

Experimental investigations to determine the thermal conductivity of the deposits are usually performed with cut-outs of pipes of heating surfaces with natural deposits. Vares et al. [30] obtained measurements in a temperature range from 300 to 500°C without the presence of water. The thickness of the observed layers varied from 0.045 to 0.23 mm, the thermal conductivity varied within the limits of 0.6 to 1.5 W/m·K. Haller et al. [31] reported thermal conductivities of deposits between 1.3–2.5 W/m·K with porosities between 0.65 to 0.75 vol-percent. Krause [24] found values of 1.2 W/m·K and 2100 kg/m^3 for thermal conductivity and density of the deposit layer, respectively. Chenoweth [32] reported that the average thermal conductivity of gypsum deposit in evaporators is 1.3 W/m·k.

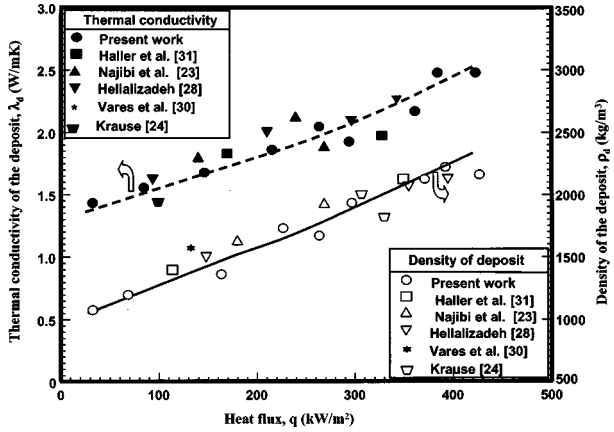

Fig. 11 Variation of the thermal conductitity and density of the deposit with heat flux

The thermal conductivity, density and porosity of the deposit are very sensitive to the deposit structure. Figure 10 shows typical pictures obtained by electron scanning microscopy of scales formed at 38,524, 120,482, and 301,205 W/m^2 respectively. A porous, needle-like structure is characteristic for the deposit formed at low heat fluxes while at high heat fluxes, the crystals are short, less porous, and more adherent. The thermal conductivity was found for a given deposit by reducing the heat flux well into the natural convection region and comparing the heat transfer coefficients with those measured with clean heat transfer surfaces under otherwise identical conditions

$$R_f = \frac{S_d}{\lambda_d} = \frac{1}{\alpha} - \frac{1}{\alpha_w} \tag{17}$$

The thickness and density of the deposit could be measured after each run. The results of the thermal conductivity and density of the observed fouling layers are summarized in Fig. 11. The results are also compared with the results reported by other investigators. These values agree with the values measured in the present investigation. The thermal conductivities obtained at high heat fluxes are higher than the values reported by Krause [24] and Chenoweth [32], probably due to the higher density of the deposits.

Modeling of Pool Boiling Heat Transfer Fouling

While the understanding of the mechanisms of scale formation under pool boiling conditions has improved, sound modeling of the change of heat transfer coefficient with time due to scale formation is not possible yet. From the above experimental results it is obvious that the traditional approach to modeling fouling as an additional heat transfer resistance in series to a more or less constant heat transfer coefficient to the fluid is not appropriate. Rather, the deposition process affects the bubble formation mechanisms and hence the heat transfer coefficient itself.

There is growing evidence that wick boiling predominates when the heat transfer surface is covered by a layer of porous deposit and that this results in boiling characteristics quite different from those with a clean surface. Porous deposits contain pores with different shapes and sizes connected to each other. McBeth [33] suggested a physical model for heat transfer through a layer of deposits, which is shown in Fig. 12. Because of the capillary

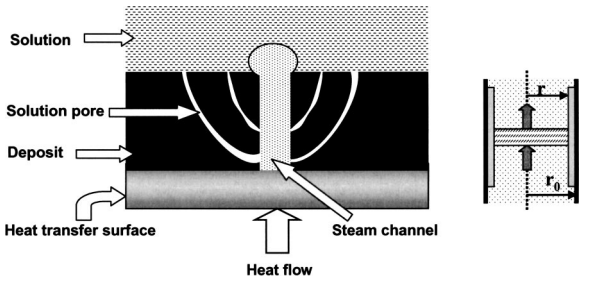

Fig. 12 Boiling from porous deposit according to McBeth [33]

forces, the liquid imbues the small pores in the direction of the heat transfer surface. The fluid pores are connected to larger pores, which are acting as ''steam chimneys''. Such a hydrodynamic model of flow in deposits works if the capillary pressure is sufficient to overcome the frictional forces in the steam chimneys to create the essential pressure gradient between the bottom and the outlet section of the steam chimneys. To achieve this, it is necessary that the diameter of the steam chimneys be larger than the diameter of the fluid pores. A close-up of the mouth of one of these steam chimneys is shown in the stereo-scan photograph of Fig. 13. These pores are of the order of 0.005 mm diameter and have a population density of typically 5000 per mm^2 [33]. The present modeling approach is concerned with the initial formation of a porous deposit followed by gradual closure and deactivation of the steam chimneys by scale precipitation.

Initial Formation of Porous Deposits. The initial porous deposits are formed in regions 1 and 2 of the heat transfer process, see Figs. 6(a–f). The duration of these two regions, i.e. the time until the heat transfer coefficient starts to decrease continuously was found to be a function of heat flux and foulant concentration. Assuming a 0th order rate equation with respect to foulant concentration, one may write

$$-\frac{dC}{dt}=k_r \tag{18}$$

Separation of variables and integration yields

$$t=\frac{C_b X}{k_r} \tag{19}$$

where X is the fractional conversion of calcium sulfate. When X approaches about 1 percent, time t approaches the transition time t_0. k_r is the reaction constant which has recently been given by Helalizadeh [28] for batch crystallization of calcium sulfate as

$$k_r=3.8\times 10^{11}\, e^{-124287/RT_s} \tag{20}$$

Hence, Eq. (19) simplifies to

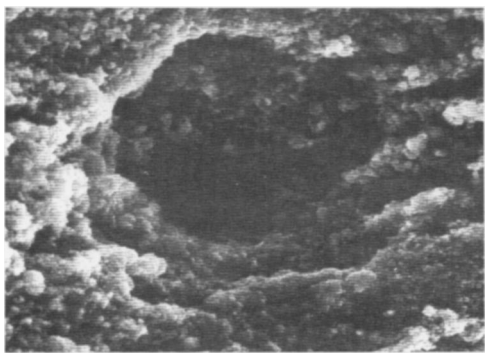

Fig. 13 Close up of picture of the mouth of a steam chimney with about 0.005 mm diameter [33]

$$t_0=0.731\times 10^{-17}\, C_b e^{-124287/RT_s} \tag{21}$$

Equation (21) predicts with good accuracy the transition time until the beginning of region 3.

Variation of Scaled Steam Channel Radius With Time The following model has been developed for the decreasing heat transfer coefficient in region 3, i.e., for $t \geqslant t_0$ It is obvious that the radius of steam chimneys is a function of time and decreases as scale deposition due to evaporation at the wall proceeds. To calculate this variation as a function of the deposition rate, the chain rule is applied

$$\frac{dr}{dt}=\frac{dC}{dt}\cdot\frac{dr}{dC} \tag{22}$$

The first term can be calculated from Eq. (15)

$$\frac{dC}{dt}=-\dot{m}_d\frac{A_c}{V_c}=-\dot{m}_d\cdot\frac{2\pi r dx}{\pi r^2 dx}=-\frac{2\dot{m}_d}{r} \tag{23}$$

The second term in Eq. (22) represents the variation of scaled steam channel radius with respect to foulant concentration. This term can be calculated from a material balance for the deposition process over a differential element of volume (see Fig. 12)

$$\dot{V}\cdot C-\dot{V}\cdot(C-dC)=\frac{dm_d}{dt}\Rightarrow \dot{\mathrm{V}}\cdot \mathrm{dC}=\frac{\mathrm{dm_d}}{\mathrm{dt}} \tag{24}$$

but

$$\frac{dm_d}{dt}=\frac{\rho_d dV_d}{dt}=\frac{\rho_d\pi(r_0^2-r^2)\cdot dx}{dt}=\frac{\rho_d\pi[(r+dr)^2-r^2]\cdot dx}{dt}$$

$$\approx 2\rho_d\pi r dr\frac{dx}{dt} \tag{25}$$

and

$$\dot{V}=\pi r^2 \mathrm{u};\quad \frac{\mathrm{dx}}{\mathrm{dt}}=u \tag{26}$$

Replacing Eqs. (25) and (26) into Eq. (24) yields

$$\frac{dr}{dC}=\frac{r}{2\rho_d} \tag{27}$$

Substituting Eqs. (23) and (27) into Eq. (22) yields

$$\frac{dr}{dt}=-\frac{\dot{m}_d}{\rho_d} \tag{28}$$

Equation (28) is applicable as long as the activity of the steam chimneys remains constant and does not decay with time.

The Rate Equation of Deactivation of the Steam Chimneys In general, the activity of the steam channels drops as salt concentration and heat flux increases, i.e., as the deposition rate in Eq. (28) increases. In analogy to solid porous catalysts, the activity of a steam channel at any time may be defined as

$$a=\frac{\dot{m}_{st}}{\dot{m}_{st,0}}\approx\frac{\dot{m}_d}{\dot{m}_{d,0}} \tag{29}$$

where $\dot{\mathbf{m}}_{\mathbf{st}}$ is the actual steam production of the steam chimneys and $\dot{\mathbf{m}}_{\mathbf{st,0}}$ is steam production before channel deactivation sets-in. It is reasonable to assume that deposit formation rate correlates with evaporation, hence **a** is also about equal to the ratio of actual rate of deposition in the steam channels, $\dot{\mathbf{m}}_{\mathbf{d}}$, to initial rate of deposition, $\dot{\mathbf{m}}_{\mathbf{d,0}}$. Levenspiel [34] proposed the following power law equation to correlate the time dependence of the activity of activation sites on the interior surface of pores

$$\frac{da}{dt}=k_d\cdot a^d \tag{30}$$

where d is called the order of deactivation, which is generally considered to be unity. Separating the variables and integrating gives

$$a = a_o\, e^{-k_d(t-t_0)} \tag{32}$$

Since a_o must be unity according to Eq. (29), Eq. (31) reduces to

$$a = e^{-k_d(t-t_0)} \tag{32}$$

Substituting Eqs. (32) and (29) into Eq. (28) yields

$$\frac{dr}{dt} = -\frac{\dot{m}_{d,0}}{\rho_d} e^{-k_d(t-t_0)} \tag{33}$$

Hence the scaled steam channel radius at any time can be obtained as a function of deposition rate from the integration of Eq. (33)

$$r = r_0 - \frac{\dot{m}_{d,0}}{\rho_d k_d}(1 - e^{-k_d(t-t_0)}) \tag{34}$$

or

$$\frac{\Delta r}{r_0} = \frac{\dot{m}_{d,0}}{\rho_d k_d r_0}(1 - e^{-k_d(t-t_0)}) \tag{35}$$

The deactivation rate constant, k_d is generally a function of temperature and follows an Arrhenius type equation [34]

$$\mathrm{k_d} = k_{d,0}\, e^{-E_d/RT} \tag{36}$$

E_d is the deactivation energy or temperature dependency of the channel deactivation process. Regression analysis of the experimental data gives

$$k_d = 1.1 \cdot 10^3\, e^{-33650/RT_s} \tag{37}$$

The low deactivation energy of steam chimney blockage indicates that this process may be considered as a physical phenomenon.

Heat Transfer Coefficient as a Function of Time. The reduction in heat transfer coefficient is a function of the reduction of steam chimney radius, i.e.,

$$\frac{\alpha}{\alpha_0} = F\left(\frac{\Delta r}{r_0}\right) \tag{38}$$

The experimental results show that this functionality can be represented by the following simple relationship:

$$\frac{\alpha}{\alpha_0} = \frac{1}{1 + \dfrac{\Delta r}{r_0}} \tag{39}$$

Substituting $\Delta r/r_0$ and $\dot{\mathbf{m}}_\mathbf{d}$ from Eqs. (15) and (35) gives

$$\frac{\alpha}{\alpha_0} = \frac{1}{1 + \Phi(C_s^i - C^*)^2(1 - e^{-k_d(t-t_0)})} \tag{40}$$

The parameter Φ and the interfacial concentration C_s^i are functions of foulant concentration and heat flux.

Calculation of Interfacial Concentration C_s^i. The relationship between the interfacial concentration of water and its concentration in the bulk of the solution is given by [35]

$$\dot{N}_W = r_W \cdot \rho \cdot \beta \ln \frac{r_w - x_w^i}{r_w - x_w^b} \tag{41}$$

where β is the mass transfer coefficient which was found to be $1.65 \cdot 10^{-4}$ m/s for calcium sulfate and calcium carbonate solutions [23,25,36]. The parameter r_w is defined as

$$r_w = \frac{\dot{N}_W}{\dot{N}_W + \dot{N}_s} \tag{42}$$

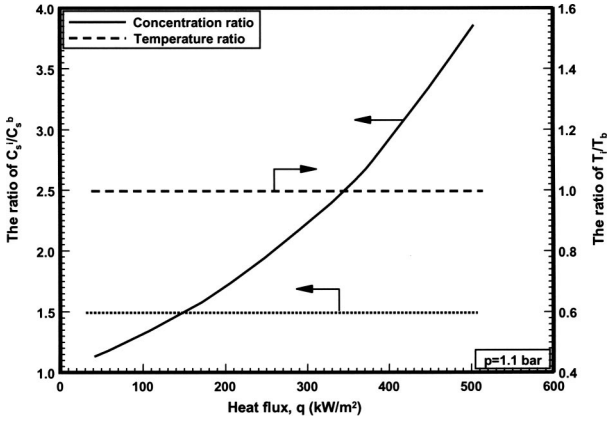

Fig. 14 The ratio of concentration and temperature of solution at interface and bulk as a function of heat flux

Since only water evaporates at the interface between the solution and the vapor bubbles, $\dot{\mathbf{N}}_\mathbf{s}$ equals zero and Eq. (42) reduces to

$$\dot{N}_W = \rho\beta \ln \frac{1 - x_w^i}{1 - x_w^b} \tag{43}$$

Therefore,

$$\frac{1 - x_w^i}{1 - x_w^b} = \frac{x_s^i}{x_s^b} = \exp\left(\frac{\dot{N}_W}{\rho\beta}\right) \tag{44}$$

Assuming that all the heat flow from the heat transfer surface passes into the bubbles in the form of latent heat, Eq. (44) becomes

$$\eta = \frac{C_S^i}{C_S^b} = \exp\left(\frac{\dot{q}}{\rho\beta\Delta h_v}\right) \tag{45}$$

Substituting the values for density, mass transfer coefficient and latent heat of evaporation, Eq. (45) simplifies for calcium sulfate solutions to

$$\eta = \frac{C_s^i}{C_S^b} = \exp(2.685 \cdot 10^{-6}\dot{q}) \tag{46}$$

The predictions of Eq. (46) are plotted in Fig. 14 for calcium sulfate solutions as a function of heat flux. Once the interfacial concentration is known, the interfacial temperature can be obtained from Eq. (3) or Fig. 4. The concentration ratio increases strongly with heat flux while the temperature ratio is almost independent of the heat flux. The reason for this behavior can be found in Fig. 4, which illustrates that doubling the concentration of the calcium sulfate concentration has almost no effect on the boiling point of the solution. Figure 14 also shows that using a constant value of η=1.5, as has been suggested previously for sub-cooled flow boiling of calcium sulfate and calcium carbonate solutions [23,36], may lead to significant inaccuracies. Instead, the heat transfer coefficient at any time can be obtained from substitution of Eqs. (46) into Eq. (40):

$$\alpha = \frac{\alpha_0}{1 + \Phi(\eta C_s^b - C^*)^2(1 - e^{-k_d(t-t_0)})} \tag{47}$$

where α_0 is the clean boiling heat transfer coefficient of the calcium sulfate solution which may be obtained from Eq. (5). The dependency of Φ on the heat flux may be calculated using all the parameters involved in the derivation of Eq. (40). However, it was found that Φ can be obtained with good accuracy from regression analysis of the experimental data

$$\Phi = \frac{1}{90.2 + 5.7 \cdot 10^{-7} \dot{q}} \tag{48}$$

Predictions of Eq. (47) over a wide range of heat fluxes and calcium sulfate concentrations have also been included in Figs. 6(a) to 6(g). The calculated trends are in good agreement with the experimental data. Equation (47) predicts all experimental data under various operating conditions and concentrations with an absolute mean average error of about 6.5 percent.

Conclusions

Sparingly soluble salts with negative solubility reduce the nucleate boiling heat transfer coefficients considerably and form deposits which further decrease the heat transfer rate. The heat transfer coefficient at the solid-liquid interface changes throughout the deposition process due to changes in the bubble formation mechanisms. Foulant concentration and heat flux have the main influence on the deposition process. The deposition rate increases and heat transfer coefficient decreases as concentration and heat flux increases. A model for pool boiling scale formation has been developed. The model includes reaction mechanisms of scale formation and concentration effects due to evaporation. The model is able to predict the effects of foulant concentration and heat flux correctly. Considering the complexity of fouling under pool boiling conditions, the quantitative agreement between measured and predicted heat transfer coefficients is very good.

Nomenclature

a and b = constants in equation (3)
a = activity of the steam chimney
A = area, m^2
C = concentration, kg/m^3
c_p = specific heat, $J/kg \cdot K$
E = activation energy, J/mole
F_p, F_q = defined by equation (6)
F_{WR}, F_{WM} = defined by equation (7)
i = van't Hoff factor
I = ionic strength of solution, $mole/m^3$
K = specific reaction rate constant
K_b = molar boiling point elevation constant of the solvent
k_r = reaction rate constant, $kg \cdot s/m^4$
k_d = deactivation rate constant, s^{-1}
m = molarity of the solution, moles of solute/kg of solvent
$\mathbf{m_d}$ = rate of deposition, kg/s
$\dot{\mathbf{m}}_\mathbf{d}$ = mass of deposition, $kg/m^2 \cdot s$
$\dot{\mathbf{m}}_\mathbf{st}$ = actual steam production of the steam chimneys, kg/s
$\dot{\mathbf{m}}_{\mathbf{st,0}}$ = initial steam production of the steam chimneys, kg/s
$\dot{\mathbf{N}}$ = rate of mass transfer, $kg/m^2 \cdot s$
p = pressure, bar
pc = capillary pressure, bar
p_r = reduced pressure
q = heat flux, W/m^2
r = steam chimney radius at time t, m
r_0 = initial steam chimney radius, m
r_w = defined by equation (42)
R = universal gas constant, $J/mol \cdot K$
R_a/R_{ao} = surface roughness correction factor
s = distance between the thermocouple location and the heat transfer surface, m
T = temperature, K
t = time, s
u = velocity, m/s
V = volume, m^3
x = mass fraction or distance
X = fractional conversion
Z = defined by equation (4)

Greek Symbols

α = heat transfer coefficient, $W/m^2 K$
β = mass transfer coefficient, m/s
η = defined by equation (45)
λ = thermal conductivity, $W/m \cdot K$
ρ = density, kg/m^3
θ = contact angle, radiant
σ = surface tension, N/m
Φ = defined by equation (48)
Δh_v = heat of evaporation, J/kg
ΔT_b = boiling point elevation, K

Subscript and Superscript

b = bulk or boiling
c = steam chimney or clean
d = deposit or de-activity
i = interface
r = reaction
ref = at reference conditions
s = surface or solute
st = steam
th = thermocouples
w = water
$*$ = saturation
o = initial or clean conditions

References

[1] Langelier, W. F., Cadwell, D. H., and Lawrence, W. B., 1957, "Scale Control in Seawater Distillation Equipment," Ind. Eng. Chem., **49**, pp. 457–465.
[2] O'Callaghan, M. G., 1986, *Heat Exchanger Sourcebook*, Hemisphere Publishing, Washington, D.C.
[3] Müller-Steinhagen, H., Jamialahmadi, M., and Robson, B., 1994, "Mitigation of Scale Formation During the Bayer Process—Measurements at the Alcoa of Australia Refinery in Kwinana," Light Metals, *Proceedings of the 1994 Light Metals Conference*, pp. 121–127.
[4] Behbahani, M. R., Jamialahmadi, M., and Müller-Steinhagen, H., 2002, "Heat Transfer in Phosphoric Acid Evaporators Under Clean and Fouling Operating Conditions," Heat Exchanger Workshop, Rabbat., Morocco.
[5] Müller-Steinhagen, H., 1993, "Fouling: The Ultimate Challenge for Heat Exchanger Design," *6th International Symposium on Transport Phenomena in Thermal Engineering*, South Korea, pp. 1–13.
[6] Sanatgar, H., and Somerscales, E. F. C., 1991, "Account for Fouling in Heat Exchanger Design," Chem. Eng. Process., **14**, pp. 53–59.
[7] Jamialahmadi, M., and Müller-Steinhagen, H., 1993, "Scale Formation During Nucleate Boiling—A Review," Journal of Corrosion Reviews, **XI**(1–2), pp. 25–54.
[8] Bott, T. R., 1995, *Chemical Engineering Monographs 26: Fouling of Heat Exchangers*, Elsevier Science.
[9] Marshal, W. L., and Slusher, R., 1964, "Aqueous Systems at High Temperature," J. Chem. Eng. Data, **9**, pp. 187–191.
[10] Najibi, H., 1996, "Heat Transfer and Heat Transfer Fouling During Subcooled Boiling of Hard Water," Ph.D. Thesis University of Surrey, UK.
[11] Wenzel, U., 1992, "Saturated Pool Boiling and Subcooled Flow Boiling of Mixtures," Ph.D. thesis, University of Auckland, New Zealand.
[12] Gorenflo, D., 2001, "State of the Art in Pool Boiling Heat Transfer of New Refrigerants," Int. J. Refrig., **24**, pp. 6–14.
[13] Thome, J. R., and Shakir, S., 1987, "A New Correlation for Nucleate Pool Boiling of Aqueous Mixtures," AIChE Symp. Ser., **83**(257), pp. 46–51.
[14] Van Wijk, W. R., Vos, A. S., and Van Stralen, J. D., 1956, "Heat Transfer to Boiling of Binary Liquid Mixtures," Chem. Eng. Sci., **11**, pp. 68–80.
[15] Schlünder, E. U., 1983, "Heat Transfer in Nucleate Boiling of Mixtures," Int. Chem. Eng., **23**, pp. 589–599.
[16] Schmitt, D. W., 1987, "Heat Transfer in Boiling of Multicomponent Mixtures," Chem. Eng. Technol., **10**, pp. 242–248.
[17] Wadekar, V. V., Hills, P. D., and Mattes, J., 1997, "Mixture Effect in Boiling of Salt Solutions," Heat Transfer—Baltimore, AIChE Symposium Series, **93**, pp. 233–238.
[18] Jamialahmadi, M., Helalizadeh, A., and Müller-Steinhagen, H., 2004, "Pool Boiling Heat Transfer to Electrolyte Solutions," Int. J. Heat Mass Transfer, **47**, pp. 729–742.
[19] Mortimer, C. E., 1986, *Chemistry*, 6th edition, Wadsworth Publishing Company.
[20] Najibi, S. H., Müller-Steinhagen, H., and Jamialahmadi, M., 1996, "Boiling and Non-Boiling Heat Transfer to Electrolyte Solutions," Heat Transfer Eng., **17**, pp. 46–63.
[21] Stephan, K., and Preusser, P., 1979, "Wärmübergang und maximale

Wämestromdiche beim Behältersieden binärer und ternärer Flüssigkeitsgemische,'' Chem. Ing. Tech., MS 649/79.
[22] Jamialahmadi, M., Blöchl, R., and Müller-Steinhagen, H., 1989, ''Bubble Dynamics and Scale Formation During Boiling of Aqueous Calcium Sulfate Solutions,'' Chem. Eng. Process., **26**, pp. 15–26.
[23] Najibi, S. H., Müller-Steinhagen, H., and Jamialahmadi, M., 1997, ''Calcium Sulphate Scale Formation During Subcooled Flow Boiling,'' Chem. Eng. Sci., **52**, pp. 1265–1284.
[24] Krause, 1986, ''Fouling an Wärmeübertragungsflächen durch Kristallisation und Sedimentbildung,'' VDI-Forschungsheft, p. 637.
[25] Bohnet, M., 1987, ''Fouling of Heat Transfer Surfaces,'' Chem. Eng. Technol., **10**, pp. 113–125.
[26] Lammers, J., 1972, ''Zur Kristallisation von Calciumsulfat bei der Verkrustung von Heizflächen,'' Dissertation, TU Berlin.
[27] Mori, H., Nakamura, M., and Toyama, S., 1996, ''Crystallization Fouling of Calcium Sulfate Di-Hydrate on Heat Transfer Surface,'' J. Chem. Eng. Jpn., **29**, pp. 166–173.
[28] Helalizadeh, 2002, ''Mixed Salt Crystallization Fouling,'' Ph.D. thesis, Department of Chemical and Process Engineering, University of Surrey, UK.
[29] Moghadasi, J., 2002, ''Particle Movement and Scale Formation in Porous Media,'' Ph.D. thesis, Department of Chemical and Process Engineering, University of Surrey, UK.
[30] Vares, V., Kruus, R., Kjaar, H., and Mikk, I., 1977, ''An Investigation of Thermal Conductivity of Inner Deposits on Boiler Tubes at 300–500°C,'' Transactions of the Tallin Polytechnic Institute, No. 416 (in Russian).
[31] Haller, K. H., Lee, R. A., and Slotnik, J. S., 1971, ''Heat Transfer and Friction Characteristics of Porous Magnetite Layers in Once-Through Boilers,'' Tech. Paper (Babcock Wilcox) TPI-40, BR-494 (presented to ASME Winter Annual Meeting, Washington).
[32] Chenoweth, J. M., 1987, ''General Design of Heat Exchangers for Fouling Conditions,'' *Proc. NATO Advanced Study Inst. On Advances in Fouling Science and Technology*, Alvor, Portugal.
[33] McBeth, R. V., 1971, ''Boiling on Surfaces Overlayed With a Porous Deposit: Heat Transfer Rate Obtainable by Capillary Action,'' AEEW-711.
[34] Levenspiel, O., 1972, *Chemical Reaction Engineering*, 2nd Ed., New York Wiley.
[35] Treybal, R. E., 1980, *Mass Transfer Operations*, Third edition, McGraw-Hill Book Company.
[36] Najibi, S. H., Müller-Steinhagen, H., and Jamialahmadi, M., 1997, ''Calcium Carbonate Scale Formation During Subcooled Flow Boiling,'' ASME J. Heat Transfer, **119**, pp. 1–9.

An Experimental Investigation of Flow Boiling Characteristics of Water in Parallel Microchannels

Mark E. Steinke

Satish G. Kandlikar
Fellow ASME

Thermal Analysis and Microfluidics Laboratory,
Mechanical Engineering Department,
Kate Gleason College of Engineering,
Rochester Institute of Technology,
Rochester, NY 14623

Microchannels are being considered in many advanced heat transfer applications including automotive and stationary fuel cells as well as electronics cooling. However, there are a number of fundamental issues from the heat transfer and fluid mechanics perspectives that still remain unresolved. The present work focuses on obtaining the fundamental heat transfer data and two-phase flow patterns present during flow boiling in microchannels. An experimental investigation is performed for flow boiling using water in six parallel, horizontal microchannels with a hydraulic diameter of 207 μm. The ranges of parameters are: mass flux from 157 to 1782 kg/m^{2}s, heat flux from 5 to 930 kW/m^2, inlet temperature of 22°C, quality from sub-cooled to 1.0, and atmospheric pressure at the exit. The corresponding single-phase, all-liquid flow Reynolds number range at the saturation conditions is from 116 to 1318. The measured single-phase, adiabatic pressure drop agreed with the conventional theory within the experimental error. The experimental single-phase Nusselt number was found to be between the constant heat flux and the constant wall temperature boundary conditions, corresponding to Nu_H and Nu_T respectively. The flow visualization demonstrates that the flow reversal condition in parallel flow channels is due to bubble nucleation followed by its rapid growth. In addition, the dry-out condition is observed, showing a change in the contact angles of the liquid-vapor interface. The local flow boiling heat transfer coefficient exhibits a decreasing trend with increasing quality. A comparison with the nucleate boiling dominant regime of a flow boiling correlation shows good agreement, except for the large peak in two-phase heat transfer coefficient observed at the onset of nucleate boiling. [DOI: 10.1115/1.1778187]

Keywords: Boiling, Enhancement, Flow, Heat Transfer, Microscale, Two-Phase

Introduction

The need to dissipate high heat fluxes is an important issue in a number of applications, including electronics cooling and MEMS devices. The first applications of small-diameter passages mainly involved aerospace systems, in the form of compact heat exchangers for managing onboard power systems. Bergles [1], in one of his pioneering works, investigated the upper limit of burnout conditions in small diameter tubes.

Tuckerman and Pease [2] presented another important paper in which they demonstrated the potential of microchannels in the cooling of integrated circuitry. The fundamental understanding of fluid flow and heat transfer has yet to catch up with their proposals. Recently, microchannel heat exchangers have been applied to miniature power systems, advanced heat sinks, fuel cell components, and several other automotive applications. The benefit of reduced channel size and the resulting heat transfer enhancement have been well established.

Literature Review

Kandlikar [3] presented an extensive review of literature on flow boiling in microchannels, and described some of the fundamental issues with two-phase flow and flow patterns. As smaller channel sizes were investigated, the terminology for classification underwent considerable changes over the past decade. In earlier studies, the term microchannel had included hydraulic diameters as large as 3.0 mm.

A wide variety of channel sizes have been investigated and reported as microchannels. A clear definition of channel size classification is necessary for consistency in comparing various results from literature. There is limited detailed local flow boiling data available in open literature for a microchannel. The present work characterizes the thermal and hydraulic performance of six parallel microchannels with a hydraulic diameter of 207 μm. The slightly larger hydraulic diameter (as compared to 200 μm for a microchannel) resulted due to the tolerances associated with the manufacturing of these channels.

Several authors have specifically addressed the issue of channel size classification. During their flow boiling studies in 1.39 to 3.69 mm diameter tubes, Kew and Cornwell [4] used confinement number, Co, to guide the channel size criterion. Mehendale et al. [5] adopted a classification based upon geometric consistency and ease of understanding. Kandlikar and Grande [6] presented a classification scheme based upon fundamental considerations of single-phase gas flow, two-phase flow patterns and channel fabrication methods and discussed further by Kandlikar [7]. Kawaji and Chung [8] recently reported a significant departure for their 100 μm microchannels from the established linear relationship between volumetric quality versus void fraction as proposed by Ali et al. [9] and [10–57] for narrow channels. The present work is not focused on developing a channel classification. There still must be more data over the entire range of channel sizes presented in literature to make a definitive decision as to which channel classifications is correct. Although the classification of minichannels ($3\text{ mm} \geqslant D_h > 200\,\mu$m) and microchannels ($200 \geqslant D_h > 10\,\mu$m) is adopted here, it should be recognized that this is merely a guideline. The actual flow phenomena will depend upon fluid properties and their variation with pressure; as well as the type of flow including single-phase, flow boiling, flow condensation, and adiabatic two-phase flow.

A review of literature on small diameter channels yielded approximately fifty research papers on flow boiling heat transfer in channels with hydraulic diameters less than 3 mm. A compilation

Contributed by the Heat Transfer Division for publication in the JOURNAL OF HEAT TRANSFER. Manuscript received by the Heat Transfer Division January 13, 2003; revision received May 20, 2004. Associate Editor: R. M. Manglik.

Table 1 Available literature for evaporation of pure liquid flows in parallel minichannel and microchannel passages

Author	Year	Fluid	D_h (mm)	Re	G ($kgm^{-2}\,s^{-1}$)	q″ (kWm^{-2})	Type*	Vis.**
Lazarek & Black [10]	1982	R113	3.150	57–340	125–750	14–380	O	N
Moriyama & Inoue [11]	1992	R113	0.140–0.438	107–854	200–1000	4.0–30	O/L	Y
Wambsganss et al. [12]	1993	R113	2.920	313–2906	50–300	8.8–90.75	L	N
Bowers & Mudawar [13]	1994	R113	2.540 & 0.510	14–1714	20–500	30–2000	O	N
Peng et al. [14]	1994	Water	0.133–0.343	200–2000	500–1626	⋯	O	N
Cuta et al. [15]	1996	R124	0.850	100–570	32–184	1.0–400	O	N
Mertz et al. [16]	1996	Water	3.100	57–210	50–300	10–110	O	N
Ravigururajan et al. [17]	1996	R124	0.425	217–626	142–411	5.0–25	L	N
Tran et al. [18]	1996	R12	2.400–2.460	345–2906	44–832	3.6–129	L	N
Kew & Cornwell [4]	1997	R141b	1.390–3.690	1373–5236	188–1480	9.7–90	L	Y
Ravigururajan [19]	1998	R124	0.850	11115–32167	3583–10369	20–700	L	N
Yan & Lin [20]	1998	R134a	2.000	506–2025	50–900	5.0–20	L	N
Kamidis & Ravigururajan [21]	1999	R113	1.540–4.620	190–1250	90–200	50–300	L	N
Lin et al. [22]	1999	R141b	1.100	1591	568	⋯	L	N
Mudawar & Bowers [23]	1999	Water	0.902	16–49	2×10^4–1×10^5	1×10^3–2×10^5	O	N
Bao et al. [24]	2000	R11/R123	1.950	1200–4229	50–1800	5–200	L	N
Lakshminarasimhan et al. [25]	2000	R11	3.810	1311–11227	60–4586	7.34–37.9	O	Y
Jiang et al. [26]	2001	Water	0.026	1541–4811	2×10^4–5×10^4	⋯	O	Y
Kandlikar et al. [27]	2001	Water	1.000	100–556	28–48	1–150	O	Y
Kim & Bang [28]	2001	R22	1.660	1883–2796	384–570	2.0–10	L	Y
Koizumi et al. [29]	2001	R113	0.500–5.000	67–5398	100–800	1.0–110	O	Y
Lee & Lee [30]	2001	R113	1.569–7.273	220–1786	52–209	2.98–15.77	L	N
Lin et al. [31]	2001	R141b	1.100	536–2955	50–3500	1–300	L	N
Hetsroni et al. [32]	2002	Vertrel XF	0.158	35–68	148–290	22.6–36	L	Y
Qu & Mudawar [33]	2002	Water	0.698	338–1001	135–402	1–1750	N	N
Warrier et al. [34]	2002	FC-84	0.750	440–1552	557–1600	1.0–50	L	N
Yen et al. [35]	2002	R123	0.190	65–355	50–300	5.46–26.9	L	Y
Yu et al. [36]	2002	Water	2.980	534–1612	50–200	50–200	L	N
Zhang et al. [37]	2002	Water	0.060	127	590	2.2×10^4	O	N
Faulkner & Shekarriz [38]	2003	Water	1.846–3.428	20551–41188	3106–6225	250–2750	O	N
Hetsroni et al. [39]	2003	Water	0.103–0.161	8.0–42	51–500	80–220	O	Y
Kuznetsov et al. [40]	2003	R21	1.810	148–247	30–50	3.0–25	L	N
Lee et al. [41]	2003	Water	0.036–0.041	22–51	170–341	0.2–301	O	Y
Lee & Garimella [42]	2003	Water	0.318–0.903	300–3500	260–1080	⋯	O	N
Molki et al. [43]	2003	R134a	1.930	717–1614	100–225	14	L	N
Park et al. [44]	2003	R22	1.660	1473–2947	300–600	10.0–20	L	N
Qu & Mudawar [45]	2003	Water	0.349	338–1001	135–402	10.0–1300	L	N
Wu & Cheng [46]	2003	Water	0.186	75–97	112	226	O	Y

*O=Overall, L=Local.
**Visualization, Y=Yes, N=No.

of some of the recent works is presented in Table 1. The fluids investigated include: water, R21, R22, R113, R123, R124, R141b, FC84, and Vertrel XF. The mass fluxes, all liquid Reynolds number, and heat fluxes range from 20 to 6225 kg/m^2s, 14 to 5236, and up to 2 MW/m^2, respectively. A visual representation of the available data is presented in Fig. 1. The all-liquid flow Reynolds number in these data sets is plotted as a function of hydraulic diameter. These data sets contain both local and overall heat transfer studies. A systematic shift toward lower Reynolds numbers with decreasing diameter is noted from Fig. 1.

The available literature is further reviewed to determine that twenty-two papers present local heat transfer data. Figure 2 shows the Reynolds number versus hydraulic diameter plot for these local data papers. The low Reynolds number range is generally encountered in microchannels, Microelectromechanical Systems (MEMS), and micro Total Analysis Systems (μTAS) applications. It can be seen from Fig. 2 that there are only two local data sets available for hydraulic diameters smaller than 200 μm. The two data sets that provide detailed local heat transfer data for $D_h < 200\,\mu$m are by Hetsroni et al. [32] and Yen et al. [35]. Neither

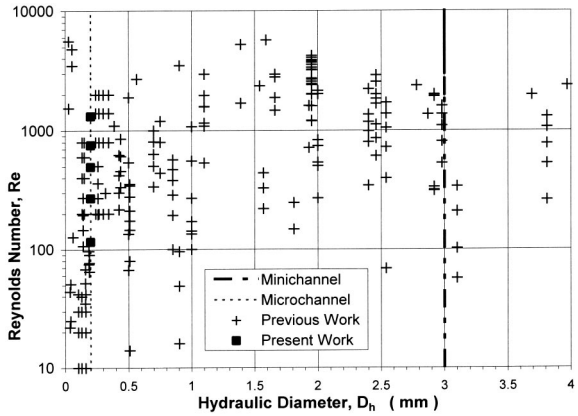

Fig. 1 Hydraulic diameter versus Reynolds number of previous studies from available literature and present work

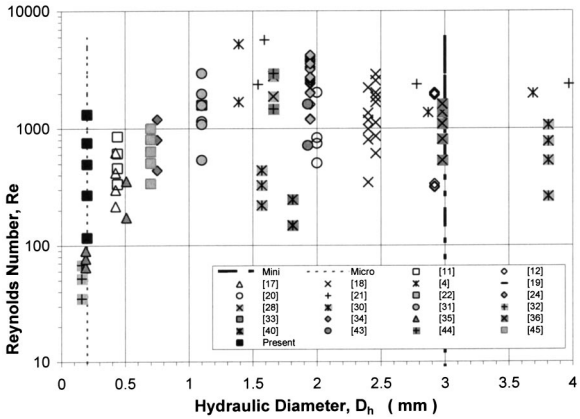

Fig. 2 Hydraulic diameter versus Reynolds number of local heat transfer data. For available literature and present work.

of these two studies have used water as the working fluid. From Table 1 and Figs. 1 and 2, it is clear that there is a need to generate more local flow boiling heat transfer data for microchannels. Knowledge of local data is essential in design, correlation development, and simulation of flow boiling systems.

Objectives of Present Work

The objectives of the present study are to investigate the heat transfer performance and two-phase flow characteristics of water heated in microchannels, as well as to generate local heat transfer data by varying mass flux, heat flux, and quality for water boiling in multiple parallel microchannels. Another goal of this study is to obtain high-speed visual images to understand the complex two-phase structure and characteristics under flow boiling conditions.

Experimental Apparatus

The experimental system consists of several sub-systems that include a water delivery system, data acquisition system, high-speed imaging system, and the experimental test sections. A schematic of the setup is shown in Fig. 3.

The working fluid for all of the present experiments is deionized and degassed water. The amount of dissolved gas in the water needs to be precisely controlled to eliminate the heat transfer changes resulting from out-gassing of dissolved gases. Steinke and Kandlikar [47] conducted an experimental investigation concerning the control of dissolved gases. They demonstrated that the effects due to the out-gassing of dissolved gases can be eliminated if the water is treated to reduce the dissolved oxygen content to 5.4 parts per million (ppm) at 25°C. To be conservative, the dissolved oxygen level used in these experiments is maintained at 3.2 ppm. The water is sampled randomly throughout the course of experimentation to ensure the dissolved oxygen level is well below this threshold limit.

The water delivery system consists of a pressure vessel, heat exchanger, throttle valve, flow meter bank, test section, and condenser. The pressure vessel provides the control of dissolved gasses and the motive force for the water. The degassing procedure described by Steinke and Kandlikar [47] is followed before beginning the experiments and consists of pressurizing the chamber to 2 atm, and then suddenly reducing the pressure to 1 atm. This causes a vigorous boiling in the chamber, driving the steam and dissolved gases from the water in the chamber. The procedure is repeated to attain the desired oxygen content.

The heat exchanger controls the inlet temperature to the test section. The throttle valve reduces the overall system pressure to an appropriate range for the flow meters and test section. The flow meter bank contains three flow meters with several different flow ranges to improve the flow measurement accuracy. The test section contains the microchannels, heaters, thermocouples, inlet and outlet plenums, and pressure connections. Finally, the condenser collects the outlet from the test section and returns the fluid into a liquid state.

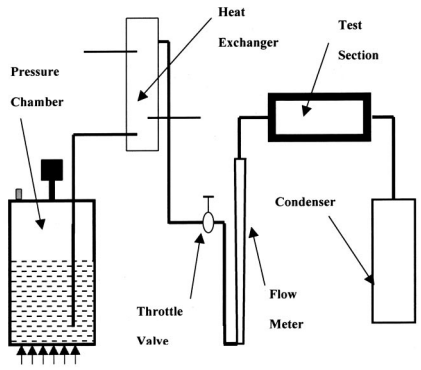

Fig. 3 Water loop sub-system. Includes: pressure cooker, flat plate heat exchanger, throttle valve, flow meter, test section, and condenser.

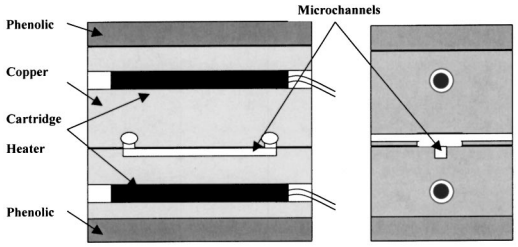

Fig. 4 Heat transfer test section. Test section constructed for data collection.

Two different test sections are studied. The test section used for flow visualization incorporates three side heating, and the test section utilized for heat transfer analysis incorperates four side heating. The water inlet and outlet plenums are included in the test sections. In each test section, the plenums are fully insulated to minimize the inlet and outlet heating of the fluid and to ensure that the heat transfer only occurs in the flow channels. In the flow visualization test section, the plenums are located in the polycarbonate top cover. In the heat transfer test section, a portion of the copper is removed and filled with an insulating epoxy. The inlet and outlet plenums are then machined in the insulating epoxy. The test section is covered with insulation to reduce the heat losses from the outer surfaces of the test section. Figure 4 shows the test section construction for the heat transfer analysis experiments.

There are six parallel microchannels machined in the copper substrate. The microchannels are tested in a horizontal orientation. The channel depth and width are measured at six locations along the flow length using a microscopic measurement system. It is observed that the channels have a slightly trapezoidal cross section, with the top and bottom widths differing by about 15 μm. The average channel dimensions are: 214 μm wide by 200 μm deep and 57.15 mm long. All measured values fall within $\pm 3\%$ of the respective average values. The individual channels are separated by a spacing of 570 μm.

Two thermocouple layers located in the copper substrate are used to determine heat fluxes and surface temperatures on the inner surface of the channel. The heater is embedded in the copper substrate furthest from the microchannel surface. Next, a layer of six thermocouples is located 6.35 mm from the microchannel surface. Then, the second layer of thermocouples is located 3.18 mm from the microchannel surface. Both of the thermocouple layers are at the same location along the flow length. The first thermocouple is located 6.35 mm, in the flow direction, from the microchannel inlet. The subsequent thermocouples are located 19.05, 25.4, 38.1, 44.45, and 57.15 mm from the inlet, respectively. A series of simple experiments are conducted to ensure that a one-dimensional heat conduction assumption is a valid. Power is applied to the test section and the surface temperature is measured using a non-contact interferometer. In addition, a finite difference model is used to validate this assumption.

Initially, a series of experiments are performed to establish the heat loss characteristics of the test section. The water is completely removed from the test section during these runs. Power is applied and the test section is allowed to reach a steady state. The heat loss is plotted against the temperature difference between the test section and the ambient air. The slope of this plot is used to determine the lost power for a given test section operating temperature.

Data Analysis

The methods used for data analysis are described in this section. The equations used for evaluating heat transfer and pressure drop characteristics are presented.

The local two-phase heat transfer coefficients are calculated along the flow length. The flow enters the microchannel as subcooled single-phase liquid. That inlet subcooling must be taken into account. The high pressure drop occurring in the microchannels causes the local saturation temperature to vary along the channel length. As a first approximation, a linear pressure variation is assumed in the channel. The pressure variation was determined from the inlet and outlet pressures measurements.

The local heat transfer coefficients are calculated using the temperature measurements from the two thermocouple layers separated by a known distance. The heat flux q'' between the two locations is determined from the thermocouple readings and the known thermal conductivity of the copper. The surface temperatures at those locations are then predicted using a linear extrapolation. The local quality is calculated from a heat balance calculation. The local heat transfer coefficients are then calculated using Eq. (1).

$$q'' = h(T_s - T_{m,w}) \tag{1}$$

The overall pressure drop is corrected for entrance and exit losses to determine the frictional losses in the microchannels. There are losses due to the contraction from the larger inlet plenum into the microchannels and the expansion from the microchannels into the larger exit plenum. The Fanning friction factor is determined from the correlation from Shah and London [48] and is given in Eq. (2).

$$f\,\mathrm{Re} = 24(1 - 1.3553\alpha^* + 1.9467\alpha^{*2} - 1.7012\alpha^{*3} + 0.9564\alpha^{*4} - 0.2537\alpha^{*5}) \tag{2}$$

For the present microchannel geometry, the $f \times \mathrm{Re}$ product is found to be 14.25. The previous equations have been used and verified in conventional channels for many years. However, the validity of Eq. (2) needs to be verified in a microchannel.

Uncertainty

The uncertainty is determined by the method of evaluating the bias and precision errors. The pressure transducer has an accuracy of ± 0.69 kPa. The temperature reading has an accuracy of ± 0.1°C. The power supply used to provide input power has accuracies for the voltage of ± 0.05 V and for the current ± 0.005 amps. The flow meter has a volumetric flow accuracy of ± 0.0588 cc/min. The power measurement has an accuracy of ± 0.5 Watts. The ΔT measurements have an uncertainty of ± 0.2°C. The resulting uncertainties are calculated for the heat transfer coefficient as 8.61%, the pressure drop is 7.19%, and friction factor is 4.80%, at a median flow case. The major source of error is the temperature reading, specifically the resulting ΔT measurements.

Results and Discussion

The major results of the present study include: single-phase pressure drop, two-phase flow patterns, local two-phase heat transfer, and the comparison of the experimental two-phase heat transfer coefficients with an existing flow boiling correlation.

Single-Phase Pressure Drop. The adiabatic single-phase friction factor for laminar flow is first determined experimentally to provide validity of the test section and measurement techniques. This experiment was performed before any diabatic experiments. The single-phase friction factor is shown in Fig. 5. There is a good agreement seen with the predicted friction factor, within 10% of the predicted values.

Flow Visualization. Flow visualization was conducted using a high speed CCD camera. Typical recording frame rates were between 500 and 2000 frames per second. The following flow patterns are observed in the microchannels: nucleate boiling, bubbly flow, slug flow (constrained bubble), annular flow, annular flow with nucleation in the thin film, churn flow, and dry-out. Steinke and Kandlikar [49] presented further details and observations. All observed flow-boiling regimes agree with those found by Kew and Cornwell [4] and many other researchers. The bubble flow or isolated bubble flow was very intermittent. The conditions to observe this flow regime had to be carefully controlled. The slug flow regime was the second most common observed flow regime. A bubble grows to the size of the channel in this pattern. Finally, the most commonly observed flow-boiling regime was annular-slug flow. In this regime, a bubble expands to fill the channel and extends into the channel causing a vapor core and wetting thin film.

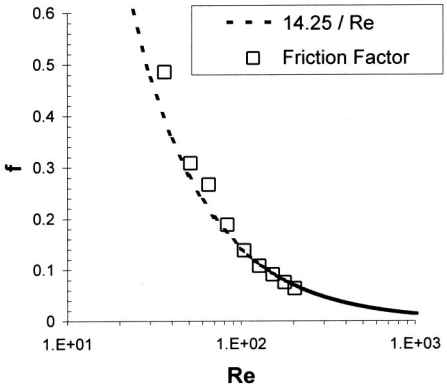

Fig. 5 Single-phase friction factor versus Reynolds number for adiabatic experiments. For: 161 kg/m² s < *G* < 1782 kg/m² s.

A commonly found flow-boiling phenomenon in parallel flow channels is flow reversal. Kandlikar et al. [27] observed this flow pattern in minichannels. During the onset of the annular-slug flow regime, the upstream interface of the vapor bubble moves counter to the flow direction. It was also observed in microchannels during the present study. Figure 6 shows the progression of flow reversal. In Fig. 6(a), a bubble nucleates in the channel. Figure 6(b) shows the vapor core expanding toward the channel exit, just as expected. The left side of the liquid vapor interface of the vapor bubble begins to move toward the channel entrance, counter to the flow direction. Finally, the right side interface continues to move

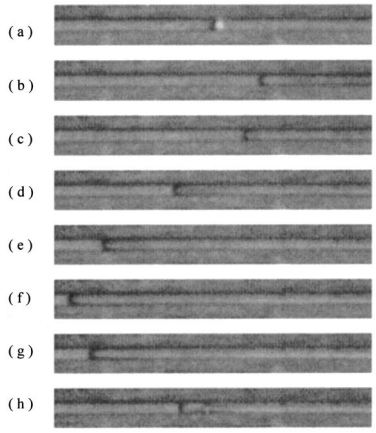

Fig. 6 Flow Reversal. Flow is from left to right, single channel shown. Counter flow interface velocity: 0.197 m/s. For: $G = 467$ kg/m² s, $V_f = 0.480$ m/s, $q''_{ts} = 140$ kW/m², $x > 0.0$, and $\Delta t = 8$ ms.

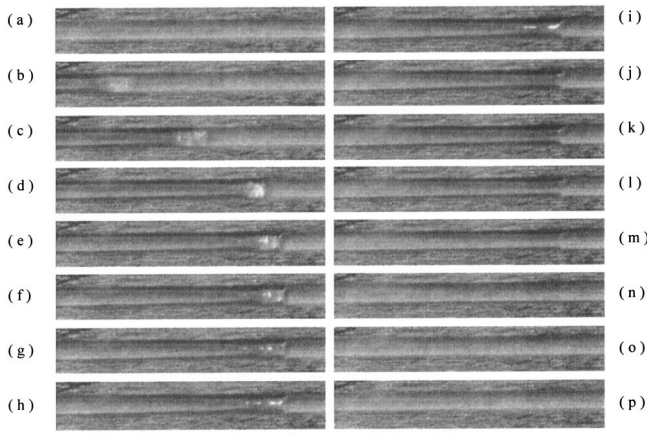

Fig. 7 Microchannel dry-out. Flow is from left to right, single channel shown. For: $G=375$ kg/m^2 s, $q''_{ts}=632$ kW/m^2, $x=0.63$, and $\Delta t=4$ ms.

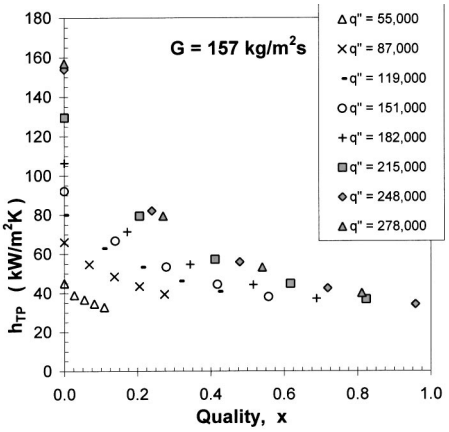

Fig. 9 Local heat transfer coefficients versus local quality. For: $G=157$ kg/m^2 s; $Re_{LO}=116$; 55 kW/m^2$<q''<$278 kW/m^2; $0<x<1$.

toward the channel exit in Fig. 6(g). The flow reversal is caused by the presence of the parallel channels, which allow a path of lower flow resistance during explosive growth of the nucleating bubbles. The flow and pressure in the other channels compensate and allow for the high pressure of vapor generation to dissipate through the other channels.

Another flow boiling phenomenon observed in the present study is the local dry-out condition. Figure 7 shows the local dry-out event. The flow is from left to right and the figure caption gives the flow details. Figure 7(a) shows the channel in a dry out condition. The local surface temperatures are rising, as there is no film on the surface. In Fig. 7(b), an annular slug comes into view. The annular slug has a head of liquid as a front cap. An advancing contact angle is seen in this frame. The slug and cap move forward a little distance. In Fig. 7(e), the interface shifts from the advancing to the receding contact angle. This signifies the onset of the dry-out condition as the interface begins to move backward toward the inlet, in Fig. 7(g). The dry-out is occurring because of the rapid evaporation of the liquid in the contact line region. This rapid movement causes a force imbalance that causes the reaction force and interface movement in the opposing direction similar to that shown in Kandlikar and Steinke [50,51]. In Fig. 7(k), the upstream vapor has joined with the vapor in the annulus. Figures 7(m) and 7(n) show the thin film interface retreating toward the inlet as the channel begins to dry-out. Finally, Fig. 7(p) shows complete dry-out in the channel.

Figure 8 shows a schematic to represent the flow boiling dry-out as seen in Fig. 7. Figure 8(a) begins with a channel in the dry-out regime. An annular slug with liquid head is introduced into the channel in Fig. 8(b). The interline, the liquid-vapor-surface contact line, is in an advancing contact position. Dry-out begins to occur in Fig. 8(c) and the interline shifts to a receding contact orientation. The dry-out is occurring because of the rapid evaporation of the liquid in the contact line region. This rapid movement causes a force imbalance that causes the reaction force and interface movement in the opposing direction, Kandlikar and Steinke [50,51]. Finally, Fig. 8(e) shows the channel returning to a post dry-out regime.

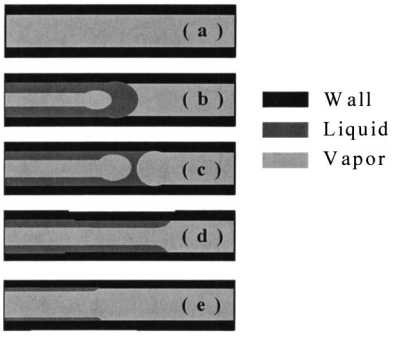

Fig. 8 Dry-out in schematic form. Representation of flow occurring in Fig. 7: (*a*) channel dry-out, (*b*) annular slug with liquid head, (*c*) contact angle shift, (*d*) vapor penetration at dry-out occurrence, and (*e*) thinning film as it returns to dry-out.

Flow Boiling Heat Transfer. The detailed flow boiling heat transfer results are presented in Figs. 9 to 13. The local heat transfer coefficient is plotted as a function of local quality. The data cover five different mass fluxes over the entire range of qualities possible with the current setup. The inlet pressure varies from 1.25 to 2.0 atm depending on the heat and mass fluxes employed.

Figure 9 presents the local heat transfer coefficients versus local quality for a mass flux of 157 kg/m^2 s. The resulting all-liquid Reynolds number for this case is 116. As the local quality increases, the heat transfer coefficient decreases. Results for several different heat fluxes are shown. It is seen that there is a dependence on heat flux for this case. This is the lowest all-liquid Reynolds number flow case studied.

The local data for a mass flux of 366 kg/m^2 s is shown in Fig. 10. The heat transfer coefficients are very high in the low quality

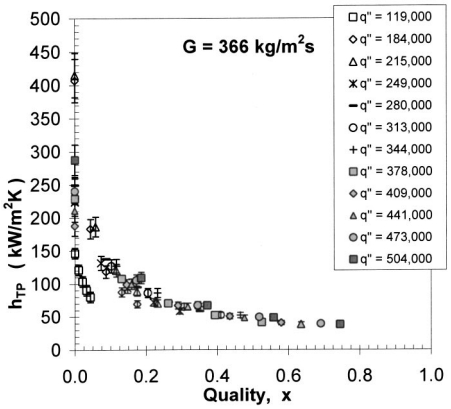

Fig. 10 Local heat transfer coefficients versus local quality. For: $G=366$ kg/m^2 s; $Re_{LO}=270$; 119 kW/m^2$<q''<$504 kW/m^2; $0<x<1$.

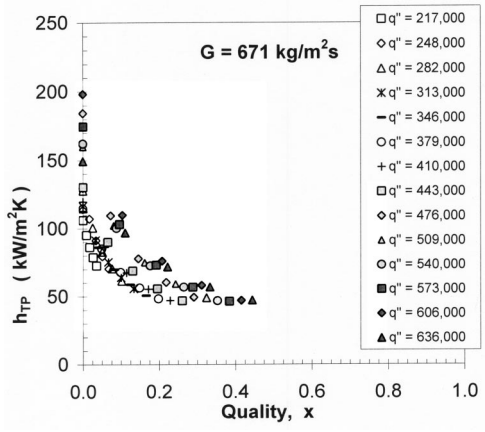

Fig. 11 Local heat transfer coefficients versus local quality. For: $G=671$ kg/m^2 s; $Re_{LO}=496$; 217 kW/m^2$<q''<$636 kW/m^2; $0<x<1$.

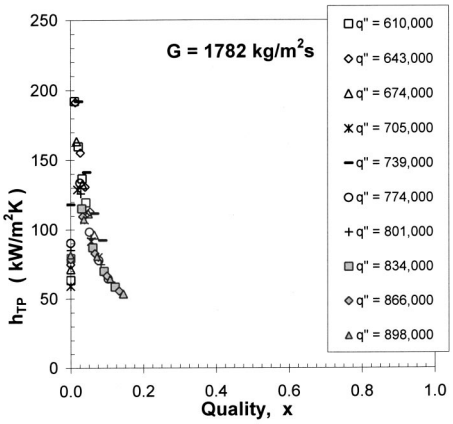

Fig. 13 Local heat transfer coefficients versus local quality. For: $G=1782$ kg/m^2 s; $Re_{LO}=1318$; 610 kW/m^2$<q''$ $<$898 kW/m^2; $0<x<1$.

region. This is believed to be due to the onset of nucleate boiling (ONB). The data then begins to sharply decline. A possible explanation could be due to the rapid growth of the bubbles, with annular slugs being generated. This may cause flow reversal, as noted in the flow visualization section. The evaporation and rewetting can lead to a very efficient means of heat transfer. After a quality of approximately 0.20, the data shows a slower decreasing trend. However, there seems to be less effect of heat flux on this flow case.

Figure 11 shows the local data for a mass flux of 671 kg/m^2 s. The heat transfer coefficient near ONB is much higher than at the other qualities. The same decreasing trend is found here. Unfortunately, the larger values of qualities could not reached for this case before critical heat flux (CHF) was achieved. However, the data seem to be converging on a single heat transfer coefficient value, approximately 40 kW/m^2 K. The local data for mass fluxes of 1022 and 1782 kg/m^2 s are given in Figs. 12 and 13 respectively. Once again, these figures show the same decreasing trend of heat transfer coefficient with respect to an increase in quality.

The trends depicted in Figs. 9 to 13 seem to match with those found in a nucleate boiling dominant flow. The decreasing heat transfer coefficient is consistent for water in the nucleate boiling dominant region, Kandlikar [52]. Yen et al. [35] also observed this trend. They studied flow boiling of a R123 in 190 μm diameter tubes. Their heat transfer coefficient magnitude is smaller than the present work, as one would expect for a refrigerant versus water. A possible explanation for the decreasing trend could be that the decreased channel size (microchannel diameters) has reduced the available space for convective flow to develop. In addition, they also saw a high heat transfer coefficient near the ONB point observed in the present data, Figs. 9 to 13.

In addition, the critical heat flux (CHF) condition was observed for each of the mass fluxes. Figure 14 shows the plot of CHF versus Reynolds number. The inlet temperature is 22°C for all these cases. A direct relationship is seen between heat flux, mass flux and Reynolds number. More data are needed with different channels before theories and correlations can be developed in this range.

Comparison With Flow Boiling Correlation. The general Kandlikar [53] flow-boiling correlation has been applied to the present experimental work for flow boiling in multiple-channels. The general correlation takes the maximum of two equations, one equation for nucleate boiling dominant flow and one for convective dominant flow. Kandlikar and Steinke [54] and Kandlikar and Balasubramanian [55] have demonstrated that the correlation can be modified to give good agreement with microchannel flow. For microchannels, the liquid only heat transfer coefficient is given by the laminar Nusselt number. In addition, only the nucleate boiling dominant portion of the flow boiling equation, Eq. (3), is used to predict h_{TP}.

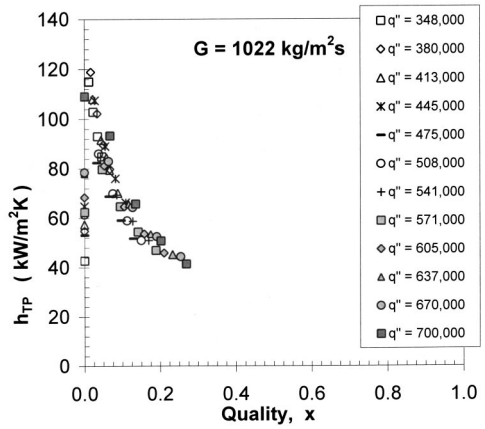

Fig. 12 Local heat transfer coefficients versus local quality. For: $G=1022$ kg/m^2 s; $Re_{LO}=756$; 348 kW/m^2$<q''<$700 kW/m^2; $0<x<1$.

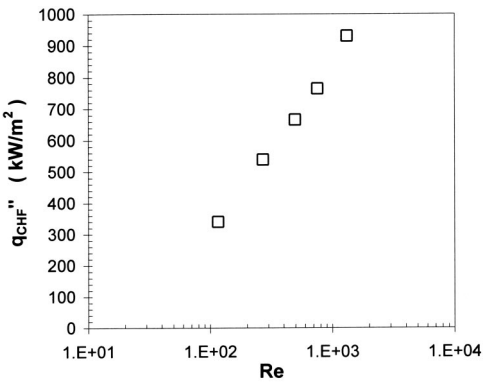

Fig. 14 Critical heat flux versus Reynolds number. For: $G=157$, 366, 671, 1022, and 1782 kg/m^{2}s; $Re_{LO}=116$, 270, 496, 756, and 1318; $q''_{chf}=340$, 539, 666, 764, and 930 kW/m^2.

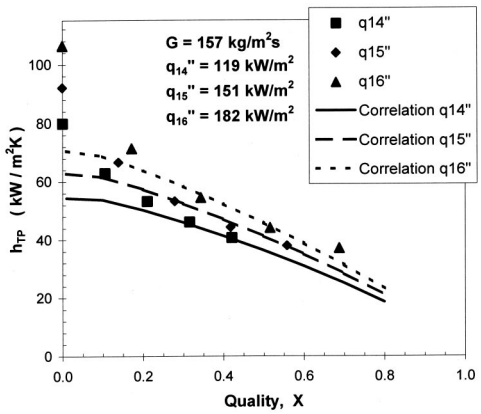

Fig. 15 Predicted heat transfer coefficient using Kandlikar modified microchannel correlation, [54]. Laminar h_{lo}, nucleate boiling dominant only. For: $G=157$ kg/m^2 s; $\mathrm{Re}_{LO}=116$; $q''=119$, 151, and 182 kW/m^2.

$$h_{TP}=h_{TP,NBD}=0.6683\mathrm{Co}^{-0.2}(1-x)^{0.8}f_2(\mathrm{Fr}_{LO})h_{LO}+1058.0\mathrm{Bo}^{0.7}(1-x)^{0.8}F_{Fl}h_{LO} \quad (3)$$

$$\mathrm{Co}=\left(\frac{\rho_g}{\rho_l}\right)^{0.5}\left(\frac{1-x}{x}\right)^{0.8} \quad (4)$$

$$\mathrm{Bo}=\frac{q''}{Gh_{fg}} \quad (5)$$

where Co is the convection number given in Eq. (4), Bo is the boiling number given in Eq. (5), Fr_{lo} is the Froude number with all liquid flow, $f_2(\mathrm{Fr}_{lo})$ is the multiplier, h_{lo} is the heat transfer coefficient with all liquid flow, and x is the quality. The F_{FL} number for water is 1.0 and the $f_2(\mathrm{Fr}_{lo})$ multiplier is 1.0 for microchannel flow due to the lack of stratified flow.

Figure 15 shows the comparison of the Kandlikar modified microchannel correlation to the experimental data. The mass flux and Reynolds number is 157 kg/m^2 s and 116, respectively. The three heat fluxes are 114, 151 and 182 kW/m^2. Figure 16 presents the comparison for another few data points. The mass flux and Reynolds number is 366 kg/m^2 s and 270, respectively. The three heat fluxes are 441, 473, and 504 kW/m^2.

The correlation predicts the magnitudes as well as the trends of the experimental data reasonably well except for the large peak observed in the experimental data at low qualities (corresponding to ONB conditions). The optimal range of the correlation is between qualities of 0.2 to 0.8. The correlation under predicts the heat transfer coefficients at the ONB condition. However, this is expected due to the rapid bubble growth observed in microchannels following nucleation. Over the quality range of 0.2 to 0.8, the mean deviation is 7.2%. Although the Kandlikar correlation does very well for the present experimental configuration, it is recommended that more local data for different channel geometries be obtained for further validating its applicability to microchannels of different aspect ratios, sizes and geometries.

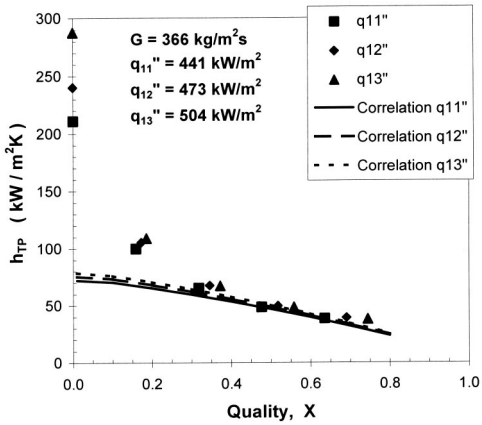

Fig. 16 Predicted heat transfer coefficient using Kandlikar modified microchannel correlation, [54]. Laminar h_{lo}, nucleate boiling dominant only. For: $G=366$ kg/m^2 s; $\mathrm{Re}_{LO}=270$; $q''=441$, 473, and 504 kW/m^2.

In a recent publication, Kandlikar [7] presented two new nondimensional groups that are thought to be important in microchannel flows. The new nondimensional groups are called K_1 and K_2 are given below.

$$K_1=\left(\frac{q''}{Gh_{fg}}\right)^2\frac{\rho_l}{\rho_g}$$

$$K_2=\left(\frac{q''}{h_{fg}}\right)^2\frac{D_h}{\sigma\rho_g}$$

The K_1 and K_2 groups are based upon the surface tension and momentum change due to evaporation, as well as the viscous shear force and the inertia force. The mass fluxes for the present work are 157, 366, 671, 1022, and 1782 kg/m^2 s. The corresponding average K_1 numbers for those mass fluxes are 4.15×10^{-4}, 2.27×10^{-4}, 1.12×10^{-4}, 6.99×10^{-5}, and 4.62×10^{-5}. The corresponding average K_2 numbers for those mass fluxes are 3.85×10^{-5}, 1.14×10^{-4}, 1.91×10^{-4}, 2.75×10^{-4}, and 5.53×10^{-4}. These numbers are reported to provide information for future researchers. In Kandlikar [7], there are K_1 and K_2 numbers presented for a variety of channel diameters as well as flow conditions.

Closing Remarks

The interest in flow boiling in microchannels continues to grow as seen from recent literature. In the recent months, a number of new publications have appeared such as; Wu and Cheng [56], Brutin et al. [57], and Pettersen [58]. The need for obtaining more experimental data has been recognized by researchers and it is expected that more data will be available in the near future.

Conclusions

An experimental investigation is conducted to study the single-phase and two-phase flow in 207 μm hydraulic diameter, trapezoidal microchannels during laminar flow. The following conclusions are drawn from the present study.

- The adiabatic single-phase friction factor for laminar flow of water in microchannels is accurately described by the established relationship for large (conventional) diameter channels.
- The single-phase flow heat transfer in the microchannel has been investigated with degassed water. The Nusselt numbers for the experimental data fall between the constant temperature and constant heat flux boundary conditions.
- A flow reversal is observed under certain conditions in microchannels, Fig. 6. The vapor interface moves in a direction counter to the bulk fluid flow. This was also seen in minichannels.
- The dry-out condition is observed in Fig. 7. The changes occurring in the interface at the dry-out condition have been visually observed and documented. The contact angles of the interface exhibit similar behavior to that found by Kandlikar and Steinke [50,51]. This indicates the need for including the contact line dynamics in developing a flow boiling critical heat flux model.
- The present work constitutes one of the first sets of local heat transfer coefficient data for flow boiling of water flow in a micro-

channel. A maximum heat flux of 930 kW/m^2 has been achieved, with heat transfer coefficients as high as 192 kW/m^{2}K. A decreasing trend in two-phase heat transfer coefficient, h_{TP}, with an increasing quality is detected. These trends are consistent with a nucleate boiling dominant flow.

• The Kandlikar flow-boiling correlation has been modified by using the laminar single-phase heat transfer coefficient and only the nucleate boiling dominant equation. The correlation shows good agreement with data between qualities of 0.2 to 0.80. However, the high heat transfer coefficients observed at the ONB condition is not predicted by the correlation. The trends seen in flow boiling data in microchannels is different from those observed in larger diameter tubes. The role of nucleate boiling is seen to be more predominant than previously thought. These aspects provide a new direction for future work in this area.

Nomenclature

A = area (m^2)
Bo = boiling number, $=q''/Gh_{fg}$
Co = convection number, $=(\rho_g/\rho_l)^{0.5}(1-x/x)^{0.8}$
d = channel depth (m)
D_h = hydraulic diameter (m)
f = friction factor
$f_2(\mathrm{Fr_{LO}})$ = Froude number multiplyer, [53]=1.0 for microchannel flow boiling
F_{FL} = liquid to Surface interaction number
Fr = Froude number, $=G^2/\rho_l^2 gD_h$
G = mass flux (kg m^{-2} s^{-1})
h = heat transfer coefficient (W m^{-2} K^{-1})
h_{fg} = heat of vaporization (J kg^{-1})
k = thermal conductivity (W m^{-1} K^{-1})
l = length (m)
$\dot{m}$ = mass flow rate (kg s^{-1})
Nu = Nusselt number, $=hD/k_f$
P = pressure (Pa)
q = heat transfer (W)
q'' = heat flux (W m^{-2})
Re = Reynolds number, $=GD_h/\mu$
t = time (s)
T = temperature (°C)
V = velocity (m s^{-1})
w = channel width (m)
x = quality

Greek

α^* = aspect ratio, $=d/w$
Δ = difference
μ = dynamic viscosity (N s m^{-2})
ρ = density (kg m^{-3})

Subscripts

cp = constant property
FD = fully developed
g = gas
H = constant Heat Flux boundary condition
i = inlet
l = liquid
LMTD = log-mean temperature difference
LO = liquid only
m = mean
NBD = nucleate-boiling dominant
o = outlet
s = surface
T = constant Temperature boundary condition
TP = two-phase
w = wall

References

[1] Bergles, A. E., 1964, ''Burnout in Tubes of Small Diameter,'' ASME Paper No. 63-WA-182, pp. 1–9.
[2] Tuckerman, D. B., and Pease, R. F. W., 1981, ''High-Performance Heat Sinking for VSLI,'' IEEE Electron Device Lett., **EDL-2**, pp. 126–129.
[3] Kandlikar, S. G., 2002, ''Fundamental Issues Related to Flow Boiling in Minichannels and Microchannels,'' Exp. Therm. Fluid Sci., **26**, pp. 389–407.
[4] Kew, P. A., and Cornwell, K., 1997, ''Correlations for the Prediction of Boiling Heat Transfer in Small-Diameter Channels,'' Appl. Therm. Eng., **17**(8–10), pp. 705–715.
[5] Mehendale, S. S., Jacobi, A. M., and Shah, R. K., 2000, ''Fluid Flow and Heat Transfer at Micro and Meso-Scales With Application to Heat Exchanger Design,'' Appl. Mech. Rev., **53**(7), pp. 175–193.
[6] Kandlikar, S. G., and Grande, W. J., 2002, ''Evolution of Microchannel Flow Passages—Thermohydraulic Performance and Fabrication Technology,'' *Proceedings of International Mechanical Engineering Congress and Exposition*, ASME, New York.
[7] Kandlikar, S. G., 2004, ''Heat Transfer Mechanisms During Flow Boiling in Microchannels,'' ASME J. Heat Transfer, **126**(1), pp. 8–16.
[8] Kawaji, M., and Chung, P. M.-Y., 2003, ''Unique Characteristics of Adiabatic Gas-Liquid Flows in Microchannels: Diameter and Shape Effects on Flow Patterns, Void Fraction and Pressure Drop,'' *Proceedings of 1st International Conference on Minichannels and Microchannels*, ASME, New York, pp. 115–127.
[9] Ali, M. I., Sadatomi, M., and Kawaji, M., 1993, ''Two-Phase Flow in Narrow Channels Between Two Flat Plates,'' *Canadian Journal of Chemical Engineering*, **71**(5), pp. 657–666.
[10] Lazarek, G. M., and Black, S. H., 1982, ''Evaporative Heat Transfer, Pressure Drop and Critical Heat Flux in a Small Vertical Tube With R-113,'' Int. J. Heat Mass Transfer, **25**(7), pp. 945–959.
[11] Moriyama, K., and Inoue, A., 1992, ''The Thermodynamic Characteristics of Two-Phase Flow in Extremely Narrow Channels (The Frictional Pressure Drop and Heat Transfer of Boiling Two-Phase Flow, Analytical Model),'' Heat Transfer-Jpn. Res., **21**(8), pp. 838–856.
[12] Wambsganss, M. W., France, D. M., Jendrzejczyk, J. A., and Tran, T. N., 1993, ''Boiling Heat Transfer in a Horizontal Small-Diameter Tube,'' ASME J. Heat Transfer, **115**(4), pp. 963–972.
[13] Bowers, M. B., and Mudawar, I., 1994, ''High Flux Boiling in Low Flow Rate, Low Pressure Drop Mini-Channel and Micro-Channel Heat Sinks,'' Int. J. Heat Mass Transfer, **37**, pp. 321–332.
[14] Peng, X. F., Peterson, G. P., and Wang, B. X., 1994, ''Heat Transfer Characteristics of Water Flowing Through Microchannels,'' Exp. Heat Transfer, **7**(4), pp. 265–283.
[15] Cuta, J. M., McDonald, C. E., and Shekarriz, A., 1996, ''Forced Convection Heat Transfer in Parallel Channel Array Microchannel Heat Exchanger,'' *International Mechanical Engineering Congress and Exposition*, ASME, New York.
[16] Mertz, R., Wein, A., and Groll, M., 1996, ''Experimental Investigation of Flow Boiling Heat Transfer in Narrow Channels,'' *Heat and Technology*, **14**(2), pp. 47–54.
[17] Ravigururajan, T. S., Cuta, J., McDonald, C. E., and Drost, M. K., 1996, ''Effects of Heat Flux on Two-Phase Flow Characteristics of Refrigerant Flows in a Micro-Channel Heat Exchanger,'' *National Heat Transfer Conference*, **7**, HTD-329, pp. 167–178.
[18] Tran, T. N., Wambsganss, M. W., and France, D. M., 1996, ''Small Circular- and Rectangular-Channel Boiling With Two Refrigerants,'' Int. J. Multiphase Flow, **22**(3), pp. 485–498.
[19] Ravigururajan, T. S., 1998, ''Impact of Channel Geometry on Two-Phase Flow Heat Transfer Characteristics of Refrigerants in Microchannel Heat Exchangers,'' ASME J. Heat Transfer, **120**, pp. 485–491.
[20] Yan, Y., and Lin, T., 1998, ''Evaporation Heat Transfer and Pressure Drop of Refrigerant R-134a in a Small Pipe,'' Int. J. Heat Mass Transfer, **41**, pp. 4183–4194.
[21] Kamidis, D. E., and Ravigururajan, T. S., 1999, ''Single and Two-Phase Refrigerant Flow in Mini-Channels,'' *Proceedings of 33rd National Heat Transfer Conference*, ASME, New York.
[22] Lin, S., Kew, A., and Cornwell, K., 1999, ''Two-Phase Evaporation in a 1 mm Diameter Tube,'' *Proceedings of 6th UK Heat Transfer Conference.*
[23] Mudawar, I., and Bowers, M. B., 1999, ''Ultra-High Critical Heat Flux (CHF) for Subcooled Water Flow Boiling—I: CHF Data and Parametric Effects for Small Diameter Tubes,'' Int. J. Heat Mass Transfer, **42**, pp. 1405–1428.
[24] Bao, Z. Y., Fletcher, D. F., and Haynes, B. S., 2000, ''Flow Boiling Heat Transfer of Freon R11 and HCFC123 in Narrow Passages,'' Int. J. Heat Mass Transfer, **43**, pp. 3347–3358.
[25] Lakshminarasimhan, M. S., Hollingsworth, D. K., and Witte, L. C., 2000, ''Boiling Incipience in Narrow Channels,'' *Proceedings of the ASME Heat Transfer Division 4*, HTD-Vol. 366–4, pp. 55–63.
[26] Jiang, L., Wong, M., and Zohar, Y., 2001, ''Forced Convection Boiling in a Microchannel Heat Sink,'' *Journal of Microelectromechanical Systems*, **10**(1), pp. 80–87.
[27] Kandlikar, S. G., Steinke, M. E., Tian, S., and Campbell, L. A., 2001, ''High Speed Photographic Observation of Flow Boiling of Water in Parallel Minichannels,'' *35th Proceedings of National Heat Transfer Conference*, ASME, New York.
[28] Kim, J., and Bang, K., 2001, ''Evaporation Heat Transfer of Refrigerant R-22

in Small Hydraulic-Diameter Tubes,'' *4th Proceedings of International Conference on Multiphase Flow*, Efstathios E. Michaelides, ed.
[29] Koizumi, Y., Ohtake, H., and Fujita, Y., 2001, ''Heat Transfer and Critical Heat Flux of Forced Flow Boiling in Vertical-Narrow-Annular Passages,'' *Proceedings of the ASME International Mechanical Engineering Congress and Exposition*, ASME, New York.
[30] Lee, H. J., and Lee, S. Y., 2001, ''Heat Transfer Correlation for Boiling Flows in Small Rectangular Horizontal Channels With Low Aspect Ratios,'' Int. J. Multiphase Flow, **27**, pp. 2043–2062.
[31] Lin, S., Kew, A., and Cornwell, K., 2001, ''Flow Boiling of Refrigerant R141B in Small Tubes,'' *Transactions of IChemE 79, Part A*, pp. 417–424.
[32] Hetsroni, G., Mosyak, A., Segal, Z., and Ziskind, G., 2002, ''A Uniform Temperature Heat Sink for Cooling of Electronic Devices,'' Int. J. Heat Mass Transfer, **45**, pp. 3275–3286.
[33] Qu, W., and Mudawar, I., 2002, ''Prediction and Measurement of Incipient Boiling Heat Flux in Microchannel Heat Sinks,'' Int. J. Heat Mass Transfer, **45**, pp. 3933–3945.
[34] Warrier, G. R., Pan, T., and Dhir, V. K., 2002, ''Heat Transfer and Pressure Drop in Narrow Rectangular Channels,'' Exp. Therm. Fluid Sci., **26**, pp. 53–64.
[35] Yen, T.-H., Kasagi, N., and Suzuki, Y., ''Forced Convective Boiling Heat Transfer in Microtubes at Low Mass and Heat Fluxes,'' *Symposium on Compact Heat Exchangers on the 60th Birthday of Ramesh K. Shah*, pp. 401–406.
[36] Yu, W., France, D. M., Wambsganss, M. W., and Hull, J. R., 2002, ''Two-Phase Pressure Drop, Boiling Heat Transfer, and Critical Heat Flux to Water in a Small-Diameter Horizontal Tube,'' Int. J. Multiphase Flow, **28**, pp. 927–941.
[37] Zhang, L., Koo, J.-M., Jiang, L., and Asheghi, M., 2002, ''Measurements and Modeling of Two-Phase Flow in Microchannels With Nearly Constant Heat Flux Boundary Conditions,'' *Journal of Microelectromechanical Systems*, **11**(1), pp. 12–19.
[38] Faulkner, D. J., and Shekarriz, R., 2003, ''Forced Convective Boiling in Microchannels for kW/cm^2 Electronics Cooling,'' *Proceedings of ASME Summer Heat Transfer Conference*, ASME, New York.
[39] Hetsroni, G., Mosyak, A., Segal, Z., and Pogrebnyak, E., 2003, ''Two-Phase Flow Patterns in Parallel Microchannels,'' Int. J. Heat Mass Transfer, **29**, pp. 341–360.
[40] Kuznetsov, V. V., Dimov, S. V., Houghton, P. A., Shamiraev, A. S., and Sunder, S., 2003, ''Upflow Boiling and Condensation in Rectangular Minichannels,'' *First International Conference on Microchannels and Minichannels*, ASME, New York.
[41] Lee, P. C., Li, H. Y., Tseng, F. G., and Pan, C., 2003, ''Nucleate Boiling Heat Transfer in Silicon-Based Micro-Channels,'' *Proceedings of ASME Summer Heat Transfer Conference*, ASME, New York.
[42] Lee, P.-S., and Garimella, S. V., 2003, ''Experimental Investigation of Heat Transfer in Microchannels,'' *Proceedings of ASME Summer Heat Transfer Conference*, ASME, New York.
[43] Molki, M., Mahendra, P., and Vengala, V., 2003, ''Flow Boiling of R-134A in Minichannels With Transverse Ribs,'' *First International Conference on Microchannels and Minichannels*, ASME, New York.
[44] Park, K. S., Choo, W. H., and Bang, K. H., 2003, ''Flow Boiling Heat Transfer of R-22 in Small-Diameter Horizontal Round Tubes,'' *First International Conference on Microchannels and Minichannels*, ASME, New York.
[45] Qu, W., and Mudawar, I., 2003, ''Flow Boiling Heat Transfer in Two-Phase Micro-Channel Heat Sinks.—I. Experimental Investigation and Assessment of Correlation Methods,'' Int. J. Heat Mass Transfer, **46**, pp. 2755–2771.
[46] Wu, H. Y., and Cheng, P., 2003, ''Liquid/Two-Phase/Vapor Alternating Flow During Boiling in Microchannels at High Heat Flux,'' Int. Commun. Heat Mass Transfer, **30**(3), pp. 295–302.
[47] Steinke, M. E., and Kandlikar, S. G., 2004, ''Control and Effect of Dissolved Air in Water During Flow Boiling in Microchannels,'' Int. J. Heat Mass Transfer, **47**, pp. 1925–1935.
[48] Shah, R. K., and London, A. L., 1978, ''Laminar Flow Forced Convection in Ducts,'' Supplement 1 to *Advances in Heat Transfer*, Academic, New York.
[49] Steinke, M. E., and Kandlikar, S. G., 2003, ''Flow Boiling and Pressure Drop in Parallel Flow Microchannels,'' *Proceedings of 1st International Conference on Minichannels and Microchannels*, ASME, New York, pp. 567–579.
[50] Kandlikar, S. G., and Steinke, M. E., 2001, ''High Speed Photographic Investigation of Liquid-Vapor Interface and Contact Line Movement During CHF and Transition Boiling,'' *Proceedings of International Mechanical Engineering Congress and Exposition*, ASME, New York.
[51] Kandlikar, S. G., and Steinke, M. E., 2002, ''Contact Angles And Interface Behavior During Rapid Evaporation of Liquid on a Heated Surface,'' Int. J. Heat Mass Transfer, **45**, pp. 3771–3780.
[52] Kandlikar, S. G., 1991, ''Development of a Flow Boiling Map for Subcooled and Saturated Flow Boiling of Different Fluids in Circular Tubes,'' ASME J. Heat Transfer, **113**, pp. 190–200.
[53] Kandlikar, S. G., 1990, ''A General Correlation for Two-Phase Flow Boiling Heat Transfer Coefficient Inside Horizontal and Vertical Tubes,'' ASME J. Heat Transfer, **112**, pp. 219–228.
[54] Kandlikar, S. G., and Steinke, M. E., 2003, ''Predicting Heat Transfer During Flow Boiling In Minichannels and Microchannels,'' ASHRAE Trans., **109**(1), pp. 1–9.
[55] Kandlikar, S. G., and Balasubramanian, P., 2003, ''Extending the Applicability of the Flow Boiling Correlation to Low Reynolds Number Flows in Microchannels,'' *Proceedings of First International Conference on Microchannels and Minichannels*, S. G. Kandlikar, ed., ASME, New York.
[56] Wu, H. Y., and Cheng, P., 2003, ''Visualization and Measurements of Periodic Boiling in Silicon Microchannels,'' Int. J. Heat Mass Transfer, **46**(14), pp. 2603–2614.
[57] Brutin, D., Topin, F., and Tadrist, L., 2003, ''Experimental Study of Unsteady Convective Boiling in Heated Minichannels,'' Int. J. Heat Mass Transfer, **46**(16), pp. 2957–2965.
[58] Pettersen, J., 2004, ''Flow Vaporization of CO2 in Microchannel Tubes,'' Exp. Therm. Fluid Sci., **28**(2–3), pp. 111–121.

The Condensation of Ammonia-Water Mixtures in a Horizontal Shell and Tube Condenser

Chris Philpott

Joe Deans

Department of Mechanical Engineering,
University of Auckland,
New Zealand

The heat transfer rates that develop when ammonia water mixtures condense within a small, un-vented, horizontal, shell and tube condenser are examined. The vapor flow within the condenser was constrained by baffles and the condensate created formed a pool that flowed along the base of the condenser. During the test program the inlet ammonia vapor concentration to the condenser varied from 0 to 10 wt % and the maximum local vapor concentration measured was 26 wt %. The experimental results demonstrate that the condensation heat transfer rates generally decrease with increasing ammonia concentration, however at low ammonia concentrations (<2 wt %) the local and overall heat transfer rates for the condenser were enhanced. When the ammonia concentration was 0.9 wt %, the vapor heat transfer rate was 34 percent greater than that predicted by the Nusselt analysis for steam at the same conditions. This enhancement is attributed to the disturbed morphology of the condensate film, created by Marangoni instabilities.
[DOI: 10.1115/1.1778188]

Keywords: Binary, Condensation, Enhancement, Surface Tension

Introduction

Ammonia-water mixtures are an industrially important working fluid, used in absorption refrigeration systems and in some new types of power cycles such as the those developed by Kalina [1]. The design of these cycles requires detailed knowledge of the mixture's behavior during a phase change. This information is particularly important for the condensation process since the performance of the entire system is dependent on the successful operation of the condenser.

There is, however, little experimental data concerning the condensation of ammonia-water mixtures. Two of the more significant studies were those of Domingo et al. [2] and Morrison et al. [3]. Domingo conducted a series of condensation experiments using an ammonia-water mixture (90 percent ammonia, 10 percent water) on the outside of a cooled vertical tube. At this concentration it was found that there was a significant degradation in the condensation heat transfer coefficient, especially at low thermal driving forces. The results from this experimental study were successfully interpreted by Pancal et al. [4] using a film model. In the study by Morrison [3,5] the ammonia water vapours flowing down a vertical duct were condensed on a short horizontal tube. This simple geometry was selected to ensure that the transport mechanisms participating in the process could be studied without the complication of an entire condenser. The maximum ammonia vapor concentration investigated in this facility was 30 wt %, and much lower than that normally employed in a Kalina cycle.

Morrison's [3] observations did demonstrate that the condensate films which formed were neither a smooth nor continuous along the axis of the tube. The results from these tests also showed that at low ammonia concentrations there was an overall increase in the heat transfer rates from the vapor compared to that found for steam condensation. When the ammonia concentration was between 0.22 percent and 0.7 percent, the vapor heat transfer coefficients were increased by 13 percent. Morrison also proposed that the nonsmooth films were created by Marangoni effects at the interface between the diffusion layer and the condensate film. Some credence to this proposal was given in the subsequent work by Morrison et al. [6] which used small concentrations of methylamine, and the subsequent work by Deans et al. [7], which compared the condensation heat transfer enhancements found when small concentrations ammonia, methylamine and trimethylamine were added to steam. All of these tests were performed on the same test rig operating at similar conditions. Most of the thermal properties for these secondary vapors additives are similar, the main difference being the values for surface tension.

The work described below extends the earlier work on the condensation of ammonia water vapors by investigating the condensation rates found in a simple horizontal shell and tube condenser when there was a range of inlet ammonia concentrations. Particular attention was paid to the concentration range where the heat transfer enhancement found by Morrison was most likely to occur.

Experimental Method

The test condenser which is schematically shown in Fig. 1. was located in the closed stainless steel circuit that contained a circulation pump accumulator and evaporator. This circuit is described in greater detail by Morrison [5] and Philpott [8]. The condenser consists of a 700 mm long, 150 mm diameter, stainless steel shell and a horizontal, 20 mm diameter, stainless steel condenser tube arranged in a counter flow, single tube and shell pass configuration. The direction of the condensate flow was similar to the vapor flow and opposite to that of the coolant flow. The shell (vapor) side was divided into six sections by a series of baffles, which produced an approximate cross-flow vapor flow pattern. Vapor composition, temperature, and pressure were measured at several points along the condenser shell and sight glasses enabled the condensation process to be observed visually. The tube was instrumented with three thermocouples embedded in the tube wall equidistant along its length. During each test the tube was rotated through 360 deg to enable circumferential surface temperature measurements to be made. Thermistors positioned along the length of a twisted tape insert inside the tube measured the tem-

Contributed by the Heat Transfer Division for publication in the JOURNAL OF HEAT TRANSFER. Manuscript received by the Heat Transfer Division June 2, 2003; revision received May 24, 2004. Associate Editor: R. M. Manglik.

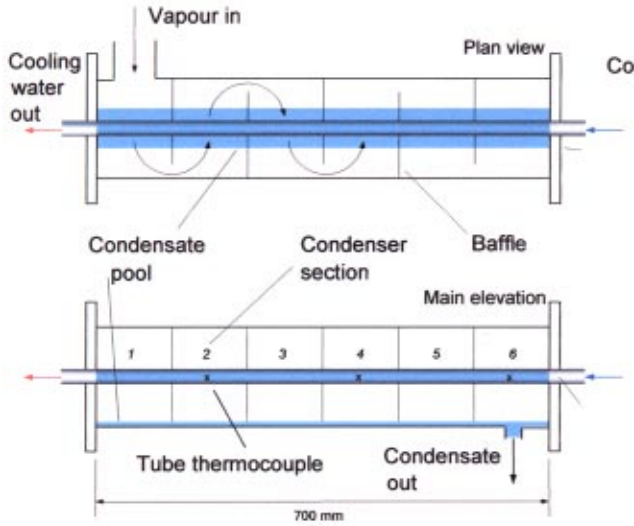

Features

- 150mm diameter stainless steel shell
- Sight glasses allow visual observation of the condensate surface
- Ports allow sampling of vapour temperature, concentration and pressure
- Tube rotates through 360 degrees.
- 20 mm outside diameter stainless steel tube.
- 2.5 mm thick tube wall.
- Tube wall embedded with thermocouples in condenser sections 2, 4 and 6.
- Internal twisted tape insert with cooling water temperature sensors.

Fig. 1 Schematic of ammonia-water test condenser

perature profile of the cooling water. This information when combined with the cooling water flow rate provided an estimate of the energy transferred to each section of the condenser tube. The ammonia concentrations at each section were measured by collecting samples of the vapor, cooling the sample and then titrating the solution. It should also be noted that this condenser operated as a total condenser and only a very small quantity of vapor was purged before each test to remove any accumulated noncondensable gas. The mass flow rate of the fluid circulating in the closed loop of the test circuit was obtained from flow meters in the condensate line.

During the condenser tests the tube wall temperature in condenser sections 2, 4, and 6 (see Fig. 1). Was measured at 30 deg intervals around the circumference of the tube. The average external tube surface temperature ($\overline{T}_{w,o}$) for each section was then calculated using the average tube wall temperature ($\overline{T}_w$), the corresponding cooling water energy balance (Q_{cw}) and an estimate of the thermal resistance between the tube wall thermocouple and the tube surface (R). (Eq. (1)). The average condensation heat transfer coefficient ($h_{w,o}$) for each section of the condenser tube was then calculated using Eq. (2). This method was verified by the experimental

$$\overline{T}_{w,o} = \overline{T}_w + \frac{Q_{cw}}{R} \tag{1}$$

$$\overline{h}_{w,o} = \frac{Q_{cw}}{A_{w,o} \cdot (T_{v,\infty} - \overline{T}_{w,o})} \tag{2}$$

results found during the commissioning tests using steam where there was good agreement with the predictions from the Nusselt's theory.

The experimental condensation heat transfer coefficients produced in the ammonia water tests were compared to both Nusselt's theory of condensation (Eq. (3)) and

$$\overline{h}_{\mathrm{Nu}} = 0.728 \cdot \left(\frac{k_l^3 \cdot g \cdot \rho_l \cdot (\rho_l - \rho_v) \cdot h_{fg}}{\mu_l \cdot (T_{v,\infty} - T_{w,o}) \cdot D} \right)^{0.25} \tag{3}$$

the numerical binary condensation model of the condenser. The theoretical results calculated using Nusselt's theory of condensation were evaluated using the properties for steam at the same vapor saturation temperature as that of the binary vapor and at a uniform outside wall temperature equal to the experimental average outside wall temperature.

The test data reduction scheme relies on accurate test measurement and all of the instrumentation used in the test program was calibrated against New Zealand Standard instruments. The errors associated with raw measurement and the derived data are given below:

Raw Data	Thermocouple temperatures	±0.2°C
	Thermistor temperatures	±0.02°C
	Cooling water flow rates	±0.004 kg·/s
	Ammonia concentration	±3 percent of measurement
Derived values	Energy Flows	±2.5 percent
	Heat Transfer Coefficients	±6 percent

All of the condensation experiments were carried out using a constant cooling water flow rate, cooling water inlet temperature and condenser heat load. The tests were characterized by relatively low bulk vapor velocities and low Reynolds numbers. Vapor velocities within the condenser ranged from near static to 0.6 m/s, producing vapor Reynolds numbers, based on tube diameter, between 30 and 400. In the Binary condensation tests the inlet vapor ammonia concentration was varied from 0 to almost 10 wt %. These tests were characterized by moderate liquid Prandtl numbers, $2 < \mathrm{Pr}_l < 5$, low modified liquid Jacob numbers, $0.02 < \mathrm{Ja}_l < 0.04$ and relatively low liquid Reynolds numbers, $20 < \mathrm{Re}_{D,l} < 60$. While the tests were concerned with the condensation of mixtures rather than pure vapors, the nondimensional numbers listed above indicate that Nusselt's analysis could be applied to the condensate film without consideration of interfacial shear stress, inertial forces and energy convection.

Model

The one-dimensional model of the condenser was based on a mass and energy balance within each of the six vapor-side sections. In each section the properties of the condensate pool and vapor were considered constant and the changing temperature of the coolant was incorporated by subdividing the tube in each section into three sequential segments and performing balances on each. A greater number of segments did not noticeably increase the accuracy and for most of the test simulations the change was less than 0.5°C per segment. The mass and energy transfer processes were driven by the condensation of the binary vapor mix-

ture at the tube surface and along with condensation/ammonia re-evaporation processes at the surface of the condensate they form the main components of the model.

The condensation model was based on the theory of Colburn and Drew [9] who considered the ''point'', or initial condensation of miscible binary vapours, on a vertical surface. Their model assumed that mass transfer existed only in the direction normal to the vapor-liquid interface and implied that the composition of the condensate was determined by condensation at that point alone. Furthermore, they postulated that at the vapor-liquid interface, the local liquid and vapor compositions could be approximated by static equilibrium conditions. They used the vapor side diffusional mass transfer resistance, derived from Ficks Law, together with the boundary conditions for the vapor film implied by the assumption of static equilibrium at the interface to derive the molar flux ($\dot{n}$) towards the condensate film (Eq. (4)).

$$\dot{n} = \frac{D_{12} c_v}{\delta_v} \cdot \ln \left| \frac{\frac{\dot{N}_1}{\dot{N}} - \omega_{v,\infty}}{\frac{\dot{N}_1}{\dot{N}} - \omega_{v,i}} \right| \tag{4}$$

The energy transferred at the condensate/vapor interface is the summation of the heat transferred by the sensible cooling of the vapor and the latent heat of condensation. This energy transfer is given by Eq. (5), which also includes the Ackermann correction factor (a). This energy transfer through the diffusion layer equals that conducted through the condensate film, Eq. (6). The temperature and composition at the vapor-liquid interface can then be determined by iteration of Eq. (5) and Eq. (6).

$$q = q_s + q_{lv} = h_v \cdot (T_{v,\infty} - T_i) \cdot \left[\frac{a}{1 - e^{-a}} \right] + h_{lv} \cdot \frac{D_{12} c_v}{\delta_v} \cdot \ln \left| \frac{\frac{\dot{N}_1}{\dot{N}} - \omega_{v,\infty}}{\frac{\dot{N}_1}{\dot{N}} - \omega_{v,i}} \right| \tag{5}$$

$$q = h_l \cdot (T_i - T_{w,o}) \tag{6}$$

A similar set of equations were used in the model to determine the energy balance in the condensate pool of each section. The mass transfer to the pool in each section was calculated from the global balance of vapor condensing on the pool surface, the addition of condensate from the tube above and the bulk re-evaporation of ammonia. The ammonia evaporation was required to maintain thermodynamic equilibrium with the vapor space. The initial mass fraction of the ammonia in the pool at entry to each section was equal to that leaving the previous section and it was further assumed that there were no concentration gradients in the pool.

The modeling of the vapor flows along the condenser was simplified because of the low vapor velocities and the ability to ignore the pressure drops between sections. In the last section of the condenser there is no exit for the vapor and consequently the mass flow rate of binary vapor entering the condenser was equal to the total flow of condensate from the condenser. This criterion was used as a check on the performance of the model. The implementation of this model depends on accurate property values for the ammonia water mixtures. The AWMix library subroutine [10] within an EES computer program was used to generate this data. A more complete description of the model together with further details of the experimental apparatus and procedures can be found in Philpott [8].

It should be noted that currently there is no complete theory to predict the heat transfer coefficients of disturbed binary condensate films. The model therefore predicted the condensate film heat transfer coefficient using Nusselt's theory, which presumes a smooth, laminar condensate film. This approach highlighted the difference between smooth and nonsmooth binary condensate film behavior.

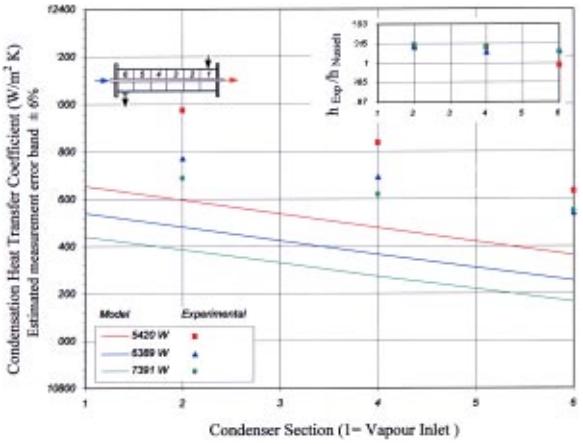

Fig. 2 Condensation heat transfer coefficient at various tube heat loads. (Inset shows experimental results relative to Nusselt analysis (Eq. 3).)

Commissioning

The condenser was commissioned using steam and the operating parameters for these tests were described earlier. Some of the results from these tests are presented in Fig. 2 where the results are presented to show the local convective heat transfer coefficients found when the condenser was tested at three different loads. These results demonstrate that the heat transfer coefficient is slightly higher at the cooling water outlet end of the tube, reflecting the higher tube surface temperature, and, hence, lower outside wall to vapor temperature difference. These trends follow the prediction from the Nusselt film condensation theory (Eq. (3)), where $\bar{h} \propto (T_s - \bar{T}_{w,o})^{-1/4}$. Figure 2 also shows that the condensation heat transfer coefficient decreases with increasing tube heat load due to the increase in the condensate film thickness that occurs with increasing heat flux.

There is good agreement between the experimental results and the prediction of both the Nusselt analysis (Eq. (3)) and the numerical model. The comparison with Eq. (3) is given in the insert in Fig. 2. The computer model of the condenser was used in these conditions by assuming that the ammonia inlet mass fraction was very low ($5*10^{-5}$) and the success of this comparison generally validates that the overall structure of the model.

Results and Discussion

In the ammonia-water condensation experiments the inlet vapor ammonia concentration was varied from 0 to almost 10 wt %. The vapor concentration increased along the condenser from inlet to condensate outlet and in this region the maximum mass fraction measured was 26 percent. In all of these tests the average outside tube wall temperatures was significantly below the bubble point of the mixture (>5°C). This along with the results from the numerical model indicated that local total condensation occurred along the length of the tube in all of the tests. The condition of local total condensation implied that the local condensate concentration and vapor-liquid interface temperature were equal to the bulk vapor concentration and bubble point temperature, respectively. Within this environment the pool of condensate in the bottom of the condenser acted to re-establish equilibrium conditions with the bulk vapor. During this process relatively high concentration ammonia vapor was emitted from the pool, enriching the bulk vapor stream with ammonia and producing a general increase in the bulk vapor ammonia concentration from vapor inlet to condensate out-

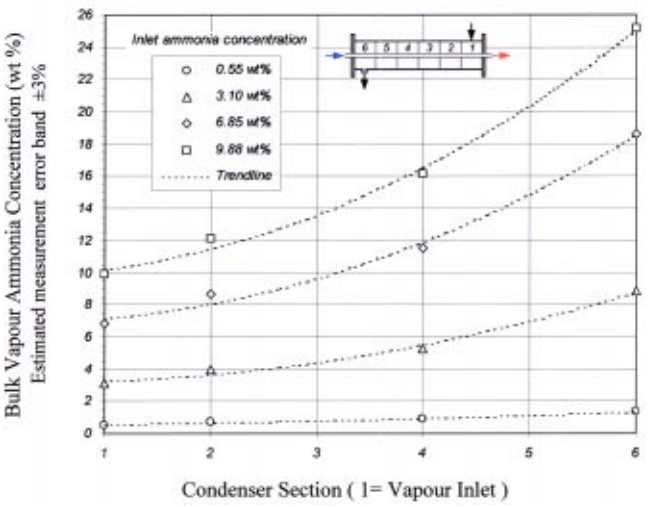

Fig. 3 Condenser bulk vapor ammonia concentration. (Note the Trend lines were derived from the numerical model and that they are depicted as a continuous line for clarity.)

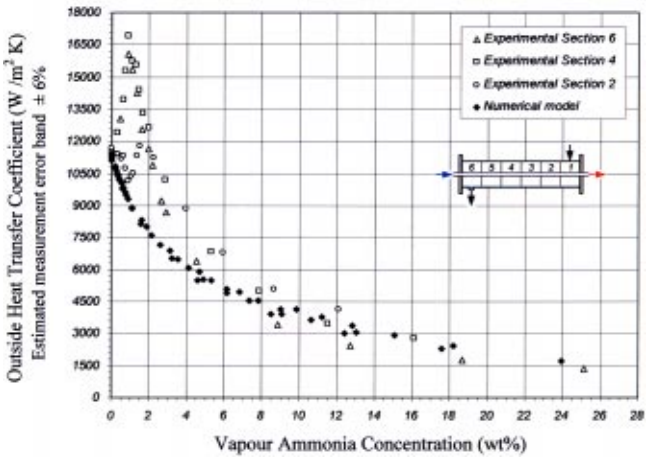

Fig. 5 Sectional condensation heat transfer coefficients

let. Figure 3 shows the increase in the vapor ammonia concentration from vapor inlet to condensate outlet, for the range of vapor inlet concentrations experimentally investigated.

When condensation takes place on a horizontal tube a distinct circumferential temperature gradient develops on the surface [11,12]. The magnitude of this variation largely depends on the ratio of the external and internal heat transfer coefficients. Within this experimental program the high thermal resistance of the 2.5 mm thick stainless steel tube wall produced a relatively low heat transfer coefficient between the outer tube surface and the bulk coolant. Thus for the steam tests and the ammonia water tests with the lowest concentration, a relatively strong temperature gradient was measured around the tube wall. As the ammonia concentration increased, the outside heat transfer coefficient was markedly reduced by the vapor diffusion layer that blanketed the tube. The circumferential tube wall temperature variation therefore tended to be reduced at high vapor ammonia concentrations, as shown in Fig. 4. Memory and Rose [11] have demonstrated that local variations in both surface temperature and heat flux have negligible effect on the mean heat transfer coefficient calculated at the average tube surface temperature. Consequently, all of the mean heat transfer coefficients found in this test program were calculated at the average tube surface temperature using the experimental method described earlier.

The experimental condensation heat transfer coefficients found in each section of the condenser are given in Fig. 5. where the general decrease in the coefficient with increasing ammonia concentration is evident. The values for the condensation heat transfer coefficient calculated using the numerical model are also superimposed on Fig. 5. At relatively high ammonia concentrations there is good agreement between the model's predictions and the experimental results. However at low concentrations the experimental heat transfer coefficients were generally higher than those predicted by the film model with a maximum difference of approximately 80 percent occurring at a vapor concentration of 0.9 wt % ammonia.

An alternative comparison of these results is given in Fig. 6 where the sectional condensation heat transfer results are compared with Nusselt's prediction for saturated steam calculated at the experimental conditions. It can be seen that when the vapor concentrations range between 0.3 and 2 wt % the experimental heat transfer coefficient was greater than that predicted by the Nusselt equation for condenser sections four and six by up to 34 percent. However, the heat transfer coefficient for section two of the condenser tube generally remained at or below the Nusselt prediction. This amomalous result was caused by a delay in the

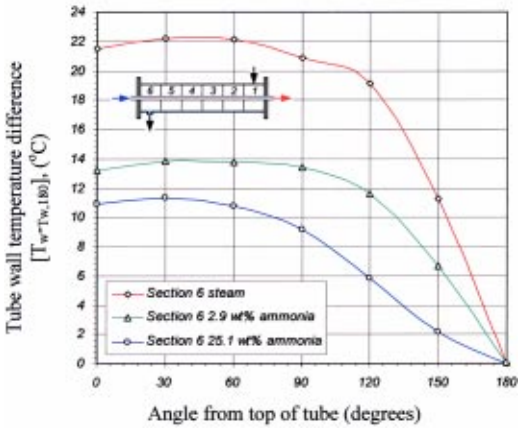

Fig. 4 Variation in tube wall temperature profile with ammonia concentration. (The wall temperature around the circumference of the tube has been normalized about the 180 deg tube wall temperature, i.e., $T_{w,\theta} - T_{w,\theta=180}$, to illustrate the tube wall temperature profile at various ammonia concentrations more clearly.)

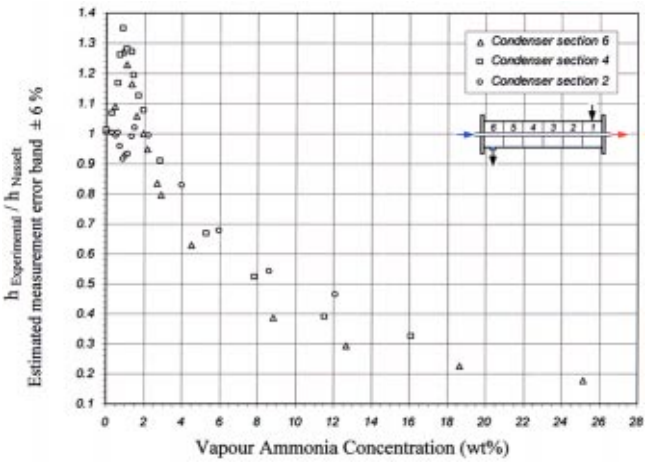

Fig. 6 Ratio of sectional condensation heat transfer coefficient to Nusselt's prediction

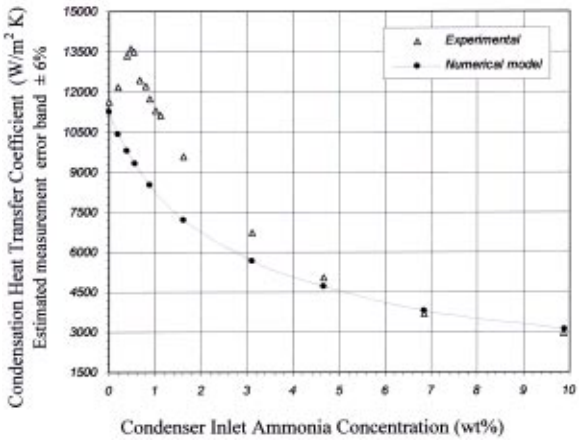

Fig. 7 Average tube condensation heat transfer coefficient

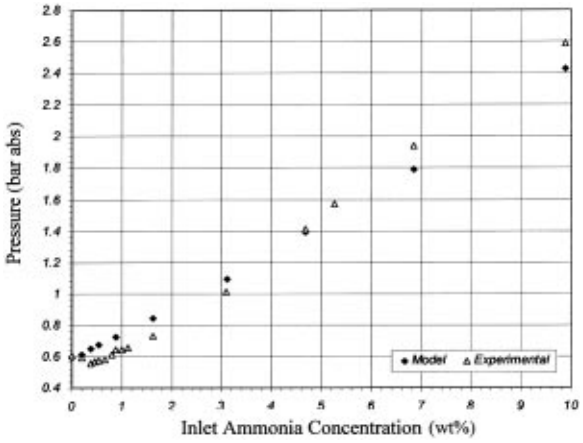

Fig. 9 Condenser pressure variation with inlet vapor ammonia concentration

axial growth of disturbed film in the early sections of the condenser. Condensate film disturbances were observed in section 2 at these ammonia concentrations; however, they preferentially developed at the edge of this section and therefore did not influence the thermocouple embedded in the tube wall near the center of the section. The measured enhancement in the condensation heat transfer coefficient at low ammonia concentrations was comparable with the earlier research of Morrison [3,5]. Morrison recorded a maximum enhancement of 13 percent at an ammonia concentration of 0.88 wt %.

The overall tube condensation heat transfer coefficients for the condenser found at various vapor inlet concentrations is given in Fig. 7. The heat transfer coefficients were calculated by averaging the sectional heat transfer coefficients on a tube area basis. The results again demonstrate that the condensation heat transfer coefficient generally decreased with increasing concentration and that at the highest ammonia concentrations investigated the numerical model agreed well with the experimental results. When the ammonia concentration of the inlet vapor was low the experimental values were markedly greater than those predicted by the model, with a maximum increase of approximately 40 percent occurring at a vapor concentration of 0.5 wt % ammonia.

Figure 8 provides a comparison of the overall condensation heat transfer coefficient results with Nusselt's prediction for saturated steam at the experimental conditions. The results show that when the ammonia vapor concentrations range from 0.2 to 0.88 wt % the condensation heat transfer coefficient exceeds the values predicted by the Nusselt solution. The maximum enhancement of this coefficient 14 percent, develops when the vapor has an ammonia concentration of 0.47 wt %. For inlet vapor concentrations greater than 0.88 wt % the ratio of the experimental condensation heat transfer coefficient to that predicted by Nusselt was less than unity, with a minimum ratio occurring at the greatest inlet concentration.

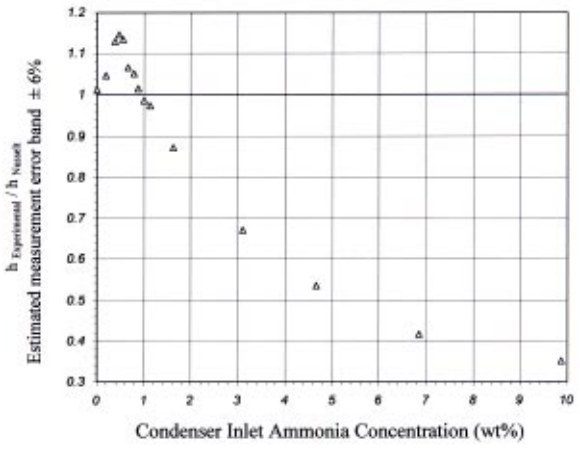

Fig. 8 Ratio of overall condensation heat transfer coefficient to Nusselt's prediction

The changes in the value of overall condensation heat transfer coefficient were reflected in changes to the condensers pressure, as shown in Fig. 9. In the region of enhanced heat transfer (0.2–0.7 wt % ammonia) the condenser pressure was slightly below that recorded for steam, while further increases in the inlet ammonia concentration produced a steady increase in the condenser pressure.

The overall thermal resistance between the between the bulk vapor and the wall is defined by Eq. (7) and the subdivision of this resistance into its components

$$R_o = \frac{(T_v - T_{w,o})}{q} \tag{7}$$

namely the vapor and condensate film resistances provide further insight into the condensation process. It was established earlier that local total condensation occurred in all of the ammonia water condensation tests and therefore the vapor-liquid interface temperature could be assumed to be the bubble point temperature of the mixture. When the interface temperature is known the individual resistances of the vapor and condensate films could be estimated using Eq. (8) and Eq. (9), respectively.

$$R_v = \frac{(T_v - T_i)}{q} \tag{8}$$

$$R_l = \frac{(T_i - T_{w,o})}{q} \tag{9}$$

Figure 10 shows the resistances of the vapor and condensate films as a function of vapor ammonia concentration for both the experiments and the numerical model. The values presented in the figures are the product of the resistance and the outside surface area of the tube section and are therefore equivalent to the inverse of the respective film heat transfer coefficients. These results show that the resistance of the vapor film was strongly dependent on the bulk vapor ammonia concentration, increasing rapidly with increasing ammonia concentration. At the lowest ammonia concentrations investigated (0.3 wt %) the vapor film resistance was almost an order of magnitude less than the condensate film heat

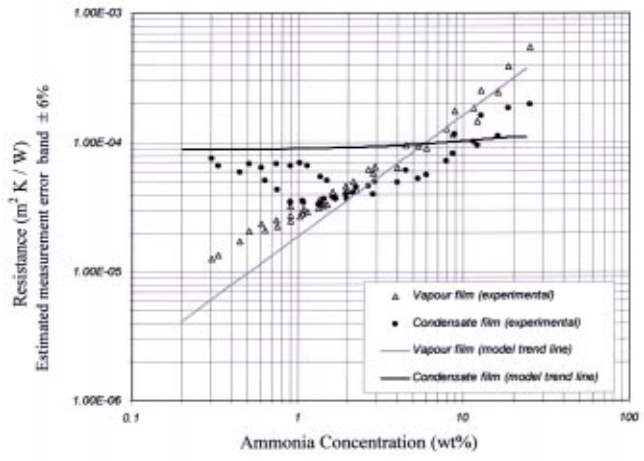

Fig. 10 Vapor and condensate film resistances

transfer resistance, while at concentrations of 1–4 wt % they were of a similar order. At higher ammonia concentrations the vapor film resistance began to dominate.

While the model was in good agreement with the experimental vapor film resistance the trends were quite different for the condensate film resistance. This was due to the fact that the model used Nusselt theory (Eq. (5)) to describe a smooth, laminar condensate film when the actual film was generally disturbed. The series of tests described by Deans [7] has shown that surface tension gradients at the vapor condensate interface are the most likely cause of these disturbances. The disturbances evolve when the surface tension in a local region increases with increasing film thickness, liquid is drawn from surrounding regions that are thinner and have lower surface tension. This reinforces the original perturbation, resulting in a stable but unevenly thick film that can be observed by the naked eye. This situation generally arises when the more volatile component of a condensing binary vapor mixture has the lower surface tension. This is certainly the case for ammonia water mixtures where liquid ammonia has a surface tension less than a tenth of that for water at 100°C.

The films observed in these ammonia water condensation tests could simply be classified as either smooth or turbulent banded in nature. However, within the turbulent banded classification there was a high degree of variation ranging from thin fast moving bands with some evidence of the beginnings of pseudo-droplet condensation to very broad slow moving bands. Figure 11 shows the condensate film at three points along the condenser for various ammonia concentrations.

The appearance of the condensate film was connected to the value of the film's thermal resistance. At low ammonia concentrations, where the film was relatively smooth (i.e., section 2 when the vapor concentration was less than 1 wt %), the experimental condensate film resistance was similar to the values predicted by the numerical model. When the ammonia vapor concentration increased the intensity of the film disturbances also appeared to increase and the experimental condensate film resistance generally decreased. The lowest film resistances were found to correspond to the most vigorous turbulent banded films observed (see for example Fig. 11(c)). This enhancement in the condensate film heat transfer is examined in further detail by Philpott and Deans [13]. Further increases in the vapor ammonia concentration tended to produce less disturbed condensate film behavior (see Figs. 11(i) and 11(l)) resulting in relatively high condensate film resistances at high ammonia concentrations ($<$10 wt %). In this region the thermal resistance of the condensate film was less than that of the diffusion layer, and the effects that the disturbed condensate film created, were minimalized. It is this region that the film models normally used to analyze binary condensation become realistic.

It is notable that the condensate film heat transfer resistance became greater than that calculated by the model for a smooth film when the concentration was greater than 10 wt %. It seems somewhat of a paradox that disturbed condensate films could display higher heat transfer resistances than smooth films, however it is postulated that circumferential surface tension gradients may have caused a general thickening of the condensate film around the tube and hence an increase in the resistance of the condensate film. Although, to the best of the author's knowledge, this phenomenon has not previously been reported during binary condensation, the thickening of binary liquid films flowing down distillation columns has been attributed to surface tension gradients [14,15].

A further point of interest is that the development of condensate film disturbances was somewhat delayed in the early sections of the condenser. This can clearly be seen in Fig. 6, where the heat transfer ratio for section 2 of the condenser remained relatively low at ammonia concentrations where peak enhancements occurred in condenser sections 4 and 6. Condensate film disturbances were observed in section 2, but at these low ammonia concentrations the disturbances were restricted to the edge of the section (see Figs. 11(a) and 11(d)). At low ammonia vapor concentrations the condensate film immediately above the thermocouple appeared smooth and consequently the average tube surface temperature measured in this section may not be a representative value. Thus, due to the geometry of the instrumentation, the experimental results tended to exaggerate the seeming lack of disturbances in section 2 of the condenser. It should be noted that the onset of Marangoni disturbances was not he focus of the present research and the test rig was therefore not suitably instrumented to give an insight into the mechanisms at work during the development of the Marangoni effect during binary condensation. Nevertheless, why the development of the condensate film disturbances was retarded in the early sections of the condenser is unknown. The onset of the Marangoni effect and the effect of thermal driving force during the condensation of ammonia water mixtures are currently being studied in detail by Korte et al. [16,17].

Conclusions

The commissioning of the simplified shell and tube test condenser was conducted using steam. The results from these commissioning tests were successfully compared with both the Nusselt equation and parts of the binary condensation model that was developed to help interpret the test data. When weak ammonia water vapors were injected into the condenser the test results generally show that the condensation heat transfer coefficient is lower than that found for steam and that this coefficient normally decreases with increasing ammonia concentration. When the bulk ammonia concentration is greater than 18 percent the heat transfer coefficient is only 20 percent of that predicted for steam at the same operating condition. At these high concentrations the results from the computer model are similar to those found in the tests. This agreement suggests that the use of a film model will become a realistic approach to the modelling of ammonia-water condensers at higher concentrations ($<$10 wt %). In these regions the diffusion layers thermal resistance will be larger than that associated with the condensate film. Some confidence in the model can be gained from its predictions regarding the increase in the ammonia concentration along the length of the unvented condenser.

The condensate films that evolved in most of the tests appeared to have a disturbed surface. At very low ammonia concentrations the films were less disturbed but they were not as smooth as the films found when steam condenses. It is believed that the disturbed films are responsible for the enhanced heat transfer rates that develop at low ammonia vapor concentrations. When the vapor's ammonia concentration is less than 2 percent, the experimentally found heat transfer coefficients are greater than those found for steam. These coefficients were enhanced by 34 percent

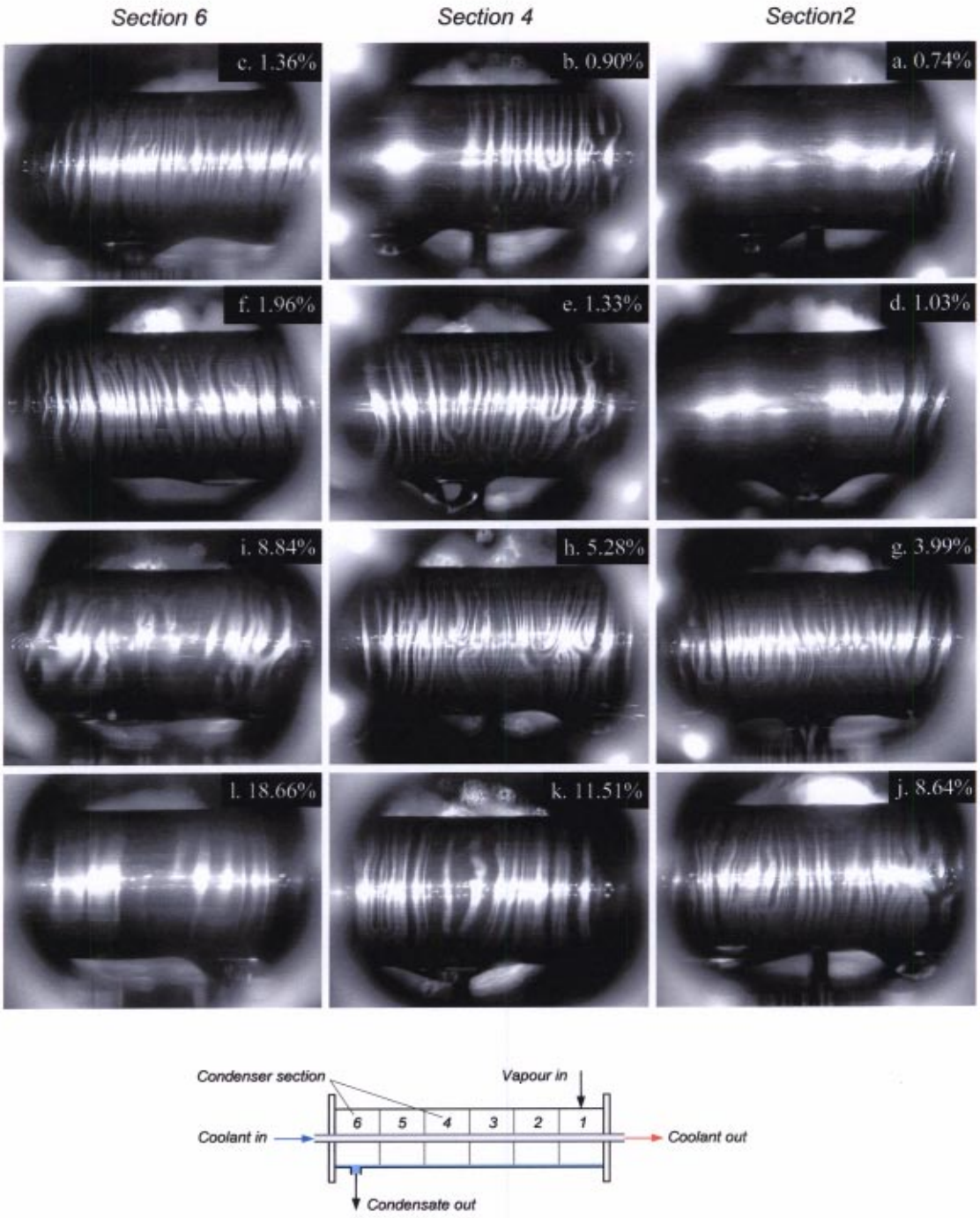

Fig. 11 (a–l) The condensate film at various vapor ammonia concentrations and positions within the condenser (left=section 6, middle=section 4, right=section 2)

when the ammonia concentration was 0.9 wt %. The source of these disturbances is believed to be surface tension instabilities at the vapor/condensate interface.

The analysis of the test conditions confirmed that total local condensation took place on the condensate surface. It is therefore possible to identify the component vapor and film resistance's that developed in each test, assuming that the condensate film was ''idealized'' as smooth and continuous. At low concentrations (>5 wt %) the computer model demonstrated that condensate film will be the dominant resistance. When the vapors ammonia concentration is higher than this value the resistance associated with the vapor film will become more important and this is the condition normally considered in binary condensation. When the vapor and condensate thermal resistance values are derived from the experimental results the values found for the condensate film resistance was lower than that predicted for the ''idealized'' binary mixture. These reduced values support the argument that the disturbed film is responsible for the enhanced rates of heat transfer and the description assists in defining the limited region of the enhancement.

Nomenclature

a = Ackermann factor,
A = area, m^2
c = molar concentration, mol/m^3
D_{12} = Diffusion coefficient, m^2/s
g = gravitational acceleration (9.81), m/s^2
h = heat transfer coefficient, $W/m^2\,K$
h_{fg} = latent heat of condensation (steam), kJ/kg
h_{lv} = latent heat of condensation (binary mixture), kJ/kg
Ja = Jacob number
k = conductivity, W/m K
$\dot{n}$ = molar flux relative to fixed axes, $mol/m^2\,s$
$\dot{N}$ = molar flow rate, mol/s
Pr = Prandtl number
Q = total heat transfer, W
q = heat flux, W/m^2
R = thermal resistance, K/W
Re = Reynolds number
T = temperature, K
wt % = weight percent

Greek Symbols

δ = film thickness, m
ρ = density, kg/m^3
μ = viscosity, $N\,s/m^2$
ω = molar fraction, mol/mol

Superscripts and subscripts

$\bar{}$ = average
w = wall
o = outside
cw = cooling water
Nu = according to Nusselt theory
l = liquid
v = vapor
∞ = bulk condition
i = interface
s = sensible heat

References

[1] Kalina, A. I., 1984, ''Combined Cycle With Novel Bottoming Cycle,'' ASME J. Eng. Gas Turbines Power, **106**, pp. 737–742.
[2] Domingo, N, Chen, F. C., and Murphy, R. W., 1992, ''Ammonia Water Mixture Experiments,'' internal report, Oak Ridge National Laboratory, TN.
[3] Morrison, J. N. A., and Deans, J., 1997, ''Augmentation of Steam Condensation Heat Transfer by Addition of Ammonia,'' Int. J. Heat Mass Transfer, **40**, pp. 765–772.
[4] Panchal, C. B., Kuru, W., Chen, F., Domingo, N., and Huang Fu, E., 1997, ''Experimental and Analytical Studies of Condensation of Ammonia Water Mixtures,'' AIChE Symp. Ser., **93**, pp. 239–244.
[5] Morrison, J. N. A., 1996, ''The Condensation of Ammonia-Water Vapours on a Horizontal Tube,'' Ph.D. thesis, The University of Auckland, New Zealand.
[6] Morrison, J. N. A., Philpott, C., and Deans, J., 1998, ''Augmentation of Steam Condensation Heat Transfer by Addition of Methylamine,'' Int. J. Heat Mass Transfer, **41**, pp. 3679–3683.
[7] Deans, J., Korte, C., and Dunstall, M., 2001, ''The Comparison of Steam Condensation Rates When There are Low Concentrations of Ammonia, Methylamine and Trimethylamine in Vapor,'' *Experimental Heat Transfer, Fluid Mechanics and Thermodynamics 2001 Conference*, Pisa.
[8] Philpott, C., 2003, ''The Condensation of Ammonia-Water Mixtures in a Horizontal Shell and Tube Condenser,'' Ph.D. thesis, The University of Auckland, Auckland, New Zealand.
[9] Colburn, A. P., and Drew, T. B., 1937, ''The Condensation of Mixed Vapors,'' Trans. AIChE, **33**, pp. 197–212.
[10] Tillner-Roth, R., and Friend, D. G., 1998, J. Phys. Chem. Ref. Data, **27**, pp. 63–96.
[11] Memory, S. B., and Rose, J. W., 1991, ''Free Convection Laminar Film Condensation on a Horizontal Tube With Variable Wall Temperature,'' Int. J. Heat Mass Transfer, **34**, pp. 2775–2778.
[12] Fujii, T., 1992, ''Overlooked Factors and Unsolved Problems in Experimental Research on Condensation Heat Transfer,'' Exp. Therm. Fluid Sci., **5**, pp. 652–663.
[13] Philpott, C., and Deans, J., 2004, ''The Enhancement of Steam Condensation Heat Transfer in a Horizontal Shell and Tube Condenser by Addition of Ammonia,'' Int. J. Heat Mass Transfer, **47**, pp. 3686–3693.
[14] Wang, K. H., Ludviksson, V., and Lightfoot, E. N., 1971, ''Hydrodynamic Stability of Marangoni Films: II. A Preliminary Analysis of the Effect of Interphase Mass Transfer,'' AIChE J., **17**, pp. 1402–1408.
[15] Ludviksson, V., and Lightfoot, E. N., 1968, ''Hydrodynamic Stability of Marangoni Films,'' AIChE J., **14**, pp. 620–626.
[16] Korte, C., Dunstall, M. G., and Deans, J., 1999, ''Onset of the Marangoni Effect During Condensation of Ammonia-Water Mixtures,'' *Two-Phase Flow Modelling and Experimentation Conference*, Pisa, pp. 405–410.
[17] Korte, C., Deans, J., and Dunstall, M. G., 2000, ''Onset of the Marangoni Effect During Condensation of Ammonia-Water Mixtures—Effect of Temperature Driving Force Variation,'' 3rd *European Thermal Sciences Conference*, Heidelberg, pp. 905–910.

A Dual-Scale Computational Method for Correcting Surface Temperature Measurement Errors

T. C. Tszeng

G. F. Zhou

Department of Mechanical, Materials and Aerospace Engineering, Illinois Institute of Technology, Chicago, IL 60616

The present paper addresses the measurement errors in temperature due to the effects of surface-mounted temperature sensors like thermocouples. Heat conduction into or from the installed thermocouple wires can alter the temperature at the thermocouple junction as well as in its immediate vicinity. As a result, the emf appearing at the thermocouple terminals does not correspond to the actual surface temperature. In this paper, we present a dual-scale computational method that can be used to calculate the transient temperatures at the multiple thermocouple junctions during heating or cooling of an object. The basis of the method is a thermocouple submodel embedded in a FEM model for the parent object. The numerical results of the dual-scale computational model are compared with that of the conventional FEM models as well as the analytical solutions available. This paper also discusses the characteristics of surface-mounted thermocouples in a range of configurations. [DOI: 10.1115/1.1773585]

Keywords: Heat Transfer, Measurement Techniques, Numerical Methods, Thermocouples

Introduction

Surface-mounted thermocouple installation is a very convenient technique to obtain the surface temperature [1,2]. Interior temperatures are usually used in the inverse heat transfer calculation for determining the surface heat transfer coefficients of an object in heating or cooling. [1–11]. Minimum time lagging and therefore better solution stability can be achieved when surface temperatures are used [1,4–11]. However, there are several important issues that need to be resolved for surface-mounted thermocouples to ensure that they produce accurate temperature measurements. To facilitate the discussion, it is important to recognize that thermocouples can be installed on the surface in at least two common configurations; namely bead-type junctions and the intrinsic junction (Fig. 1). In the latter approach two dissimilar thermocouple wires are usually spot-weld directly onto the surface; with the spacing between the junctions ranging between one to two wire diameters (Saraf [1], Park et al. [3]). Since the junctions lie directly on the object surface, the temperature appearing at the thermocouple junction is usually thought to be the actual surface temperature. Nonetheless there are errors in the measured temperature using intrinsic or bead junctions [5,12,13]. Essentially, heat conduction into or from the attached thermocouple wires can alter the temperature at the thermocouple junction as well as in its immediate vicinity. It is believed that such error is a more serious problem in applications involved high rate of heating or cooling. For instance, the high heating/cooling rate in laser processing and dilatometry tests can be as high as a thousand degrees per second. The accuracy of measured temperature is important for assessing the rapid microstructural changes [14].

A number of methods and simplifications have been utilized in modeling the transient thermal response of surface-mounted thermocouples [13,15–18]; a review is furnished in [5]. One of the authors developed an embedded submodel for calculating the transient temperature at the intrinsic thermocouple junction [5]. The present paper reports the study on general characteristics of the surface-mounted thermocouples based on a combination of the thermocouple submodel and the FEM modeling in a dual-scale computational approach. The numerical results of the dual-scale computational model are compared with those of the conventional FEM models as well as the analytical solutions available.

Contributed by the Heat Transfer Division for publication in the JOURNAL OF HEAT TRANSFER. Manuscript received by the Heat Transfer Division January 8, 2003; revision received April 20, 2004. Associate Editor: A. F. Emery.

Dual-Scale Computational Method

A schematic of intrinsic surface-mounted thermocouples is shown in Fig. 1. In practice, thermocouple wire is usually very thin (with a radius typically less than 0.5 mm) compared to the radius of curvature on the parent object's surface. Therefore, an axi-symmetric model is a good approximation to the heat transfer phenomena in the thermocouple wire and the material in the vicinity of thermocouple junction. Because of the small size of the thermocouple wire, the parent object does not feel the existence of the thermocouple except in the immediate vicinity of the junction. Indeed, the heat transfer analysis in the parent object is carried out without considering the existence of thermocouples. In the immediate vicinity of the junction, the multi-dimensional nature of the heat transfer becomes more apparent.

The calculation of the detailed multi-dimensional distribution of temperature close to the junction calls for an analysis in a region whose size is comparable to the length scale of the junction. One such model of small length scale is depicted in Fig. 2, which is one half of an axisymmetric model. The model consists of two portions; the first one is the body of thermocouple wire and the second portion is a finite volume of the parent object in the vicinity of the junction. When the parent object is subjected to a changing temperature, so is the submodel. The top surface of the submodel (parent object and the thermocouple wire) is exposed to the environment (see Fig. 2). As discussed earlier, the temperature at a location away from the immediate vicinity of the junction is assumed not to be significantly affected by the presence of the thermocouple. Thus, the material along the lower and right boundaries of the model should have the same temperature as that in the object assuming no disturbance from the thermocouple. These undisturbed temperatures can be calculated easily with the FEM model if the rate of heat transfer on the surface of parent object is known. The appropriate boundary conditions are also shown in Fig. 2.

The dimensions of the submodel are normalized by the radius of the portion of parent object in the submodel, as shown in Fig. 2. The actual size of the submodel is determined by scaling on the

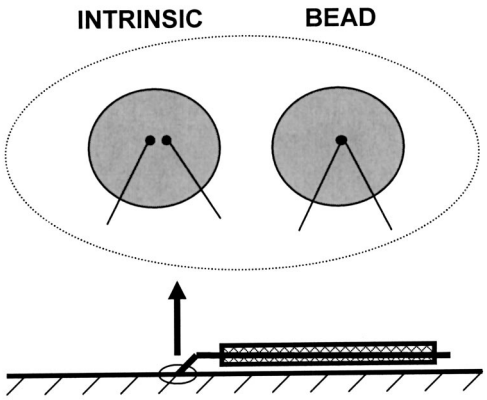

Fig. 1 Two types of junction for installing surface-mounted thermocouples

diameter of the thermocouple wire. The submodel is superimposed at the actual location of surface-mounted thermocouples on the parent object that does not include thermocouple in the FEM mesh. Since the heat conduction in the thermocouple affects the local temperature distribution, care must be taken to properly account for changes in thermal properties of both the parent material and the thermocouple. It needs to be remarked that the thermocouple submodel can be placed at any location of the surface-mounted thermocouples on the parent object; it does not necessarily have to lie along the symmetric axis of the parent object. Therefore, the proposed computational model has the great flexibility of considering the multiple surface-mounted thermocouple wires in two- or three-dimensional analysis. The computational procedure follows the standard FEM time stepping technique in which the time domain is subdivided into many small steps. At the beginning of each time step, the temperature field throughout the parent object in the absence of the thermocouples is obtained by solving the heat transfer equations by FEM. The temperatures in the thermocouple submodel(s) are then obtained from the parent object by spatial interpolation. Actually, only those boundary nodes with temperature-specified boundary conditions will carry the interpolated temperatures. If applicable, the time-varying heat transfer coefficient appears on the outer surface of the thermocouple submodel as well as of the parent object. A separate FEM calculation is then carried out to determine the temperature field in each of the thermocouple submodel(s). At the completion of the current step, the solutions for both the parent object and the thermocouple submodel(s) are saved for the next time step. The computational algorithm is implemented in the FEM-based software system HOTPOINT [19].

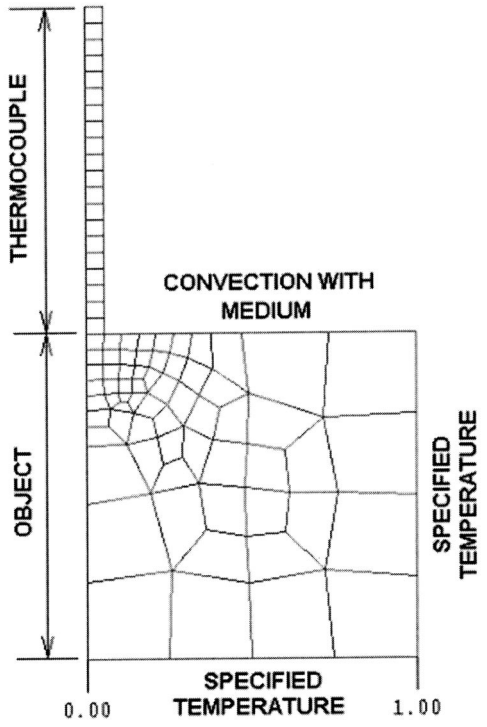

Fig. 2 Embedded computational model for calculating the temperature field in and around the thermocouple

Evaluation of the Developed Method

In this section, the developed dual-scale computational method is evaluated by comparing the numerical results with the analytical solutions available in the literature. Keltner and Beck [16] obtained analytical solutions to the transient heat transfer problems of an intrinsic thermocouple attached to a substrate that experiences a uniform temperature change. The thermocouple is perfectly insulted on lateral surface. The surface onto which the thermocouple is installed is considered to be adiabatic [16]. The solution of temperature at the junction, T_J, was obtained when the entire object (substrate) experiences a unity step temperature change. For the dimensionless time $\tau=\alpha_1 t/a^2 \geqslant 0.1$, the solution of temperature, T_J, at the junction is given in [16] by $\Phi(\tau)=1-C_1 rerfc(C_2\sqrt{\tau})$, where $C_1=\beta/(8/\pi^2+\beta)$, $C_2=4/(8/\pi+\beta\pi)$, $rerfc(x)=\exp(x^2)(1-\mathrm{erf}(x))$, $\beta=K/\sqrt{A}$, α=thermal diffusivity of substrate, a=thermocouple wire radius, $K=k_2/k_1$ (where k=thermal conductivity) and $A=\alpha_2/\alpha_1$. Subscripts 1 and 2 represent parent object (substrate) and thermocouple, respectively.

In order to evaluate the dual-scale computational method against the above-mentioned analytical solutions, we examine the case similar to that mentioned above [16], in which the top surface is adiabatic. However, instead of the entire substrate, only the bottom surface is assumed to experience a step change of temperature. In the case of constant thermal diffusivity, the temperature at the junction is given in [20] by the use of Duhamel's integral:

$$T_J(\tau)=D(0)\Phi(\tau)+\int_0^\tau \Phi(\tau-s)\frac{dD(s)}{ds}ds, \qquad (1)$$

where D is the temperature disturbance at the junction; Φ is the unsteady temperature at the junction resulting from a stepwise unit disturbance (step response function). The step response Φ is given in previous paragraph for the dimensionless time $\tau=\alpha_1 t/a^2>0.1$. The temperature disturbance, D, is obtained by considering a step temperature change appears on both surfaces of a plate of thickness $2L$. Assuming constant thermal conductivity and constant heat capacity, the temperature $T(x,t)$ at any location x measured from the centerline of the plate is given by [20]:

$$\frac{T(x,t)-T_s}{T_o-T_s}=2\sum_{n=0}^{\infty}\frac{(-1)^n}{\lambda_n L}e^{-\alpha\lambda_n^2 t}\cos\lambda_n x, \qquad (2)$$

where T_o and T_s are, respectively, the initial (uniform) and surface temperature on the plate; α=thermal diffusivity, $\lambda_n L=(2n+1)\pi/2$, n=0, 1, 2, 3, etc. The junction temperature $T_J(\tau)$ is thus obtained by replacing the disturbance function D in Eq. (1) by the temperature $T(0,t)$, of Eq. (2).

In the following numerical calculations, the bottom surface of the thin plate is assumed to experience a step change of 100°C in temperature. The thermocouple wire radius a=0.1 mm, and the plate thickness is 3 mm. The properties are $k_1=k_2=10$ w/m/k, $(\rho c)_1=(\rho c)_2=1\times10^6$ J/m^3/k; which corresponds to $\beta=1$. Fig-

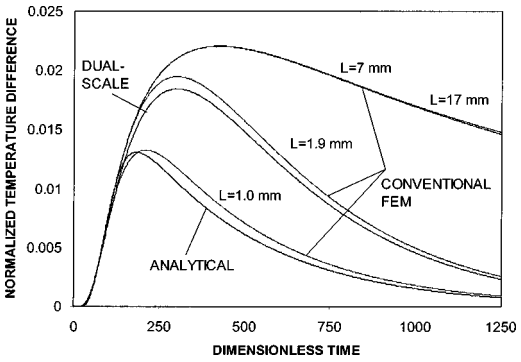

Fig. 3 Difference between the undisturbed surface temperature and calculated temperature at junction, ($T_U - T_J$). The calculated temperature normalized by the maximum temperature (100°C), and the dimensionless time is given by $\tau = \alpha_1 t / a^2$. The bottom surface of the thin plate experiences a step change of 100°C in temperature. The thermocouple wire radius a=0.1 mm, and the thickness is 3 mm. $k_1 = k_2 = 10$ w/m/k, $(\rho c)_1 = (\rho c)_2 = 1 \times 10^6$ J/m^3/k. The conventional FEM model is shown in Fig. 4.

ure 3 shows the differences between the undisturbed surface temperature (T_U) and that at the junction (T_J) as computed by the analytical solution, Eqs. (1) and (2) and the ''conventional FEM'' where the temperature is normalized by the temperature change of 100°C at the bottom surface of the substrate. In addition to the analytical solution, this figure shows the results from the conventional FEM model for three different lengths (L) of thermocouple. A finite element analysis that incorporates the detailed thermocouple model with the parent material will be referred to as a ''conventional FEM'' model throughout the present paper. The grid of one such FEM models, corresponding to a thermocouple length $L = 1.9$ mm, is shown in Fig. 4(a) where a fine mesh is used in the vicinity of thermocouple junction for better solution

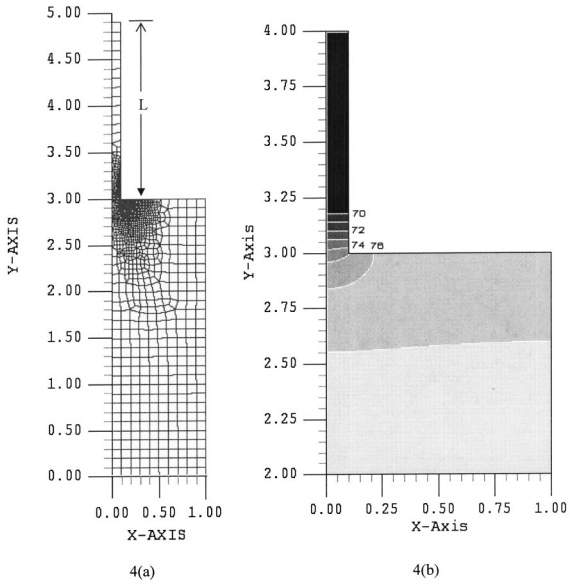

Fig. 4 Conventional FEM mesh for half of an axisymmetric model that features a thermocouple of radius $a = 0.1$ mm on a substrate whose thickness is 3 mm; length of thermocouple $L = 1.9$ mm. The base of the substrate is brought to 100°C at $t = 0$; other surfaces are adiabatic. Thermophysical properties are the same as that of Fig. 3. The contour plot is the temperature distribution in the vicinity of junction at a normalized time $\tau = 400$.

accuracy. The thermocouple junction is represented by the element edge between the thermocouple stem and the parent object. It is observed that the temperature is actually not constant along this junction, Fig. 4(b). For the purpose of comparison, an average temperature along this element edge is considered to be the thermocouple junction temperature.

These results in Fig. 3 indicate that the difference between T_U and T_J increases during the initial stage of heating; and decreases in the later stage. As seen in the figure, the conventional FEM result for a thermocouple length of $L = 1$ mm agrees well with the analytical result in which the thermocouple length is not considered. The agreement between the analytical solution and the conventional FEM model for this very short length is taken as justification for benchmarking the dual-scale FEM model against the conventional FEM results.

For a thermocouple of 0.2 mm diameter, the dual-scale FEM model of Fig. 2 has a thermocouple length (L) of 1.9 mm. The calculated difference between T_U and T_J by using the developed dual-scale FEM model is shown in Fig. 3. The result agrees well with the result from conventional FEM model when the same thermocouple length of 1.9 mm is used. Given that the differences between the undisturbed surface temperature (T_U) and that at the junction (T_J) are indeed very small (about 2°C out of 100°C) in the considered case, the dual-scale FEM model is judged to be sufficiently accurate to investigate the effects of thermocouple attachment.

Figure 3 also indicates that the difference between T_U and T_J increases with increasing length L. However, at large lengths L, further increases of L do not lead to a greater effect since the behavior of the thermocouple leads is approaching that of an infinitely long fin. Thus the influence is greatest for short lengths—as shown, there is essentially no difference between the cases of $L = 7$ mm and 17 mm.

The case in the following is similar to that of Fig. 3 but closer to actual applications. The initial temperature is 20°C in a specimen of 3 mm thickness, and the temperature on the opposite side of the adiabatic surface is brought to 1000°C suddenly. At the end of a holding period of one (1) second, the surface temperature is brought back to 20°C. The thermal properties of AISI 4140 steels are taken from [5]. The thermocouple wires are assumed to have the same thermophysical properties as that of the base specimen materials. Thermocouple wire is assumed to be perfectly insulated. By using the dual-scale computational method, the calculated temperature on the adiabatic surface as well as that on the thermocouple junctions is shown in Fig. 5(a) for thermocouple wire of 0.30 mm diameter (0.15 mm in radius). As indicated in the figure, the temperature at thermocouple junctions falls behind the changing temperature on the adiabatic surface. That is, the junction temperature is lower than the undisturbed surface temperature in heating, and the reverse is true in cooling. The error due to surface-mounted thermocouple (the temperature difference between thermocouple junctions and the adiabatic surface) are shown in Fig. 5(b). Several different thermocouple wire radii are considered, ranging between 0.02 mm and 0.15 mm. The discrepancy grows at a larger thermocouple wire diameter. For a thermocouple wire size of 0.15 mm in radius, the discrepancy in temperature can be as large as 30°C in the case study. It is thus concluded that smaller thermocouple size is desirable for lower measurement error.

Characteristics of Surface-Mounted Thermocouples

In this section, the developed dual-scale computational method is used to examine the issues regarding characteristics of surface-mounted thermocouples; namely, (1) thermocouple wire diameter; and (2) heat convection on thermocouple surface. Specifically, we examine the situation in which the surface of thermocouple is exposed to an environment in which there is heat exchange between the thermocouple and the environment. The heat flux, q,

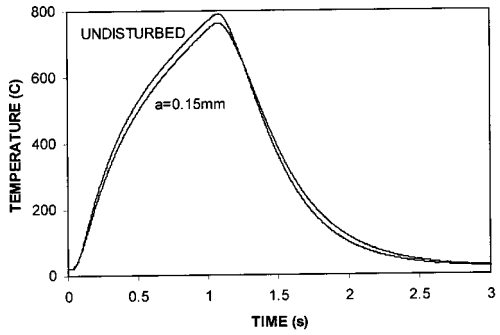

5(a)

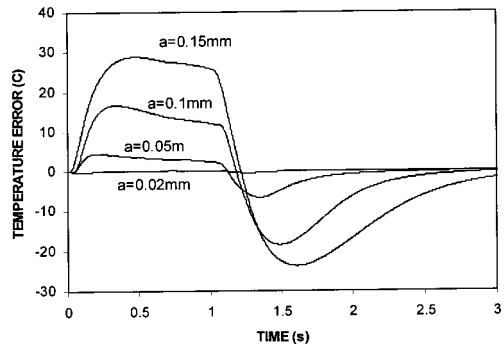

5(b)

Fig. 5 Calculated histories of temperature for rapid heating, short holding and rapid quenching from the bottom surface of the thin plate of 3 mm thickness. The thermocouple is a Chromel. Actual thermophysical properties of 4140 steel [5] are used. (*a*) The calculated temperature for wire radius of 0.15 mm; (*b*) The error in temperature as predicted by dual-scale FEM.

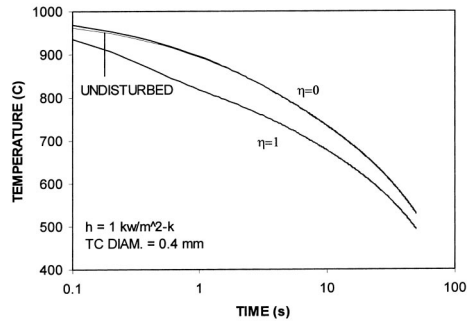

(a)

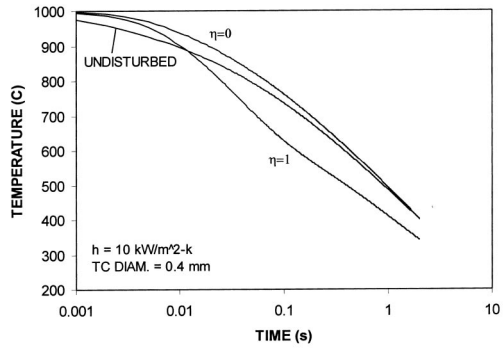

(b)

Fig. 6 Calculated histories of temperature by using the dual-scale computation for rapid quenching from the top surface of the parent object. The thermocouple is a Chromel. Wire radius of 0.4 mm. η is the normalized heat transfer coefficient on the surface of insulation sleeve. (*a*) Heat transfer coefficient $h=1$ kW/m^2 K; (*b*) Heat transfer coefficient $h=10$ kW/m^2 K.

through the surface follows the general relation $q=h(T_s-T_\infty)$, in which, q is the surface heat flux, h is the heat transfer coefficient, T_s is the surface temperature, and T_∞ is the environment temperature. A real-world example is the insulation on thermocouple wires; which is not always thermally perfect. It is known that the insulation thickness increases with the size of the insulation sleeve.

Let a normalized heat transfer coefficient η be defined by the ratio of effective surface heat transfer coefficient on the thermocouple surface $(\bar{h})$ to that on the object surface (h), i.e., $\eta=\bar{h}/h$. Hence, $\eta=0$ corresponds to perfect insulation, and $\eta=1$ is no insulation (bare surface). The case to be examined is a simple two-dimensional axisymmetric model with a surface-mounted thermocouple on a parent object. The top surface of the parent object and the thermocouple wire surface are exposed to the environment; all other surfaces are assumed to have zero heat flux (insulated). Only the parent object needs to be meshed; the initial temperature is 1000°C. Heat is extracted from the surface of a plate through convection with a heat transfer coefficient h. An intrinsic thermocouple junction is installed on the same surface. The actual thermal properties of AISI 4140 steel are used [5]. The calculated temperatures at the thermocouple junction as well as that on the surface are shown in Fig. 6 for two levels of heat transfer coefficient on the specimen's surface (i.e., $h=1$ and 10 kW/m^2 K). In this calculation, Chromel thermocouples of two wire diameters are considered. The measurement errors at the thermocouple junction are shown in Fig. 7 for heat transfer coefficient $h=1$ kW/m^2 K and two thermocouple wire diameters. Overall, the magnitude of temperature error decreases with the effectiveness of insulation, η. In the present case of cooling, the junction temperature is mostly lower than the actual, undisturbed surface temperature. At a lower effective surface insulation ratio η, the junction temperature is closer to the undisturbed surface temperature. At a large thermocouple diameter combined with a lower effective surface insulation ratio η (e.g., $\eta=0$ in Fig. 7), the junction temperature can be slightly higher than the undisturbed surface temperature, particularly in the earlier stage of cooling because the thermocouple junction acts as an insulator. In summary, it is noted that bare thermocouple wires always lead to large measurement error. In contrast, perfect insulation tends to minimize the error. According to Figs. 6 and 7, low temperature error can be obtained at a normalized heat transfer coefficient η smaller than or equal to 0.1.

Conclusions

The present study investigated the error in measured temperature by using surface-mounted thermocouples. In order to overcome the difficulty of calculating the temperature field associated with surface-mounted thermocouples attached at an arbitrary location on the object, a dual-scale computational model is developed and used in conjunction with a FEM model for the multidimensional calculation of the heating or cooling of a part. By using analytical solutions and numerical calculations, it is shown that the developed dual-scale computational model offers accurate prediction of the temperature at the junction of thermocouple wire. The actual effects of thermocouple on measured temperatures depend on the diameter of thermocouple wire; generally smaller wire gauge leads to smaller measurement error. The effectiveness of insulation decreases with wire size. Particularly, the insulation becomes very ineffective on thin gauge thermocouple when the

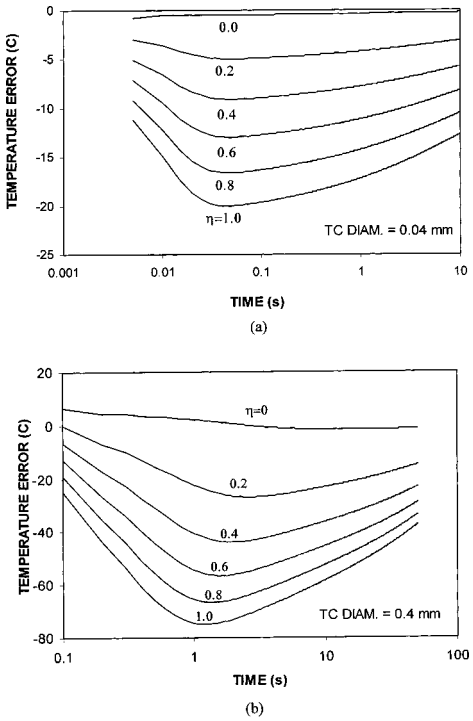

Fig. 7 Calculated errors in temperature by using the dual-scale computation for rapid quenching from the top surface of the parent object. The thermocouple is a Chromel. Heat transfer coefficient $h=1$ kW/m^2 K. η is the normalized heat transfer coefficient on the surface of insulation sleeve (*a*) wire radius of 0.04 mm; (*b*) wire radius of 0.4 mm.

heat transfer rate is low. For minimum measurement error, it is advisable to use bare thermocouple wires of smaller diameters than highly insulated thermocouple wire of larger diameters.

Acknowledgment

The help from Associate Editor Professor A. Emery is gratefully acknowledged. This project is partially funded by the Thermal Processing Technology Center at Illinois Institute of Technology; Professor P. Nash is the Director.

References

[1] Saraf, V., 2001, ''Distortion Characterization and Quench Process Modeling in Heat Treated Components of IN 718 Superalloy and AISI 4142 Steel,'' M.S. thesis, Department of Mechanical, Materials and Aerospace Engineering, Illinois Institute of Technology, Chicago, IL.

[2] Cross, M. F., Bennett, J. C., Jr, and Bass, R. W., 1999, ''Developing Empirical Equations for Heat Transfer Coefficients on Metallic Disks,'' 19th ASM-HTS Conference Proceedings, pp. 335–342.

[3] Park, J. E., Childs, K. W., Ludtka, G. M., and Chu, W., 1991, ''Correction of Errors in Intrinsic Thermocouple Signals Recorded During Quenching,'' *National Heat Treat Conference*, Minneapolis, MN.

[4] Zhou, G. F., and Tszeng, T. C., 2002, ''Determination of Heat Transfer Coefficients by Inverse Calculation in Conjunction With Embedded Model for Surface Mounted Thermocouples,'' paper in preparation.

[5] Tszeng, T. C., and Saraf, V., 2003, ''A Study of Fin Effects in the Measurement of Temperature Using Surface Mounted Thermocouples,'' ASME J. Heat Transfer, **125**, pp. 926–935.

[6] Gummadam, K. C., 2002, ''Characterizing the Inverse Computational Method for the Determination of Surface Heat Transfer Coefficients,'' M.S. thesis, Department of Mechanical, Materials and Aerospace Engineering, Illinois Institute of Technology, Chicago, IL.

[7] Bass, R. W., 1998, *Heat Transfer of Turbine Disks in Liquid Quench*, Techxperts, Inc., Tolland, CN.

[8] Tszeng, T. C., 2000, ''Determination of Heat Transfer Boundary Conditions of Quenching Operations in Heat Treating Processes,'' *Heat Treating and Hardening of Gears*, SME Technical Paper CM00-123, SME, Dearborn, MI.

[9] Beck, J. V., and Osman, A. M. 1992, ''Analysis of Quenching and Heat Treating Processes Using Inverse Heat Transfer Method,'' *Proceedings of the First International Conference on Quenching and Control of Distortion*, G. E. Totten, ed., ASM International, pp. 147–153.

[10] Beck, J. V., Blackwell, B., and St. Clair, Jr., C. R., 1985, *Inverse Heat Conduction: Ill-Posed Problems*, Wiley-Interscience, New York.

[11] Gummadam, K. C., and Tszeng, T. C., 2001, ''An Integrated Approach to Estimate the Surface Heat Transfer Coefficients in Heat Treating Processes,'' ASM International/IFHTSE Symposium on Quenching and Control of Distortion.

[12] Moffat, R. J., 1962, *The Gradient Approach to Thermocouple Circuitry, From Temperature—Its Measurement and Control in Science and Industry*, Reinhold, New York.

[13] Hennecke, D. K., and Sparrow, E. M., 1970, ''Local Heat Sink on a Convectively Cooled Surface—Application to Temperature Measurement Error,'' Int. J. Heat Mass Transfer, **13**, pp. 287–304.

[14] Shi, G., Tszeng, T. C., and Nash, P., 2003, ''Modeling of the Austenitization in a Lamellar Pearlite Microstructure of Eutectoid Steels at High Temperatures,'' Mater. Sci. Eng., A, in press.

[15] Sparrow, E. M., 1976, *Measurement in Heat Transfer*, 2nd ed., E. R. G. Eckert and R. J. Goldstein, eds., Hemisphere Publishing Corp, Chap. 1.

[16] Keltner, N. R., and Beck, J. V., 1983, ''Surface Temperature Measurement,'' ASME J. Heat Transfer, **105**, pp. 312–318.

[17] Litkouhi, B., and Beck, J. V., 1985, ''Intrinsic Thermocouple Analysis Using Multinode Unsteady Surface Element Method,'' AIAA J., **23**, pp. 1609–1614.

[18] Segall, A. E., 1994, ''Corrective Solutions for Intrinsic Thermocouples Under Polynominal Substrate Loading,'' ASME J. Heat Transfer, **116**, pp. 759–761.

[19] Tszeng, T. C., 2001, *HOTPOINT System Manual, 2001*, Illinois Institute of Technology, Chicago, IL.

[20] Arpaci, V. S., 1966, *Conduction Heat Transfer*, Addison-Wesley Publishing Co., Reading, MA.

Experimental Investigation of the Potential of Metallic Porous Inserts in Enhancing Forced Convective Heat Transfer

Bogdan I. Pavel
e-mail: pavelb@enme.ucalgary.ca

Abdulmajeed A. Mohamad
e-mail: amohamad@enme.ucalgary.ca

The University of Calgary,
Department of Mechanical
and Manufacturing Engineering,
Calgary, AB, T2N 1N4, Canada

The present experimental work investigates the effect of a metallic porous matrix, inserted in a pipe, on the rate of heat transfer. The pipe is subjected to a constant and uniform heat flux. The effects of porosity and thickness of the porous matrix on the heat transfer rate and pressure drop are investigated. That is, the surface temperature distribution along a heated section of the pipe, the pressure drop over this section, as well as the inlet temperature of the air were continuously monitored with a data acquisition system and recorded when steady-sate conditions were attained. The results obtained for a range of Reynolds numbers 1000–4500, comprise both laminar and turbulent regime. Also, the results are compared with the clear flow case where no porous insert was used. It is shown that higher heat transfer rates are achieved when using porous inserts at the expense of a reasonable pressure drop, which depends on the permeability of the porous matrix.
[DOI: 10.1115/1.1773586]

Keywords: Convection, Enhancement, Experimental, Heat Transfer, Porous Media

1 Introduction

The employment of different types of porous materials in forced convection heat transfer has been extensively studied due to the wide range of potential engineering applications such as electronic cooling, drying processes, solid matrix heat exchangers, heat pipe, enhanced recovery of petroleum reservoirs, etc. Al-Nimr and Alkam [1] numerically investigated the problem of transient forced convection flow in a concentric annuli partially filled with porous substrates located either on the inner or the outer cylinder. An increase of up to 12 times in the Nu number was reported in comparison with the clear annuli case and the superiority in thermal performance of the case when the porous substrate was emplaced to the inner cylinder was outlined. Based on the results obtained, Alkam and Al-Nimr [2] further investigated the thermal performance of a conventional concentric tube heat exchanger by emplacing porous substrates on both sides of the inner cylinder. Numerical results obtained showed that porous substrates of optimum thicknesses yield the maximum improvement in the heat exchanger performance with moderate increase in the pumping power. Recently, Mohamad [3] numerically investigated the heat transfer augmentation for flow in a pipe or a channel partially or fully filled with porous material emplaced at the core of the channel. It was shown that partially filling the channel with porous substrates can reduce the thermal entrance length by 50% and increase the rate of heat transfer from the walls. Although the porous material contributes to the pressure drop along the channel, an optimum thickness of about 60% of the channel height was found to offer a substantial increase in the Nu number at the expense of a reasonable pressure drop. Ichimiya [4] proposed a new method for evaluation of heat transfer between solid material and fluid in a porous medium by conducting both experimental and numerical work. In the first stage, the local Nusselt numbers were numerically obtained based on different dimensionless heat transfer coefficients, which enclosed in their forms the volumetric heat transfer coefficient between the fluid and solid in a porous medium. The numerical model assumed thermal nonequilibrium between the fluid and the solid in the porous medium. The experimental Nusselt numbers were determined by measuring the temperatures along the channel as well as the heat flux to the wall. The volumetric heat transfer coefficient was evaluated by comparing the experimental Nusselt numbers with the numerical ones. Fu et al. [5] experimentally demonstrated that a channel filled with high conductivity porous material subjected to oscillating flow is a new and effective method for cooling electronic devices. Angirasa [6] performed experiments that proved the augmentation of heat transfer by using metallic fibrous materials with two different porosities, namely 97% and 93%. The experiments were carried out for different Reynolds numbers (17,000–29,000) and power inputs (3.7 and 9.2 W). The improvement in the average Nusselt number was about 3–6 times in comparison with the case when no porous material was used.

It is worth mentioning that the literature contains a large number of numerical investigations on the use of porous materials for natural and forced flow applications. However, the experimental work carried out in this area is limited. Since the topology of porous materials varies drastically from one application to another, a carefully controlled experimental work is highly desirable.

The present experimental study aims at demonstrating the potential of metallic porous inserts in enhancing the convective heat transfer. The experiments were carried out for Reynolds numbers between 1000 and 4500, the power input was set at 13.2 W, and 12 different porous media, whose porosities varied between 96.6% and 99.1%, were examined. The maximum increase in the length-averaged value of the Nusselt number of about 5.2 times in comparison with the clear flow case was achieved with a porous medium fully filling the pipe (porosity 98.1% and a Reynolds number of about 4500).

2 Experimental Setup and Procedure

The porous media used for experiments were manufactured from commercial aluminum screen (wire diameter 0.8 mm, density 2770 kg/m^3, thermal conductivity 177 W/m^2 K) cut out at various diameters (D) and then inserted on steel rods, see Fig. 1. That is, 12 different porous materials, whose properties are pre-

Contributed by the Heat Transfer Division for publication in the JOURNAL OF HEAT TRANSFER. Manuscript received by the Heat Transfer Division January 4, 2004; revision received April 23, 2004. Associate Editor: P. M. Ligrani.

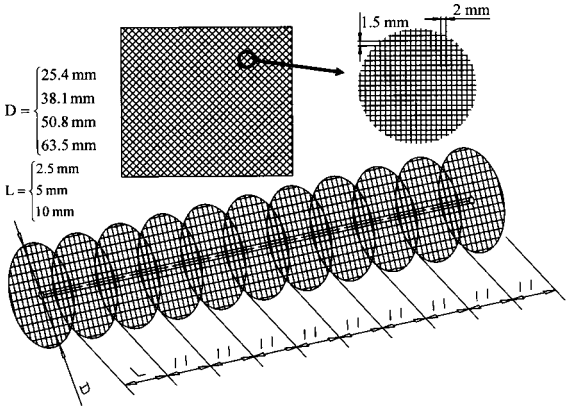

Fig. 1 Porous medium manufactured from aluminum screens

sented in Table 1, were obtained by varying the screen diameter and the distance between two adjacent screens (L).

The schematic diagram of the experimental facility is depicted in Fig. 2. Tests were carried out using a rig composed of four copper pipe sections ($D_p = 63.5$ mm), joined together by flanges and screws. The last section (10) was heated at the exterior over its entire length with a uniform heat flux generated by a flexible Kapton heater (33.4 Ω), and thermally insulated from the developing region (9) with Teflon gaskets and from the environment

Table 1 Porous medium characteristics

	D (mm)	L (mm)	Rp	Porosity ε (percent)
Porous medium 1	25.4	10	0.4	97.9 (Large)
Porous medium 2	25.4	5	0.4	97.4(Medium)
Porous medium 3	25.4	2.5	0.4	96.6 (Small)
Porous medium 4	38.1	10	0.6	98.8 (Large)
Porous medium 5	38.1	5	0.6	98.3(Medium)
Porous medium 6	38.1	2.5	0.6	97.5 (Small)
Porous medium 7	50.8	10	0.8	99.1 (Large)
Porous medium 8	50.8	5	0.8	98.6(Medium)
Porous medium 9	50.8	2.5	0.8	97.8 (Small)
Porous medium 10	63.5	10	1.0	99.3 (Large)
Porous medium 11	63.5	5	1.0	98.8(Medium)
Porous medium 12	63.5	2.5	1.0	98.1 (Small)

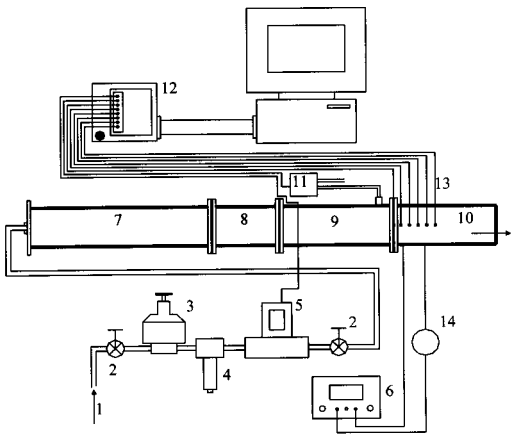

1.Compressed air
2. Valve
3. Pressure regulator
4. Filter
5. Gas flow meter
6. DC Power supply
7. Settling region (760 mm)
8. Straightener (120 mm)
9. Developing region (260 mm)
10. Heated section (500 mm)
11. Differential pressure transmitter
12. Signal conditioning unit
13. Thermocouples
14. Ammeter

Fig. 2 Experimental setup

with 3 layers of fiber glass with a total thickness of about 5 cm. The magnitude of the heat flux was adjusted by varying the intensity of the current measured with the ammeter (14) and supplied by the direct current power supply (6). A honeycomb rectifier of 50 mm length installed at the entrance of section (8), followed by three screens, 10 mm apart from one another, were employed in order to remove eddies and provide a more uniform velocity profile. The pressure drop caused by inserting different porous media inside the heated section (10) was measured by connecting one of the ports of the differential pressure transmitter (11) to a pressure tap, welded in the proximity of the flanges between section (9) and (10), and leaving the other one free to the atmosphere. Temperatures of the air entering the heated section and those of the surface of (10), at five axial positions (0, 49.4, 98.8, 148.2, and 247 mm) were recorded using six K-type thermocouples. The mass flow rate of air flowing inside the rig, adjusted with the help of valves (2) and pressure regulator (3), was measured using the gas flow meter (5), protected by the 50μ filter (4). Electrical signals generated by the sensors were transmitted to the signal conditioning unit, where they were selectively processed (the following operations were performed on the signals generated by the thermocouples: linearization, cold junction compensation, amplification). The resulting analog signals were further converted into digital signals by a DAQ card installed into a PC and recorded with an application developed in LabView. The characteristics and accuracy of instruments used for experiments are summarized in Table 2.

Tests were carried out for all porous media manufactured, at different mass flow rates of air and for the same power input 13.26 W. The procedure followed during each experiment is as follows. A constant power input was supplied and the mass flow rate was adjusted so that the initial value of the Re number was around 1000. The temperature of the air, the temperatures along the heated section, the mass flow rate of air as well as the pressure drop were continuously monitored, with a scanning frequency of 1200 Hz. Usually an initial period of approximately 3–4 hours was required before reaching steady-state conditions (considered to be attained, when the temperatures along the pipe didn't vary with more than ± 0.3°C within a period of about 2 minutes). To effectively remove the noise specific to each sensor as well as the noise induced in the electric wires by the surrounding electromagnetic fields, each data point acquired was obtained by averaging 300 discrete values acquired with the above mentioned frequency of 1200 Hz. After collecting a set of data at steady-state conditions, the mass flow rate of air was increased so that the next value of the Re number differed from the previous one by about 250 units. A new set of data was collected when steady-state conditions were reached again, usually within a period of approximately 30 minutes. That is, the mass flow rate of air was increased progressively until a maximum value (limited by the source of compressed air) of Re$\sim$4500 was reached.

Heat losses from the heated section (10) to the adjacent section (9) by conduction, to the atmosphere by radiation and natural convection were accounted for by performing separate experimental tests for each porous medium. The procedure followed in this case is as follows. Small amounts of heat were supplied by the electrical heater without having air flowing inside the rig. After reaching steady-state conditions, temperatures along the heated surface were recorded and averaged. The heat input supplied was considered to be the same as the heat losses that occur during forced convection. This assumption holds as long as the temperature potential between the heated section (10) and the ambient air, driving the above mentioned phenomena, is the same. In the present study the temperature of the compressed air was very close to the ambient temperature in the room. Hence, by doing a least-square fit, heat losses were expressed as functions of the average temperature of the heated surface. The coefficients re-

Table 2 Instrumentation used for data acquisition

	Characteristics	Manufacturer
FMA-1600 Mass Flow Meter	Accuracy: ±1%	Omega
SCXI-1000 Chassis	···	National Instruments
SCXI-1328 High Accuracy	Accuracy:	
Isothermal Terminal Block	±5% (15−30°C)	National Instruments
SCXI-1125 8-Channel Isolated	Offset error: ±1.5mV/gain	National Instruments
Analog Input Module	Gain error: ±0.03%	
PX277 Differential Pressure Transmitters with Field Selectable Ranges	Accuracy: ±1%	Omega
SA1-K Thermocouples	Accuracy: ±0.3%	Omega

sulted from the polynomial regression were updated every time a new porous medium was tested and the heat losses were deducted from the heat input.

In order to test the repeatability of the measurements, different sets of readings were collected on different days using the same porous medium 10 (see Table 1). The results plotted in Fig. 3 indicate that the maximum deviation between the two sets of data is less than 5%.

3 Results and Discussion

Figures 4 present the surface temperatures measured on section (10) at the above specified axial positions, as well as the temperature of the air at the inlet of section (10) at steady state conditions for various Re and different porous media. It can be seen that the temperatures of the surface increase with the increase in the axial position for a fixed value of Re and decrease with the increase in Re.

A careful examination of the cases when a porous medium was inserted in the core of section (10) (Figs. 4(*b*–*e*)) in comparison with the clear flow case (Fig. 4(*a*)) reveals that a more uniform temperature distribution along the pipe surface is achieved with higher Re and higher Rp.

It is well established that the local Nu number for a thermally fully developed laminar flow in a pipe subjected to a constant heat flux is 4.36. In the present experiment, the thermally fully developed condition was not satisfied, since the minimum value of the local Nu number recorded for the clear flow case (Re=1002) at the position of the 5th thermocouple, was 5.73. It should be mentioned that the nature of the present experimental study is to compare the rate of heat transfer obtained with and without porous materials.

An evaluation of the potential of the porous material to enhance the rate of heat transfer between the surface of the heated section (10) and the air flowing inside it can be done by comparing the

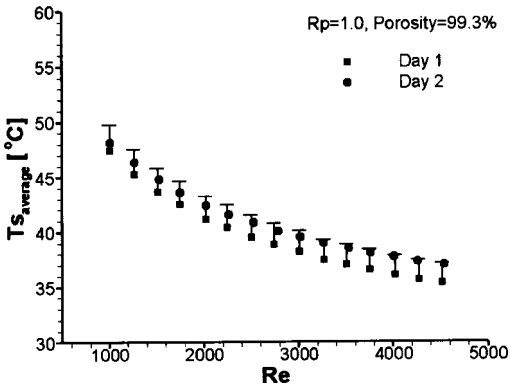

Fig. 3 Repeatability test

average temperature of the surface at two different Re numbers recorded for the clear flow case (Fig. 4(*a*)) and the case of fully filling the pipe with the porous material of porosity 98.1% (Fig. 4(*e*)). The temperature drop due to the presence of the porous material is about 16°C at a Re of about 1000 and 18°C for a Re of about 4500.

Figures 5(*a*) and (*b*) present the length-averaged temperature of the surface and length-averaged Nusselt number, respectively. The length-averaged values were obtained by averaging the local values of the corresponding parameters. The local convective heat transfer coefficient was calculated using the following equation:

$$h(x)=\frac{q''}{[T_s(x)-T_m(x)]} \tag{1}$$

where the local mean thermodynamic temperature of the air was deducted from an energy balance over an elementary control volume [7] located at an axial distance x

$$T_m(x)=T_{\text{in}}+\frac{q''(\pi D_p)}{\dot{m}c_p}x \tag{2}$$

Hence, the local values for the Nusselt number were computed using the following relation:

$$\text{Nu}(x)=\frac{h(x)D_p}{k_f} \tag{3}$$

Comparing the length-averaged Nusselt number corresponding to the porous media with the same porous ratio Rp (Fig. 5(*b*)) it can be seen that a small decrease in porosity doesn't influence the rate of heat transfer when $Rp=0.4$ and $Rp=0.6$. But this is not the case for $Rp=0.8$ and $Rp=1.0$ where a small decrease in porosity results in a significant increase in $\text{Nu}_{\text{average}}$. The variation in porosity for the case where $Rp=1.0$ has a much stronger influence upon $\text{Nu}_{\text{average}}$ than the other cases due to the additional heat transfer by conduction resulted from the contact between the pipe surface and the porous medium. When Rp decreases to 0.8 the increase in the value of $\text{Nu}_{\text{average}}$ with the decrease in porosity is due to a channeling effect. A decrease in porosity translates into a poorer capability of the fluid to penetrate through the porous medium; hence the fluid tends to flow in the annular channel, which is created between the cylindrical porous medium and the interior surface of the pipe, at higher velocities due to the reduction in the cross sectional area available for fluid flow. This effect can be observed by studying the axial velocity profiles obtained by employing a numerical simulation, as described by Mohamad [3] and Al-Nimr [1]. Besides the channeling effect, which causes a flow redistribution, another factor that can be reasoned to enhance heat transfer is the radiative heat transfer occurring between the pipe surface and the porous medium placed in the core of the pipe. In this case a smaller porosity would be more desirable in order to increase the radiative heat transfer.

Figures 5(*a*) and (*b*) also illustrate the strong effect the porous

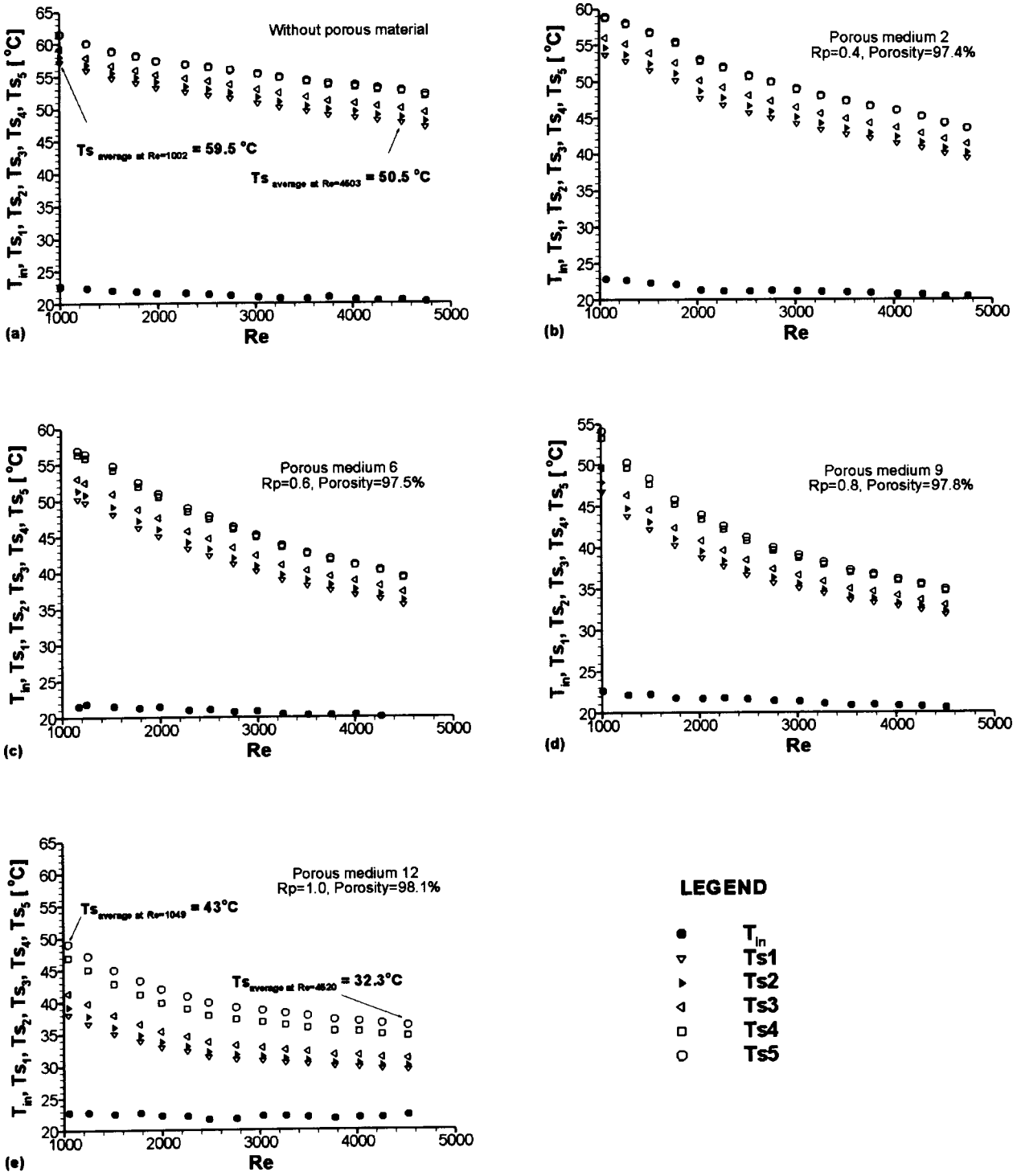

Fig. 4 Temperatures recorded: (*a*) clear flow case; (*b*) porous medium 2; (*c*) porous medium 6; (*d*) porous medium 9; and (*e*) porous medium 12

medium ratio Rp has on enhancing heat transfer. By comparing the $Nu_{average}$ curves obtained with $Rp=0.4$, 0.6, 0.8, and 1.0 with the clear flow case it can be concluded that higher heat transfer rates can be achieved by increasing Rp culminating with the case of a fully porous channel. It is also worth noticing that the porous medium with $Rp=1.0$ and largest porosity 99.3% is less effective in enhancing the rate of heat transfer than the porous medium with $Rp=0.8$ and porosity 97.8% starting with Re numbers corresponding to the transient flow regime. The same observation is true in comparison with the porous medium with $Rp=0.8$ and porosity 98.6% starting with Re numbers corresponding to the beginning of the turbulent flow regime.

It should be mentioned that increasing Re (Fig. 5(*b*)), which translates into higher flow rates, results in higher heat transfer rates regardless of the value of porosity and porous material ratio.

Heat transfer enhancement also arises from the modification of the thermal conductivity of the medium inside the pipe, as it was also mentioned by other authors [1,3]. For the clear flow case

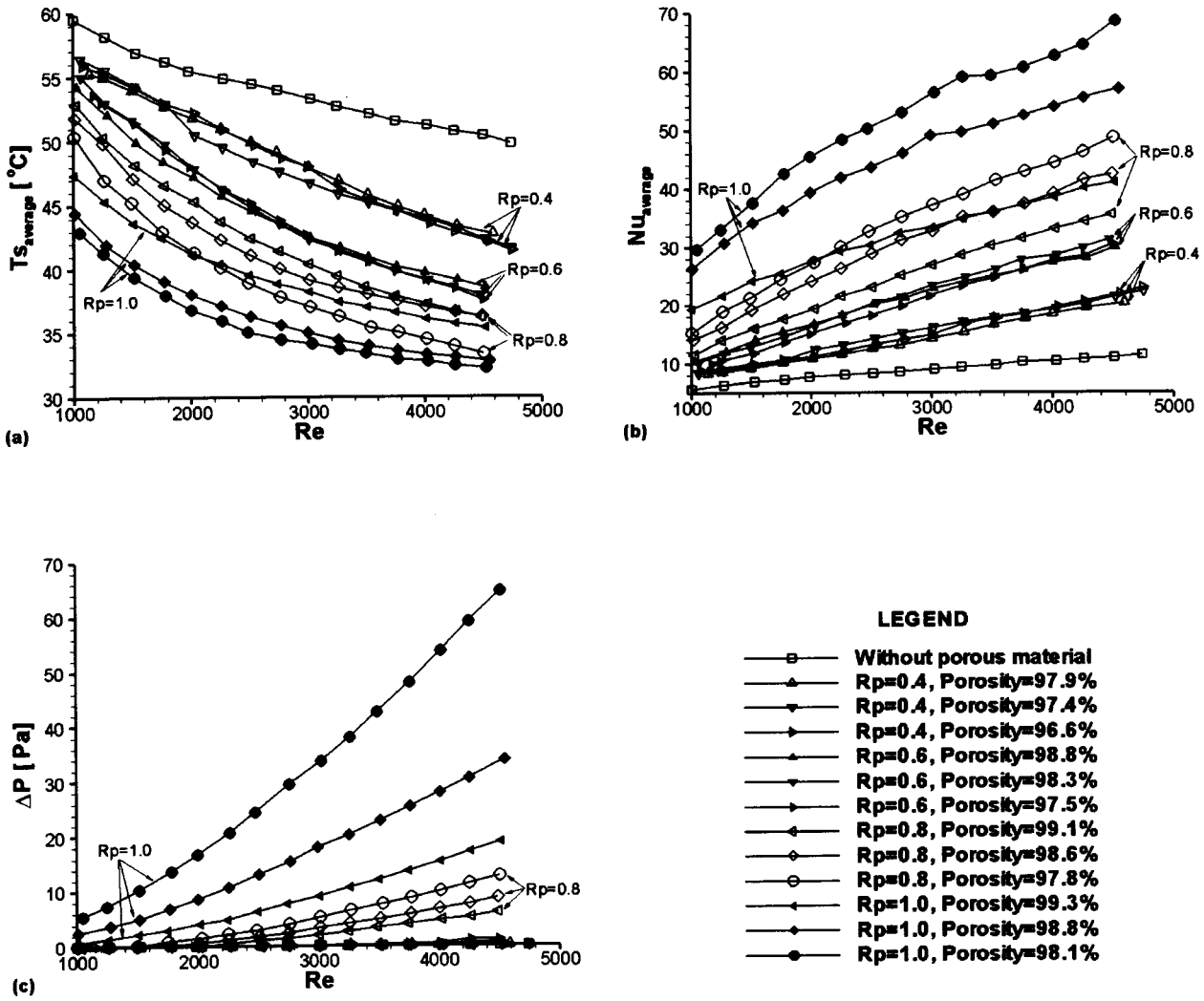

Fig. 5 Experimental data: (*a*) length-averaged temperature of the heated section; (*b*) length-averaged Nusselt number; and (*c*) pressure drop

thermal conductivity of the medium inside the pipe is that of the air, which is very small (about 0.026 W/mK), but when an aluminum porous medium is employed the resulting effective thermal conductivity is increased. The magnitude of this increase depends on porosity.

An important factor that has to be considered when employing porous media for the purpose of enhancing heat transfer is the penalty arising from the increased pressure drop. Figure 5(*c*) presents the pressure drops measured over the experimentally tested porous media at different Re. As expected the largest pressure drops correspond to the cases that offer the best thermal performance, namely $Rp=0.8$ and $Rp=1.0$.

The results showing the influence of porous materials on the rate of heat transfer and pressure drop are presented in Figs. 6 and 7. Figure 6 presents the percentage increase in the value of the Nusselt number in comparison with the clear flow case. For each Rp, the minimum and maximum increases correspond to the lowest and highest Re, respectively. Figure 7 shows the pressure drop recorded for all cases, the previous observations regarding the minimum and maximum values being the same.

4 Conclusions

This study presents an experimental investigation of the potential of porous inserts to enhance the rate of heat transfer occurring between the surface of a pipe heated with a constant and uniform heat flux and the air flowing inside it. The following conclusions may be drawn:

Heat transfer enhancement can be achieved using porous inserts whose diameter approach the diameter of the pipe. For a constant diameter, further improvement can be attained by using a porous insert with a smaller porosity. Care should be exercised since both

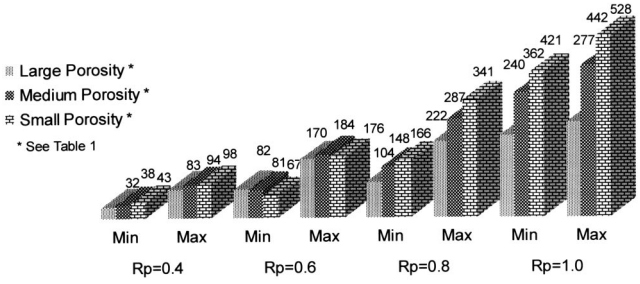

Fig. 6 Evaluation of the improvement in Nu number generated by each porous medium in comparison with the clear flow case

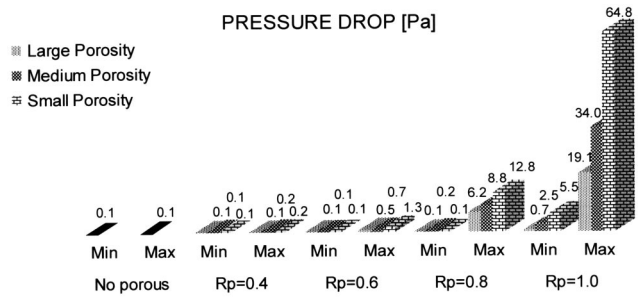

Fig. 7 Evaluation of the hydrodynamic performance of each porous medium

of these two parameters, namely porosity and diameter, have a positive influence upon heat transfer and negative impact on pressure drop, consequently on the pumping power.

The main mechanisms reasoned to be the basis for the heat transfer enhancement when using porous materials are as follows: flow redistribution (flow channeling), thermal conductivity modification, and enhancement of the radiative heat transfer.

The highest increase in the Nusselt number of approximately 5.28 times was obtained by fully filling the pipe at the expense of the highest pressure drop of 64.8 Pa. In comparison with fully filling the pipe, a partial filling has the advantage of a comparable increase in the Nusselt number and a smaller increase in the pressure drop.

Nomenclature

c_p = specific heat of air at constant pressure
D_p = internal diameter of the pipe
h = local convective heat transfer coefficient
k_e = effective thermal conductivity
k_f = thermal conductivity of the fluid
Nu = local Nusselt number, hD_p/k_f
q'' = exterior heat flux applied to section (10)
Re = Reynolds number, $\rho u_m D_p/\mu$
Rp = ratio of the porous material, $2r_p/D_p$
r_p = radius of the porous material
T_{in} = temperature of the air at the inlet of the heated section (10)
T_m = local mean thermodynamic temperature of the air
T_s = local temperature measured on the heated section (10)
x = axial position measured from the beginning of the heated section (10)

Greek Symbols

ε = porosity
μ = dynamic viscosity of the fluid
ρ = fluid density

Subscripts

e = effective
f = fluid
s = surface
sm = solid matrix

References

[1] Al-Nimr, M. A., and Alkam, M. K., 1997, ''Unsteady Non-Darcian Forced Convection Analysis in an Annulus Partially Filled With a Porous Material,'' ASME J. Heat Transfer, **119**, pp. 799–804.
[2] Alkam, M. K., and Al-Nimr, M. A., 1999, ''Improving the Performance of Double-Pipe Heat Exchanger by Using Porous Substrates,'' Int. J. Heat Mass Transfer, **42**, pp. 3609–3618.
[3] Mohamad, A. A., 2003, ''Heat Transfer Enhancements in Heat Exchangers Fitted With Porous Media. Part I: Constant Wall Temperature,'' Int. J. Heat Mass Transfer, **42**, pp. 385–395.
[4] Ichimiya, K., 1999, ''A New Method for Evaluation of Heat Transfer Between Solid Material and Fluid in a Porous Medium,'' ASME J. Heat Transfer, **121**, pp. 978–983.
[5] Fu, H. L., Leong, K. C., Huang, X. Y., and Liu, C. Y., 2001, ''An Experimental Study of Heat Transfer of a Porous Channel Subjected to Oscillating Flow,'' ASME J. Heat Transfer, **123**, pp. 162–170.
[6] Angirasa, D., 2002, ''Experimental Investigation of Forced Convection Heat Transfer Augmentation With Metallic Fibrous Materials,'' Int. J. Heat Mass Transfer, **45**, pp. 919–922.
[7] Incropera, F. P., and DeWitt, D. P., 2002, *Introduction to Heat Transfer*, John Wiley & Sons, New York, pp. 445–447, Chap. 8.

Effect of Squealer Geometry on Tip Flow and Heat Transfer for a Turbine Blade in a Low Speed Cascade

Vikrant Saxena

Srinath V. Ekkad
e-mail: ekkad@me.lsu.edu

Mechanical Engineering Department,
Louisiana State University,
Baton Rouge, LA 70803

A detailed investigation on the effect of squealer geometries on the blade tip leakage flow and associated heat transfer is presented for a scaled up high pressure turbine blade in a low-speed wind tunnel facility. The linear cascade is made of four blades with the two corner blades acting as guides. The tip profile of a first stage rotor blade is used to fabricate the two-dimensional blade. The wind tunnel accommodates an 116° turn for the blade cascade. The mainstream Reynolds number based on the axial chord length based on cascade exit velocity is 4.83×10^5. An upstream wake effect is simulated with a spoked wheel wake generator placed upstream of the cascade. A turbulence grid placed even farther upstream generates a free-stream turbulence of 4.8%. The center blade has a tip clearance gap of 1.56% with respect to the blade span. Static pressure measurements are obtained on the blade surface and the shroud. Results show that the presence of the squealer alters the tip gap flow field significantly and produces lower overall heat transfer coefficients. The effects of different squealer arrangements are basically to study the effect of squealer rim placement on tip leakage flow and associated heat transfer. Detailed heat transfer measurements are obtained using a steady state liquid crystal technique. The effect of periodic unsteady wake effect is also investigated by varying the wake Strouhal number from 0–0.4. Results show that suction side squealers may be favorable in terms of overall reduction in heat transfer coefficients over the tip surface. However, the presence of a full squealer is most beneficial in terms of reducing overall heat load on the tip surface. There is reasonable effect of wake induced periodicity on tip heat transfer. [DOI: 10.1115/1.1777580]

Introduction

Turbine blade tip heat transfer has been a strong focus of ongoing studies recently. Turbine blade tips are exposed to a pressure driven leakage flow across the tip from the pressure side to the suction side of the blade. The leakage flow cannot be eliminated due to a required clearance between the rotating blade and the stationary casing or shroud. The leakage flow causes high heat load to the tip region and leads to oxidation and cracking resulting in significant losses to overall power and efficiency. The ''squealer'' tip where an outer rim extends along the blade tip edge causing the tip surface to act as a labyrinth seal is one of the efforts focused on designing the blade tip region to reduce leakage flow and thus reduce overall heat load and delay failure initiation processes. The tip geometry is called ''squealer'' in industry terminology as it squeals the flow.

Bindon [1] and Morphis and Bindon [2] studied tip clearance loss, using a linear cascade under low-speed conditions, and concluded that the losses varied linearly with gap size. Using static pressure measurements and flow visualization, Bindon observed a separation bubble on the blade pressure edge that mixes with a high-speed leakage jet induced at mid-chord. The leakage flow was defined as sink-like flow on the pressure side and source-like flow on the suction side of the blade. Yaras et al. [3] also observed the presence of a separation bubble away from the leading edge and concluded that flow towards the leading edge had little effect on overall losses. In Yaras' study, a high-speed test rig was used. Yamamoto [4] also found that leakage vortices were sensitive to incident angle and the blade tip gap height. Kaiser and Bindon [5] investigated various effects on tip leakage flow and associated losses in a rotating turbine rig.

Mayle and Metzger [6] investigated heat transfer on a two-dimensional rectangular tip with rotating and stationary shroud. They established that the effects of relative motion between a blade model and the shroud have negligible effects on heat transfer data. Metzger et al. [7] and Chyu et al. [8] investigated the effects of varying the recess depth on the tip heat transfer of a blade tip model. It was determined that tip heat transfer was reduced under the presence of a cavity. The cavity simulated the squealer tip geometry. Leakage flow was reduced until the depth reached $D/W=0.2$.

Metzger et al. [9] measured tip heat flux on a rotating turbine rig using multiple heat flux sensors. Yang and Diller [10] made discrete point measurements on the tip of a blade in a linear cascade under blowdown conditions using a single heat flux gage. Bunker et al. [11] published the first study with detailed blade tip heat transfer measurements on actual blade tips. The measurements were made for a first stage power generation blade using a steady state liquid crystal technique. They varied the curvature of the blade tip edges (rounded and sharp). They found that the blade with a tip edge radius had greater leakage flow and higher heat transfer coefficients. Bunkeret al. [11] also reported that an increase in free stream turbulence intensity increased the heat transfer coefficient. The authors observed an area of low heat transfer toward the blade leading edge, referred to as the sweet spot. Ameri and Bunker [12] used CFD simulations to reproduce the results for the same blade geometry shown by Bunker et al. [11]. They concluded that the assumption of periodic flow was invalid for tip heat transfer calculations because the entire passage had to

Contributed by the Heat Transfer Division for publication in the JOURNAL OF HEAT TRANSFER. Manuscript received by the Heat Transfer Division June 2, 2003; revision received May 4, 2004. Associate Editor: H. S. Lee.

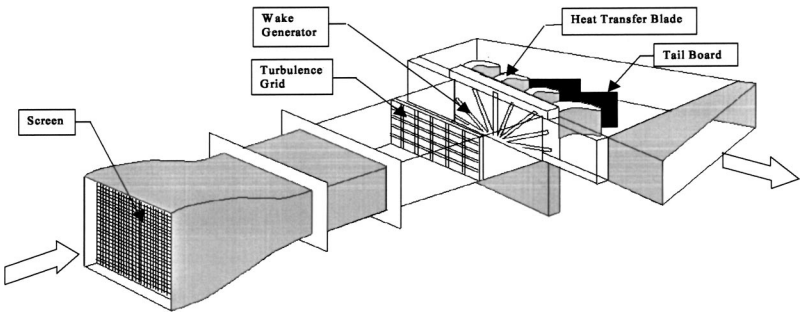

Fig. 1 Illustration of the low-speed cascade

be modeled. Their numerical results for the radi used edge showed better agreement with the experimental data than that of the sharp edge.

Azad et al. [13] performed heat transfer investigation on blade tips in which three different tip clearance gaps ($t/H=1$, 1.5, 2.5%) were used. They used a GE-E^3 engine blade and a cascade inlet total-to-outlet static pressure ratio of 1.2 in a five-blade cascade. They measured heat transfer coefficients using a transient liquid crystal technique. The results of this experiment showed that a larger gap causes higher heat transfer coefficient on the tip. A second study by Azad et al. [14] investigated the effects of a recessed tip ($D/H=3.77\%$) on the heat transfer coefficient. It was determined that the squealer tip produced a lower overall heat transfer coefficient compared to the plain tip. The squealer redirected the airflow over the tip forcing the flow to move from the leading edge pressure side to the trailing edge suction side.

Bunker and Bailey [15] and Azad et al. [16] examined the different squealer geometries for reducing tip leakage flow and associated heat transfer, including single and double squealers. The single squealer was a thin extension running from tip to tail, located on the camber line, pressure edge or suction edge. The double squealer consists of two strips: a full perimeter strip, a pressure side strip from tip to tail and a short chord strip, and a suction side strip from tip to tail and a short chord strip. The single squealer produced lower heat transfer coefficients on the tip than the double squealers. The mid-chord squealer and the suction side squealers produced the best leakage reduction and heat transfer. Recently, Dunn and Haldeman [17] presented time averaged heat flux measurements on a recessed tip, the lip of the recess of a rotating blade in a full-scale rotating stage at transonic vane exit conditions. Nasir et al. [18] studied the effect of partial squealers on heat transfer over a blade tip in a blowdown tunnel. They indicated that the suction side squealer placement was as effective as a full squealer. Pressure side squealers cause highly accelerated flow separation and reattachment resulting in higher heat transfer coefficients on the tip that are higher than the plain tip.

There have been several studies that have focused on the effect of periodic unsteady wakes on linear cascades [19–20]. Wittig et al. [21] and Han et al. [22] focused on the blade surface heat transfer under the effect of periodic unsteady wakes. These early studies simulated rotor-stator interactions with an upstream rotating rod wake generator. This technique has been accepted as a solution to simulating upstream unsteady wake effects on blades in low-speed cascades. Teng et al. [23] presented detailed heat transfer coefficient distributions on a large-scale blade tip with different tip gaps. The effect of unsteady wake on tip heat transfer was investigated. They concluded that a reduced tip clearance gap produces lesser effect of the upstream unsteady wake thereby producing lower heat transfer coefficients. However, they did not investigate the effects of squealer geometries under unsteady wake effects. Also, they used the mid-span section of the blade to simulate the leakage flow and not the tip section. This can produce nontypical leakage flow over the tip compared to the tip section because the pressure distribution around the blade surface is different. Saxena et al. [24] presented detailed heat transfer coefficient and pressure distributions over turbine blade tips in low-speed flow conditions. They studied the effect of cross-wise strips on tip flow and heat transfer. They oriented the trips in different directions with respect to the leakage flow and indicated that slight reductions in heat transfer were observed for trips placed against the leakage flow direction compared to the plain tip. This study is a continuation of the study by Saxena et al. [24] and uses the same experimental test rig and technique.

The present study focuses on different squealer geometries that provide an understanding of the placement of squealer rim and their effect on leakage flow and associated heat transfer. The results indicate the effectiveness of single squealers with respect to full squealers. Detailed heat transfer measurements are obtained using the steady-state liquid crystal technique. The HSI based technique is described in detail by Camci et al. [25]. A typical high-pressure turbine blade was used in a four-blade linear cascade. Heat transfer measurements are presented for different squealer arrangements for one tip gap clearance of 1.56% of the blade span (20.32 cm). The effect of unsteady wake and free-stream turbulence is investigated for each of the proposed tip geometry.

Experimental Setup

A schematic of the experimental setup is shown in Fig. 1. The test setup consists of a suction type blower, a low-speed wind tunnel with an inlet-nozzle. Three screens are inserted at the inlet and exit of the nozzle section to help reduce and breakdown the large-scale turbulence entering the wind tunnel. The wind tunnel is designed to accommodate the turning angle of the blade cascade. The flow turning angle for the cascade is 116°. The flow passes through a rectangular section where a turbulence grid can be inserted to increase the free-stream turbulence approaching the four-blade linear cascade. The turbulence grid is placed 46.67-cm upstream of the cascade leading edge. The grid is made of 6.35-mm thick circular rods arranged in a cross-bar fashion with a spacing of 25.4-mm between the rods in both directions. A spoked-wheel wake generator similar to previous studies [21–23] is used to generate the periodic unsteady flow simulating rotor-stator interaction on the cascade and is 17.15-cm upstream of the blade cascade. The wake generator has 32 rods, each 0.63 cm in diameter simulating the upstream trailing edge of the guide vane. The wake Strouhal number can be adjusted by adjusting the rotating speed of the rods using a frequency controller. The cascade inlet velocity can be varied using a frequency controller for the blower to adjust the required inlet velocity for different inlet flow conditions.

The cascade has four 4× scaled up blades with an axial chord length of 12-cm, span of 20.32-cm, and blade spacing of 19.06-cm at cascade inlet. The two end blades form the outer edge of the cascade guide the flow through the middle three passages. One of the middle blades serves as the test blade. The blade can be interchanged to obtain pressure or heat transfer measurements. The test

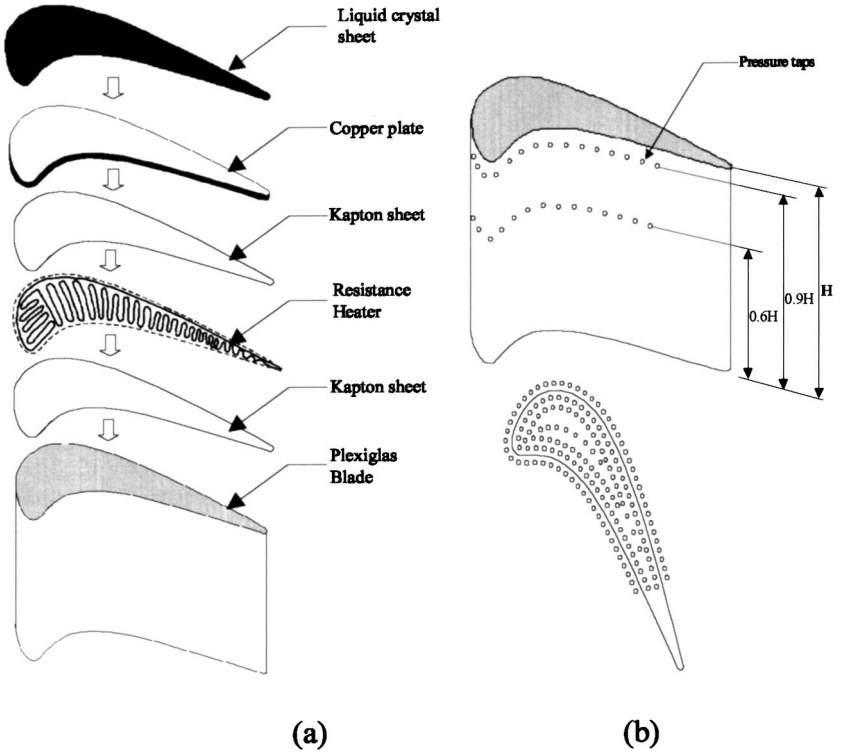

Fig. 2 (*a*) **Heat transfer blade; and** (*b*) **pressure blade and shroud taps.**

blade is the only blade that has a tip gap clearance. All the blades are machined out of plexiglass. The blade shapes were cut out of 5.04-cm thick plexiglass sheet and four cuts were stacked up and glued together to obtain one blade for the cascade. The cascade inlet and exit velocity profile was monitored and the results show uniform flow through the three passages. The uniform flow was obtained by adjusting the tailboards behind the cascade. Figure 2(*a*) shows the heat transfer blade. The heat transfer blade is first instrumented with a Kapton sheet, a resistance wire of known length was designed with a certain distribution and is attached to the underneath of a thin copper plate (0.79 mm) using another Kapton sheet. The wire is connected to an 110VAC source for power. The liquid crystal sheet of known color range (R30C5W) with red beginning at 30°C and a bandwidth of 5°C was then glued to the top of the copper plate. The heater system provided an almost uniform heat flux on the blade tip. The regions along the blade edges may produce some non-uniformities although they are not visible during the tests.

Figure 2(*b*) shows the test blade with surface pressure taps of diameter of 1.59 mm. Pressure taps were drilled on the blade surface at 60% span and 90% span to measure the static pressure distributions on the blade surface at different span locations. Static pressure taps were also drilled on the shroud of the blade as shown in Fig. 2. The shroud pressure distributions were obtained to characterize the leakage flows with different tip sealing geometries. Each static pressure tap was connected to a 32-channel NetScanner system from Pressure Systems, Inc with rigid tubing in the hole and to the system using flexible tubes.

Figure 3 presents the five squealer geometry cases studied. The squealer rims are made of cork strips that are attached to the tip surface using adhesive. The cork material is nonconducting so there is no heat loss through the extended rims. Case 1 is the plain tip case with the tip clearance at 1.56%. Case 2 is the suction side squealer where the rim (0.32 cm) exists only on the suction side edge of the tip. Case 3 is the pressure side squealer where the rim exists only on the pressure side rim. Case 4 is the camberline squealer where the rim exists along the camberline of the tip profile. Case 5 is the baseline full squealer case where the rim covers the entire edge of the tips surface. The tip gap above the squealer rim is maintained at 1.56% of the blade span.

A high-resolution RGB camera is placed right above the tip surface of the heat transfer blade location. Lights are mounted on the frame that holds the camera in position. The RGB camera is connected to a 24-bit color frame grabber board inside a PC. An image processing software is used to capture and analyze the liquid crystal color images on the blade tips.

Procedure and Data Reduction

Liquid Crystal Calibration. The first step in the experimental procedure is to calibrate the liquid crystal color to temperatures. The calibration was done in-situ with a thermocouple placed on the liquid crystal sheet. The camera was focused on the region around the thermocouple. The liquid crystal sheet was heated by

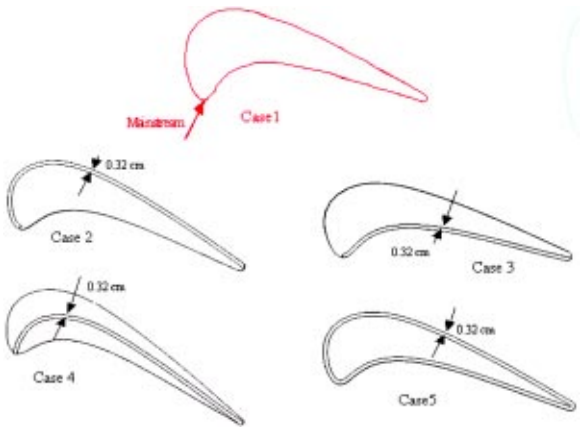

Fig. 3 Different squealer tip geometries studied

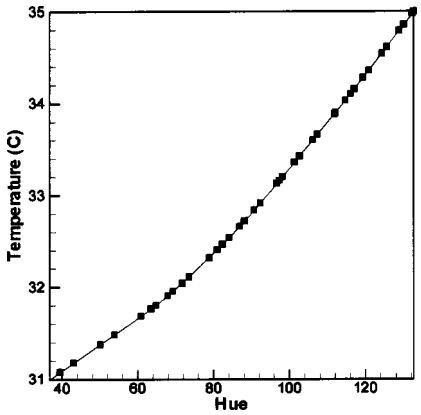

Fig. 4 Hue versus temperature curve for liquid crystal sheet

turning on the heater underneath the sheet. The heater temperature was slowly increased by about 0.2°C and allowed to come to steady state. In the HSI method, the color signal is broken into three components, Hue, Saturation, and Intensity. These three contribute to the color signal as a combination of the three base colors, Red, Green, and Blue. The Hue of the color was recorded by the image processing unit through an inbuilt macro and the temperature was measured using a temperature recorder. The Hue of the color was then plotted against the temperature to obtain the calibration curve. Camci et al. [23] provide a detailed description of Hue-based liquid crystal measurement technique. A Hue-Temperature relationship is obtained from the curve. Figure 4 shows the temperature vs. hue curve. This relationship for the present set-up is given as

$$\text{Temperature} = 0.047^{*}\text{Hue} + 28.619$$

Heat Transfer Experiment. The camera is focused on the test surface. The suction blower is turned on to start the mainstream flow through the cascade. Once the flow is steady, the heater is turned on using an electrical supply and a variac. The variac is used to control the current and voltage into the heating wire. The heater wire heats up the copper plate and the copper plate heats up the liquid crystal layer. The heat flux is increased till most of the blade is either green or red. The Hue calibration is not very reliable in the blue color range as the curve tends to plateau with increasing temperature. To avoid this, color changes are limited to red and green. Once the surface is mostly green, the heat flux is maintained constant till the test surface achieves steady state. This typically takes about 30–45 minutes. The image is then captured and the local Hue values are obtained at every pixel on the blade tip surface. The Hue is then converted to the local surface temperature using the above hue-temperature relation. The wall surface heat flux is calculated from the known voltage and current and the blade tip surface area. The local heat transfer coefficient is calculated from the relation:

$$h = \frac{q''_{\text{elec}} - q''_{\text{loss}}}{(T_w - T_\infty)},$$

where q''_{elec} is the applied electrical power per unit area, and q''_{loss} is the losses due to conduction, natural convection, and radiation. This was estimated to be about 6% of the applied heat flux over the entire tip surface. Heat loss was estimated by running the heater without air flow and making surface temperature measurements for different heat flux ratings. The local wall temperature T_w is calculated from the local hue measurement and T_∞ is the oncoming free-stream temperature measured upstream of the cascade.

The experimental uncertainties in the local heat transfer coefficient measurement are calculated with 95% confidence [24]. The uncertainty in Hue measurement, the Hue-temperature relation, free-stream temperature measurement, and heat flux input, and loss estimation affect the heat transfer coefficient measurement. The individual uncertainties are listed below:

Voltage measurements (V):	±2.5%
Current measurements (I):	±2%
Mainstream Temperature (T_∞):	±1°C
Hue measurements (Hue):	±5%
Wall Temperature (T_w):	±1.6°C
Area measurements (A):	±1% (machining tolerance)

Therefore, the average experimental uncertainties in the measurement of local heat transfer coefficient calculated based on Kline and McClintock [26] is ±6.54 %. However, near the edges of the tip, lateral conduction causes non-uniform heat flux resulting in higher errors. However, when a squealer rim is used, this region is covered by cork material and no results are presented. Similarly the experimental uncertainty in pressure measurement is ±0.2% and in the velocity measurements is ±5%.

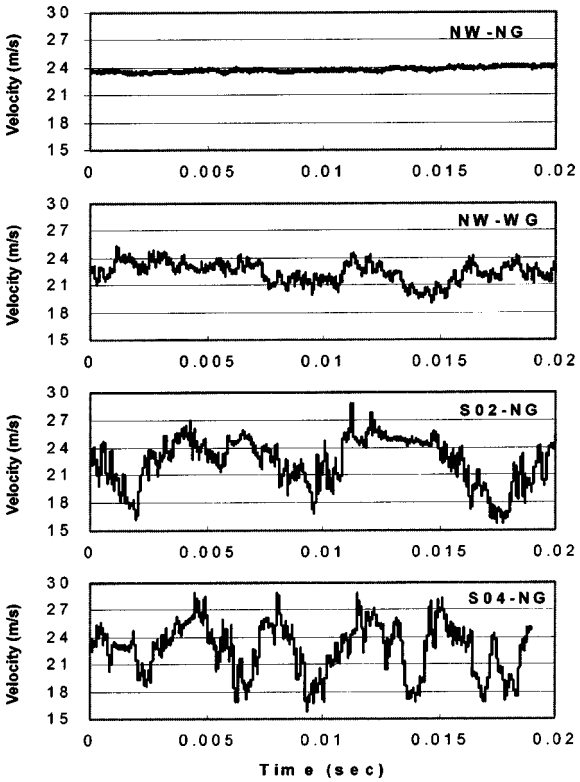

Fig. 5 Velocity signature for the four flow conditions

Results and Discussion

Flow Measurements. The free-stream velocity at cascade inlet is 23 m/s and 58 m/s at the cascade exit. The cascade Reynolds number based on axial chord length and cascade exit velocity is 4.83×10^5. Four different flow conditions were studied for each tip geometry. The no grid, no wake case has a baseline turbulence intensity of around 1.4% and the upstream grid produces a turbulence intensity of 4.9% upstream of the cascade. Two different wake generator rotational speeds produce wake Strouhal numbers of 0.2 and 0.4. Figure 5 shows the velocity signature from four flow conditions. A TSI hot wire system was used with a probe model 1260A-T15 for the velocity and turbulence measurements. The baseline case with no wake and no grid (NW-NG) produced a turbulence intensity of 1.4%. The turbulence intensity with the no wake and turbulence grid (NW-WG) was 4.8%. With the unsteady

Table 1 List of flow conditions

Flow condition	Rods	Grid	Turbulence Intensity	Wake Strouhal No. (S)
NW-NG	No	No	1.4%	0
NW-WG	No	Yes	4.8%	0
S02-NG	Yes	No	1.4%	0.2
S04-NG	Yes	No	1.4%	0.4
S04-WG	Yes	Yes	4.8%	0.4

wake superimposed on the grid, the periodicity of the wake passing is clearly evident. For the case with Strouhal number of 0.2, the wake passing period is 0.007 seconds. The case for the Strouhal number of 0.4 produces half the wake passing period of $S = 0.2$ as expected. The periodicity for the passing wake is clearly evident from the velocity signatures. Table 1 summarizes the flow conditions and the associated turbulence intensity for each case.

Pressure Measurements. The flow in all the three blade passages were equalized by repositioning the tailboards behind the cascade. The tailboards were adjusted till the leading edge velocities were uniform for all the three passages. Velocities were measured using a pitot probe traversing across the inlet line of the cascade. Figure 6 presents the surface normalized static pressure distributions $\{P_s/P_t\}$ for the test blade at 60% and 90% span locations versus the axial distance normalized with axial chord length (x/c). The static pressure measurements were used to calculate the local dynamic pressure for three different flow conditions. Results show that the upstream flow condition, whether wake or grid, does not affect the static pressure distributions on the blade surface significantly. This is true at both span locations. The pressure side shows almost uniform pressure over the entire surface. The lowest pressure occurs around 0.45C on the suction surface. The flow accelerates from the leading edge to 0.45C on the suction surface and then decelerates towards the trailing edge.

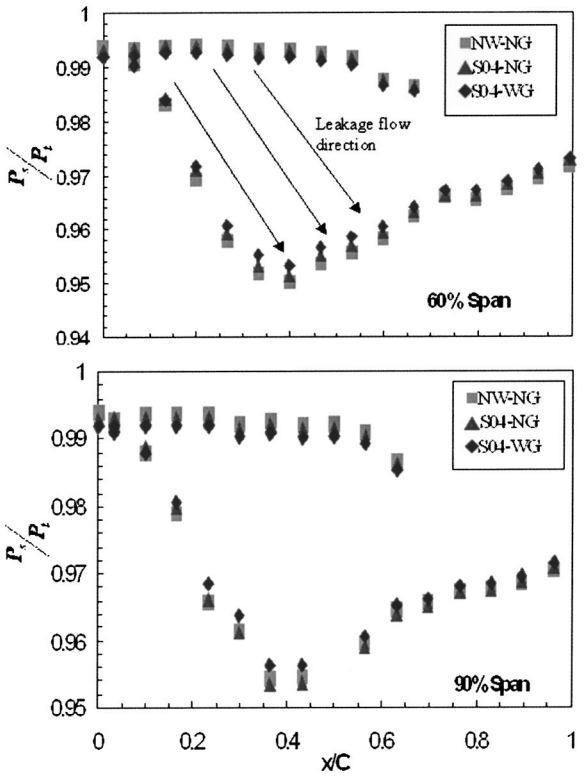

Fig. 6 Surface pressure distributions on the test blade at different span locations

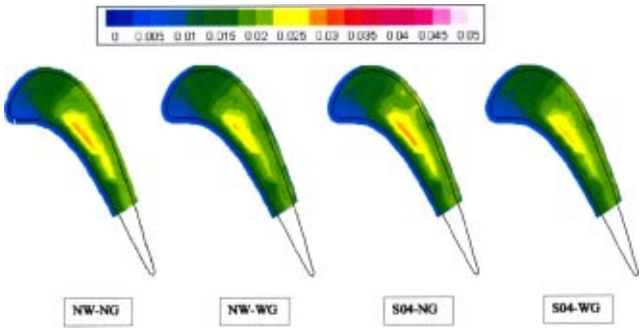

Fig. 7 Static pressure distributions $\{(P_t\text{-}P_s)/P_t\}$ on the shroud for the plain tip under different flow conditions

Figure 7 presents the normalized dynamic pressure distributions $\{(P_t\text{-}P_s)/P_t\}$ on the shroud for the plain tip with four different flow conditions. The presence of wake appears to show little effect on the shroud pressure distributions. However, the presence of grid-generated turbulence appears to reduce the low pressure region in the middle of the blade due to increased mixing.

Figure 8 presents the shroud pressure distributions for various tip geometries. The pressure distributions clearly show that the least pressure drop is obtained for the geometry with the suction side squealer (case 2). All the other cases show a large low-pressure zone in the middle of the tip surface. The pressure side squealer (case 3) shows almost similar pressure gradients as the plain tip (case 1) indicating that it may not be providing much resistance to the leakage flow. The other squealer geometries show lower pressure gradients than the plain tip.

Heat Transfer Measurements. Figure 9 presents detailed heat transfer distributions for the plain tip under different upstream flow conditions. The baseline case is the no wake, no grid case with a low turbulence intensity of 1.4%. For this condition, heat transfer coefficient is highest along the blade tip trailing edge region. The lowest heat transfer coefficients are obtained in the middle of the leading edge region. This region of low heat transfer was observed by previous studies. Bunker and Bailey [15] referred to it as the ''sweet spot.'' From the pressure distributions on the shroud (Fig. 8), it is clear that bulk of the leakage flow will follow the line along the strongest pressure gradient across the tip which is downstream of the leading edge region around $X/C = 0.4–0.5$. Further downstream, the heat transfer coefficient is higher due to highly accelerated flow over the tip. With a change in mainstream flow condition, the high heat transfer region seems to be unaffected. However, the sweet spot region sees higher heat transfer coefficients. It can be summarized that the increase in free-stream turbulence enhances heat transfer closer to the leading edge due to increased mixing caused by the introduction of the grid and wake into the flow.

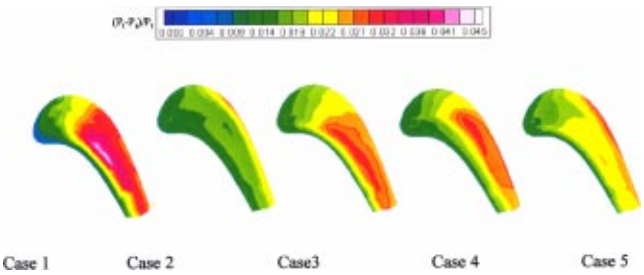

Fig. 8 Static pressure distributions $\{(P_t\text{-}P_s)/P_t\}$ on the shroud for all the different tip configurations

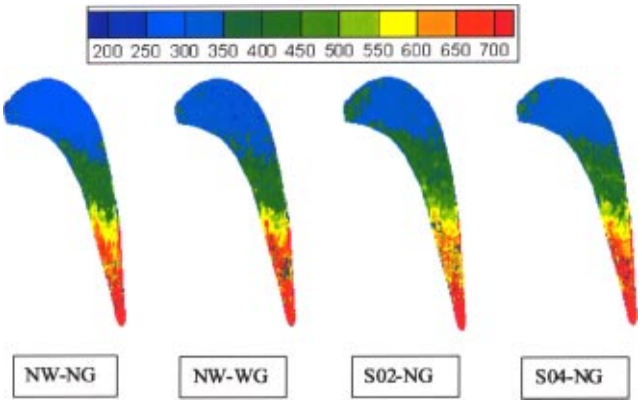

Fig. 9 Detailed heat transfer coefficient distributions on plain tips

Figure 10 compares the heat transfer coefficient distributions on the tip for all the different tip geometry configurations for the baseline flow condition of no wake, no grid. The scale for heat transfer coefficients is on the right side of the cases. For the squealer geometries, there are no measurements on the rim surfaces. It is expected that the heat transfer coefficients on the rim itself will be significantly higher than the tip surface. This may cause the overall average heat transfer over the tip surface including the rim surface area to be higher than measured. However, the increase in surface area and reduced leakage flow can reduce the enhancement due to the presence of rims. Also, these rims can be expendable pieces that can be brazed on the surface after several hours of operating and thus protecting the actual tip from loss of material.

The suction side squealer produces lower heat transfer coefficients over the entire tip surface. For this case, the blockage is not affecting the leakage flow till the flow reaches the suction side rim. This causes the leakage flow to enter the tip gap and move along the tip towards the trailing edge causing slightly higher h values at the trailing edge. Pressure side squealer produces slightly similar heat transfer coefficients on the leading edge as compared to baseline case. Because of the squealer on the pressure side, the leakage flow finds an obstruction at starting which causes detachment of this flow over the blade tip. This in turn reduces the heat transfer coefficient over the tip along the leading edge. For the camberline squealer, due to the presence of the squealer at the mean camberline the leakage flow finds an obstruction that causes bifurcation of leakage flow. This causes even levels of heat transfer coefficients on both sides of the squealer. The full squealer produces lowest heat transfer coefficients over the entire tip surface as compared to all the tip geometries proposed. This is because the groove or cavity acts as a labyrinth seal to increase the resistance to the flow and thus reduces the leakage flow and the associated heat transfer. There is some flow attachment near the leading edge but the weaker leakage flow reduces overall heat transfer.

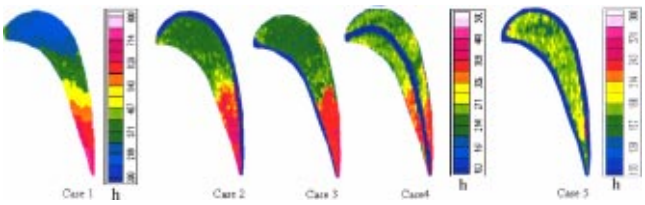

Fig. 10 Detailed heat transfer coefficient distributions for different tip configurations

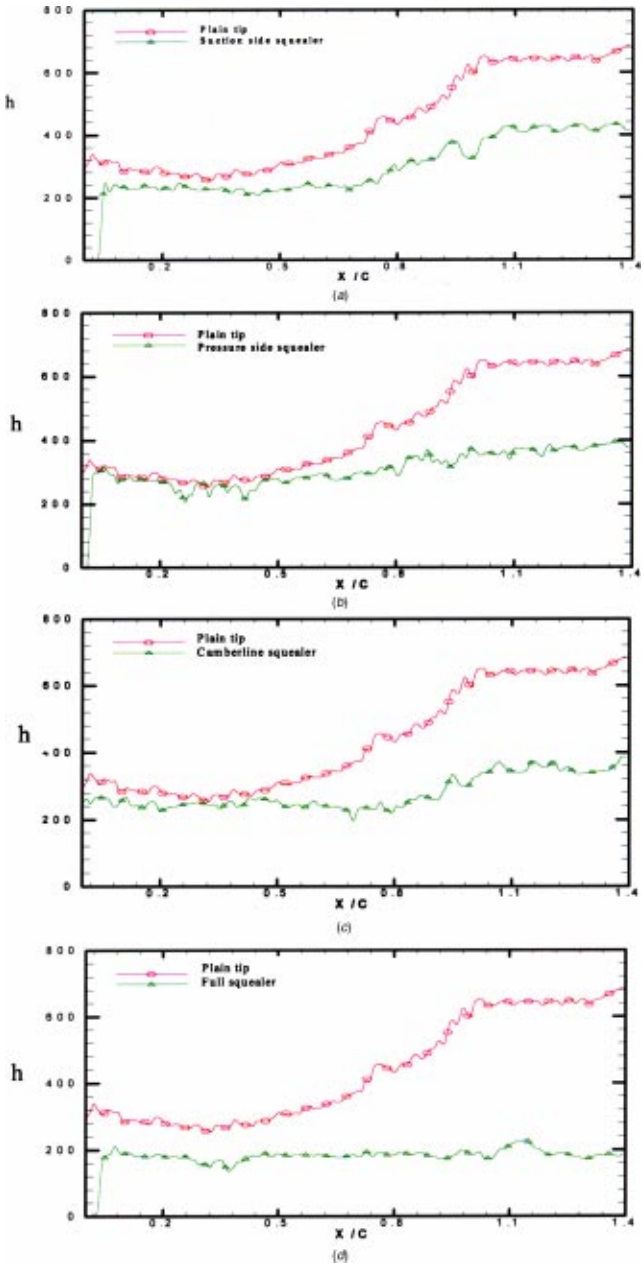

Fig. 11 Comparison of camberline heat transfer for each squealer tip with the plain tip: (*a*) suction side squealer; (*b*) pressure side squealer; (*c*) camberline squealer; and (*d*) full squealer.

Figure 11 presents the local heat transfer coefficients along the camberline for each squealer geometry and compares the case with the baseline plain tip case. The suction side squealer (case 5) produces lower heat transfer coefficients over the entire tip surface as compared to baseline tip as seen in Fig. 10. The pressure gradient across the tip is lowest, which indicates that leakage flow may be reduced. In this case, flow has similar condition to the plain tip with more clearance gap until it reaches suction side where it sees the suction side partial squealer. This squealer causes the detachment of the flow at the suction side of the tip. This reduces the tip heat transfer coefficient especially in the trailing edge region compared to other tip geometries.

The pressure side squealer produces slightly similar heat transfer coefficients on the leading edge as compared to baseline case as seen in Fig. 10. Because of the squealer on the pressure side,

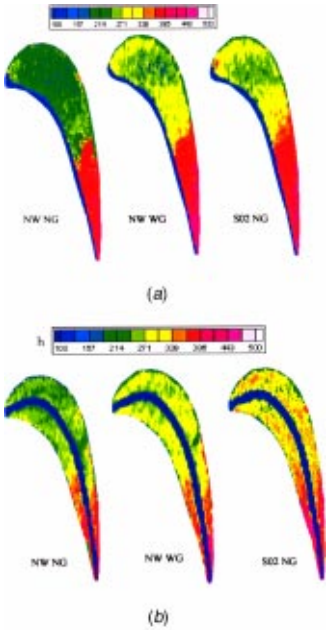

Fig. 12 Detailed heat transfer distributions under various flow conditions for different squealer geometries: (*a*) pressure side squealer; and (*b*) camberline squealer.

the leakage flow finds an obstruction on the pressure side rim, which causes detachment of this flow over the edge of the blade tip. But as the flow reattaches again on the tip, the flow gets accelerated. The pressure gradient increases after the pressure side squealer but this is lower compared to baseline case.

The camberline squealer produces slightly lower heat transfer coefficients on the leading edge as compared to baseline case as seen in Fig. 10. Due to the presence of the squealer at the mean camberline, the leakage flow finds an obstruction that causes detachment and bifurcation of this flow. But as the flow reattaches, the flow gets accelerated as seen in Fig. 8, the pressure gradient increases after the mean camberline squealer but this is lower compared to baseline case. This causes the reduction in the heat transfer coefficients on the trailing edge as compared to the baseline case.

The full squealer produces lowest heat transfer coefficients over the entire tip surface as compared to all the tip geometries proposed. This is because the groove or cavity acts as a labyrinth seal to increase the resistance to the flow and thus reduces the leakage flow and the associated heat transfer. Because of the flow recirculation in cavity, the heat transfer coefficient reduces 30–40% as compared to the baseline case that can be seen in Fig. 10. Overall, it appears that the full squealer produces the largest reduction in heat transfer coefficients over the entire blade tip.

Figure 12 presents the effect of upstream flow condition on surface heat transfer coefficients over two different tip geometries. The suction side squealer and the full squealer cases did not show any significant effect of the upstream flow condition on heat transfer. For the pressure side squealer, the heat transfer coefficient is almost similar in $X/C=0.05-0.6$ region as seen in Fig. 12. But for $X/C=0.62-1.1$, there is large increase in the heat transfer coefficient with the introduction of grid and wake. Thus in this case, with the introduction of unsteady effects there is increase in the heat transfer coefficient along the trailing edge region.

For camberline squealer, with the introduction of grid and wake, there is large increase in the overall tip heat transfer coefficient over the entire tip region as seen in Fig. 12. Thus in this case, the unsteady effects are dominant over the entire tip region. Because the squealer is placed on the midchord, the leakage flow entering the clearance gap through the leading edge is bifurcated along the pressure side rim and suction side rims resulting in the even heat transfer from leading edge to trailing edge on both sides of the squealer.

Conclusions

A systematic investigation of the use of squealer tips and their effects on flow and heat transfer over a turbine blade tip in a low speed cascade was performed. A Hue-based steady state liquid crystal technique was used to make detailed heat transfer coefficient measurements. Several squealer tips were investigated for leakage flow and associated heat transfer characteristics. Results show that the full squealer produces reduced leakage flow and lowest heat transfer coefficient over the tip compared to the other cases. The suction side squealer also significantly reduces leakage flow and heat transfer. However, the pressure side squealer is almost similar to the plain tip and does not appear to reduce heat transfer over the tip.

The effect of upstream flow condition with the presence of a grid to generate free-stream turbulence of 4.8% and to simulate passing wake due to upstream NGV trailing edge was also investigated. The presence of the wake and free-stream turbulence produced higher heat transfer coefficients on the plain tip. However, the pressure side squealer and the camberline squealer show some effect of upstream flow condition. Overall, it appears that the full squealer performs the best in reducing overall heat transfer on the tip.

Acknowledgment

This work was supported partly through a grant from NSF under the GOALI program and through a grant from NASA EPSCoR–LaSPACE. Acknowledgements are due to the program managers Drs. A. Emery, S. Thynell, and R. Smith from NSF and to Dr. John Wefel of LaSPACE consortium. Acknowledgments are also due to Dr. R. S. Bunker from General Electric Global R&D center, for sharing his technical expertise. Acknowledgements are also due to Dr. S. Acharya, Mr. L. Bonadona, Mr. J. Watkins, and Ms. S. Dupree for their help with the cascade facility.

Nomenclature

C = blade axial chord length (12 cm)
d = wake rod diameter (cm)
D = depth of squealer cavity from tip of rim
h = local heat transfer coefficient (W/m^2-K)
H = tip gap height
HSI = Hue-Saturation-Intensity
n = number of rods on wake generator
N = speed of rotating rods (rpm)
P_s = local static pressure
P_t = total pressure at inlet (atmospheric pressure)
q'' = surface heat flux (W/m^2)
Re = free-stream Reynolds number ($V_2 C_X/\nu$)
RGB = Red-Green-Blue
S = wake Strouhal number, $2\pi Ndn/(60V_1)$
t = tip clearance gap
T_m = mainstream temperature
T_w = local wall temperature
Tu = free-stream mean turbulence intensity at cascade inlet
V_1 = cascade inlet velocity (m/s)
V_2 = cascade exit velocity (m/s)
W = width of squealer cavity
X = streamwise distance from leading edge to trailing edge
ν = kinematic viscosity of inlet air

References

[1] Bindon, J. P., 1989, "The Measurement and Formation of Tip Clearance Loss," ASME J. Turbomach., **111**, pp. 257–263.
[2] Morphis, G., and Bindon, J. P., 1988, "The Effect of Relative Motion, Blade

Edge Radius and Gap Size on the Blade Tip Pressure Distribution in an Annular Turbine Cascade with Clearance,'' AMSE Paper 88-GT-256.
[3] Yaras, M., Yingkang, Z., and Sjolander, S. A., 1989, ''Flow Field in the Tip Gap of a Planar Cascade of Turbine Blades,'' ASME J. Turbomach., **111**, pp. 276–283.
[4] Yamamoto, A., 1989, ''Endwall Flow/Loss Mechanisms in a Linear Turbine Cascade With Blade Tip Clearance,'' ASME J. Turbomach., **111**, pp. 264–275.
[5] Kaiser, I., and Bindon, J. P., 1997, ''The Effect of Tip Clearance on the Development of Loss Behind a Rotor and a Subsequent Nozzle,'' ASME Paper 97-GT-53.
[6] Mayle, R. E., and Metzger, D. E., 1982, ''Heat Transfer at the Tip of an Unshrouded Turbine Blade,'' *Proceedings of the 7th International Heat Transfer Conference*, **3**, pp. 87–92.
[7] Metzger, D. E., Bunker, R. S., and Chyu, M. K., 1989, ''Cavity Heat Transfer on a Transverse Grooved Wall in a Narrow Flow Channel,'' ASME J. Heat Transfer, **111**, pp. 73–79.
[8] Chyu, M. K., Moon, H. K., and Metzger, D. E., 1989, ''Heat Transfer in the Tip Region of Grooved Turbine Blades,'' ASME J. Turbomach., **111**, pp. 131–138.
[9] Metzger, D. E., Dunn, M. G., and Hah, C., 1990, ''Turbine Tip and Shroud Heat Transfer,'' *Proceeding of International Gas Turbine and Aeroengine Congress and Exposition*, Brussels, Belgium, September 1990, Paper No. 90-GT-333.
[10] Yang, T. T., and Diller, T. E., 1995, ''Heat Transfer and Flow for a Grooved Turbine Blade Tip in a Transonic Cascade,'' *Proceedings of International Mechanical Engineering Congress and Exposition*, San Francisco, ASME Paper No. 95-WA/HT-29.
[11] Bunker, R. S., Bailey, J. C., and Ameri, A. A., 1999, ''Heat Transfer and Flow on the First Stage Blade Tip of a Power Generation Gas Turbine: Part 1—Experimental Results,'' ASME J. Turbomach., **122**, pp. 263–271.
[12] Ameri, A. A., and Bunker, R. S., 1999, ''Heat Transfer and Flow on the First Stage Blade Tip of a Power Generation Gas Turbine: Part 2—Simulation Results,'' ASME J. Turbomach., **122**, pp. 272–277.
[13] Azad, Gm. S., Han, J. C., and Teng, S., 2000, ''Heat Transfer and Pressure Distributions on a Gas Turbine Blade Tip,'' *Proceedings of International Gas Turbine and Aeroengine Congress and Exposition*, ASME paper 2000-GT-194.
[14] Azad, G. S., Han, J. C., and Boyle, R. J., 2000, ''Heat Transfer and Flow on the Squealer Tip of a Gas Turbine Blade,'' *Proceedings of International Gas Turbine and Aeroengine Congress and Exposition*, Munich, Germany, 2000-GT-195.
[15] Bunker, R. S., and Bailey, J. C., 2001, ''Effect of Squealer Cavity Depth and Oxidation on Turbine Blade Tip Heat Transfer,'' *International Gas Turbine and Aeroengine Congress and Exposition*, New Orleans, June 2001.
[16] Azad, G. S., Han, J. C., Bunker, R. S., and Lee, C. P., 2001, ''Effect of Squealer Geometry Arrangement on Gas Turbine Blade Tip Heat Transfer,'' *Proceedings of International Mechanical Engineering Congress and Exposition*, New York, New York, November 2001, IMECE2001/HTD-2431.
[17] Dunn, M. G., and Haldeman, C. W., 2000, ''Time-Averaged Heat Flux for a Recessed Tip, Lip and Platform of a Transonic Turbine Blade,'' ASME Paper 2000-GT-0197.
[18] Nasir, H., Ekkad, S. V., Kontrovitz, D. M., Bunker, R. S., and Prakash, C., 2003, ''Effect of Tip Gap and Squealer Geometry on Detailed Heat Transfer Measurements over a HPT Rotor Blade Tip,'' IMECE 2003-41294, ASME IMECE 2003, Washington, D.C.
[19] Wittig, S., Schulz, A., Dullenkopf, K., and Fairbank, J., 1988, ''Effects of Free-Stream Turbulence and Wake Characteristics on the Heat Transfer Along a Cooled gas Turbine Blade,'' ASME Paper No. 88-GT-179.
[20] Han, J. C., Zhang, L., and Ou, S., 1993, ''Influence of Unsteady Wake on Heat Transfer Coefficient from a Gas Turbine Blade,'' ASME J. Heat Transfer, **115**, pp. 904–911.
[21] Teng, S., Han, J. C., and Azad, Gm. S., 2001, ''Detailed Heat Transfer Coefficient Distributions on a Large Scale Gas Turbine Blade Tip,'' ASME J. Heat Transfer, **123**, pp. 803–809.
[22] Saxena, V., Nasir, H., and Ekkad, S. V., 2003, ''Effect of Blade Tip Geometry on Tip Flow and Heat Transfer for a Blade in a Low Speed Cascade,'' ASME GT2003-38176, ASME IGTI Conference, Atlanta, GA, June 2003.
[23] Camci, C., Kim, K., and Hippensteele, S. A., 1991, ''A New Hue Capturing Technique for Quantitative Interpretation of Liquid Crystal Images Used in Convective Heat Transfer Studies,'' ASME Paper 91-GT-277.
[24] Kline, S. J., and McClintock, F. A., 1953, ''Describing Uncertainties in Single Sample Experiments,'' Mech. Eng. (Am. Soc. Mech. Eng.), **75**, pp. 3–8.

The Effects of Nozzle Diameter on Impinging Jet Heat Transfer and Fluid Flow

Dae Hee Lee
e-mail: mechdhl@inje.ac.kr

Jeonghoon Song

Technology Innovation
Center for Automotive Parts,
School of Mechanical and Automotive
Engineering, Inje University, 607,
Obang-dong, Kimhae, Kyongnam 621-749 Korea

Myeong Chan Jo
School of Mechanical and Automotive
Engineering,
Inje University

The effects of nozzle diameter on heat transfer and fluid flow are investigated for a round turbulent jet impinging on a flat plate surface. The flow at the nozzle exit has a fully developed velocity profile. A uniform heat flux boundary is created at the plate surface by using gold film Intrex, and liquid crystals are used to measure the plate surface temperature. The experiments are performed for the jet Reynolds number (Re) of 23,000, with a dimensionless distance between the nozzle and plate surface (L/d) ranging from 2 to 14 and a nozzle diameter (d) ranging from 1.36 to 3.40 cm. The results show that the local Nusselt numbers increase with the increasing nozzle diameter in the stagnation point region corresponding to $0 \leqslant r/d \leqslant 0.5$. This may be attributed to an increase in the jet momentum and turbulence intensity level with the larger nozzle diameter, which results in the heat transfer augmentation. In the mean time, the effect of the nozzle diameter on the local Nusselt numbers is negligibly small at the wall jet region corresponding to $r/d > 0.5$. [DOI: 10.1115/1.1777583]

1 Introduction

Impinging jets greatly enhance heat and mass transfer and have thus been widely used in a variety of engineering applications, such as cooling hot steel plates, tempering glass, drying papers and films, cooling turbine blades and electronic components, and the production of thin film transistor—liquid crystal diodes (TFT-LCDs). Previous studies on impinging jets have considered the effects of multiple jets and of Reynolds number, nozzle to plate distance, nozzle geometry, jet temperature, target shape orientation, cross flow, surface shape of the flow, etc.

Several reviews and summary papers on impinging jet heat transfer have been published, including those by Martin [1], Down and James [2], Goldstein et al. [3], and Viskanta [4]. Most of the previous impinging jet studies have considered only a flat surface. Hoogendoorn [5] used both a long straight pipe and a smoothly converging nozzle to study the effects of turbulence on heat transfer at the stagnation point. Lee et al. [6] and Yan [7] measured the heat transfer coefficient obtained from a fully developed jet impinging on a flat plate, and Goldstein and Franchett [8] studied the heat transfer to a jet impinging on a plane surface at different oblique angles. Lee and his colleagues [9–11] researched the characteristics of heat transfer and fluid flow from an impinging jet on concave and convex plates, using liquid crystals to measure surface temperatures.

The literature survey shows some previous studies that deal with the dependence of Nusselt number on nozzle diameter of the impinging jet. Garimella and Nenaydykh [12] studied the effect of square-edged nozzle diameter and aspect ratio on the local heat transfer from an impinging submerged and confined liquid jet. Womac et al. [13] used free and submerged circular liquid jet having a uniform velocity profile and Steven and Webb [14] carried out the experiments with fully developed free liquid jet. They all found that increasing the nozzle diameter for the same Reynolds number resulted in an increase in stagnation point Nusselt number.

The present study is undertaken to investigate the effects of nozzle diameter on impinging jet heat transfer and fluid flow. Local Nusselt numbers are determined for a submerged air jet issuing from a long straight, circular pipe. The distributions of the mean velocity and turbulence intensity along the free jet centerline are also measured. The experiments are carried out for the jet Reynolds number of Re=23,000, the nozzle diameters of $d = 1.36$, 2.16, and 3.40 cm, and the dimensionless nozzle-to-surface distance ranging from $L/d = 2$ to 14.

2 Test Apparatus

A schematic diagram of the experimental apparatus is shown in Fig. 1. It is nearly identical to the one used for the study by Lee et al. [11] except for the impinging surface geometry. Laboratory air, delivered by a 2 horsepower centrifugal blower, first enters a 6.35 cm inner diameter copper pipe. This pipe section contains a cross-flow heat exchanger, with water from a constant temperature bath circulating inside. This heat exchanger is used to adjust the air temperature so that the jet issuing from the nozzle exit is maintained to within ±0.2°C of the ambient temperature. The copper pipe then connects to a 6.3 cm inner diameter cast acrylic pipe with an ASME orifice plate flow meter. The mass flow rate of the air through the pipe is determined from the pressure drop measured across this orifice plate, using a MERIAM/34MB2-TM micro-manometer (which has an accuracy of ±0.001 cm of water differential pressure).

Located 150 cm downstream end of the pipe is a smooth transition pipe, which connects to a smaller cast acrylic pipe. Three different diameters ($d = 1.36$, 2.15, and 3.40 cm) and lengths ($Z = 79$, 125, and 197 cm) of pipe are used to investigate the diameter effect on heat transfer and fluid flow. These pipes have a development length-to-pipe diameter ratio z/d of 58, and produce a fully developed round jet, which impinges perpendicularly upon test surface. The piston-cylinder type arrangement of the pipe system permits the distance between the nozzle and the test surface to be set to different values (with an accuracy of ±0.05 cm) up to a maximum value L of 48 cm.

The jet temperature is measured using a thermocouple, which is constructed of 0.025 cm diameter Chromel-Alumel thermocouple wire, and placed in the air stream at a location 10 cm upstream from the nozzle exit. Three thermocouples of the same type and gauge are used to measure the ambient temperature. The signal produced by each of these thermocouples is acquired using a data acquisition system, which consists of Strawberry Tree/Data Shuttle 12-bit A/D board and Pentium PC computer. Each thermo-

Contributed by the Heat Transfer Division for publication in the JOURNAL OF HEAT TRANSFER. Manuscript received by the Heat Transfer Division August 21, 2003; revision received December 16, 2003. Associate Editor: J. H. Lienhard V.

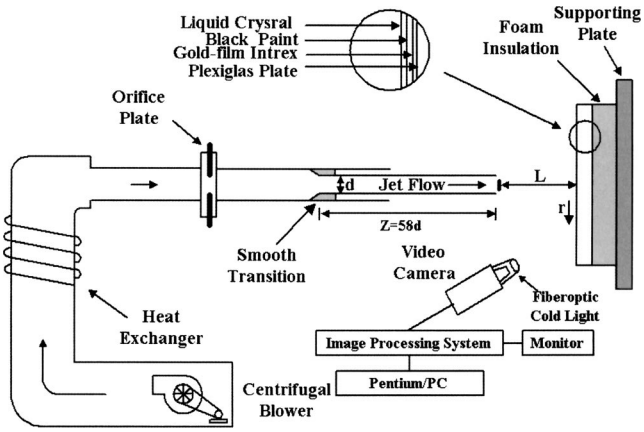

Fig. 1 Schematic diagram of the test apparatus for a jet impinging on a flat plate surface

couple is calibrated in a NESLAB/RTE-221D constant temperature bath within ±0.1°C accuracy, using a PRT(Platinum Resistance Thermometer) as a temperature standard.

The test plate is a clear 1 cm thick Plexiglas sheet. This material is chosen for its low thermal conductivity, to minimize heat conduction to the wall. A sheet of Intrex is glued to the surface of the plate. Copper foil strip electrodes are attached to either end of the Intrex surface, and silver-loaded paint is used to establish a good electrical contact. Passing an AC current through the Intrex creates an essentially uniform wall heat flux boundary. An airbrush is then used to apply the black paint and the micro-encapsulated thermo-chromic liquid crystal to the Intrex surface. The liquid crystal used in this experiment is Hallcrest R35C1W. It has a narrow band of approximately 1°C over which the entire color spectrum occurs. A foam insulation plate is placed behind the test plate to minimize conduction heat losses. The entire plate assembly is mounted vertically, with the test surface perpendicular to the direction of the jet flow.

A digital color image processing system is used to accurately determine the temperature corresponding to liquid crystal color. The liquid crystal is calibrated within ±0.2°C by utilizing the same calibration apparatus used by Lee et al. [11]. The image processing system consists of Sony FX310 CCD camera, DARIM/Visible Office frame grabber, and Pentium PC. A white light source from an optical fiber that emits little heat radiation is used to minimize any radiation effects from the lighting. A TSI IFA-300 hot-wire anemometer is used to measure the centerline velocity and turbulence intensity along the free jet centerline. The anemometer signals are low pass filtered at 5 kHz through a signal conditioner, then digitized by a universal waveform analyzer with a sampling frequency of 10 kHz. A total of 20 ensembles of 4096 data sets for the mean and RMS velocities are averaged.

3 Experimental Analysis

The measurement technique used in this study, described by Lee et al. [10,11,15], provides a method of using liquid crystal to determine surface temperatures. An essentially uniform wall heat flux is established by electrically heating the very thin gold coating on the Intrex surface. The heat flux is adjusted by changing the current passing through the Intrex, which changes the surface temperature. Under the uniform wall heat flux condition, an isotherm on the Intrex surface corresponds to a contour of a constant heat transfer coefficient. The local heat transfer coefficient is then calculated from

$$h = \frac{q_v}{T_w - T_j} \tag{1}$$

Table 1 Nusselt number uncertainty analysis

X_i	value	δX_i	$(\frac{\delta X_i}{Nu}\frac{\partial Nu}{\partial X_i})\times 100(\%)$	
			r/d=0	5.09
f	1	0.02	2.00	2.00
T_w	35.5 (°C)	0.20	1.44	1.43
T_i	21.5; 21.4 (°C)	0.15	1.04	0.95
q_c	0 (W/m^2)	22.17; 6.55	0.97	0.89
V	34.88; 19.48 (V)	0.125	0.36	0.64
1	3.79; 2.17 (A)	0.01	0.26	0.46
d	2.16 (cm)	5.0×103	0.22	0.23
ε	0.9	0.05	0.19	0.60
A	0.0576 (m^2)	5.0×103	0.09	0.09
	Total Nu uncertainty	δNu/Nu=2.90		2.96

where the net heat flux q_v was obtained by subtracting the heat loss from the total heat flux through the Intrex; i.e.,

$$q_v = \frac{fIV}{A} - \varepsilon\sigma(T_w^4 - T_\alpha^4) - q_c \tag{2}$$

Here f is the ratio of the local electrical heating to the average heating and is a measure of the uniformity of the gold coating on the Intrex. Baughn et al. [16] found the uniformity to be as high as 98 percent for a carefully selected small area of the Intrex corresponding in size to that of the present experiment. Therefore, for the heat flux calculations we assumed $f \approx 1$, but f was maintained in Eq. (2) because it contributed to the overall uncertainty (see Table 1).

The uncertainty in the local Nusselt numbers is estimated with a 95 percent confidence level using the methods suggested by Kline and McKlintock [17]. Table 1 shows that the overall uncertainty in the Nusselt number is estimated to be 2.90 perent when Re=23,000, $L/d=6$, and $r/d=0$, and 2.96 percent when Re =23,000, $L/d=6$, and $r/d=5.09$. The contribution of each measured variable to the overall uncertainty is also shown in Table 1 for the specified conditions. The uncertainty in the gold coating uniformity factor, *f*, is the largest contributor to the overall uncertainty. Another important source of uncertainty is the liquid crystal measurement of the plate wall temperature, T_w.

4 Results and Discussion

Lee et al. [15] proved in their research that a jet flow has a fully developed velocity profile at the nozzle exit, and the present research uses the same flow test apparatus. Therefore, this study measures the local heat transfer coefficient, the centerline velocity, and the turbulence intensity when a fully developed round jet impinges perpendicular to a flat plate.

Figures 2 and 3 show the distributions of the mean velocity and turbulence intensity along the free jet centerline for nozzle diam-

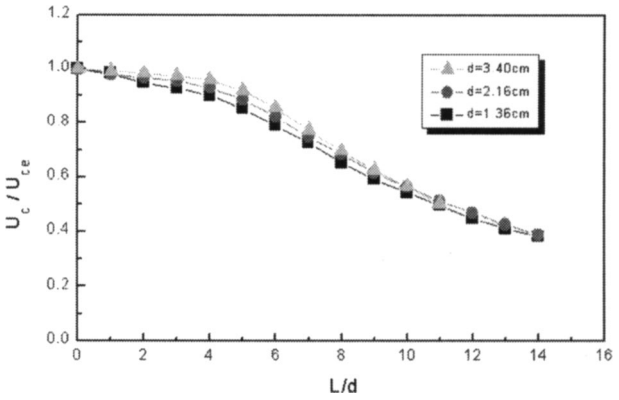

Fig. 2 Velocity profiles along the free jet centerline for Re=23,000

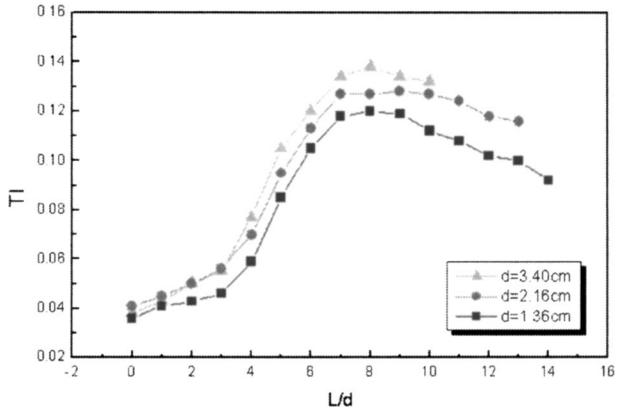

Fig. 3 Turbulence intensity profiles along the free jet centerline for Re=23,000

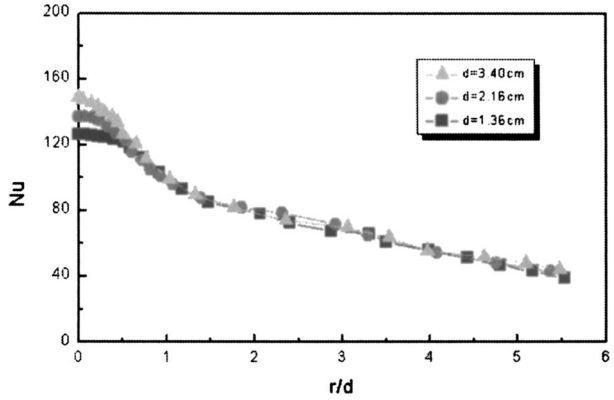

Fig. 5 Effect of nozzle diameter on the local Nusselt number distributions for $L/d=6$ and Re=23,000

eters of $d=1.36$, 2.16, and 3.40 cm when Re=23,000. Giralt et al. [18] defines the potential core length as the distance from the nozzle exit to the point where the centerline velocity (U_c) is 98 percent of the nozzle exit velocity (U_{ce}). According to this definition, the potential core lengths, when $d=1.36$, 2.16, and 3.40 cm, are 2.3, 2.7, and 3.0 times the nozzle diameter, respectively. Thus, it follows that the potential core length increases with an increasing nozzle diameter. Figure 2 also shows that at the same L/d, the larger nozzle diameter produces the bigger mean velocity (or bigger jet momentum).

It can be seen from Fig. 3 that for all nozzle diameters, the turbulence intensity within the potential core maintains their magnitudes at the levels of 4~5 percent. However, outside the potential core, magnitudes of the turbulence intensity level rapidly increase until $L/d\approx 7$ to 8, due to an active mixing of the jet flow with an ambient air. Figure 3 also shows that beyond $L/d=8$, the turbulence intensity gradually decreases.

Figure 4 shows the effect of the nozzle diameter on the stagnation point Nusselt number Nu_{st}. When $d=3.40$ cm, Nu_{st} is 10.0 percent and 19.1 percent larger than the values obtained when $d=2.16$ and 1.36 cm, respectively. The similar trend can be seen from the results by Yan [7] for circular and straight pipe with nozzle diameter of $d=4.03$ cm and the same Reynolds number of Re=23,000. Yan's Nu_{st} is 4.7 percent larger than the value obtained in the present study with $d=3.40$ cm. This may be attributed to the increase in the mass flow rate, jet momentum, and turbulence intensity with the larger nozzle diameter.

Gau and Chung [19] report that the size of the vortices that impinge on a plate increases as the nozzle diameter becomes larger, which in turn results in the heat transfer augmentation.

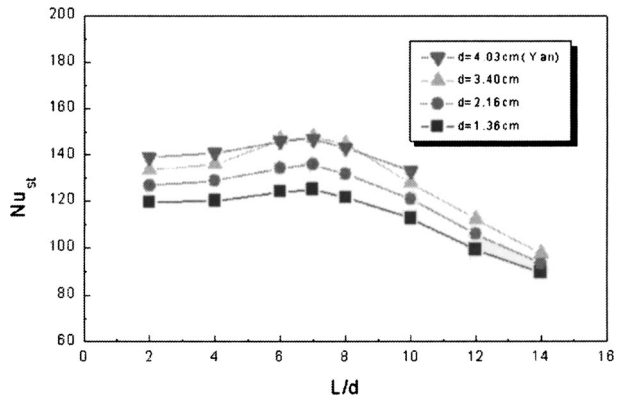

Fig. 4 Effect of nozzle diameter on the stagnation point Nusselt number for Re=23,000

They also show that the maximum Nu_{st} occurs at $L/d\approx 7$. These behaviors are consistent with our experimental results. Lee et al. [15] and Kataoka et al. [20] too report that the maximum Nu_{st} occurs at $L/d\approx 7$ where the turbulence intensity reaches roughly a maximum value, which is in excellent agreement with the results in the present study shown in Figs. 3 and 4. In the mean time, the effect of nozzle diameter on Nu_{st} is gradually diminished when $L/d>8$, and does not seem to exist beyond $L/d=18\sim 20$.

Figure 5 shows the local Nusselt number distributions when Re=23,000 and $L/d=6$ for different nozzle diameters. The Nusselt numbers increase with the increasing nozzle diameter at the stagnation point region corresponding to $0\leqslant r/d\leqslant 0.5$. However, the effect of the nozzle diameter on the Nusselt numbers is negligibly small at the wall jet region corresponding to $r/d>0.5$. This is because the impinging jet flow characteristics are nearly lost in the process of the re-development of the boundary layer after the jet impinges on the plate. It should be noted that the local Nusselt number measurements were made for the range of $L/d=2$ to 14, and the results at $L/d=6$ only are selected as a representative case. However, the results at other L/d's (not shown here) indicate that the diameter effect on the stagnation point region is more marked for $2\leqslant L/d\leqslant 8$ and its effect gradually diminishes as L/d changes from 10 to 14.

5 Summary and Conclusions

The effects of nozzle diameter and nozzle-to-surface distance on heat transfer and fluid flow are investigated for a round turbulent jet impinging on a flat surface at a uniform heat flux boundary condition. The flow at the nozzle exit has a fully developed velocity profile. The jet Reynolds number Re is 23,000, and the dimensionless nozzle-to-surface distance L/d ranges from 2 to 14. Three nozzle diameters d of 1.36, 2.16, and 3.40 cm are considered. Local Nusselt number distributions are determined from surface temperatures, which are measured on the flat surface using thermochromic liquid crystals and a digital color image processing system. Important observations from the experimental data are noted and summarized below.

1. According to the distributions of the mean velocity and turbulence intensity along the free jet centerline when Re =23,000, the potential core lengths for nozzle diameters of $d=1.36$, 2.16, and 3.40 cm, are 2.3, 2.7, and 3.0 times the nozzle diameter, respectively. Thus, the potential core length increases with an increasing nozzle diameter. In other words, for the same L/d, the larger nozzle diameter produces the bigger mean velocity (or bigger momentum). In the mean time, the turbulence intensity within the potential core maintains their magnitudes at the levels of 4~5 percent. However, outside the potential core, the turbulence intensity rap-

idly increases up to $L/d \approx 8$, due to an active mixing of the jet flow with an ambient air, and gradually decreases beyond $L/d = 8$.

2. When $d = 3.40$ cm, the stagnation point Nusselt number Nu_{st} is 10.0 percent and 19.1 percent larger than the values obtained when $d = 2.16$ and 1.36 cm, respectively. This may be attributed to the increase in the jet momentum and turbulence intensity with the larger nozzle diameter, which in turn results in the heat transfer augmentation at the stagnation point. In the mean time, the effect of nozzle diameter on Nu_{st} is gradually diminished when $L/d > 8$, and does not seem to exist beyond $L/d = 18 \sim 20$.
3. When Re=23,000 and for all nozzle diameters tested, the maximum Nu_{st} occurs at $L/d \approx 7$, which is consistent with the results from other investigations. It turns out that the physical mechanism for the maximum Nu_{st} to occur at $L/d \approx 7$ is that the turbulence intensity reaches roughly a maximum value in that region.
4. The local Nusselt numbers increase with the increasing nozzle diameter at the stagnation point region corresponding to $0 \leqslant r/d \leqslant 0.5$. However, the effect of the nozzle diameter on the local Nusselt numbers does not exist at the wall jet region corresponding to $r/d > 0.5$. This may be attributed to the fact that the impinging jet flow characteristics are almost lost in the process of the re-development of the boundary layer after the jet impinges on the plate.

Nomenclature

A = surface area of the gold film Intrex (m^2)
d = pipe nozzle diameter (cm)
f = gold coating uniformity factor
h = heat transfer coefficient ($W/m^2 K$)
I = current across the gold film Intrex (A)
k_a = thermal conductivity of air (W/mK)
L = distance from the nozzle to the plate surface (cm)
Nu = local Nusselt number, hd/k
Nu_{st} = stagnation point Nusselt number
q_c = conduction heat loss (W/m^2)
q_r = radiation heat loss (W/m^2)
q_v = net heat flux (W/m^2)
r = streamwise distance from the stagnation point (cm)
Re = Reynolds number, Ud/ν
T_a = ambient temperature (°C)
T_j = jet temperature (°C)
T_w = wall temperature (°C)
u = fluctuating velocity along the free jet centerline (m/s)
U = jet mean velocity inside the pipe nozzle (m/s)
U_c = mean velocity along the free jet centerline (m/s)
U_{ce} = jet centerline mean velocity at the nozzle exit (m/s)
TI = turbulence intensity along the free jet centerline, $\sqrt{\overline{u^2}}/U_{ce}$
V = voltage across the gold film Intrex (V)

Greek symbols

ε = emissivity of the liquid crystal and black-paint-coated surface
ν = kinematic viscosity of air (m^2/s)
σ = Stefan-Boltzmann constant ($W/m^2 K^4$)

References

[1] Martin, H., 1977, "Heat and Mass Transfer Between Impinging Gas Jets and Solid Surfaces," *Advances in Heat Transfer*, Academic Press, New York, pp. 1–60, Chpt. 13.
[2] Down, S. J., and James, E. H., 1987, "Jet Impinging Heat Transfer—A Literature Survey," ASME Paper No. 87-H-35.
[3] Goldstein, R. J., Behbahani, A. I., and Heppelmann, K. K., 1986, "Streamwise Distribution of the Recovery Factor and the Local Heat Transfer Coefficient to an Impinging Circular Air Jet," Int. J. Heat Mass Transfer, **29**(8), pp. 1227–1235.
[4] Viskanta, R., 1993, "Heat Transfer to Impinging Isothermal Gas and Frame Jet," Exp. Therm. Fluid Sci., **6**, pp. 111–134.
[5] Hoogendoorn, C. J., 1977, "The Effect of Turbulence on Heat Transfer at Stagnation Point," Int. J. Heat Mass Transfer, **20**, pp. 1333–1338.
[6] Lee, D. H., Grief, R., Lee, S. J., and Lee, J. H., 1995, "Heat Transfer From a Surface to a Fully Developed Axisymmetric Impinging Jet," ASME J. Heat Transfer, **117**, pp. 772–776.
[7] Yan, X., 1993, "A Preheated-Wall Transient Method Using Liquid Crystals for the Measurement of Heat Transfer on External Surfaces and in Ducts," Ph.D. dissertation, University of California, Davis, CA.
[8] Goldstein, R. J., and Franchett, M. E., 1988, "Heat Transfer From a Flat Surface to an Oblique Impinging Jet," ASME J. Heat Transfer, **110**, pp. 84–90.
[9] Chung, Y. S., Lee, D. H., and Lee, J. S., 1999, "Heat Transfer Characteristics of an Axisymmetric Jet Impinging on the Rib-Roughened Convex Surface," Int. J. Heat Mass Transfer, **42**, pp. 2102–2110.
[10] Lee, D. H., Chung, Y. S., and Kim, M. G., 1999, "Turbulent Heat Transfer From a Convex Hemispherical Surface to a Round Impinging Jet," Int. J. Heat Mass Transfer, **42**, pp. 1147–1156.
[11] Lee, D. H., Chung, Y. S., and Won, S. Y., 1999, "The Effect of Concave Surface Curvature on Heat Transfer From a Fully Developed Round Impinging Jet," Int. J. Heat Mass Transfer, **42**, pp. 2489–2497.
[12] Garimella, S., and Nenaydykh, B., 1996, "Nozzle-Geometry Effects in Liquid Jet Impingement Heat Transfer," Int. J. Heat Mass Transfer, **39**, pp. 2915–2923.
[13] Womac, D. J., Ramadhyani, S., and Incropera, F. P., 1993, "Correlating Equations for Impingement Cooling of Small Heat Sources With Single Circular Liquid Jets," ASME J. Heat Transfer, **115**, pp. 106–115.
[14] Stevens, J., and Webb, B. W., 1991, "Local Heat Transfer Coefficients Under an Axisymmetric, Single-Phase Liquid Jet," ASME J. Heat Transfer, **113**, pp. 71–78.
[15] Lee, D. H., Chung, Y. S., and Kim, D. S., 1997, "Turbulent Flow and Heat Transfer Measurements on a Curved Surface With a Fully Developed Round Impinging Jet," Int. J. Heat Mass Transfer, **18**(1), pp. 160–169.
[16] Baughn, J. W., Ireland, P. T., Jones, T. V., and Saniei, N. A., 1989, "Comparison of the Transient and Heated-Coating Methods for the Measurements of the Local Heat Transfer Coefficients on a Pin Fin," ASME J. Heat Transfer, **111**, pp. 877–881.
[17] Kline, S. J., and McKlintock, F. A., 1953, "Describing Uncertainties in Single Sample Experiments," Mech. Eng. (Am. Soc. Mech. Eng.), **75**, pp. 3–8.
[18] Giralt, F., Chia, C., and Trass, O., 1977, "Characterization of the Impingement Region in an Axisymmetric Turbulent Jet," Ind. Eng. Chem. Fundam., **16**, pp. 21–28.
[19] Gau, C., and Chung, C. M., 1991, "Surface Curvature Effect on Slot-Air Jet Impingement Cooling Flow and Heat Transfer Process," ASME J. Heat Transfer, **113**, pp. 857–864.
[20] Kataoka, K., Sahara, R., Ase, H., and Harada, R., 1987, "Role of Large Scale Coherent Structures in Impinging Jet Heat Transfer," J. Chem. Eng. Jpn., **20**, pp. 71–76.

Melting Heat Transfer Characteristics of Microencapsulated Phase Change Material Slurries With Plural Microcapsules Having Different Diameters

Hideo Inaba
e-mail: inaba@mech.okayama-u.ac.jp

Myoung-Jun Kim

Akihiko Horibe

Department of Mechanical Engineering
Faculty of Engineering,
Okayama University, Tsushimanaka 3-1-1,
Okayama 700-8530, Japan

The present study has been performed for obtaining the heat transfer enhancement characteristics of the plural microencapsulated solid-liquid phase change materials (PCM) slurry having different sizes, which flows in a straight tube heated under a constant wall heat flux condition. In the turbulent flow region, the friction factor of the plural PCM slurry was found to be lower than that of pure water flow due to the drag reducing effect of the PCM slurry. The heat transfer coefficient of the plural PCMs slurry flow in the tube was increased by both effects of latent heat evolved in phase change process and microconvection around plural microcapsules with different diameters. The experimental results revealed that the average heat transfer coefficient of the plural PCMs slurry flow was about 2~2.8 times greater than that of a single phase of water.
[DOI: 10.1115/1.1773584]

Keywords: Forced Convection, Heat Transfer, Melting, Phase Change, Spheres

Introduction

The use of microencapsulated phase change material slurry has been widely spread in practice since a couple of decades because of high energy storage density owing to latent heat absorption during a phase change process [1]. Especially, the possibility of PCM slurry transportation in a pipe was discussed by Mehalick and Tweedie [2]. Kasza and Chen [3] elucidated that the heat transfer coefficient of microencapsulated phase change suspension flow was increased three times as much as that of pure water flow in a straight pipe. Hart and Thornton [4] reported a two-fold increase in the effective specific heat of suspension and showed that the PCM microcapsules ranging of 5 μm to 50 μm in diameter could be pumped without destroying microcapsule's shell. The heat transfer characteristics of PCM slurry flow in circular ducts were clarified numerically by Charunyakorn et al. [5]. They showed that the heat transfer coefficient obtained by the PCM slurry were about 2~4 times higher than a pure water flow. Choi et al. [6] observed the physical mechanism of the convection heat transfer enhancement due to the PCM particles in a turbulent slurry pipe flow. The melting and solidification heat transfer characteristics of the microencapsulated PCM slurry flowing in a heat transfer tube were examined experimentally and numerically for the uniformly small size of microcapsules by authors [7].

The purpose of the present study is to examine heat transfer and flow drag characteristics of the microencapsulated PCM slurry composed of plural microcapsules in different diameters as well as different kinds of phase change materials (different melting points and latent heats) in a straight tube. According to the author's previous study [8], the optimum concentration of the uniformly small sized PCM particles (1.5 μm in diameter) in the microencapsulated PCM slurry was 20 mass percent by considering both the transmitted amount of heat and pumping power of the PCM slurry flow. The present experimental study was carried out to examine the flow drag and heat transfer characteristics by the mixing effect of large size microcapsules of 17 μm in diameter into the uniformly microencapsulated PCM slurry with small size microcapsules of 1.5 μm in diameter in the straight tube.

The proposed plural microencapsulated PCMs slurry composed of two kinds of PCMs having different melting points and diameters is applicable for cooling and heating air-conditioning demand, in which the microcapsules in a certain diameter are packed with PCM at a low melting point and other side those in the different diameter are packed with PCM at a high melting point. Therefore, the present study attempts to elucidate the relationship between the transmitted heat of plural PCMs slurry flow and its pumping power.

Physical Characteristics and Properties of PCM Slurry

The previous paper [7] by the authors concluded that the optimum mass concentration of PCM packed into microcapsules with a small size of 1.5 μm in diameter was $C_{sma}=20$ mass percent by considering both heat transfer and pumping power (pipe friction factor) in a straight tube heat exchanger. In order to increase the heat transfer coefficient of a mono-sized (PCM particles of 1.5 μm in diameter) and encapsulated PCM slurry in a tube flow, the plural PCMs slurry was produced by mixing larger PCM particles of 17 μm in diameter into a small size of PCM slurry at a concentration of $C_{sma}=20$ mass percent. As shown in Table 1, a melting point of small sized PCM (main constituent of paraffin waxes, n-tetradecane, $C_{14}H_{30}$) is $T_m=278.9$ K and a melting point of larger sized PCM (n-docosane, $C_{22}H_{46}$) is $T_m=318.2$ K. The purpose of the present study is to investigate the mixing effect of larger sized PCM particles under the condition without a phase change on the small sized PCM slurry with a phase change. Therefore, the temperature conditions in the present experiments were set below 318 K.

Contributed by the Heat Transfer Division for publication in the JOURNAL OF HEAT TRANSFER. Manuscript received by the Heat Transfer Division June 30, 2003; revision received April 16, 2003. Associate Editor: C. Amon.

Table 1 Physical properties of two kinds of phase change materials

Physical properties/ Phase change material	Small PCM particle n-tetradecane ($C_{14}H_{30}$)	Large PCM particle n-docosane ($C_{22}H_{46}$)
Melting temperature, T_m (K)	278.9	318.2
Latent heat of melting, L (kJ/kg)	229	189
Density	803 at 278 K	815 at 317 K
ρ (kg/m^3)	765 at 280 K	789 at 320 K
Specific heat	1.8 at 278 K	1.7 at 317 K
C_p (kJ/kg·K)	2.1 at 280 K	2.1 at 320 K
Thermal conductivity	0.273 at 278 K	0.281 at 317 K
λ (W/m·K)	0.211 at 280 K	0.224 at 320 K

Figure 1 presents the diameter frequency (percent) of the PCM particles for various mass ratios C_{big} of the large size PCM particles of 17 μm in diameter to those of 1.5 μm in diameter.

The average diameter d_{ave} of the plural microencapsulated PCMs particles dispersed in water is calculated by an arithmetic average method of mass raito C_{big} and two different diameters of PCM particles as shown in Eq. (1) and the total concentration, C_{tot} of the plural PCMs particles in the PCM slurry is also calculated by Eq. (2).

$$d_{ave}=\frac{d_{sma}+d_{big}C_{big}}{1+C_{big}} \tag{1}$$

$$C_{tot}=\frac{C_{sma}+C_{sma}C_{big}}{1+C_{sma}C_{big}} \tag{2}$$

The symbols in Figs. 2(a–d) show the measured data of density ρ_b, specific heat Cp_b, thermal conductivity k_b and viscosity μ_b of the plural microencapsulated PCMs slurry with temperature T, respectively. Those thermo-physical properties were obtained by the previous measuring methods [7] and [16] which were used with a densimeter (measuring error ± 3 percent) for density, a differential Scanning Calorimeter (measuring error ± 3 percent) for specific heat, a transient hot wire device (measuring error ± 7 percent) for thermal conductivity and a rotating viscometer (measuring error ± 6 percent) for viscosity, respectively. The solid, dot and dash lines in Fig. 2 were estimated from Eq. (3) for density and Eq. (4) for specific heat which were derived by the additional properties law [7] and Eq. (5) for thermal conductivity and Eq. (6) for viscosity were calculated by Maxwell's correlation and by Vand's correlation [10], respectively. The physical properties obtained from Eq. (3) to Eq. (6) were estimated from the averaged physical properties (constant value according to a solid or liquid phase condition) of two PCMs indicated in Table 1 and those of water with a temperature dependency.

$$\text{Density, } \rho_b:\rho_b=\rho_w\times(1-C_{tot})+\rho_p\times C_{tot} \tag{3}$$

$$\text{Specific heat, } Cp_b:Cp_b=Cp_pC_{tot}+Cp_w\times(1-C_{tot}) \tag{4}$$

$$\text{Thermal conductivity, } k_b:\ \frac{k_b}{k_w}=\frac{2+\frac{k_p}{k_w}+2C^*_{tot}\left(\frac{k_p}{k_w}-1\right)}{2+\frac{k_p}{k_w}-C^*_{tot}\left(\frac{k_p}{k_w}-1\right)} \tag{5}$$

In Eq. (5), the value of k_p corresponds to the average thermal conductivity of both PCMs.

The k_p was estimated as $k_p=(k_{sma}+k_{big}C_{big})/(1+C_{big})$.

$$\text{Viscosity, } \mu_b:\ \frac{\mu_b}{\mu_w}=(1-C^*_{tot}-1.16C^{*2}_{tot})^{-2.5} \tag{6}$$

Where C^*_{tot} means the volume concentration of the plural PCM particles in the PCM slurry.

From Figs. 2(a–d), it is noticed that the measured data of the physical properties are in good agreement with those estimated from Eqs. (3)–(6).

Experiment Apparatus and Method

Figure 3 shows the schematic diagram of experimental apparatus used to elucidate the flow drag and heat transfer characteristics of the plural microencapsulated PCMs slurry flow in a straight tube. The experimental apparatus consisted mainly of a heat transfer horizontal tube as a test section maintained at a constant wall heat flux, the PCM slurry circulating loop and a cooling tank with a refrigerator to solidify PCM in the microcapsules dispersed in water. And also the detail of the test section is shown at the lower part of Fig. 3. The test section was made of a stainless steel tube of 15 mm inside diameter, 0.8 mm in thickness and 5.85 m in length.

The constant heating wall heat flux condition was obtained by supplying directly DC electricity on the stainless steel tube from a DC power supply unit. The uncertainty of obtained data on the heat flux q_{hw} was estimated within ± 2 percent by measuring the electric current with a precision ammeter and voltage with a precision voltmeter across the stainless steel tube. The thermocouples which were insulated by applying the electric insulation material.

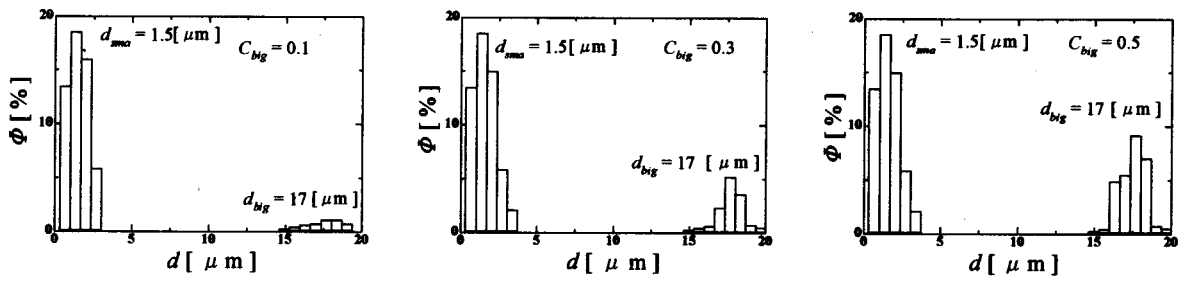

Fig. 1 The diameter distribution of the plural PCMs particles

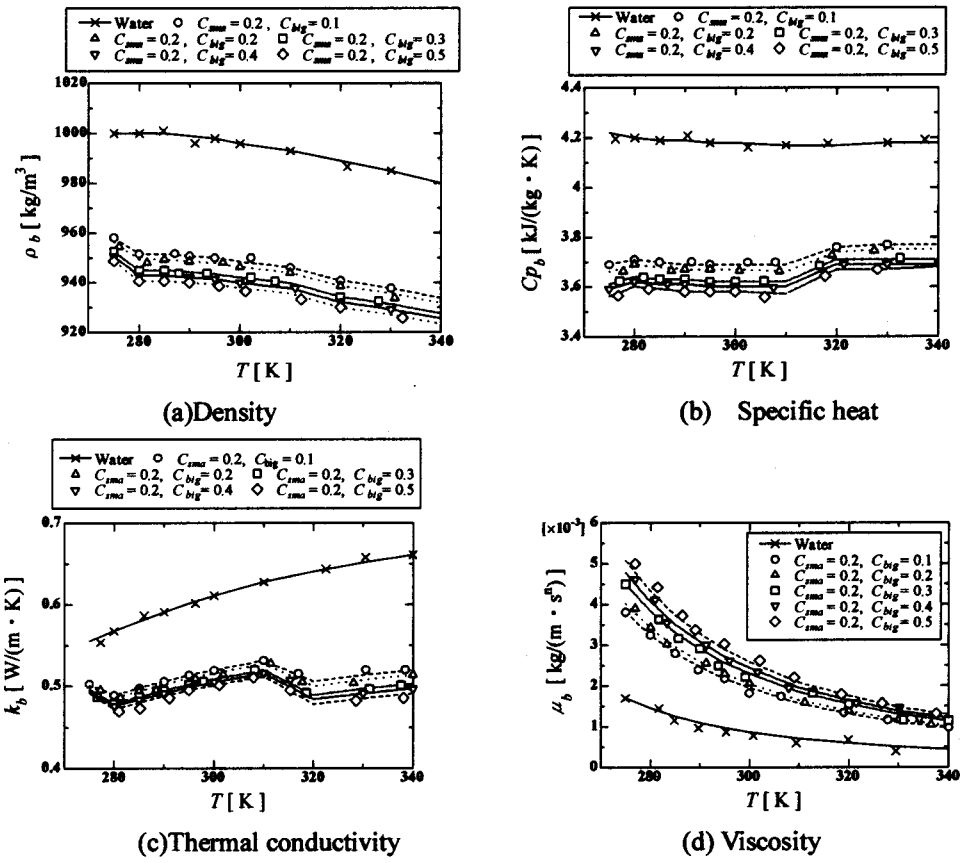

Fig. 2 Thermophysical properties of the plural PCMs slurry

Those thermocouples were bonded to the tube exterior by an adhesive. The measuring error of temperatures obtained by those thermocouples was estimated within 0.05 °C from calibrating results before the test runs.

In order to prevent the heat loss from the test section to the circumference environment, a two layer thermal insulator composed of 20 mm thickness glass wool insulating material and 30 mm thickness urethane foam insulating material was installed around the test section. As a result, the total heat loss was controlled within ±3 percent as compared with the total heat transmitted to the plural PCMs slurry. The measuring accuracy of heat transfer coefficient h for a pure water flow by a preliminary experiment was also coincided with the reference value [11] within ±5 percent. In order to measure the pressure loss difference ΔP of the plural PCMs slurry flow between inlet and outlet of the test section, a precision manometer (measuring error within ±1 percent) was set between 3 mm diameter pressure drop taps mounted on the inlet and outlet of the test tube. The fanning friction factor f_b of the plural PCMs slurry was calculated by the following Eq. (7).

The mass flow rate of the test slurry was estimated by the weighting method of a precision scale (measuring error within ±1 percent). The uncertainty of mass flow rate data was estimated about ±1 percent as regards to the reading error of the scale.

$$f_b = \frac{\Delta P_b / l_{te}}{(1/2)\rho_b U_b^2 / D} \times \frac{1}{4}, \quad f_w = \frac{\Delta P_w / l_{te}}{(1/2)\rho_w U_b^2 / D} \times \frac{1}{4} \tag{7}$$

Concerning the experimental procedure, at first, the cooling and mixing of plural PCM slurry in the cooling bath as shown in Fig. 3 were continued until two kinds of microencapsulated phase change materials in the slurry were solidified at the temperature of about 278 K. Then, the plural PCM slurry was charged into the test section of the stainless steel tube at a constant flow rate by controlling the frequency inverter of electric power mounted on the pump and adjusting the bypass valve set near the exit of cooling bath. The plural PCM slurry heated from the heating test tube was stored into the storage bath. The solidification rate of PCM in small microcapsules were measured by a volumeter set at the

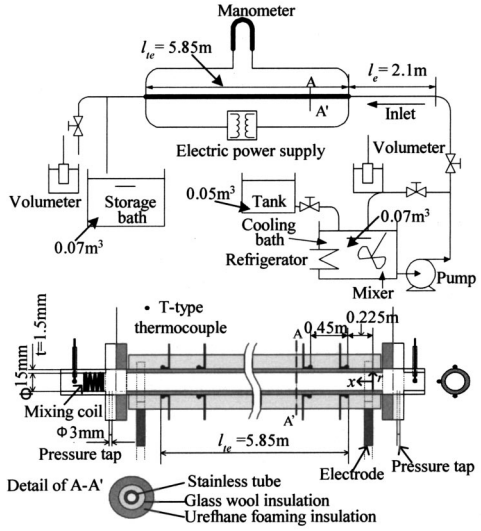

Fig. 3 Schematic diagram of experimental apparatus

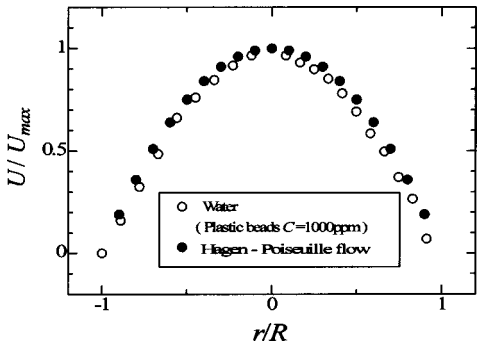

Fig. 4 Nondimensional velocity profile of water in the radial direction

branch part from the stainless steel tube after the test tube. All measurements of temperatures, heat flux, flow rate and pressure difference of the PCM slurry flow in the test section were carried out after reaching thermally and hydrodynamically the steady-state condition. All data were recorded into a data acquisition system.

Experiment Results and Discussion

Velocity Profile of the Plural PCMs Slurry in the Radial Direction. In the present experiment, the flow velocity of the microencapsulated PCM particles in the slurry was measured using Ultra Sonic Velocity Profiler (UVP). The UVP device could obtain the information on flow velocity of fine solid particles suspended in the fluid. Its principle is based on measuring the time period of ultrasound beam which reflects on fine solid particles suspended at a low concentration in the fluid [16]. Figure 4 presents the nondimensional velocity ($U/U_{\max}$) profile in the nondimensional radial direction (r/R) for a mixture of water and fine plastic beads (density ρ=995 kg/m^3, 20 μm in diameter) at a concentration of 1000 ppm. It is seen that nondimensional velocity profile, $U/U_{\max}$, of water-plastic beads slurry agrees well with Hagen-Poiseuille's equation. However, in the case of high concentration of the microencapsulated PCM particles in the slurry like the present experiments, the obtained flow velocity by the UVP device might be a mixture velocity of the PCM slurry flow.

From Fig. 5, it is demonstrated that the triangle symbols indicating the nondimensional velocity profile ($U/U_{\max}$) for the uniformly small sized PCM slurry ($C_{\text{big}}=0$, $C_{\text{sma}}=20$ percent) are above those (open circles) of water as a Newtonian fluid in the range of $r/R>0.3$. Moreover, in the case of the plural PCMs slurry for $C_{\text{big}}=0.5$ and $C_{\text{sma}}=0.2$ (solid symbol in Fig. 5), the values of $U/U_{\max}$ as indicated in open square symbols become greater than those of the uniformly small sized PCM slurry in the

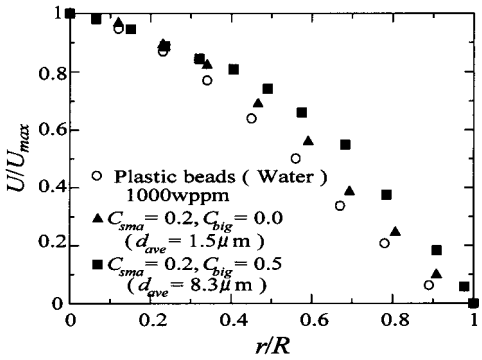

Fig. 5 Nondimensional velocity profiles in the radial direction

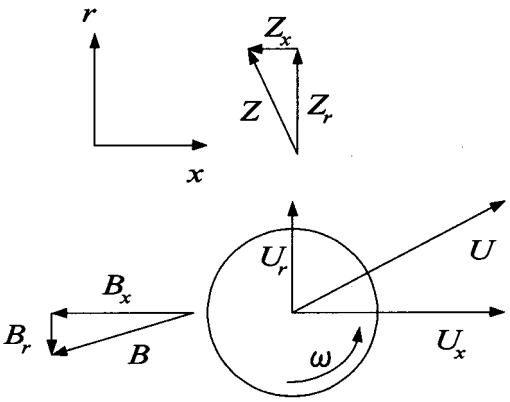

Fig. 6 Momentum model of a sphere

range of $r/R>0.4$. This difference of $U/U_{\max}$ between the plural PCMs plural PCMs slurry and the small sized PCM slurry might be qualitatively explained from the results by the following analytical model for the momentum of a spherical particle in Fig. 6.

The momentum balance on a spherical particle as a microencapsulated PCM particle consists of drag force B and lift force Z in the axial direction and radial direction and they can be expressed by Eq. (8) using these forces in Newton's law of momentum.

$$\sum F_x=\rho_p V_p\left(\frac{dU_x}{dt}\right), \quad \sum F_r=\rho_p V_p\left(\frac{dU_r}{dt}\right) \tag{8}$$

Moreover, the balance equation in the axial direction is derived from Eq. (9).

$$-Z_x-B_x=\rho_p V_p\left(\frac{dU_x}{dt}\right), \quad -\rho_p V_p g+Z_r-B_r=\rho_p V_p\left(\frac{dU_r}{dt}\right) \tag{9}$$

where, the drag and lift forces are defined as,

$$Z=\frac{1}{2}\rho_p C_Z U^2 S, \quad B=\frac{1}{2}\rho_p C_B U^2 S \tag{10}$$

where, C_Z and C_B are coefficients of lift force and drag force, respectively. The values of these coefficients are shown in Fig. 7, where S is the projected area of the spherical particle.

The flow motion for a microencapsulated PCM particle can be obtained from the above equations as follows.

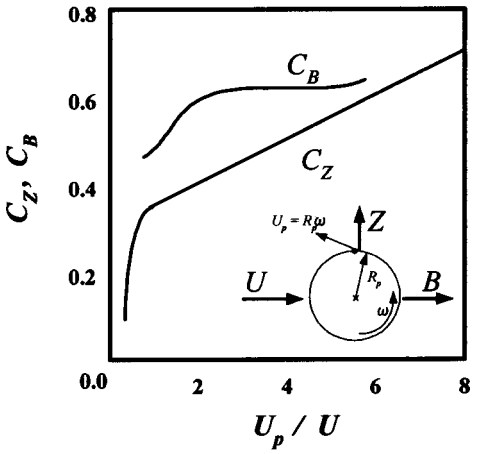

Fig. 7 Coefficient of lift force and drag force of a sphere

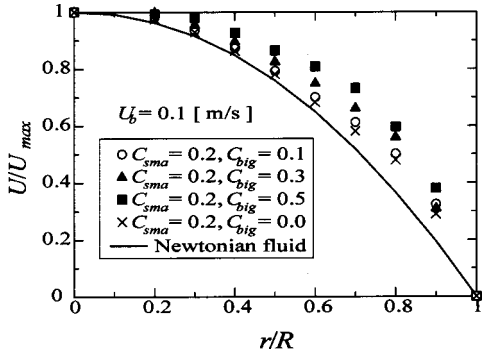

Fig. 8 Calculated nondimensional velocity profile in the radial direction

$$\left.\begin{aligned} -\frac{1}{2}\rho_p C_B U_x^2 S &= \rho_p V_p\left(\frac{dU_x}{dt}\right) \\ -\rho_p V_p g + \frac{1}{2}\rho_p C_Z U_r^2 S &= \rho_p V_p\left(\frac{dU_r}{dt}\right) \end{aligned}\right\} \tag{11}$$

The condition in which the spherical particle group does not interfere to each other is assumed. In addition, drag force in radial direction B_r and lift force in axial direction Z_x are omitted.

Assuming that the flow is fully developed and the velocity ratio of U_r/U_x is constant, the velocity of main stream U_x is given like the following Eq. (12).

$$\left.\begin{aligned} \int_{U_{x0}}^{U_x}\frac{dU_x}{U_x^2} &= -\frac{C_B\cdot S\cdot t}{2\cdot V_p} \\ U_x &= \frac{1}{\dfrac{1}{U_{x0}}+\dfrac{C_B\cdot S\cdot t}{2\cdot V_p}} \end{aligned}\right\} \tag{12}$$

After developing the above equations in the radial direction, the velocity profile U_r of PCM slurry at the instantaneous time can be defined by Eq. (13) and velocity of the PCM particle in the slurry in a tube is arranged as indicated in Eq. (14).

$$U_r = -gt - \frac{C_Z}{C_B}\left(\frac{U_{x0}}{1+\dfrac{\rho_p C_B S U_{x0} t}{2\rho_p V_p}}\right) = -gt + \frac{C_Z}{C_B}(U_{x0}-U_x) \tag{13}$$

$$U^2 = U_x^2 + U_r^2 = U_x^2\left[1+\left(\frac{U_r}{U_x}\right)^2\right] \tag{14}$$

Figure 8 shows the nondimensional velocity profiles ($U/U_{\max}$) of water (solid line), small sized PCM slurry (symbol: ×) and plural PCMs slurry for various C_{big}. It is seen from Fig. 8 that values of $U/U_{\max}$ increase with an increase in mass ratio C_{big}. Therefore, it is evident that the difference of $U/U_{\max}$ between plural PCMs particles and single-small sized PCM particles could be explained qualitatively by mixing effect based on the above-mentioned momentum analysis of the spherical particle.

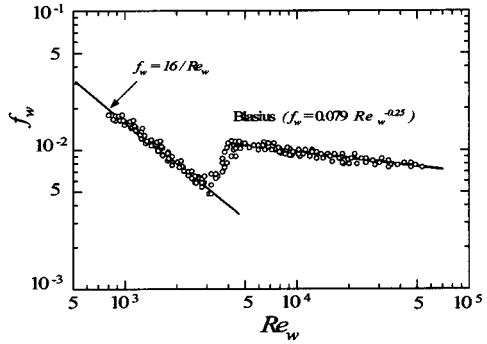

Fig. 9 Fanning friction factor of water

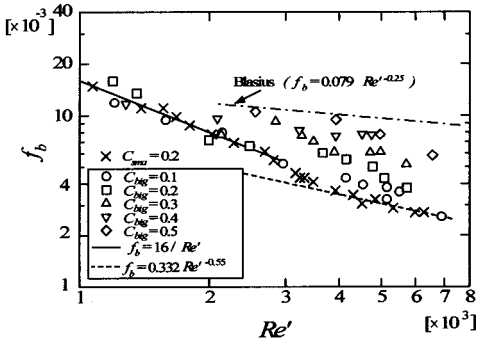

Fig. 10 Fanning friction factor of the plural PCMs slurry and uniformly small sized PCM slurry

Friction Factor. Figure 9 shows the relationship between friction factor f_w and Reynolds number Re($=\rho_w U_w D/\mu_w$) for water flow in the test section. From Fig. 9, it is clear that the fanning friction factor for water f_w in both laminar and turbulent regions show a good agreement with the correlations of Hagen-Poiseuille and Blasius ($f_w = 0.79\,\mathrm{Re}_w^{-0.25}$) within ±3 percent. On the other hand, the data of fanning friction factor f_b for the plural PCMs

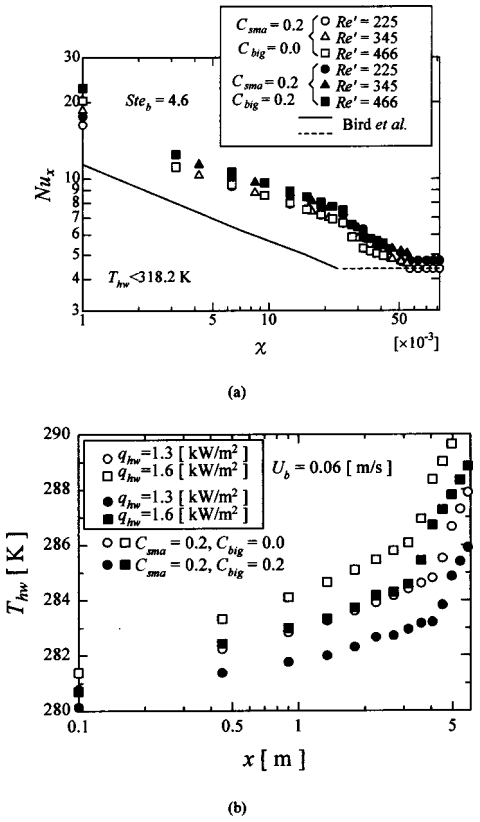

Fig. 11 (*a*) Variation of local Nusselt number with nondimension distance in the tube axis; and (*b*) Variation of surface wall temperature of test section tube with nondimension distance in the tube axis

Table 2 Nondimensional parameters

Local Nusselt number	$Nu_x=\dfrac{h_{hx}D}{k_b}$
Non-dimensional axial distance	$\chi=\dfrac{x}{D}\cdot\dfrac{1}{\mathrm{Re}'\cdot\mathrm{Pr}'}$
Modified Reynolds number based on power viscosity law	$\mathrm{Re}'=8^{1-n}\left[\dfrac{3n+1}{4n}\right]^{-n}\left[\dfrac{\rho_b U^{2-n}D^n}{\mu_b}\right]$
Modified Prandtl number based on power viscosity law	$\mathrm{Pr}'=\left[\dfrac{3n+1}{4n}\right]^{n}\left[\dfrac{8U}{D}\right]^{n-1}\dfrac{\mu_b Cp_b}{k_b}$
Stefan number	$Ste_b=\dfrac{Cp_b\rho_b\lvert q_{hw}R/k_b\rvert}{C_{\mathrm{tot}}L\rho_p}$

slurry flow at various mass ratios C_{big} show the different tendency from the data for water flow in the turbulent region in Fig. 10. That is, it is understood that the fanning friction factor of the plural PCMs slurry f_b exists between both correlations of Blasius for Newtonian fluid ($f_b=0.079\,\mathrm{Re}'^{-0.25}$) and non-Newtonian fluid ($f_b=0.332\,\mathrm{Re}'^{-0.55}$) by Ng [12].

In Fig. 10, it is seen that the friction factor data f_b for the uniformly small sized PCM slurry at $C_{\mathrm{sma}}=20$ mass percent and $C_{\mathrm{big}}=0$ percent in the turbulent flow region approaches to the equation of $f_b=0.332\,\mathrm{Re}'^{-0.55}$ for Newtonian fluid proposed by the reference [12] which could be applicable to the drag reducing visco-elastic polymer solution flow. This result revealed that a cluster of fine PCM particles have a function as flow drag reducing additives such as Toms effect which suppresses the occurrence of turbulence flow and declines the turbulent structure. The same behavior of flow drag reduction for the microcapsule PCM slurry in the present experiments was reported by the previous paper [6] which mentioned the flow drag reducing effect for the fine PCM particles (about 100 μm in diameter) slurry. It is also understood from Fig. 10 that the value of f_b increases with an increase in the mass ratio C_{big} of the larger size PCM particles due to its mixing effect.

Heat Transfer Coefficient. Figure 11(*a*) presents the variation of local Nusselt number Nu_x, with nondimensional axial distance χ for the plural PCMs slurry at various modified Reynolds number, Re'.

The nondimensional numbers used in the present study were defined in Table 2 as follows;

Local Nusselt number: $\mathrm{Nu}_x=\dfrac{h_{hx}D}{k_b}$

Nondimensional axial distance: $\chi=\dfrac{x}{D}\cdot\dfrac{1}{\mathrm{Re}'\cdot\mathrm{Pr}'}$

Modified Reynolds number based on pseudoplastic viscosity law on non–Newtonian fluid:

$$\mathrm{Re}'=8^{1-n}\left[\frac{3n+1}{4n}\right]^{-n}\left[\frac{\rho_b U^{2-n}D^n}{\mu_b}\right] \tag{15}$$

Modified Prandtl number based on pseudoplastic viscosity law on non–Newtonian fluid:

$$\mathrm{Pr}'=\left[\frac{3n+1}{4n}\right]^{n}\left[\frac{8U}{D}\right]^{n-1}\frac{\mu_b Cp_b}{k_b}$$

Stefan number: $\mathrm{Ste}_b=\dfrac{Cp_b\rho_b\lvert q_{hw}R/k_b\rvert}{C_{\mathrm{tot}}L\rho_p}$

where the value of n is the power index of the pseudoplastic viscosity. The power index of the plural PCMs slurry ranged from $n=0.92$ to 0.96. The Stefan number in Eq. (15) includes the parameter of $q_{hw}R/k_b$ whose unit corresponds to the temperature difference. Therefore, the proposed Stefan number means the energy ratio of sensible heat to latent heat. The same Stefan number based on the constant wall heat flux condition was used in the previous paper [5] for the microencapsulated PCM slurry. The experiments were performed under the conditions that the PCM particles in a small size of 1.5 μm in diameter absorbs the latent heat by melting, while those in a large size of 17 μm in diameter flow without absorbing its latent heat because the operating temperature is below its melting point of 318.2 K in the present experiments. The open symbols in Fig. 11(*a*) show the local Nusselt number of the uniformly small sized PCM slurry with PCM particles of 1.5 μm in diameter. The solid and dash lines correspond to the following correlation equations for the slurry flow without a phase change by Bird [13,14].

$$\mathrm{Nu}_x=1.41\cdot\left[\frac{(3n+1)}{4n}\right]^{1/3}\cdot\chi^{-1/3}\left(\chi^{-1}>25\pi\right)$$
$$\mathrm{Nu}_\infty=\frac{8(5n+1)(3n+1)}{31n^2+12n+1} \tag{16}$$

It is noticed from Fig. 11(*a*) that the data of local Nusselt number for small sized PCM slurry are greater than those calculated from the correlation Eq. (16) without a phase change. These increase in Nu_x for the small sized PCM slurry is caused by keeping the thermal boundary temperature at around a melting point of the PCM particles due to latent heat absorption during the phase change. Furthermore, it is clear from Fig. 11(*a*) that the closed symbol's data of Nu_x for the plural PCMs slurry with two kinds of PCM particles in different diameters are over those for the small sized PCM slurry as indicated in open symbols. This increase in Nu_x for the plural PCMs slurry would be brought by the microconvection around the plural particles due to the mixed convection of natural (buoyant force by PCM particles) and forced convections. This heat transfer enhancement of the microconvection in the microcapsules PCM slurry was observed by the previous papers [15,16].

From Fig. 11(*b*), it is noticed that the wall surface temperatures of heating tube wall surface T_{hw} for the plural PCMs slurry by the closed symbols are lower than those for small sized PCM slurry. Basing on the experimental data of T_{hw}, q_{hw}, and T_b, the wall surface local heat transfer coefficient h_{nx} under the constant wall heat flux condition was calculated by Eq. (17).

$$h_{hx}=\frac{q_{hw}}{(T_{hw}-T_b)} \tag{17}$$

Figure 12 shows the variation of the mean Nusselt number Nu_m with modified Reynolds number Re'. It is seen that the data of

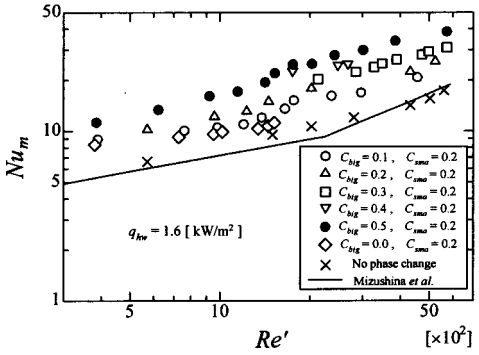

Fig. 12 The relationship between Mean Nusselt number and modified Reynolds number

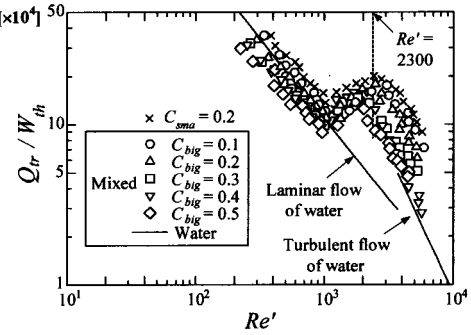

Fig. 13 The relationship between Q_{tr}/W_{th} and Re′

Nu_m for the plural PCMs slurry are greater than those for the small sized PCM slurry (symbol: ◇) and the slurry without phase change (symbol: ×). As the mass ratio C_{big} increases, the mean Nusselt number Nu_m is increased by the above-mentioned mixing effect by large sized PCM particles. As a result, It is understood that value of Nu_m for $C_{\mathrm{big}}=0.5$ is 2.8 times greater than that for the slurry without phase change.

When the microcapsules were suspended in a carrier fluid like water and circulated through the heating tube, Kasza and Chen [3] and Choi et al. [6] observed that the convective heat transfer coefficient was increased by the mixing effect of the microconvection around solid particles, which promotes mass transfer between carrier fluids with different temperatures inside and outside of thermal boundary layer developed from the heating tube surface. The present study elucidated also the enhancement of heat transfer coefficient based on mixing effect of microconvection around microcapsule particles by numerical simulation of particle motion in Fig. 8 and velocity profile of microcapsule PCM slurry obtained with a UVP in Fig. 5.

Heat Transfer and Pumping Power of the Plural PCM Slurries. Referring to application of the plural PCMs slurry, it is necessary to investigate the relationship between the transmitted heat in a heat exchanger Q_{tr} and its pumping power W_{th}.

First, the transmitted heat quantity through a circular tube for the plural PCMs slurry Q_{tr} was calculated from the following Eq. (18) as the sum of latent heat quantity and sensible heat quantity exchanged through the circular tube.

$$Q_{tr}=m_b\times(Cp_b\times\Delta T+L_b) \tag{18}$$

In Eq. (18), ΔT is the temperature difference of the plural PCMs slurry at the inlet and outlet position of the circular tube according to experimental conditions.

On the other hand, the theoretical pumping power W_{th} was calculated by measuring pressure drop difference ΔP, of the plural PCMs slurry at the inlet and outlet position of the circular tube as mentioned in the former section as follows:

$$W_{th}=\frac{D^2}{4}\pi U_b\Delta P_b \tag{19}$$

Figure 13 shows the variation of the ratio of Q_{tr} to W_{th} for the plural PCMs slurry with modified Reynolds number Re′. It is understood that the value of Q_{tr}/W_{th} decreases with increasing the mass ratio C_{big}. This tendency of Q_{tr}/W_{th} is caused by the fact that the increase in pumping power based on the viscosity of the plural PCMs slurry surpasses the increase in the transmitted heat quantity as the mass ratio C_{big} increases. It is intriguing that there appears a local maximum of Q_{tr}/W_{th} at around $\mathrm{Re}'=2300$.

Characteristic of Heat Transfer and Drag Reduction. Figure 14 presents the results shown in Figs. 6 and 8 replotted as friction factor ratio DR versus nondimensional heat transfer parameter ratio HTR as defined in Eq. (20).

$$DR=\frac{f_{nf}-f_b}{f_{nf}},\quad \mathrm{HTR}=\frac{j_{Hnf}-j_{Hb}}{j_{Hnf}},$$
$$j_{Hb}=St\cdot\mathrm{Pr}'^{2/3},\quad j_{Hnf}=\mathrm{St}\cdot\mathrm{Pr}^{2/3} \tag{20}$$

where, f_{nf} and j_{Hnf} correspond to the friction factor and nondimensional heat transfer parameter of water as Newtonian fluid, respectively, and also f_b and j_{Hb} correspond to those for the plural PCMs slurry. The data in Fig. 14 indicate that the tendency of DR or HDR varies at around the point of $\mathrm{Re}'\approx2300$. In the range of $500<\mathrm{Re}'<2300$, the data of HTR are greater than those of DR. On the other hand, in the range of $2300<\mathrm{Re}'<6000$, the data of HTR are lower than those for DR. Concerning the application of the plural PCMs slurry to the heat carrier medium for a heat exchanger, these results reveal that the modified Reynolds number should be controlled in the turbulent region ($\mathrm{Re}'>2300$) to require the effect of drag reduction. On the contrast, in order to need the effect of heat transfer enhancement, the modified Reynolds number must be controlled in the laminar region ($\mathrm{Re}'<2300$).

Concluding Remarks

The heat transfer enhancement of the plural PCMs slurry has mainly been investigated experimentally under the flow conditions of both laminar and turbulent flow in a circular tube with a constant wall heat flux. The influence of latent heat evolved during the phase change process and microconvection around the PCM particles were clarified for both small sized PCM and plural PCMs slurries. The main conclusions and the results of experiments are summarized as follows:

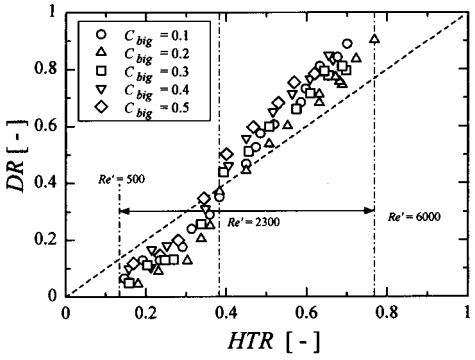

Fig. 14 The relationship between drag force ratio *DR* and nondimensional heat transfer ratio HTR

- It was seen that the generation of turbulence in the plural PCMs slurry with PCM particles in different diameters was suppressed by the Toms effect of PCM particles dispersed in water in the turbulent region such as flow drag reducing surfactant additives.
- The local Nusselt number of the plural PCMs slurry showed greater value than that without phase change due to the mixing effect by the microconvection and latent heat adsorption during melting process of phase change material dispersed in water.
- Concerning the application of the plural PCMs slurry to a heat transfer medium of heat exchanger, it was concluded that the modified Reynolds number should be controlled in the turbulent region ($Re' > 2300$) to require the effect of drag reduction. On the other hand, the modified Reynolds number should be limited in the laminar region ($Re' < 2300$) in order to take advantage the heat transfer enhancement by the plural PCMs slurry.

Nomenclature

B = drag force of sphere, Pa
C = mass concentration of plural PCM particles in the PCM slurry
C^* = volume concentration of plural PCM particles in the PCM slurry
C_B = drag coefficient of sphere
C_{big} = mass ratio of large size PCM particles (17 μm in diameter) to small size PCM particles (1.5 μm in diameter)
C_{sma} = mass concentration of small size PCM particles (1.5 μm in diameter) in the PCM slurry
C_Z = lift coefficient of sphere
C_P = specific heat, kJ/(kg·K)
D = inside diameter of tube, m
DR = drag force ratio as defined in Eq. (18)
d = diameter of microcapsule, m
F = force, N
f = fanning friction factor
g = gravitational acceleration, m/s^2
HTR = nondimensional heat transfer ratio as defined in Eq. (20)
h = heat transfer coefficient, W/(m^2·K)
j_H = nondimensional heat transfer parameter
k = thermal conductivity, W/(m·K)
L = latent heat of PCM, kJ/kg
l = tube length, m
m = mass flow rate, kg/s
n = power law index of non–Newtonian fluid
Nu = Nusselt number
P = pressure, Pa
Pr = Prandtl number
Pr′ = modified Prandtl number based on pseudoplasticity viscosity as defined in Eq. (8)
q = heat flux, W/m^2
Q = amount of heat, W
R = tube radius, m
r = radial distance, m
Re = Reynolds number
Re′ = modified Reynolds number based on pseudoplasticity viscosity as defined in Eq. (15)
S = projective surface area of sphere, m^2
St = Stanton number
Ste = Stefan number
T = temperature, K
t = time, s
U = velocity, m/s
V = volume, m^3
W_{th} = theoretical pumping power, W
x = tube axial distance, m
Z = lift force of sphere, Pa
Δ = difference

Greek Symbols

μ = pseudoplasticity viscosity, kg/(m·s^n)
ρ = density, kg/m^3
χ = nondimensional tube distance
Φ = frequency (percent) of microcapsule diameters
ω = angular velocity of sphere, s^{-1}

Subscripts

ave = average
b = bulk
big = microcapsule particle of 17 μm in diameter
e = entrance region
hw = heating wall
hx = local position on the heating wall in x-direction
m = melting point
nf = Newtonian fluid
p = particle
r = radial direction
sma = microcapsule particle of 1.5 μm in diameter
te = test section
th = theoretical
tot = total
tr = transfer
w = water
x = tube axial direction
$x0$ = center of tube

References

[1] Hale, D. V., Hoover, M. J., and O'Neil, M. J., 1971, *Phase Change Materials Handbook*, NASA CR-61363.
[2] Mehalick, E. M., and Tweedie, A. T., 1975, "Two Component Thermal Energy Storage Material," *Report NSF/RANN/SE/AER-74-09186*, National Science Foundation, Washington, D.C.
[3] Kasza, K. E., and Chen, M. M., 1982, "Development of Enhanced Heat Transfer/Transport/Storage Slurries for Thermal System Improvement," *ANL-82-50*, Argonne National Lab., IL.
[4] Hart, R., and Thornton, F., 1982, "Microencapsulation of Phase Change Materials," *Final Report Contract No. 82-80*, Ohio Department of Energy, OH.
[5] Charunyakorn, P., Sengupta, S., and Roy, S. K., 1991, "Forced Convection Heat Transfer in Microencapsulated Phase Change Material Slurries: Flow in Circular Ducts," Int. J. Heat Mass Transfer, **34**, pp. 819–833.
[6] Choi, E.-S., Cho, Y.-I., and Harold, G. L., 1994, "Forced Convection Heat Transfer With Phase-Change-Material Slurries: Turbulent Flow in a Circular Tube," Int. J. Heat Mass Transfer, **37**, pp. 207–215.
[7] Inaba, H., Kim, M.-J., and Horibe, A., 2002, "Cold Heat Storage Characteristics of Latent Heat Microcapsule-Water Mixture Flowing in a Pipe With Constant Temperature Wall," Trans. JSME, **68**, pp. 156–163.
[8] Inaba, H., Kim, M.-J., and Horibe, A., 2002, "Melting Heat Transfer Characteristics of Latent Heat Microcapsule-Water Mixed Slurry Flowing in a Pipe With Constant Wall Heat Flux (Experimenal Study)," *Trans. JSRAE*, **19**, pp. 13–22.
[9] Maxwell, J. C., 1954, *A Treatise on Electricity and Magnetism*, 3rd ed., **1**, Dover, New York, pp. 440–441.
[10] Vand, V., 1945, "Theory of Viscosity of Concentrated Suspensions," Nature, **155**, pp. 364–365.
[11] Gnielinski, V., 1976, "New Equations for Heat and Mass Transfer in Turbulent Pipe and Channel Flow," Int. Chem. Eng., **16**, pp. 359–368.
[12] Ng, K. S., Hartnett, J. P., and Tung, T. T., 1977, "Heat Transfer of Concentrated Drag Reducing Viscoelastic Polyacrylamide Solutions," AIChE Pap., *Heat Transfer Conf.*, 17th, pp. 74.
[13] Bird, R. B., Armstrong, R. C., and Hassager, O., 1977, *Dynamics of Polymeric Liquids*, **1**, Wiley, New York.
[14] Bird, R. B., Stewart, W. E., and Lightfoot, E. N., 1960, *Transport Phenomena*, Wiley, New York.
[15] Mizushina, T., Ito, R., Kuriwake, K., and Yahikazawa, K., 1967, "Boundary Layer Heat Transfer in a Circular Tube to Newtonian and non-Newtonian Fluids," Kagaku Kogaku Ronbunshu, **31**, p. 250.
[16] Takeda, Y., 1995, "Velocity Profile Measurement by Ultrasonic Doppler Method," Exp. Therm. Fluid Sci., **10**, pp. 444–453.

Basil T. Wong
e-mail: btung01@engr.uky.edu

M. Pinar Mengüç
e-mail: menguc@engr.uky.edu

Department of Mechanical Engineering,
University of Kentucky,
151RGAN Building,
Lexington, KY 40506

R. Ryan Vallance
e-mail: vallance@gwu.edu
Mechanical and Aerospace Engineering,
The George Washington University,
738 Academic Center,
801 22nd St., N.W.,
Washington, DC 20052

Nano-Scale Machining Via Electron Beam and Laser Processing

It is recently conceptualized that nano-scale machining might be achieved by coupling electron emission with radiation transfer. A laser may be used to heat a workpiece to a threshold temperature, and a nano-probe might then transfer additional energy via electron emission to remove a minute amount of material. To investigate this hypothesis, a detailed numerical study is presented. The electron-beam transport is modeled using a Monte Carlo approach, and a radiation transfer model that includes Fresnel reflections is adapted to simulate laser heating. The numerical study suggests that approximately 0.5 W from a single electron-beam is sufficient to initialize local evaporation from a gold film. With the use of a laser, the required power can be halved if the film is sufficiently thin. This paper describes the details of the numerical study and establishes guidelines for such nano-scale machining processes. [DOI: 10.1115/1.1777581]

Keywords: Heating, Heat Transfer, Machining, Monte Carlo, Nanoscale

Introduction

Nano-manufacturing is receiving significant attention in industry and research institutions due to the ever-growing interest in nanotechnology. Nano-structures are usually manufactured via two-step processes that generate a pattern (e.g., electron-beam lithography) and then develop the pattern (e.g., etching). Recently, our group hypothesized that single-step or direct-write nano-scale machining might be achieved by coupling nano-probe field emission with radiation transfer [1]. A laser may be used to heat a workpiece within a microscopic region that encloses an even smaller nanoscopic region subjected to a focused electron beam. The electron-beam supplies marginal heat sufficient to remove a minute volume of material by evaporation or sublimation. Experimentally investigating this hypothesis requires an estimate of the power needed in the electron-beam. In this paper, a detailed numerical study is conducted to study electron-beam processing; the governing equations are outlined and a solution scheme is discussed. Finally, a series of representative results are presented for the case of a gold film on a quartz substrate.

Traditional electron-beam processing [2] employs electrons from an electron-gun that emits many electrons and projects them onto a solid workpiece. The key feature of this method is the use of electrons with large kinetic energies. These electrons penetrate into the lattices of the target solid and transfer significant energy to the workpiece via inelastic collisions. This penetration and energy transfer induces ''melting'' and ''evaporating,'' to manufacture the desired patterns.

The interaction between energetic electrons and solid materials is very complex. Since accelerated electrons are extremely small, they easily penetrate the lattice of atoms in a solid workpiece. When energetic electrons strike and interact with a solid material, they are scattered in various directions. An elastic scattering refers to the re-direction of a propagating electron while an inelastic scattering re-directs the electron and attenuates its energy. Electron scattering within the workpiece affects the penetration depth, which depends upon the initial energy of the electrons.

Due to the complicated interactions between propagating electrons and the solid material, obtaining a realistic analytical solution is difficult. In this work, a Monte Carlo Method (MCM) is used to statistically simulate the electron-beam transport; a large number of electron ensembles penetrating the workpiece surface are traced according to the material properties of the workpiece [3]. The change in the temperature of the workpiece is modeled using the Fourier heat conduction equation. Reasons for employing this equation are discussed later in the paper. Further consideration of using the Boltzmann transport equation (BTE) in place of Fourier's law is being considered and developed to determine the validity of the law in micro and/or nano systems [4].

The interactions between electrons and solid materials have been investigated in the literature both theoretically and experimentally [5–7]. Particularly, Whiddington's work [7] is important as it relates the electron penetration range R_p (m) with the electron acceleration voltage V (Volt) and the mass density of the metal ρ (kg/m^3), which is given as

$$R_p = 2.2\times 10^{-11}\, V^2/\rho. \tag{1}$$

Here, R_p is the depth that the penetrating electrons reach as they are incident on the target surface, indicating that most of the energy from the propagating electrons is absorbed within this range. However, this expression is incorrect at low applied voltages ($<$20 kV) since the curve fit was done at a much higher voltage range. In order to properly predict the penetration depth at low voltages, a more rigorous approach is needed, and for that reason we used the MCM to simulate the electron-beam transport.

With high acceleration voltages much of the energy is absorbed below the surface of the workpiece; a 30-kV electron-beam penetrates about 1 μm into a gold surface. As a result, the highest temperature would occur below the surface because energy is absorbed throughout the penetration range. For more modest acceleration voltages, the profile of absorbed energy is concentrated near the surface; a 4-kV electron-beam penetrates only 60 nm (as predicted by the MCM), but this limits the total energy that can be delivered via the electron-beam. For this reason, nano-machining may require threshold heating in conjunction with an electron-beam of modest acceleration voltage.

Problem Description and Assumptions

Our objectives are to model the electron-beam transport, to predict the temperature field in the workpiece, and to determine the electron-beam power to effectively remove atoms from a workpiece and achieve nano-machining. We are in search of the sufficient number of energized electrons supplied per unit time (or

Contributed by the Heat Transfer Division for publication in the JOURNAL OF HEAT TRANSFER. Manuscript received by the Heat Transfer Division January 21, 2003; revision received May 12, 2004. Associate Editor: G. Chen.

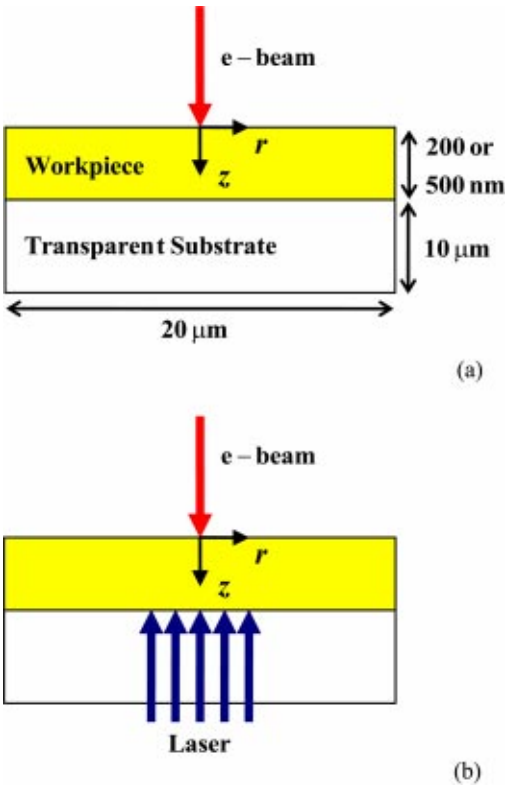

Fig. 1 Schematic for the nano-scale machining process considered. A workpiece is positioned on top of a substrate. The substrate is assumed transparent to the incident laser. Two different evaporation methods are considered: (a) electron-beam impinges perpendicularly on the top of the workpiece, and (b) electron-beam and laser impinge normally on the workpiece at opposite directions.

current) to elevate local workpiece temperatures near the melting, evaporation, or sublimation temperatures. It should be realized that the concepts of ''melting'', ''evaporating'', and ''sublimation'' at nano-scales are loosely used here, and they require further investigation, particularly in conjunction with detailed experiments. The models and predictions developed in this work will subsequently serve as experimental guidelines for finding suitable nano-probes for nano-machining.

Schematic of the problem is depicted in Fig. 1. We consider two possible scenarios. The first uses only the electron-beam as the source of heating, which is illustrated in Fig. 1(a). In the second one we consider auxiliary heating using a laser at the interface between the workpiece and the substrate, in addition to the electron-beam heating (see Fig. 1(b)). For our current investigations, the type of the electron source used in the simulations is irrelevant as long as it can emit sufficient electrons without failing. In simplifying our current investigation, it is assumed that there are no electron sources or drains imposed on the workpiece. Such additional applied voltages across the workpiece would alter the propagation of penetrating electrons from the electron-beam and may also cause non-uniform joule heating within the workpiece. These details will be included in future models as joule heating can serve as a means of assisting the nano-machining process by providing additional heat beside the electron-beam and laser.

In this study, we choose a thin gold film as the solid target (or workpiece), which is deposited on a 10-μm semitransparent substrate (quartz). Both the workpiece and the substrate are assumed to have a radial dimension of 10 μm. The thickness of gold film is considered to be either 200 nm or 500 nm. Although the actual thickness of the substrate in the experiments would possibly be a few hundred microns thick, it would not affect our final results since the 10-μm quartz is ''infinitely thick'' with respect to heat waves (not to mention a 100-μm quartz). We assume that quartz does not absorb any radiant energy (i.e., it is transparent to the laser). A single electron source is considered to emit electrons, with predetermined initial kinetic energies, directly onto the top surface of the workpiece. A laser with a wavelength of 355 nm is chosen to heat the workpiece from the bottom of the substrate. The laser wavelength is selected to minimize reflection of the incident radiation, as gold reflects radiation significantly at wavelengths beyond 355 nm. Although the workpiece and the laser are specified in the calculations, the numerical approach presented in this work is general and can be extended to other materials or laser wavelengths.

The origin of the coordinate frame is set at the point where electron bombardment occurs. A cylindrical coordinate system is used for the computations since both the electron-beam and the laser impinge normally on the workpiece and the solution will be axisymmetric along the z-direction. The choice of distances between the electron-beam, the laser, and the workpiece are not so critical at this stage of simulations since they only affect the incident profiles of the electrons and photons at the boundaries; these parameters can easily be modified in later studies. Our current interest focuses on the material removal using a single probe; therefore, only a single electron-beam is used for the machining process. Machining paradigms based on multiple beams are under consideration [8], and these will be discussed in a future work.

In vacuum, the only two possible heat transfer mechanisms are radiation and conduction. The emission of radiation from the workpiece at high temperatures is inevitable and needs to be considered. However, radiation heat transfer at nano-scale levels requires intense studies and investigations, and the radiative properties (i.e., emissivity and absorptivity) at nano-scales and temperatures beyond melting are not readily available for gold. In addition, emission of radiation depends greatly on surface areas (which are extremely small in this problem); therefore, they may not have any impact in the energy balance at all. For these reasons emission is omitted in this study. Hence, we assume that the top of the workpiece, the bottom of the transparent substrate and side walls are considered insulated, and the problem of this sort is naturally unsteady since there are no heat losses. In terms of the computational domain, the overall geometry is a dual layer of cylinders. If the computed temperatures near the side wall of the cylinder are equal to the room temperature, then the solution is physically equivalent to a plane-parallel workpiece with infinite side walls at room temperature. In addition, we assume that the medium is homogeneous and free of defects and cracks. Such an assumption simplifies the heat transfer analysis, as electron and photon scatterings become extremely complicated when there are impurities in the medium.

Computational Grid

The computational grid, depicted in Fig. 2, is expressed in cylindrical coordinates with the grid index m corresponding to the radial direction r, and the grid index n corresponding to the axial direction z. The MC simulations for the electron-beam transport are performed in the uniform grid, which is the domain given by $(r\times z)=(R_1\times L_1)$ and spans from $m=0$ to $N_{R1}-1$ and $n=0$ to $N_{L1}-1$. Since the boundary conditions are defined far away from the incident electron-beam and laser, the use of a uniform grid within the entire computational domain for the conduction problem would be impractical. To overcome this, we increase the grid spacing as we move away from the origin. Generally, the radial distribution of the laser would be larger than that of the electron-beam; therefore, the uniform grid is extended from $(R_1\times L_1)$ to $((R_1+R_2)\times(L_1+L_2))$ when the conduction is modeled. The ex-

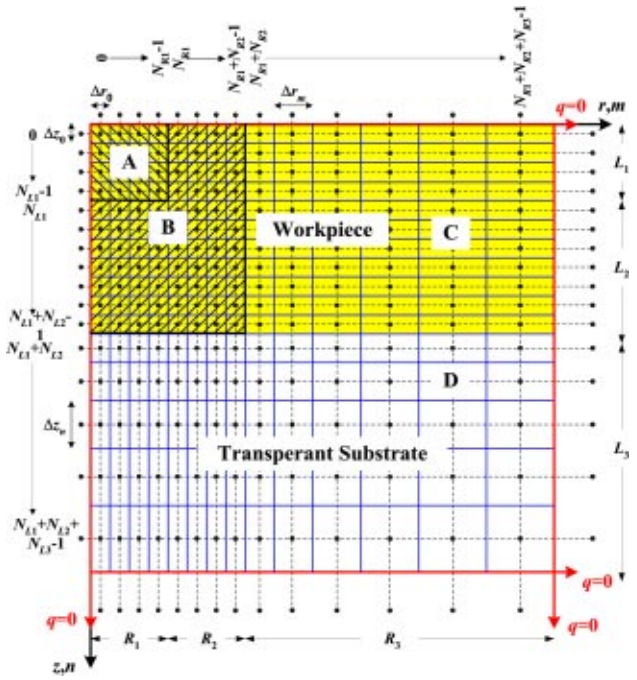

Fig. 2 The grid setup used in modeling the electron-beam transport, the laser propagation, and the heat conduction inside the workpiece. The grid is sub-divided into two zones: (1) A and B with uniform spacings in both *r* and *z*-directions, and (2) C and D with non-uniform spacings where the grid is stretched along *r* and *z*-directions with independent factors. A is where the MC simulation in the electron-beam transport is performed while B extends A uniformly in both *r* and *z*-directions in order to account for the laser heating. The boundary conditions are (a) adiabatic at $r=0$ due to symmetry and (b) adiabatic at $r=R_1+R_2+R_3$, $z=0$ and $z=L_1+L_2+L_3$ since it is assumed that there are no convection and radiation losses.

tended uniform grid is then connected to the nonuniform grid with stretching factors in both *r* and *z*-direction. The grid is set up so that the thickness of the workpiece is described as L_1+L_2 (i.e., $n=0$ to $N_{L1}+N_{L2}-1$) while the thickness of the substrate is denoted L_3 (i.e., $n=N_{L1}+N_{L2}$ to $N_{L1}+N_{L2}+N_{L3}-1$). The number of grid points required for the calculations, i.e., N_{R1}, N_{R2}, N_{R3}, N_{L1}, N_{L2}, and N_{L3} can be determined easily using the *R*'s, the *L*'s, and the ratios of the two adjacent grid spacing (particularly, the latter over the former) for the *r* and *z*-directions.

Monte Carlo Method for the Electron-Beam Transport

The distribution of energy deposited in a workpiece due to electron bombardment can be determined using a Monte Carlo Method (MCM). For the case of electrons penetrating a workpiece, a MCM simulates the propagation of electrons inside a workpiece based on cumulative probability distribution functions (CPDFs). The MCM treats an electron-beam as discrete electrons, where all the electrons have equal energy. Each electron undergoes a series of elastic and inelastic scatterings inside the workpiece. The histories of many propagating electrons form the resultant profile of absorbed energy.

MCM is used extensively for the solution of the Radiative Transfer Equation (RTE). However, the propagations of photons follow different scattering and absorption probability distributions than electrons [3,9]. The scattering characteristics of electrons in a solid target based on MCMs are well outlined in the literature [3,10–12], which we adopt here.

The MCM simulation starts by initializing data such as the number of ensembles, the location of emission, the initial launching direction, etc. An ensemble represents a bundle of quantum particles (i.e., electrons or photons). Each ensemble is launched, one after the complete propagation of another, assuming that interferences between ensembles do not exist. The distance of interaction, which is the distance the ensemble can propagate before interacting with the medium, is drawn according to the material properties of the medium. The ensemble is then moved from its current position to the next, covering the distance of interaction with its initial direction of emission. If it exits the medium, then it will either contribute to the reflection or transmission. Otherwise, its weight or energy is altered accordingly and a new propagating direction is determined. The above procedures are then repeated with drawing another distance of interaction.

In order to carry out a MC simulation, we need to obtain the CPDFs of the scattering direction and the penetration distance, replace them with random numbers ranging from 0 to 1, and then invert the expressions to get the direction and distance as a function of random numbers [9]. The CPDF of electron scattering direction is derived according to the scattering cross section, which is a measure of the scattering intensity. There is a simple and explicit expression derived from the screened Rutherford elastic scattering cross section for determining the scattering angle Θ as a function of a random number Ran_Θ, the atomic number Z of the solid, and the electron energy E, which is given as [13]

$$\cos(\Theta)=1-\frac{2\alpha \mathrm{Ran}_\Theta}{1+\alpha-\mathrm{Ran}_\Theta} \tag{2}$$

where

$$\alpha=3.4\times10^{-3}\frac{Z^{0.67}}{E} \tag{3}$$

However, Eq. (2) incorrectly represents the scattering phenomena at low electron energies of a few kiloelectronvolts (keV) [10]. Therefore, the Mott elastic scattering cross section is better suited for this application. The derivation of the Mott cross-section can be found in [14], which will not be repeated here. Once the Mott differential elastic scattering cross-section (i.e., $d\sigma_{\mathrm{el}}/d\Omega$) is obtained, the total elastic scattering cross section $\sigma_{\mathrm{el,total}}$ is evaluated as

$$\sigma_{\mathrm{el,total}}=\int_{\Omega=4\pi}\frac{d\sigma_{\mathrm{el}}}{d\Omega}d\Omega=\int_0^{2\pi}\int_0^{\pi}\frac{d\sigma_{\mathrm{el}}}{d\Omega}\sin\theta d\theta d\phi. \tag{4}$$

The CPDF of the scattering cross section is obtained using $\sigma_{\mathrm{el,total}}$ and assuming azimuthal symmetry (i.e., $d\sigma_{\mathrm{el}}/d\Omega$ is not a function of ϕ) where

$$R(\Theta)=\frac{2\pi}{\sigma_{\mathrm{el,total}}}\int_0^{\Theta}\frac{d\sigma_{\mathrm{el}}}{d\Omega}\sin\theta d\theta. \tag{5}$$

Unfortunately, this equation cannot be inverted analytically to obtain Θ. Hence, as discussed in [3], a table containing the CPDFs as a function of Θ for gold is desired. When a random number is generated, it is compared with the CPDFs and the corresponding Θ is selected from the table using a linear interpolation. Since azimuthal symmetry is assumed, the azimuthal angle is given as

$$\phi=2\pi\mathrm{Ran}_\phi \tag{6}$$

The CPDF of an electron penetrating a distance S without being scattered is given as [10]

$$R(S)=\exp(-S/\lambda), \tag{7}$$

where

$$\lambda=\frac{A}{N_a\rho\sigma_{\mathrm{el,total}}} \tag{8}$$

λ is the elastic mean free path of the penetrating electrons, which depends on the atomic number Z, the atomic weight A, the density

ρ of the solid target, and the electron energy E. Replacing the CPDF by a random number Ran_S, the interaction distance is determined as

$$S = -\lambda \ln(\mathrm{Ran}_S) \tag{9}$$

To account for the attenuation of the electron energy, the stopping power (i.e., dE/dS), which describes the amount of energy attenuated per unit distance, is needed. The most common expression for the stopping power is the modified Bethe relationship, which is given as [10]

$$\frac{dE}{dS} = -78{,}500\frac{Z}{AE}\log\left(\frac{1.166(E+0.85J)}{J}\right), \tag{10}$$

where J is the mean ionization potential. The Bethe stopping power is typically valid until $E=50$ eV, which is about a few percent of the initial energy of each electron accelerated by a few keV. The use of this relation in determining the amount of energy loss for electrons within the workpiece yields small error (a few percent) in the predicted absorption profile, which is acceptable. In this work, however, we use the experimental stopping power obtained by Luo et al. [15] as given in [16], where the data points are given for electron energies as low as 3 eV.

The energy absorbed from the electron-beam is modeled as internal heat generation when solving the heat conduction problem. The results of the MC simulations are the energy absorbed from the electron-beam at elements within the grid. The energy is adapted into a normalized energy density $\Psi_{m,n}$ by dividing the absorbed energy by the volume of the element and the total energy of incident electron ensembles, and it is mathematically expressed as

$$\Psi_{m,n} = \frac{\psi_{m,n}}{2\pi r_m \Delta r_m \Delta z_n N_{en} E_0} \tag{11}$$

where $\psi_{m,n}$ is the total kinetic energy of electrons deposited at the (m,n) element, N_{en} is the total number of electron ensembles used (i.e., for the statistical MC simulation, not the actual number of electrons incident on the solid target), E_0 is the initial energy of the electrons, and the quantity $2\pi r_m \Delta r_m \Delta z_n$ is the volume of the (m,n) element. The internal heat generation at a given element (m,n), $\dot{q}^{\mathrm{elec}}_{m,n}$, is then computed with the following expression

$$\dot{q}^{\mathrm{elec}}_{m,n} = \dot{E}\Psi_{m,n} \tag{12}$$

where $\dot{E}$ is the input power of the electron-beam.

Laser Heating

A collimated laser is considered for additional heating of the workpiece within a specified radius R_{laser} (see Fig. 3). We assume that the substrate is transparent to the incident laser beam (i.e., no absorption within the substrate) while the metal layer is absorbing. Since the absorption cross-section in a metal is much larger than the scattering cross-section, the laser heating is analyzed in one dimension along the direction of incidence.

The Fresnel reflections at the mismatched interfaces (i.e., different indices of refraction) where the laser is incident need to be considered. For the normal incident case, the fraction of the incident radiant energy reflected, $R_{i\to t}$, as the laser propagates from medium i to t, is given as [17]

$$R_{i\to t} = \left(\frac{\tilde{n}_t - \tilde{n}_i}{\tilde{n}_t + \tilde{n}_i}\right)\left(\frac{\tilde{n}_t - \tilde{n}_i}{\tilde{n}_t + \tilde{n}_i}\right)^* \tag{13}$$

where $\tilde{n}_i$ and $\tilde{n}_t$ are the complex indices of refraction of the incident and the transmitted media, respectively. In the simulations, the initial heat flux q''_0 of the laser beam propagating through the substrate is prescribed (see Fig. 3). As the laser first hits the quartz-gold interface, a fraction of the heat flux, $R_{s\to w}(=0.75)$ is reflected while the remainder transmits through the interface. When the laser propagates within the gold film its energy decreases exponentially with respect to the distance traveled due to absorption. Therefore, the radiant heat flux as a function of depth in the z-direction within the radial area of incidence is given as

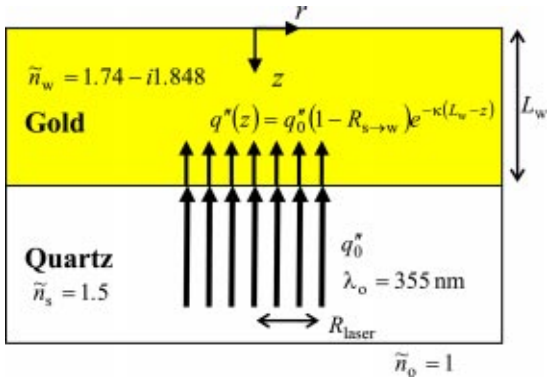

Fig. 3 Schematic for the radiative transfer inside the workpiece. The impinging laser has a radial dimension of R_{laser} and a wavelength of 355 nm. Since the absorption of radiant energy in a metal is strong, a one-dimensional radiation model with exponential decaying of radiant energy in the direction of propagation is employed; scattering of photons is neglected. The complex index of refraction of gold is at the wavelength of the laser. $R_{s\to w}$ is the reflectivity at the interface between gold and quartz when the incident direction is from quartz to gold.

$$q''(z) = (1 - R_{s\to w})q''_0 e^{-\kappa(L_w - z)} \tag{14}$$

where κ is the absorption coefficient of the workpiece. The absorption coefficient is determined using the imaginary refractive index of the workpiece, $n_{\mathrm{I,w}}$, according to the expression [18]

$$\kappa = \frac{4\pi n_{\mathrm{I,w}}}{\lambda_o} \tag{15}$$

where λ_o is the wavelength of the laser in vacuum. Normally, the incident photons are strongly absorbed within the first few tens of nanometers in a metal. For a $\lambda_o = 355$ nm laser, κ of gold (i.e., $n_{\mathrm{I,w}} = 1.848$ [19]) is about 0.0654 nm^{-1} so that 95 percent of the penetrating photons are absorbed within 46 nm into the gold film. The thickness of the film considered in this work is sufficiently large that the penetrating photons would never reach the other surface of the workpiece. Hence, there is no need in considering the interference effect between incoming photons from one end and the reflected ones (if there is any) from the other.

To determine the amount of radiant energy per unit volume absorbed by a computational element in the workpiece within a radius of R_{laser}, the radiant heat flux is divided by the Δz_n and it is expressed as

$$\dot{q}^{\mathrm{rad}}_{m,n} = \frac{q''(z)}{\Delta z_n}, \tag{16}$$

for $m = 0,1,\ldots,N_{R\mathrm{laser}} - 1$ and $N_{R\mathrm{laser}}$ is the radial index at R_{laser}.

Heat Conduction

In general, heat conduction refers to the transport of energy by electrons and phonons. Electrons are the dominant energy carriers in metals while phonons are solely responsible for heat transport in insulators. In semiconductors, both electrons and phonons are equally important. Phonons exist in all materials, and they serve as the main source of electron scattering in metals although their heat capacities are much smaller than those of electrons. In our problem, electrons originated from the electron-beam and photons from the laser penetrate the target workpiece. Therefore, significant amount of energy and momentum are transferred to electrons

inside the workpiece causing these electrons to become "hot" while phonons remain "cold." Then through scatterings between these propagating electrons and phonons, the incident energies are distributed (or, conducted) within the workpiece. Both electrons and phonons eventually reach thermal equilibrium.

The mean free path and the mean free time of the energy carriers are important in the heat transport analysis [20]. The mean free path of an energy carrier is the average distance that the carrier travels without involving any collision with other carriers; the mean free time of an energy carrier is the average time that the carrier is "free" (i.e., the time required to penetrate a distance equivalent to the mean free path). If the size of the physical domain far exceeds the mean free path and the time scale is much larger than the mean free time, then macroscopic models, such as Fourier's law, are used to solve the heat transport phenomena. If the physical length scales are at the same order of magnitude as the mean free path or the observation time is comparable to the mean free time, then special attention should be paid to the propagation of individual energy carriers, especially the collisions and scatterings between carriers [21].

Mean free paths of electrons in materials are usually less than a few nanometers, and speeds of electrons are on the order of 10^6 m/s; both depend on the energies of the electrons [22]. This leads to mean free times for electrons on the order of femtoseconds. Unlike electrons, mean free paths of phonons span from nanometers to micrometers depending on the temperature, and their mean free times range from picoseconds to nanoseconds since phonons travel at about the speed of sound (i.e., 10^3 to 10^4 m/s) [23]. In this work, the thicknesses of the gold film and the quartz substrate are 200 or 500 nm and 10 μm, respectively. For the metal where electrons are of concern, the thickness considered far exceeds the electron mean free paths; therefore, the transport behavior is spatially diffusivelike. In addition, we are interested in machining within nano-second intervals, which is at a time-scale much larger than mean free times of the electrons; hence, the ballistic behavior of electrons is not important. As a result, the electronic thermal conduction should be macroscopic within the gold film. Unfortunately, mean free paths for phonons can be comparable to the thickness of the workpiece depending on the temperature, producing questionable results if the macroscopic approach is employed. In the context of this work, the temperature range (i.e., 300 K–3129 K) involved is vast, and mean free paths of phonons at the higher temperatures can easily be as small as a few nanometers or even less, meaning that the phonon transport is likely to be diffusive.

Of the concerns regarding heat conduction at nano-scales, especially those for phonons, more detailed theoretical approaches and experiments are required to clarify and prove the validity of various approaches, which is beyond the scope of this work. Since temperatures in this application are undoubtedly high so that both the electron transport and the phonon transport could be diffusive, and since electrons play the major role in heat transport within metals (although electrons and phonons can exist at different temperatures), we assume the Fourier law is acceptable for the heat conduction. Consideration of other models for more accurate electron-phonon transport will be carried out in future works.

The derivation of the energy balance for each element within the workpiece and the substrate is not shown here since the procedures are fairly standard and well-known [24] except that the heat generation term at each element (m,n) in the computational domain will include the sum of both the deposition of electron energy and the absorption of radiant energy.

$$\dot{q}_{m,n} = \dot{q}^{\text{elec}}_{m,n} + \dot{q}^{\text{rad}}_{m,n}. \tag{17}$$

Solving the System of Equations and Accounting for "Melting" and "Evaporation". After discretizing the entire computational domain, the differenced equations for all the nodal points are collected to form a system of linear equations. It is given in matrix representation as

$$\underline{B}\,\overline{T} = \overline{D}, \tag{18}$$

where B is a $(N_R \times N_L) \times (N_R \times N_L)$ matrix, $\overline{T}$ is the temperature field, and $\overline{D}$ is known from the discretizations, which contains temperatures at the previous time step and heat generation terms at various nodes. We solve Eq. (18) for $\overline{T}$ using the point successive overrelaxation (SOR) numerical scheme [25].

In order to properly account for "melting" and "evaporation" the latent heats of fusion and evaporation need to be included in the solution scheme. In solving the system of equations, the point SOR solves the nodal temperature one after another, which can be conveniently modified to account for "melting" and "evaporation." In our current solution scheme, the code detects any nodal temperatures beyond the "melting" or "evaporation" temperature at any given time step. If there are any nodal temperatures computed at a given time step beyond the specified temperatures, the code re-solves the system of equations with those nodal temperatures fixed at either one of the temperatures, accordingly. With the newly solved temperature field, the energy balance is performed at each node to determine the heat generation term q_{gen}. Each calculated q_{gen} is the energy required to maintain that particular nodal temperature at the "melting" or "evaporation" temperature. Note that at this particular time step, energies are still supplied by electrons from the electron-beam to those nodes. A fraction (i.e., the calculated q_{gen}) of the supplied energy is then used for sustaining the specified temperature while the rest of it is stored at the corresponding node to overcome the latent heat of fusion, followed by the latent heat of evaporation.

Once a node has enough latent heat, its temperature is allowed to increase at the next time step. The stored heat never exactly equals the specified latent heats of fusion and evaporation because the increment time interval and hence the energy supplied are fixed. Therefore, when an element overcomes the latent heat at a given time step, the excess energy from the electron-beam is added to the same element at the next time step, preventing unrealistic energy destruction.

Results and Discussions

Computational Parameters. In principle, material properties such as the thermal conductivity, the specific heats, etc. are temperature-dependent, especially in this application where the variation of temperatures across the workpiece is large. Also, they may change depending on air pressure. Unfortunately, these properties at temperatures beyond melting and at various air pressures are not readily available either theoretically or experimentally. Therefore, we use constant material properties at the ambient condition. In this work, gold is the selected workpiece, which has density (ρ_w) of 19,300 kg/m^3, specific heat (C_w) of 129 J/kg-K, and conductivity (k_w) of 317 W/m-K at the room temperature. The melting temperature of gold is given as 1336 K while its evaporation temperature is 3129 K [24]. The complex index of refraction of gold at the wavelength of 355 nm is given as 1.74-il.848 [19]. Its atomic number (Z) and the atomic weight (A) are 79 and 196.97 g/mol, respectively; the corresponding mean ionization potential (J) is 0.790 keV [10]. For the transparent substrate we select quartz, which has $\rho_s = 2{,}650$ kg/m^3, $C_s = 765.85$ J/kg-K, and $k_s = 1.77$ W/m-K [24]. A typical value of 1.5 is assumed for the index of refraction of quartz [18].

The incident profile of the electron-beam is a Gaussian distribution with a $1/e^2$ radius of R_{electron} [26]. In this work, two beam profiles are assumed; one of which is with $R_{\text{electron}} = 50$ nm, and the second is twice the former (i.e., $R_{\text{electron}} = 100$ nm). The initial energies of electrons originating from the electron-beam are considered to be either 4 or 6 keV. All the temperature distributions are determined after about one nano-second (ns) of machining process.

Selection of the Computational Time Steps, Grid Spacings, and Tolerances for SOR. If very fine grid spacing were adapted in the simulations, a significant amount of computational time would be needed for both the Monte Carlo and the conduction heat transfer simulations to converge. Since the computational domains for both models need to be overlapped, a finer grid on the MC simulation would lead to an over-refined grid for the conduction problem.

The computational grid requirements are determined after a number of preliminary numerical experiments. It is found that an effective grid scheme uses $\Delta r = 1.25$ nm and $\Delta z = 1.25$ nm with 10 percent increases in the r and 5 percent increases in the z-grid spacings starting from $m = N_{R1} + N_{R2}$ and $n = N_{L1} + N_{L2}$, respectively (see Fig. 2). The size of the uniform grid is taken to be either $(r \times z) = (400\ \text{nm} \times 200\ \text{nm})$ or $(400\ \text{nm} \times 500\ \text{nm})$ when the thickness of gold film considered is 200 nm or 500 nm, accordingly. These values keep the computational time reasonable while maintaining acceptable resolutions for the MC predictions. A change of temperature on the order of 1 K is observed when halving the grid spacings while holding other computational variables constant. Decreasing the grid stretching effect also inflicts a temperature change of order 1 K. The Δt's in the various simulated cases are chosen in such a way that accurate (i.e., within O(1 K)) temperature distributions are obtained. In addition, the convergent tolerance for the SOR scheme is chosen to be 10^{-6}, guaranteeing a convergence of the temperature distribution to within O(1 K). As a result, we expect an overall uncertainty on the order of 1 K for the temperature field in all our calculations.

Normalized Energy Density Deposited Due to Electron Beam. Figure 4 depicts the electron energy deposited within gold as determined by the MCM for two selected beam profiles (i.e., $R_{\text{electron}} = 50$ nm and 100 nm) and two initial kinetic energies of electrons (i.e., $E_0 = 4$ keV and 6 keV). Each of the sub-figures depicts the average result of five separate MC runs and the number of statistical ensembles was about 10×10^6 for each run to ensure smooth spatial distributions. One important observation is that by decreasing the incident E_0, the peak amount of electron energy deposited per unit volume within the workpiece increases although the penetration depth decreases (see (a) and (c) in Fig. 4). This might seem rather confusing since one might expect electrons with higher initial energy to deposit more energy per unit volume within the workpiece. Although more energy is deposited within the workpiece, it is distributed over a wider space since electrons penetrate deeper into the workpiece with higher initial energy.

Similarly, when the incident electron-beam profile is wide, the incident electrons are more dispersed compared to the case where the incident beam profile concentrates at the point of incidence. Subsequently, this causes the dispersion of the electron energy absorbed within the metal over a wider range; therefore, we observe that the energy deposited per unit volume within gold in Fig. 4(a) is less than that in Fig. 4(b) near the axis of the incident beam.

Temperature Distribution Due to Electron Beam. Using the normalized energy densities obtained from the MC simulations, the temperature distributions were determined with the Fourier law. We are interested in the material removal during a period of about one nano-second; therefore, the conduction code runs until the element at the origin evaporates (i.e., latent heat of evaporation is overcome and $T > T_{\text{evap}} = 3129$ K). The temperature distribution due to the electron energy deposited within gold for the case where $R_{\text{beam}} = 100$ nm and $E_0 = 4$ keV (see Fig. 4(a)) is illustrated in Fig. 5(a). The evaporated region is portrayed in white color. The time required for evaporation to occur is found to be at about $t = 0.9$ ns for an electron-beam power of 0.5 W. The required current or the number of electrons needed per unit time equals 125 μA or 7.8×10^{14} electrons/s for a power of 0.5 W at 4 keV. Since a 500-nm gold layer on top of a 10-μm transparent

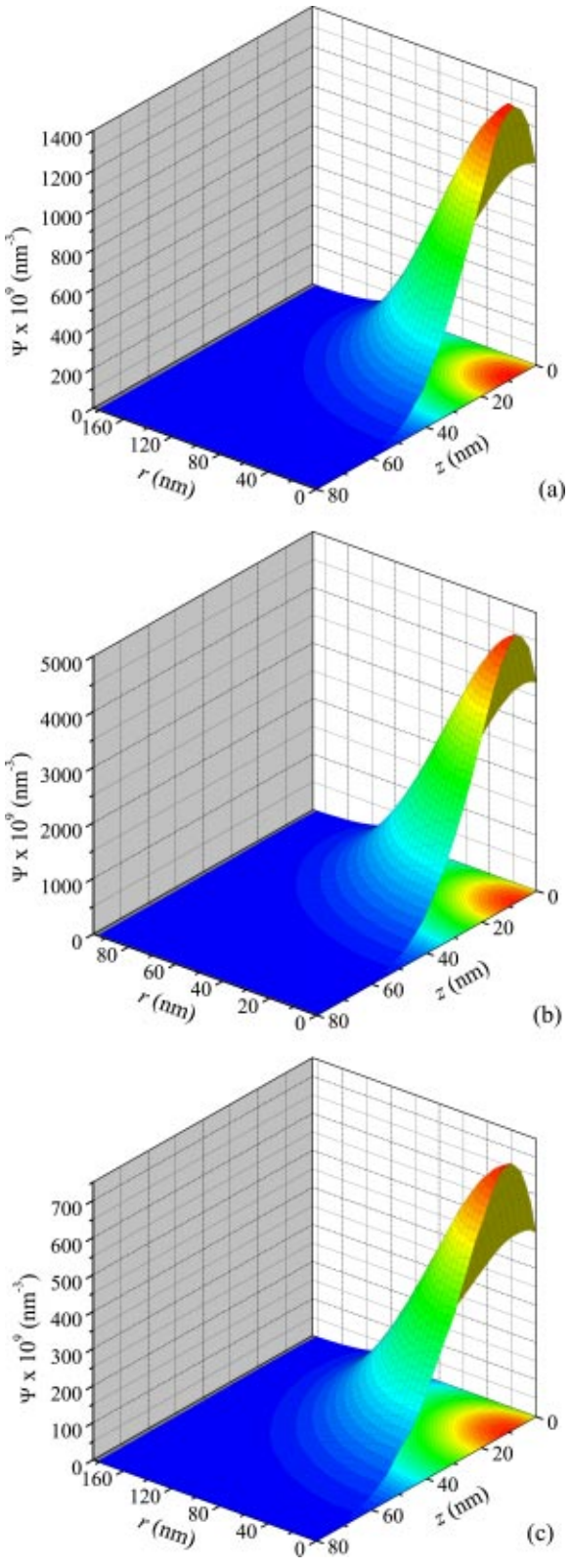

Fig. 4 Normalized electron energy $\Psi \times 10^9$ (nm^{-3}) (see Eq. (11)) deposited inside gold film Results are obtained from the Monte Carlo simulation in the electron-beam transport. The incident beam has a Gaussian profile in the r-direction with (a) a $1/e^2$ radius of $R_{\text{electron}} = 100$ nm and the initial kinetic energy of $E_0 = 4$ keV, (b) $R_{\text{electron}} = 50$ nm and $E_0 = 4$ keV, and (c) $R_{\text{electron}} = 100$ nm and $E_0 = 6$ keV.

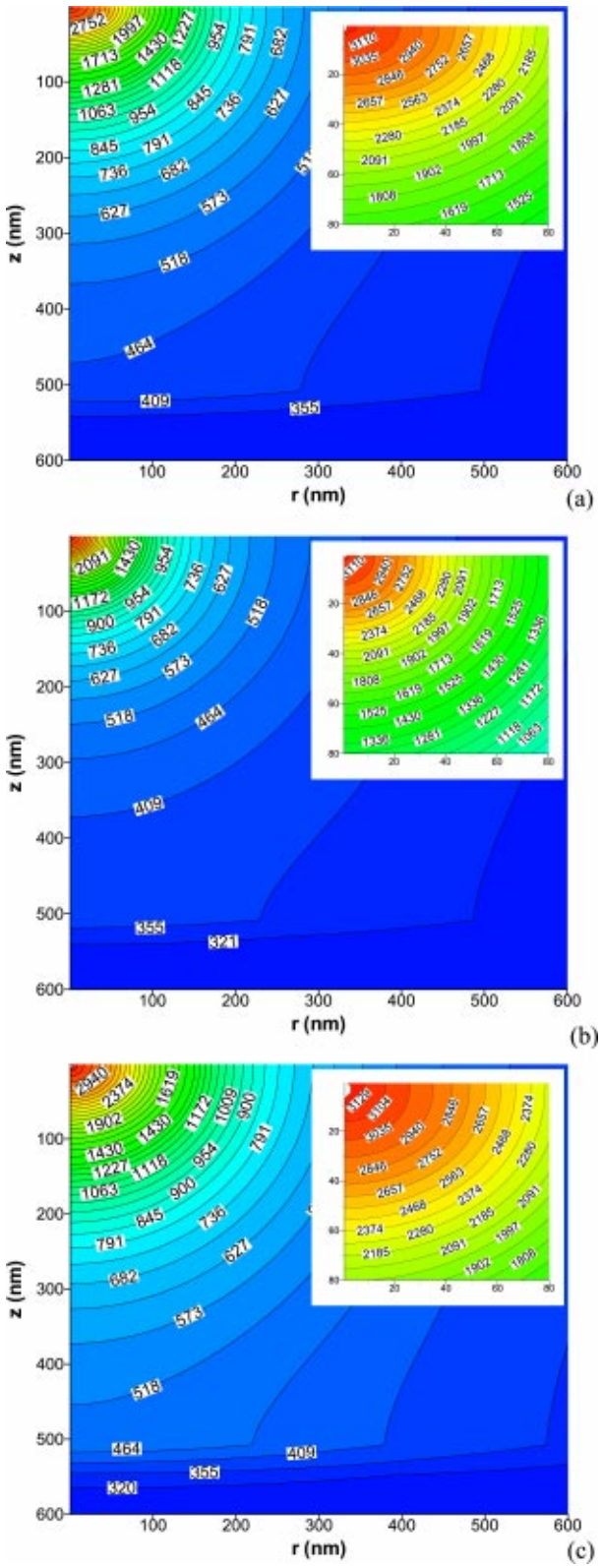

Fig. 5 (a) **Temperature distribution** (K) **within gold film at** $t=0.9$ **ns. The electron-beam impinges on the top of workpiece (i.e.,** $z=0$**). A Gaussian beam profile is considered with a** $1/e^2$ **radius of** $R_{electron}=100$ **nm and an initial kinetic energy of** $E_0=4$ **keV. The power of the beam is set to** $\dot{E}=0.5$ **W. The** Δt **used in the simulation is 0.005 ps. The thicknesses of the workpiece and the substrate, which are gold and quartz, are assumed to be 500 nm and 10** μ**m, respectively. In the figure there is a sharp bending for the isothermal lines at** $z=500$ **nm, which is where the interface of the two different materials. Note that this is the snapshot of the temperature field right at the moment when the first computational element nearest the origin overcomes the latent heat of evaporation and starts to evaporate. The small inset in top right-hand corner portrays an up-close temperature field for an area of** $(r\times z)=(120\text{ nm}\times 120\text{ nm})$ **near the origin. (b) Temperature distribution** (K) **within gold at** $t=0.7$ **ns using the same conditions in (a) except that** $R_{electron}=50$ **nm,** $E_0=4$ **keV, and** $\dot{E}=0.305$ **W. (c) Temperature distribution** (K) **within gold at** $t=1.0$ **ns using the same conditions in (a) but with** $R_{electron}=100$ **nm,** $E_0=6$ **keV, and** $\dot{E}=0.615$ **W.**

substrate was assumed, the isotherms bend sharply at $z=500$ nm as the material properties change at the interface. Note that the figure portrays only the portion of the computational domain where the highest temperatures exist. The element at the origin where evaporation occurs is removed in the figure as shown by a white spot at the upper left-hand corner.

Using the MC result given in Fig. 4(b), the temperature distribution for an incident electron-beam of $R_{\text{electron}}=50$ nm is computed and depicted in Fig. 5(b). In this case the power of the electron-beam was 0.305 W and evaporation started at $t=0.7$ ns. Note that the beam has less power, yet evaporation occurs sooner compared to the previous case (i.e., $R_{\text{electron}}=100$ nm), demonstrating that the required power for evaporation can be reduced when the beam is narrow. It also indicates that the temperature of gold film can be increased much faster at the origin if the electron-beam is more focused, and that if wider machining area is desired, then a wider beam should be used even though this slows down the process and may require greater beam power.

Figure 5(c) shows the temperature distribution within gold film at $t=1$ ns for an incident electron-beam of 6 keV with an input power of 0.615 W. It is obvious that increasing the applied voltage tends to spread the electron energy over a deeper range since the penetration depth is also increased; this in turn elevates the input power required from the beam. This is evident from the comparison between (a) and (c) in Fig. 5. To compare the current required between the two (i.e., $E_0=4$ keV versus 6 keV with the same R_{beam}), the evaporation time should be identical in both cases. Therefore, it is essential to determine the required input power for the 6-keV beam to cause evaporation at $t=0.9$ ns instead of 1 ns. An extra simulation with a beam power of 0.625 W was performed, and it was determined that the evaporation time is at 0.8 ns. Assuming a linear relationship between the time for evaporation and the power, it takes approximately 0.62 W for the 6-keV electron-beam to start evaporation at 0.9 ns as opposed to 0.5 W for the 4-keV one. This leads to a current of 103 μA for the former and 125 μA for the latter. It looks as though the current required for achieving evaporation is actually reduced when the beam energy increases. However, this preliminary conclusion should not be generalized since there are other factors affecting the outcome such as the evaporation time and the thicknesses of the film. In-depth calculations and explorations are needed for further clarification of the affects of other parameters.

Another interesting thing to note in Fig. 5(c) is that evaporation first occurs layers beneath the surface creating the gold vapor, which is expected. It is clear from Fig. 4(c) that the region with highest density of energy deposited by the electron beam is not at the surface but a few nanometers beneath it. However, the vapor is trapped inside the material since the surface has not been evaporated. At the instance the element at the origin is removed, the vapor is released, leaving a noticeable evaporated region as seen in the figure. Further examinations on the temperature distributions reveal similar trend in both (a) and (b) in Fig. 5 except that the evaporated regions are smaller. Although it would be informative to compare among the electron-beam powers or currents required for various cases to evaporate the exact volume and shape, it is impractical since the penetration depth varies depending on the incident kinetic energy of the electron-beam.

Temperature Distribution Due to Electron-Beam and Laser An alternative to reduce the power required from the CNT is to supply additional heat via a laser. To investigate this, additional numerical simulations were carried out. Figure 6 shows the temperature distribution obtained with laser heating for the same conditions used in Fig. 5(a). To be consistent with other cases, the result given here is at the instance where the element at the origin evaporates. With the help of a laser heat flux of 5.09 μW/nm^2 ($=q_0''$) incident on the bottom of the gold layer within an area of a radius of $R_{\text{laser}}=300$ nm measured from the z-axis, the time required for evaporation is shortened from $t=0.9$ ns (as in Fig. 5(a)) to 0.5 ns. By coupling the laser heat flux required, the incident area, and the Fresnel reflection when the laser first enters the vacuum-substrate interface, the laser power needed for this specific case is calculated to be about 1.5 W. Although this approach can reduce the power required from the electron-beam, the thickness of the workpiece is a limiting factor since the laser heats from the back of the workpiece. In addition, the absorption of radiant energy in a metal is strong; therefore, the gold film thickness needs to be as small as possible in order for the laser heating to affect the material in the vicinity of the incident electron-beam.

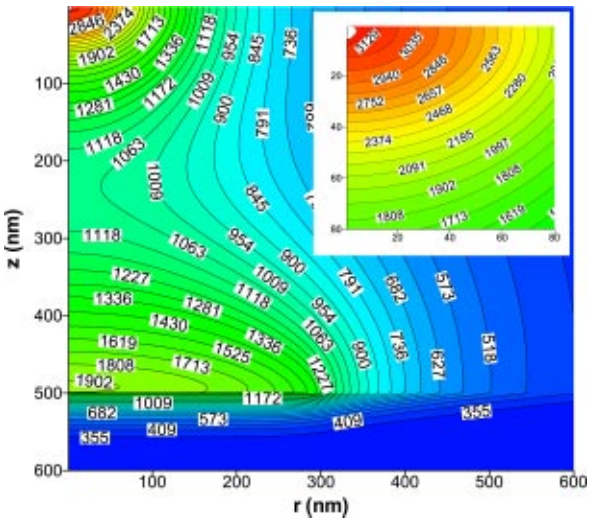

Fig. 6 Temperature distribution (K) within gold film at $t=0.5$ ns. Both the electron-beam and the laser are considered. The input parameters are the same as those in Fig. 5(a). The power of the laser is 1.5 W and it covers a radius of $R_{\text{laser}}=300$ nm from the z-axis. With the assistance from the laser, the time required for the first element at the origin to evaporate is improved from $t=0.9$ ns (as in Fig. 5(a)) to 0.5 ns.

For the simulation results depicted in Fig. 7, the thickness of the gold layer is 200 nm. The specifications of the electron-beam and the laser remain the same as in Fig. 6. In this case, the laser heating is more effective in reducing the power required from the electron-beam. Figure 7(a) is the temperature field at about 1 ns where evaporation occurs at the origin for a reduced electron-beam power of 0.25 W while Fig. 7(b) depicts the time required for evaporation as a function of various powers of the electron-beam, with or without the use of a laser, for a 200-nm layer of gold film. One obvious observation from the figure is that the time to evaporation is reduced when the laser is employed for heating from the back of the workpiece. Notice also that the evaporation time increases as the electron-beam power is decreased. For a strong electron-beam, using a laser would not be necessary since the evaporation time is so short that the workpiece starts to evaporate before the heat provided by the laser is conducted to the top.

Only if both the electron-beam and the laser are directed towards the same point of incidence can the most advantage of the laser heating be obtained. This would require that both beams to be obliquely oriented, which would require revisions to the model that can be investigated in future work.

Transient Temperature of the Origin. Figure 8 shows the transient temperatures of the element at the origin around an infinitesimal radius of $\Delta r=1.25$ nm and a depth of $\Delta z=1.25$ nm under different conditions. The descriptions of the various cases can be found in the figure caption. In short, Case 1 sets the standard for the remaining four cases. Case 2 refers to a more focused electron-beam Case 3 the inclusion of laser heating, Case 4 reduced gold thickness with laser heating, and Case 5 an electron-beam with higher incident kinetic energy.

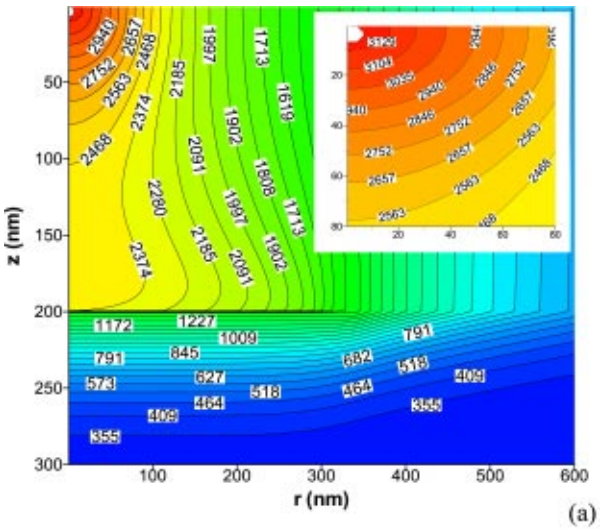

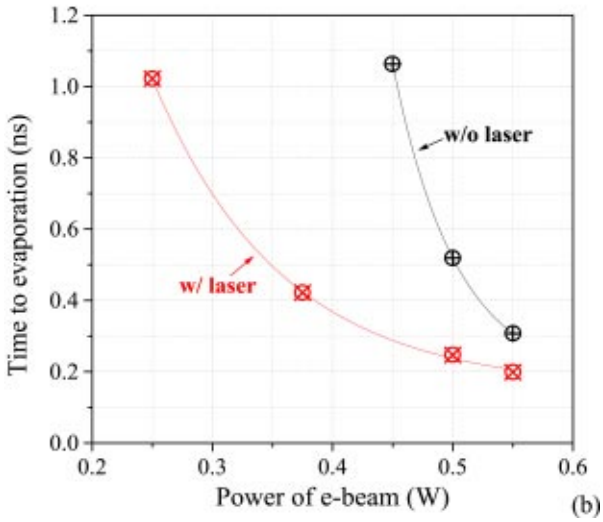

Fig. 7 (a) Temperature distribution (K) within gold at $t=1$ ns. Both the electron-beam and the laser heating are considered. The thickness of gold film is reduced to 200 nm and the power of the electron-beam is set to 0.25 W. The rest of the input parameters follow those given in Fig. 6(b). The time required for evaporation as a function of the input power from the electron-beam for the 200-nm gold film.

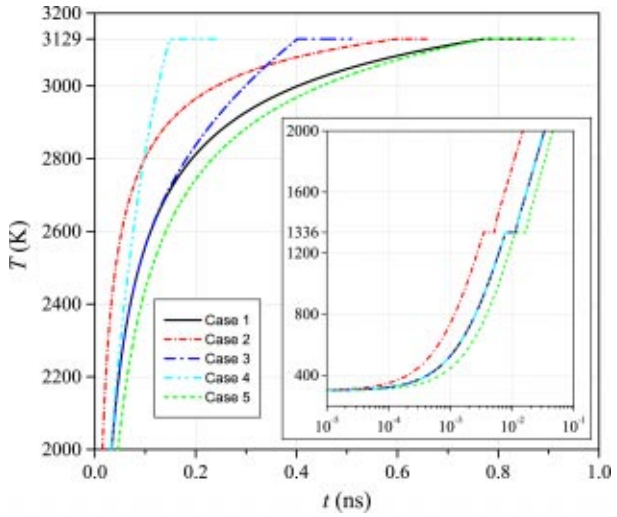

Fig. 8 Transient temperatures at the origin around an infinitesimal area with radius of $\Delta r=1.25$ nm and depth of $\Delta z=1.25$ nm. The first case is set as the reference at which the inputs for the electron-beam are $R_{electron}=100$ nm, $E_0=4$ keV and $\dot{E}=0.5$ W. The gold film thickness is assumed to be 500 nm. The second has the same inputs as the reference except that the beam is focused narrower with $R_{electron}=50$ nm. The third is the same as the first case but with laser heating. The power of the laser used is 1.5 W. The fourth has a gold film thickness of 200 nm while the rest of the inputs are the same as the third case. The electron-beam of the final case has $R_{electron}=100$ nm, $E_0=6$ keV and $\dot{E}=0.615$ W with the laser turned off.

It is observed that the transient curve shifts to the left as the electron-beam is focused narrower (see Cases 1 and 2), indicating that the transient temperature at the origin is always higher for the latter case. This shows that a highly-focused electron-beam is desired in elevating local temperatures in this application and shortening the evaporation time. When the laser heating is used simultaneously with the electron-beam, it has no effect on the temperature of the origin until $t=0.15$ ns at which the temperature starts to increase more compared to that of the case where it is excluded (see Cases 1 and 3). Certainly, the starting time for the laser to aid the heating process at the origin can be reduced by decreasing the thickness of the workpiece, which can be evident from the transient curve of Case 4. Note that all the cases have the same input power for the electron-beam except the final case where the incident beam energy is lowered to 6 keV. This is because the computational cost required for the case where a 6-keV electron-beam of 0.5 W is used is relatively expensive; therefore, the power is increased to 0.615 W to reduce the cost while maintaining the trend that the temperature at the origin as heated by a lower-energy beam is lower at all time (see Cases 1 and 5).

Conclusions

In this work, we investigated the possibility of achieving nano-scale machining on a thin metallic film deposited on a transparent substrate. The effects of simultaneous electron and photon processing are considered. The propagation of the electron-beam inside the gold film is modeled using a MC simulation while the laser heating is treated as a one-dimensional problem. Both the electron and photon energy accumulated inside the workpiece are considered as heat generation in the conduction heat transfer model. Hence, the temperature field inside the workpiece is predicted. The results show that a power input of half-a-watt supplied from an electron-beam alone is sufficient to start local evaporation during about 1 ns. This can be achieved by using either a 4 or 6-keV electron-beam, provided the spatial distribution of the emitted electrons from the electron-gun is no greater than 100 nm and closely resembles a Gaussian distribution. With the help of focused laser heating, the power required from the electron-beam can be reduced by a factor of 50 percent if the workpiece is sufficiently thin. Although a comprehensive theoretical frame work is presented here for predicting the power and current required for nano-scale machining, the model needs further modifications, improvements, and fine-tuning for applications to real systems. Some of these requirements are briefly outlined below.

The accuracy of the electron energy deposition profiles predicted using the MC simulation for the electron-beam transport can be further improved by employing a Discrete Inelastic Scattering Approach (DISA) (see [27] for further details) instead of a Continuous Slowing-Down Approach (CSDA), which we adapted here. The DISA uses the experimental optical data for the workpiece to treat all the scattering events discretely, which is more

accurate than using the stopping power as in the CSDA, especially if the incident energy of the electron-beam is around 1 keV. In addition, the propagations of secondary electrons as a result of the inelastic scatterings (i.e., energy lost from the primary electrons of the electron-beam to the electrons inside the workpiece) would further spread the incident energy from the electron-beam over a wider volume, which is not accounted for in the current MC model.

The radiation losses and the pressure- and temperature-dependent material properties need to be incorporated in the conduction modeling. With these effects included, the required power for the electron-beam could either be lower or higher. If radiative losses were added, the required power is definitely higher since the workpiece would lose heat (if it is significant). However, it is known that materials become more temperature-resistant as the temperature increases; therefore, it implies that heat loss by conduction at the heating region would be reduced. As a result, the input power needed from the electron-beam would be reduced as well, which certainly benefits the case of using only the electron-beam.

The use of Fourier heat conduction model implies that both electrons and phonons are at the same temperature. This approximation needs to be replaced by a two-temperature model (TTM) [23]. The TTM allows electrons and phonons to exist at different temperatures, which is important since the electron-beam first transfers energy to electrons inside the workpiece and causes elevation of the electron temperature. Consequently, electrons exist at a temperature much higher than that of phonons. Interactions between electrons and phonons subsequently establish equilibrium at which both immerse at a single temperature [28].

Acknowledgment

This work is supported by an NSF Nanoscale Interdisciplinary Research Team (NIRT) award from the Nano Manufacturing program in Design, Manufacturing, and Industrial Innovation (DMI-0210559). In addition, Basil T. Wong has received the Dissertation Year Fellowship granted by the University of Kentucky during this study.

Nomenclature

A = atomic weight (kg/mol-atom)
C = specific heat (J/kg-K)
E = electron energy (keV)
E_0 = initial energy of the electron beam (keV)
$\dot{E}$ = input power of electron beam (W)
J = mean ionization potential (keV)
k = thermal conductivity (W/m-K)
L = z-dimension of the geometry (m)
N = total number of elements (−)
N_{en} = total number of statistical ensembles (−)
N_a = Avogadro number ($=6.023\times10^{23}$ atoms/mol)
n_1 = real part of refractive index (−)
$\tilde{n}$ = complex refractive index (−)
q'' = heat flux (W/m^2)
$\dot{q}$ = heat generation (W/m^3)
q_0'' = initial laser heat flux incident on the workpiece (W/m^2)
q_{gen} = rate of heat generation (W)
r = radial axis (−)
Δr = grid spacing in r-direction (m)
R = r-dimension of the geometry (m)
$R(\bullet)$ = cumulative probability distribution (−)
$R_{i\rightarrow t}$ = fraction of laser energy reflected propagating from medium i to t (−)
Ran = a random number (−)
R_{electron} = the l/e^2 radius of the Gaussian distribution (m)
R_{laser} = the radius of the area where the laser uniformly heats (m)
R_p = electron penetration range (m)
S = distance of interaction (m)
t = time (s)
Δt = time increment (s)
T = temperature (K)
V = voltage (V)
z = z-axis (−)
Δz = grid spacing in z-direction (m)
Z = atomic number (−)

Greek Symbols

ϕ = azimuthal angle (rad)
κ = absorption coefficient (m^{-1})
λ = mean free path of electrons (m)
λ_o = wavelength of light in vacuum (m)
θ = polar angle (rad)
Θ = scattering angle (rad)
ρ = density of solid (kg/m^3)
σ_{el} = elastic scattering cross section (m^2)
$\sigma_{\text{el,total}}$ = total elastic scattering cross section (m^2)
Ω = solid angle (sr)
ψ = energy deposited (keV)
Ψ = normalized electron energy density (m^{-3})

Subscripts

i = incident
m = grid index in the r-direction
n = grid index in the z-direction
o = vacuum
s = substrate
t = transmitted
w = workpiece

Superscripts

elec = refers to electron transport
p = time step
rad = refers to radiative transfer

References

[1] Vallance, R. R., Rao, A. M., and Menguc, M. P., 2003, ''Processes for Nanomachining Using Carbon Nanotubes,'' U.S. Patent No. 6,660,959, issued to University of Kentucky Research Foundation, Lexington, KY.
[2] Taniguchi, N., Ikeda, M., Miyamoto, I., and Miyazaki, T., 1989, *Energy-Beam Processing of Materials: Advanced Manufacturing Using Various Energy Sources*, Oxford University Press, New York.
[3] Wong, B. T., and Mengüç, M. P., 2004, ''Monte Carlo Methods in Radiative Transfer and Electron-Beam Processing,'' J. Quant. Spectrosc. Radiat. Transf., **84**, pp. 437–450.
[4] Wong, B. T., and Mengüç, M. P., 2003, ''Electronic Thermal Conduction in Thin Gold Films,'' ASME Summer Heat Transfer Conference, Las Vegas, Nevada, Paper No. 47172.
[5] Archard, G. D., 1961, ''Back Scattering of Electrons,'' J. Appl. Phys., **32**(8), pp. 1505–1509.
[6] Kanaya, K., and Okayama, S., 1972, ''Penetration and Energy-Loss Theory of Electrons in Solid Targets,'' J. Phys. D, **5**, pp. 43–58.
[7] Whiddington, R., 1912, ''The Transmission of Cathode Rays Through Matter,'' Proc. R. Soc. London, Ser. A, Containing Papers of a Mathematical and Physical Character, **86**(588), pp. 360–370.
[8] Trinkle, C. A., Vallance, R. R., Mengüç, M. P., Bah, A., Javed, K., Rao, A. M., and Jin, S., 2002, ''Nanoprobe Concepts for Field Emission Nanomachining,'' Proceedings of the 17th Annual Meeting of the American Society for Precision Engineering, St. Louis, MO.
[9] Wong, B. T., and Mengüç, M. P., 2002, ''Comparison of Monte Carlo Techniques to Predict the Propagation of a Collimated Beam in Participating Media,'' Numer. Heat Transfer, Part B, **42**, pp. 119–140.
[10] Joy, D. C., 1995, *Monte Carlo Modeling for Electron Microscopy and Microanalysis*, Oxford University Press, New York.
[11] Murata, K., Matsukawa, T., and Shimizu, R., 1971, ''Monte Carlo Calculations on Electron Scattering in a Solid Target,'' Jpn. J. Appl. Phys., **10**(6), pp. 678–686.
[12] Shimizu, R., Ikuta, T., and Murata, K., 1972, ''The Monte Carlo Technique as Applied to the Fundamentals of Epma and Sem,'' J. Appl. Phys., **43**, pp. 4233–4249.
[13] Newbury, D. E., and Myklebust, R. L., 1981, *Analytical Electron Microscopy*, R. H. Geiss eds., San Francisco Press, San Francisco, pp. 91.
[14] Czyzewski, Z., MacCalium, D. O. N., Romig, A., and Joy, D. C., 1990, ''Cal-

culations of Mott Scattering Cross Section,'' J. Appl. Phys., **68**(7), pp. 3066–3072.
[15] Luo, S. C., Zhang, X., and Joy, D. C., 1991, ''Experimental Determinations of Electron Stopping Power at Low Energies,'' Radiat. Eff. Defects Solids, **117**, pp. 235–242.
[16] Joy, D. C., ''A Database of Electron-Solid Interactions,'' http://web.utk.edu/~srcutk/.
[17] Hecht, E., 1998, *Optics*, Addison Wesley Longman, Inc.
[18] Modest, M. F., 1993, *Radiative Heat Transfer*, McGraw-Hill, Inc.
[19] Palik, E. D., 1985, *Handbook of Optical Constants of Solids*, Academic Press, New York.
[20] Majumdar, A., 1998, ''Microscale Energy Transport in Solids,'' *Microscale Energy Transport*, C. L. Tien eds., Begell House, New York, pp. 1–93.
[21] Cahill, D. G., Ford, W. K., Goodson, K. E., Mahan, G. D., Majumdar, A., Maris, H. J., Merlin, R., and Phillpot, S. R., 2003, ''Nanoscale Thermal Transport,'' Applied Physics Reviews, **93**(2), pp. 793–818.
[22] Ashcroft, N. W., and Mermin, N. D., 1976, *Solid State Physics*, Saunders Company, Philadelphia, PA.
[23] Tzou, D. Y., 1997, *Macro- to Microscale Heat Transfer*, Taylor & Francis, Washington, DC.
[24] Incropera, F. P., and DeWitt, D. P., 1996, *Fundamentals of Heat and Mass Transfer*, John Wiley & Sons, New York.
[25] Matthews, J. H., and Fink, K. D., 1999, *Numerical Methods Using Matlab*, Prentice Hall, Inc., New Jersey.
[26] Jacques, S. L., and Wang, L., 1995, ''Monte Carlo Modeling of Light Transport in Tissues,'' *Optical-Thermal Response of Laser-Irradiated Tissue*, Welch and V. Gemert eds., Plenum Press, New York, pp. 73–100.
[27] Ding, Z. J., and Shimizu, R., 1996, ''A Monte Carlo Modeling of Electron Interaction With Solids Including Cascade Secondary Electron Production,'' Scanning, **18**, pp. 92–113.
[28] Hohlfeld, J., Wellershoff, S.-S., Güdde, J., Conrad, U., Jähnke, V., and Matthias, E., 2000, ''Electron and Lattice Dynamics Following Optical Excitation of Metals,'' Chem. Phys., **251**, pp. 237–258.

Finite Size Effects in Determination of Thermal Conductivities: Comparing Molecular Dynamics Results With Simple Models

Patrice Chantrenne
Thermal Center of Lyon (CETHIL),
UMR 5008 CNRS, INSA,
Bât. S. Carnot, 20 Av. A. Einstein, 69621
Villeurbanne Cedex,
France

Jean-Louis Barrat
Laboratoire de Physique de la Matière
Condensée et Nanostructures,
UMR 5586 CNRS, UCBL,
Bât. L. Brillouin, 43 Bd. du 11 Nov. 1918, 69622
Villeurbanne Cedex,
France

The thermal conductivity of nanometric objects or nanostructured materials can be determined using nonequilibrium molecular dynamics (NEMD) simulations. The technique is simple in its principle, and resembles a numerical guarded hot plate experiment. The "sample" is placed between a hot source and a cold source consisting of thermostatted sets of atoms. The thermal conductivity is obtained from the heat flux crossing the sample and the temperature profile in the system. Simulation results, however, exhibit a strong dependence of the thermal conductivity on the sample size. In this paper, we discuss the physical origin of this size dependence, by comparing MD results with those obtained from simple models of thermal conductivity based on harmonic theory of solids. A model is proposed to explain the variation of the thermal conductivity with system size.
[DOI: 10.1115/1.1777582]

Keywords: Heat Transfer, Molecular Dynamics, Nanoscale

1 Introduction

As with other transport or thermodynamic properties, the thermal behavior of nanostructured materials or nanoelectronic devices cannot be simply inferred by extrapolating macroscopic behavior to small scales. Instead, when the typical size of the device becomes comparable to interatomic distances, a discussion of properties and models at the atomic scale becomes essential. The total conductance of nanowire or nanowire arrays, superlattices, thin films and periodic thin film structures will depend on the thermal conductivity of each component and on the thermal resistance between them, all of which will be scale dependent. The aim of experimental and theoretical studies is to predict or to measure these characteristics [1–14]. However, the best experimental resolution is still larger than 100 nm. At smaller scales, atomistic numerical simulation appears to be an appropriate tool to predict thermophysical properties.

Using atomistic modeling [15,16], three methods are available for computing thermal conductivities. The first one, mostly used for bulk systems, is equilibrium molecular dynamics (MD) [17] using the appropriate Einstein or Green-Kubo relations. This approach can be extended to the determination of contact resistances [18]. An alternative route is to use nonequilibrium molecular dynamics (NEMD) [19–21], and is more appropriate for inhomogeneous systems [22]. The last approach combines a microscopic determination of phonon dispersion relations with a transport theory of the Landauer-Buttiker-type (which is generally used to calculate electronic transport properties) [23].

In this paper, we present NEMD simulations of heat transfer in finite size structures. The technique mimics numerically a guarded hot plate experiment. The "sample" is placed between a hot source and a cold source consisting of thermostatted sets of atoms. The thermal conductivity is obtained from the heat flux crossing the sample and the temperature profile in the system. NEMD is therefore well adapted to study the influence of structural defects and solid interfaces. We show that the simulation results exhibit a strong dependence on sample size, and also on the type of boundary conditions. In order to understand the physical origin of these dependences, we compare our simulation results with a simple approach based on phonon transport theory.

The type of effects we are interested in are generic in nature, and our study a methodological one. Therefore no attempt was made to model a specific material in a realistic manner. Rather, we favor computational efficiency by using a simplistic model of particles interacting through a classical, pairwise, Lennard-Jones potential:

$$E_p(r) = 4\varepsilon\left[\left(\frac{\sigma}{r}\right)^{12} - \left(\frac{\sigma}{r}\right)^{6}\right] \quad (1)$$

Molecular dynamics simulations with Lennard-Jones potential allow to recover with a good accuracy the properties of the element of group VIII of the chemical periodic table (rare gas) [15,16]. Solid argon is considered as an example in this paper because it has been previously widely studied with MD and lots of experimental data are available in the litterature. All the results in the following will be given in Lennard-Jones units. $\varepsilon=1$, $\sigma=1$ and $m=1$. For the calculations, a modified version of the parallel MD code LAMMPS [24] was used.

Finally, we want to emphasize that our calculations are purely classical, which limits their applicability to cases where heat transport is essentially phononic, i.e., insulators or bad electrical conductors.

The paper is organized as follows: in the next section, we describe our NEMD simulation method and we present the influence of the boundary conditions, simulation parameters and system size on heat transfer and the thermal conductivity. Section 3 describes a semianalytical approach used to rationalize our results, and section 4 summarizes our conclusions.

Contributed by the Heat Transfer Division for publication in the JOURNAL OF HEAT TRANSFER. Manuscript received by the Heat Transfer Division June 11, 2003; revision received May 17, 2004. Associate Editor: G. Chen.

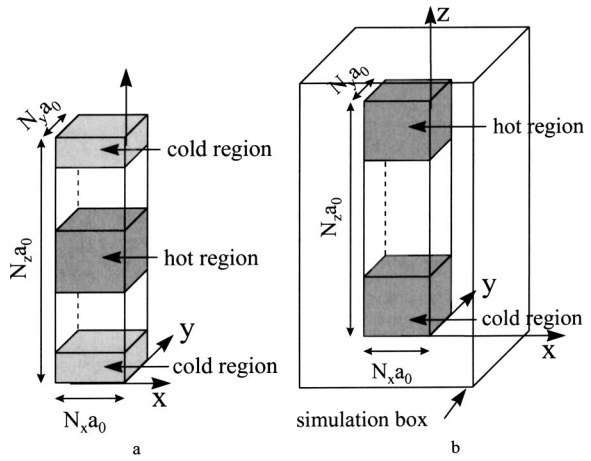

Fig. 1 Geometric configuration of the simulations: (a) for periodic boundary condition, the system and the simulation box have the same size; (b) for free surfaces, the size of the simulation box is larger than the system size

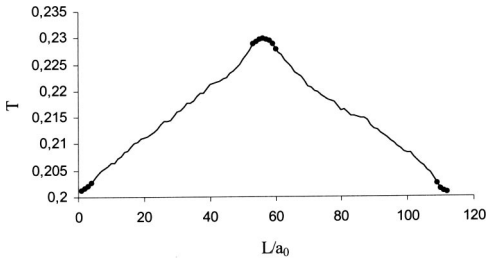

Fig. 2 Temperature profile in a system with thermostatted zones as a function of the nondimensional position in the direction of heat transfer. Periodic boundary conditions are used in all directions. The dots indicate the thermostatted zones.

2 NEMD Simulation Methodology and Its Influence on the Thermal Conductivity

Several papers describe the methodology used to simulate heat transfer with NEMD. A hot thermal reservoir and a cold thermal reservoir are used to create a temperature gradient in the system (Fig. 1). To create these hot and cold regions it is possible to control the energy given or taken from the thermal reservoir either by rescaling the velocity field of the hot and cold region or by exchanging particles between them [13,25–27]. With this method, the heat flux is perfectly controlled and constant during the simulation. However, the temperature gradient is not controlled. We used the alternative method of controlling the temperature of the hot and cold region by rescaling the velocity field of these regions in order to maintain their average temperature constant [11,14,18,28–30]. The total temperature gradient is perfectly controlled and the comparison of the heat flux given to the hot region and taken from the cold region is a good mean to check that the simulation is energy conservative. Three simulation parameters are important: the frequency of rescaling, the fraction of rescaling and the size of the thermostatted zones. Their influence on the thermal conductivity is studied in section 2.1.

As expected, temperatures and heat fluxes experience instantaneous fluctuations. The mean value of the heat fluxes and temperature profile are calculated over a large range of time step after the steady state heat transfer has been reached.

All the simulations are performed in a simulation cell containing a FCC lattice of Lennard-Jones atoms at mass density $\rho=1.075\ \mathrm{m}/\sigma^3$. The lattice parameter a_0 is equal to 1.5496σ. The LJ inter-atomic potential of Eq. (1) is used. For computational reasons and energy conservation, this potential has been smoothly cut-off at a distance 3σ. The size of the crystal is N_xa_0, N_ya_0, and N_za_0 in the x, y, and z-directions (Fig. 1). The hot and cold regions are sets of atoms forming a slab parallel to the (x,y) plan so that heat transfer is unidimensional in the z-direction. The size of the simulation cell and the location of the hot and cold region depends on the boundary conditions that are used, as shown on Fig. 1(a) and 1(b). For periodic boundary conditions, the simulation cell has the same size than the crystal. For free or fixed boundary surfaces, the size of the simulation cell is larger than the crystal size by at least the cut-off distance of the LJ potential. The influence of the boundary conditions and the system size on the thermal conductivity are presented in section 2.2.

The time step used for all the simulations is equal to 0.001 in Lennard-Jones units. As the aim of the simulations is to study the influence of the simulation parameters and the system size, the choice of the temperature level is almost arbitrary. The average temperature should not be too high to limit the instantaneous variations and the problems that can be encountered for free surfaces boundary conditions. The average temperature of the system and the temperature difference between the hot and cold region are then equal to 0.2123 and 0.0274 in LJ units. This correspond to an average temperature of 25 K for solid argon. A similar value of 0.27 in LJ units for the average temperature was used by Lukes et al. [25] to study the thermal conductivity of thin films of solid argon. Under these conditions, the steady state is attained after about 50,000 time steps (depending on the sizes of the hot and cold regions). Then the simulations last several hundred thousand time steps (typically between 500,000 and 1,000,000) in order to have a good accuracy on the temperature gradient between the hot and cold region and the heat fluxes. The method proposed by Lukes et al. [25] to calculate the uncertainties has been implemented. This led to an uncertainty on the thermal conductivity which lies between 15 and 20 percent.

Two important characteristics of the reservoirs must be well understood in order to avoid an incorrect interpretation of the simulation results. At first, the heat source and the heat sink cannot be considered as classical boundary conditions of a continuous medium. They are part of the system, so that phonon modes are characterized by the whole dimension of the system and not by the size of the intermediate zones. Secondly, as a heat flux requires a temperature gradient, if the thermal reservoirs are isothermal then no heat flux can flow to or from them. So, there is a temperature gradient within the thermal reservoirs, which depends on the heat flux.

2.1 Influence of the Thermostatted Zones. Due to heat transfer, there is theoretically no local thermal equilibrium. This equilibrium is characterized by the Maxwell-Boltzmann distribution function of the velocity. Actually, the deviation from the equilibrium distribution function is expected to be very small [29] so that local temperature can still be defined and calculated. In our case, the instantaneous temperature profile in the z-direction is determined from the temperature of each atomic layer in the (x,y) planes

$$T_z = m\sum_{i}^{N_{xy}} \frac{v_i^2}{3N_{xy}k_b} \quad (N_{xy}:\ \text{number of atoms considered}) \tag{2}$$

in accordance with the equipartition principle.

The local velocity distribution function has been determined in a system during a heat transfer simulation. The system size is $10a_0$, $10a_0$, and $116a_0$ in the x, y, and z-directions. Periodic boundary conditions are used and the thickness of the cold and hot regions is equal to $8a_0$. The temperature profile in the system during this simulation is shown in Fig. 2. As expected, the temperature profile in the thermostatted zones is not constant: it exhibits a parabolic shape as for macroscopic systems with heat sources. For each atomic layer, the velocity distribution function

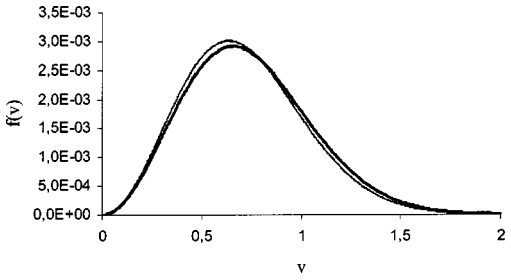

Fig. 3 Velocity repartition function. Bold line: repartition function in the middle of the hot source. Thin line: repartition function in the middle of the intermediate bloc. In both cases, numerical and theoretical repartition functions are superimposed.

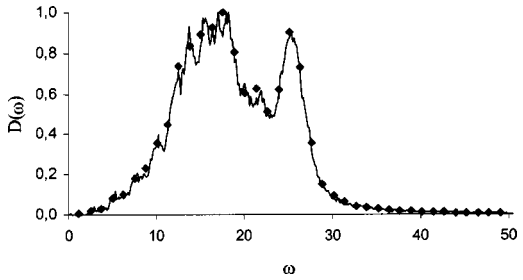

Fig. 4 Density of states D (in arbitrary units) versus angular frequency (Lennard-Jones units). Line: results for system at equilibrium; Diamonds: results for system with thermostatted zones.

is compared to the equilibrium Maxwell distribution function [32] at the same temperature. Two such distribution functions are presented in Fig. 3, for layers taken in the middle of the heat source and in the middle of the intermediate (not thermostatted) zone. The two functions are different due to the temperature difference, but visually, there is no significant difference between the numerical distribution and the Maxwell-Boltzmann distribution. Actually, the differences do not exceed 2 percent, which confirm the validity of local thermal equilibrium assumption.

The other effect that might be induced by the NEMD simulation method is due to the rescaling of the velocity field in the thermostatted regions. If the rescaling significantly modifies the vibration modes, it would modify the heat transfer in the system and the simulation results may not be valid. As already said, three numerical parameters govern the rescaling: the period of rescaling, the fraction of rescaling and the size of the hot and cold region. In Table 1, the thermal conductivity calculated for a system for different rescaling periods and fractions. The results show that the thermal conductivity does not depend on these parameters. All the subsequent simulations used a systematic rescaling (period equal to the time step and rescaling fraction equal to 1).

The effective density of states (i.e., the Fourier transform of the velocity autocorrelation of a particle) has been determined for a system at equilibrium. It is compared to the density of states of a system with a heat source and heat sink such that the average temperature of the system is also equal to the temperature of the system at equilibrium. The two curves are superimposed in Fig. 4. Our conclusion is that the thermostats do not significantly modify the microscopic dynamics of our system, and are therefore appropriate for performing heat transport simulations.

For a system of size equal to $50a_0$ in all directions, with periodic boundary conditions, the thermal conductivity was calculated for two sizes of the thermostated zones: $10a_0$ and $15a_0$, and no significant differences were found (Fig. 5). However, the results exhibit a large dispersion if the number of free atoms between the thermal reservoirs is too large because the system then requires more time to reach the steady state.

Table 1 Influence of the rescaling factor and period on the thermal conductivity. System size: $10a_0$, $10a_0$ and $116a_0$ in the *x*, *y*, and *z*-directions. Periodic boundary conditions are used in the *x* and *y*-directions, fixed boundary atoms in the *z*-direction. Thickness of the cold and hot regions equal to $8a_0$.

rescaling period	rescaling fraction	thermal conductivity (LJ unit)
1	1	41+/−8
10	1	45+/−9
100	1	42+/−7
1	0.1	45+/−8

2.2 Influence of the Boundary Conditions and System Size.. In MD simulations, the system is placed in a simulation box of finite size. To predict bulk properties, the standard approach is to use periodic boundary conditions (PBC), in which the simulation box is periodically repeated in each direction [15,16]. The system is finite, but completely homogeneous.

To study properties of nanometric structures free surfaces are used in all directions for a three-dimensional object, in two directions for a wire and in one direction for a film. The object is embedded in a much larger simulation cell (Fig. 1(b)). Studying solids under these conditions can be difficult since evaporation can result in unwanted shape changes. To prevent the formation of the vapor phase, the system can be delimited by either with a set of fixed (''dead'') atoms (hard wall) or with ''phantom'' atoms, i.e., weak harmonic springs that bind the atoms located on the system surface to their equilibrium position. The spring constant is chosen such that the associated vibrational frequency is smaller than the Einstein frequency, so as to minimize the influence of this constraint on vibrational dynamics [18].

The thermal conductivity of a cube of dimension $L=Na_0$ has been determined using NEMD. The cube size ranged between $10a_0$ to $80a_0$. Four kinds of boundary conditions were used: periodic boundary surfaces in the three directions, free surfaces with fixed (''dead'') atoms, free surfaces with phantom atoms in all three directions, and unconstrained free surfaces. Due to the evaporation problem mentioned above, only one reliable data point could be obtained for the unconstrained case. Figure 5 compares the results for the thermal conductivity obtained with these different boundary conditions, as a function of system size. The error bars are plotted assuming the maximum uncertainty of 20 percent. Free surfaces with dead or phantom atoms yield, within numerical accuracy, the same conductivity, which confirms the results obtained by Lukes et al. [25]. The thermal conductivity is

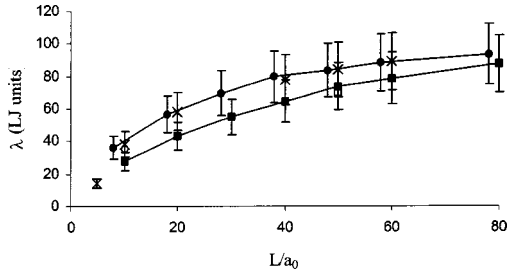

Fig. 5 Thermal conductivity in LJ units as a function of the system size. Line with squares: periodic boundary conditions. Empty square: result for another thermostat dimension. Line with circles: free surfaces with dead atoms. Stars: free surfaces with phantom atoms. Empty circle: result for a system with really free surfaces.

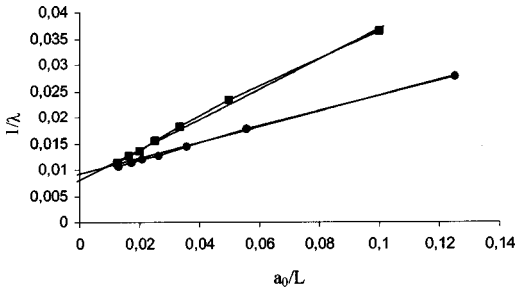

Fig. 6 Inverse of thermal conductivity as a function of the inverse of the system size. The extrapolation of the regression line to an infinite system size gives the bulk thermal conductivity.

smaller for the periodic boundary conditions than for free surfaces. The difference is systematic, but remains in the uncertainty domain.

For free surfaces and periodic boundary conditions, the thermal conductivity exhibits a strong dependence on the system size. This variation can be explained by the increase of the number of modes when the system size increases. This ''mode counting'' effect is in principle similar for periodic boundary conditions and systems with free boundaries. The other explanation of the size influence on the thermal conductivity is the possible increase of the phonon mean free path when the system size increases. For small systems, if the phonon mean free path due to phonon scattering is larger than the system size then phonons will be more frequently scattered. This is quite obvious for systems with free surfaces, but for systems with periodic boundary conditions, this effect has not been clearly pointed out [33–35]. As the thermal conductivity is smaller for periodic boundary conditions, this would mean that periodic boundary conditions result in stronger phonon scattering than free surfaces. This point will be discussed in section 3.3.

Plotting the inverse of the thermal conductivity as a function of the inverse of the system size results in a nearly linear relationship, both for free and periodic boundary conditions. This linear behavior can be predicted from the analytical analysis in part 3.2. The bulk thermal conductivity is obtained from the extrapolation of the regression line to system of infinite length (Fig. 6). The difference between the two asymptotic values is less than ten percent. Using the potential parameter of Argon ($\varepsilon/k_b=120$ K, $\sigma=0.34$ nm) the bulk thermal conductivity is found to be equal to 1.4 ± 25 percent W/(mK) at 25 K, which is in good agreement with the value found in the literature (1.2 W/mK at 30 K increasing when the temperature decreases) [36]. The minimum cube size that would be required to obtain the bulk thermal conductivity with an accuracy better than 3 percent is determined using the extrapolation curve: it is equal to $1170a_0$ for a system with periodic boundary conditions and $590a_0$ for a system with free surfaces. These systems are much too large (more than 10^9 atoms) to be considered for MD, which justify the use of smaller systems and the extrapolation procedure.

3 Simple Models for the Size Dependence of the Thermal Conductivity

3.1 Analytical Expression of the Thermal Conductivity In a system of volume V at temperature T, the number of phonons with wave vector K and polarization p is given by the Planck distribution function [37,38]

$$\langle n_{K,p}\rangle = \frac{1}{(e^x-1)} \tag{3}$$

with $x=\hbar\omega(K,p)/k_bT$ and where $\omega(K,p)$ is given by the dispersion curve.

The internal energy of the phonons (K,p) per unit volume is the product of the number of phonons and their individual energy [37,38]:

$$U(K,p)=\frac{\hbar\omega(K,p)}{V(e^x-1)} \tag{4}$$

which leads to its volume specific heat

$$C(K,p)=\frac{\partial U(K,p)}{\partial T}=k_bx^2\frac{e^x}{V(e^x-1)^2} \tag{5}$$

The total volume specific heat is then equal to the sum over all the wave vectors and polarizations

$$C=\sum_p\sum_K k_bx^2\frac{e^x}{V(e^x-1)^2} \tag{6}$$

If ω were constant then the expression for the volume specific heat would be the same as the one given by the Einstein model. Using elementary kinetic theory, the thermal conductivity in a direction x associated with the phonons (K,p) can be written as [37,38]

$$\lambda_x(K,p)=C(K,p)v^2(K,p)\tau(K,p)\cos^2(\theta_x(K)) \tag{7}$$

with v the group velocity of the phonons (K,p):

$$v(K,p)=d\omega/dK \tag{8}$$

and $\tau(K,p)$ the phonon relaxation time.

The total thermal conductivity is then the sum of the individual conductivities for all the wave vectors and polarizations:

$$\lambda_x=\sum_K\sum_p \lambda_x(K,p)$$

$$=\sum_K\sum_p C(K,p)v^2(K,p)\tau(K,p)\cos^2(\theta_x(K)) \tag{9}$$

If the material is isotropic, and if the group velocity and the relaxation time are assumed to be constant, the classical expression for the thermal conductivity for an infinite system is obtained

$$\lambda=\frac{1}{3}v^2\tau\sum_K\sum_p C(K,p)=\frac{1}{3}Cv^2\tau \tag{10}$$

The thermal conductivity is constant and does not depend on the system dimension. So, to illustrate the influence of the system size on the thermal conductivity, it is necessary to take into account the actual variation of the group velocity and the relaxation time with the wave vector.

If the system is isotropic and its size infinite, the sum in (9) becomes an integral, which is most conveniently re-expressed using a change of variables from wavevector K to angular velocity ω (through the dispersion curve and density of states). The result for λ reads

$$\lambda=\frac{\hbar^2}{3k_bT^2V_{\mathrm{mol}}}\int_0^{\omega_R} v(\omega)^2\tau(\omega)D(\omega)\frac{\omega^2e^{\hbar\omega/k_bT}}{(e^{\hbar\omega/k_bT}-1)^2}d\omega \tag{11}$$

This expression has been used by Rosenblum et al. [33] for example, with the assumption of constant group velocity, to compute thermal conductivities of diamond crystals. It was named the ''Phonon Spectrum'' (PS) method since it requires the knowledge of the density of states, $D(\omega)$, which can be determined previously from equilibrium MD. For a perfect crystal, a general expression representing the phenomenological variation of the relaxation time is used

$$\tau^{-1}(\omega)=\tau_U^{-1}(\omega)+\tau_{BC}^{-1}(\omega) \tag{12}$$

with the relaxation time due to the Umklapp processes [38,39]

$$\tau_U^{-1}(\omega) = A\omega^2 T^{\xi} \exp(-B/T) \tag{13}$$

and the relaxation time due to the presence of the system boundaries

$$\tau_{BC}^{-1}(\omega) = v/(\alpha\Lambda) \tag{14}$$

An other empirical formula [40] was proposed for τ_{BC}

$$\tau_{BC}^{-1}(\omega) = v^*(1-s)/\Lambda \tag{15}$$

where s represents the fraction of all phonon specularly scattered from the boundary surfaces ($s \in [0-1]$). Here Λ is the distance traveled between two scattering events by the boundaries.

Rosenblum et al. [33] assume Λ to be constant and equal to the characteristic length of the system. *A*, *B*, ξ, α are identified in order to fit the calculated thermal conductivity to an experimental value. The *PS* method allows the prediction of the thermal conductivity of an infinite medium (*L* infinite leads to $\tau_{BC}^{-1}(\omega) = 0$), or of a finite object with characteristic length *L* in the three directions of space from the knowledge of the density of state and a few experimental values. As shown in the previous section, the density of states can be calculated from simple molecular dynamics simulation at equilibrium. This method requires much less CPU time than NEMD and the results do not depend on the way heat transfer is simulated. However, the continuous integral over the angular frequency range implies the following:

1. The phonon properties do not depend on the wave vector direction. Since Λ is assumed constant for all wave vectors, it is then not possible to study the size effects in nanowires or nanofilms. For such structures, Λ is a function of the wave vector direction and can be considered infinite in one or two directions.
2. The number of modes is infinite. The number of modes is equal to $3N-3$ where *N* is the number of atoms in the system. If the system size is small, the sums in Eq. (6) can not be accurately transformed into a continuous integral.

To calculate the thermal conductivity of small systems, it seems therefore preferable to use Eq. (8) which contains more information on the wave vector: the number of modes, the group velocity, the relaxation time, the angular properties and their variation with the wave vector direction. This should in principle allow for proper inclusion of size and geometry effects, both in the mode counting and in the scattering. This method will be described in the following as the Wave Vectors (WV) method.

3.2 Vibrational Properties of Argon. The thermal conductivity has been calculated with the *WV* method (Eq. (8)) for a cube made of solid argon in order to compare the *WV* model results to the NEMD results for periodic boundary conditions and fixed boundary surfaces. For the periodic boundary conditions, two other geometries are studied: a nanofilm and a nanowire. To implement Eq. (8), vibrational properties of argon must be known.

Solid argon has an fcc structure which unit cell is described by the three primitive vectors: $a_1(0,a_0/2,a_0/2)$, $a_2(a_0/2,0,a_0/2)$ and $a_3(a_0/2,a_0/2,0)$ where a_0 is the lattice parameter of the conventional FCC cell. For a FCC crystal of dimension $(N_x a_0, N_y a_0, N_z a_0)$ in the *x*, *y*, and *z*-directions, with periodic boundary conditions in the three directions, the wave vectors describing the crystal vibrations are linear combination of

$$K_x = 2n_x\pi/(N_x a_0) \quad \text{with} \quad n_x \in]-N_x, N_x] \tag{16}$$

$$K_y = 2n_y\pi/(N_y a_0) \quad \text{with} \quad n_y \in]-N_y, N_y] \tag{17}$$

$$K_z = 2n_z\pi/(N_z a_0) \quad \text{with} \quad n_z \in]-N_z, N_z] \tag{18}$$

and

$$-3\pi/a_0 < K_x + K_y + K_z \leqslant 3\pi/a_0 \tag{19}$$

$$-3\pi/a_0 < K_x - K_y + K_z \leqslant 3\pi/a_0 \tag{20}$$

$$-3\pi/a_0 < K_x + K_y - K_z \leqslant 3\pi/a_0 \tag{21}$$

$$-3\pi/a_0 < -K_x + K_y + K_z \leqslant 3\pi/a_0 \tag{22}$$

(the wave vector are in a cube).

(These later conditions allow the truncation of the cube on its eight corners).

Equations (19)–(21) and the conditions on n_x, n_y, n_z (Eqs. (15–17)) allow the wave vectors to belong to the first Brillouin zone of an FCC structure, which is a cube truncated on its eight corner in the reciprocal space [37]. The number of wave vectors is equal to $4N_xN_yN_z$ which is the number of atoms. To simulate a cube, $N_x = N_y = N_z$, for a nanofilm: N_x is finite and N_y and N_z tend to and infinite value. For a nanowire: $N_x = N_y$ and N_z tends to an infinite value.

If the same crystal now have fixed boundary surfaces, the wave vectors describing the crystal vibrations are linear combination of

$$K_x = p_x\pi/(Na_0) \quad \text{with} \quad n_x \in [1,2(N_x-2)] \tag{23}$$

$$K_y = p_y\pi/(Na_0) \quad \text{with} \quad n_y \in [1,2(N_y-2)] \tag{24}$$

$$K_z = p_z\pi/(Na_0) \quad \text{with} \quad n_z \in [1,2(N_z-2)] \tag{25}$$

and

$$K_x + K_y + K_z < 3\pi/a_0 \tag{26}$$

The number of wave vectors is still equal the number of atoms: $4N^3$. But for fix boundary conditions the wave vectors are confined in 1/8 of the Brillouin zone of the FCC structure due to Eq. (26) and the conditions on n_x, n_y, n_z (Eqs. (23)–(25)). We choose to calculate the thermal conductivity of the cube with fixed boundary surfaces and with periodic boundary conditions, so that $N_x = N_y = N_z = N$. For fixed boundary condition, the real cube size that must be considered is equal to $(N-2)a_0$ in order to take into account the external layer of atoms that are fixed.

The dispersion curves of Argon should be known in order to calculate the angular and the group velocities for each wave vector. Assuming an harmonic crystal, there are one longitudinal mode (ω_l) and two degenerate transverse modes (ω_t) for each wave vector direction, which can be modeled as

$$\omega_t(K) = \omega_{Mt} \sin\left(\frac{\pi}{2}\frac{K}{K_M}\right) \tag{27}$$

$$\omega_l(K) = \omega_{Ml} \sin\left(\frac{\pi}{2}\frac{K}{K_M}\right) \tag{28}$$

The associated group velocities are given by the first derivative of the dispersion relations (Eq. (8))

$$V_t(K) = V_{Mt} \cos\left(\frac{\pi}{2}\frac{K}{K_M}\right) \tag{29}$$

$$V_l(K) = V_{Ml} \cos\left(\frac{\pi}{2}\frac{K}{K_M}\right) \tag{30}$$

For simplicity, it is also assumed that the dispersion curves are isotropic, with K_M the maximum wave vector length in the first Brillouin zone. Considering the data for Argon in the literature [37,41], the maximum angular and group velocities are equal to

$\omega_{Ml} = 1.35\ \ 10^{13}$ rad/s and

$v_{Ml} = 1800$ m/s for the longitudinal mode and

$\omega_{Mt} = 0.6^* \omega_{Ml}$ and

$v_{Mt} = 0.6^* v_{Ml}$ for the two transverse modes

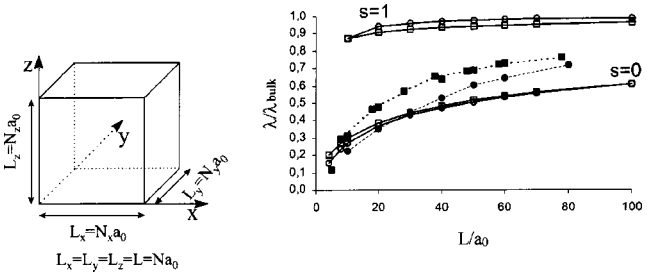

Fig. 7 Normalized thermal conductivity of a cube as a function of its characteristic length. Comparison between the WV model (full lines) with NEMD (dashed lines) for periodic boundary conditions (lines with squares) and fixed boundary surfaces (lines with circles).

Using Eqs. (12), (13), and (15), the relaxation time can be written as

$$\tau^{-1}(K)=A\omega^2(K)T^{\xi}\exp(-B/T)+v(K)*(1-s)/\Lambda(K) \tag{31}$$

For a cube, $\Lambda(K)$ is equal to the characteristic length of the cube. But, for the wire and the film, $\Lambda(K)$ is defined as the maximum length a wave can travel in the system between two boundaries. It is then calculated for each wave vector direction. At a given temperature, the value of $AT^{\xi}\exp(-B/T)$ is determined so that the asymptotic value of the thermal conductivity calculated with the WV model for an infinite length is equal to the experimental thermal conductivity of Argon ($\lambda_{bulk}=1.4$ W/(mK) at 25 K). All the results are normalized by this bulk value.

3.3 Results for Nano-Particles. The thermal conductivity is calculated for a cube of Argon at 25 K for the two limiting values of the scattering parameter: $s=1$ and $s=0$ (Fig. 7). For symmetry reasons, the thermal conductivity is isotropic. The direction is then not specified.

For $s=1$: only specular reflections occur at the boundaries. For this value of s, the relaxation time is not govern by the presence of the boundary conditions (Eq. (31)). This condition is used to study the influence of the number of wave vectors on the thermal conductivity, independently of the system geometry. This is of course an artificial construction, which cannot be directly compared to MD simulations. The thermal conductivity of this cube made of an FCC solid argon is smaller than $0.97*\lambda_{bulk}$ for a dimension less than $50a_0$ for the periodic boundary conditions and $120a_0$ for the fixed boundary surfaces. Above these dimensions, mode counting effects can reasonably be neglected. The thermal conductivity of the system with free surfaces is smaller than the one of the periodic system: for periodic boundary conditions, the first Brillouin zone is uniformly sampled while, for fixed boundary surfaces, wave vectors are not allowed on the limit of the first Brillouin zone.

For $s=0$: phonons are diffusely scattered at the system boundaries. The relaxation time is then influence by the system size (Eq. (31)) through the value of Λ(K). The smaller the system size, the smaller the relaxation time. This leads to a smaller thermal conductivity than in the bulk value. Assuming that $\Lambda(K)$ is equal to the characteristic system size L, assuming a constant relaxation time τ_u due to the phonon-phonon scattering process, a constant group velocity v and an isotropic system, then substituting $\tau(K)$ by its expression (Eq. (31)) in Eq. (9) gives

$$\lambda=\frac{1}{3}Cv^2/(\tau_u^{-1}+v*(1-s)/L) \tag{32}$$

which shows that the inverse of the thermal conductivity should, at first order, depend linearly on the inverse of the system size. This dependence has been recovered from the MD simulation results (Fig. 6).

The normalized values of the thermal conductivity obtained from NEMD simulations has also been plotted on Fig. 7 to be compared with the analytical results. It is clear that for $s=1$, the analytical model does not allow to recover the NEMD simulation results. For $s=0$, there is a good qualitative agreement between the analytical and NEMD results. The relative variations are of the same order of magnitude and the thermal conductivity of the cube with fixed boundary condition is greater than the one of the cube with periodic boundary conditions. This result is quite surprising since, as s is interpreted as the fraction of the phonon specularly scattered at the boundaries, it means that for periodic boundary conditions, phonons are diffusively scattered at the boundary surfaces. This is an unexpected conclusion since with periodic boundary conditions, wave modes should remain coherent. This point certainly need further discussion.

Quantitatively the variation of the thermal conductivity due to the boundary conditions is much larger with NEMD than with the WV model, and the asymptotic value is reached for smaller system sizes with NEMD than with the WV model. These differences can easily be explained by the following assumptions, made in the WV model, and which may in fact not be valid: (1) vibration modes are plane waves, (2) the system is harmonic, and (3) the phonon properties do not depend on the wave vector direction. Note also that we have used the same value of the scattering parameter s for the two situations. By adjusting the value of s to an intermediate value, it would of course be possible to increase, in the *WV* model, the difference between fixed and periodic boundary conditions, so that the *WV* results would be qualitatively closer to the NEMD results.

Another important difference between *MD* and *WV* model lies in the specific heat. In molecular dynamics simulations, the energy of each vibration mode is equal to k_bT. This leads to a constant specific heat, k_b, for all the vibration modes. Actually, as phonons follow the Planck distribution function, the specific heat depends on the wave vector and the temperature (Eq. (3)). This effect can never be taken into account in classical *MD* simulations. Using the *WV* model and assuming a constant specific heat for all wave vectors, it is clear that the equipartition of energy in *MD* simulations leads to an overestimation of the thermal conductivity; we have checked, however, that the relative variations with system size are similar if the classical formula, rather than the correct Planck distribution, is used for the specific heat. This is reasonable, since finite size effects are dominated by long wavelength phonons, for which the classical formula is most accurate. Moreover, at high temperature, the phonon specific heat (Eq. (3)) tends to k_b, so that the error in *MD* simulations due to this classical treatment of lattice vibrations will decrease.

3.4 Results for Nano-Films and a Nano-Wires. As the *WV* model qualitatively reproduces the size dependence of the thermal conductivity of a nanoparticle, we have extended it to study the size dependence of the thermal conductivity of nanofilms and nanowires. Only periodic boundary conditions are considered since the difference with fixed boundary surfaces is small. The scattering parameter s is equal to zero. Films and wires actually have two characteristic lengths:

1. The thickness e and the characteristic dimension L in the (y,z) plane for the nanofilm (Fig. 8(a)).
2. The characteristic length 1 of the wire section (in the (x,y) plane) and the length L of the nanowire in the z-direction (Fig. 9(a)).

If the thickness of the film and the section of the wire were large toward the interatomic distance and the phonon mean free path due to the Umklapp process, then the systems could be considered isotropic as for macroscopic material. However, as long as we are concerned by nanowires and nanofilms, the thermal conductivity does not remain isotropic. For symmetry reason, the thermal conductivities, λ_x and λ_y, in the x and y-directions are identical and might differ from the thermal conductivity λ_z in the

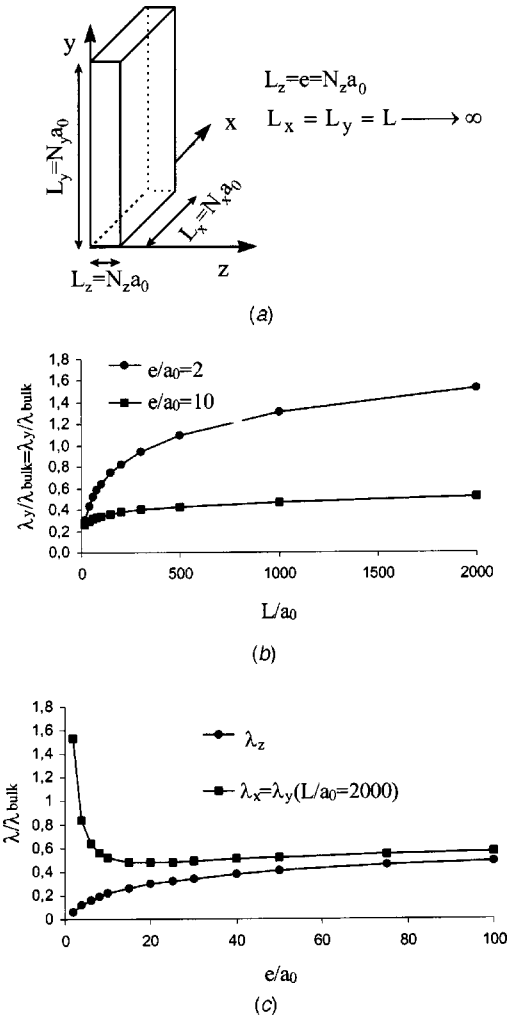

Fig. 8 Normalized thermal conductivity of a film (a), as a function of L for two thicknesses (b), and as a function of its thickness for $L=2000a_0$ (c)

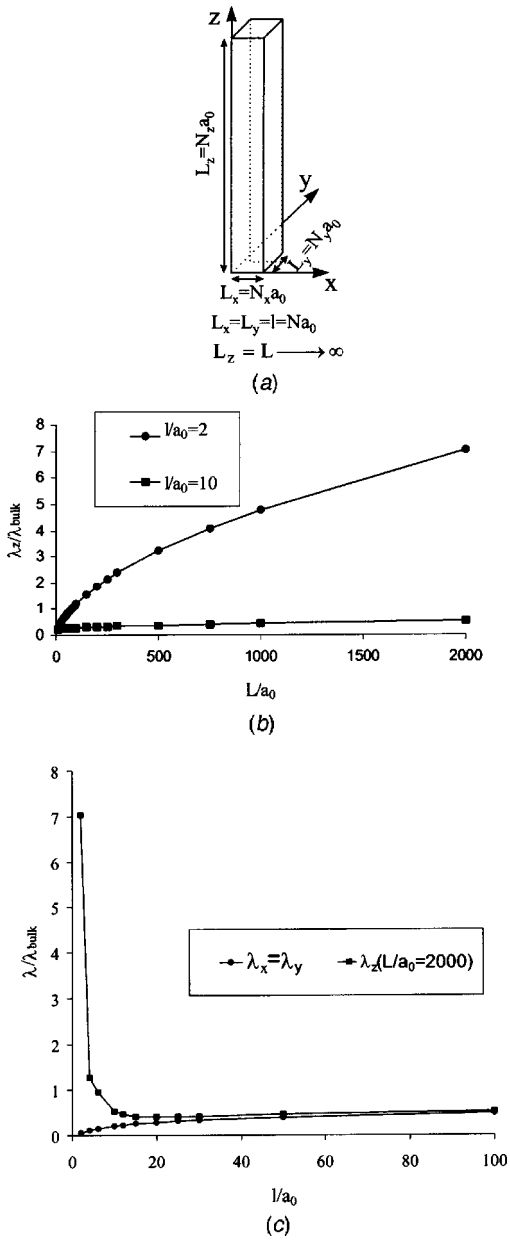

Fig. 9 Normalized thermal conductivity of a wire (a), as a function of L for two values of 1 (b), and as a function of 1 for $L=2000a_0$ (c)

z-direction. The thermal conductivities in the directions parallel to the larger dimension $\lambda_x(e,L)=\lambda_y(e,L)$ for the film and $\lambda_z(1,L)$ for the wire are calculated within the *WV* model for increasing values of L (Figs. 8(b) and 9(b)). On these figures, the thermal conductivity appears to diverge for large values of L, at fixed e and 1. The divergence becomes evident when e and l decrease. Such a divergence is typical of low dimensional systems [42], and results from the particular role of the wave vectors that are parallel to the longer dimension (i.e., those with $k_z=0$ in the film, with $k_x=k_y=0$ in the wire). For these wavevectors, boundary scattering is absent, and the sum over (k_x,k_y) (film) or k_z (wire) yields a divergent integral in the limit of large L. In practical cases, this divergence (which, in our model, is actually slightly overestimated [30]) will be cutoff either by the device dimension or by a typical distance between defects in the larger dimension.

For a value of $L=2000a_0$ (arbitrarily value corresponding to a typical device size of 1 micrometer), the thermal conductivities $\lambda_x(e,L)=\lambda_y(e,L)$ for the film and $\lambda_z(1,L)$ for the wire have been plotted as a function of e and l (Figs. 8(c) and 9(c)). For the same characteristic length (l and e), the thermal conductivity of the film is larger than the thermal conductivity of the wire. This is expected, since boundary scattering is stronger in wires. An interesting feature is the non-monotonic behavior with the lateral characteristic size. As e or l decrease, the conductivity first decreases as the scattering by boundaries becomes more efficient, but eventually increases again at small thickness, when the low dimensional character and the associated divergence prevail. This nonmonotonic behavior illustrates the difficulties encountered in extrapolating data obtained over a limited range of sizes in the range of nanometric scales.

The thermal conductivity in the direction perpendicular to the film surface, $\lambda_z(e,L)$, does not depend on the size of the film but strongly depends on it thickness (Fig. 8(c)). Due to the boundary scattering, $\lambda_z(e,L)$ is smaller than the in-plane thermal conductivity of the film. As the film thickness increase, the thermal conductivity becomes isotropic.

Similarly, for the wire, the thermal conductivity in the section plan $\lambda_x(1,L)=\lambda_y(1,L)$ does not depend on the wire length, but on the section size. Its value is smaller than the thermal conductivity in the z-direction. We also see that as the section size increase, the thermal conductivity becomes isotropic.

4 Conclusion

NEMD is one of the possible tools for determining the thermal conductivity of a material on an atomic scale. Even if NEMD is

widely used, its reliability has sometimes been questioned. In this paper, the influence of the thermal reservoir, the boundary conditions and the system size on the thermal conductivity is studied by use of NEMD simulations of an fcc structure and a Lennard-Jones potential.

It has been shown that, when the thermal reservoirs are thermostatted with a systematic velocity rescaling, the density of state remains the same as the one obtained for an equilibrium system. Moreover, the temperature gradient between the thermostats is linear and the local velocity distribution function is nearly the Maxwell distribution function (the difference are smaller than 2 percent. Thus, it is believed that the local thermal equilibrium is achieved everywhere in the system. The thermal conductivity can then be calculated from the temperature gradient and heat flux.

An analytical model of the thermal conductivity is developed in order to give qualitative explanations of the thermal conductivity variations with the system size. In this model, the total thermal conductivity is considered as the sum of the individual thermal conductivity of all the phonon modes. This is the Wave Vector method. The phonon properties required are determined from the literature data for Argon, in order to compare the WV model results to NEMD results. All the wave vectors should be characterized but, for simplicity, the thermal conductivity has been calculated assuming that phonon properties are the same for all the wave vector directions.

The system size dependence of the thermal conductivity is confirmed with our NEMD results. The bulk thermal conductivity can be recovered from the extrapolation of the simulation results for finite systems towards an infinite system size. Qualitatively, the analytical model shows that the size dependence of the thermal conductivity is due to the discretisation of the wave vectors for small systems and the influence of the phonon scattering the boundary surfaces.

Due to the surface scattering, the size dependence of the thermal conductivity is expected for the system with free surfaces. Moreover, it is shown that the thermal conductivity does not depend on the way free surfaces are modeled: hard wall, phantom atoms and really free surfaces. For the system with periodic boundary conditions, the thermal conductivity also exhibits a size dependence and values smaller than those obtained for the system with free surfaces.

The wave vector model was used to study the size dependence of the thermal conductivity of a nanofilm and a nanowire. For thin films and wires, the thermal conductivity is strongly anisotropic. The thermal conductivity is larger in the direction parallel to the longer length. As the film thickness or the section typical length of the wire decrease, the thermal conductivity decreases as expected. However, for small enough film thickness or wire section (typically less than 20 lattice parameters for solid argon) the thermal conductivity increases and can become larger than the bulk thermal conductivity. This is due to the vibrational behavior of the film and wire which then resembles the one of a two-dimensional and one-dimensional system, respectively, for which the thermal conductivity diverges with the system length.

Acknowledgment

This work was supported by the CINES (CNRS) and the CDCSP (Univ. Lyon 1) for computer facilities.

Nomenclature

a_0 = lattice parameter (m)
C = volume specific heat ($J \cdot K^{-1} \cdot m^{-3}$)
D = density of states
e = film thickness (m)
h = Planck constant (J·s) ($\hbar = h/2\pi$)
k_b = Boltzmann constant ($J \cdot K^{-1}$)
K = wave vector (m^{-1})
l = section characteristic length (m)
L = largest dimension of a cube, a wire and film (m)
m = mass (kg)
n = indice for the mode counting
N = number of unit cell
p = indice for polarization
t = time (s)
T = temperature (K)
v = sound velocity ($m \cdot s^{-1}$)
V = volume (m^3)
Δt = time step (s)
ε = minimum energy of the Lennard Jones potential (J)
λ = thermal conductivity ($W \cdot m^{-1} \cdot K^{-1}$)
Λ = wave vector largest path in a system (m)
ω = angular frequency (s^{-1})
σ = zero energy distance of the Lennard Jones potential (m)
τ = relaxation time (s)
θ = angle (rad)

Subscript

x, y, z = direction
l = longitudinal
t = transverse

References

[1] Cahill, D. G., Goodson, K., and Majumdar, A., 2002, "Thermometry and Thermal Transport in Micro/Nanoscale Solid State Devices," ASME J. Heat Transfer, **124**(2), pp. 223–241.
[2] Chen, G., and Shakouri, A., 2002, "Heat Transfer in Nanostructures for Solid State Energy Conversion," ASME J. Heat Transfer, **124**(2), pp. 242–252.
[3] Kulish, V. V., Lage, J. L., Komorov, P. L., and Raad, P. E., 2001, "A Fractional-Diffusion Theory for Calculating Thermal Properties of Thin Films From Surface Transient Thermoreflectance Measurements," ASME J. Heat Transfer, **123**(6), pp. 1133–1138.
[4] Mazumber, S., and Majumdar, A., 2001, "Monte Carlo Study of Phonon Transport in Solid Thin Films Including Dispersion and Polarization," ASME J. Heat Transfer, **123**(4), pp. 749–759.
[5] Zeng, T., and Chen, G., 2001, "Phonon Heat Conduction in Thin Films: Impact of Thermal Boundary Resistance and Internal Heat Generation," ASME J. Heat Transfer, **123**(2), pp. 340–347.
[6] Wang, X., Hu, H., and Xu, X., 2001, "Photo-Acoustic Measurement of Thermal Conductivity of Thin Films and Bulk Materials," ASME J. Heat Transfer, **123**(1), pp. 138–144.
[7] Li, B., Pottier, L., Roger, J. P., Fournier, D., Watari, K., and Hirao, K., 1999, "Measuring the Anisotropic Thermal Diffusivity of Silicon Nitride Grains by Thermoreflectance Microscopy," J. Eur. Ceram. Soc., **19**, p. 1631.
[8] Gomes, S., Trannoy, N., Grossel, Ph., Depasse, F., Bainier, C., and Charraut, D., 2001, "Scanning Thermal Microscopy: Characterization and Interpretation of the Measurement," Int. J. Thermophys., **40**, pp. 949–958.
[9] Hmina, N., and Scudeller, Y., 1998, "Thermal Interface Resistance and Subsurface Effusivity of Submicron Metallic Films on Dielectric Substrates: An Experimental Method for Simultaneous Determination," Int. J. Heat Mass Transfer, **41**(18), pp. 2781–2798.
[10] Bincheng, L., Potier, L., Roger, J. P., and Fournier, D., 1999, "Thermal Characterization of Thin Superconducting Films by Modulated Thermoreflectance Microscopy," Thin Solid Films, **352**(1–2), pp. 91–96.
[11] Maruyama, S., 2002, "A Molecular Dynamics Simulation of the Heat Conduction in Finite Length SWNTs," Physica B, **323**, pp. 193–195.
[12] Berbert, S., Kwon, Y. K., and Tomanek, D., 2000, "Unusually High Thermal Conductivity of Carbon Nanotubes," Phys. Rev. Lett., **84**(25), pp. 4613–4616.
[13] Jund, P., and Jullien, R., 1999, "Molecular-Dynamics Calculation of the Thermal Conductivity of Vitreous Silica," Phys. Rev. B, **59**(21), pp. 13707–13711.
[14] Daly, B. C., and Maris, H. J., 2002, "Calculation of the Thermal Conductivity of Superlattices by Molecular Dynamics Simulations," Physica B, **316–317**, pp. 247–249.
[15] Allen, M. P., and Tildesley, D. J., 1987, *Computer Simulation of Liquid*, Oxford University Press Inc., New York.
[16] Frenkel, D., and Smit, B., 1996, *Understanding Molecular Simulation*, Academic Press, San Diego.
[17] Kubo, R., Toda, M., and Hashitsume, N., 1985, *Statistical Physics II*, Springer, Berlin.
[18] Barrat, J. L., and Chiaruttini, F., 2003, "Kapitza Resistance at the Liquid Solid Interface," Mol. Phys., **101**, p. 1605.
[19] Evans, D. J., and Morris, G. P., 1990, *Statistical Mechanics of Nonequilibrium Liquids*, Academic Press, New York.
[20] Baranyai, A., 1996, "Heat Flow Studies for Large Temperature Gradients by Molecular Dynamics Simulations," Phys. Rev. E, **54**(6), pp. 6911–6917.
[21] Hansen, D. P., and Evans, D. J., 1994, "A Generalized Heat Flow Algorithm," Mol. Phys., **81**(4), pp. 767–779.
[22] Maiti, A., Mahan, G. D., and Pantelides, S. T., 1997, "Dynamical Simulations

of Nonequilibrium Processes—Heat Flow and the Kapitza Resistance Across Grain Boundaries,'' Solid State Commun., **102**(7), pp. 517–521.
[23] Zheng, Q., Su, G., Wang, J., and Guo, H., 2002, ''Thermal Conductance for Single Wall Carbon Nanotubes,'' Eur. Phys. J. B, **25**, pp. 233–238.
[24] Plimpton, S. J., 1995, J. Comput. Phys., **117**(1) code available at http://www.cs.sandia.gov/tech8reports/ssjplimp.
[25] Lukes, J. R., Li, D. Y., Liang, X. G., and Tien, C. L., 2000, ''Molecular Dynamics Study of Solid Thin Film Thermal Conductivity,'' ASME J. Heat Transfer, **122**, p. 536.
[26] Müller-Plathe, F., 1997, ''A Simple Non-Equilibrium Molecular Dynamics Method for Calculating the Thermal Conductivity,'' J. Chem. Phys., **106**(14), p. 6082.
[27] Ikeshoji, T., and Hafskjold, B., 1994, ''Non-Equilibrium Molecular Dynamics Calculation of Heat Conduction in Liquid and Through Liquid Gas Interface,'' Mol. Phys., **81**, pp. 251–261.
[28] Kotake, S., and Wakuri, S., 1994, ''Molecular Dynamics Study of Heat Conduction in Solid Materials,'' JSME Int. J., Ser. B, **37**(1), pp. 103–108.
[29] Olischlger, C., and Schön, J. C., 1999, ''Simulation of Thermal Conductivity and Heat Transport in Solids,'' Phys. Rev. B, **59**(6), pp. 4125–4133.
[30] Chantrenne, P., and Barrat, J. L., 2004, ''Analytical Model for the Determination of Thermal Conductivity in Nanostructures,'' Superlattices Microstruct., to be published.
[31] Chapman, S., and Cowling, T. G., 1970, *The Mathematical Theory of Non-Uniform Gases: An Account of the Kinetic Theory of Viscosity, Thermal Conduction and Diffusion in Gases*, third ed., Cambridge University Press.
[32] Fujita, S., 1996, *Statistical and Thermal Physics*, Part I, R. E. Krieger Publishing Company, Malabar, FL.
[33] Rosenblum, I., Adler, J., and Brandon, S., 1998, ''Calculation of Thermal Properties of Diamond From Simulated Phonon Spectra,'' Comput. Mater. Sci., **12**, pp. 9–25.
[34] Che, J., Çagin, T., and Goddard, W. A., 2000, ''Thermal Conductivity of Carbon Nanotubes, Nanotechnology,'' Nanotechnology, **11**, pp. 65–69.
[35] Volz, S., and Chen, G., 1999, ''Lattice Dynamic Simulation of Silicon Thermal Conductivity,'' Physica B, **263–264**, pp. 709–712.
[36] Motoyama, S., Ichikawa, Y., Hiwatari, Y., and Oe, A., 1999, ''Thermal Conductivity of Uranium Dioxide by Nonequilibrium Molecular Dynamics Simulation,'' Phys. Rev. B, **60**(1), pp. 292–298.
[37] Kittel, C., 1996, *Introduction to Solid State Physics*, Wiley, New York.
[38] Ashcroft, N. W., and Mermin, N. D., 1976, ''*Solid State Physics*,'' Harcourt College Publishers, Fort Worth, TX.
[39] Chaikin, P. M., and Lubensky, T. C., 1995, *Principle of Condensed Matter Physics*, Cambridge Press University.
[40] Zou, J., and Balandin, A., 2001, ''Phonon Heat Conduction in a Semiconductor Nanowire,'' J. Appl. Phys., **89**(5), pp. 2932–2938.
[41] Quesnel, D. J., Rimai, D. S., and DeMejo, L. P., 1993, ''Elastic Compliances and Stiffnesses of the FCC Lennard-Jones Solid,'' Phys. Rev. B, **48**(10), pp. 6795–6807.
[42] Lepri, S., Livi, R., and Politi, A., 2003, ''Thermal Conduction in Classical Low-Dimensional Lattices,'' Phys. Rep., **377**, pp. 1–80.

A. Rubinov
Computational Mechanics Laboratory,
Faculty of Mechanical Engineering,
Technion—Israel Institute of Technology,
Haifa 32000, Israel

V. Erenburg

A. Yu. Gelfgat
e-mail: gelfgat@eng.tau.ac.il

E. Kit

School of Mechanical Engineering,
Tel-Aviv University,
Ramat Aviv 69978,
Israel

P. Z. Bar-Yoseph

A. Solan

Computational Mechanics Laboratory,
Faculty of Mechanical Engineering,
Technion—Israel Institute of Technology,
Haifa 32000, Israel

Three-Dimensional Instabilities of Natural Convection Flow in a Vertical Cylinder With Partially Heated Sidewall

The three-dimensional axisymmetry-breaking instability of an axisymmetric convective flow in a vertical cylinder with a partially heated sidewall is studied numerically. The central part of the sidewall is maintained at constant temperature, while its upper and lower parts are thermally insulated. The dependence of the critical Grashof number on the cylinder aspect ratio (A=height/radius) is obtained for a fixed value of the Prandtl number, $Pr=0.021$, and fixed length of the heated central region, equal to the cylinder radius. Three different modes of the most dangerous three-dimensional perturbations, which replace each other with the variation of the aspect ratio, are found. Comparison with experiment shows a good agreement at the aspect ratio $A=8$ and 12, while at $A=4$ a significant disagreement is observed. Possible reasons for this disagreement are discussed. At $A=4$, the dependence of the critical Grashof number on the Prandtl number is studied in the range $0<Pr<0.05$, to rule out the possibility that the disagreement is due to uncertainty in values of fluid properties. The similarities and differences of instabilities in the cylindrical and rectangular geometries are examined. The computations are carried out using two independent numerical approaches, which cross-validate each other.
[DOI: 10.1115/1.1773588]

Keywords: Convection in Cylinder, Heat Transfer, Numerical Methods, Stability

Introduction

Axisymmetry-breaking bifurcations of axisymmetric convective flows have been extensively studied mainly in connection with convective instabilities in various crystal growth devices [1–3]. Since the early experiments of Hurle [4] it is known that convective instabilities resulting in supercritical oscillatory flows lead to an undesirable lattice structure of a growing crystal (additional examples can be found in [1,2]). Thus, the numerous and continuing attempts to produce high-quality crystals aboard a spacecraft [5] are mainly motivated by the possibility to avoid instabilities of buoyancy convection in the microgravity environment. Both ground-based and microgravity crystal growth technologies need tools for the investigation and control of stability. Numerical modeling can be used for parametric studies, which may be impossible or unaffordable in laboratory experiments. Such numerical results must be validated. This is done by comparison either with experiments which are rare or with independent numerical results. In the present paper we perform a parametric three-dimensional stability analysis by two independent numerical approaches and compare our results with previously published experimental data [6]. We show how the stability properties of the flow change with the governing parameters, and discuss physical mechanisms responsible for the instability onset and possible reasons of a certain disagreement with the experiment.

Studies of three-dimensional axisymmetry-breaking convective instabilities started from a relatively simple model of instability of a motionless conducting state in vertical cylinders heated from below (Rayleigh-Bénard configuration) [7–9]. However, from the practical point of view, the consideration of more complicated heating conditions, which result in a developed convective base flow state, is needed [10,11]. In this paper we focus our attention on conditions that are axisymmetric (which is usually the case in many crystal growth devices), but lead to the appearance of a finite amplitude convective flow at any nonzero temperature gradient applied. The numerical study of the stability of such flows requires special numerical methods [12–17], which include the calculation of an initial axisymmetric steady finite-amplitude convective flow and then the analysis of its stability with respect to all possible infinitesimal three-dimensional bifurcations. The study of the axisymmetry-breaking instabilities of finite-amplitude steady convective flows began with the analysis of secondary instabilities of finite-amplitude flows in the Rayleigh-Bénard configuration [7,18–20]. More complicated heating conditions were applied in [20–24]. Most of these studies approached the transition to three-dimensionality by unsteady nonlinear three-dimensional solvers, which lead to heavily CPU-time consuming calculations and do not allow a parametric investigation of the stability properties of the flow. A numerical method for a comprehensive three-dimensional stability analysis of convective flow under arbitrary axisymmetric heating conditions was proposed in [15,20] and was used for a parabolic temperature distribution on the cylindrical sidewall in [23].

Among many numerical studies of three-dimensional convective flows arising from various axisymmetric heating conditions [7–9,18–24], a comparison with experimental results is reported only in [17,18,20,21,24] and the agreement, as a rule, is only qualitative. It was shown that the stability properties of convective flows are strongly dependent on variations of geometry and the Prandtl number [25–27]. A similar stiff dependence on a variation of the heating conditions can also be expected. Therefore, to compare numerical and experimental results it is necessary to reproduce correctly the Prandtl number and the boundary conditions in a numerical model.

In the present paper we carry out a three-dimensional stability analysis, similar to that in [23], for a configuration of an experiment that was focused on the axisymmetry-breaking instability of an axisymmetric convective flow [6]. Natural convection in a ver-

Contributed by the Heat Transfer Division for publication in the JOURNAL OF HEAT TRANSFER. Manuscript received by the Heat Transfer Division July 1, 2003; revision received April 12, 2004. Associate Editor: P. S. Ayyaswamy.

tical cylinder, whose vertical wall is heated in the middle and is thermally insulated above and below the heated zone, is considered. The top and bottom are maintained at a constant "cold" temperature. This configuration is associated with floating zone crystal growth [6]. Following the experimental setup we fix the size of the heated zone to be equal to the cylinder radius and the Prandtl number to be 0.021 (the experimental liquid was gallium) and compute the dependence of the critical Grashof number on the aspect ratio of the cylinder. Together with this dependence we obtain the patterns of the most dangerous perturbation and in the case of oscillatory instability—the frequency of oscillations at the bifurcations points. Similarly, we fix the aspect ratio to be 4 (the reason for this choice is explained below) and calculate the dependence of the critical Grashof number on the Prandtl number.

Two independent numerical approaches are used to solve the problem. One is based on the global Galerkin method as described in [15]. It was successfully used in [20,23] for similar problems. The other, which is the main approach used here, is based on the second-order finite volume discretization and uses the Newton and Arnoldi iteration techniques to solve for the steady states and for the leading eigenvalues and eigenvectors, respectively. The results obtained by the two independent numerical approaches cross-validate each other over the whole interval $2 \leqslant A \leqslant 8$ considered, where $A =$ height/radius is the aspect ratio.

Our calculations show that at $\mathrm{Pr}=0.021$ there are three different three-dimensional perturbation modes, which replace each other when the aspect ratio is varied between 2 and 8. Comparison with the experimental results [6] is possible only for the aspect ratios equal to 4, 8, and 12. The comparison shows a very good agreement in the value of the critical Grashof number and the pattern of supercritical three-dimensional flow at $A=8$ and 12. A disagreement between the computations and the experiment is observed for $A=4$ and is attributed to the secondary instability of the three-dimensional flow that develops after the numerically predicted steady axisymmetry-breaking bifurcation.

The stability of convective flows in a two-dimensional rectangular cavity with similarly heated/insulated sidewalls was studied in [28,29], where among several bifurcations of different type we found multiple steady states. Here we discuss the similarities in the onset of instability in the two-dimensional rectangular cavity and in the cylindrical enclosure, as well as the possibility of the multiple states expected in the supercritical regimes.

Formulation of the Problem

The convective flow of a Boussinesq fluid in a vertical cylinder $0 \leqslant r \leqslant R$, $0 \leqslant z \leqslant H$ is considered (Fig. 1). All the boundaries are no-slip. The top and the bottom are maintained at a constant low temperature θ_{cold}. The central section of the cylindrical boundary in the interval $h_1 \leqslant y \leqslant h_2$ is maintained at a high temperature θ_{hot}. The remaining parts of the cylindrical boundary are thermally insulated.

To render the governing equations dimensionless, we introduce the scales R, R^2/ν, ν/R, $\rho(\nu/R)^2$ for length, time, velocity and pressure respectively, where ν is the kinematic viscosity and ρ is the density. The temperature is rescaled as $\theta \rightarrow (\theta-\theta_{\mathrm{cold}})/(\theta_{\mathrm{hot}}-\theta_{\mathrm{cold}})$. With the Boussinesq approximation, the Navier-Stokes and energy equations for the nondimensional velocity $\mathbf{v}=\{\mathrm{v_r},\mathrm{v}_\theta,\mathrm{v_z}\}$, temperature θ and pressure p in cylindrical coordinates (r,θ,z) read

$$\frac{\partial \mathbf{v}}{\partial t}+(\mathbf{v}\cdot\nabla)\mathbf{v}=-\nabla p+\Delta \mathbf{v}+\mathrm{Gr}\ \theta \mathbf{e}_z \tag{1}$$

$$\frac{\partial \theta}{\partial t}+(\mathbf{v}\cdot\nabla)\theta=\frac{1}{\mathrm{Pr}}\Delta\theta, \tag{2}$$

$$\nabla\cdot\mathbf{v}=0. \tag{3}$$

The boundary conditions are:

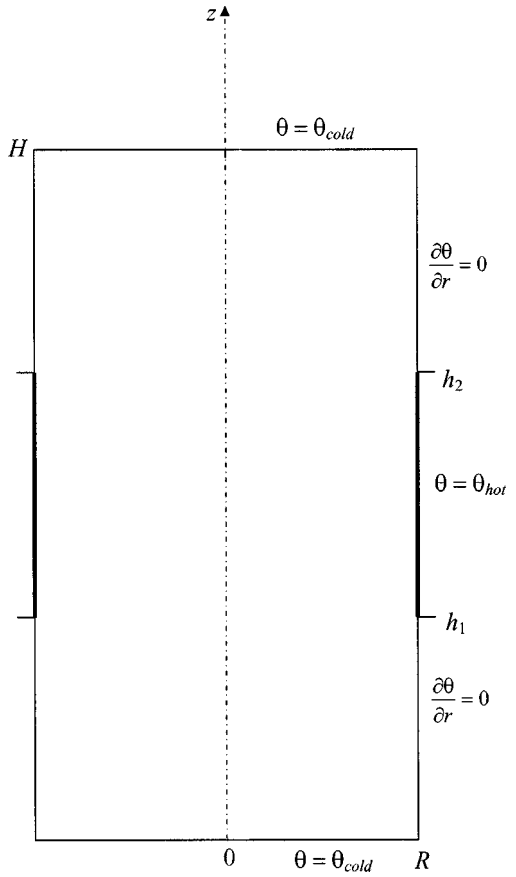

Fig. 1 Geometry of the problem

$$\mathbf{v}=\mathbf{0} \quad \text{on all the boundaries} \tag{4}$$

$$\theta=0 \quad \text{at } z=0,A \tag{5}$$

$$\theta=1 \quad \text{at } r=0; \quad a_1 \leqslant z \leqslant a_2 \tag{6}$$

$$\frac{\partial\theta}{\partial r}=0 \quad \text{at } r=0; \quad r=1 \quad \text{and} \quad z<a_1 \quad \text{or} \quad z>a_2 \tag{7}$$

Here $\mathrm{Gr}=g\beta(\theta_{\mathrm{hot}}-\theta_{\mathrm{cold}})R^3/\nu^2$ is the Grashof number, $\mathrm{Pr}=\nu/\chi$ the Prandtl number, $A=H/R$ the aspect ratio of the cylinder, $a_1=h_1/R$ and $a_2=h_2/R$ are the dimensionless borders of the heated region, g is the gravity acceleration, β the thermal expansion coefficient, χ the thermal diffusivity, and $\mathbf{e}_z$ the unit vector in the vertical direction. The study is focused on the steady solutions of (1)–(7) and their stability, therefore the initial conditions are not specified. Since our study is motivated by the experiments reported in [6], the values of Pr, a_1, and a_2 are not varied in the calculations and are chosen to be $\mathrm{Pr}=0.021$, $a_1=A/2-1/2$, $a_2=A/2+1/2$, that correspond to the experimental setup [6]. The parametric study is performed in the parameter space of the Grashof number and the aspect ratio. An additional study for a varying Prandtl number is performed for $A=4$.

Numerical Techniques

The problem was solved numerically using two independent approaches based on the global Galerkin and finite volume methods. Both approaches treat the three-dimensional solutions of (1)–(7) as Fourier expansions in the 2π-periodic azimuthal direction

$$\langle \mathbf{v},p,\theta\rangle=\sum_{k=-\infty}^{k=\infty}\langle \mathbf{v}_k(r,z,t),p_k(r,z,t),\theta_k(r,z,t)\rangle e^{ik\varphi} \tag{8}$$

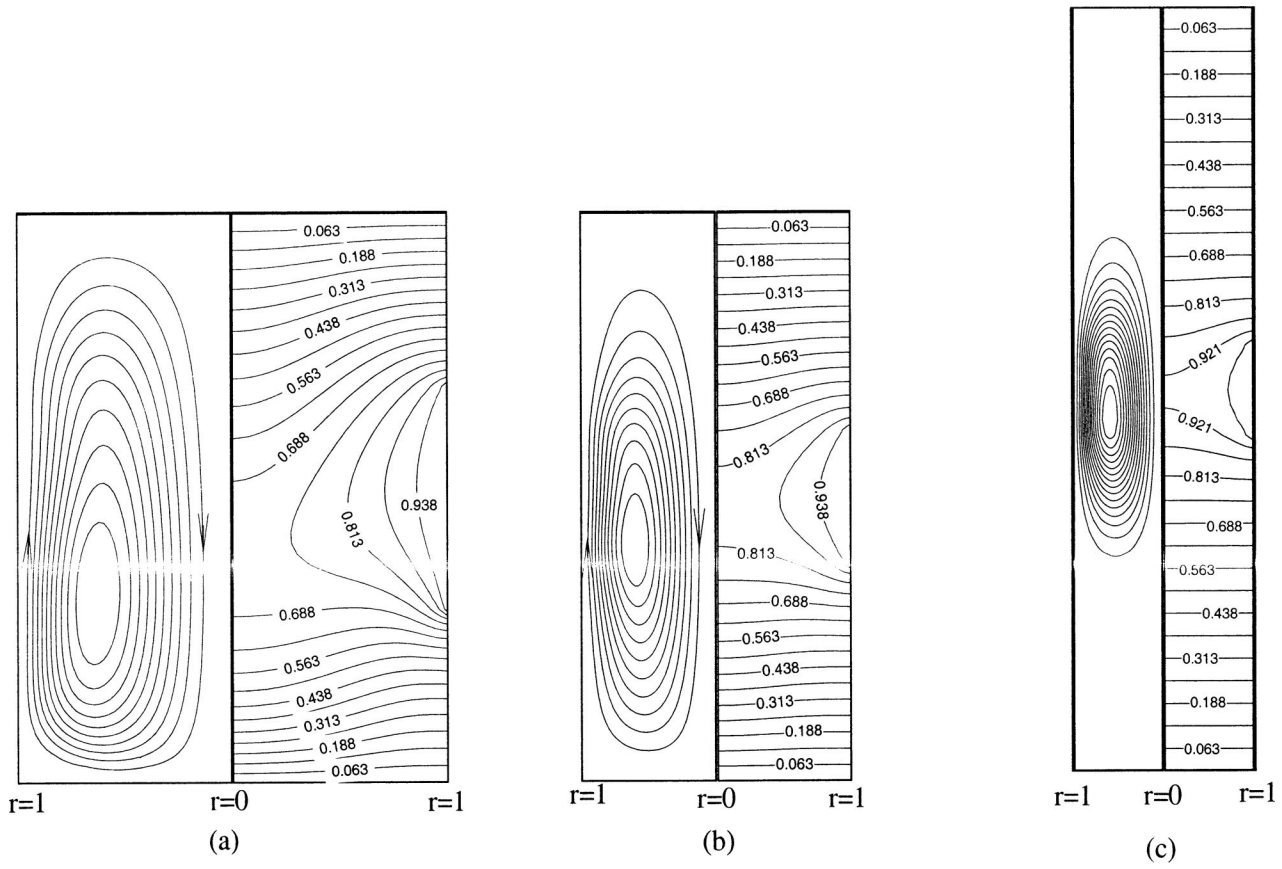

Fig. 2 Streamlines (left frames) and isotherms (right frames) of base axisymmetric flow. All isolines are equally spaced. The temperature varies between 0 and 1: (a) $A=2.5$, $\mathrm{Gr}_{cr}=1.12\times10^5$, $\psi_{\max}=23.59$; (b) $A=4$, $\mathrm{Gr}_{cr}=3.18\times10^5$, $\psi_{\max}=6.20$; (c) $A=8$, $\mathrm{Gr}_{cr}=1.82\times10^4$, $\psi_{\max}=2.01$.

The zero Fourier mode ($k=0$) corresponds to the axisymmetric solution of (1)–(7), whose stability is to be studied. The modes corresponding to nonzero values of the azimuthal wavenumber k are k-fold periodic in the azimuthal direction, i.e., are invariant with respect to a rotation over the angle $2\pi/k$ around the axis. The functions $\mathbf{v}_k(r,z)$, $p_k(r,z)$, $\theta_k(r,z)$ are defined in the meridional plane and are calculated by the global Galerkin and the finite volume methods.

The discretization by the global Galerkin method and the subsequent three-dimensional stability analysis are described in [15,20]. The treatment of the discontinuous boundary condition at $r=1$ is done in the same way as in [28,29]. The second-order discretization by the finite volume method is done on the staggered uniform grid. Both methods use Newton iteration for the calculation of steady state solutions. The linear stability problem separates for each azimuthal wavenumber k. The corresponding eigenproblems are solved by the QR-decomposition algorithm in the case of the global Galerkin discretization and by the shift-and-inverse Arnoldi iteration in the case of the finite volume discretization.

In the Fourier-decomposition of the solution (8) the mode with $k=0$ corresponds both to the base axisymmetric flow state and to the axisymmetric perturbation. The modes with $k\neq0$ correspond only to the three-dimensional perturbations. Two different ways are used to represent a calculated three-dimensional perturbation graphically. First, we note that the requirement that all the results represented by (8) are real functions yields

$$\mathbf{v}_k=\overline{\mathbf{v}}_{-k}, \quad p_k=\overline{p}_{-k}, \quad \theta_k=\overline{\theta}_{-k}, \tag{9}$$

where overbar means complex conjugation. Thus, to represent the three-dimensional pattern of a perturbation of the velocity of the temperature we plot the real part of $[\mathbf{v}_k(r,z)e^{ik\varphi}]$ or $[\theta_k(r,z)e^{ik\varphi}]$. In the case of steady bifurcation (zero imaginary part of the leading eigenvalue) these functions represent the perturbation itself. In the case of oscillatory instability (nonzero imaginary part of the leading eigenvalue equal to ω_{cr}) these functions represent a snapshot of the unsteady perturbation, proportional to $\exp[i(\omega_{cr}t+k\varphi)]$, which rotates around the axis with the angular velocity ω_{cr}/k. Obviously, the direction of rotation is arbitrary. The choice of a time moment to plot the perturbation is also arbitrary, since nonzero times add only an azimuthal phase shift to the whole pattern. To gain a better description of the amplitude of a certain perturbation mode we plot also the modulus of the above functions, which reduces to $|\mathbf{v}_k(r,z)|$ and $|\theta_k(r,z)|$. The latter do not depend on the azimuthal angle and the time scale and therefore are axisymmetric time-independent functions.

The most usual case of oscillatory instability is the *Hopf* bifurcation, which takes place when a pair of complex-conjugated eigenvalues cross the imaginary axis and some other conditions hold. When the axisymmetry is broken by the *Hopf* bifurcation the resulting flow at small supercriticalities evolves into either a traveling or a standing wave. The traveling wave states correspond to the growth of the most unstable perturbation and can be represented as, for example $\mathbf{v}_0(r,z)+\varepsilon\mathbf{v}_k(r,z)\exp[i(\omega t+k\varphi)]$, where $\mathbf{v}_0(r,z)$ is the axisymmetric steady solution, $\mathbf{v}_k(r,z)$ is the eigenfuction of the corresponding linearized problem, while the amplitude ε and the frequency of a nonlinear oscillatory regime ω must be obtained from a nonlinear analysis (a numerical realization of such analysis for the axisymmetric *Hopf* bifurcation of steady flows is described in [15]). The traveling wave rotates around the axis with the angular velocity ω/k. There exists also another traveling wave $\mathbf{v}_0(r,z)+\varepsilon\mathbf{v}_{-k}(r,z)\exp[i(\omega t-k\varphi)]$ differing from the

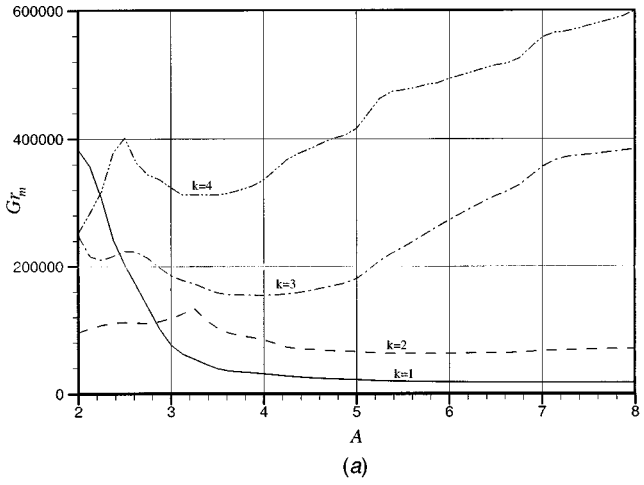

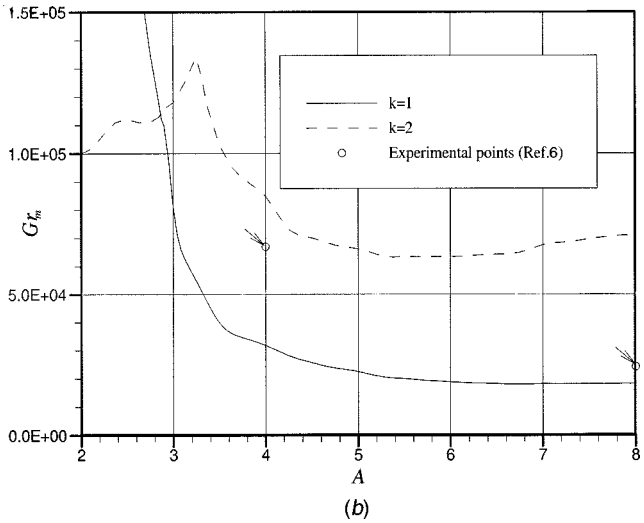

Fig. 3 Stability diagram: (a) Marginal Grashof number versus the aspect ratio for $1 \leq k \leq 4$; and (b) Two most critical marginal stability curves for $k=1$ and 2 and comparison with experimental points [6].

first one only by the direction of rotation, so that the direction of rotation of the resulting nonlinear traveling-wave state is arbitrary. The third possibility is a nonlinear state resulting from the interaction of the two traveling waves, which results in a nonlinear standing wave regime. It is stressed, however, that the examination of possible three-dimensional nonlinear regimes is not a purpose of the present paper, which is focused on the stability properties of the flow only. The methods developed for three-dimensional linear stability analysis allow us to avoid heavy computations and provide practically important answers in cases when stabilization of fluid flows is the primary goal. The details of the numerical validation are outlined in the appendix.

Results

The streamlines and isotherms of the axisymmetric convective flows, whose stability is to be studied, are shown in Fig. 2. The fluid heated near the hot part of the cylindrical wall ascends along it and then descends near the cylinder axis. Note that in tall cylinders (Fig. 2(c)) the convective vortex is located in the central part of the cylinder, so that the motion near the top and the bottom is very weak. Note also that in the lower part of the cylinder the fluid is stably stratified (cold fluid is located below), while in the upper part the stratification is unstable (cold fluid is located above). For a two-dimensional cavity it was shown that these two

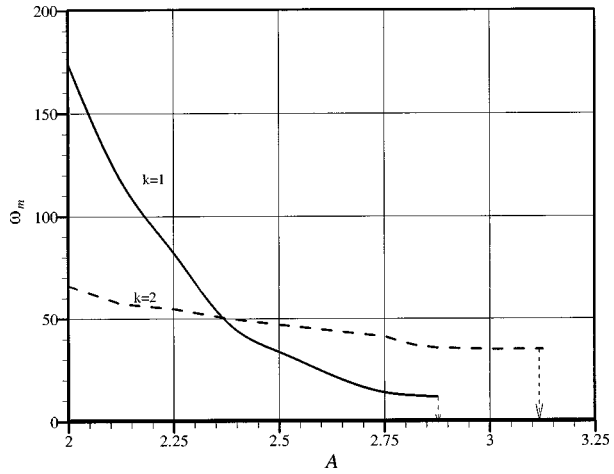

Fig. 4 Marginal frequency of the azimuthal traveling wave for the modes $k=1$ and 2 (only non-zero ω_m are shown)

stratifications play a crucial role in the onset of instability and can lead to a multiplicity of flow patterns [28,29]. The effect of the cylindrical geometry is discussed below.

The stability of the axisymmetric flows was examined for $k=0$, 1, 2, 3, 4. For each azimuthal wavenumber k the marginal Grashof number $\mathrm{Gr}_m(k)$, corresponding to the instability with respect to a $2\pi/k$—periodic perturbation, was calculated for rather densely selected values of A in the range $2 \leq A \leq 8$. Obviously, the critical Grashof number corresponds to the minimal $\mathrm{Gr}_m(k)$ over all possible values of k.

Varying the Aspect Ratio for a Fixed Prandtl Number, Pr =0.021. The dependence of the marginal Grashof numbers on the aspect ratio for the fixed Prandtl number $\mathrm{Pr}=0.021$ is shown in Fig. 3(a). As mentioned, this value of the Prandtl number corresponds to the liquid gallium used in the experiments [6]. The values of Gr_m corresponding to the axisymmetric perturbation with $k=0$ are always larger than those shown in Fig. 3(a), and in fact are above the value of 6×10^5 (see Table 3 of appendix). This shows that beyond a certain value of the Grashof number the axisymmetric calculations are not valid (similar conclusions were drawn also in [15,20,23]). The calculations show that there are three most dangerous instability modes, corresponding to the azimuthal wavenumbers $k=1$ and 2, which replace each other at $A=2.87$ and 2.9. The aspect ratio dependence of these two modes is zoomed out in Fig. 3(b), where we show also two experimental points reported in [6]. The agreement between the present computations and the experiment is discussed below. We performed also several calculations for $k>4$ to ensure that the marginal Grashof numbers of the axisymmetric and higher azimuthal modes are well above the value 6×10^5.

The three-dimensional flow that develops after the instability onset can be steady or oscillatory. The spatial pattern and temporal properties of developed three-dimensional states can be studied by non-linear three-dimensional calculations, which are beyond the scope of the present study. In the framework of the present linear stability analysis we can distinguish, first of all, between the monotone and the oscillatory growth of the dominant perturbation. This is defined by the imaginary part of the dominant eigenvalue, which can be zero (monotone growth), or nonzero (oscillatory growth indicating a *Hopf* bifurcation). The nonzero imaginary parts of the most dangerous azimuthal modes ($k=1$ and 2) are shown in Fig. 4. The Fourier mode $k=2$ is the most dangerous for $2 \leq A \leq 2.87$ (Fig. 3(a)) and remains oscillatory in this subinterval. The Fourier mode $k=1$ becomes the most dangerous at $A=2.87$. For $A \leq 2.9$ the most unstable perturbation is oscillatory,

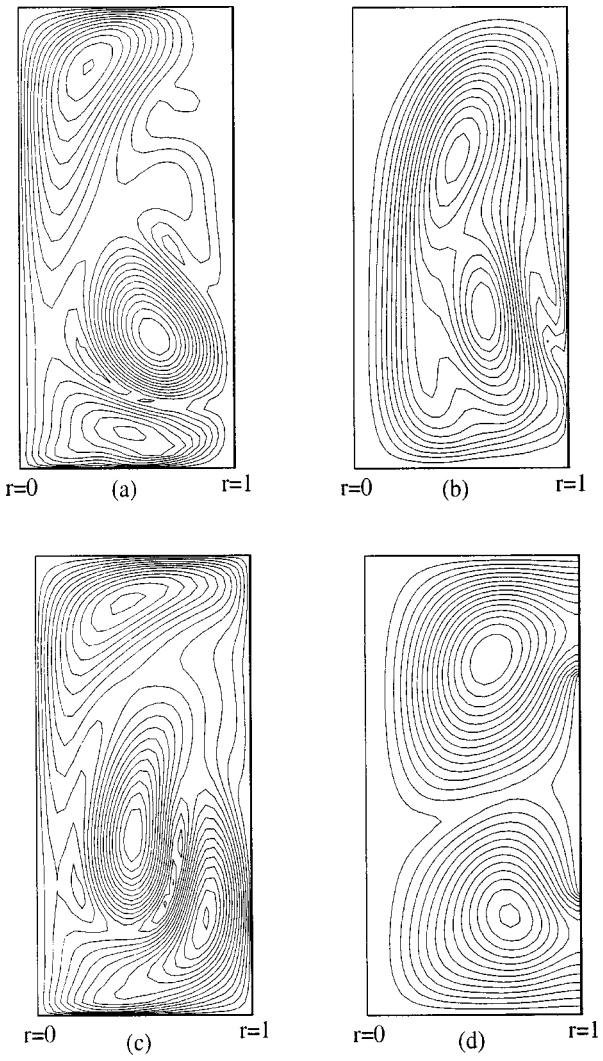

Fig. 5 Amplitudes of the perturbations of (a) radial, (b) vertical, (c) azimuthal velocities, and (d) temperature. $A=2.5$, $Gr_{cr}=1.12\times10^5$, $k=2$.

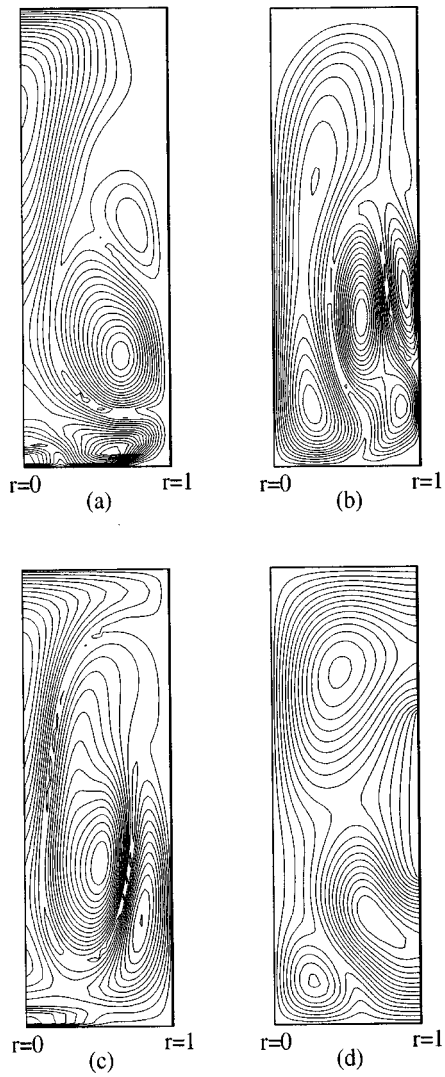

Fig. 6 Amplitudes of the perturbations of (a) radial, (b) vertical, (c) azimuthal velocities, and (d) temperature. $A=2.9$, $Gr_{cr}=1.10\times10^5$, $k=1$.

but is replaced by the steady one for larger aspect ratios up to $A=8$. Within the linear model considered the switch from the oscillatory to the steady perturbation takes place abruptly and the corresponding perturbations have different patterns in spite of the same $2\pi/k$ circumferential periodicity. Therefore, there are three different perturbation modes to be described: one is the oscillatory mode with $k=2$ that is most dangerous in the interval $2\leqslant A\leqslant2.87$; the second is the oscillatory mode with $k=1$ that becomes most dangerous in the narrow interval $2.87\leqslant A\leqslant2.9$; the third one is the steady mode with $k=1$ which is the most dangerous for $A>2.9$.

The patterns of the most dangerous perturbations are shown in Figs. 5–14. Figures 5–9 show the isolines of the perturbation amplitudes, which are defined in the (r,z) plane. Spatial patterns of the temperature perturbations are shown in Figs. 10–14. Comparison of the perturbation amplitude isolines (Figs. 5–9) shows that the three perturbation modes have different patterns and, therefore, are caused by different physical mechanisms. Since the perturbations are defined to within a multiplication by a constant [15] the values of the functions depicted in Figs. 5–14 are not shown. All the isolines and isosurfaces are equally distributed between the minimal and the maximal values of the corresponding functions.

The isolines of the amplitudes of the oscillatory perturbation at $A=2.5$, $k=2$ (Fig. 5) are distributed over the whole region of the flow. Note that the intensity of the temperature and velocity perturbations is almost the same in the upper and the lower parts of the cylinder, which is not the case in the tall cylinders (see below). Since the perturbations are not visibly affected by the stable and unstable temperature stratifications this instability can be assumed to originate from a hydrodynamic mechanism, i.e., the velocity field itself becomes unstable while the temperature perturbations do not play a significant role in the instability onset. To verify this assumption we calculated the most unstable perturbations for $A=2.5$ and $Pr=0$ (for which the heat transfer is governed by the conduction only and the temperature field is not perturbed at all) and obtained a similar perturbation pattern. Since the axisymmetry breaking instability is oscillatory ($\omega_m\neq0$) the three-dimensional perturbation is an azimuthal traveling wave [15], whose spatial pattern is shown in Fig. 10. As noted above, this pattern rotates around the axis with the angular velocity ω_m/k, and the direction of rotation is arbitrary.

The next oscillatory mode shown in Figs. 6 and 11 for $A=2.9$ is 2π-periodic ($k=1$). The corresponding instability can lead to a precession of the deformed, initially toroidal, vortex around the axis, as was experimentally observed for larger aspect ratios [6], or to a development of a standing wave (not observed experimen-

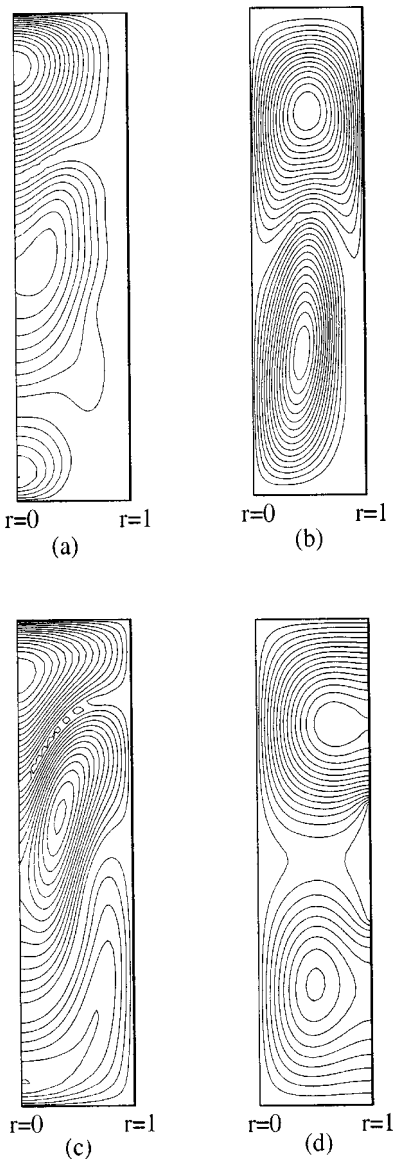

Fig. 7 Amplitudes of the perturbations of (a) radial, (b) vertical, (c) azimuthal velocities, and (d) temperature. $A=4$, $Gr_{cr}=3.18\times10^5$, $k=1$.

tally). Note, that the perturbations of velocity in this case are located in the lower part of the cylinder (Fig. 6), where the fluid is stably stratified. As above, this implies the purely hydrodynamic origin of this instability. The spatial pattern of the temperature perturbation (Fig. 11) also shows that its amplitude is stronger in the lower part of the cylinder. Consider the supercritical flow pattern in a meridional cross-section of the cylinder (say, in the plane $\theta=\theta_0$ and $\theta_0+\pi$). Since the amplitude of the perturbation varies as $\exp(i\theta)$, the amplitude in the cross-section will be an odd function with respect to the axis $r=0$. The flow pattern in this cross-section will be similar to that calculated for the two-dimensional cavity with partially heated vertical walls [6,29] in the case of an instability due to a *Hopf* bifurcation that causes the break of reflectional symmetry.

The third type of the perturbation pattern shown in Figs. 7–9 and 12–14 belongs to the same continuous marginal stability curve corresponding to the steady axisymmetry-breaking bifurcation with $k=1$ (Fig. 3(b)). Belonging to the same curve means that the instability sets in due to the same physical mechanism for the whole interval $2.9\leqslant A\leqslant 8$. Looking first at the patterns corresponding to $A=4$ (Figs. 7 and 12), we notice that the perturbations are intense in the whole cylinder. Moreover, the amplitude of the temperature perturbation is similar to those observed for the oscillatory three-dimensional instability in a lower cylinder (cf. Figs. 5 and 7). These can lead to the above conclusion about the purely hydrodynamic nature of the instability. However, this conclusion appears to be wrong, which is seen from the perturbation

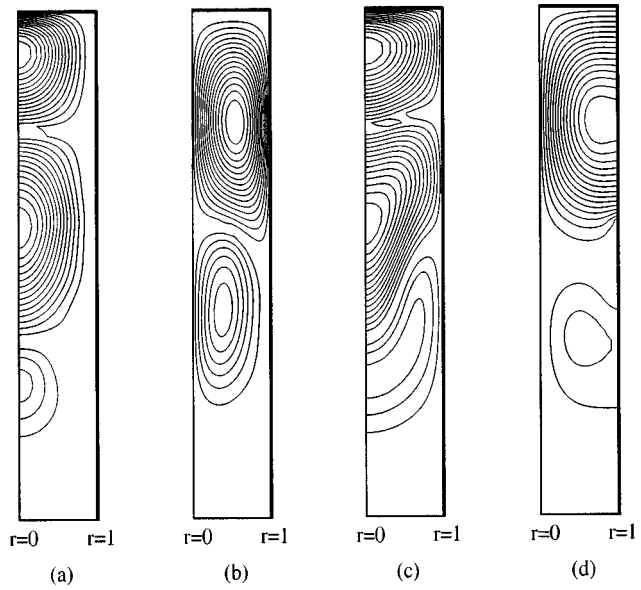

Fig. 8 Amplitudes of the perturbations of (a) radial, (b) vertical, (c) azimuthal velocities, and (d) temperature. $A=6$, $Gr_{cr}=1.88\times10^4$, $k=1$.

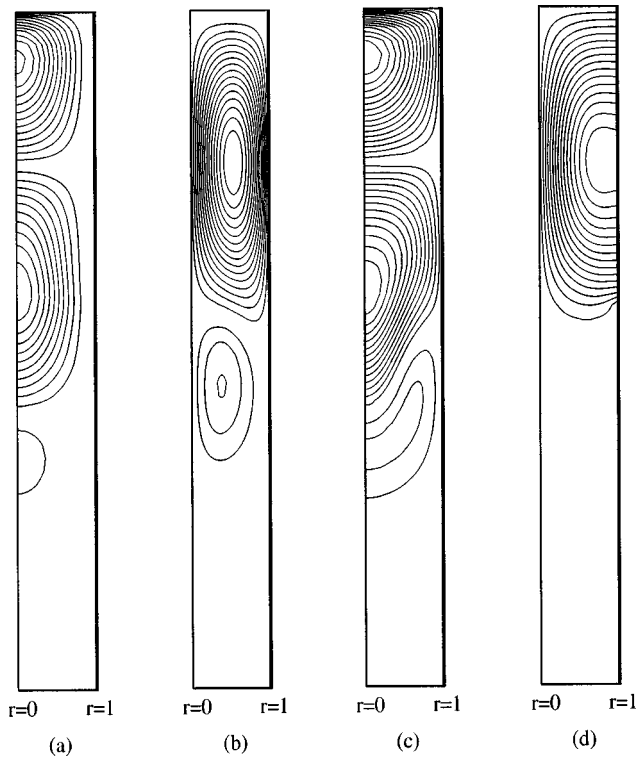

Fig. 9 Amplitudes of the perturbations of (a) radial, (b) vertical, (c) azimuthal velocities, and (d) temperature. $A=8$, $Gr_{cr}=1.82\times10^4$, $k=1$.

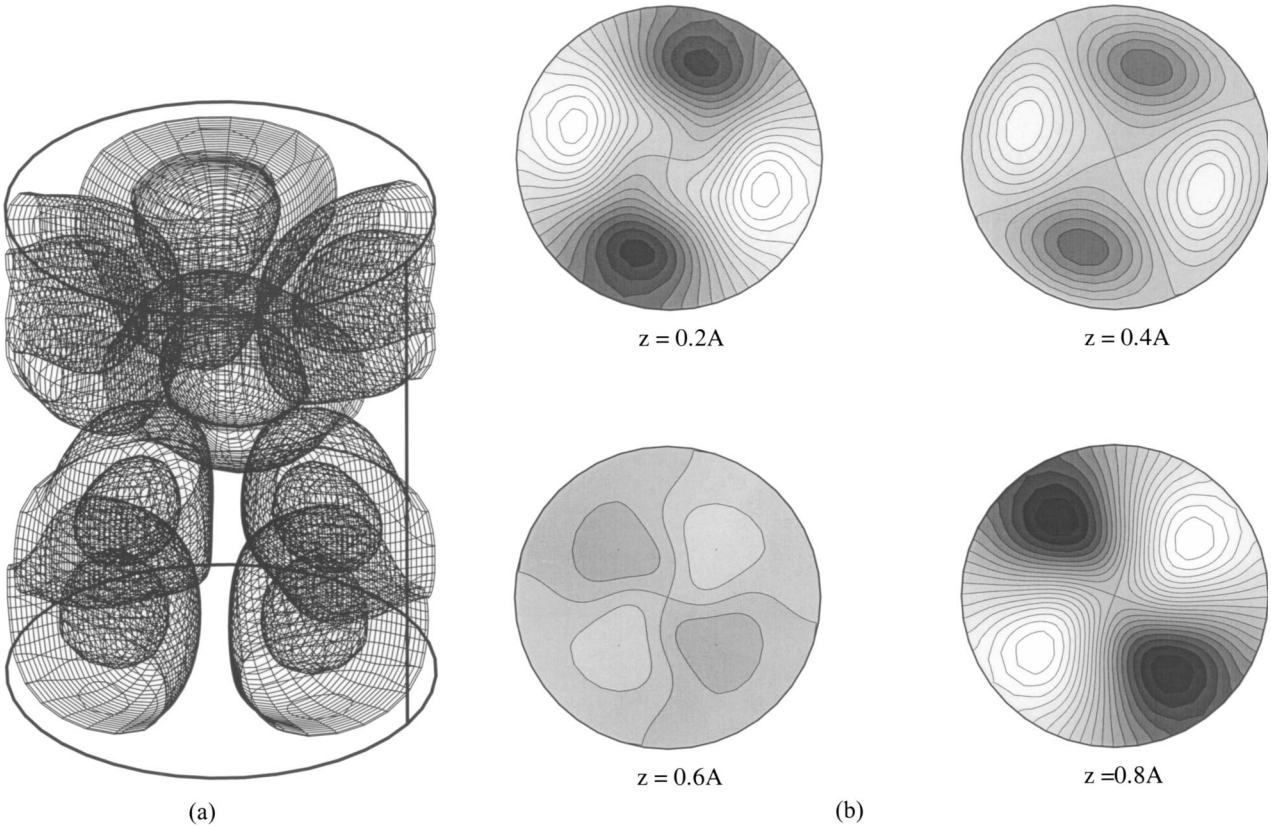

Fig. 10 Pattern of the temperature perturbation at $A=2.5$, $Gr_{cr}=1.12\times10^5$, $k=2$: (a) four equally spaced isosurfaces; and (b) 21 equally spaced isolines in four different axial cross-sections.

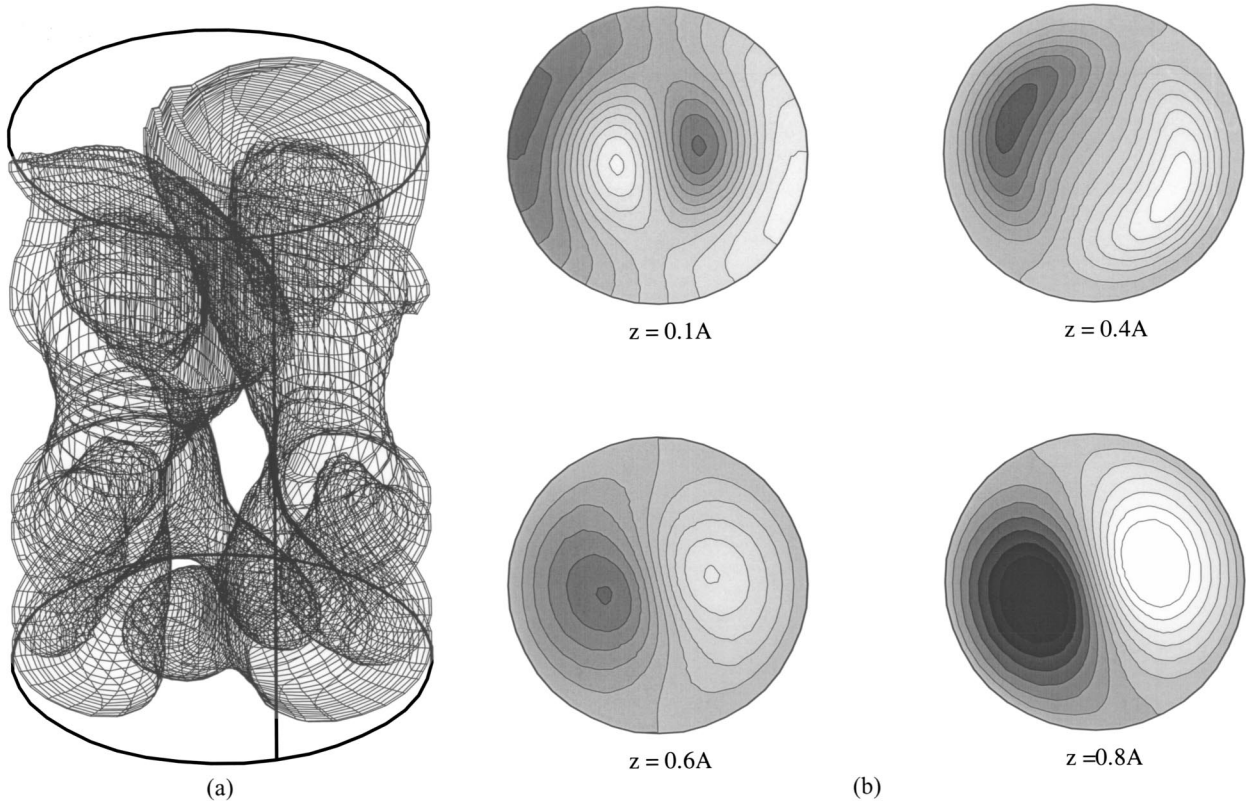

Fig. 11 Pattern of the temperature perturbation at $A=2.9$, $Gr_{cr}=1.10\times10^5$, $k=1$: (a) four equally spaced isosurfaces; and (b) 21 equally spaced isolines in four different axial cross-sections.

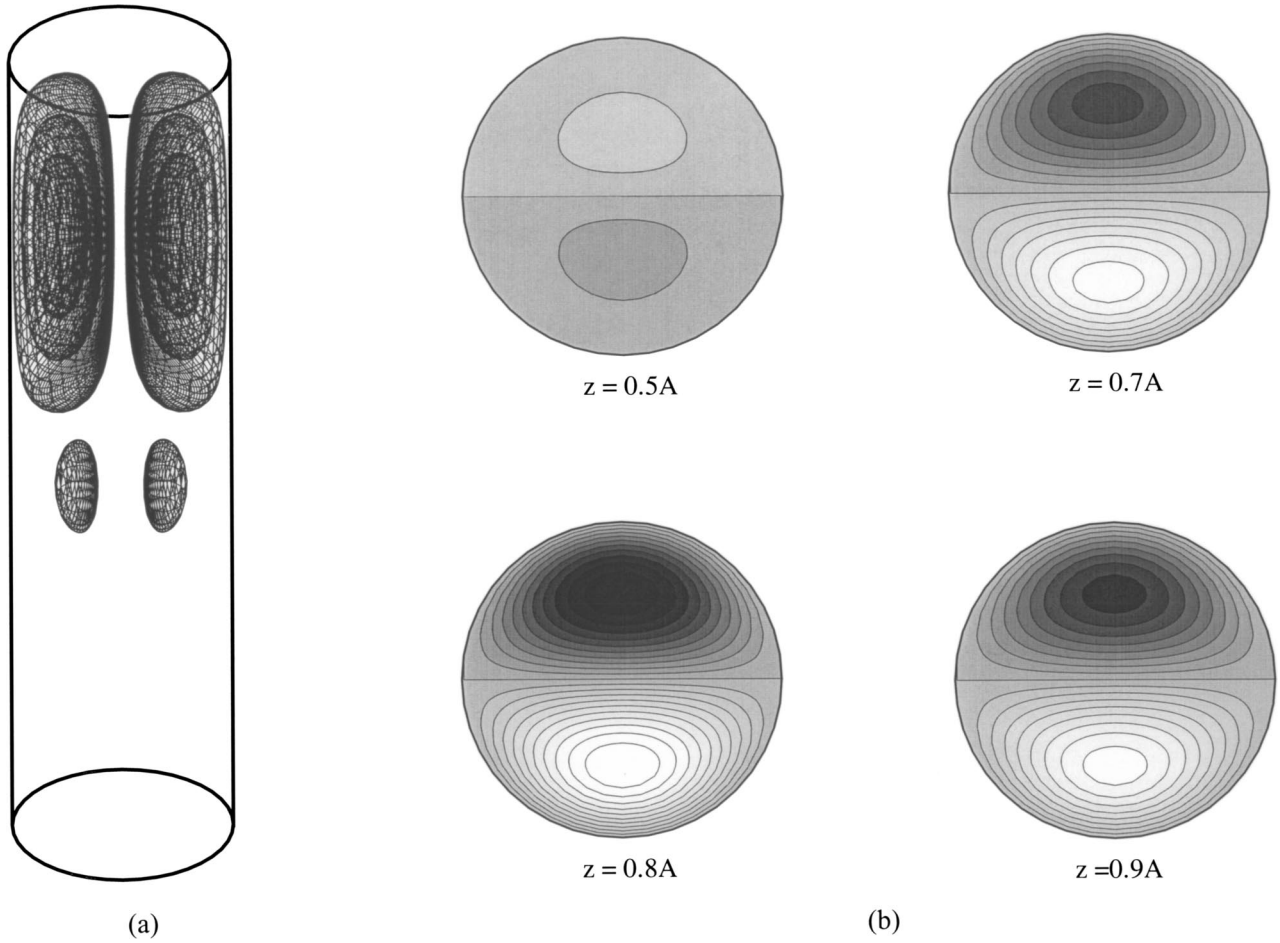

Fig. 12 Pattern of the temperature perturbation at $A=4$, $Gr_{cr}=3.18\times10^4$, $k=1$: (a) four equally spaced isosurfaces; and (b) 21 equally spaced isolines in four different axial cross-sections.

patterns at higher aspect ratios. With the growth of the cylinder height all the patterns remain qualitatively similar, but are shifted upwards with the increase of A (cf. Figs. 7, 8, and 9). This shift can be explained by the growth of the stably stratified fluid layer in the lower part of the cylinder (Fig. 2), where the perturbations are suppressed. As a result, the instability sets in the upper part of the cylinder, where the fluid is stratified unstably.

In tall two-dimensional cavities with locally heated sidewalls the instability was shown to set in due to the Rayleigh-Bénard mechanism, leading to the appearance of the convective roll in the upper part of a cavity [28,29]. To show that the same mechanism drives also the instability in the cylinder geometry, we consider the three-dimensional patterns of the temperature and the vertical velocity perturbations. The latter are shown in Fig. 14. Note that the perturbation patterns shown in Figs. 10–14 are antisymmetric functions with the darker and lighter color corresponding to the minimum and the maximum of a function. Thus comparing the perturbations of the temperature and the axial velocity in the axial cross-sections $z=0.7A$ and $0.9A$ we notice that the instability causes the downflow of the cold fluid from the upper boundary (darker parts in Figs. 13(b) and 14(b)) in one half of the cross-section, while in another half the hot fluid is ascending (lighter parts in Figs. 13(b) and 14(b)). Taking into account the unstable temperature stratification developed in the upper part of the cylinder, where the perturbations are located, we interpret the arising instability as an appearance of a three-dimensional Rayleigh-Bénard roll in the upper part of the cylinder. The motion inside this roll can be described as follows. Dividing the cylinder in two halves by the zero isosurface of the temperature (or axial velocity) perturbation, one will observe the upflow of the hot fluid in one half and downflow of the cold fluid in the other half. Note that the zero isosurface coincides with one of the meridional planes. Its orientation in space is arbitrary.

The description of the supercritical fluid motion in a tall cylinder with $A=8$ given above completely agrees with the experimental observations [6]. It also agrees qualitatively with the numerical results obtained for the two-dimensional cavity with partially and symmetrically heated sidewalls [28,29]. In lower cylinders, up to $A\approx2.9$, the instability also sets in due to the Rayleigh-Bénard mechanism. However, at lower aspect ratios the motion inside the Rayleigh-Bénard roll will create, by continuity, an opposite motion just below it. A secondary vortex will develop below the primary Rayleigh-Bénard roll. The relatively intensive perturbations in the lower part of the cylinder at $A=4$ (Figs. 7 and 12) correspond to this secondary vortex. With the growth of the aspect ratio the secondary vortex is suppressed by the growing stably stratified liquid layer: the perturbations near the midplane and below it become weaker with the increase of A (cf. Figs. 7, 8, and 9).

The developed three-dimensional regime at $A=8$ was experimentally observed at $Gr_{exp}=2.4\times10^4$ (see also Fig. 3(b)) [6]. According to our calculations, the critical value is $Gr_{cr}=1.8\times10^4$, which is below the experimentally observed value. This difference can be explained by the fact that the experiment reports the flow with an observable large finite deviation from the axial symmetry, while the computed critical value corresponds to the zero amplitude of the three-dimensional perturbation. Except for this nu-

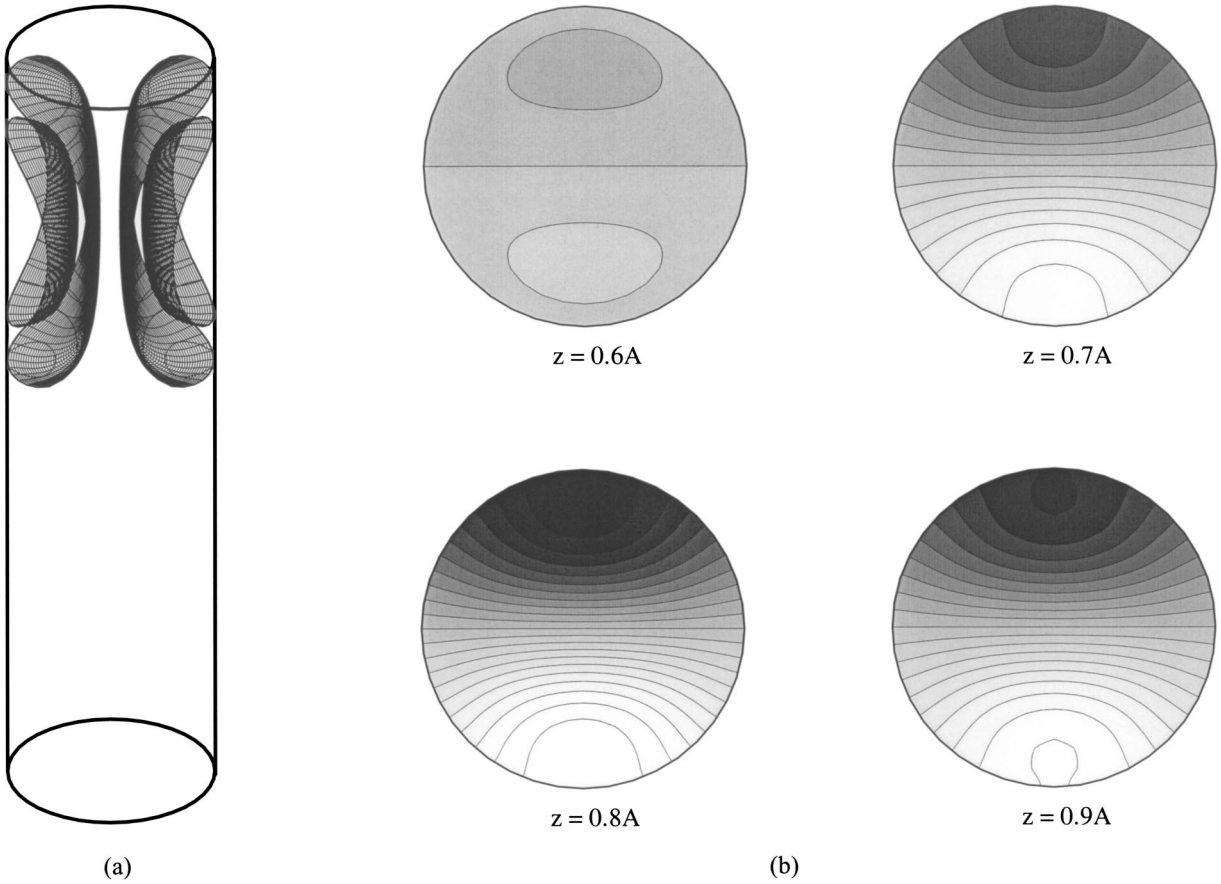

Fig. 13 Pattern of the temperature perturbation at $A=8$, $Gr_{cr}=1.82\times10^4$, $k=1$: (a) four equally spaced isosurfaces; and (b) 21 equally spaced isolines in four different axial cross-sections.

merical difference the experimentally observed flow pattern, i.e., steady convective roll in the upper part of the cylinder, completely agrees with the pattern of the most dangerous perturbation calculated here. Therefore, we conclude that in this case the numerical predictions agree with the experimental observations. Furthermore, we calculated the critical Grashof number for $A=12$ (using 80×100 finite volume grid) and found that the three-dimensional instability sets in at $Gr_{cr}=2.18\times10^4$ with $\omega_{cr}=0$ and $k_{cr}=1$. This completely agrees with the experimentally observed pattern and the critical Grashof number equal to $Gr_{exp}=2.20\times10^4$.

At $A=4$ the disagreement between the calculations and the experiment is qualitative. The present result predicts a steady axisymmetry-breaking bifurcation, setting in at $Gr_{cr}=3.18\times10^4$, similar to that observed at $A=8$. However, the experiment reports transition to the three dimensional oscillatory state at $Gr_{exp}=6.7\times10^4$ with the period of oscillations at $Gr=9.67\times10^4$ approximately 10 sec. Rescaling the period to the dimensionless circular frequency ($R=0.955\times10^{-2}$ m, $\nu=3.37\times10^{-7}$ m^2/s for gallium at 37°C [25]) we obtain the dimensionless circular frequency of oscillations $\omega\approx185$. The pattern of the observed oscillatory flow is described as a precession of the deformed convective vortex around the axis, which corresponds to the axisymmetry-breaking *Hopf* bifurcation with $k=1$. We checked ten leading eigenvalues corresponding to this Fourier mode and found that their imaginary parts (i.e., frequencies of oscillations) are less than 100. Since the numerically predicted critical Grashof number is less than one half of the observed one we offer the following explanation of the disagreement between the numerical results and experimental observations. The first transition from the steady axisymmetric to steady three-dimensional flow takes place when the Grashof number exceeds the value of $Gr_{cr}=3.18\times10^4$. However, the amplitude of the deviation from axisymmetry grows very slowly, so that it does not exceed the tolerance of the experimental measurements. This assumption can be supported by the fact that the measured azimuthal deviations of the temperature at $A=8$ were less than 0.5°C and are even less at $A=4$ (Figs. 7 and 9 of [6]). With the growth of the Grashof number the steady three-dimensional state loses stability with respect to an oscillatory perturbation which has the same azimuthal wavenumber $k=1$. The numerical modeling of such instability requires a three-dimensional nonlinear steady solver combined with the three-dimensional Floquet analysis, which is beyond the scope of the present study.

Another, and perhaps simpler, reason for the disagreement may be connected with the geometrical and heating imperfections of the experiment. The cylindrical cavity cannot be made absolutely circular, and it cannot be placed absolutely vertically. The cylindrical wall also cannot have a sharp jump from the perfect conduction at the heated region to the perfect insulation outside of it. These imperfections can shift the oscillatory-steady mode exchange at $A=2.9$ to larger aspect ratios, so that the instability at $A=4$ still will be oscillatory. The fact that with the growth of the aspect ratio the agreement between the present calculations and the experiment becomes better also suggests imperfections in the experimental thermal boundary conditions. Thus, if the heating ring is not perfectly axisymmetric the effect of asymmetry will vanish as the relative width of the heating ring with respect to the sidewall size decreases. Another possibility is the temperature dependence of the Prandtl number, which can lead to drastic changes in the stability properties of the flow [25,27]. Note that the numerical results were cross validated by the independent numerical techniques (see appendix) and therefore the disagreement cannot be simply attributed to a lack of numerical accuracy.

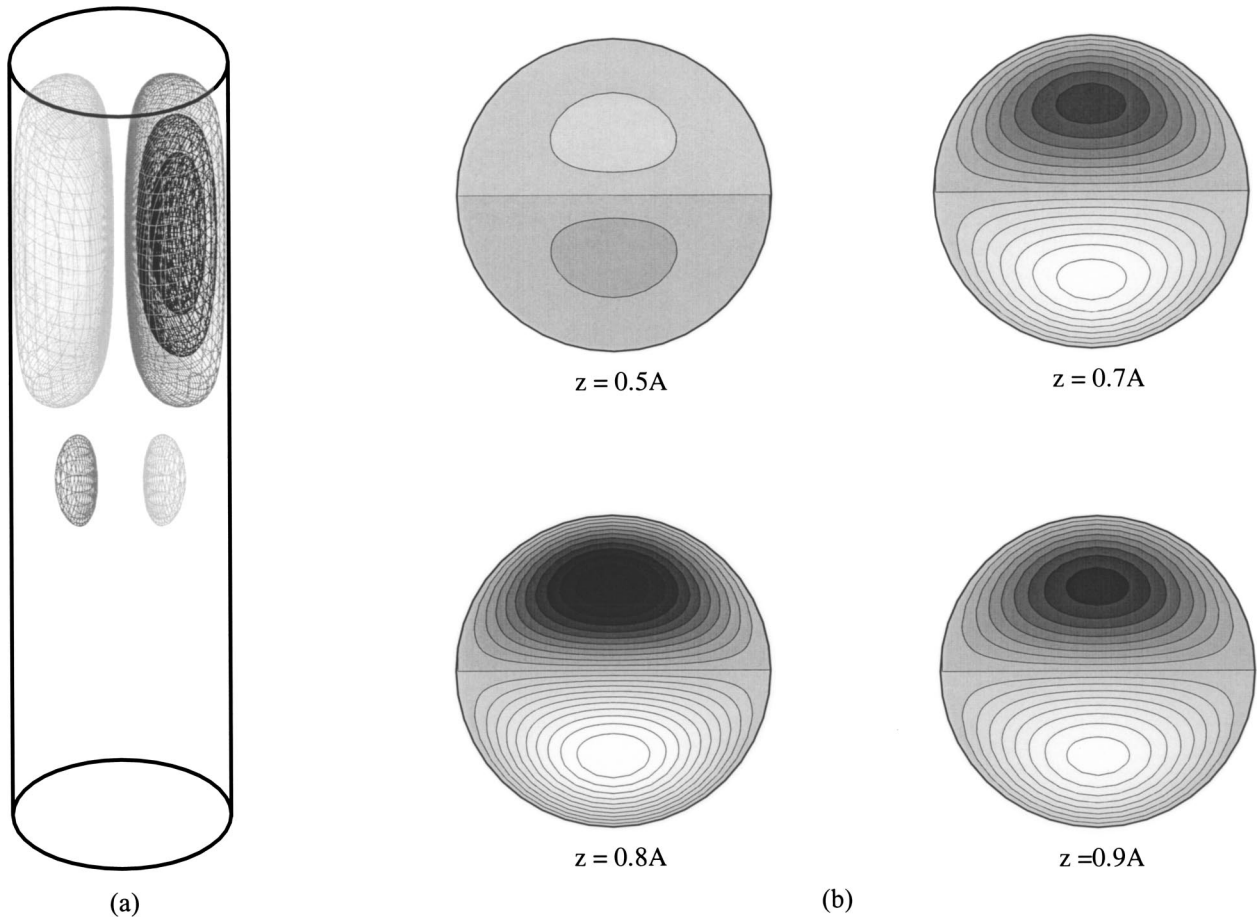

Fig. 14 Pattern of perturbation of the vertical velocity at $A=8$, $Gr_{cr}=1.82\times10^4$, $k=1$: (a) six equally spaced isosurfaces; and (b) 21 equally spaced isolines in four different axial cross-sections.

Varying the Prandtl Number for a Fixed Aspect Ratio $A=4$. To study a possible effect of the Prandtl number variation on the stability properties of the flow and, in particular, to examine whether the reported disagreement with the experiment can be explained by the temperature dependence of the viscosity and thermal diffusivity, the calculations were performed for $0\leqslant Pr\leqslant 0.05$ and $A=4$, which is the aspect ratio at which the present result disagrees with the experimental observations [6]. Note that the zero Prandtl number $Pr=0$ corresponds to the case of very large thermal diffusivity at which the convective heat transfer can be neglected. At this limiting case the temperature is not altered by the convective motion, its distribution over the volume is defined by the steady heat conduction only and does not depend on the Grashof number. Consequently, in this limiting case the temperature perturbations are excluded from the stability problem. Since the temperature field is not altered, the corresponding instability is caused by the instability of the resulting flow and we referred to it in the above as to the purely ''hydrodynamic instability.'' With the increase of the Prandtl number the role of the temperature perturbations in the instability onset increases. The interaction between the velocity and temperature perturbations leads to other instability modes, which are referred to as ''convective'' instability. Obviously at a certain value of the Prandtl number the ''hydrodynamic'' instability is replaced by a ''convective'' one (see also [23,25,27]).

The marginal stability curves $Gr_m(Pr)$ for $A=4$ are shown in Fig. 15. At very small Prandtl numbers, the most dangerous instability mode is steady and corresponds to $k=2$, which is replaced by the mode corresponding to $k=1$ already at $Pr\approx0.002$. The most dangerous instability mode corresponding to $k=1$ is oscillatory up to $Pr\approx0.011$ and then is replaced by another, steady mode. The maximal critical circular frequency of oscillations of the oscillatory mode is approximately 33, which is still far below the experimental value of 185. The leading eigenvalues corresponding to higher Fourier modes ($k>1$) are real up to the corresponding marginal values of the Grashof number. Therefore, the disagreement at $A=4$ cannot be attributed to an uncertainty in the determination of the Prandtl number.

It was found that the excitation of the mode $k=2$ at small Prandtl numbers is caused by a drastic change of the flow pattern taking place when the Prandtl number is reduced from approximately 0.01 to zero. Figure 16 illustrates the change of the flow patterns at $Pr=0$ and the Grashof number growing from $Gr=10^3$ up to its critical value $Gr_{cr}=2.3\times10^5$. The temperature distribution in this case (left frame in Fig. 16) is governed by the heat conduction only and therefore is reflection-symmetric with respect to the $z=A/2$ plane. The streamlines at low Grashof numbers (e.g., $Gr=1000$) are also almost reflection-symmetric. With the increase of the Grashof number the maximum of the stream function shifts downwards, so that at the critical point $Gr\approx2.3\times10^5$ the flow becomes significantly more intensive in the lower part of the cylinder than in the upper part. The shift of the stream function maximum can be explained by the fact that the fluid ascends along the no-slip cylindrical wall slower than it descends along the axis. As a result the flow near the bottom becomes more intensive. The patterns of the corresponding perturbations are also characterized by sharp maxima in the lower part of the cylinder. With the increase of the Prandtl number this effects disappears. This is illustrated in Fig. 17, where the streamlines and isotherms

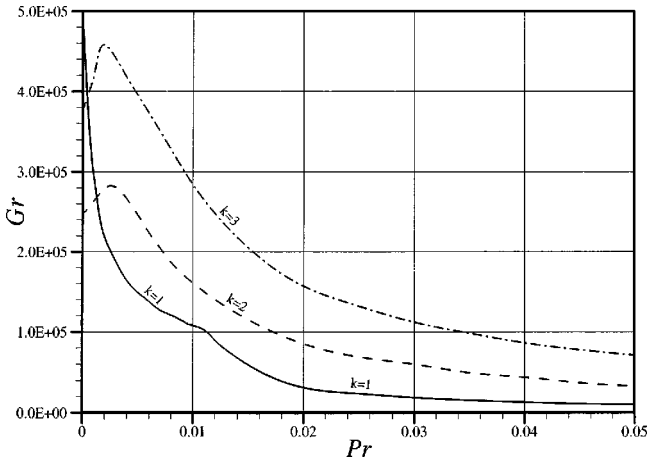

Fig. 15 Marginal Grashof number versus the Prandtl number for $A=4$ and $1\leqslant k\leqslant 3$

are shown for $Gr_{cr}=2.3\times10^5$ and Pr=0.005 and 0.01. Apparently, convective effects slow down the descending of the fluid along the axis tending to sharpen the stable stratification in the lower part of the cylinder.

Conclusions

The three-dimensional stability analysis of axisymmetric convective flows was carried out numerically for the experimental configuration of [6]. The computations were carried out by two independent numerical approaches, which cross validate each other. For a fixed value of the Prandtl number, Pr=0.021, and a fixed size of the heated part of the cylindrical sidewall the dependence of the critical Grashof number on the aspect ratio is obtained. Beyond the critical Grashof number the axisymmetric flows are unstable. It is found that depending on the aspect ratio the axisymmetry breaking instability leads to a steady or oscillatory three-dimensional flow. Three different three-dimensional patterns of the most dangerous perturbation replace each other with the variation of the aspect ratio. It was found that in low cylinders with $2\leqslant A\leqslant 2.87$ the primary instability sets in due to oscillatory perturbation in the form of π-periodic azimuthal traveling wave ($k_{cr}=2$). In taller cylinders with $2.87<A\leqslant 2.9$ the instability is also oscillatory, but sets in due to a traveling-wave-type 2π-periodic perturbation, which can lead to a precession of the deformed, initially axisymmetric, toroidal convective vortex around the axis. The supercritical flow in these two cases can develop in the form of travelling or standing waves. In tall cylinders, with $A>2.9$ and at least up to $A=8$, the instability sets in as a 2π-periodic Rayleigh-Bénard roll located in the upper part of the cylinder.

A comparison with experiment is possible only for the aspect ratios $A=4$, 8, and 12, for which the experimental observations are reported. For $A=8$ and 12 the value of the critical Grashof number and the pattern of the most dangerous three-dimensional perturbation are in a good agreement with the experimental results. However, at $A=4$ the numerical predictions, obtained by two independent numerical approaches, disagree with the experimental observations both for the critical value of the Grashof number and for the pattern of supercritical flow. We suggest that a possible reason for disagreement is that the experimentally observed oscillatory instability is secondary, while the primary steady instability had been overlooked because of its small amplitude. Alternatively, the disagreement can be caused by imperfections in the experimental geometry and heating conditions. The calculated dependence of the critical Grashof number on the Prandtl number showed that the disagreement cannot be attributed to the temperature dependence of the physical properties of gallium. It was shown also that the flow pattern, as well as the most unstable perturbation, undergo qualitative changes when the Prandtl number is decreased below the value Pr=0.005.

It would be interesting to repeat the experiment [6] and to try to observe two oscillatory three-dimensional modes at lower aspect ratios. Apparently, the disagreement at $A=4$ can be resolved by experiment combined with fully three-dimensional time-dependent computations.

A two-dimensional instability in a two-dimensional rectangular cavity with similar heating conditions was studied in [28,29]. It was already argued [29] that the steady symmetry-breaking bifurcation in the rectangular cavity is similar to the steady axisymmetry-breaking bifurcation in a cylinder of the same height. The similarity can be seen by a comparison of the amplitudes of the most dangerous perturbations in both models, which are reported in [29] for $A=8$. We noticed above that the axisymmetry-breaking *Hopf* bifurcation with $k=1$, observed here for $A\leqslant 2.9$ is similar to the symmetry-breaking Hopf bifurcation in the two-dimensional rectangular cavity. Note that the axisymmetric perturbation in the present case corresponds to the reflectionally symmetric perturbation in the two-dimensional cavity,

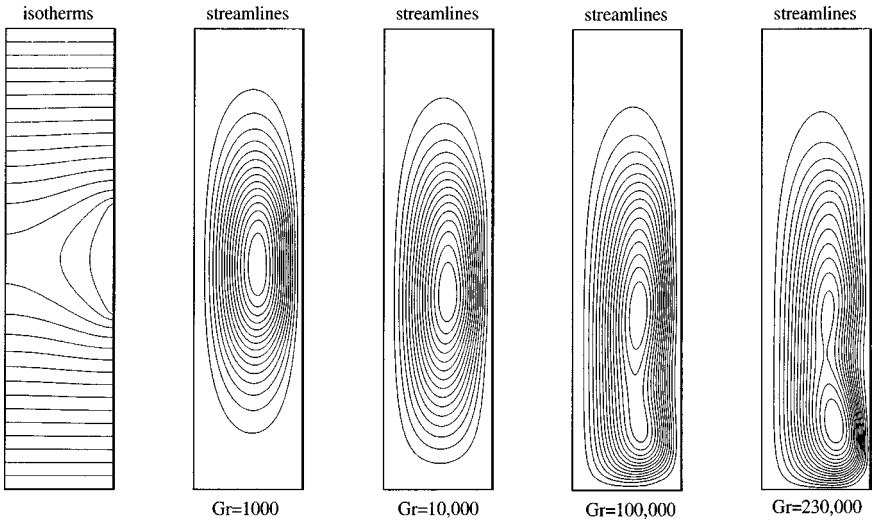

Fig. 16 Isotherms (left frame) and streamlines for Pr=0 and growing Grashof number

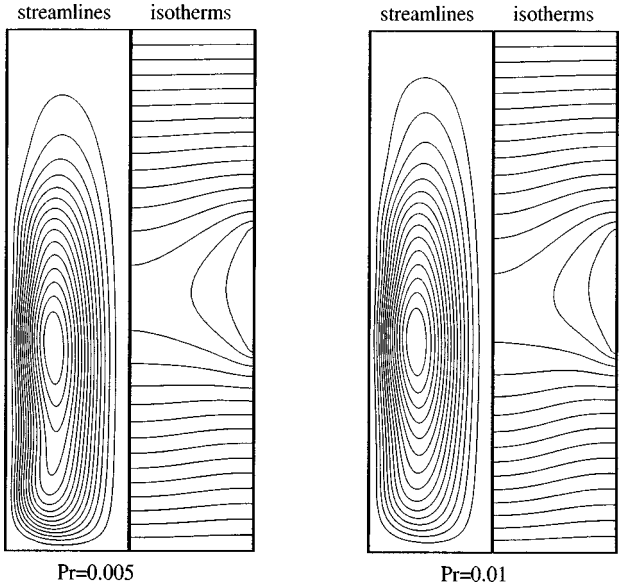

Fig. 17 Streamlines and isotherms of the flow for Gr=2.3 $\times 10^5$ and the Prandtl numbers slightly different from zero

neither of which ever becomes the most dangerous (Fig. 2 and the stability diagram in [29]). Note also that the three-dimensional perturbations with $k>1$ correspond to the three-dimensional perturbations in a rectangular box, which were not considered in [29]. The multiple supercritical flow states observed in the two-dimensional box [28,29] should be expected also in the cylindrical enclosure for the Grashof numbers above the critical one. Apparently, these multiple states, if they exist, are three-dimensional.

Acknowledgment

This work was supported by the Israel Ministry of Science (Grant 8575-1-98), the Israel Science Foundation (Grant 240/01), the Israel Ministry of Immigrant Absorption (to A. Rubinov, V. Erenburg and A. Gelfgat), the Fund for the Promotion of Research at the Technion, and the Y. Winograd Chair of Fluid Dynamics and Heat Transfer at Technion. The authors would like to acknowledge the use of computer resources belonging to the High Performance Computing Unit, a division of the Inter University Computing Center, which is a consortium formed by research universities in Israel.

Appendix

Validation of Numerical Techniques. To validate the numerical results we examined the convergence of both techniques and compared the converged results. The performance of the global Galerkin method was studied in [15,23], where very fast, sometimes spectral, convergence was reported. For the cylindrical configuration with aspect ratio varied from 1 to 4 it was possible to obtain convergence up to three or four decimal digits using 30×30 basis functions in the r- and z-directions.

Table 1 Convergence of the critical Grashof number and the critical frequency for $A=1$, $k=4$, and Pr=0.015 for the finite volume method. Parabolic heating of the sidewall. The converged result obtained by the Galerkin method is $Gr_{cr}=3.5922\times10^5$ and $\omega_{cr}=632.18$.[23]

Grid	$Gr_{cr}\times10^{-5}$	ω_{cr}
20× 20	3.9177	641.68
40× 40	3.8011	638.20
50× 50	3.4426	620.43
80× 80	3.6004	631.66
100×100	3.5927	632.42
120×120	3.5923	632.23
140×140	3.5923	632.20

Table 2 Convergence of the critical Grashof number and the critical frequency for $A=2$ and $k=1$ for the finite volume method

A	Grid, $N_r\times N_z$	$Gr_{cr}\times10^{-5}$	ω_{cr}
2	20× 20	4.2987	164.25
	30× 30	4.3702	162.80
	40× 40	3.8466	171.72
	50× 50	3.8291	173.55
	80× 80	3.8283	173.37
	100×100	3.8281	173.37
	125×125	No change	No change
	150×150		
4	20× 20	2.9348	0
	20× 40	3.1688	0
	30× 60	3.1716	0
	40× 60	3.1790	0
	40× 80	3.1792	0
	40×100	No change	0
	60×100		0
	80×100		0
8	20× 20	1.8283	0
	20× 40	1.8266	0
	30× 60	1.8139	0
	40× 60	1.8168	0
	40× 80	1.8171	0
	40×100	No change	0
	60×100		0
	80×100		0

The results of [23] were used for the validation of the finite volume method. The configuration considered in [23] differs from the present one only by the thermal boundary condition at the cylindrical wall: a continuous parabolic temperature profile $\theta(r=1)=z(1-z)/4$ was imposed instead of the discontinuous boundary condition (6),(7). The converged result obtained by the global Galerkin method states that at $A=1$ the instability sets in at $Gr_{cr}=3.5922\times10^5$ as a three-dimensional azimuthally traveling wave with the azimuthal wavenumber $k=4$ and the circular oscillation frequency $\omega_{cr}=632.18$. The convergence of the finite volume method for this case is shown in Table 1. The 100×100 grid yields a result that coincides with that obtained by the Galerkin method to three decimal digits. With further mesh refinement (120×120 or finer) we obtained agreement to the fourth decimal digit. Note that an accurate computation of critical values requires the accurate approximation of both the steady flow and the dominant eigenvector. The sufficiently accurate computation of both by the finite volume approach is validated in the present example.

The convergence of the finite volume method for the present case of discontinuous heating is illustrated in Table 2. It is seen that the use of 80×80 nodes for $A=2$, and 40×80 nodes for $A=4$ and 8 yields at least four converged decimal digits in the critical Grashof number and critical frequency. On the other hand, the convergence of the global Galerkin method slows down in the present case. The slow down is caused by the discontinuities of the normal derivative of the temperature in the boundary conditions at $z=a_1$ and a_2. These discontinuities lead to the Gibbs phenomenon, i.e., to the appearance of spurious oscillations near a point of discontinuity. The Gibbs phenomenon can be smoothed by a proper choice of the collocation points at the boundary (for details see [28,29]) and remains small when the axisymmetric steady flows are calculated, so that the pointwise difference (calculated via all grid nodes) between the solutions obtained by the two numerical methods is less than 1% for a rather coarse discretization: 50×50 uniform finite volume grid against 20×20 Galerkin

Table 3 Comparison of results obtained by the global Galerkin and finite volume methods

		Discretization, $N_r \times N_z$		Critical Grashof number		Critical frequency	
A	k	Finite volume	Galerkin	Finite volume	Galerkin	Finite volume	Galerkin
2	0	80×80	20×58	6.391×10^5	6.279×10^5	375.1	372.8
2	1			3.828×10^5	3.5565×10^5	173.3	178.8
2	2			9.610×10^4	9.3822×10^4	66.11	66.26
2	3			2.476×10^5	2.596×10^5	0	0
2	4			2.529×10^5	2.4855×10^5	0	0
4	0	40×80	20×56	1.055×10^6	1.047×10^6	194.6	192.7
4	1		20×72	3.179×10^4	3.174×10^4	0	0
4	2		20×82	8.504×10^4	8.496×10^4	0	0
4	3		20×44	1.548×10^5	1.547×10^5	0	0
4	4		20×56	3.363×10^5	3.3934×10^5	0	0
6	0	40×80	20×48	1.303×10^6	1.314×10^6	163.4	163.6
6	1		20×64	1.882×10^4	1.893×10^4	0	0
6	2		20×66	6.332×10^4	6.321×10^4	0	0
6	3		20×48	2.732×10^5	2.728×10^5	0	0
6	4		20×48	4.942×10^5	5.028×10^5	0	0
8	0	40×80	16×64	1.492×10^6	1.491×10^6	163.7	163.1
8	1		20×72	1.817×10^4	1.805×10^4	0	0
8	2		16×88	7.093×10^4	7.041×10^4	0	0
8	3		20×88	3.845×10^5	3.687×10^5	46.0	44.44
8	4		20×64	5.991×10^5	6.0320×10^5	0	0

basis functions with 72 collocation points at the boundary. However, the Gibbs phenomenon becomes stronger when three-dimensional perturbations are calculated. The strongest effect is observed in low-aspect ratio cylinders, where the relative size of the heated element is larger.

The Gibbs phenomenon can be significantly reduced by a smoothing of the boundary conditions. However, our experience in flow stability studies [15,20,23,26–29] shows that stability properties of the flow can change drastically with a small, seemingly negligible, change of geometry or boundary conditions. Since the Gibbs phenomenon is observed to be strongest in the patterns of three-dimensional perturbations, we prefer to refrain from any alteration of the boundary conditions. Thus, we used the global Galerkin method for validation purposes only, and conducted the parametric stability study by the finite volume method.

The critical parameters obtained by both numerical approaches for different aspect ratios and the azimuthal wavenumbers are shown in Table 3. At large aspect ratios the agreement between the two methods is better since the Gibbs phenomenon is weaker. The largest disagreement between the two numerical methods is observed at $A=2$, but it does not exceed 10 percent. Nevertheless, the use of the independent global Galerkin approach allowed us to obtain additional validation of the results. The stability study reported below is done using the finite volume approach, which does not exhibit the convergence slowdown (see Table 2).

References

[1] Müller, G., 1993, ''Convective Instabilities in Melt Growth Configurations,'' J. Cryst. Growth, **128**, pp. 26–36.

[2] Müller, G., and Ostrogorsky, A., 1994, ''Convection in Melt Growth,'' in *Handbook of Crystal Growth*, D. T. J. Hurle, ed., **2**, North-Holland, Amsterdam, pp. 711–781.

[3] Jaluria, Y., 2001, ''Fluid Flow Phenomena in Materials Processing—The 2000 Freeman Scholar Lecture,'' ASME J. Fluids Eng., **123**, pp. 173–210.

[4] Hurle, D. T. J., 1966, ''Temperature Oscillations in Molten Metals and Their Relationship to Growth Striae in Melt-Grown Crystals,'' Philos. Mag., **13**, pp. 305–310.

[5] Benz, K. W., and Dold, P., 2002, ''Crystal Growth Under Microgravity: Present Results and Future Prospects Towards the International Space Station,'' J. Cryst. Growth, **237–239**, pp. 1638–1645.

[6] Selver, R., Kamotani, Y., and Ostrach, S., 1998, ''Natural Convection of a Liquid Metal in Vertical Cylinders Heated Locally From the Side,'' ASME J. Heat Transfer, **120**, pp. 108–114.

[7] Rosenblat, S., 1982, ''Thermal Convection in a Vertical Cylinder,'' J. Fluid Mech., **122**, pp. 395–410.

[8] Neumann, G., 1990, ''Three-Dimensional Numerical Simulation of Buoyancy-Driven Convection in Vertical Cylinders Heated From Below,'' J. Fluid Mech., **214**, pp. 559–578.

[9] Hardin, G. R., Sani, R. L., Henry, D., and Roux, B., 1990, ''Buoyancy-Driven Instability in a Vertical Cylinder: Binary Fluids With Soret Effect. Part 1. General Theory and Stationary Stability Results,'' Int. J. Numer. Methods Fluids, **10**, pp. 79–117.

[10] Garandet, J. P., and Albousiérre, T., 1999, ''Bridgman Growth: Modeling and Experiments,'' Prog. Cryst. Growth Charact. Mater., **38**, pp. 73–131.

[11] Monberg, E., 1994, ''Bridgman and Related Growth Techniques,'' in *Handbook of Crystal Growth*, D. T. J. Hurle, ed., North-Holland, Amsterdam, pp. 52–97.

[12] Cliffe, K. A., Spence, A., and Tavener, S. J., 2000, ''The Numerical Analysis of Bifurcation Problems With Application to Fluid Mechanics,'' Acta Numerica, **9**, pp. 39–131.

[13] Gadoin, E., Le Quere, P., and Daube, O., 2001, ''A General Methodology for Investigating Flow Instabilities in Complex Geometries: Application to Natural Convection in Enclosures,'' Int. J. Numer. Methods Fluids, **37**, pp. 175–208.

[14] Sanchez, J., Marques, F., and Lopez, J. M., 2002, ''A Continuation and Bifurcation Technique for Navier-Stokes Flows,'' J. Comput. Phys., **180**, pp. 78–98.

[15] Gelfgat, A. Yu., 2001, ''Two- and Three-Dimensional Instabilities of Confined Flows: Numerical Study by a Global Galerkin Method,'' Computational Fluid Dynamics Journal, **9**, pp. 437–448.

[16] Gelfgat, A. Yu., and Bar-Yoseph, P. Z., 2004, ''Multiple Solutions and Stability of Confined Convective and Swirling Flows—A Continuing Challenge,'' Int. J. Numer. Methods Heat Fluid Flow, **14**, pp. 213–241.

[17] Baumgartl, J., Budweiser, W., Müller, G., and Neumann, G., 1989, ''Studies of Buoyancy Driven Convection in a Vertical Cylinder With Parabolic Temperature Profile,'' J. Cryst. Growth, **97**, pp. 9–17.

[18] Müller, G., Neumann, G., and Weber, W., 1984, ''Natural Convection in Vertical Bridgman Configuration,'' J. Cryst. Growth, **70**, pp. 78–93.

[19] Wanschura, M., Kuhlmann, H. C., and Rath, H. J., 1996, ''Three-Dimensional Instability of Axisymmetric Buoyant Convection in Cylinders Heated From Below,'' J. Fluid Mech., **326**, pp. 399–415.

[20] Gelfgat, A. Yu., Bar-Yoseph, P. Z., Solan, A., and Kowalewski, T., 1999, ''An Axisymmetry—Breaking Instability in Axially Symmetric Natural Convection,'' Int. J. Transport Phenomena, **1**, pp. 173–190.

[21] Barwölff, G., König, F., and Seifert, G., 1997, ''Thermal Buoyancy Convection in Vertical Zone Melting Configurations,'' ZAMM, **10**, pp. 757–766.

[22] Kaiser, Th., and Benz, K. W., 1998, ''Floating-Zone Growth of Silicon in Magnetic Fields. III. Numerical Simulation,'' J. Cryst. Growth, **183**, pp. 564–572.

[23] Gelfgat, A. Yu., Bar-Yoseph, P. Z., and Solan, A., 2000, ''Axisymmetry Breaking Instabilities of Natural Convection in a Vertical Bridgman Growth Configurations,'' J. Cryst. Growth, **220**, pp. 316–325.

[24] Szmyd, J. S., Jaszczur, M., and Ozoe, H., 2002, ''Numerical Calculation of Spoke Pattern in Bridgman Top Seeding Convection,'' Numer. Heat Transfer, Part A, **41**, pp. 685–695.

[25] Braunsfurth, M. G., and Mullin, T., 1996, ''An Experimental Study of Oscillatory Convection in Liquid Gallium,'' J. Fluid Mech., **327**, pp. 199–219.

[26] Gelfgat, A. Yu., Bar-Yoseph, P. Z., and Yarin, A. L., 1997, ''On Oscillatory Instability of Convective Flows at Low Prandtl Number,'' ASME J. Fluids Eng., **119**, pp. 823–830.
[27] Gelfgat, A. Yu., Bar-Yoseph, P. Z., and Yarin, A. L., 1999, ''Stability of Multiple Steady States of Convection in Laterally Heated Cavities,'' J. Fluid Mech., **388**, pp. 315–334.
[28] Erenburg, V., Gelfgat, A. Yu., Kit, E., Bar-Yoseph, P. Z., and Solan, A., 2002, ''Natural Convection in a Rectangular Cavity With Piece-Wise Heated Vertical Walls: Multiple States, Stability and Bifurcations,'' *Proc. 12th Heat Transier Conf.*, Grenoble, France, pp. 459–464.
[29] Erenburg, V., Gelfgat, A. Yu., Kit, E., Bar-Yoseph, P. Z., and Solan, A., 2003, ''Multiple States, Stability and Bifurcations of Natural Convection in Rectangular Cavity With Partially Heated Vertical Walls,'' J. Fluid Mech., **492**, pp. 63–89.

Numerical Analysis of Natural Convection and Mixing in Two-Fluid Stratified Pools With Internal Heat Sources

A. A. Gubaidullin[1]

B. R. Sehgal
e-mail: sehgal@ne.kth.se
Professor
Fellow ASME

Division of Nuclear Power Safety,
Royal Institute of Technology (KTH),
Drottning Kristinas väg 33 A,
100 44 Stockholm, Sweden

The heat transport in two-layer fluid systems has been investigated numerically for slice-type semicircular pools with internal heat sources. The fixed interface model has been applied to study natural convection in the system of the immiscible fluids. The double-diffusion model has been employed to describe the heat transfer and mixing for the miscible fluids. The numerical results are compared to data measured in the SIMECO experiments. Based on the numerical simulations, the effect of the ratio of the fluid properties has been quantified. The results are of interest for the corium melt coolability in a postulated severe accident scenario in a light water reactor.
[DOI: 10.1115/1.1777578]

Keywords: Computational, Double Diffusion, Heat Transfer, Natural Convection, Stratified

1 Introduction

Research interest in natural convection has been motivated by its relevance in many applications including geophysical, chemical, and nuclear. In particular, thermal convection driven by internal heat sources plays an important role in the post-accident heat removal problem in the event of a core meltdown accident in a nuclear power reactor. The success of in-vessel retention (IVR) severe accident management strategy depends among other factors on the thermal loadings imposed by the convecting melt pool [1,2]. The motivation for this work arises from the results of RASPLAV experiments [3] which show that the melt separation into heavy and light fluids with a jump of uranium and zirconium concentrations at the boundaries may occur for some corium compositions. The melt stratification of its oxidic components affects the thermal convection heat transfer. Thus, its effects on local heat flux distribution and average energy transport must be evaluated.

Much research effort has been directed at the problem of natural convection in a uniform pool with internal heat generation [4]. However, only a few studies have focused on the subject of thermal convection in volumetrically heated stratified layer pool. The first experimental studies of natural convection in a double-layer system with volumetric heat sources, motivated by issues related to the post-accident heat removal in liquid-metal-cooled fast breeder reactors, were reported in 1970s. Fieg [5] investigated the natural convection characteristics of two stratified immiscible liquid layers with an internally heated lower layer. The temperature was maintained equal at the top and bottom boundaries. Heptane and water were used as lighter and heavier liquids, respectively. The important conclusion was that the two layers behaved as if separated by a rigid highly conductive wall. The correlation for the Rayleigh-Bénard convection in the upper layer and that for the lower layer internally heated and bounded by the isothermal walls were applied and the calculated values agreed with the experimental data to within ± 10 percent accuracy. Schramm and Reineke [6] studied experimentally and numerically the natural convection in a rectangular channel filled with two immiscible fluids of different physical properties. No heat flux data were obtained in their experiments. They found that their computational isotherms were quite similar to those observed in their experiments. Kulacki and Nguen [7] studied hydrodynamic instability and thermal convection in a horizontal system of two immiscible fluid layers with internal heat generation in the lower layer. In their study, the systems of heptane-water or silicone oil-water were bounded in a square cavity from below by a rigid, insulated surface and from above, by an isothermal wall. The heat was generated internally in the lower layer. Experimental measurements of transient and steady state convection up to Rayleigh numbers of 10^{11} were obtained. The Nusselt numbers based on the average heat transfer coefficient for different layer thickness ratios were obtained from the experiments and correlated. The uncertainty in the measured Nu and Ra was reported to be less than 5.2 percent. The numerical predictions in the vorticity-stream function formulation for a uniform computational domain of 28×40 were found to be in general agreement with the data. The interface was treated as a semi-solid conducting sheet with interfacial shear transmitted from the lower layer to the upper layer. In addition, simulations were performed with the interface assumed to be hydrodynamically rigid. It was concluded that for either interface, the overall flow pattern was not much affected by the hydrodynamics at the interface. However, predicted Nusselt number for the case of a hydrodynamically rigid interface was about 10 percent lower. Gubaidullin [8] developed two semiempirical correlations that may be employed to evaluate the heat fluxes in a horizontal double layer fluid system with internal heat generation in the lower layer.

Recently, the SIMECO (SImulation of MElt COolability) experimental program [9] was focused to study the effects of density stratification on heat transfer characteristics. A number of tests were performed in a semicircular vessel which is a slice geometry representation of the hemispherical lower head of a PWR such as Westinghouse's AP600 reactor. The system of two immiscible fluids were composed of paraffin oil as the top layer, and water as the lower one [10]. The experiments were conducted for $\mathrm{Ra}\sim10^{13}$, various depth ratios $L_{12}=\{4:26,6:26\}$ with the lower layer heated, and $L_{12}=\{12:14,8:18,4:22\}$ for the case when both layers are heated. The choice of the Rayleigh number was defined by the size of the facility. In the prototypical reactor case the expected Rayleigh numbers are higher ($\mathrm{Ra}\sim10^{15}$–10^{16}).

[1]Present address: Commissariat à l'Energie Atomique (CEA), 17 rue des Martyrs, 38054 Grenoble, France.

Temperature distributions, local and averaged heat fluxes, ratio of energy transferred upwards to downwards, Q_{12} were presented. The presence of an upper layer, heated from within or without heat sources, significantly decreased the upwards heat transfer. The local heat flux peaked below the interface and was found to be greater than that in the corresponding single layer experiments. No dependency on L_{12} was observed for cases of heat generation in the lower layer. No mixing between the two fluids was observed, and the interface did not deform.

Tests employing salt water for the lower layer, and fresh water for the upper layer (miscible fluids) were conducted as well [11]. The density difference between the upper and the lower layer was varied from $\Delta\rho=2$ percent to $\Delta\rho=30$ percent. For $\Delta\rho<5$ percent, a blurred interface was observed, and for $\Delta\rho>5$ percent the interface was defined by a distinct boundary. Mixing time was found to be dependent on $\Delta\rho$ and the heat generation rate. The energy split, Q_{12}, defined as $q_{up}\cdot A_{up}/q_d\cdot A_d$, took values much less than those in the corresponding uniform pool and did not change significantly during quasi-steady state, when partial mixing occurs at the interface and side boundaries. As rapid total mixing occurred between the layers, Q_{12} increased reaching the value for the uniform pool and the temperature of the pool decreased to the values of the corresponding single-layer pool. Temperature distributions, local and averaged heat fluxes, ratio of energy transferred upwards to downwards (sidewards), Q_{12} were measured and the mixing process was recorded on video. Some of these two-layer pool tests were repeated with the two fluids separated at the interface by a thin (about 1 mm) copper plate [12]. The tests were carried out for two different fluid layer combinations, water-water and paraffin oil-water, in order to determine: (1) the effect of a rigid interface on heat transfer, as compared with a case of direct contact between the immiscible layers; (2) the effect of a rigid interface in the of case of water-water, as compared with a diffuse interface in the case of salt water-water; and (3) the effects of different thermophysical property ratios. The experimental values of Q_{12} showed that for the immiscible fluids system (paraffin oil-water), the rigid interface has nearly no effect on heat transfer and the average value of the energy splitting is the same as in the case of direct contact between the two layers. This agrees with the conclusions based on experiments, reported by Haberstroh and Reinders [13] that the thermal convection heat transfer in an oil-water system is not affected when the two layers are separated by a thin conductive plate. In cases of salt water-water versus water-water with separation, the average values of Q_{12} were similar to each other. However, the data scatter around the average values was much more pronounced in the first case. It was concluded that the diffuse interface, prior to complete mixing of the layers, has no significant effect on the average heat transfer characteristics.

No numerical studies on thermal convection in a double-layer system, miscible or immiscible, for case of complex semicircular geometry have been reported so far.

In this paper, computational fluid dynamics (CFD) analyses have been performed to study the natural convection heat transfer in two-layered miscible (salt water-water) and immiscible systems with internal heat generation in a semicircular vessel. The objective of the work is to delineate the effects of stratification and mixing on heat transport in a two-fluid density-stratified pool. We have also performed a parametric study to assess the effect of physical properties on the heat transfer characteristics to complement results obtained from experiments by means of CFD simulations for a range of lower Rayleigh number and to combine the experimental data and the computational results.

In the present study, we do not attempt to provide any reactor assessment by using the obtained numerical results. There are large uncertainties in the current knowledge about related prototypical reactor situations. In fact, reactor conditions involves number of other complicating factors. These include physical chemistry of core melt, radiation heat transfer from the pool top surface, metal layer focusing of heat flux to name but few. These complex issues are not within the scope of this paper.

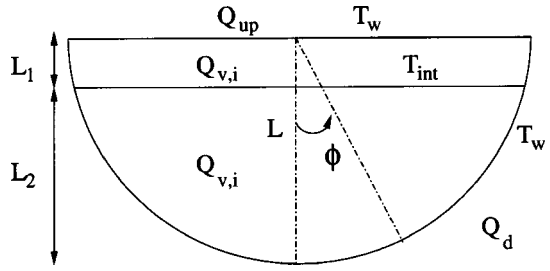

Fig. 1 Problem formulation and boundary conditions employed in CFD simulations

In section 2, two mathematical models for double-layer thermal convection in immiscible system and for double-diffusion are introduced. The description of numerical methods and code are given. Application of the models and results of computations are demonstrated and discussed in section 3. First, heat transport in stratified pools is compared to those in the uniform pool. The role of the nature of interface on the average heat transfer characteristics is investigated in several numerical tests. In the next part, the predictions of SIMECO tests at Rayleigh number lower than those in the tests are described. Results of a parametric study on effects of the upper fluid layer properties and height ratio on heat transfer follows. In the last part of section 3, mixing of two miscible layers is studied. Appropriate dimensionless parameters are identified and their effect on mixing time is investigated. Finally, a summary can be found in section 4.

2 Modeling of Natural Convection in a Double-Layer System

2.1 Fixed Interface Model. We consider the heat transport in two layers of incompressible immiscible fluids with internal heat generation. By ''immiscible'' layers, we assume that fluids composing different layers can not mix at the molecular level and no mass transfer, across the interface, takes place by convection and diffusion. The fluids have separate velocity and temperature fields and exchange momentum and energy through the interface. The liquid-liquid interface is assumed to be horizontal and does not deform. The interfacial forces due to the variations of the surface tension produced by temperature gradients (Marangoni effects) are assumed to be negligible. This approach was used previously in the numerical studies reported in [14–16].

We consider two immiscible fluid layers of depths L_1 and L_2; the upper fluid is designated as 1 and the lower fluid as 2. The fluids are enclosed in a two-dimensional semicircular cavity of radius L. The geometry configuration and the fluid height ratios L_{12} are chosen as in the SIMECO tests. Heat $Q_{v,i}$ is generated volumetrically either in both layers or in the lower layer. Two fluids are bounded by isothermal surface at temperature T_w. No-slip boundary conditions are applied along the rigid walls. Initially, the fluids are quiescent and at uniform temperature. Schematic of the problem and boundary conditions employed are shown in Fig. 1. The Boussinesq approximation is assumed for the buoyancy force. The independent variables are scaled as x/L_2, $\mathbf{u}L_2/\nu_2$, $t\nu_2/L_2^2$, $(T-T_w)/(Q_vL_2^2/k_2)$, $pL_2^2/\rho_2\nu_2^2$. The conservation equations in dimensionless form for fluid 1 are

$$\nabla\cdot\mathbf{u}=0 \tag{1}$$

$$\frac{\partial\mathbf{u}}{\partial t}+(\mathbf{u}\cdot\nabla)\mathbf{u}=-\rho_{12}^{-1}\nabla p+\beta_{12}(\mathrm{Ra}_2/\mathrm{Pr}_2)\Delta T\mathbf{j}+\nu_{12}\nabla^2\mathbf{u} \tag{2}$$

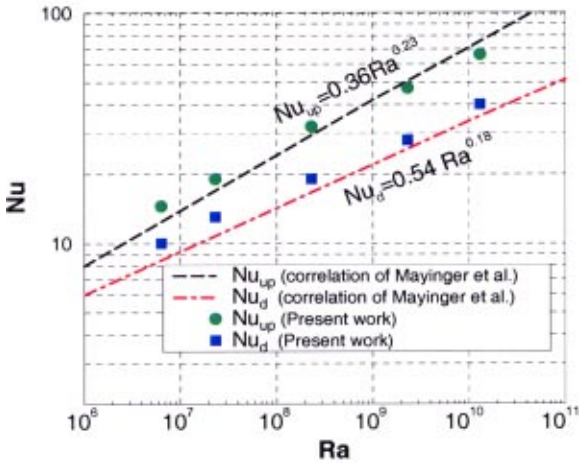

Fig. 2 Variation of the average Nusselt number with the Rayleigh number for a uniform pool

$$\frac{\partial T}{\partial t}+\mathbf{u}\cdot\nabla T=\frac{\alpha_{12}}{\mathrm{Pr}_2}\nabla^2 T+\frac{\alpha_{12}}{k_{12}\mathrm{Pr}_2} \tag{3}$$

and for fluid 2

$$\nabla\cdot\mathbf{u}=0 \tag{4}$$

$$\frac{\partial \mathbf{u}}{\partial t}+(\mathbf{u}\cdot\nabla)\mathbf{u}=-\nabla p+(\mathrm{Ra}_2/\mathrm{Pr}_2)\Delta T\mathbf{j}+\nabla^2\mathbf{u} \tag{5}$$

$$\frac{\partial T}{\partial t}+\mathbf{u}\cdot\nabla T=\frac{1}{\mathrm{Pr}_2}\nabla^2 T+\frac{1}{\mathrm{Pr}_2} \tag{6}$$

$$\begin{gathered}\mu_{12}\cdot\frac{\partial u_1}{\partial y}=\frac{\partial u_2}{\partial y}\\ k_{12}\cdot\frac{\partial T_1}{\partial y}=\frac{\partial T_2}{\partial y}\\ u_1=u_2\\ v_1=v_2=0\\ T_1=T_2\end{gathered} \tag{7}$$

The motion of fluid in a double-layer system not only depends on a Ra and Pr, but also on the ratios of physical properties. With a number of new dimensionless parameters that enter the governing equations, the investigation of the two-layer problem becomes significantly more complicated than that of a single-layer.

2.2 Double-Diffusion Model. The subject of double-diffusive convection had its beginnings in the 1950s with interest in it coming mainly from oceanography. It is concerned with the study of fluids in which there are gradients of two (or more) properties with different molecular diffusivities. Double-diffusive convection has been studied extensively in the environmental sciences [17,18]. Direct simulation of double-diffusive layered convection has been reported in [19,20]. However, a numerical study of double-diffusive convection with internal heat generation has not, to the author's knowledge, been reported so far.

As in the previous part, we consider a semicircular two-dimensional enclosure of radius L bounded by isothermal surfaces ($T=T_w$). Initially, the fresh water layer ($S_1=0$) of depth L_1 rests on the top of the salt water layer of concentration S_2 and the maximum depth L_2. The two-layer system can be destabilized and mixed by heating due to the uniform heat sources Q_v located in both layers and cooling at the boundaries. The nondimensional quantities introduced are defined as $\mathbf{x}=\mathbf{x}/L$, $\mathbf{u}=\mathbf{u}L/\nu$, $t=t\nu/L^2$, $p=pL^2/\rho\nu^2$, $T=(T-T_w)/(Q_vL^2/k)$, $S=(S-S_1)/(S_2-S_1)$. Hence, the conservation equations for the Boussinesq fluid may be written in the following dimensionless form:

$$\nabla\cdot\mathbf{u}=0 \tag{8}$$

$$\frac{\partial \mathbf{u}}{\partial t}+(\mathbf{u}\cdot\nabla)\mathbf{u}=-\nabla p+\mathrm{Ra/Pr}(\Delta T-\lambda_Q\Delta S)\mathbf{j}+\nabla^2\mathbf{u}, \tag{9}$$

$$\frac{\partial T}{\partial t}+\mathbf{u}\cdot\nabla T=\frac{1}{\mathrm{Pr}}\nabla^2 T+\frac{1}{\mathrm{Pr}} \tag{10}$$

$$\frac{\partial S}{\partial t}+\mathbf{u}\cdot\nabla S=\frac{1}{\mathrm{LePr}}\nabla^2 S. \tag{11}$$

where S_1 and S_2 are initial minimum and maximum solute concentrations [wt %]. For the sake of simplicity we have used the same notation for dimensionless parameters as for corresponding dimensional quantities. The new dimensionless parameters are λ_Q, a stability number which is a measure of the ratio of density changes due to the stabilizing effect of the solute stratification divided by the destabilizing effect of internal heating and external cooling, and Le, the Lewis number, which is a ratio of thermal and solute diffusivities. Le and λ_Q are defined as

$$\begin{gathered}\lambda_Q=\frac{\gamma(S_2-S_1)}{\beta Q_v L^2/k}\\ \mathrm{Le}=\frac{\alpha}{D}\end{gathered} \tag{12}$$

2.3 Computational Details. The numerical calculations were performed using the general-purpose CFX-4.1 code[2]. The transport equations are discretized using a conservative finite-difference method with all variables defined at the center of control volumes which fill the physical domain being considered. For most of the present work, if not stated otherwise, third-order accurate CCCT upwind scheme for treatment of the advection term, fully implicit backward difference time stepping procedure and SIMPLEC velocity-pressure coupling have been used [21]. The performance of CCCT scheme has been compared to other numerical schemes available in the code and chosen for its low numerical diffusion [22]. The above described models are implemented into the code by means of the code user FORTRAN routines.

Benchmarking of the Code. The fixed interface model was tested on the two-layer Couette flow benchmark and on the heat conduction problem of two fluids having different conductivities. In addition, the model was validated against the experimental correlation of Kulaki and Nguen [7] in the previous study [23]. For the miscible case, the validation against the experimental data of Bergman and Ungan [24] was made in the earlier study of the two-layer mixing in a rectangular, salt-stratified pool destabilized by heating and cooling on lateral boundaries [22]. Previously, the CFX code was successfully employed in the extensive study of natural convection in single-layer pools with volumetric heat sources [25,26].

Grid Independence Study. The computational mesh is constructed using a multi-block approach. Up to 17 blocks are attached to form the full domain for the fixed interface model. The flow domain is divided in two sub-domains coupled through the boundary conditions at the interface. In order to correctly resolve heat transfer near the interface and isothermally cooled walls, a very dense mesh was used in these regions. An example of grid employed for calculations is given in the appendix, Fig. 14(a). Grid sensitivity tests were performed. Several different grid systems were tested for each model and for each configuration. The

[2]Property of AEA Technology, U.K.

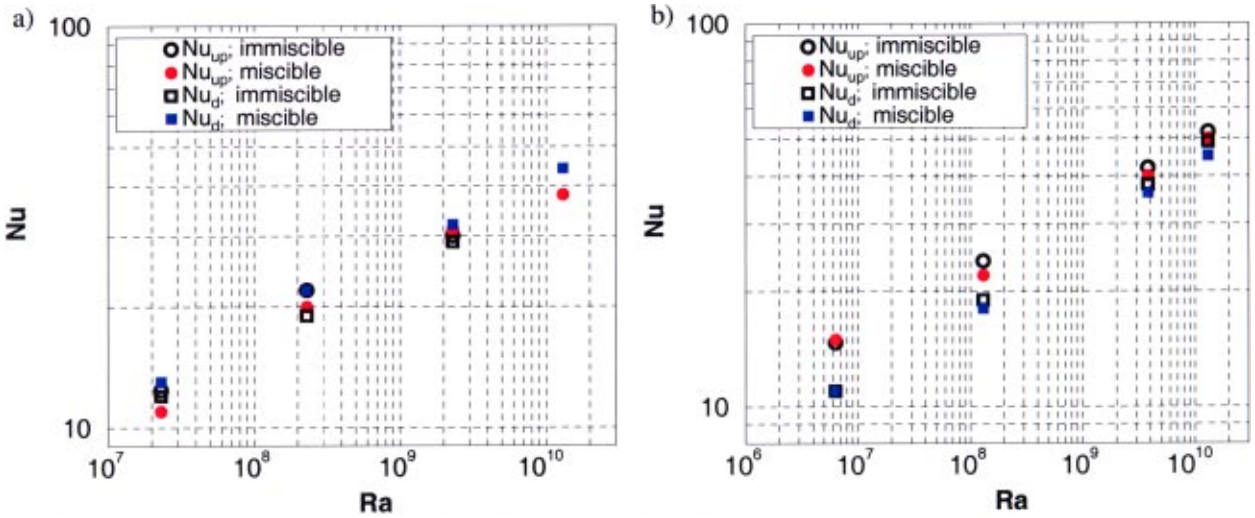

Fig. 3 The mean Nusselt number as a function of the Rayleigh number for (a) $L_{12}=4:22$, Pr=6.5, $Q_{v,1}=Q_{v,2}$; (b) $L_{12}=8:18$, Pr=6.5, $Q_{v,1}=Q_{v,2}$

criterion for the grid choice was the convergence of the value of the mean Nusselt number. An example of the mesh independence study is presented in appendix, Table 1. The grid chosen for simulations of convection of immiscible fluids was about $13\cdot10^3$ nodes. For the double-diffusion model, a typical mesh is presented in appendix, Fig. 14(b). As a result of the grid independence study (Fig. 13), the mesh with about $17\cdot10^3$ nodes was chosen. The time scales of development of the interfacial instabilities and mixing of layers are very short, hence, very small time steps were chosen $\Delta Fo_c < O(10^{-7})$. Eight iterations are performed at each time step to assure the mass balance. In total, each run comprises of about six thousand time steps. The total CPU time for each run in case of miscible layers was of order $O(10^5)$ s on one processor of Cray J90 workstation.

3 Results and Discussion

3.1 Comparison of Convective Heat Transfer in Miscible and Immiscible Fluid Systems. In this part we would like to compare different stratification conditions with immiscible fluids and double diffusive system.

Uniform Pool. The purpose of these single-layer tests is twofold: (1) to benchmark the computational method against well accepted data from the uniform pool case, and (2) to obtain heat transfer data that can be directly compared with the stratified pool cases studied here.

The set of the Navier-Stokes Eqs. (1)–(3) is integrated numerically for $\alpha_{12}=\nu_{12}=\beta_{12}=\rho_{12}=1$ and $L_{12}=0$. The Rayleigh number, Ra, based on the reference value of the radius L is varied from $5\cdot10^6$ to $1.3\cdot10^{10}$ and the Prandtl number Pr=6.5. The time integration is performed until a statistical steady state is achieved. During calculations, the overall energy balance in the pool has been checked. The resulting heat fluxes and, consequently, the overall energy balance exhibits an oscillatory behavior due to turbulence. The amplitude of oscillations increase with the increase of the Rayleigh number, and it is considerably larger on the top surface where intensive turbulent mixing occurs. It should be noted that turbulence in buoyancy-driven flows exhibits itself already at relatively low Rayleigh numbers. The computed flows under consideration are partially turbulent. For higher Rayleigh numbers, it is known that two-dimensional direct simulation (without an additional turbulence model or an application of any kind of wall-functions) of the equations of motion results in underprediction of heat transfer due to strong turbulence [25], and three-dimensional simulation (DNS or "quasi-DNS") is required to represent correctly the turbulent mixing. The available

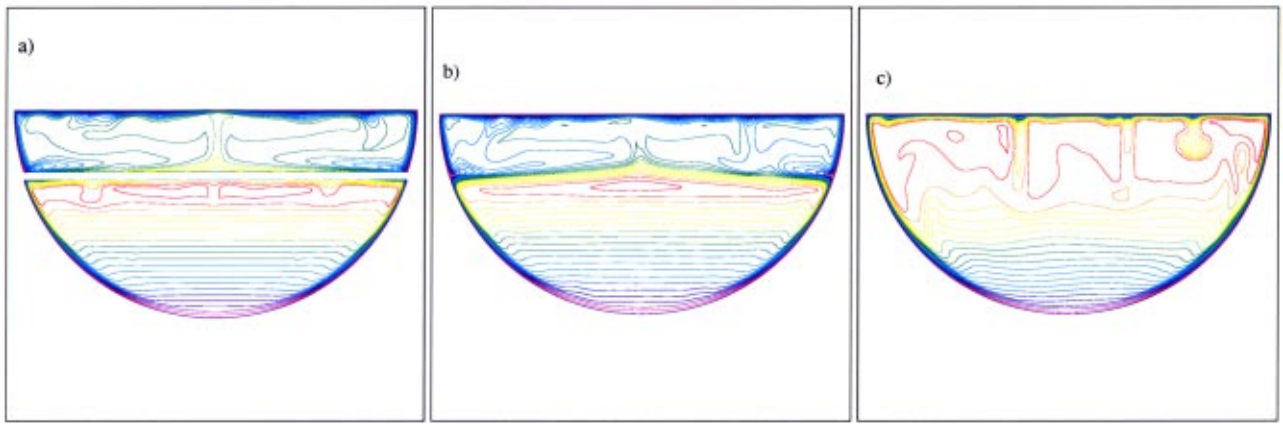

Fig. 4 Normalized with T_{max} isotherm patterns in case of (a) stratified immiscible fluids; (b) stratified miscible fluids ($Ra=1.3\cdot10^{10}$, $Ra_2=2\cdot10^9$, $L_{12}=8:18$, $Q_{v,1}=Q_{v,2}$); (c) one fluid

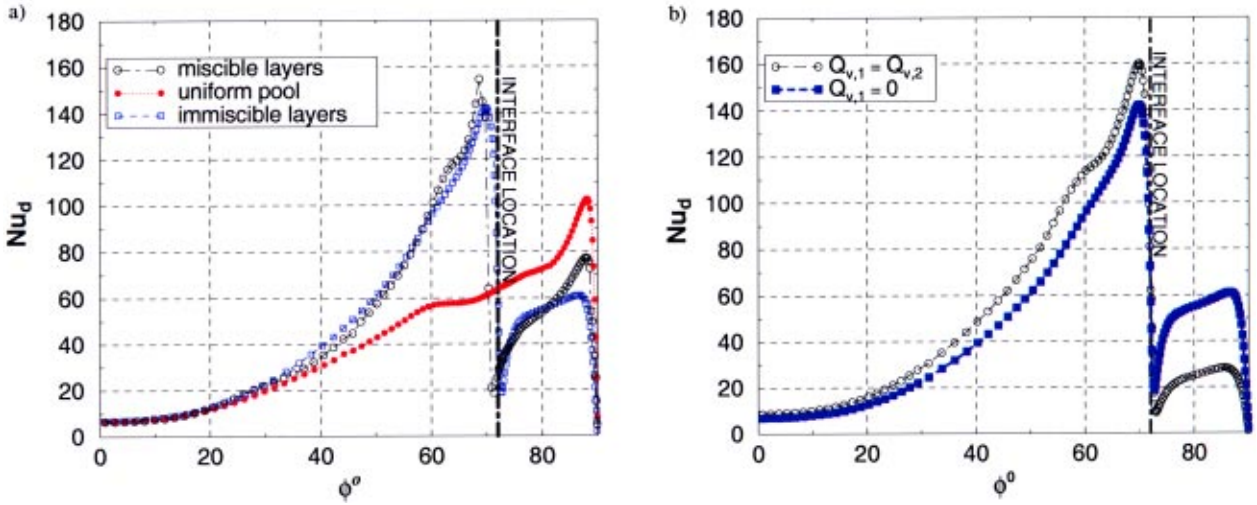

Fig. 5 Variation of the average Nusselt number over the side wall (Ra=2·10⁹, Pr=6.5, L_{12}=8:18): (a) heat generation in both layers; (b) with and without heat generation in the upper layer

turbulence models were critically reviewed in [27]. The application of the Reynolds-averaged Navier-Stokes (RANS) turbulence models (e.g., the two-equation eddy-viscosity $k-\epsilon$ models) to thermal convection in stratified pools at high Ra did not give satisfactory results [27]. Therefore, we have limited our study to the moderate Rayleigh numbers where the two-dimensional direct integration of the Navier-Stokes equations without the additional turbulence model gives reliable results. For the detailed discussion on modeling issues related to thermal buoyant flows, a reader can be addressed to [28,29].

The computed time and space averaged Nusselt numbers are compared with the experimental correlations of Mayinger et al. [30]. The heat fluxes are estimated as $q=k\times\partial T/\partial n$ with the first-order approximation used at the boundary. The computed results presented in Fig. 2 are in good agreement (±15 percent) with experimental data. The computed average values of Q_{12} are about unity, the value obtained from the Mayinger correlation. The value of Q_{12} increases with the increase of the Rayleigh number, i.e., more heat is being transferred upwards. For Ra$\sim 10^{13}$, the correlation gives $Q_{12}\sim 2$, the value measured in uniform pool, water SIMECO tests.

Immiscible Fluid Layers. The set of Eqs. (1)–(6) along with the boundary conditions Eqs. (7) are solved numerically. Two height ratios are considered: L_{12}=4:22 ("thin" layer) and L_{12}=8:18 ("thick" layer). The Rayleigh number, Ra, is varied from $2.3\cdot 10^7$ to $1.3\cdot 10^{10}$. The fluid properties of the top layer fluid are equal to those of the lower layer (Pr=6.5). The heat is generated in both layers.

Miscible Fluid Layers. The set of Eqs. (8)–(11) is solved numerically. Simulations are performed for Pr=6.5, Le=100, and L_{12}=4:22 or L_{12}=8:18. The Rayleigh numbers are taken as in the previous, immiscible layers case. The stability number λ_Q is taken equal to about 0.07 for most of the calculations. For this relatively high value of λ_Q, the system reaches thermal equilib-

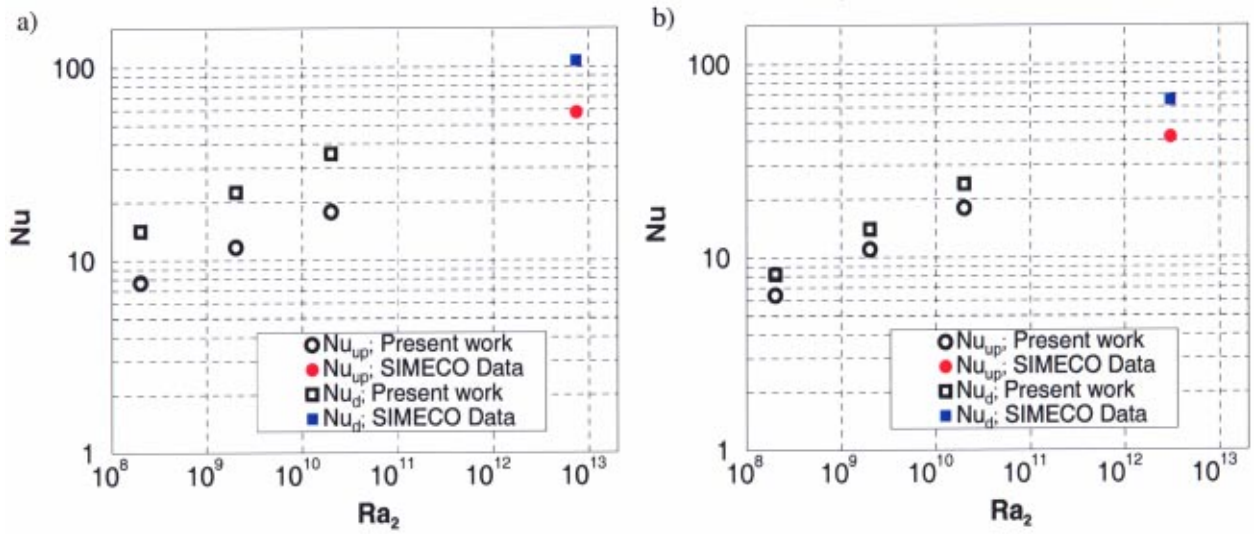

Fig. 6 The mean Nusselt number as a function of the Rayleigh number for (a) L_{12}=4:22, $Q_{v,1}=Q_{v,2}$; (b) L_{12}=8:18, $Q_{v,1}=Q_{v,2}$

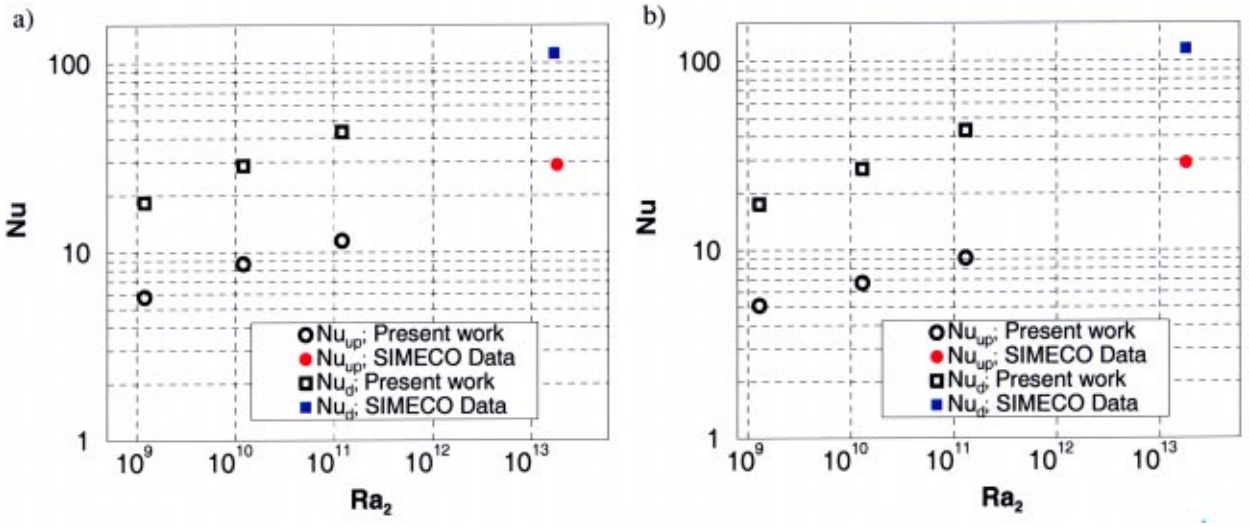

Fig. 7 The mean Nusselt number as a function of the Rayleigh number for (a) $L_{12}=4:26$, $Q_{v,1}=0$; (b) $L_{12}=6:26$, $Q_{v,1}=0$

rium at times corresponding to the Fourier number, $Fo_c \sim O(10^{-3})$ when the mass diffusion effects are negligible and no mixing has occurred. At these times the interface remains sharp and horizontal. In general, the interface stability depends on Ra, the stability number λ_Q and the height ratio L_{12}. It should be recognized that the mixing in a two-layer fluid subjected to shear-free turbulence is a very complex hydrodynamic phenomena [29]. We have addressed the issues associated with the interface stability and mixing in the last part of this study.

We would like to compare the mean heat transfer characteristics in miscible layers with those in immiscible ones. The results of simulations are presented in Fig. 3. The average Nu_{up} is lower and Nu_d is higher in the double-layer system than in the uniform pool. This indicates higher thermal loading on the side walls. The energy splitting, Q_{12}, is mostly affected by fluid stratification. In the miscible case, the average values of $Q_{12}\sim 0.6$ for $L_{12}=4:22$, and $Q_{12}\sim 0.8-0.7$ for $L_{12}=8:18$. In the immiscible case, the mean values of $Q_{12}\sim 0.7$ for $L_{12}=4:22$, and $Q_{12}\sim 0.8-0.7$ for $L_{12}=8:18$. Thus, the fraction of heat released within the layer, that is transferred to the side walls, is significantly greater than that in the uniform pool ($Q_{12}\sim 1.3$ for $Ra\sim 10^{10}$). It is interesting to note that the heat transfer sidewards is not considerably affected by the increase in L_{12}, while the heat transfer upwards is higher for the case of the thicker upper layer. This might be explained (a) the presence of heat sources in the top layer (more heat is being generated within the thicker top layer); and (b) more efficient convective heat transfer mechanism upwards. The comparison of the results for the immiscible and miscible systems demonstrates that there is little difference (less than 10 percent) between the average Nusselt numbers (Fig. 3). Figure 4 presents the computed temperature fields in three different cases. The calculated flow field in case of stratified fluids, both immiscible and miscible, can be separated into three distinct regions. The flow pattern in the upper layer resembles the one typical for the Rayleigh-Bénard convection regime. The flow field in the bottom layer include: (1) inverted thermals descending from the interface whose temperature is lower than that of the lower core region. This creates a relatively well-mixed unstably-stratified convection-dominated region in the upper part of the bottom layer; (2) a steep boundary layer descending down along the curved side wall; and (3) a stably-stratified conduction-dominated lower pool. In miscible system, there is a thin layer of quiescent diffused interface. The heat transfer in this layer is mainly by conduction. Since the interface temperature is higher than T_w and, as a result, the inverse temperature gradients are lower, the thickness of the unstably-

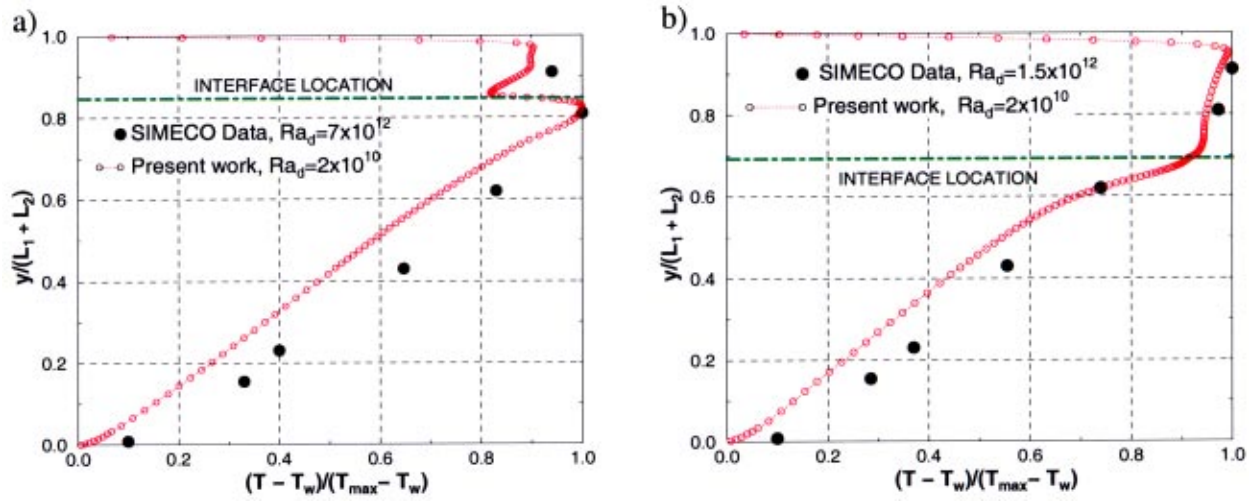

Fig. 8 Time average centerline temperature distributions for (a) $L_{12}=4:22$, $Q_{v,1}=Q_{v,2}$; (b) $L_{12}=8:18$, $Q_{v,1}=Q_{v,2}$

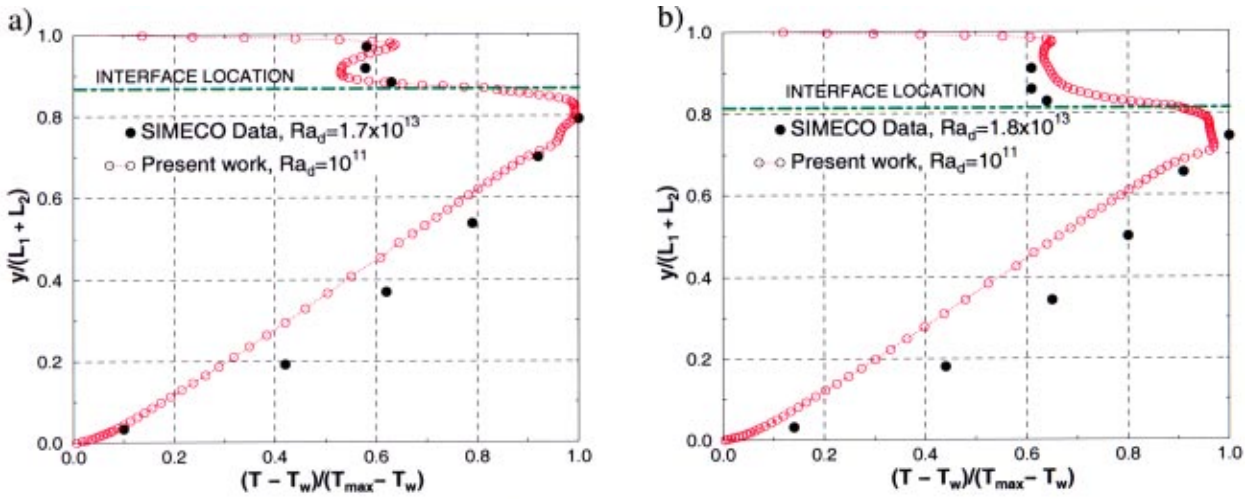

Fig. 9 Time average centerline temperature distributions for (a) $L_{12}=4:26$, $Q_{v,1}=0$; (b) $L_{12}=6:26$, $Q_{v,1}=0$

stratified region in the double-layer fluid is considerably smaller than the one in the uniform pool. Figure 5 presents the angular distribution of the local Nusselt number at the side vessel wall. The side wall heat flux gradients over the interface are less sharp in the miscible system due to the diffused nature of the interface. It can be seen that in the stratified pool the thermal load differs dramatically from the one-fluid pattern. The heat flux increases with angle ϕ. However, it reaches its maximum value in the region just below the interface. As ϕ passes through ϕ_{int}, the heat flux abruptly decreases reaching its minimum value at the interface. In the top layer, the heat flux increases to its local maximum close to the upper wall and decreases soon after to zero value. This behavior reflects the development of the boundary layer on the side wall interrupted by a stagnation point of the interface intersection with the side wall. The instantaneous local Nusselt number distribution at the side wall is practically identical for cases of miscible and immiscible fluids (Fig. 5(a)), i.e., the nature of the kinematically stable, diffused interface seems to play little role in determining the heat transfer characteristics at times $\text{Fo}_c \ll 1$. The presence of the heat sources does not seemingly affect the heat transfer sidewards in the lower layer (Fig. 5(b)).

3.2 Computations for the SIMECO Tests Configurations The objective of these numerical experiments is to perform a parametric study to assess the effect of physical properties on the heat transfer characteristics as well as to complement results obtained from the SIMECO experiments by means of CFD simulations for a range of lower Rayleigh numbers and to combine the experimental data and the computational results to cover a greater range of Ra numbers. Simulations are performed for the double-layer immiscible system. Two cases are considered: the case of heat generation in both layers ($L_{12}=4:22$ or $L_{12}=8:18$), and the case of heat sources in the bottom layer ($L_{12}=4:26$ or $L_{12}=6:26$). The physical properties of the bottom layer fluid taken are those of water and the properties of the top layer fluid are those of paraffin oil. The conductivity and the viscosity ratios of two fluids are $k_{12}=1:3$ and $\mu_{12}=20$. The Prandtl numbers are $\text{Pr}_1=370$, $\text{Pr}_2=4$. The Rayleigh number based on the lower layer properties, Ra_2, ranges from 10^9 to 10^{11}.

The computed and experimental mean Nusselt numbers are presented in Figs. 6 and 7. It can be seen that the extrapolation of the predicted Nusselt numbers result in values consistent with those measured in the experiments. The time-averaged centerline temperature profiles are presented in Figs. 8 and 9. The experimental values were obtained from time-averaged measurements with thermocouple probes located at the centerline of the pool. These normalized values are compared to the numerical results for lower Rayleigh numbers. The deviation in the experimental values from the computed linear profile is likely to be due to the fluid motion present in the lower layer at much higher Rayleigh number in the

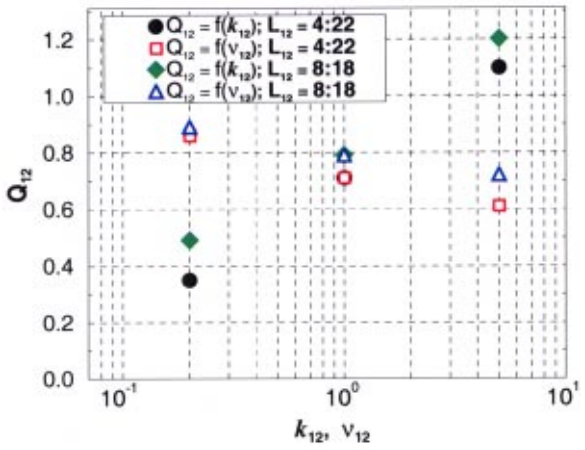

Fig. 10 Effect of upper layer physical properties on Q_{12} ($Q_{v,1}=Q_{v,2}$)

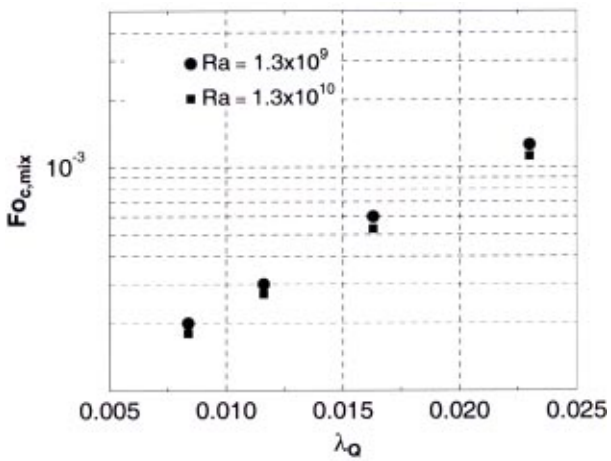

Fig. 11 Predicted mixing times

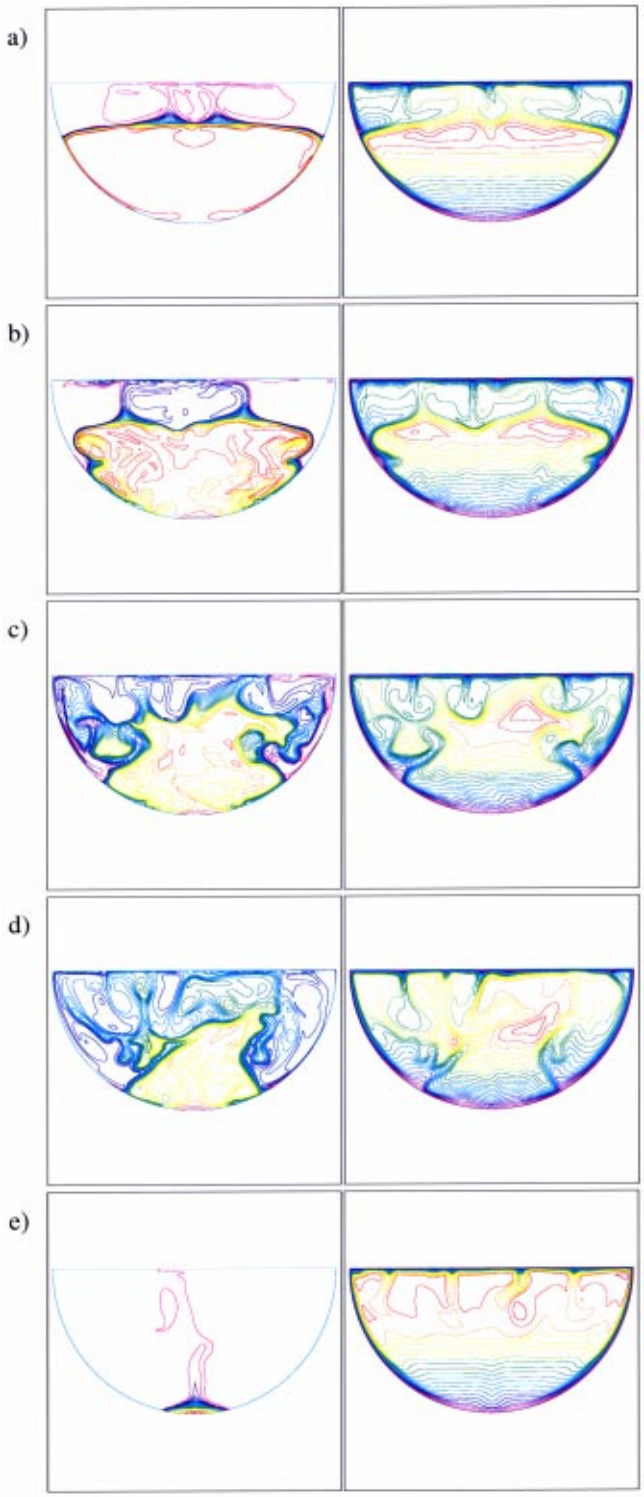

Fig. 12 Concentration (left-hand column) and temperature (right-hand column) fields for $Ra=1.3\cdot10^9$, $\lambda_Q=2.33\cdot10^{-2}$ (a) $Fo_c=8.3\cdot10^{-4}$, $S_{max}=1.0$; (b) $Fo_c=10\cdot10^{-4}$, $S_{max}=0.99$; (c) $Fo_c=11.5\cdot10^{-4}$, $S_{max}=0.98$; (d) $Fo_c=12.8\cdot10^{-4}$, $S_{max}=0.96$; (e) $Fo_c=14.2\cdot10^{-4}$, $S_{max}=0.94$

tests. The temperature distribution in the lower layer is almost linear in all cases and indicates that fluid is stably stratified in the region. Both computed and experimental values show a sharp gradient across the interface. For the case of heat generation in the lower layer, the profiles in the upper layer are typical for those of Rayleigh-Bénard convection.

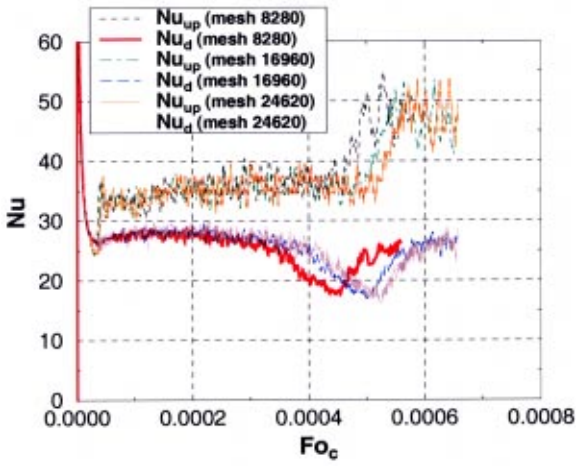

Fig. 13 Transient average Nusselt numbers for $Ra=1.3\cdot10^9$, $\lambda_Q=1.16\cdot10^{-2}$

3.3 Effect of the Upper Layer Physical Properties. In general, the heat transfer in a multilayered system depends on a multitude of parameters such as ratios of thermophysical properties, layers thickness, heat generation rates, etc. The correlation between the energy split and the thermophysical parameters of interest is not known for a semicircular geometry as it was obtained for a rectangular case [12]. Therefore the assessment of the effect of properties at a specified thickness ratio of the layers by means of CFD is desirable. We would like to determine the effect of the key parameters, i.e., conductivity and viscosity ratios k_{12}, μ_{12}, on the heat transfer process for stratified layers. The values of k_{12} and μ_{12} considered are 5:1, 1:1, 1:5. The Rayleigh number Ra_2 is chosen equal to $1.2\cdot10^{10}$. The simulations are performed for two configurations of $L_{12}=4:22$ and $L_{12}=8:18$ and same heat generation rate in both layers. Figure 10 presents the effect of different k_{12} and μ_{12} on the mean energy split Q_{12}. A strong dependency of Q_{12} on k_{12} can be observed. For cases of $k_{12}\leqslant1$, the upper layer introduces additional thermal resistance and thus, decreases heat transferred upwards. Again, Q_{12} is higher for the thicker layer due to the heat sources present in the upper layer. The maximum value of side wall heat flux can be much higher than in the corresponding uniform pool case and is located right below the interface. The effect of viscosity is less significant. Lower viscosity in the upper layer increases the convection intensity and the heat transfer. The difference in Q_{12} for $\mu_{12}=5:1$ and 1:5 is about 30 percent.

3.4 Mixing of Double-Layer Salt-Stratified System. In this part, we would like to perform the numerical analysis for a layered salt-stratified system, destabilized and mixed, by internal heating. The purpose of these calculations is to delineate the effect of the Rayleigh number, Ra, and the stability ratio, λ_Q, on mixing time $Fo_{c,mix}$ of the layers. Calculations are performed for Le=100, Pr=6.5, $Ra=1.3\cdot10^9$, and $L_{12}=8:18$. Different values of λ_Q are considered. In the absence of convective motion the layers are mixed in times $Fo_{c,mix}\sim O(1)$. It is practically impossible to cover computationally the whole range of mixing times from the minimum value which corresponds to an almost homogeneous pool upto the case of mixing due to diffusion only. Besides computational expense and the problems associated with numerical diffusion which may affect the results of the simulations, there could be different regimes of mixing depending on values of Ra, λ_Q, Fo_c. Here, we consider only such initial parameters that the mixing of layers occurs in times $Fo_{c,mix}\ll1$. More precisely we consider mixing which may occur in times less than $Fo_{c,mix}<10^{-3}$ which corresponds to few hours for a pool of characteristic size

$L \sim 10^{-1}$ m. The density difference due to salinity was varied between 0.5 percent and 2 percent. We define the mixing time, $Fo_{c,mix}$, as the time that corresponds to a sudden increase in heat transfer.

The results of simulations are presented in Fig. 11. As expected, the mixing time increases with increase of λ_Q. For λ_Q values smaller than $3 \cdot 10^{-2}$ which corresponds to initial density difference of about 2 percent the mixing of the layers was not achieved in times $Fo_{c,mix}$ less than $O(10^{-3})$. The interface, for these cases, remained almost horizontal. Once thermal equilibrium has been reached, the average heat transfer characteristics do not change in the time period considered. The dynamics of mixing is depicted in Fig. 12. The convecting cells in both layers cause the formation of cusps at the interface. The interface adjacent to the cooled walls moves downwards. The quasi-steady state, when thermal equilibrium has been achieved, can be attained prior to mixing depending on the value of λ_Q for a given Ra. Fluid, flowing down along the side boundaries, penetrates the diffusive interface trapping the hot core region below the interface from the sides and at some point the interface is ruptured. As energy is released from the core region, the heat transfer upwards increases to its maximum value and the mixed system is approaching quasi-steady state rapidly. The partially unmixed salt region accumulates at the bottom of the vessel. The time- and space-averaged Nusselt numbers of the system in the mixed state are in good agreement (± 15 percent) with the experimental correlations of Mayinger et al. [30]. The transient Nusselt number is presented in Fig. 13. The quasi-steady state prior to mixing is clearly observed. The jump in Nu_{up} indicates the break-up of the trapped core region with subsequent energy release to the upper boundary.

4 Conclusions

CFD analysis has been performed to study the effect of fluid stratification on heat transport in two-layer pools. Miscible and immiscible fluid systems are considered. The liquid-liquid interface in immiscible fluids is assumed to be horizontal and nondeformable (fixed interface model). Computations are performed for the complex semicircular geometry for Rayleigh numbers up to 10^{11}.

Both fixed interface and double-diffusion models are applied to investigate natural convection phenomena in semicircular pools. Calculations have been performed for the cases of ''thin'', 4:22, and ''thick'', 8:18, upper layers with heat sources either in only the lower layer or in both layers. The comparison of the results for the immiscible and miscible systems before mixing demonstrates that there is little difference (less than 10 percent) between the average Nusselt numbers. Both fixed interface and double-diffusive models provided almost the same local Nusselt number distribution on the side wall. The side wall heat flux gradient over the interface is less sharp in the miscible system due to the diffuse nature of the interface. The local and the average Nusselt numbers are presented and compared to those of uniform pools. The results of CFD simulations show that the maximum value of the downward heat flux can be much higher in the stratified pool than in the corresponding case of a uniform pool. The average upward Nusselt number is lower, and the average downward Nusselt number is higher, for the double-layer system than for the uniform pool.

The simulations are conducted for a paraffin oil-water system, and results are compared to data obtained in the SIMECO experiments. Different layers depth ratios, L_{12}, were considered: {4:22,8:18,4:26,6:26}. The major trends in the vessel wall heat flux and temperatures can be predicted by the CFD model. A case of heat generation in both layers is considered also and the fluid properties of the upper layer are varied parametrically. The energy splitting was found to be strongly dependent on the conductivity ratio. The dependence on the viscosity ratio is weak.

A numerical analysis is performed for a two-layer salt-stratified system, destabilized and mixed by internal heating in a semicircular vessel. The motion of the initially planar interface between the two stably stratified layers of fluid is computed once the convection began. The development of interfacial instabilities leading to a rapid mixing of the layers is predicted. The shape of the interface during mixing becomes highly nonlinear and is characterized by multiple vortices. The physical mechanisms responsible for the mixing of the stratified layers in an internally-heated system are elucidated.

We believe that the present study is the first attempt to describe different stratification conditions with immiscible fluids and double-diffusive system in semicircular cavities with internal heat generation.

Nomenclature

A = surface area, m^2
C = constant
$c_{p,ij}$ = ratio of *i*-layer to *j*-layer specific heat
D = solute diffusivity, m^2/s
Fo_c = Fourier number, $Fo_c = t \cdot D/L^2$
$\mathbf{i}, \mathbf{j}, \mathbf{k}$ = unit vectors in *x*, *y*, *z* directions
k = heat conductivity, W/m·K
k_{ij} = ratio of *i*-layer to *j*-layer conductivity
L = total height of the pool, m
L_{ij} = ratio of *i*-layer height to *j*-layer height
Le = Lewis number, $Le = \alpha/D$
$\mathbf{n}$ = normal vector
Nu_{up} = mean Nusselt number at the upper surface, $Nu_{up} = q_{up}L/k_2\Delta T$
Nu_d = mean Nusselt number at the curved surface, $Nu_d = q_d L/k_2 \Delta T$
Pr = Prandtl number, $Pr = \nu/\alpha$
p = dynamic pressure, N/m^2
Q = heat transfer rate, W
Q_v = volumetric heat generation rate, W/m^3
Q_{12} = mean ratio of heat transferred upwards to heat transferred downwards or sidewards
q = heat flux, W/m^2
Ra = internal Rayleigh number, $Ra = g\beta Q_v L^5/\nu\alpha k$
Ra_2 = Rayleigh number based on the reference values of the lower layer
S = solute concentration
T = temperature, K
t = time, s
$\mathbf{u}$ = velocity vector, m/s
(x,y,z) = Cartesian coordinates, m
x_i = coordinate, *i*, m

Greek

β = coefficient of thermal expansion, $-1/\rho_0 \partial\rho/\partial T$, 1/K
β_{ij} = ratio of *i*-layer to *j*-layer coefficient of thermal expansion
γ = coefficient of fractional expansion due to solute
δ_t = thermal boundary layer thickness, m
Δ = difference between two values of some parameter
λ_Q = stability number, $\lambda_Q = \gamma\Delta S/\beta Q_v L^2/k$
μ_{ij} = ratio of *i*-layer to *j*-layer dynamic viscosity
∇ = vector operator, $\nabla = \mathbf{i}\partial/\partial x + \mathbf{j}\partial/\partial y + \mathbf{k}\partial/\partial z$
ρ_{ij} = ratio of *i*-layer to *j*-layer density

Subscripts

1 = top layer
2 = lower layer
exp = experimental
comp = computational, computed
corr = correlation
d = related to the curved or lower surface
int = interface
max = maximum
up = related to the upper surface
w = wall

List of Acronyms

LWR = Light Water Reactor
PWR = Pressurized Water Reactor
RPV = Reactor Pressure Vessel
SIMECO = SImulation of MElt COolability
SIMPLE = Semi-Implicit Method for Pressure Linked Equations.

Appendix

Table 1 Example of the mesh sensitivity test ($L_{12}=4:26$, $Ra_2=1.2\times10^{11}$)

Mesh	Number of blocks	Number of nodes	Nu_d	Nu_{up}
1	7	4685	36	12
2	12	8358	39	10
3	17	13,696	43	9
4	17	15,768	43	9

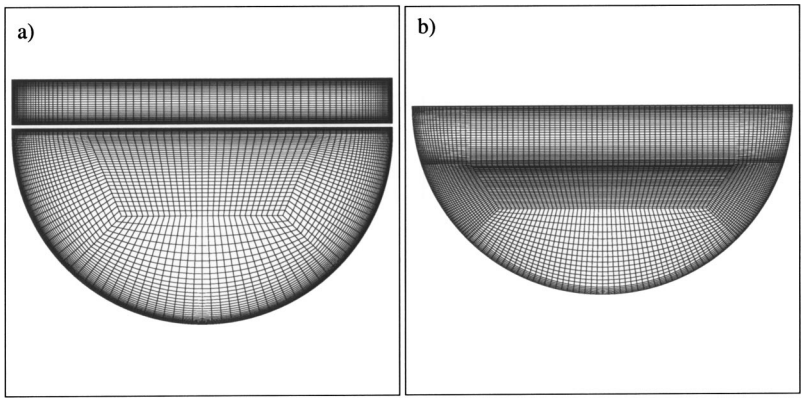

Fig. 14 Computational domain of semicircular cavity for (a) immiscible layers ($L_{12}=6:26$); (b) miscible layers ($L_{12}=8:18$)

References

[1] Theofanous, T. G., Liu, C., Additon, S., Angelini, S., Kymaelaeinen, O., and Salmassi, T., 1997, ''In-Vessel Coolability and Retention of a Core Melt,'' Nucl. Eng. Des., **169**, pp. 1–48.
[2] Tuomisto, H., and Theofanous, T. G., 1994, ''A Consistent Approach to Severe Accident Management,'' Nucl. Eng. Des., **148**, pp. 171–183.
[3] Asmolov, V., Ponomarev-Stepnoy, N., Strizhov, V., and Sehgal, B. R., 2001, ''Challenges Left in the Area of In-Vessel Melt Retention,'' Nucl. Eng. Des., **209**, pp. 87–96.
[4] Dhir, V. K., 1997, ''Heat Transfer From Heat-Generating Pools and Particulate Beds,'' Adv. Heat Transfer, **29**, pp. 1–57.
[5] Fieg, G., 1976, ''Experimental Investigation of Heat Transfer Characteristics in Liquid Layers With Internal Heat Sources,'' *Proc. Int. Meet. on Fast Reactor Safety and Related Physics*, USERDA Conf. 761001, pp. 2047–2055.
[6] Schramm, R., and Reineke, H. H., 1978, ''Natural Convection in a Horizontal Layer of Two Different Fluids With Internal Heat Sources,'' *Proc. 6th Int. Heat Transfer Conf.*, **2**, Paper NC-20, National Research Council of Canada.
[7] Kulacki, F. A., and Nguen, A. T., 1981, ''Hydrodynamic Instability and Thermal Convection in a Horizontal Layer of Two Immiscible Fluids With Internal Heat Generation,'' NUREG/CR-2619 Report.
[8] Gubaidullin, A. A., 2003, ''Correlations for Natural Convection Heat Transfer in Two-Layer Fluids With Internal Heat Generation,'' Int. J. Heat Mass Transfer, **46**, pp. 3935–3940.
[9] Sehgal, B. R., Bui, V. A., Dinh, T. N., Green, J. A., and Kolb, G., 1998, ''SIMECO Experiments on In-Vessel Melt Pool Formation and Heat Transfer With and Without a Metallic Layer,'' NEA/CSNI/R(98)18, Proc. OECD/CSNI Workshop on In-Vessel Core Debris Retention and Coolability, Garching, Germany.
[10] Kolb, G., Theerthan, S. A., and Sehgal, B. R., 2000, ''Natural Convection in Stable Stratified Layers With Volumetric Heat Generation in the Lower Layer,'' CD Proc. 34th National Heat Transfer Conf., Aug. 20–22, Pittsburgh, PA.
[11] Theerthan, S. A., Kolb, G., and Sehgal, B. R., 2001, ''Double-Diffusive Convection in a Semicircular Slice With Internal Heat Generation in One or Both Layers,'' Exp. Heat Transfer, **14**(4), pp. 283–297.
[12] Gubaidullin, A. A., 2002, ''Natural Convection Heat Transfer in Two-Fluid Stratified Pools With Internal Heat Sources,'' Ph.D. thesis, Royal Institute of Technology (KTH), Stockholm, Sweden.
[13] Haberstroh, R. D., and Reinders, R. D., 1974, ''Conducting-Sheet Model for Natural Convection Through a Density-Stratified Interface,'' Int. J. Heat Mass Transfer, **17**, pp. 307–311.
[14] Simonovskii, I. B., 1979, ''Numerical Investigation of Convection in a System of Two Immiscible Fluids Heated From Below,'' Convection Flows and Hydrodynamic Stability, Sverdlovsk (in Russian).
[15] Prakash, A., and Koster, J. M., 1996, ''Steady Rayleigh-Bénard Convection in Two-Layer System of Immiscible Liquids,'' ASME J. Heat Transfer, **118**, pp. 366–373.
[16] Koster, J. M., and Nguen, K., 1996, ''Steady Natural Convection in a Double Layer of Immiscible Liquids With Density Inversion,'' Int. J. Heat Mass Transfer, **39**(3), pp. 467–478.
[17] Huppert, H. E., and Turner, J. S., 1981, ''Double-Diffusive Convection,'' J. Fluid Mech., **106**, pp. 299–329.
[18] Gebhart, B., Jaluria, Y., Mahajan, R. L., and Sammakia, B., 1988, *Buoyancy-Induced Flows and Transport*, Springer, Chap. 9.
[19] Wirtz, R. A., 1976, ''The Effect of Solute Layering on Lateral Heat Transfer in an Enclosure,'' Int. J. Heat Mass Transfer, **20**, pp. 841–846.

[20] Hyun, M. T., and Bergman, B. L., 1995, ''Direct Simulation of Double-Diffusive Layered Convection,'' ASME J. Heat Transfer, **117**, pp. 334–339.
[21] CFDS-FLOW3D, 1994, Release 3.3, User Manual.
[22] Gubaidullin, A. A., and Sehgal, B. R., 2000, ''Numerical Analysis of Mixing in a Double-Diffusive System,'' CD Proc. 34th ASME National Heat Transfer Conference, Aug. 20–22, Pittsburgh, PA.
[23] Gubaidullin, A. A., and Sehgal, B. R., 2001, ''Numerical Analysis of Natural Convection in a Double-Layer Immiscible System,'' CD Proc. 9th International Conference on Nuclear Engineering (ICONE-9), April 8-12, Nice, France.
[24] Bergman, B. L., and Ungan, A., 1988, ''A Note on Lateral Heating in a Double-Diffusive System,'' J. Fluid Mech., **194**, pp. 175–186.
[25] Nourgaliev, R. R., Dinh, T. N., and Sehgal, B. R., 1997, ''Effect of Fluid Prandtl Number on Heat Transfer Characteristics in Internally Heated Liquid Pools With Rayleigh Numbers up to 10^{12},'' Nucl. Eng. Des., **169**, pp. 165–184.
[26] Nourgaliev, R. R., and Dinh, T. N., 1997, ''An Investigation of Turbulence Characteristics in an Internally Heated Unstably Stratified Fluid Layer,'' Nucl. Eng. Des., **178**, pp. 235–258.
[27] Dinh, T. N., and Nourgaliev, R. R., 1997, ''Turbulence Modeling for Large Volumetrically Heated Liquid Pools,'' Nucl. Eng. Des., **169**, pp. 131–150.
[28] Hanjalić, K., 2002, ''One-Point Closure Models for Buoyancy-Driven Turbulent Flows,'' Annu. Rev. Fluid Mech., **34**, pp. 321–347.
[29] Turner, J. S., 1968, ''The Coupled Turbulent Transport of Salt and Heat Across a Sharp Density Interface,'' Int. J. Heat Mass Transfer, **8**, pp. 759–767.
[30] Mayinger, F., Jahn, M., Reineke, H. H., and Steinbrenner, V., 1976, ''Examination of Thermal-Hydraulic Processes and Heat Transfer in a Core Melt,'' BMFT RS 48/1, Institut für Verfahrenstechnik der T. U., Hanover FRG.

A Computational Study on Flame-Solid Radiative Interaction in Flame Spread Over Thin Solid-Fuel

Amit Kumar

Kevin Tolejko

James S. T'ien

Department of Mechanical and Aerospace Engineering,
Case Western Reserve University,
Cleveland, OH 44106

A detailed, two-dimensional, laminar, flame spread model over a thin solid is solved in both a normal gravity downward spread configuration and in a microgravity quiescent atmosphere configuration. The radiation transfer equation is solved using discrete ordinates methods. While flame radiation plays only a secondary role in normal gravity spread, it is crucial in microgravity. By using the solid fuel total emittance and total absorptance as parameters, systematic computations have been performed to isolate the roles of flame radiative loss to the ambient, absorption of flame radiation by the solid and solid emission. Computations show that depending on the values of the solid radiation parameters, trend reversals in spread rate and extinction limits between flames in normal gravity and in microgravity can occur. [DOI: 10.1115/1.1773196]

Keywords: Flame, Heat Transfer, Microgravity, Modeling, Radiation

Introduction

Flame spread over a solid fuel can be described as a diffusion flame propagating parallel to a solid fuel surface. The flame is formed by a reaction between oxygen in the atmosphere and fuel vapor, which originates at the solid fuel surface and diffuses into the surroundings. A part of the thermal energy released by the flame from the chemical reactions heats up the solid ahead of the flame and also pyrolyzes the solid into fuel vapor. When enough fuel vapor blends with the air, a combustible mixture is formed and the flame advances across the surface.

Traditionally, flame spread over solids is classified (based on flow direction relative to the flame) as opposed-flow spread, where the flame spreads against the flow direction, or concurrent flow spread, where the flame spreads in the direction of the flow. The flow can be buoyancy induced, forced or a combination of both. In purely buoyant flows, the downward flame spread is an opposed-flow spread. The purely forced case can only be achieved in zero gravity (0g) or microgravity (μg) (for the purpose of this work we will use these two terms interchangeably). An interesting special case of opposed-flow flame spread in μg is the self-propagation of the flame in a quiescent atmosphere where there is no external flow with respect to the laboratory coordinates. However, since the flame is spreading, the spread rate is itself the relative convective velocity between the flame and the ambient atmosphere. In flame-fixed coordinates, this yields the limiting case of opposed flame spread in a forced flow situation.

The flame-spread rate in an opposed-flow is primarily controlled by heat transfer forward to the unburnt solid fuel. As illustrated in Fig. 1, the solid consists of two zones: a pyrolysis zone (l_p), where the fuel vapor is produced, and a preheat (stabilization) zone (l_{ph}), where the flame transfers heat upstream to the unburnt solid. In the preheat zone, both stream-wise and cross-stream heat and mass transfer are important. Therefore, the governing differential equations are elliptic. To be consistent with the heat and mass transfer treatment, the momentum equations must be the full Navier-Stokes equations. In the opposed-flow flame spread, the preheat zone coincides with the flame stabilization zone. Here the gaseous reaction is initiated (with respect to the upstream oxygen flow). By including finite-rate chemical kinetics and by resolving the structure of this zone, flame-spread limits can be analyzed.

Heat transfer takes place in the gas-phase by the mechanisms of conduction, convection and radiation. In the solid, the heat transfer is mostly by conduction and solid radiation. Conduction in thermally thin solids is not a rate-controlling process, and classical analysis has focused mostly on the gas-phase conduction/convection mechanism [1]. Radiation becomes important in flame spread in microgravity (μg) because of the reduction of convection [2–7]. While radiant emission from a hot solid serves as a heat loss mechanism, the flame (gas-phase) radiation has at least two contributions: one as a heat loss mechanism to the ambient and other as a heat feedback mechanism to the solid fuel. The interaction of flame radiation with the solid can be complex, depending on the solid radiation properties. There are relatively few studies of flame spread that account for flame radiation. In opposed flame spread modeling, Bhattacharjee, Altenkirch and their collaborators [3,4,8] included flame radiation in their model. Comparisons of their modeling results with space experiments support the importance of radiation in microgravity. Lin and Chen [9] also included a radiation model in their downward flame spreading computations in reduced gravity.

One of the difficulties of including flame radiation in the combustion problem is that the gas radiation, which even by itself is a very complex process, is coupled to the reactive flow and the solid pyrolysis process. In addition, gas radiation is spectral. The gas-phase radiatively participating species include the combustion product gases (CO_2 and H_2O), fuel vapor, and possibly soot (however, in certain flames in microgravity, soot is practically absent [10,11]). Although it is now possible to use spectral analyses, such as the narrow-band model [12], in computing one-dimensional flames their adoption to this class of coupled multi-dimensional flame problems is still computationally prohibitive. Furthermore, in the combustion of most solid fuels the detailed thermal decomposition and gas-phase reactions are not well understood and therefore empirical one-step kinetic models are often used. To be compatible in the sense of overall accuracy, a radiation model using mean absorption coefficients is adopted. The details on how the mean absorption coefficients are determined will be described later.

Contributed by the Heat Transfer Division for publication in the JOURNAL OF HEAT TRANSFER. Manuscript received by the Heat Transfer Division February 28, 2003; revision received March 17, 2004. Associate Editor: S. T. Thynell.

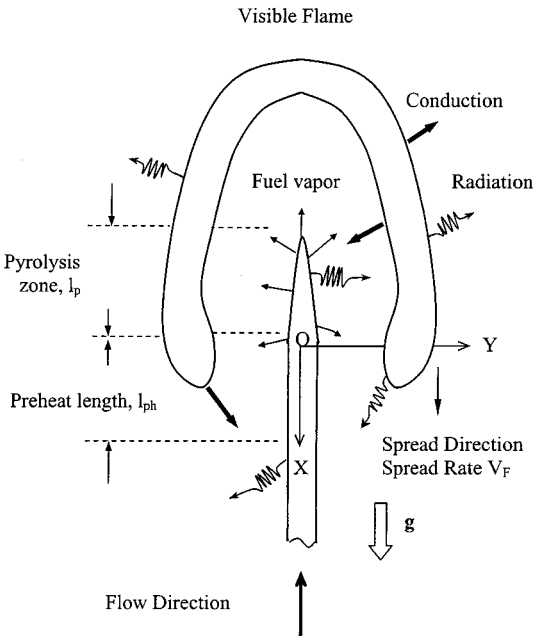

Fig. 1 Schematic of opposed (downward/self-propagating) flow spreading flame

The purposes of this study are to use a two-dimensional, laminar, opposed-flow flame spreading model with flame radiation to: (1) compare the characteristics of self-propagating flames in μg with the downward propagating flames in normal gravity (1g); and (2) investigate the nature of flame-solid radiative interaction by parametrically varying the solid radiation properties and by turning flame radiation in the model on and off to guide further modeling improvements as well as experiments for the determination of physicochemical and radiative properties.

Model Description

The present numerical model of opposed-flow flame spread has evolved from a previous (and the most up-to-date) version of a flame-spread model in concurrent flow [6], which has successfully predicted experimental observations on concurrent flame spread (both purely buoyant and purely forced) over thin solids [13]. A schematic of the domain and flame spread configuration is shown in Fig. 1. The flame-fixed coordinate system is located at the pyrolysis front ($X=0$) of the solid, where the fuel thickness is 95% of the fresh fuel thickness. In these co-ordinates, the solid fuel is fed at the flame-spread rate ($\overline{V_F}$) into the stationary flame and the flow approaches the flame base with a relative velocity of $\overline{U_R}(x,y)=\overline{U_B}(x,y)+\overline{V_F}$ for the buoyant downward spreading flame. Here $U_B(x,y)$ is the local buoyancy induced velocity with respect to the laboratory frame of reference. For the microgravity self-propagating case, $\overline{U_R}(x,y)=\overline{V_F}$. The domain is open to the atmosphere and extends far into the ambient. The flame is assumed to be symmetric with respect to the thin solid fuel; therefore only half of the domain needs to be computed. The governing equations for the gas-phase and the solid phase are described next. The property values used in this work can be found in the Nomenclature section.

Gas-Phase. The gas-phase model consists of two-dimensional, steady, laminar, full Navier-Stokes equations along with the conservation equations of mass, energy and species. The energy equation includes radiation effects in the form $\nabla\cdot\vec{q}_r$, which is obtained by solving the radiation transfer equation. The species equations are for the fuel vapor, oxygen, carbon dioxide and water vapor. Nitrogen forms the balance of the gas mixture. A one-step, second-order, global reaction between fuel vapor and oxygen of Arrhenius type is assumed. The complete set of governing equations and the boundary conditions in the gas-phase can be found elsewhere [6]. Only the nondimensional energy equation and the radiation treatment will be detailed below.

Energy Equation

$$\rho c_p(uT_x+vT_y)=c_p\left[\left(\frac{\kappa}{c_p}T_x\right)_x+\left(\frac{\kappa}{c_p}T_y\right)_y\right]+\left(\frac{\kappa}{c_p}\right)[(c_p)_xT_x+(c_p)_yT_y]+\sum_i\frac{\rho D_i c_{pi}}{Le_i}[(Y_i)_xT_x+(Y_i)_yT_y]-\frac{\nabla\cdot q_r}{c_pBo}-\sum_{i=1}^{N}\varpi_i h_i$$

here

$$Bo=(\rho^* c_P^*\overline{U_R})/(\sigma\overline{T_\infty^3})$$

$$\nabla\cdot\vec{q}_r=K(4T^4-G)$$

$$\varpi_i=f_i\varpi_F=f_iDa\rho^2Y_FY_{O2}\exp\left(\frac{-E_g}{T}\right)$$

Solid Phase. The solid is a thin cellulosic material (Kimwipes) with chemical formula $C_6H_{10}O_5$. It is assumed to be both thermally and aerodynamically thin. The thickness of the fuel (h_s) changes as pyrolysis occurs, but the solid density remains constant. The governing equations in the solid phase consist of the continuity and energy conservation equations along with a solid pyrolysis law of zeroth-order Arrhenius kinetics [14,15]. The solid-phase equations are given below:

Pyrolysis Model

$$\dot{m}''=A_s\rho_s\exp\left(\frac{-E_s}{T_s}\right)=\rho v_w$$

Mass Conservation

$$\frac{dh_s}{dx}=\frac{A_s}{V_F}\exp\left(\frac{-E_s}{T_s}\right)$$

Energy Equation

$$q_c+\frac{q_r^y}{Bo}+\Gamma h_s\frac{dT_s}{dx}=\Gamma\frac{dh_s}{dx}[-L+c(T_s-T_L)+(T_L-T_s)]$$

where

$$\Gamma=(\overline{\rho_s}\overline{c_s}\overline{V_F})/(\rho^* c_P^*\overline{U_R})$$

$$c=c_P^*/\overline{c_s}$$

$$q_c=\kappa T_y|_{y=0}$$

Boundary Conditions

$$x=x_{\min},\quad h_s=\tau,\quad T_s=1$$

The first term on the left side of the solid-phase energy equation is the conductive/convective contribution from the gas-phase, the second term is the net radiative heat flux from the gas-phase, the third term represents the bulk solid heat-up term and the term on the right hand side represents the energy exchange due to the latent heat of vaporization (the latent heat is defined at temperature T_L).

As pointed out previously [6,15], the solid radiation term is inversely proportional to $\overline{U_R}$, the relative opposing velocity, and the gas radiation term is inversely proportional to $\overline{U_R^2}$. This is because, in addition to the linear dependence of Boltzmann number on $\overline{U_R}$, the nondimensional radiation source term picks up

another $\bar{U}_R$ dependence as length is nondimensionalized by $L_R = \alpha^*/\bar{U}_R$. As $\bar{U}_R$ is decreased (e.g., from a normal gravity flame to a microgravity flame), the gas radiation effect is amplified partly because the radiating layer (or, equivalently, the flame thickness) is thicker and partly because conduction is reduced (due to larger flame standoff distance). Although at 1g the solid radiation emission loss is greater than that from the gaseous flame, the flame radiation effects amplify faster than the solid radiation effects as the opposing velocity (or gravity) is reduced.

Treatment of Radiation. A direct treatment of radiation involves solving the radiative transfer equation for the intensity distribution over the field of interest. Since solving the radiative transfer equation with spectral accuracy is computationally prohibitive for this coupled multi-dimensional problem, the use of mean absorption coefficients will be adopted. The transfer equation for radiation intensity (in nondimensional form) passing in a specified direction $\vec{\Omega}$ through a small differential volume in an emitting, absorbing and non-scattering medium, in two dimensional co-ordinates can be written as

$$\xi I_x(x,y,\Omega) + \eta I_y(x,y,\Omega) + K(x,y)I(x,y,\Omega) = K(x,y)I_b(x,y)$$

The thin solid fuel is assumed to be diffusively emitting, transmitting and reflecting. The solid radiation properties for the thin solid in this model are specified by the total emittance (ε) and total absorptance (α) (integrated over the entire wave length). Note that a part of the incident radiation can transmit through the thin solid fuel. Since the flame is symmetric with respect to the solid, the transmission is equivalent to reflection. Therefore, the solid total absorptance is sufficient to characterize the response of the solid to the incident radiation. The outgoing radiative intensity from the solid ($y = y_{\min} = 0$) can be expressed as

$$I(x,0,\Omega) = \varepsilon I_b(x,0) + \left[\frac{1-\alpha}{\pi}\right] \int_{n\cdot\Omega'<0} |n\cdot\Omega'| I(x,0,\Omega')\, d\Omega'$$

$$n\cdot\Omega > 0$$

In the above expression total emittance (ε) and total absorptance (α) do not have to be equal. The reason for this will be discussed later. Once the radiative intensity field is obtained, the total incident radiation, radiative flux, and the divergence of radiative heat flux in the rectangular domain are obtained from the following formulas:

$$G(x,y) = \int_{4\pi} I(x,y,\Omega)\, d\Omega$$

$$q_r^{x+}(x,y) = \int_{\xi>0} \xi\cdot I(x,y,\Omega)\, d\Omega \quad q_r^{x-}(x,y)$$

$$= \int_{\xi<0} \xi\cdot I(x,y,\Omega)\, d\Omega$$

$$q_r^{y+}(x,y) = \int_{\eta>0} \eta\cdot I(x,y,\Omega)\, d\Omega \quad q_r^{y-}(x,y)$$

$$= \int_{\eta<0} \eta\cdot I(x,y,\Omega)\, d\Omega$$

$$q_r^x = q_r^{x+} + q_r^{x-}, \quad q_r^y = q_r^{y+} + q_r^{y-}$$

$$\nabla\cdot\vec{q}_r(x,y) = K(x,y)[4T^4(x,y) - G(x,y)]$$

Here, a mean absorption coefficient $K(x,y)$ for the gas mixture is needed. In this work, the participating gases are carbon dioxide and water vapor. Soot is assumed to be absent based on experimental observations of flames in low-speed flow and low oxygen atmospheres [10]. The simplest way is to assign a constant absorption coefficient, which is treated as a parameter [16]. A more sophisticated treatment of gas radiation has been proposed by Bhattacharjee et al. [3]. Here the gas radiation is treated as a heat loss term in the energy equation with a constant absorption coefficient, the value of this coefficient is evaluated from a global radiation energy balance. The radiation heat feedback to the solid is then obtained in a similar fashion. The overall radiative transfer is ensured in a self-consistent manner, but only a single absorption coefficient is used for the entire flame. However, it is believed that the absorption coefficient can vary significantly from one location to another in the flame. In the work by Lin and Chen [9], with an optically thin-limit approximation, variable absorption coefficients based on the local mixture composition and temperature were used and the two-dimensional radiative transfer equation was solved using the P-1 approximation. In the concurrent flame spread case, Jiang [15] solved the radiation transfer equation using discrete ordinates methods. Here again an optically thin flame was assumed with the adoption of a local Planck-mean absorption coefficient.

One-dimensional studies [12,17] have shown that even for a flame as thin as one or two centimeters, the flame is not optically thin. This is caused by self-absorption by radiatively active species. Furthermore, in comparison with the more accurate results obtained from a narrow-band radiation model in one-dimensional flames, it was shown that the Planck-mean results over predict net emission from the flame [12,17]. Therefore, to improve the computed heat flux at the solid or to the ambient, a correction is needed. One such procedure has been proposed in [17] and is adopted in this work. This procedure is described briefly below.

The local Plank-mean absorption coefficient for the mixture can be given by $K_p = P_{CO2}\cdot K_{p(CO_2)} + P_{H2O}\cdot K_{p(H_2O)}$, where P_i represents the partial pressure of species i. The values of K_p for each species are taken from [18] as a function of temperature. A novel feature used here is the incorporation of a calibration procedure [17] for the mean absorption coefficient. The calibration of the absorption coefficient against the narrow-band results through a quasi-one-dimensional flame is to account for the different optical lengths in different parts of the flame and the effect of spectral self-absorption of gaseous species. Therefore the local absorption coefficient K used in this work is set equal to CK_p, where C is the correction factor. In the downstream flame region, $X<0$, C is determined by an optical traverse in the Y-direction (perpendicular to the solid) and by applying the empirical relation proposed in [17]. For the region $X>0$, where the flame is highly two-dimensional, two traverses are made from $X=Y=0$, one in the Y-direction and the other in the X-direction toward the upstream. The correction factor is the average of these two traverse values and a uniform value is assumed in this region. Note that since the steady flame solution is obtained iteratively (to be described later), the distribution of C is also determined iteratively. The spatial distribution of C along X has been presented in [19] for an opposed-flow spreading flame and in [6] for a concurrent flow spreading flame.

Numerical Scheme

The SIMPLER algorithm [20] is used for the fluid flow and combustion equations. In the flame-spread problem, the radiative heat emission in the flame zone and the net radiative heat flux onto the solid are the primary quantities of concern. The net radiative heat flux on the solid is determined by the zone near the flame where the influences of ray effects and false scattering are quite small. Furthermore, the divergence of the radiative heat flux in the gas-phase becomes negligibly small away from the flame zone due to small absorption coefficients. Based on these considerations, the radiation transfer equation is solved using the S-N discrete ordinates method [21,22]. The two-dimensional S4 scheme with 12 ordinate directions was chosen for use in the current computations by considering the balance of numerical accuracy and computational expense [15]. The higher order

schemes, S6 and S8, were investigated by Jiang [15] but S4 yielded adequate resolution (within 6%) of the radiative heat flux distribution on the solid.

Since the equation of radiative transfer and the conservation equations are coupled, they are solved iteratively. In most computations, the gas radiation routine is invoked once for every five gas-phase iterations to update both $\nabla \cdot \vec{q}_r$ in the gas-phase energy equation and the radiative flux term in the solid energy equation. The solid-phase equations, which are coupled to the gas-phase system, are solved by finite-difference techniques. The steady flame spread rate (the eigenvalue of the whole system) is determined iteratively using the bisection method to force the pyrolysis front (95% of the fresh fuel thickness) to occur at $X=0$.

The computations for a given case are initialized by using a previously converged solution of a case with similar input parameters. Convergence is ensured in the continuity and momentum equations and by a steady flame spread rate. The flame is considered to be extinct when the maximum temperature in the computational domain is not in the gas phase.

The computations are carried out on a non-uniform mesh. In the *Y*-direction, the grid nodes are clustered near the solid and expand away from the surface. In the *X*-direction, a fine grid structure is used in the flame stabilization region (near the flame's leading edge) to capture the drastic variations in the flame; the grids then expand upstream and downstream. A fine grid structure near the solid burnout region (the trailing edge) is also needed to resolve the region adequately. Since the pyrolysis length is not known a priori, an adaptive gridding scheme is used for this purpose. For all the calculations, the grid structure is consistent near the flame stabilization zone. The smallest grid size (0.05 thermal lengths) is in the flame stabilization zone. The domain extends to 200/350 thermal lengths in the *Y*-direction and 250/450 thermal lengths in the downstream *X*-direction as measured from the pyrolysis front for μg/1g flames. The upstream extent of the domain for the 1g case extends to 500 thermal lengths. In the calculations for self-propagating μg flames, the upstream extent has a prescribed length of 10 cm, which is a dimensional constraint for the forced opposed-flow simulation [19]. However, this length is found to be sufficient to completely resolve all variations upstream of the flame. We further note that the smallest length scale in this problem is the thermal length in the flame stabilization zone which is the length scale used to non-dimensionalized the governing equations. By solving the equations non-dimensionally and by choosing a grid size that is a small fraction of the thermal length, parametric studies on flame-solid interactions can be carried out with a desired numerical accuracy.

For a typical case of a μg flame at 21% O_2 there are 119 and 59 grid nodes in the *X* and *Y*-directions, respectively; in the 1g case, there are 157 and 62 grid nodes in the *X* and *Y*-directions, respectively. The computational time is typically about 1 to 2 hours on a 667 MHz Compaq XP1000 workstation.

Results

The computed results will be presented in two sections. First, microgravity self-propagating flames will be compared with normal gravity downward propagating flames. Next, the solid radiation properties (α and ε) will be varied independently to investigate the nature of flame-solid radiation interactions in microgravity flames.

Comparison of Normal Gravity (1g) and Microgravity Flames (μg). Figures 2(*a*) and (*b*) show, respectively, the structural details of a 1g downward spreading flame and a μg self-propagating flame in a quiescent ambiance of 21% O_2 and one atmospheric pressure. The radiative properties of the solid are $\varepsilon=1$, $\alpha=1$ (fully absorbing and emitting solid). Several fuel vapor reaction rate contours are presented. The outer most reaction rate

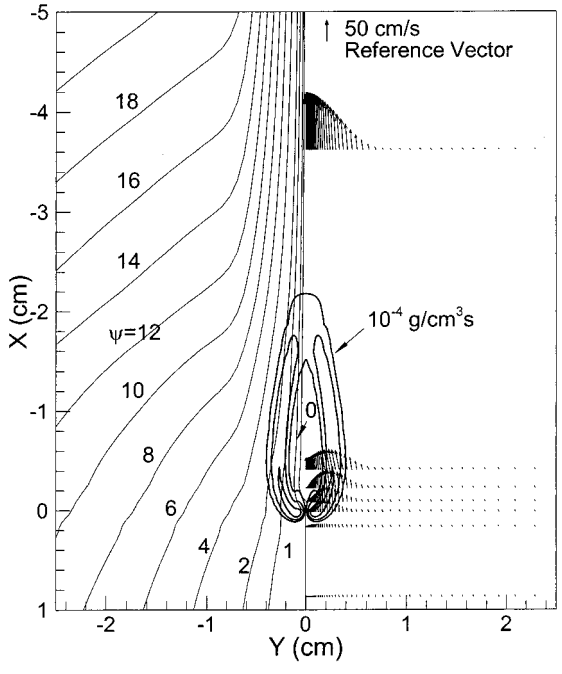

(a)

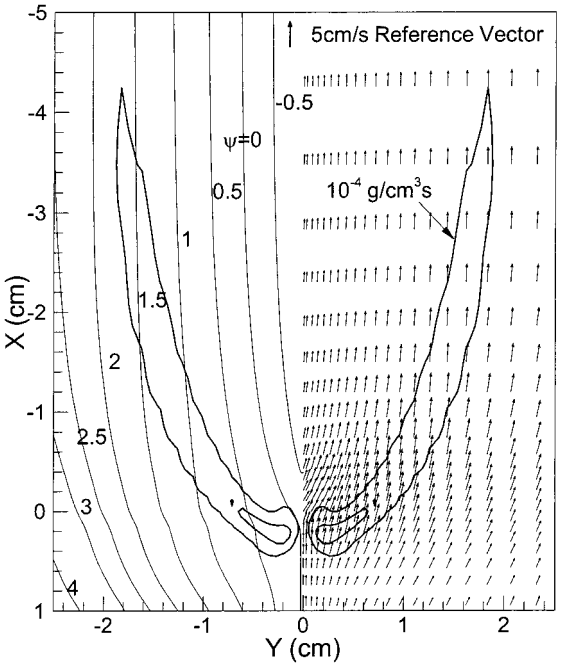

(b)

Fig. 2 (*a*) Normal gravity (1g) downward spreading flame at 21% O_2, solid radiative properties of ($\varepsilon=\alpha=1$), flame is represented by fuel reaction rate contours. Left half: stream functions, Right half: velocity vectors with respect to flame; and (*b*) microgravity (μg) self-propagating flame at 21% O_2, solid radiative properties ($\varepsilon=\alpha=1$), flame is represented by fuel reaction rate contours. Left half: stream functions, Right half: velocity vectors with respect to flame.

contour of $\varpi_F=10^{-4}$ g/cm^3/s is taken to represent the boundary of the visible flame [10]. The other contours have values increasing by a factor of 10 from the outside to the core of the flame. We see some drastic differences between the 1g and the μg flames. The 1g flame is shorter (due to a much smaller pyrolysis length, to

be discussed later), narrower and the downstream tip of the flame is closed. In comparison, the μg flame is longer and much wider along with having open tips. These computed features of the appearances of the visible flames agree well with experiments both in normal gravity and microgravity [7]. It should be noted that the opposed-flow model successfully captures the qualitative differences between these two flames. However, while the flame size in normal gravity agrees well between the model and experiments, the computed flame in microgravity is about twice as large as the experimental one [7]. The difference is believed to be due to the three-dimensional nature of the experiment (note the present model is two-dimensional). This will be discussed further later.

In addition, Fig. 2 shows stream functions plotted on the left half of the symmetry plane and the velocity vectors on the right half, both based on the flame-fixed coordinate system. Figure 2(*a*) shows that in the downstream direction the flow is continuously accelerated by buoyancy (at X=3.5 cm, the peak velocity at the center plane is already 1.5 m/s). This accelerating flow entrains the surrounding fluid towards the center, which pushes the flame closer to the center plane and thereby closing the flame tips. In contrast, the μg flame in Fig. 2(*b*) has much lower relative velocities with respect to the flame. The maximum velocity is less than 5 cm/s (note the different velocity vector scales in Figs. 2(*a*) and (*b*)). The streamlines become divergent downstream, which is characteristic of flames in pure forced flows [14,15]. The lower velocities for the μg flame result in a much larger flame standoff distance from the solid and consequently have a much smaller flame conductive feedback to the solid fuel. This has profound implications on the heat transfer mechanisms in flame spreading and extinction, as discussed next.

Figures 3(*a*) and (*b*) present the heat flux distributions along the solid for the 1g and μg flames shown in Fig. 2. The gas phase conductive heat flux is q_c and gas-radiation feedback is $(q_r)_{\text{in}}$. The radiation leaving the solid, $(q_r)_{\text{out}}$, consists of emission from the solid, the reflected $(q_r)_{\text{in}}$ and the transmitted radiation from the other side of the solid. A positive value of the heat flux indicates heat gain for the solid and a negative value indicates heat loss from the solid. The sum of $(q_r)_{\text{in}}$ and $(q_r)_{\text{out}}$ gives $(q_r)_{\text{net}}$, the net radiative heat flux. The total net heat flux to the solid is $q_{\text{net}}(=q_c+(q_r)_{net})$. The distribution of q_c depends primarily on the local flame stand-off distance from the solid. The conductive heat flux, q_c, has a peak near the flame leading edge (slightly upstream of the pyrolysis front, $X=0$) where the flame is closest to the solid. Here q_c is substantially greater than $(q_r)_{\text{in}}$ and is the dominant mode of heat transfer to the solid. While conduction/convection is always dominant in the flame attachment zones for both flames, the flame radiation feedback to the solid can exceed convection in both the upstream preheat zone and the downstream pyrolysis zone for the μg flame, as shown in Fig. 3(*b*). We note that the peak value of q_c for the μg flame is several times smaller than that for the 1g flame, a consequence of the larger flame standoff distance discussed earlier (note the different scales used in Figs. 3(*a*) and (*b*)). In the region upstream of the flame leading edge, q_c drops sharply as heating by conduction is now against the opposing convective flow. This effect is more prominent in the 1g flame where the buoyancy induced opposing flow is much greater than the flame spread rate (spread rate is the effective opposing velocity for the μg flame). Interestingly for the μg flame (inset on the upper right corner of Fig. 3(*b*)), over a certain region upstream of the pyrolysis front ($X>0$) q_c is negative, indicating heat conduction from a hotter solid to a relatively colder gas phase, due to upstream heating by the flame radiation $(q_r)_{\text{in}}$. Radiation has a much longer reach than conduction, especially in an opposed-flow situation. The gas-phase radiation feedback, $(q_r)_{\text{in}}$, is the dominate heat transfer mechanism to the solid fuel in the farther upstream regions, away from the flame leading edge. Flame radiation is a significant forward heat transfer mechanism in microgravity opposed-flow flame spread [3,9]. By contrast, although Fig. 3(*a*) indicates some contribution of the solid radiative loss in the solid energy balance, the contribution of the flame radiation is very small for the 1g flame.

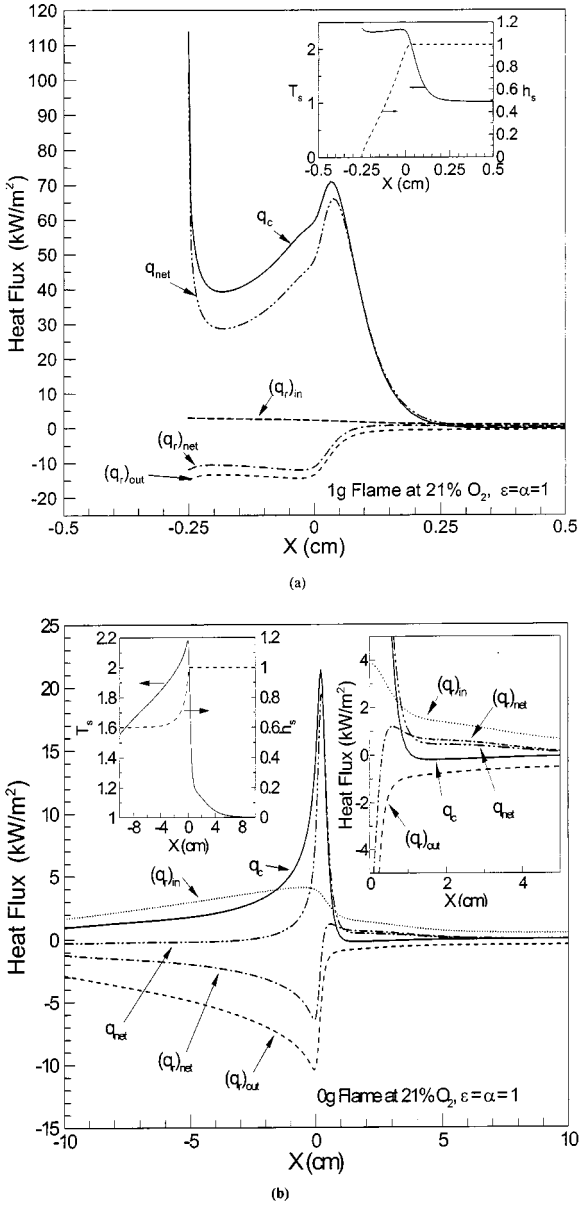

Fig. 3 Heat flux distribution on the solid for (*a*) normal gravity downward spreading flame at 21% O_2 ($\varepsilon=\alpha=1$); and (*b*) microgravity (μg) self-propagating flame at 21% O_2 ($\varepsilon=\alpha=1$)

The spread rates for the 1g and μg flames are 1.24 cm/s and 2.02 cm/s, respectively. As discussed before, the flame-spread rate is proportional to the forward heat transfer to the fuel. The net heat transfer to the fuel is obtained by integrating and adding together the contributions of the radiative heat feedback, $(q_r)_{\text{net}}$, and conductive heat feedback, q_c, over the fuel preheat region (defined as the region upstream of the pyrolysis front $X=0$). The contributions for the 1g flame are $\int(q_r)_{\text{net}}dx=2.1$ W/m and $\int q_c dx=50.5$ W/m and for the μg flame are $\int(q_r)_{\text{net}}dx=27.1$ W/m and $\int q_c dx=55.3$ W/m. We note that the flame spread rate of the μg flame is higher than that of the 1g flame in proportion to the total heat feedback to the solid fuel in the preheat region. The above values clearly show that the net contribution of radiation is negligible in the normal gravity flame and conduction is the primary mode of heat transfer to the solid. We also observe that although conductive heat flux in the normal

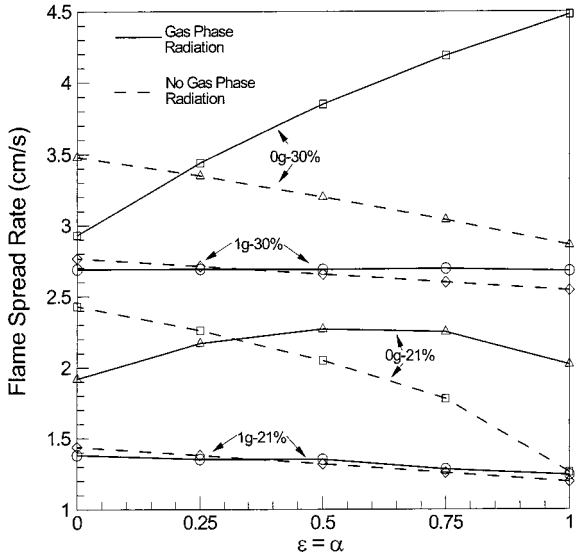

Fig. 4 Flame spread rate as a function of radiation properties of the solid $\varepsilon(=\alpha)$, in normal gravity (1g) and microgravity (μg) environment

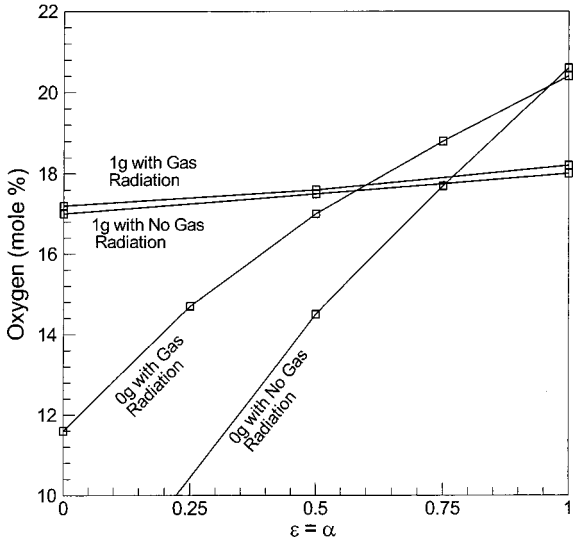

Fig. 5 Limiting Oxygen Index (LOI) as a function of radiation properties of the solid $\varepsilon(=\alpha)$, in 1g and μg environment

gravity flame is much higher than that for the μg flame, it acts over a very small preheat region and in this particular case the integrated net contribution of conduction is close to that for the μg flame.

The 1g flame also has a short pyrolysis length. The inset in Fig. 3(*a*) shows that the solid burns out at $X=-0.25$ cm (a pyrolysis length of 2.5 mm only). The solid temperature in the pyrolysis zone is nearly uniform, verified by numerous experiments, e.g., [23]. At the burnout point, the conductive heat flux rises sharply. In contrast, for the μg flame, the left inset in Fig. 3(*b*) shows that the solid temperature in the pyrolysis zone drops continuously towards downstream. Figure 3(*b*) shows that the net heat flux becomes slightly negative for locations downstream of $X<-2.67$ cm. In this region, the solid radiative loss exceeds the heat gain from the flame. As a consequence, the solid temperature drops and local pyrolysis rate (dependent on solid temperature) becomes small, and therefore unburnt solid is left downstream of the flame. Whether or not the solid will completely burnout or if material will remain depends on a number of parameters. A more detailed discussion on this aspect can be found in [19].

The results shown so far assume that both ε and α are unity. Next we will show the effect of nonunity ε and α (but both are assumed equal to each other) on flame spread rates and extinction limits. In addition, to isolate the effects of flame radiation from solid radiation, cases with of no gas radiation have also been computed and compared.

Figure 4 presents the flame-spread rate as a function of $\varepsilon(=\alpha)$. The dashed curves correspond to computations without the inclusion of gas-phase radiation in the model and the solid curves represent computations with gas-phase radiation included in the model. Each of the two curves is plotted for 1g and μg and for two different oxygen levels of 30% and 21%. For both 21% O_2 and 30% O_2, flame radiation has little influence one 1g flames. The two spread rate curves (with and without radiation) are close to each other. The effect of varying $\varepsilon(=\alpha)$ is also small, reflecting the secondary role of radiation on downward flame spread in normal gravity. On the other hand, the influence of both flame and solid radiation on microgravity (μg) flame spread is large. At 30% O_2, the μg flame spread rate increases monotonically as $\varepsilon(=\alpha)$ increases. This flame-spread trend reflects the dominating role of the flame radiation feedback to the solid. This trend was also reported by Bhattacharjee et al. [3] based on their computations on ashless filter paper at 50% O_2 and an ambient pressure of 1.5 atm. Interestingly at 21% O_2, the μg flame spread rate exhibits a nonmonotonic dependence on $\varepsilon(=\alpha)$. The flame spread rate first increases to a maximum, with increasing $\varepsilon(=\alpha)$, and then decreases. This nonmonotonic behavior is due to the competing effects of heat loss by solid emission and heat gain by absorption of the flame radiation. At even lower oxygen concentration (for example at 15% O_2, not shown here), the μg flame spread rate decreases monotonically with increases in $\varepsilon(=\alpha)$ until extinction.

The effect of radiation properties of the solid on the minimum ambient oxygen percentage capable of supporting flame spread is shown in Fig. 5 (to be referred to as LOI, limiting oxygen index). Again, the 1g flames show little effect of flame radiation on LOI. There is a small decrease in LOI with decreasing $\varepsilon(=\alpha)$. In the 1g regime, the flame extinguishes by the 'blow off' mechanism, where the reactants do not get enough time to complete the reaction [24]. In this small Damkohler number limit, the reaction heat release per unit volume is high, therefore, the radiation influence is minimal. The μg flames, on the other hand, are controlled largely by radiative heat transfer and are therefore sensitive to changes in radiative properties of the solid. Figure 5 shows that the LOI for the μg flame, both with and without flame radiation, decreases rapidly with $\varepsilon(=\alpha)$. In computations without flame radiation, the only loss is by emission from the solid. Decreasing $\varepsilon(=\alpha)$ reduces the loss, and, hence, lowers the LOI. In computations with flame radiation, there is an additional loss from the gas phase but there is also a radiation feedback to the solid, which increases the solid burning rate and strengthens the flame. These two effects compete with each other. Figure 5 shows that, except near $\varepsilon=\alpha=1$, the heat feedback prevails, which results in a higher LOI for the case with flame radiation considered in the model.

Comparing the 1g and μg cases in Fig. 5, we note a crossover of the LOI curves between the two cases. When $\varepsilon(=\alpha)$ is close to unity, the flame in 1g is more flammable (i.e., has lower LOI). When $\varepsilon(=\alpha)$ is reduced (e.g., <0.5), the μg flame is more flammable. This is a *flammability limit reversal* phenomenon. The possibility of flammability limit reversals between 1g and μg environments was first suggested by T'ien [25]. Experimentally, Honda and Ronney [26] demonstrated its existence by mixing different inert gases with the ambient atmosphere. Here, we show that the radiative properties of the solid can also produce a reversal in flammability limit.

To compare with available experimental data, we found that it is possible to obtain reasonable agreement on flame size, spreading rates and extinction limit for normal gravity flames. We noted that radiation only plays a minor role in normal gravity. On the

other hand, the model predicts a higher spread rate and a large flame size than the present available microgravity data [21,26] within reasonable ranges of radiation parameters, kinetic constants and fuel Lewis number. By examining the details of the model results, we feel this discrepancy is due to the three-dimensional nature of the experiment. The microgravity experiments were performed using solid samples of widths between 3 and 5 cm. While this is enough for a two-dimensional approximation in 1g, since the preheating distance is short (of the order of millimeters), this is not enough in μg flames where the preheat distance is of the order of 5 cm, due to flame radiation. The three-dimensional effect is not limited to the preheat zone (which affects the spread rate) but also affects the flame size. The longer action length of flame radiation causes the experimental μg flame to be three-dimensional. The lateral radiative loss reduces the flame temperature and flame size.

Flame Radiation-Solid Interaction. We have shown that both radiative transfer within the flame and emission by the solid can have large effects on the flame-spread rates and the extinction limits of μg self-propagating flames. The computed results shown so far assume that ε and α are equal. It should be noted that while ε determines the solid emission loss, the interaction between the flame radiation and the solid is controlled by α. To enhance our understanding of this interaction further, we now treat the total emittance (ε) and the total absorptance (α) as independent parameters and consider the following cases:

$\varepsilon=1$, $\alpha=1$: full solid emission, full solid absorption
$\varepsilon=1$, $\alpha=0$: full solid emission, no solid absorption
$\varepsilon=0$, $\alpha=1$: no solid emission, full solid absorption
$\varepsilon=0$, $\alpha=0$: no solid emission, no solid absorption

Although the cases $\varepsilon=\alpha=1$ and $\varepsilon=\alpha=0$ are the natural limiting conditions for solid radiation properties, the unequal cases for ε and α (i.e., $\varepsilon=1$, $\alpha=0$ and $\varepsilon=0$, $\alpha=1$) may appear to be unrealistic and deserve an explanation. Using Fourier transform infrared techniques (FTIR), it has been found that the radiative absorption and emission of thin cellulose solids (i.e., the solid fuel considered in this work) are spectral [27]. To represent the total radiative energy emitted by the solid and the total radiative energy from the flame that is absorbed by the solid, the total emittance (ε) and total absorptance (α) are used, as mentioned previously. These two "total" quantities are the integrated values over the entire range of wavelengths. Since incident gas radiation (which is also spectral) originates from high temperatures while emission from the solid occurs at lower temperatures, the solid total absorptance (α) and the solid total emittance (ε) do not have to be equal [27]. For example, for Kimwipes $\varepsilon>\alpha$ ($\varepsilon\approx0.5$ and $\alpha\approx0.25$) and the latter is estimated based on approximate flame properties [27]. The case $\varepsilon=1$, $\alpha=0$ represents an extreme limit to bracket those cases where $\varepsilon>\alpha$. The case $\varepsilon=0$, $\alpha=1$ also seems drastic for practical materials, but it is actually a good simulation of the *radiation response* of flame spread over a liquid or a solid with a very low vaporization temperature. Although the solid emission is negligible, due to the low solid temperature, the solid can still absorb flame radiation.

In addition to the four above cases, the adiabatic case (no solid and flame radiation) and pure solid radiative loss case (with $\varepsilon=1$ and no flame radiation) are also included for comparisons. These two are important limiting cases that have been traditionally adopted in flame spreading models [28].

In the adiabatic case, shown in Fig. 6, the flame spread rate decreases with decreasing O_2 slightly steeper than a linear dependence. The lowest oxygen percentage computed for this case is 5%, with a flame spread rate of 0.1 cm/s. It appears that there is no low oxygen limit (LOI) for the adiabatic case. With inclusion of emission from the solid ($\varepsilon=1$; no flame radiation), an LOI of 0.21 is obtained and the spread rates are much lower than the adiabatic cases for the same O_2%. Using these two cases as reference, the other four cases with flame radiation are examined. For the $\varepsilon=0$, $\alpha=0$ case, all the flame radiation is lost to the ambient but there is no radiation loss from the solid. The spread rates are slightly lower than the adiabatic case and the LOI is 0.12. For the $\varepsilon=1$, $\alpha=0$ case both the solid radiation and all the flame radiation is lost to the ambient, which results in the lowest spread rates and the highest LOI of 0.28. For the $\varepsilon=1$, $\alpha=1$ case part (approximately one half) of the flame radiation is absorbed by the solid. Here the spread rates are higher than those of the adiabatic case at high O_2% but lower than those of the adiabatic case at low O_2%. This crossover phenomenon will be analyzed later in more detail. The computed LOI for this case is 0.20. Lastly, for the $\varepsilon=0$, $\alpha=1$ case (no solid radiative loss but complete absorption of the flame radiation feedback) the spread rates are always higher than the adiabatic case and this case has a rather low LOI of 0.06. The inset in Fig. 6 shows the four cases for 1g flames. Both solid and flame radiation have only small influence on the spread rates and the LOI, as expected.

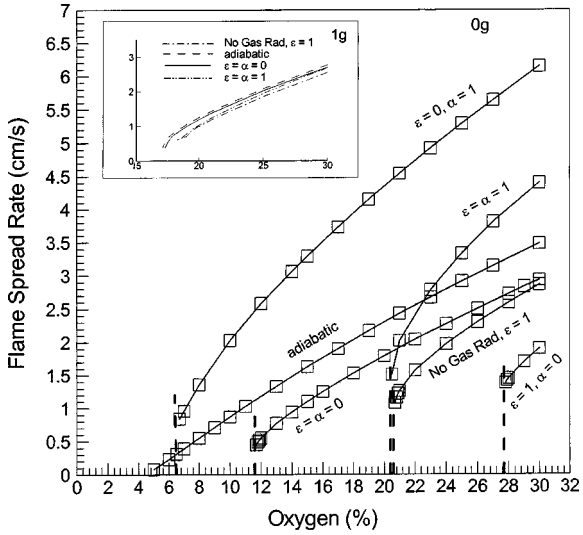

Fig. 6 Parametric study of flame solid interaction in μg self-propagating flame. Inset shows equivalent curves for 1g flame.

The spread rate curves between the $\varepsilon=1$, $\alpha=1$ case and the adiabatic case in μg show a crossover. At high oxygen concentration (e.g., 30% O_2) the spread rate for the $\varepsilon=1$, $\alpha=1$ case is higher than the corresponding adiabatic case and at low oxygen levels (e.g., 21% O_2) the spread rate is lower than that of the adiabatic case. This crossover in spread rate trend can be understood in terms of the competing effects of the solid radiation loss, the flame radiation loss and the heat feedback to the solid. At high oxygen levels the strong flame radiation feedback to the solid, $\int(q_r)_{in}dx$, over shoots the drop in conduction feedback, $\int q_c dx$, (due to a drop in the flame temperature as a result of flame radiation loss to the ambient) and the solid radiative loss, $\int(q_r)_{out}dx$. The numerical values are shown in Table 1. The flame radiation feedback and the conduction feedback, both being strong functions of flame temperature, drop with decreases in oxygen level whereas the solid radiative loss, which is a function of solid temperature, is less sensitive to changes in oxygen concentration and drops slowly. The result is that at low oxygen levels, the solid radiative loss becomes dominant and thus reduces the net heat feedback to the solid.

The heat flux distributions on the solid for the four cases in μg, at 30% O_2 and with flame radiation included are shown in Figs. 7(*a*,*b*,*c*,*d*). The inset in the figures show the net radiation flux vectors near the leading edge of the flame (represented by the fuel reaction rate contour for 10^{-4} g/cm^3/s and gas phase temperature contours). In Fig. 7(*a*), the solid is radiatively non-participating ($\varepsilon=\alpha=0$). The entire flame radiation incident on the solid is reflected back to the gas phase ($(q_r)_{in}=(q_r)_{out}$). Therefore, close to

Table 1 Contribution of conductive and radiative heat feedback to the preheat zone and solid emissive loss

O_2 %		$\int q_c dx$ W/m	$\int (q_r)_{in} dx$ W/m	$\int (q_r)_{out} dx$ W/m
30	Adiabatic	145.26	⋯	⋯
	$\varepsilon=1$, $\alpha=1$	109.81	162.1	71.68
21	Adiabatic	102.05	⋯	⋯
	$\varepsilon=1$, $\alpha=1$	55.34	92.76	65.66

the solid the net radiative flux vectors are parallel to the solid. Conduction from the gas phase is the only mode of heat transfer to the solid. The net radiation flux vectors shown in the inset are directed away from the flame towards the ambient, indicating radiative heat loss to the surroundings. In Fig. 7(*b*), the solid emits radiation like a black surface but does not absorb any flame radiation ($\varepsilon=1$, $\alpha=0$). Here, all of the incident gas-phase radiation, $(q_r)_{\text{in}}$, on the solid is reflected back to the ambient along with addition of the emitted solid radiation. Again, as in the previous case, only the gas phase conduction is the source of heat gain for the solid. The net radiation flux vectors are nearly perpendicular to the solid, which indicates strong emission loss from the solid. A black absorbing but non-emitting solid ($\varepsilon=0$, $\alpha=1$) is presented in Fig. 7(*c*). The flame radiation feedback effect is highlighted here. The inset in the figure shows the direction of the net radiative heat flux vectors, including those on the solid. The net radiation flux vectors near the solid point toward the solid indicating heat feedback to the solid by flame radiation ($(q_r)_{\text{in}}=(q_r)_{\text{net}}$, $(q_r)_{\text{out}}=0$). Note that the conductive heat flux, q_c, peaks near the flame stabilization zone but $(q_r)_{\text{in}}$ is dominant in the regions away from the stabilization zone, both upstream and downstream of the flame. Figure 7(*d*) shows a black absorbing and emitting solid. As shown in the inset, radiation flux vectors on the solid change their

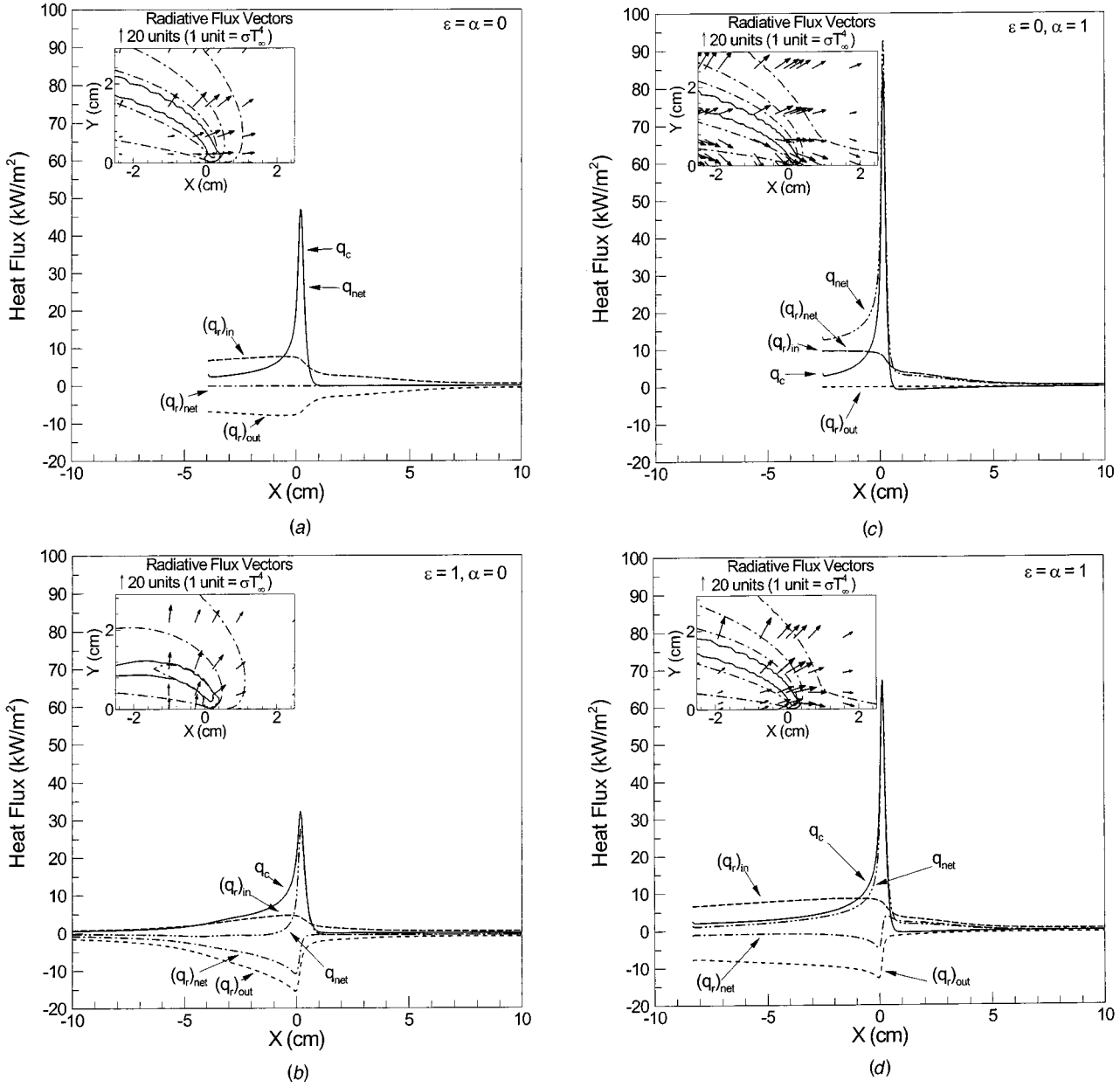

Fig. 7 Heat flux distribution on the solid (*a*) ($\varepsilon=\alpha=0$); (*b*) ($\varepsilon=1$, $\alpha=0$); (*c*) ($\varepsilon=0$, $\alpha=1$); and (*d*) ($\varepsilon=1$, $\alpha=1$)

directions: pointed away from the solid in the pyrolysis zone ($X<0$, a loss) and toward the solid in the preheat zone ($X>0$, a gain). In all four cases, it is seen that the net radiation flux vectors display two-dimensional character near the flame anchor point.

Conclusions

A detailed two-dimensional flame-spreading model in opposed-flow has been formulated and solved with emphasis on the effects of flame radiation. The radiation transfer equation was solved using discrete ordinates methods that enabled a detailed accounting of the interaction of flame radiation with the solid fuel. The following conclusions can be drawn from this study:

1. A comparison of the computed flame profiles between normal gravity downward spreading flames and microgravity self-spreading flames show profound qualitative difference in pyrolysis length, flame size and shape, flow pattern and heat transfer characteristics.
2. While its effect is negligible in normal gravity, flame radiation plays a significant role in microgravity flames due to of the reduction of convection. In self-spreading flames in microgravity, flame radiation constitute a significant portion (in certain cases it could be more than one half) of the total heat flux in the preheat zone, confirming a previous finding in [3].
3. Since the length of the preheat zone caused by flame radiation can exceed 5 cm, data from currently available microgravity experiments using sample widths of 5 cm or less are expected to have three-dimensional effects.
4. The flame spread rate and extinction limit are sensitive to the radiative properties of the solid fuels. With different total emittance and total absorptance, there can be a reversal between the microgravity and the normal gravity flame spread rates and extinction limits for thin solids.
5. Because solid radiation properties can be spectral, the total emittance and total absorptance do not have to be equal to each other and varying them independently can produce a drastic variation of radiative interaction between the flame and the solid. In the case of a high absorbing and low emitting solid (or liquid), the flame-spread rate can exceed the spread rate predicted by an adiabatic flame.

Acknowledgment

This research has been supported by NASA grants NCC3-633 and NCC3-669 under the technical monitoring of Dr. Kurt Sacksteder.

Nomenclature

A_s = nondimensional solid phase pre-exponential factor ($A_s=\overline{A_s}/\overline{V_F}$)
$\overline{A_s}$ = solid phase pre-exponential factor (3.8×10^5 m/s)
Bo = Boltzmann number ($=\rho^* c_P^* \overline{U_R}/(\sigma \overline{T_\infty^3})$)
$\overline{B_g}$ = gas-phase pre-exponential factor (1.58×10^9 m^3/kg/s)
C = correction factor
c_P = nondimensional gas-phase specific heat ($=\overline{c_P}/c_P^*$)
c_s = nondimensional solid-fuel specific heat ($=\overline{c_s}/c_P^*$)
$\overline{c_s}$ = solid-phase specific heat (1.386 kJ/kg/K)
c_P^* = reference gas-phase specific heat (1.386 kJ/kg/K)
D_i = diffusion coefficient of species i
Da = Damkohler number ($=\alpha^*\rho^*\overline{B_g}/\overline{U_R^2}$)
E_g = nondimensional gas-phase activation energy ($=\overline{E_g}/R_u/\overline{T_\infty}=45.3$)
$\overline{E_g}$ = gas-phase activation energy (11.30×10^4 kJ/kg mol)
E_s = nondimensional solid-phase activation energy ($=\overline{E_s}/R_u/\overline{T_\infty}=50.3$)
$\overline{E_s}$ = solid-phase activation energy (12.56×10^4 kJ/kg mol)
f_i = stoichiometric mass ratio of species i/fuel
G = nondimensional incident radiation ($=\overline{G}/(\sigma\overline{T_\infty^4})$)
h_i = nondimensional enthalpy of species i ($h_i=(h_i^0+\int_{\overline{T_0=298\text{ K}}}^{\overline{T}}\overline{c_{Pi}}d\overline{T})/(c_P^*\overline{T_\infty})$)
$\overline{h_i^0}$ = enthalpy of formation of species i (gives heat of combustion, $\Sigma_{i=1}^N\overline{\varpi}_i\overline{h_i^0}/(c_P^*\overline{T_\infty})=-40.4$)
h_s = nondimensional solid fuel thickness ($=\overline{h_s}/\overline{L_R}$)
I = nondimensional radiative intensity ($=\overline{I}/(\sigma\overline{T_\infty^4})$)
$\overline{K_P}$ = Planck mean absorption coefficient
K_P = nondimensional Planck mean absorption coefficient ($=\overline{K_P}\overline{L_R}$)
$\overline{K}$ = mean absorption coefficient ($=CK_p$)
$\overline{L_R}$ = reference length (thermal length, $\alpha^*/\overline{U_R}$)
L = nondimensional latent heat of solid ($=\overline{L}/\overline{c_s}/\overline{T_\infty}$)
$\overline{L}$ = dimensional latent heat of solid (-754 kJ/kg)
Le_i = Lewis number of species i ($\text{Le}_F=1$, $\text{Le}_{O2}=1.11$, $\text{Le}_{CO2}=1.39$, $\text{Le}_{H2O}=0.83$, $\text{Le}_{N2}=1$)
$\overline{P_\infty}$ = reference pressure
$\overline{P_T}$ = ambient pressure
$\overline{P_i}$ = dimensional partial pressure ($=X_i\overline{P_T}$)
P_i = nondimensional partial pressure (P_i/P_∞)
$\dot{m}''$ = nondimensional mass flux from solid ($=\overline{\dot{m}}/\rho^*/\overline{U_R}$)
n = outward normal to the wall
q_c = conductive heat flux
$\vec{q}_r$ = radiative heat flux vector
q_r^{x+}, q_r^{x-} = positive/negative components of $\vec{q}_r$ along x
q_r^{y+}, q_r^{y-} = positive/negative components of $\vec{q}_r$ along y
q_r^x = net radiative heat flux in x-direction
q_r^y = net radiative heat flux in y-direction
R_u = universal gas constant
T = nondimensional gas temperature ($=\overline{T}/\overline{T_\infty}$)
T_L = nondimensional temperature at which L is given ($=\overline{T_L}/\overline{T_\infty}=1$)
T_s = nondimensional solid temperature ($=\overline{T_s}/\overline{T_\infty}$)
$\overline{T_\infty}$ = ambient temperature (300 K)
$\overline{U_R}$ = reference velocity ($=\overline{U_B}(x,y)+\overline{V_F}$)
$\overline{U_B}$ = reference buoyant velocity
u = nondimensional velocity along x ($=\overline{u}/\overline{U_R}$)
v = nondimensional velocity along y ($=\overline{v}/\overline{U_R}$)
$\overline{V_F}$ = flame spread rate
X_i = molar fraction of species i
Y_i = mass fraction of species i
α^* = reference thermal diffusivity (2.13×10^{-4} m^2/s)
α = solid total absorptance
ε = solid total emittance
κ = nondimensional gas thermal conductivity ($=\overline{\kappa}/\kappa^*$)
κ^* = reference gas thermal conductivity (8.08×10^{-2} J/m/s/K)
η = direction cosine in y-direction
ρ = nondimensional gas density ($=\overline{\rho}/\rho^*$)
ρ_s = nondimensional solid density ($=\overline{\rho_s}/\rho^*$)
$\overline{\rho_s}$ = dimensional solid density (236 kg/m^3)
ρ^* = reference gas density (2.75×10^{-1} kg/m^3)
σ = Stefan-Boltzmann constant (5.67×10^{-8} W/m^2/K^4)
τ = nondimensional fresh fuel half thickness ($\tau=\overline{\tau}/\overline{L_R}$)

$\bar{\tau}$ = fuel half thickness (3.8×10^{-5} m)
ξ = direction cosine in x-direction
Ω = ordinate direction (ξ,η)
ϖ_i = source or sink term for species $i(=f_i\varpi_F)$
ϖ_F = nondimensional fuel source term

Subscript

b = black body
F = flame or fuel
i = species i
min = minimum
max = maximum
R = reference
s = solid phase
w = value at wall
x = along the x, or derivative with respect to x
y = along the y, or derivative with respect to y
∞ = value at far field

Superscript

x = along the x, or derivative with respect to x
y = along the y, or derivative with respect to y
$*$ = evaluated at T^* (1250 K)

References

[1] De Ris, J. N., 1969, ''Spread of a Laminar Diffusion Flame,'' Proc. Combust. Inst., Pittsburgh, PA, **12**, pp. 241–252.
[2] Fakheri, A., and Olson, S. L., 1989, ''The Effects of Radiative Heat Loss on Microgravity Flame Spread,'' AIAA Paper No. 89-0504.
[3] Bhattacharjee, S., and Altenkirch, R. A., 1990, ''Radiation Controlled, Opposed-Flow Flame Spread in a Microgravity Environment,'' Proc. Combust. Inst., Pittsburgh, PA, **23**, pp. 1627–1633.
[4] Bhattacharjee, S., Altenkirch, R. A., Olson, S. L., and Sotos, R. G., 1991, ''Heat Transfer to a Thin Solid Combustible in Flame Spreading at Microgravity,'' ASME J. Heat Transfer, **113**, pp. 670–676.
[5] Chen, C.-H., and Cheng, M.-C., 1994, ''Gas Phase Radiative Effects on Downward Flame Spread in Low Gravity,'' Combust. Sci. Technol., **97**, pp. 63–83.
[6] T'ien, J. S., Shih, H. Y., Jiang, C. B., Ross, H. D., Miller, J., Fernandez-Pello, A. C., Torero, J. L., and Walther, D., 2001, ''Mechanisms of Flame Spread and Smolder Wave Propagation,'' in *Microgravity Combustion: Fire in Free Fall*, H. Ross, ed., Academic Press.
[7] Olson, S. L., Ferkul, P. V., and T'ien, J. S., 1988, ''Near-Limit Flame Spread Over a Thin Fuel in Microgravity,'' Proc. Combust. Inst., **22**, pp. 1213–1222.
[8] Bhattacharjee, S., Altenkirch, R. A., and Sacksteder, K., 1996, ''The Effect of Ambient Pressure on Flamespread Over Thin Cellulosic Fuel in a Quiescente, Microgravity Environment,'' ASME J. Heat Transfer, **118**, pp. 181–190.
[9] Lin, T.-H., and Chen, C.-H., 1999, ''Influence of Two-Dimensional Gas Phase Radiation on Downward Flame Spread,'' Combust. Sci. Technol., **141**, pp. 83–106.
[10] Grayson, G., Sacksteder, K. R., Ferkul, P. V., and T'ien, J. S., 1994, ''Flame Spreading Over a Thin Solid in Low-Speed Concurrent Flow-Drop Tower Experimental Results and Comparison With Theory,'' Microgravity Sci. Technol., **7**(2), pp. 187–195.
[11] Dietrich, D. L., Ross, H. D., Shu, Y., Chang, P., and T'ien, J. S., 2000, ''Candle Flame in Non-Buoyant Atmospheres,'' Combust. Sci. Technol., **156**, pp. 1–24.
[12] Bedir, H., T'ien, J. S., and Lee, H. S., 1997, ''Comparison of Different Radiation Treatments for a One-Dimensional Diffusion Flame,'' Combust. Theory Modell., **1**, pp. 395–404.
[13] Feier, I. I., Shih, H. Y., Sacksteder, K. R., and Tien, J. S., 2002, ''Upward Flame Spread Over Thin Solids in Partial Gravity,'' Proc. Combust. Inst., Pittsburgh, PA, **29**, pp. 2569–2577.
[14] Ferkul, P. V., and T'ien, J. S., 1994, ''A Model of Low-Speed Concurrent Flow Flame Spread Over a Thin Fuel,'' Combust. Sci. Technol., **99**, pp. 345–370.
[15] Jiang, C. B., 1995, ''A Model of Flame Spread Over a Thin Solid in Concurrent Flow With Flame Radiation,'' Ph.D. thesis, Case Western Reserve University, Cleveland, OH.
[16] Di Blasi, C., 1995, ''Predictions of Wind-Opposed Flame Spread Rates and Energy Feedback Analysis for Charring Solids in a Microgravity Environment,'' Combust. Flame, **100**, pp. 332–340.
[17] Rhatigan, J. L., Bedir, H., and T'ien, J. S., 1998, ''Gas-Phase Radiative Effects on the Burning and Extinction of a Solid Fuel,'' Combust. Flame, **112**, pp. 231–241.
[18] Tien, C. L., 1968, ''Thermal Radiation Properties of Gases,'' *Advances in Heat Transfer*, Academic Press, New York, **5**, pp. 234–254.
[19] Kumar, A., Shih, H., and T'ien, J. S., 2003, ''A Comparison of Extinction Limits and Spreading Rates in Opposed and Concurrent Spreading Flames Over Thin Solids,'' Combust. Flame, **132**, pp. 667–677.
[20] Patankar, S. V., 1980, *Numerical Heat Transfer and Fluid Flow*, Hemisphere Pub. Co., New York.
[21] Fiveland, W. A., 1984, ''Discerete Ordinates Solutions of the Radiative Transfer Equation for Rectangular Enclosures,'' ASME J. Heat Transfer, **106**, pp. 699–706.
[22] Kim, T. K., and Lee, H. S., 1989, ''Radiative Transfer in Two-Dimensional Anisotropic Scattering Media With Collimated Incidence,'' J. Quant. Spectrosc. Radiat. Transf., **42**, pp. 225–238.
[23] Frey, Jr., A. E., and T'ien, J. S., 1976, ''Near-Limit Flames Over Paper Samples,'' Combust. Flame, **26**, pp. 263–289.
[24] T'ien, J. S., 1986, ''Diffusion Flame Extinction at Small Stretch Rates: The Mechanism of Radiative Loss,'' Combust. Flame, **65**, pp. 31–34.
[25] T'ien, J. S., 1990, ''The Possibility of a Reversal of Material Flammability Ranking From Normal Gravity to Microgravity,'' Combust. Flame, **80**, pp. 355–357.
[26] Honda, L. K., and Ronney, P. D., 1988, ''Effect of Ambient Atmosphere on Flame Spread at Microgravity,'' Combust. Sci. Technol., **133**, pp. 267–291.
[27] Pettegrew, R., Street, K., Plitch, N., T'ien, J. S., and Morrison, P., 2003, ''Measurement and Evaluation of the Radiative Properties of a Thin Solid Fuels,'' AIAA Paper No. 2003-0511.
[28] Bhattacharjee, S., and Altenkirch, R. A., 1991, ''The Effect of Surface Radiation on Flame Spread in a Quiescent, Microgravity Environment,'' Combust. Flame, **84**, pp. 160–169.

Reverse Monte Carlo Method for Transient Radiative Transfer in Participating Media

Xiaodong Lu

Pei-feng Hsu
e-mail: phsu@fit.edu

Mechanical and Aerospace Engineering Department,
Florida Institute of Technology,
150 West University Blvd.,
Melbourne, FL 32901

The Monte Carlo (MC) method has been widely used to solve radiative transfer problems due to its flexibility and simplicity in simulating the energy transport process in arbitrary geometries with complex boundary conditions. However, the major drawback of the conventional (or forward) Monte Carlo method is the long computational time for converged solution. Reverse or backward Monte Carlo (RMC) is considered as an alternative approach when solutions are only needed at certain locations and time. The reverse algorithm is similar to the conventional method, except that the energy bundle (photon ensemble) is tracked in a time-reversal manner. Its migration is recorded from the detector into the participating medium, rather than from the source to the detector as in the conventional MC. There is no need to keep track of the bundles that do not reach a particular detector. Thus, RMC method takes up much less computation time than the conventional MC method. On the other hand, RMC will generate less information about the transport process as only the information at the specified locations, e.g., detectors, is obtained. In the situation where detailed information of radiative transport across the media is needed the RMC may not be appropriate. RMC algorithm is most suitable for diagnostic applications where inverse analysis is required, e.g., optical imaging and remote sensing. In this study, the development of a reverse Monte Carlo method for transient radiative transfer is presented. The results of non-emitting, absorbing, and anisotropically scattering media subjected to an ultra short light pulse irradiation are compared with the forward Monte Carlo and discrete ordinates methods results. [DOI: 10.1115/1.1773587]

Keywords: Heat Transfer, Nonintrusive Diagnostics, Numerical Methods, Radiation, Transient

Introduction

Recent research on the propagation of ultra-short light pulse inside the absorbing and scattering media has lead to some interesting applications in the area of material properties diagnostics, optical imaging, remote sensing, etc. The time scales of such processes are usually on the order of 10^{-12} to 10^{-15} seconds. In the case of remote sensing using a short light pulse, the pulse width can be in the order of 10^{-9} seconds. The corresponding spatial and temporal variations of radiation intensity in these processes are comparable. Therefore, the consideration of the transient term in the radiation transport equation is necessary. The simulation of transient radiation process is more complex than that in the steady state due to the hyperbolic wave equation coupled with the in-scattering integral term. Several numerical strategies have been developed, which include discrete ordinate method [1,2], finite volume method [3,4], integral equation models [5–7], and Monte Carlo method [8,9].

The Monte Carlo method is a numerical technique of solving various scientific and engineering problems by the simulation of random variables. Monte Carlo is one of the most versatile and widely used numerical methods, very suitable for solving multi-dimensional problems, especially when deterministic solutions are difficulty to obtain. Monte Carlo simulations have consumed a significant fraction of high performance computing time. With the advancement of the low-cost Beowulf cluster [10] and inherently high parallel efficiency of the Monte Carlo method [11,12], its usage will only grow over time.

However, the Monte Carlo method can be computationally very time consuming due to its root-mean-square error being limited by the number of sampling in the form of $O(N^{-0.5})$, in which N is the sampling number. That is why much of the effort in Monte Carlo development has been in construction of variance reduction methods that speed up the computation. The other approach, which has shown promising results, is the utilization of deterministic number sequences instead of random numbers for integration [13]—this belongs to the so-called quasi-Monte Carlo (QMC) method [14,15]. In theory, the *upper* error bound of QMC is proportional to $O(N^{-1}(\log N)^D)$, where D is the dimension of integration or the number of deterministic number sequence. In practice, depending on the quality of the number sequences and the nature of the problem, the error bound is typically between $O(N^{-0.5})$ to $O(N^{-1})$ [16] and special arrangements of the deterministic number sequences are frequently needed [17].

In the case of detecting radiation signals at some selected positions and/or given time intervals, the reverse Monte Carlo (RMC) method becomes very advantageous. Since computational results in the whole spatial and temporal domains are not always necessary, either MC or QMC becomes unnecessarily inefficient. The RMC method is based on the reciprocity principle in radiative transfer theory [18]. The RMC algorithm is similar to the conventional method, except that the energy or photon bundle is tracked in a time-reversal manner. Its migration is recorded from the detector into the participating medium, rather than from the source to the detector as in the conventional MC method. There is no need to keep track of the bundles that do not reach a particular detector. Thus, the RMC method takes up much less computation time than the conventional MC method. On the other hand, one should always note that the RMC method will generate far less information than the corresponding MC method.

Collins et al. [19] reported the earliest work on RMC relevant

Contributed by the Heat Transfer Division for publication in the JOURNAL OF HEAT TRANSFER. Manuscript received by the Heat Transfer Division August 4, 2003; revision received April 23, 2004. Associate Editor: S. T. Thynell.

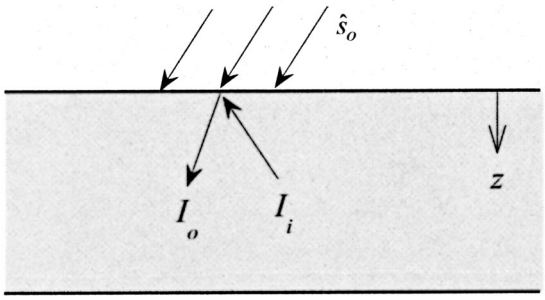

Fig. 1 Geometry of the collimated irradiation

to radiation transfer calculations. Adams and Kattawar [20] adopted the same concept of Collins, et al. in their study of spherical shell atmospheric radiation. They also provided justifications of RMC, which will be expanded in this study. In a series of rocket plume base heating calculations by Nelson [21], the RMC method was also found to be a practical tool to include various effects, e.g., spectral properties and scattering. To provide a more rigorous theoretical foundation to the RMC method, Walters and Buckius [22] utilized the reciprocity relations developed by Case [18]. Recently, Modest [23] used their results and applied to singular light source problems. The only RMC treatments for transient radiation processes reported so far, to the best of the authors' knowledge, are by Wu and Wu [7] and Andersson-Engels et al. [24]. However, the details of the RMC algorithm were not given in either paper and the RMC results of the latter work were inconsistent. This study will present a detailed and validated RMC method to simulate transient radiation process, particularly for light pulse propagation within scattering media, with validated solutions. The utilization of a Beowulf cluster for simulation demonstrates the RMC method has the potential for real time inverse analysis. Although only one-dimensional geometry is considered in this study, the algorithm can be readily extended to treat nonhomogeneous media and multi-dimensional geometry. The nonhomogeneous media problem was considered in a follow-up study [25,26].

Transient Radiation Transport

Consider a one-dimensional slab containing an absorbing and scattering medium, the radiative transfer equation (RTE) in a given direction $\hat{s}$ is [27]:

$$\frac{\partial I(\hat{r},\hat{s},t)}{c\,\partial t}+\frac{\partial I(\hat{r},\hat{s},t)}{\partial s}=-\kappa(\hat{r})I(\hat{r},\hat{s},t)+\frac{\sigma(\hat{r})}{4\pi}\int_{\Omega'=4\pi}I(\hat{r},\hat{s}',t)\Phi(\hat{s}',\hat{s})d\Omega' \tag{1}$$

where κ and σ are the extinction coefficient and scattering coefficient, respectively, c the speed of light in the medium, $\hat{s}$ the light propagation direction, and $\Phi(\hat{s}',\hat{s})$ the scattering phase function. The medium is assumed to be cold and gray.

The geometry of a collimated pulsed irradiation on the top surface of the slab medium is shown in Fig. 1. $I(\hat{s}_o,t)$ is the collimated irradiation intensity in direction $\hat{s}_o$. I_o is the intensity leaving the wall toward the medium and I_i the intensity coming from the medium toward the wall. It is convenient to use a concept similar to Olfe's [28] modified differential approximation by splitting the intensity into two components: one contributed by incident radiation and the other by medium emission and scattering. The former can be solved exactly with the boundary condition containing singular emission source and the latter by various numerical schemes. The approach has successfully treated various radiative transport problems, e.g., Liou and Wu [29] and Ramankutty and Crosbie [30,31]. With the time-dependent, incident collimated irradiation, e.g., a light pulse, one can separate the intensity into two parts

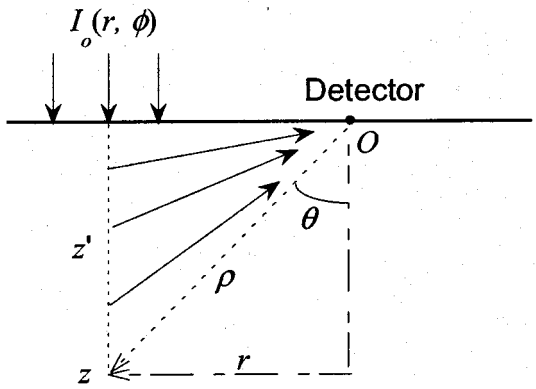

Fig. 2 Geometry of integrated intensity received at the detector

$$I(x,\hat{s},t)=I_c(x,\hat{s},t)+I_d(x,\hat{s},t) \tag{2}$$

In this equation, I_c is the attenuated intensity of the collimated beam, and I_d is the diffuse intensity, which is the in-scattered radiation into direction $\hat{s}$. Substitution of Eq. (2) into Eq. (1) and normalizing the terms give the dimensionless RTE,

$$\frac{\partial I_d(z^*,\hat{s},t^*)}{\partial t^*}+\mu\frac{\partial I_d(z^*,\hat{s},t^*)}{\partial z^*}+I_d(z^*,\hat{s},t^*)=\frac{\omega}{4\pi}\int_{4\pi}\Phi(\hat{s}',\hat{s})I_d(z^*,\hat{s}',t^*)d\Omega'+S(z^*,\hat{s},t^*) \tag{3}$$

where $t^*=\kappa ct$ and $z^*=\kappa z$. In the above equation, the out-scattered radiation source formed from the collimated irradiation contributes to the source term and is described by

$$S(z^*,\hat{s},t^*)=\frac{\omega}{4\pi}\int_{4\pi}\Phi(\hat{s}',\hat{s})I_c(z^*,\hat{s}',t^*)d\Omega' \tag{4}$$

where $I_c(z^*,\hat{s},t^*)$ is obtained by solving the RTE governing the attenuation of the collimated beam. In the case of a collimated beam in the z-direction the solution is

$$I_c(z^*,\hat{s},t^*)=I_o e^{-z^*}[H(t^*-z^*)-H(t^*-t_p^*-z^*)]\delta(\hat{s}-\hat{s}_o) \tag{5}$$

with $t_p^*=\kappa ct_p$ and t_p is the pulse width, δ the Dirac delta distribution, and H the Heaviside step function. Equation (4) becomes

$$S(z^*,\hat{s},t^*)=\frac{\omega}{4\pi}I_o e^{-z^*}[H(t^*-z^*)-H(t^*-t_p^*-z^*)]\Phi(\hat{s}_o,\hat{s}) \tag{6}$$

$\Phi(\hat{s}',\hat{s})=1+a\mu\mu'$ where μ is the direction cosine of $\hat{s}$. If the medium is isotropically scattering, then $a=0$. The collimated source function is then equivalent to the isotropic blackbody emission term. However, it is a time-dependent ''emission'' term.

Reverse Monte Carlo Method

In this section, the rationale and advantage of using the RMC method, in comparison of using the conventional Monte Carlo, are first demonstrated with a steady-state radiation source example. It is then followed by a discussion of the validity of RMC method based on the reciprocity principle developed by Case [18]. A subsection on detailed description of RMC algorithm is given at the end.

Figure 2 demonstrates the geometry of the intensity received at

the detector from a collimated source. For simplicity, consider the collimated irradiation, which spans from $r=0$ to $r=\infty$, to be a steady-state source. Consideration of transient sources in this geometry will have no effect on the discussion below of comparing the MC and RMC integrations. The collimated source irradiates normally on a semi-infinite, absorbing, and scattering medium. The detector is located at origin, *O*, and assumed to be of point size. The source is attenuated in the medium and, in particular, the source at a cylindrical coordinate position (r,z) shown in the figure is considered. The problem can be treated as axisymmetric with respect to the $r=0$ axis.

Integrating the steady-state RTE within the isotropic scattering and non-emitting medium, the intensity at any position *z*, including $z=0$, can be found as

$$I(z,\hat{s})=I(0,\hat{s})e^{-\kappa z}+\frac{\kappa}{4\pi}\int_0^{\infty}\int_{4\pi}I(z',\hat{s})e^{-\kappa(z-z')}d\Omega_s dz' \tag{7}$$

If only singly scattered photons are considered, that is, the collimated intensity being attenuated at position z' and then scattered to the detector, then the $I(z',\hat{s})$ inside the integral will be the attenuated collimated intensity, i.e., $I_o(r,\phi)e^{-\kappa z'}$. The intensity at the detector, $I(z=0,\hat{s})$, does not include the direct contribution from the collimated source in direction $\hat{s}_o$, i.e., the first term on the right hand side of Eq. (7). The integrated intensity over the incoming (lower) hemisphere at the detector can then be expressed as

$$G(0)=\frac{\kappa}{4\pi}\int_0^{\infty}\int_{2\pi}I_o(r,\phi)e^{-\kappa z'}e^{-\kappa\rho}d\Omega_d dz' \tag{8}$$

It should be pointed out that the $d\Omega_s$ in Eq. (7) is the solid angle from all in-scattered directions and $d\Omega_d$ in Eq. (8) is the solid angle viewed from the detector to position z'. The $G(0)$ represents the signal received at the detector. From Fig. 2,

$$d\Omega_d=\frac{dr(rd\phi)\cos\theta}{\rho^2} \tag{9}$$

Substitute into Eq. (8),

$$G(0)=\frac{\kappa}{4\pi}\int_0^{\infty}\int_0^{2\pi}\int_0^{\infty}\frac{I_o(r,\phi)e^{-\kappa z'}e^{-\kappa\rho}\cos\theta}{\rho^2}rdrd\phi dz' \tag{10}$$

Converting the (r,ϕ,z) coordinates into spherical coordinates of (ρ,ϕ,θ) with $r=\rho\sin\theta$, $z=\rho\cos\theta$, and the Jacobian of the transformation, Eq. (10) becomes

$$G(0)=\frac{\kappa}{4\pi}\int_0^{\infty}\int_0^{2\pi}\int_0^{\pi/2}I_o(r,\phi)e^{-\kappa\rho\cos\theta}e^{-\kappa\rho}\times\sin\theta\cos\theta d\theta d\phi d\rho \tag{11}$$

Equation (10) is the equivalent of Monte Carlo integration and Eq. (11) is the counter part of RMC integration. Two problems are immediately observed in Eq. (10): First, a truncation of *r* has to be determined, because if *r* is too large then sampling in some regions may not contribute much to the detector signal. Second, the ρ^2 in the denominator causes large statistical oscillation in the results for small ρ. By considering the same problem with the view point from the detector in Eq. (11), both of these problems are eliminated. It should be noted that the determination of radiative flux at the detector could be similarly obtained, although the sampling of the bundle direction will be different due to a different, cumulative distribution function.

Case [18] derived a fundamental identity that was based on the RTE. From that identity, the reciprocity principle used in this study is simply a special case. Implicitly assumed in the principle is $\Phi(\hat{s}',\hat{s})=\Phi(-\hat{s},-\hat{s}')$, i.e., the scattering phase function has time reflection symmetry. The most basic reciprocity principle states that

$$I(\hat{r}_1,-\hat{s}_1;\hat{r}_2,\hat{s}_2)=I(\hat{r}_2,-\hat{s}_2;\hat{r}_1,\hat{s}_1)$$

That is, the intensity at $\hat{r}_1$ and direction $-\hat{s}_1$ due to the point source at $\hat{r}_2$ in the direction $\hat{s}_2$ equals to the intensity at $\hat{r}_2$ and direction $-\hat{s}_2$ due to the point source at $\hat{r}_1$ in the direction $\hat{s}_1$. Several other reciprocity relations can be obtained from this. In the sense of Monte Carlo simulation, the bundles (photons) that finally reached the detector can be backtracked in both temporal and spatial manner.

As the bundle travels from the detector position back into the medium, the diffuse intensity caused by the collimated source (Eq. 6) must be integrated along the path length encountered by the bundle

$$I_d(z^*,\hat{s},t^*)=\int_0^{l^*}S(z^*,\hat{s},t^*)\exp(-\kappa l^{*\prime})dl^{*\prime} \tag{12}$$

In a steady-state source problem, the backtracking bundle will encounter the source at a certain path length. Otherwise, I_d is zero. In ultra-short light pulse propagation or transient problem, since both the bundle and source are moving in temporal and spatial space, the determination of when and where the bundle and source will meet needs to be considered carefully. With such information, the lower and upper bounds of the above integration can be found. The consideration can be greatly simplified by noting that $dt=ds/c$, i.e., the space and time are not two independent variables, and using the Lagrangian view point for bundle movement. The consideration is similar to that in the discussion leading to the "domain of influence" described in Tan and Hsu [5]. A detailed analysis and discussion how this determination can be carried out are given below.

RMC Algorithm.

1. Assume *N* bundles arrive at the detector. Start the first bundle and pick a backtracking direction and time t_1, which is the bundle arrival time at the detector. The direction can be uniformly distributed to minimize the fluctuation in the result. The direction is decided by the cumulative distribution functions of θ and ϕ that are, in turns, dependent on the radiation information needed at the detector, e.g., integrated intensity or heat flux over a finite solid angle.
2. Pick a path length (l_κ) based on κ, the extinction coefficient.
3. At the end of the path length, check the new (and earlier) time $t_2\,(=t_1-l_\kappa/c)$ to see if it is still greater than 0 and if the pulse, also at t_2, would have encountered the bundle. If so, integrate the collimated source according to Eq. (12). The integration limits are determined by the following procedure. Since the pulse has a certain temporal width t_p that spans over a finite spatial distance ct_p, it is necessary to check how the bundle at the earlier time t_2 and position z_2 would have intersected with the pulse, whose leading edge was at position $z_{p2}=ct_2$. There are three possible scenarios, which are depicted in Fig. 3(*a*) and discussed below in detail. Note that in Fig. 3(*a*) the three path lengths $\overline{oa}$, $\overline{ob}$, and $\overline{oc}$ are equal to the pulse travel distance $(z_{p1}-z_{p2})$. The two other path lengths, $\overline{o'a}$ and $\overline{o'c}$, are also equal to the pulse travel distance but are not drawn to the scale.

(a) $(z_{p2}-ct_p)\leq z_2\leq z_{p2}$—the bundle lands inside the pulse. The upper limit of the source integration (Eq. 12) is $z_U=z_2$. As for the lower limit of the integration z_L, there are two possibilities:

(1) $(z_{p1}-ct_p)\leq z_1\leq z_{p1}$: the point that the bundle and pulse would meet at a time after t_2 is also inside the pulse, then $z_L=z_1$. Note that $z_{p1}=ct_1$ is the position of the pulse's leading edge at time t_1. The backtracking bundle's path is shown in Fig. 3(*a*) as line $\overline{o'a}$.

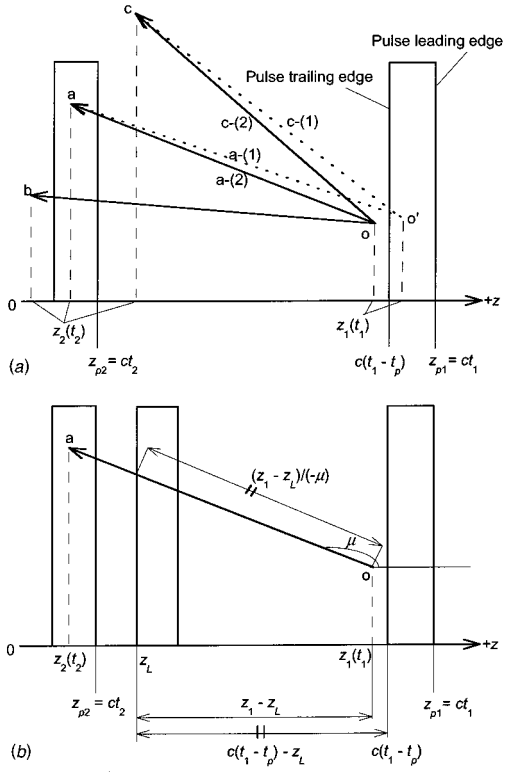

Fig. 3 (*a*) Three possible scenarios that a backtracking bundle's path would have positioned relative to the pulse at a time t_2. The end points a, b, and c corresponds to the cases (a), (b), and (c), respectively, described in the algorithm section step 3; (*b*) The relation of backtracking bundle path length, i.e., case (a)-part(2), and pulse's travel distance from t_2 to t_1. The path length of $(z_1-z_L)/(-\mu)$ equals the pulse travel distance at the same time interval. The equality leads to the determination of z_L. In this case z_U is z_2.

(2) $(z_{p1}-ct_p)>z_1$: the point that the bundle and pulse would meet at a time after t_2 is between z_1 and z_2. Also the intersection point must be at the trailing edge of the pulse. The backtracking bundle's path is shown in Fig. 3(*a*) as line $\overline{oa}$. Since the bundle and pulse travel distances are the same,

$$\frac{z_1-z_L}{-\mu}=c(t_1-t_p)-z_L$$

Thus,

$$z_L=\frac{\mu c(t_1-t_p)+z_1}{1+\mu} \tag{13}$$

where μ is the direction cosine of the path from z_1 to z_2. The derivation of Eq. (13) can be easily obtained with the aid of Fig. 3(*b*).

Go to step 4.

(b) $z_2<(z_{p2}-ct_p)$—the pulse would not have met the bundle. That is, the bundle was lagging behind the pulse and their path lengths would never intersect. Go to step 4.

(c) $z_2>z_{p2}$—the pulse would have met and moved across the backtracking bundle while traveling from z_{p2} to z_{p1}. The paths of bundle and pulse intersected at two positions. The first or earlier intersection position is the upper limit of the source integration, z_U, which must be between z_1 and z_2 and is also at the leading edge of the pulse,

$$z_U=\frac{\mu ct_1+z_1}{1+\mu} \tag{14}$$

Similar to Eq. (13), a diagram like Fig. 3(*b*) can be drawn to prove Eq. (14). As for the second or later intersection position, i.e.,the lower limit of the source integration z_L, there are also two possibilities:

(1) $(z_{p1}-ct_p)\leqslant z_1\leqslant z_{p1}$: the later intersection position at a time after t_2 is inside the pulse, then $z_L=z_1$. The backtracking bundle's path is shown in Fig. 3(*a*) as line $\overline{o'c}$.

(2) $(z_{p1}-ct_p)>z_1$: the later intersection position at a time after t_2 is between z_1 and z_2. This intersection point must be at the trailing edge of the pulse. The backtracking bundle's path is shown in Fig. 3(*a*) as line $\overline{oc}$. Following the same procedure in obtaining Eq. (13), the lower integration limit is

$$z_L=\frac{\mu c(t_1-t_p)+z_1}{1+\mu} \tag{15}$$

Also in this case, since the bundle and pulse would have never met at any time earlier than t_2, terminate the bundle backtracking, go to step 1, and start a new bundle from the detector;

4. At the end of path length, calculate the absorption decay and determine whether the bundle is absorbed or scattered from the albedo. If scattered, pick a new direction based on phase function and return to step 2. If absorbed, go to next step;
5. Go to step 1 for a new bundle and complete the tally of all N bundles.

For a nonhomogeneous medium, step 2 needs to be modified to consider the variation of radiation properties in the path length. Walter and Buckius [22] suggested that absorption suppression can be used to determine the path length, based on the scattering coefficient, to speed up the calculation, as shown by Modest [23]. If this approach was used, then step 4 will not be needed. The nonhomogeneous media treatment and absorption suppression are considered in authors' follow-up work [25,26]. In the case of multi-dimensional geometry, the algorithm remains the same. The only difference is the bundle's travel position has to be considered in the corresponding coordinate system. In one-dimensional slabs, only a z-coordinate is needed. In the case of nonhomogeneous media, additional consideration of volume to volume variation of properties in the source path length integration has to be treated.

An important advantage of the above RMC method is that it can provide the solution at a specific time or over a time interval. It is unlike other solution methods or MC method that the complete time history from $t=0$ to any time of interest has to be computed. The information over specific time interval is of interest to time-gated measurements. This particular advantage of the RMC method further reduces the amount of computation and may have the potential of being used in the real-time signal processing and inverse analysis for optical image re-construction and remote sensing.

Results and Discussion

The parallel computer architecture used in this study is simply a collection of computers with commodity processors and parts. The coding is based on the Single Program Multiple Data model and uses the Message Passing Interface (MPI) library [32,33]. The system consists of one master or root node and many slave or compute nodes. The communication among nodes, in this case, is through a private, channel-bonded FastEthernet. A 48-node IBM Linux cluster was used in this study. This system can be extended to 96 processors with dual processors in each node. Currently, except the head node, only one processor is installed in each of the compute nodes. Each compute node is an IBM ×330 x-Series with a Pentium III 866 MHz processor and 512 MB SDRAM. The

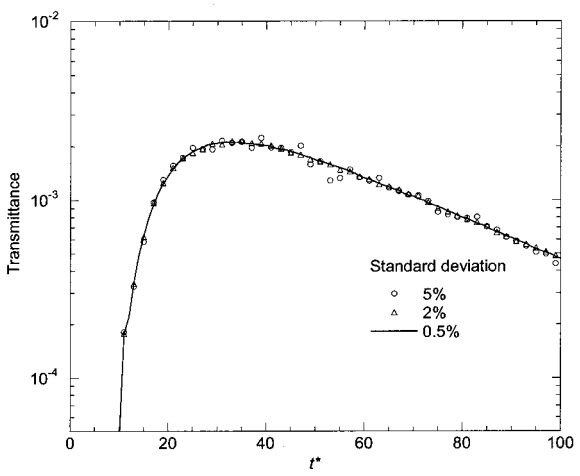

Fig. 4 The convergence of solutions with different variance. The medium has an isotropic scattering phase function, scattering albedo=0.998, and optical thickness=10.

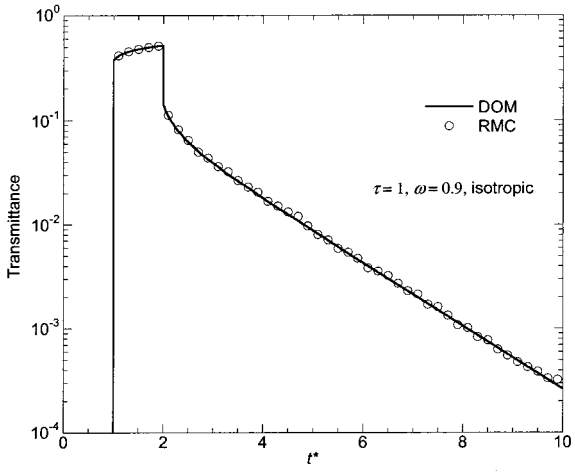

Fig. 5 Wave front resolution of the RMC method

total system memory space is 24 GB. Detailed hardware and software configuration information is given in the website at http://olin.fit.edu/beowulf/.

The geometry solved in this paper is a one-dimensional slab, with radiation signal solved on the opposite side of the source. As a first test of the RMC algorithm used in this study, it is used to solve a slab medium of $\tau=10$ and large scattering albedo 0.998 subjected to a collimated pulse irradiation [9]. The incident pulse width $t_p^*=1$ is modeled by two consecutive Heaviside unit step functions at the boundary $z=0$ and the normalized collimated intensity is equal to 1. The solution improves as the standard deviation is reduced from 5 percent, 2 percent, to 0.5 percent (Fig. 4). The 5 percent curve shows moderate statistical oscillations and 0.5 percent curve is very smooth. The temporal transmittance curve is consistent with those reported by our earlier work.

Many existing numerical schemes to simulate transient radiative transport simply fail to resolve the wave front correctly, e.g., Mitra et al. [34], leading to incorrect propagation speed. A part of the rigorous tests of transient radiation transfer numerical schemes, including Monte Carlo algorithms, is to demonstrate the capability of wave front resolution. Figure 5 depicts the excellent agreement between the RMC method and DOM, as well as the sharp collimated pulse front in this regard. The medium has unit optical thickness and isotropic scattering with albedo being equal to 0.9. The DOM solution was validated with our prior integral equation and Monte Carlo solutions.

To further verify the RMC algorithm, the simulations of forward anisotropically, isotropically, and backward anisotropically scattering media are compared with the discrete ordinates method with which accurate transient solutions were obtained [1]. Comparison with a forward Monte Carlo method [33] is also made on the same plot (Fig. 5). A 5 percent RMC solution takes about 12 seconds using MPI parallel library on 10 nodes of the aforementioned Beowulf cluster. It takes about two hours by the Monte Carlo method using a serial code on a 633 MHz 21164A Alpha processor workstation [9]. The run time is shorter if the albedo is smaller. It should be emphasized that the typical application of RMC solution of pulse propagation may be over a time interval, not from $t=0$ to a given time. As previously discussed, RMC is suitable for problems with radiation information needed only at limited locations and time. It is not a replacement for the conventional Monte Carlo method in other situations. Therefore, a direct comparison of computational time between MC and RMC was not made.

Figure 6 shows good agreement between the MC and RMC solutions and somewhat small difference with the discrete ordinates solutions in three cases of linear anisotropic scattering media. In this figure the difference between MC and RMC solutions can hardly be seen. The temporal transmittance curves of three different cases are shown. The number of energy bundles used in the simulation at different time step varies from 10^5 to 2×10^5 by setting the standard deviation of the solution to be 5 percent and it takes about 12 seconds to finish. It takes 47 seconds by setting standard deviation at 2 percent with the bundle number varying from 10^5 to 1.6×10^6. In comparison, the number of bundles used by Monte Carlo is 2×10^7 and the total number of bundles by the RMC method is about an order of magnitude larger with 2 percent standard deviation. It is noted that the results by Monte Carlo method with this bundle number still show a large degree of oscillation [9]. This indicates more energy bundles need to be used in the MC simulation to reduce the statistical oscillations at long time [25]. Setting the standard deviation to be 0.5 percent, the RMC solution become much smoother and the corresponding bundle numbers vary from 3.2×10^6 to 1.28×10^7. The total computational time is 11 minutes using 10 nodes with 0.5 percent standard deviation setting.

Figure 7 shows the variation of the bundle number used in each time instant and for three different phase functions. The result is based on the 2 percent standard deviation setting. A similar trend is found in other standard deviation settings. First, the bundle

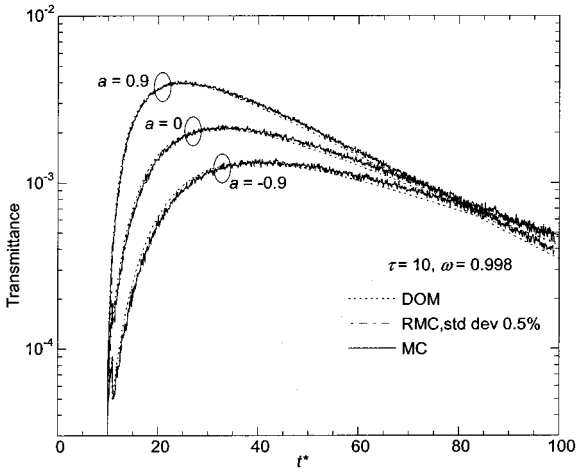

Fig. 6 Comparison of RMC, MC, and Discrete Ordinates Method solutions for isotropic scattering slab with a collimated pulse irradiation

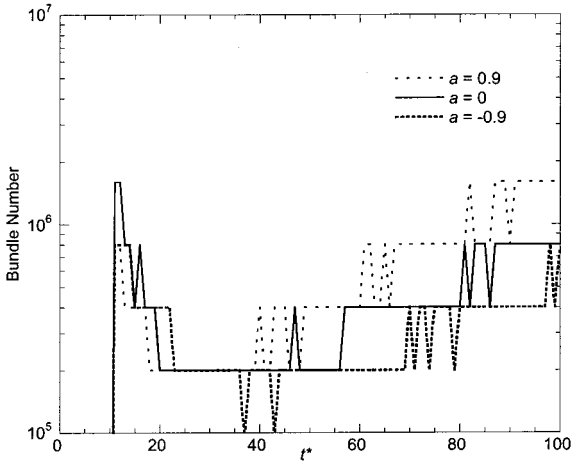

Fig. 7 Bundle number used in three difference scattering phase functions used in Fig. 6. The converged solutions have 2 percent standard deviation.

number decreases as the transmittance signal reaches its peak. Then, the bundle number increases as the transmittance signals gradually levels off. Secondly, for $t^*>30$, i.e., after the pulse passes the medium, the bundle number used is higher for forward scattering medium and lower for backward scattering medium. In the backward scattering medium, the bundles tend to stay inside the medium longer, and the chance to encounter a pulse is thus higher. This leads to quicker convergence with fewer number of bundles used. The behavior of bundle movement is similarly described in our earlier work on the DOM [1]. At any given t^*, the appropriate amount of energy bundles used to meet the standard deviation setting indicates that the RMC method is very efficient in controlling the number of bundles needed for simulation.

A series of tests of the proposed RMC algorithm shows that it can provide accurate simulations at given locations or time with significant reduction in computational time when compared to the traditional MC method. The RMC method will be used to compare pulsed laser measurements of three-dimensional scattering media in a follow-up publication.

In transient problems, one of the forward Monte Carlo methods can carry out the time stepping of the simulation of all the N bundles simultaneously at a given time step [9]. While this approach consumes very large amount of memory, it can achieve good parallel efficiency. A different approach is to trace the bundle one at a time and record the time history accordingly [12]. This second approach does not perform time marching for all bundles simultaneously, but rather it ''assembles'' the temporal information of all bundles at the end. In this way, the memory requirement is not an issue, but it can not provide the variance of the simulations during the calculation. It should be pointed out that the coarse grain parallelism is retained in all of the above MC and RMC algorithms. As far as the requirements of reducing memory usage and obtaining solution variance during the calculation, the reverse Monte Carlo algorithm is more suitable.

Conclusions

The RMC simulations are conducted for transient radiative transfer process within absorbing, scattering, and non-emitting participating media. Details about the RMC algorithm are developed and discussed. The solutions are validated with existing solutions obtained by Monte Carlo and discrete ordinates methods. The RMC method was shown to be a very effective way to reduce the long computational time and memory requirements compared to the Monte Carlo method when only certain spatial and temporal domain information is needed. This method provides a computationally efficient scheme for remote sensing and optical imaging inverse analysis. It is possible to apply the method in real-time applications because of the small amount of time used in a cluster system.

Acknowledgment

The parallel computing system used in the simulations was provided by a grant from the National Science Foundation, Grant No. EIA-0079710. Dr. Rita V. Rodriguez is the program director.

Nomenclature

a = linear anisotropic scattering phase function coefficient
c = propagation speed of radiation transport in the medium, m/s
D = dimension of integral
G = integrated intensity, W/m^2
I = radiation intensity, W/m^2 sr
I_o = radiation intensity at boundary $z=0$, W/m^2 sr
L = total slab thickness, m
N = number of samplings or energy bundles
r = radial coordinate, m
$\hat{r}$ = position vector of a location (x,y,z) in space
s = geometric path length, m
$\hat{s}$ = unit vector along a given direction
t = time, s
t_p^* = pulse parameter, $c\kappa t_p$
z = coordinate, m

Greek Symbols

Φ = scattering phase function
ϕ = azimuthal angle
κ = extinction coefficient, m^{-1}
μ = direction cosine in z-direction
θ = polar angle
ρ = distance, m
σ = scattering coefficient, m^{-1}
τ = optical thickness of the one-dimensional slab medium, κL
Ω = solid angle, sr
ω = scattering albedo, σ/κ

Superscripts

$'$ = dummy variables
$*$ = normalized variables
$\wedge$ = vector

Subscripts

c = collimated or direct attenuation component
d = detector location
L = lower limit of source integration
o = collimated pulse direction
p = pulse
s = multiply scattered or diffuse component; in-scattering direction
U = upper limit of source integration

References

[1] Sakami, M., Mitra, K., and Hsu, P.-f., 2000, ''Transient Radiative Transfer in Anisotropically Scattering Media Using Monotonicity-Preserving Schemes,'' *Proceedings, the ASME 2000 Int. Mechanical Engineering Congress & Exposition*, Orlando, FL.
[2] Sakami, M., Mitra, K., and Hsu, P.-f., 2002, ''Analysis of Light-Pulse Transport Through Two-Dimensional Scattering and Absorbing Media,'' J. Quant. Spectrosc. Radiat. Transf., **73**(2–5), pp. 169–179.
[3] Chai, J. C., 2003, ''One-Dimensional Transient Radiation Heat Transfer Modeling Using a Finite-Volume Method,'' Numer. Heat Transfer, **44**(2), pp. 187–208.
[4] Lu, X., Hsu, P.-f., and Chai, J. C., 2003, ''Transient Radiative Transfer of Light Pulse Propagation in Three-Dimensional Scattering Media With Finite Volume Method and Integral Equation Model,'' ASME Paper No. HT2003-47455.

[5] Tan, Z.-M., and Hsu, P.-f., 2001, ''An Integral Formulation of Transient Radiative Transfer,'' ASME J. Heat Transfer, **123**(3), pp. 466–475.
[6] Wu, C.-Y., 2000, ''Propagation of Scattered Radiation in a Participating Planar Medium With Pulse Irradiation,'' J. Quant. Spectrosc. Radiat. Transf., **64**(5), pp. 537–548.
[7] Wu, S.-H., and Wu, C.-Y., 2000, ''Integral Equation Solutions for Transient Radiative Transfer in Nonhomoegeneous Anisotropically Scattering Media,'' ASME J. Heat Transfer, **122**(4), pp. 818–822.
[8] Brewster, M. Q., and Yamada, Y., 1995, ''Optical Properties of Thick, Turbid Media From Picosecond Time-Resolved Light Scattering Measurements,'' Int. J. Heat Mass Transfer, **38**, pp. 2569–2581.
[9] Hsu, P.-f., 2001, ''Effects of Multiple Scattering and Reflective Boundary on the Transient Radiative Transfer Process,'' Int. J. Therm. Sci., **40**(6), pp. 539–545.
[10] Sterling, T., Becker, D. J., Savarese, D., Dorband, J. E., Ranawak, U. A., and Packer, C. V., 1995, ''Beowulf: A Parallel Workstation for Scientific Computation,'' *Sagamore Computer Conference on Parallel Processing*, Pennsylvania State Univ. Press, University Park, PA.
[11] Siegel, R., and Howell, J. R., 2002, *Thermal Radiation Heat Transfer*, 4th ed., Taylor & Francis, New York, NY.
[12] Sawetprawichkul, A., Hsu, P.-f., and Mitra, K., 2002, ''Parallel Computing of Three-Dimensional Monte Carlo Simulation of Transient Radiative Transfer in Participating Media,'' AIAA paper No. 2002-2901.
[13] O'Brien, D. M., 1992, ''Accelerated Quasi Monte Carlo Integration of the Radiative Transfer Equation,'' J. Quant. Spectrosc. Radiat. Transf., **48**(1), pp. 41–59.
[14] Holton, J. H., 1960, ''On the Efficiency of Certain Quasi-Random Sequences of Points in Evaluating Multi-Dimensional Integrals,'' Numerische Mathematik, **2**, pp. 84–90.
[15] Niederreiter, H., 1978, ''Quasi-Monte Carlo Method and Pseudo-Random Numbers,'' Bull. Am. Math. Soc., **84**(6), pp. 957–1041.
[16] Bratley, P., Fox, B. L., and Niederreiter, H., 1992, ''Implementation and Tests of Low-Discrepancy Sequences,'' ACM Trans. Model. Comput. Simul., **2**(3), pp. 195–213.
[17] Spanier, J., and Li, L., 1997, ''Quasi-Monte Carlo Methods for Integral Equations,'' in *Proceedings, Monte Carlo and Quasi-Monte Carlo Methods in Scientific Computing Conf.* the University of Salzburg, Salzburg, Austria, July 9–12, 1996, *Springer Lecture Notes on Statistics* #127, Springer, New York.
[18] Case, K. M., 1957, ''Transfer Problems and the Reciprocity Principle,'' Rev. Mod. Phys., **29**(4), pp. 651–663.
[19] Collins, D. G., Blattner, W. G., Wells, M. B., and Horak, H. G., 1972, ''Backward Monte Carlo Calculations of the Polarization Characteristics of the Radiation Emerging From Spherical-Shell Atmospheres,'' Appl. Opt., **11**(11), pp. 2684–2696.
[20] Adams, C. N., and Kattawar, G. W., 1978, ''Radiative Transfer in Spherical Shell Atmospheres—I. Rayleigh Scattering,'' Icarus, **35**, pp. 139–151.
[21] Nelson, H. F., 1992, ''Backward Monte Carlo Modeling for Rocket Plume Base Heating,'' AIAA J., **6**(3), pp. 556–558.
[22] Walters, D. V., and Buckius, R. O., 1992, ''Rigorous Development for Radiation Heat Transfer in Nonhomogeneous Absorbing, Emitting, and Scattering Media,'' Int. J. Heat Mass Transfer, **135**(12), pp. 3323–3333.
[23] Modest, M. F., 2003, ''Backward Monte Carlo Simulations in Radiative Heat Transfer,'' ASME J. Heat Transfer, **125**, pp. 57–62.
[24] Andersson-Engels, S., Enejder, A. M. K., Swarting, J., and Pifferi, A., 2000, ''Accelerated Monte Carlo Models to Simulate Fluorescence of Layered Tissue,'' in *Photon Migration, Diffuse Spectroscopy, and Optical Coherence Tomography: Imaging and Functional Assessment*, S. Andersson-Engels and J. G. Fujimoto, eds., SPIE, **4160**, pp. 14–15.
[25] Lu, X., and Hsu, P.-f., 2004, ''Reverse Monte Carlo Simulations of Light Pulse Propagation in Nonhomogeneous Media—Part I: Theoretical Development,'' accepted by *the Fourth Int. Symp. of Radiation Transfer*, Istanbul, Turkey.
[26] Lu, X., and Hsu, P.-f., 2004, ''Reverse Monte Carlo Simulations of Light Pulse Propagation in Nonhomogeneous Media—Part II: Numerical Simulations,'' accepted by *the Fourth Int. Symp. of Radiation Transfer*, Istanbul, Turkey.
[27] Ozisik, M. N., 1973, *Radiative Transfer and Interaction with Conduction and Convection*, J. Wiley, New York.
[28] Olfe, D. B., 1970, ''Radiative Equilibrium of a Gray Medium Bounded by Nonisothermal Walls,'' AIAA *Progress in Astronautics and Aeronautics*, **23**, pp. 295–317.
[29] Liou, B.-T., and Wu, C.-Y., 1997, ''Ray Effects in the Discrete-Ordinate Solution for Surface Radiation Exchange,'' Int. J. Heat Mass Transfer, **32**, pp. 271–275.
[30] Ramankutty, M. A., and Crosbie, A. L., 1997, ''Modified Discrete-Ordinates Solution of Radiative Transfer in Two-Dimensional Rectangular Enclosures,'' J. Quant. Spectrosc. Radiat. Transf., **57**(1), pp. 107–140.
[31] Ramankutty, M. A., and Crosbie, A. L., 1998, ''Modified Discrete-Ordinates Solution of Radiative Transfer in Three-Dimensional Rectangular Enclosures,'' J. Quant. Spectrosc. Radiat. Transf., **60**(1), pp. 103–134.
[32] Lu, X., and Hsu, P.-f., 2003, ''Parallel Computing of an Integral Formulation of Transient Radiation Transport,'' AIAA *J. Thermophysics Heat Transf.*, **17**(4), pp. 425–433.
[33] Sawetprawichkul, A., Hsu, P.-f., and Mitra, K., 2000, ''A Monte Carlo Study of the Transient Radiative Transfer Within the One-Dimensional Layered Slab,'' *Proceedings, ASME 2000 Int. Mechanical Engineering Congress & Exposition*, ASME HTD-Vol. 366-1, pp. 145–153, Orlando, FL.
[34] Mitra, K., Lai, M.-S., and Kumar, S., 1997, ''Transient Radiation Transport in Participating Media Within a Rectangular Enclosure,'' AIAA *J. Thermophysics Heat Transf.*, **11**(3), pp. 409–414.

A Two-Temperature Model for the Analysis of Passive Thermal Control Systems

Shankar Krishnan

Jayathi Y. Murthy

Suresh V. Garimella
e-mail: sureshg@ecn.purdue.edu

Cooling Technologies Research Center,
School of Mechanical Engineering,
Purdue University, West Lafayette, IN
47907-2088

Passive control of steady and unsteady thermal loads using effective thermal conductivity enhancers, such as metal foams, internal fins and metal filler particles, is being explored for a variety of electronics applications. The interstices are filled with air, phase change materials, or other fluids. Local thermal equilibrium between the solid filler and the matrix is not ensured in such systems since their thermal diffusivities are frequently very different. The use of a single volume-averaged energy equation for both the phases cannot be justified in such situations. A two-medium approach is used in the present work to account for the local thermal non-equilibrium. Separate energy equations are written for the solid and fluid respectively, and are closed using a steady-state interphase heat transfer coefficient between the two phases. A general momentum equation which includes the Brinkman-Forchheimer extension to Darcy flow is employed. The resulting equations are solved implicitly using a fully transient method on fixed orthogonal co-located finite volumes. Unsteady natural convection in a metal-foam filled cavity is computed. The influence of various parameters such as the ratios of solid-to-fluid thermal conductivities and heat capacities, Rayleigh number, Prandtl number and Darcy number on the thermal and flow fields is investigated. The results illustrate that local thermal equilibrium is not assured, either during the transient or at steady state for the range of parameters considered. Furthermore, even if the steady-state solid-to-fluid temperature differences are small, large temperature differences are seen during the unsteady response. [DOI: 10.1115/1.1773194]

Keywords: Enhancement, Heat Transfer, Natural Convection, Non-Equilibrium, Porous Media

Introduction

Thermal management of electronics is becoming increasingly challenging as chip-level heat fluxes increase at a rapid rate. Cooling can be achieved either by using conventional techniques that utilize active components like fans, or with passive techniques such as phase change thermal storage units and heat pipes. In many emerging cooling designs, thermal conductivity enhancers such as metallic foams, internal fins and metallic particles are used. The interstices contain either fluid or air. In thermal energy storage applications, for example, phase change materials (PCMs) are used. These materials are particularly attractive for transient applications where the heat generation experiences frequent short spikes in its magnitude. In addition to a high latent heat of melting, phase change materials used in electronics cooling must have high thermal diffusivity to quickly conduct away the dissipated heat into the bulk of the PCM. Though typical PCMs in popular use (e.g., paraffins) have very high latent heats of melting (order of 10^5 J/kg or more) [1] and isobaric specific heat capacities (order of 1000 J/kg K or more) [1], they suffer from very low thermal conductivities (order of 1 W/mK or less). Further discussion of the characteristics of solid/liquid and liquid/vapor PCMs is available in [2,3]. It is therefore necessary to increase the effective thermal conductivity of the PCM through the use of internal fins, foams or filler particles. In high power electronics applications, metal foams with high porosity have been proposed to provide increased surface area for passive single-phase heat transfer.

In general, metal foams are mathematically modeled using the technique of volume-averaging owing to the complexity involved in modeling the metal foam and saturating fluid separately. Hunt and Tien [4] explored forced convection in metal foams saturated with water. They studied the effects of thermal dispersion on forced convection using a single energy equation assuming a local thermal equilibrium between the metal foam and fluid phase.

Amiri and Vafai [5,6] used a semi-heuristic model to account for local thermal nonequilibrium for steady and transient forced convective flows through a bed of spherical particles. They explored the importance of non-Darcian terms and thermal dispersion effects on thermal and flow characteristics. Error maps were introduced to quantify the results. The solid-to-fluid thermal conductivity ratio was found to have a profound influence on the local thermal equilibrium. Lee and Vafai [7] performed an analytical study of forced convective flows in a porous bed. An electrical network was developed to represent the heat transfer through the porous medium. The validity of a single volume-averaged energy equation was discussed based on the solid and fluid temperature differentials obtained from a two-energy equation model. The error in using the one-equation model was found to increase with a decrease in the ratio of effective conductivity of the fluid to that of the solid and with a decrease in Biot number based on the interstitial heat transfer coefficient. Lu et al. [8] developed an analytical model for the convection heat transport through metal foams. Simplifying assumptions were made and guidelines for optimum foam structures were proposed for maximum heat transfer for a given power input. Minkowycz et al. [9] performed a theoretical study to analyze the validity of assuming local thermal equilibrium in heat transfer through a porous fluidized bed. It was shown that local thermal equilibrium depends on the size of the porous layer, pore size, interstitial heat transfer coefficient and thermophysical properties. Calmidi and Mahajan [10] performed an experimental investigation of forced convection in metal foams with air and water as fluid phases. An empirical correlation was also reported. Alazmi and Vafai [11] analyzed a variety of porous me-

Contributed by the Heat Transfer Division for publication in the JOURNAL OF HEAT TRANSFER. Manuscript received by the Heat Transfer Division June 2, 2003; revision received March 24, 2004. Associate Editor: K. S. Ball.

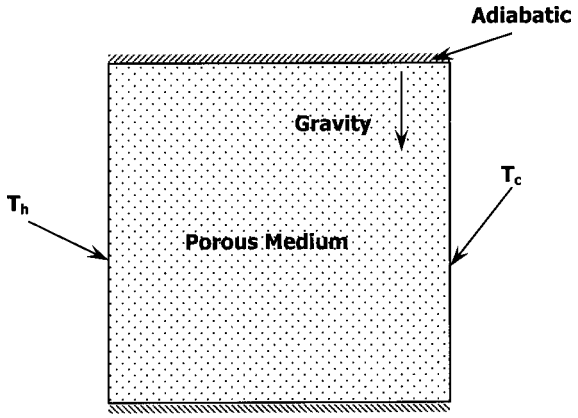

Fig. 1 Schematic diagram of the problem considered

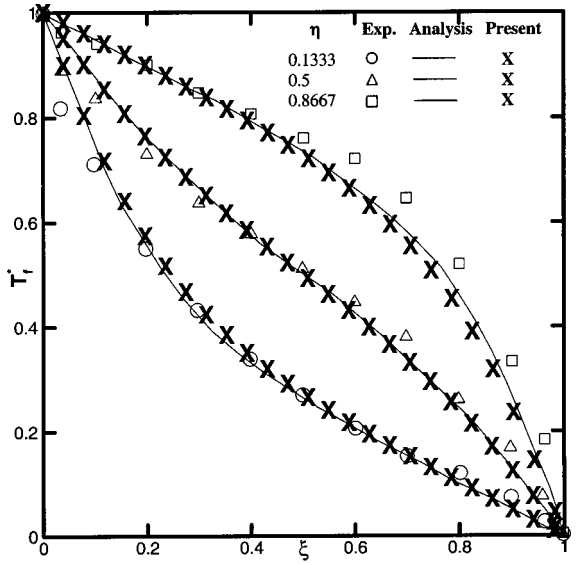

Fig. 2 Comparison of the present work (×) with experimental and numerical predictions of Beckermann and Viskanta [20]

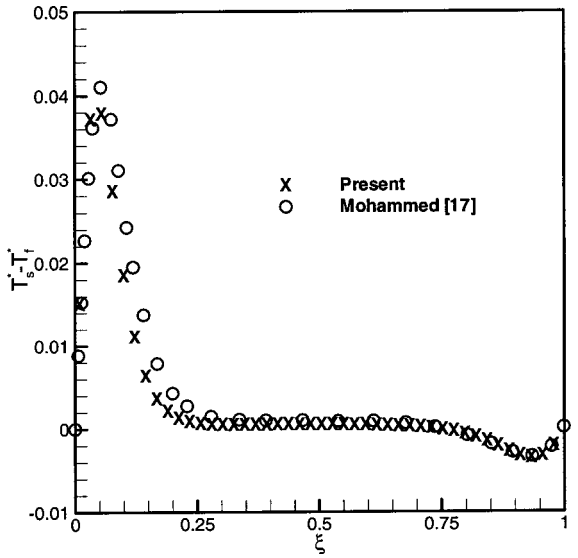

Fig. 3 Comparison of the predicted temperature difference between solid and fluid phases (×) with the numerical predictions of Mohammed [18] (○) at η=0.25 for Pr=1 and thermal conductivity ratio=1.0

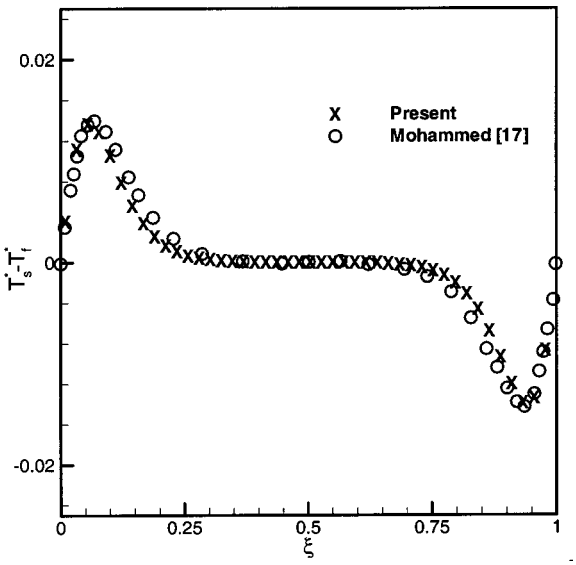

Fig. 4 Comparison of the predicted temperature difference between solid and fluid phases (×) with the numerical predictions of Mohammed [18] (○) at η=0.5 for Pr=1 and thermal conductivity ratio=1.0

dia transport models for forced convection in porous beds. The effects of variations in existing semi-heuristic models, effects of porosity, thermal dispersion and local thermal equilibrium were reported. Calmidi and Mahajan [12] reported an experimental and numerical study of forced convection in metal foams under local thermal non-equilibrium conditions. Hwang et al. [13] performed experiments on metal foams. They measured the interstitial convective heat transfer and frictional drag for forced convective flows using a transient single-blow technique. Empirical correlations for interstitial heat transfer coefficient were reported. Further details of the thermal non-equilibrium modeling of forced convection can be obtained from [14].

Natural convection in porous media is also encountered in many applications [15,16]. However, while many studies have

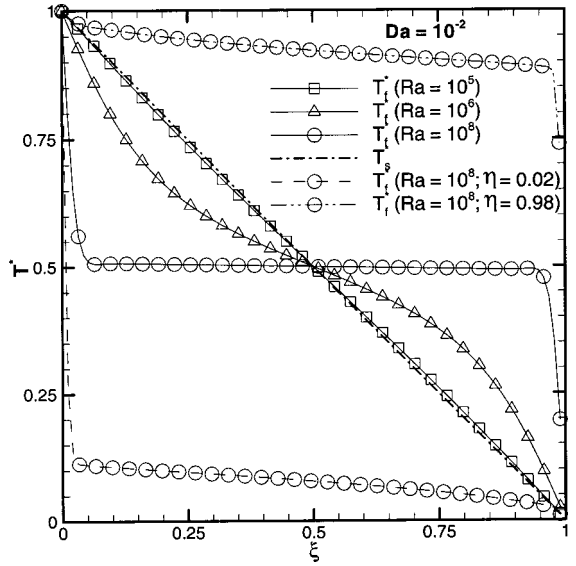

Fig. 5 Spatial variation of solid and fluid temperature distribution for zero inter-phase heat transfer coefficient (Nu_f=0). For all Rayleigh numbers the solid temperature distribution is a straight line.

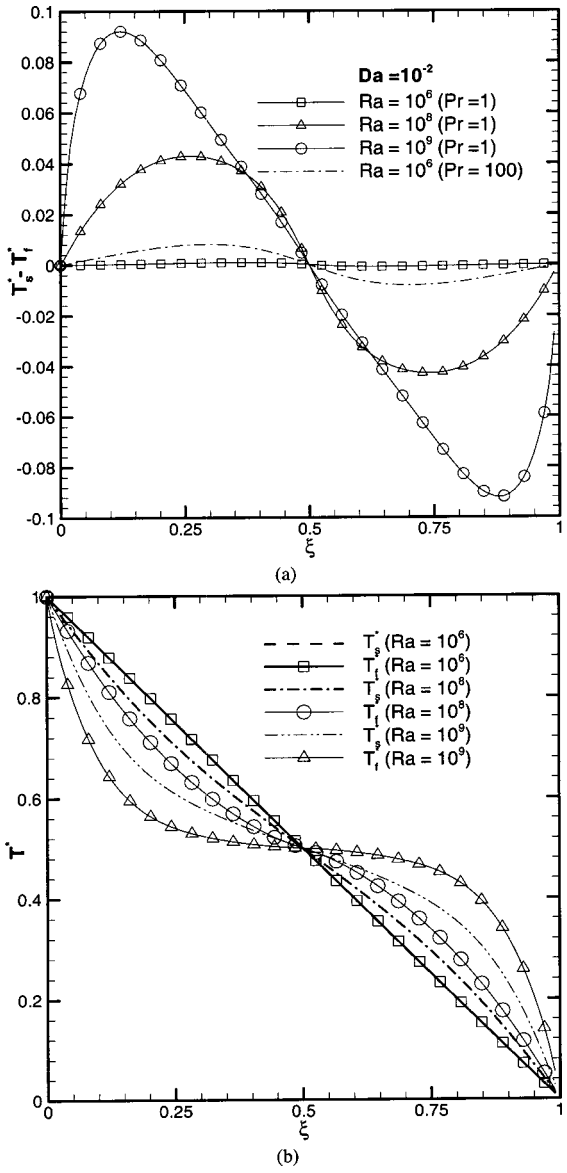

Fig. 6 Predicted temperature variation at steady-state for various Rayleigh numbers at the mid-height of the domain (η=0.5): (*a*) solid-to-fluid temperature difference, and (*b*) solid (broken line) and fluid (solid lines with symbols) temperature distributions

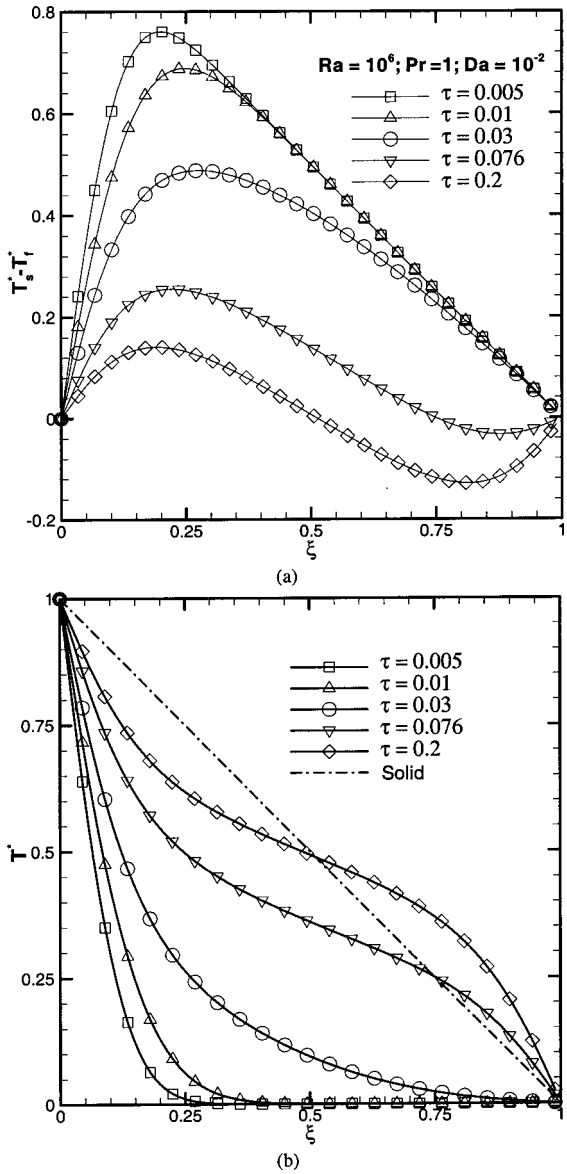

Fig. 7 Predicted temporal evolution of thermal field for Ra $=10^6$, $Nu_f=0$, Pr=1, and Da$=10^{-2}$ at the mid-height of the domain (η=0.5): (*a*) solid-to-fluid temperature difference, and (*b*) solid (broken line) and fluid (solid lines with symbols) temperature distribution. Solid (broken line) reaches a steady state very fast.

investigated forced convective flow through porous media under local non-equilibrium thermal conditions, fewer have considered natural convection. Deiber and Bortolozzi [17] performed a natural convection study in a vertical porous annulus composed of spheres without assuming local thermal equilibrium to exist between the solid matrix and saturating fluid. They reported that a two-energy equation model should be used at high Rayleigh and Darcy numbers. Mohammed [18] performed a parametric study for natural convection in a porous enclosure under steady-state conditions. The effects of varying the Darcy, Rayleigh, and Prandtl numbers and the solid-to-fluid thermal conductivity ratio on the temperature differentials between solid and fluid were reported. Rees and Pop [19] also reported the existence of non-equilibrium conditions for steady-state flows. Beckermann and Viskanta [20] experimentally and numerically analyzed natural convection inside a porous enclosure with a local thermal equilibrium assumption. Recently, Phanikumar and Mahajan [21] reported numerical and experimental results for natural convective flow in a rectangular domain partially filled with a porous medium (metal foam) and heated from below. Heat transfer enhancement due to the presence of the foam against that with no foam was studied. Effects of thermal dispersion and the Darcy number on the heat transfer were explored. They concluded that a local thermal nonequilibrium model better describes the underlying heat transfer phenomena in metal foams.

The present work undertakes a parametric analysis of natural convection inside enclosures containing metal foams for the transient thermal management of electronics. Only single-phase flows without phase change are considered to elucidate the basic physics. The paper examines the transient effects of different parameters including the Rayleigh, Darcy and Prandtl numbers, solid-to-fluid thermal conductivities, and the Nusselt number for interphase heat transfer, on the temperature differentials between

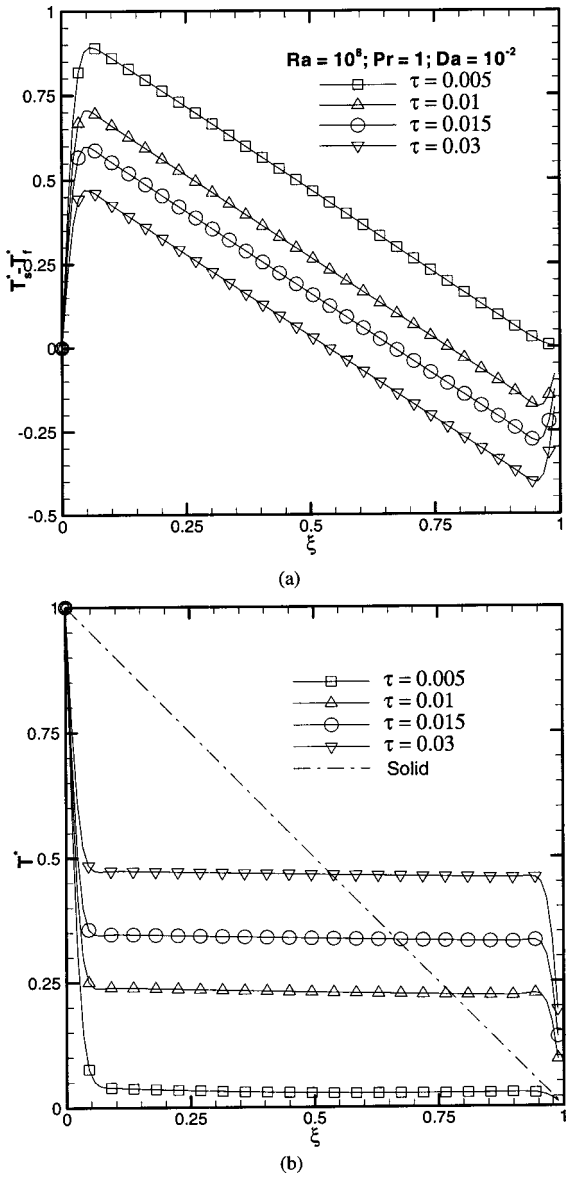

Fig. 8 Predicted temporal evolution of thermal field for Ra $=10^8$, $Nu_f=0$, Pr=1, and Da$=10^{-2}$ at the mid-height of the domain (η=0.5): (*a*) solid-to-fluid temperature difference, and (*b*) solid (broken line) and fluid (solid lines with symbols) temperature distribution. Solid (broken line) reaches a steady state very fast.

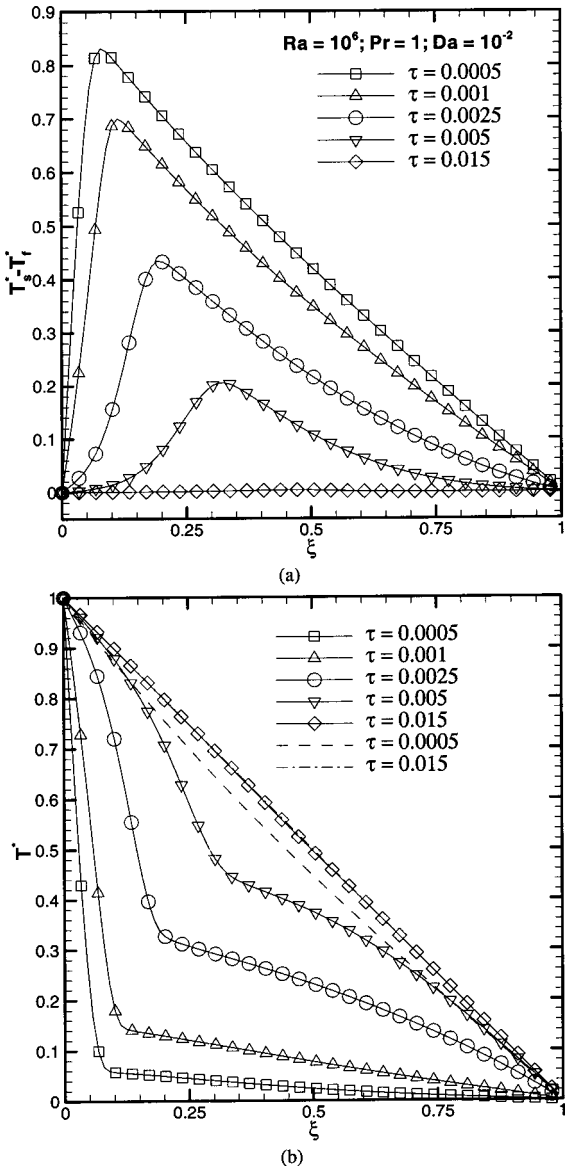

Fig. 9 Predicted temporal evolution of thermal field for Ra $=10^6$, $Nu_f\neq0$, Pr=1, and Da$=10^{-2}$ at the mid-height of the domain (η=0.5): (*a*) solid-to-fluid temperature difference, and (*b*) solid (broken line) and fluid (solid lines with symbols) temperature distribution

the solid and fluid under local thermal non-equilibrium conditions. The physics governing the existence of thermal non-equilibrium during the transient are explored.

Mathematical Formulation and Numerical Modeling

A schematic of the problem considered is shown in Fig. 1. A porous medium saturated with fluid is contained in a square enclosure of side H. The left and right walls are held at constant temperatures T_h and T_c, respectively. The top and bottom walls are adiabatic. The fluid and solid media are at equilibrium initially, and at temperature T_c. At $\tau=0$, the temperature of the left wall is raised to T_h. The objective of the work is to examine the temporal evolution of the solid and fluid temperature fields. The liquid is assumed to be incompressible and Newtonian. The momentum equations include the Brinkman's term and Forchheimer's extension to Darcy flow. The solid is assumed to be isotropic and rigid. Thermophysical properties of the solid and fluid phases are assumed to remain constant and isotropic over the range of temperatures considered. The Boussinesq approximation is invoked in the fluid phase. Dispersion effects are neglected. Using the dimensionless variables

$$\xi=\frac{x}{H};\quad \eta=\frac{y}{H};\quad \tau=\frac{t\alpha_f}{H^2};\quad \mathbf{U}=\frac{uH}{\alpha_f};\quad P=\frac{pH^2}{\rho_f v_f \alpha_f}$$

$$T_s^*=\frac{(T_s-T_c)}{(T_h-T_c)};\quad T_f^*=\frac{(T_f-T_c)}{(T_h-T_c)}$$

the dimensionless volume-averaged continuity and momentum equations [20] in the fluid phase are

$$\nabla\cdot\mathbf{U}=0 \tag{1}$$

Table 1 (a) Predicted times for solid and fluid to reach steady state for various Rayleigh, Prandtl and Darcy numbers for $Nu_f=0$, and (b) predicted solid-to-fluid temperature differences at steady state

Darcy Number	Prandtl Number	Rayleigh Number	Time[1] for solid to reach steady state	Time[1] for fluid to reach steady state
10^{-2}	1	10^5	0.00055	0.45
		10^6	0.00055	0.2
		10^8	0.00055	0.03
		10^9	0.00055	0.015
	100	10^6	0.00055	0.1925
		10^8	0.00055	0.0275
10^{-3}	1	10^6	0.00055	0.55
		10^8	0.00055	0.175
	100	10^6	0.00055	0.58
		10^8	0.00055	0.171

(a)

Darcy Number	Prandtl Number	Rayleigh Number	$(T_s-T_f)_{max}$ at $\eta=0.5$	$(T_s-T_f)_{max}$
10^{-2}	1	10^5	0.01	0.15
		10^6	0.13	0.57
		10^8	0.44	0.86
		10^9	0.48	0.91
	100	10^6	0.13	0.575
		10^8	0.44	0.86
10^{-3}	1	10^6	0.0002	0.017
		10^8	0.13	0.61
	100	10^6	0.00015	0.0168
		10^8	0.128	0.61

(b)

[1]Nondimensional time.

$$\frac{1}{\mathrm{Pr}}\left(\frac{1}{\varepsilon}\frac{\partial U}{\partial \tau}+\frac{1}{\varepsilon^2}(\mathbf{U}\cdot\nabla)\mathbf{U}\right)=-\nabla\mathbf{P}+\frac{1}{\varepsilon}\nabla^2\mathbf{U}-\left(\frac{1}{\mathrm{Da}^2}+\frac{F}{\mathrm{Pr}\cdot\mathrm{Da}}|\mathbf{U}|\right)\mathbf{U}+\mathrm{Ra}\cdot T_f^* \quad (2)$$

The governing intrinsic phase-averaged energy equations are written for the solid and fluid phases separately. These macroscopic continuum equations for solid and fluid are valid at every point in the domain. The two energy equations can be closed either using an unsteady closure [22] or a steady-state closure [5]. A steady-state closure has been found to be sufficient for most problems [22], and is used in this work. The dimensionless energy equations are

$$\Omega\frac{\partial T_s^*}{\partial \tau}=\lambda\nabla^2 T_s^*-\frac{(\mathrm{Nu})_f}{(1-\varepsilon)}(T_s^*-T_f^*) \quad (3)$$

$$\frac{\partial T_f^*}{\partial \tau}+\frac{1}{\varepsilon}(\mathbf{U}\cdot\nabla)T_f^*=\nabla^2 T_f^*-\frac{(\mathrm{Nu})_f}{\varepsilon}(T_f^*-T_s^*) \quad (4)$$

The dimensionless parameters governing the flow and heat transfer are

$$\mathrm{Pr}=\frac{v_f}{\alpha_f};\quad \mathrm{Ra}=\frac{g\beta_f H^3(T_h-T_c)}{\alpha_f v_f};\quad \mathrm{Da}=\frac{\sqrt{K}}{H};\quad (\mathrm{Nu})_f=\frac{h_v H^2}{k_f}$$

$$\lambda=\frac{k_s}{k_f};\quad \Omega=\frac{(\rho C_p)_s}{(\rho C_p)_f};\quad \delta=\frac{\mathrm{d}}{\mathrm{H}}$$

$$F=0.068 \quad \text{(for metal foams)}$$

$$F=\frac{1.75}{\sqrt{150\varepsilon^3}} \quad \text{(for flow over spherical particles)}$$

Two different volumetric heat transfer coefficients are used. For forced convection through a packed bed of spheres [16,23] the expression is

$$(\mathrm{Nu})_p=\frac{h_v d^2}{k_f}=6(1-\varepsilon)[2+1.1\mathrm{Pr}^{1/3}(\mathrm{Re})^{0.6}] \quad (5)$$

This correlation is valid up to Re of 8500. For forced flow through metal foams, the following correlation is used

$$(\mathrm{Nu})_p=\frac{h_v d^2}{k_f}=0.376(\mathrm{Re})^{0.644}(\mathrm{Pr})^{0.37} \quad (6)$$

It is important to note the limitations of Eq. (6) in modeling inter-phase heat transfer. The correlation in [13] was developed for metal foams in air, for a Reynolds number Re* ($=uL/v$, L being the test-section length) in the range $1900<\mathrm{Re}^*<7900$. To use it for typical PCMs, a scaling factor for Prandtl number similar to that in Phanikumar and Mahajan [21] was included. Further, for high Pr, the flow in the core of the domain is of relatively low velocity, and the Reynolds number may be far lower than the lower Re* limit of Eq. (6); it is also clear that Eq. (6) does not correctly recover the conduction ($\mathrm{Re}^*=0$) limit. To the authors' knowledge, there are no available correlations in the literature describing the inter-phase heat transfer coefficient in the high-Prandtl number and low-Reynolds number limit. Therefore, Eq. (6) is used despite these limitations.

The volumetric heat transfer coefficient in the above equations can be expressed in terms of the inter-phase heat transfer coefficient as

$$h_v=h_{sf}a_{sf} \quad (7)$$

In Eq. (7), a_{sf} is the specific surface area. These correlations are expected to be approximately valid for natural convection as well. The Reynolds number in Eqs. (5) and (6) was interpreted as the local Reynolds number, defined based on the local mean velocity

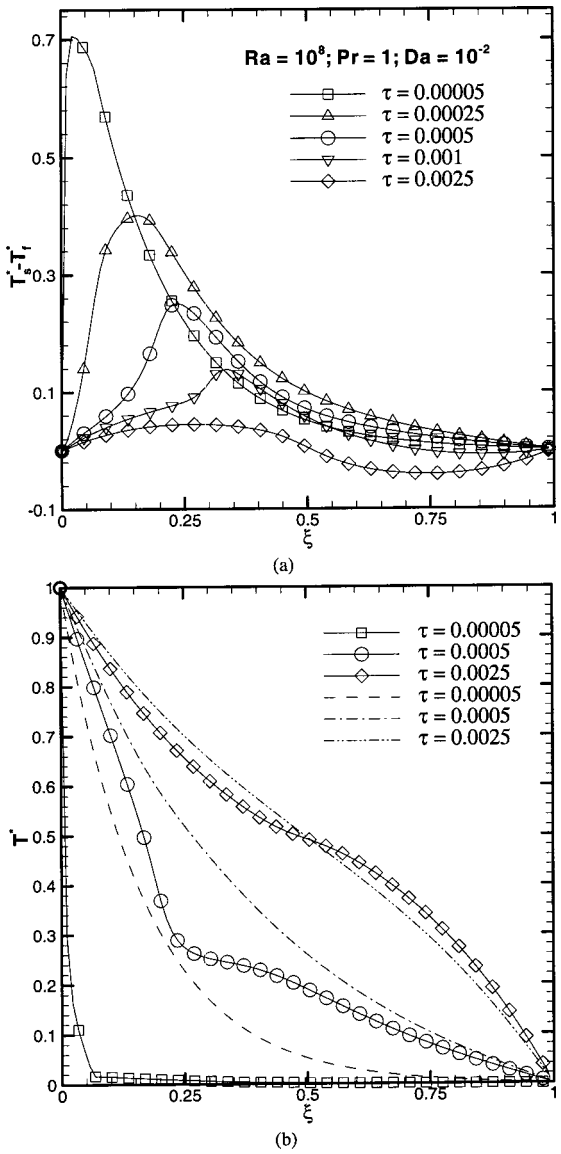

Fig. 10 Predicted temporal evolution of thermal field for Ra $=10^8$, $Nu_f \neq 0$, Pr=1, and Da$=10^{-2}$ at the mid-height of the domain (η=0.5): (*a*) solid-to-fluid temperature difference, and (*b*) solid (broken line) and fluid (solid lines with symbols) temperature distribution

($u_{mean}d/\nu$). The relations for permeability and inertial coefficient used for spherical particles can be obtained from [5,6]. For metal foams, a porosity of 0.8 is used and the inertial coefficient is 0.068 [13].

The computational domain is discretized into finite volumes using an orthogonal mesh. Pressure, velocity and the two temperatures are stored at the cell centroids. A central differencing scheme with a deferred correction [24,25] is used for convective fluxes. A central differencing scheme is used for discretizing diffusive fluxes. A second order Euler implicit (three time level) scheme is used for the transient terms. The SIMPLE algorithm is employed for obtaining the velocity fields. The linearized systems of equations are solved using the strongly implicit procedure (SIP) [25]. Additional details about the numerical approach are available in [2,26]. The calculations are terminated when the residual has dropped at least below 10^{-6} for all governing equations.

Code Validation

Because experimental results are not available in the literature for natural convection inside porous metal foams, the code was validated against studies on convection in a packed bed of spheres. Beckermann and Viskanta [20] performed an experimental and numerical study of natural convection in a porous enclosure comprising spherical (glass) particles with gallium as the interstitial fluid. A fixed porosity of 0.385 was considered. Predictions from the present work are compared to those in [20] in Fig. 2 at different vertical (η-direction) locations. In the current predictions, Eq. (5) was used to represent the inter-phase heat transfer coefficient. The predicted thermal fields agree well with the numerical predictions in [20] and also show satisfactory agreement with the experimental measurements [20].

Predictions from the present model are also compared in Figs. 3 and 4 with those of Mohammed [18] who also employed a two-temperature model for the analysis of natural convection in a packed bed of spheres. The comparison is shown for the case of Prandtl number=1.0, and the agreement is seen to be excellent.

Grid and time-step independence for the mesh and time-step sizes used in the present simulations was also established. A Rayleigh number of 10^8, a Darcy number of 10^{-3} and a Prandtl number of 1 were used for this set of calculations. Grid independence was tested using three different non-uniform grids, 46×46 (mesh #1), 92×92 (mesh #2) and 182×182 (mesh #3). For mesh #1, a deviation of 6.48% in the maximum solid-to-fluid temperature difference was observed with respect to mesh #3, with this deviation between mesh #2 and mesh #3 reducing to 0.33%. Therefore, mesh #2 (92×92) was chosen for all the calculations in this study. For establishing time-step independence, three different time step values, 1.25×10^{-4}, 2.5×10^{-4} and 5×10^{-4} were evaluated with the 92×92 mesh. The deviation in the results for the maximum solid-to-fluid temperature difference compared to the smallest time step was less than 0.01% for both larger time steps. Since refinement in the time-step did not produce discernible improvements in accuracy, a nondimensional time-step value of 2.5×10^{-4} was used for most of the computations in this work.

Results and Discussion

Passive thermal storage units used in electronics cooling would feature solid-to-fluid thermal conductivity ratios (λ) in the range of 10^2 to 10^5 and Prandtl numbers of 1 to 100. The porosity of the metal foam considered in this study is held constant at 0.8 with a pore size corresponding to $d/H=0.0135$. The ratio of the average ligament diameter of the foam to the mean cell size of the foam is 0.1875 with average ligament diameter being equal to 0.36 mm [13]. In the range of thermal conductivity ratios of interest ($\lambda \sim 10^3-10^5$), the results did not vary much with λ, and hence a value of 10^3 was used for all cases.

Steady State. The case of zero inter-phase heat transfer ($Nu_f=0$) is first considered, in which there is no thermal interaction between the solid and fluid phases. Figure 5 shows the variation of solid and fluid temperature profiles for different Rayleigh numbers at mid-height (η=0.5); the fluid temperature variation at η=0.02 and η=0.98 for Ra$=10^8$ is also shown for contrast. The solid profile is expected to be a straight line and is independent of the Prandtl number and η location. The fluid profile is also a straight line if the Rayleigh number is low and, as a result, the solid-to-fluid temperature difference $\Delta T^* \sim O(0)$ everywhere in the domain. As the Rayleigh number increases the fluid temperature profile deviates from the solid temperature profile as thermal boundary layers develops near the heated and cooled walls. The thickness of the boundary layer scales as $\sim(\mathrm{RaDa}^2)^{-1/4}$ [27]. It can be seen from Fig. 5 that the numerical predictions agree with the scaling analysis. For example, for Ra$=10^8$ and Da$=10^{-2}$ the numerically predicted boundary layer thickness is approximately 0.09 and that from scaling analysis is 0.1. As the Rayleigh number increases, the thermal boundary layer in the fluid is increasingly confined to a thin layer near the wall, with the core being at a temperature $T_f^* \sim 0.5$. Thus, the geometric center of the cavity is a point of zero temperature difference between solid and fluid. The

Table 2 (a) Predicted times for solid and fluid to reach steady state for various Rayleigh, Prandtl and Darcy numbers for $Nu_f \neq 0$, and (b) predicted solid-to-fluid temperature differences at steady state

Darcy Number	Prandtl Number	Rayleigh Number	Time[1] for solid to reach steady state	Time[1] for fluid to reach steady state
10^{-2}	1	10^6	0.0075	0.00935
		10^8	0.0023	0.00235
	100	10^6	0.015	0.0225
		10^8	0.0027	0.00275
10^{-3}	1	10^6	0.02345	0.0929
		10^8	0.00735	0.0086
	10	10^6	0.0125	0.15
	100	10^6	0.00055	0.2245
		10^8	0.01475	0.02175

(a)

Darcy Number	Prandtl Number	Rayleigh Number	$(T_s - T_f)_{max}$ at $\eta=0.5$	$(T_s - T_f)_{max}$
10^{-2}	1	10^6	0.000865	0.0248
		10^8	0.0429	0.1506
	100	10^6	0.0081	0.08385
		10^8	0.1638	0.3758
10^{-3}	1	10^6	0.00004	0.0041
		10^8	0.00087	0.02635
	10	10^6	0.00005	0.0064
	100	10^6	0.000075	0.0091
		10^8	0.0081	0.0884

(b)

[1]Nondimensional time.

maximum temperature difference is expected to occur at the edge of the thermal boundary layer, with a value $\Delta T^* \sim O(0.5)$ at the mid-height ($\eta=0.5$) of the domain for high Rayleigh numbers. At $\eta=0$ and 1, the maximum temperature difference is $\sim O(1)$ for high Ra as expected.

The next case considered is one in which the solid and fluid exchange energy in a steady-state mode through inter-phase transfer ($Nu_f \neq 0$). Figure 6(*a*) shows the dimensionless solid-to-fluid temperature difference $T_s^* - T_f^*$ at mid-height ($\eta=0.5$) for several Rayleigh numbers, for $Da=10^{-2}$, $\lambda=10^3$, $\Omega=1$, and $d/H=0.0135$. Figure 6(*b*) shows dimensionless solid and fluid temperature variations at mid-height for $Pr=1$. The effect of the inter-phase heat transfer coefficient is to lower the solid-to-fluid temperature difference. For low Rayleigh numbers ($Ra<10^6$), the maximum temperature difference is seen to be $\sim O(0)$ as explained previously. The solid-to-fluid temperature difference increases with increasing Ra, but is always less than that in the $Nu_f=0$ case, i.e., less than O(0.5). Indeed, for $Ra=10^9$ a maximum temperature difference of about 10% is seen. Comparing Fig. 6(*b*) with Fig. 5 it can be seen that for high Ra, the dimensionless solid temperature variation at the mid-height of the enclosure ($\eta=0.5$) is not linear but follows the fluid temperature variation due to inter-phase heat exchange between solid and fluid phases.

Figure 6(*a*) also shows that for a Rayleigh number of 10^6, increasing the Prandtl number from $Pr=1$ to $Pr=100$ increases the solid-to-fluid temperature difference by a small extent. The vertical velocity in the rectangular domain scales as [27]

$$V = \frac{v\,d}{\alpha_f}\frac{H}{d} = \mathrm{Re}\,\mathrm{Pr}\left(\frac{H}{d}\right) \sim (\mathrm{RaDa}^2)^{1/2} \tag{8}$$

The inter-phase heat transfer coefficient scales as

$$\mathrm{Nu}_p = \frac{h_v d^2}{k_f} = 0.376(\mathrm{Re})^{0.644}\mathrm{Pr}^{0.37} \sim 0.376\left\{(\mathrm{RaDa}^2)^{1/2}\left(\frac{d}{H}\right)\right\}^{0.644}\mathrm{Pr}^{-0.274} \tag{9}$$

Thus, the inter-phase Nusselt number depends on the Prandtl number, and tends to decrease as the Prandtl number increases, causing the two media to act in a more uncoupled manner. This dependence assumes that the Prandtl number variation in Eq. (6) is valid at high Pr.

Unsteady Flow. As in the steady-state cases, in order to understand the effect of the inter-phase heat transfer on the solid-to-fluid temperature difference we first consider the $Nu_f=0$ case. In the absence of inter-phase heat exchange, the solid-to-fluid temperature difference depends on the relative response time of the two phases. The solid reaches steady state in time scales of order (H^2/α_s) or a dimensionless time scale of $\tau_s \sim \Omega/\lambda$. The fluid response time depends on Ra. For low Rayleigh numbers the time to reach steady state scales as H^2/α_f, corresponding to a dimensionless scale $\tau_f \sim O(1)$. For high Rayleigh numbers, the fluid time-to-steady-state scales as the inverse of the vertical velocity, and, hence,

$$V \sim (\mathrm{RaDa}^2)^{1/2} \qquad \tau_f \sim 1/V \sim (\mathrm{RaDa}^2)^{-1/2} \tag{10}$$

Figure 7(*a*) shows the variation of dimensionless solid-to-fluid temperature difference along $\eta=0.5$ at different times for $Ra=10^6$, $Da=10^{-2}$, $Pr=1$, $\Omega=1000$, and $\lambda=1$. Figure 7(*b*) shows the fluid and solid temperature distributions at the mid-height of the domain. The solid response time is much faster than that of the fluid due to its higher thermal diffusivity, and it is seen to reach a steady state much faster. In Fig. 7(*b*), the solid has reached a steady state even before the fluid field starts to develop. Thus, at

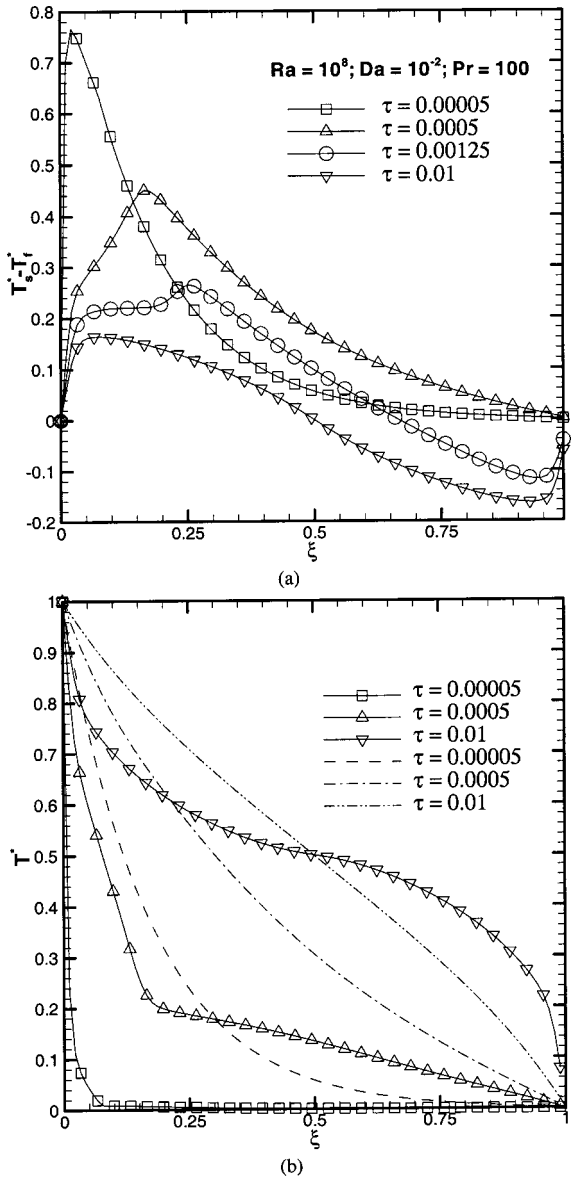

Fig. 11 Predicted temporal evolution of thermal field for Ra $=10^8$, $Nu_f \neq 0$, Pr=100, and Da$=10^{-2}$ at the mid-height of the domain (η=0.5): (a) solid-to-fluid temperature difference, and (b) solid (broken line) and fluid (solid lines with symbols) temperature distribution

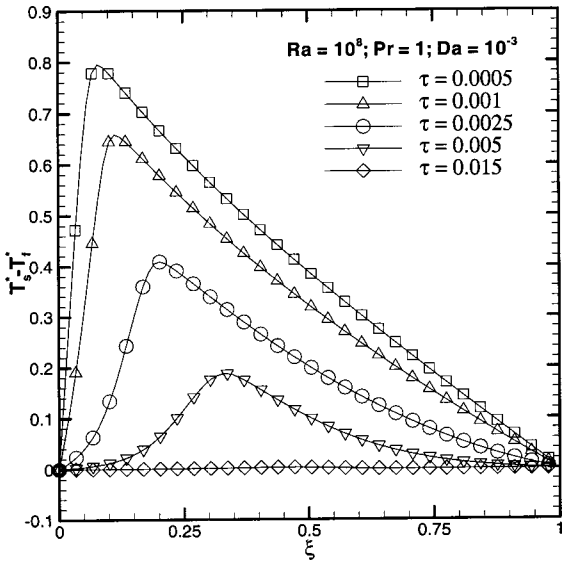

Fig. 12 Predicted temporal evolution of solid-to-fluid temperature difference at the mid-height of the domain (η=0.5) for Ra $=10^8$, $Nu_f \neq 0$, Pr=1, and Da$=10^{-3}$

early times, the solid-to-fluid temperature difference is high ($\sim O(1)$) and the temperature difference progressively decreases with time, reaching its steady-state value over the fluid time scale. The ratio of the solid-to-fluid time to reach steady state is given by

$$\frac{\tau_s}{\tau_f} \sim \frac{\Omega(\mathrm{RaDa}^2)^{1/2}}{\lambda} \tag{11}$$

As the Rayleigh number increases, the fluid response time decreases. This is seen in Fig. 8(*a*) which shows a plot of temperature difference variation along the mid-height of the domain for Ra$=10^8$, Da$=10^{-2}$, Pr=1, and $Nu_f=0$. Figure 8(*b*) shows the variation of solid and fluid temperature fields along the mid-height of the domain. Due to the high Rayleigh number, the core fluid is at a temperature of $T_f^*=0.5$ and the boundary layer is confined to a very thin layer near the heated and cooled walls. The time to reach a steady state and the solid-to-fluid temperature difference at steady state are listed in Tables 1(a) and 1(b) for various Darcy, Prandtl and Rayleigh numbers. The process is declared to have reached a steady state if T^* at $(\eta,\xi)=(0.78,0.98)$ is within 1% of its steady-state value. It is clear from Tables 1(a) and 1(b) that for $Nu_f=0$, the time to reach steady state is independent of Pr, as expected. For low Darcy number (Da$=10^{-3}$), the fluid flow is so strongly retarded by the porous medium that the time to reach a steady-state is governed by the fluid diffusion scale, $\tau_f \sim O(1)$; correspondingly, the solid-to-fluid temperature difference is relatively low.

The results for $Nu_f \neq 0$ are considered next. Here, the behavior is governed by the relative magnitude of three interacting scales: the response time of the solid, the response time of the fluid, and the response time of the solid-fluid interface. If the interface response time is very long, the solid and fluid evolve separately and large temperature differences exist at steady state. If, on the other hand, the interface response time is much shorter than either the solid or the fluid response time, the two phases will evolve in a coupled manner, with the faster-responding phase imprinting its temperature on the slower-responding phase. A measure of the dimensionless response time of the interface is Nu_f^{-1} $(=h_v H^2/k_f)^{-1}$. For $Nu_f \gg 1$, the two phases will evolve in equilibrium. Figure 9(*a*) shows the temporal evolution of the solid-to-fluid temperature difference for a Rayleigh number of 10^6, Pr=1 and Da$=10^{-2}$. The dimensionless solid and fluid temperature distribution at η=0.5 is shown in Fig. 9(*b*). The solid has the fastest response time, and reaches a steady state on a time scale $\tau_s \sim \Omega/\lambda$. The fluid time scale for this low value of $\mathrm{RaDa}^2(=100)$ is relatively large, leading to a slow approach to steady state. Thus, the fluid is essentially at its initial condition during the time the solid reaches a steady state, and initial temperature differences in Fig. 9(*a*) are $O(1)$. However, it is seen that the solid-to-fluid temperature difference is driven to zero over a time scale $\tau \sim$O(0.015), far faster than the response time of the fluid. This is a result of the response time of the inter-phase heat transfer, which is intermediate between the solid and fluid scales. This allows the solid to impose its imprint on the fluid temperature profile, which also assumes a straight line shape, leading to nearly zero temperature difference at steady state. For the uncoupled case (Fig. 7(*b*)), the fluid temperature is not a straight line for the same set of parameters.

In contrast, the interface time-scale is competitive with the solid time scale in Figs. 10(*a*) and 10(*b*), which shows the solid-to-fluid

temperature difference and the solid and fluid temperature variation at mid-height for $Ra=10^8$, $Pr=1$, and $Da=10^{-2}$. The ratio of the interface time scale to the solid response time is $\sim(Nu_f\Omega/\lambda)^{-1}$. Here, the solid is not allowed to reach a steady state before losing heat to the fluid. Instead, the temperature difference begins to fall well before $\tau\sim\tau_s$ and reaches equilibrium with the fluid on a time scale of $\tau\sim0.0025$. Because the fluid time scale is more competitive with the solid for this high value of $RaDa^2(=10^4)$, we see that the solid temperature profile is not imposed on the fluid and a nonzero temperature difference exists at steady state. The time to reach steady-state and the steady state solid-to-fluid temperature difference for several Ra, Pr, and Da are listed in Tables 2(a) and 2(b), respectively. Since the two phases are coupled, the time to reach steady state is of the same order for both. This is especially true as Ra and Da increase, since Nu_p increases with $RaDa^2$.

The effect of Prandtl number on the solid-to-fluid temperature difference and the temporal evolution of the solid and fluid temperature fields is brought out in Figs. 11(*a*) and 11(*b*) for which $Ra=10^8$, $Pr=100$, and $Da=10^{-2}$. From Eq. (2), it can be seen that an increase in Prandtl number causes a decrease in the inter-phase heat transfer coefficient, and, hence, the phases act in a more uncoupled manner. The temporal evolution is faster than the uncoupled case (Figs. 8(*a*) and 8(*b*)) and the solid-to-fluid temperature difference is higher than the corresponding $Pr=1$ and $Nu_f\neq0$ case. It is important to note, however, that these results are subject to the assumption that Eq. (6) describes the inter-phase heat transfer.

The effect of Darcy number can be seen by comparing Fig. 12 with Fig. 9. Figure 9 has been plotted for $Ra=10^6$, $Da=10^{-2}$ while Fig. 12 has been plotted for $Ra=10^8$, $Da=10^{-3}$. The fluid velocity scales approximately as $\sim(RaDa^2)^{1/2}$. As a result, the temperatures differences in the two figures are almost identical; the response times are also very similar.

Conclusions

A fully transient analysis of natural convection inside a porous enclosure containing a metal foam was carried out using a two-temperature formulation. Based on the results of a parametric study, local thermal equilibrium is not ensured, either during the transient or at steady state in such systems. For transient applications, the temperature difference between the solid and the fluid is governed by the response time of the two phases as well as the time scale of the solid-fluid interface. The results demonstrate that even if the steady-state temperature differences are small, the temperature difference during the unsteady response may be quite large. Single-temperature formulations are expected to yield incorrect predictions when the inter-phase heat transfer time scale is longer than the fastest response time of either the fluid or solid phase. For metal/air or metal/PCM systems, the faster-responding phase for typical ranges of Ra and Da is the solid. In this limit, two-temperature formulations are necessary when $Nu_f<1$.

The present study did not consider phase change. When phase change is included, an additional time scale associated with the latent heat of melting is introduced in the problem, and depending on the value of the Stefan number, can change the results obtained here. Yet another time scale appears when pulsed heating is used. The interaction of pulse periodicity with these competing scales determines the validity of single-temperature formulations. These effects will be investigated in the future. Another research need is the development of interphase Nusselt number correlations for high Prandtl number and low-Reynolds number flows, as well as correlations for pure conduction heat transfer in PCM-impregnated foams. These correlations are necessary to correctly capture inter-phase heat transfer in the frozen as well as the low-velocity sections of the computational domain.

Nomenclature

a_{sf} = Ratio of specific surface area to volume, m^{-1}
C_p = Specific heat, $J\,kg^{-1}\,K^{-1}$
Da = Darcy number
d = Particle diameter or mean pore diameter, m
F = Inertial coefficient
g = Acceleration due to gravity, ms^{-2}
H = Height of enclosure, m
h_{sf} = Inter-phase heat transfer coefficient, $W\,m^{-2}\,K^{-1}$
h_v = Volumetric heat transfer coefficient, $W\,m^{-3}\,K^{-1}$
K = Permeability, m^2
k = Thermal conductivity, $W\,m^{-1}\,K^{-1}$
Nu = Nusselt number based on height of the enclosure
P = Pressure, $N\,m^{-2}$
Pr = Prandtl number
Ra = Rayleigh number
Re = Reynolds number
T = Temperature, K
t = Time, s
U = Velocity vector, ms^{-1}
u, v = Velocity in x and y directions, ms^{-1}
x, y = Cartesian coordinates

Greek Symbols

α = Thermal diffusivity, $m^2\,s^{-1}$
β = Thermal expansion coefficient, K^{-1}
ΔH = Enthalpy of freezing/melting, $J\,kg^{-1}$
Δt = Time step
$\Delta x, \Delta y$ = Spatial mesh sizes, m
δ = Ratio of mean pore diameter to height of enclosure
ε = Porosity
η = Dimensionless y coordinate
λ = Ratio of thermal conductivities of solid and fluid
μ = Dynamic viscosity, $N\,s\,m^{-2}$
ν = Kinematic viscosity, $m^2\,s^{-1}$
ρ = Density, $kg\,m^{-3}$
τ = Dimensionless time
ξ = Dimensionless x coordinate
Ω = ratio of volumetric heat capacities of solid and liquid

Subscripts

c = cold
ef = effective fluid property
es = effective solid property
f = fluid
h = hot
l = liquid
p = pore or particle
s = solid

Superscripts

$*$ = dimensionless quantity
ss = steady state

Acknowledgment

Support for this work from industry members of the Cooling Technologies Research Center, an NSF Industry/University Cooperative Research Center (www.ecn.purdue.edu/CTRC), is gratefully acknowledged.

References

[1] Himran, S., Suwono, A., and Mansoori, G. A., 1994, ''Characterization of Alkanes and Paraffin Waxes for Application as Phase Change Energy Storage Medium,'' Energy Sources, **16**, pp. 117–128.
[2] Krishnan, S., 2002, ''Analysis of Phase Change Energy Storage Systems for Pulsed Power Dissipation,'' M.S.M.E. thesis, Purdue University, West Lafayette, IN.
[3] Krishnan, S., Murthy, J. Y., and Garimella, S. V., 2002, ''A Two-Temperature Model for the Analysis of Passive Thermal Control Systems for Electronics,'' *Proc. of IMECE 2002*, ASME Paper No. 33335, ASME, New York.
[4] Hunt, M. L., and Tien, C. L., 1988, ''Effects of Thermal Dispersion on Forced

Convection in Fibrous Media,'' Int. J. Heat Mass Transfer, **31**(2), pp. 301–309.
[5] Amiri, A., and Vafai, K., 1994, ''Analysis of Dispersion Effects and Non-Thermal Equilibrium, Non-Darcian, Variable Porosity Incompressible Flow Through Porous Media,'' Int. J. Heat Mass Transfer, **37**(6), pp. 939–954.
[6] Amiri, A., and Vafai, K., 1998, ''Transient Analysis of Incompressible Flow Through a Packed Bed,'' Int. J. Heat Mass Transfer, **41**(24), pp. 4259–4279.
[7] Lee, D. Y., and Vafai, K., 1999, ''Analytical Characterization and Conceptual Assessment of Solid and Fluid Temperature Differentials in Porous Media,'' Int. J. Heat Mass Transfer, **42**(3), pp. 423–435.
[8] Lu, T. J., Stone, H. A., and Ashby, M. F., 1998, ''Heat Transfer in Open-Cell Metal Foams,'' Acta Mater., **46**(10), pp. 3619–3635.
[9] Minkowycz, W. J., Haji-Sheikh, A., and Vafai, K., 1999, ''On Departure from Local Thermal Equilibrium in Porous Media due to a Rapidly Changing Heat Source: the Sparrow Number,'' Int. J. Heat Mass Transfer, **42**(18), pp. 3373–3385.
[10] Calmidi, V. V., and Mahajan, R. L., 1999, ''The Effective Thermal Conductivity of High Porosity Fibrous Metal Foams,'' ASME J. Heat Transfer, **121**, pp. 466–471.
[11] Alazmi, B., and Vafai, K., 2000, ''Analysis of Variants Within the Porous Media Transport Models,'' ASME J. Heat Transfer, **122**, pp. 303–326.
[12] Calmidi, V. V., and Mahajan, R. L., 2000, ''Forced Convection in High Porosity Metal Foams,'' ASME J. Heat Transfer, **122**, pp. 557–565.
[13] Hwang, J. J., Hwang, G. J., Yeh, R. H., and Chao, C. H., 2002, ''Measurement of Interstitial Convective Heat Transfer and Frictional Drag for Flow Across Metal Foams,'' ASME J. Heat Transfer, **124**, pp. 120–129.
[14] Kuznetsov, A. V., 1998, ''Thermal Nonequilibrium Forced Convection in Porous Media,'' *Transport Phenomena in Porous Media*, Ingham, D. B., and Pop, I., eds., Elsevier, Oxford, pp. 103–129.
[15] Nield, D. A., and Bejan, A., 1992, *Convection in Porous Media*, 1st ed. Springer-Verlag, New York, NY.
[16] Kaviany, M., 1995, *Principles of Heat Transfer in Porous Media*, 2nd ed., Springer-Verlag, New York, NY.
[17] Deiber, J. A., and Bortolozzi, R. A., 1998, ''A Two-Field Model for Natural Convection in a Porous Annulus at High Rayleigh Numbers,'' Chem. Eng. Sci., **53**, pp. 1505–1516.
[18] Mohammed, A. A., 2000, ''Non-Equilibrium Natural Convection in a Differentially Heated Cavity Filled With a Saturated Porous Matrix,'' ASME J. Heat Transfer, **122**, pp. 380–384.
[19] Rees, D. A. S., and Pop, I., 2000, ''Vertical Thermal Boundary Layer Flow in a Porous Medium Using a Thermal Non-Equilibrium Model,'' J. Porous Media, **3**, pp. 31–44.
[20] Beckermann, C., and Viskanta, R., 1988, ''Natural Convection Solid/Liquid Phase Change in Porous Media,'' Int. J. Heat Mass Transfer, **31**(1), pp. 35–46.
[21] Phanikumar, M. S., and Mahajan, R. L., 2002, ''Non-Darcy Natural Convection in High Porosity Metal Foams,'' Int. J. Heat Mass Transfer, **45**(18), pp. 3781–3793.
[22] Moyne, C., 1997, ''Two-Equation Model for a Diffusive Process in Porous Media Using the Volume Averaging Method With an Unsteady-State Closure,'' Adv. Water Resour., **20**, pp. 63–76.
[23] Wakao, N., and Kaguei, S., 1982, *Heat and Mass Transfer in Packed Beds*, Gordon and Beach, New York, NY.
[24] Khosla, P. K., and Rubin, S. G., ''A Diagonally Dominant Second-Order Accurate Implicit Scheme,'' Comput. Fluids, **2**, pp. 207–209.
[25] Ferziger, J. H., and Peric, M., 1995, *Computational Methods for Fluid Dynamics*, Springer-Verlag, Berlin.
[26] Simpson, J. E., Garimella, S. V., and deGroh, III, H. C., 2002, ''An Experimental and Numerical Investigation of Bridgman Growth of Succinonitrile,'' AIAA J. Thermophysics and Heat Transfer, **16**(3), pp. 324–335.
[27] Bejan, A., 1995, *Convection Heat Transfer*, 2nd ed., John Wiley and Sons, New York, NY.

Local Pool Boiling Coefficients on the Inside Surface of a Horizontal Tube

Myeong-Gie Kang
Department of Mechanical Engineering Education, Andong National University 388 Songchun-dong, Andong-city, Kyungbuk 760-749, Korea

Nucleate pool boiling heat transfer of water on the inside surface of a horizontal tube of 51 mm internal diameter has been studied experimentally at atmospheric pressure. Experiments were performed at four different azimuthal angles (0 deg, 45 deg, 120 deg, and 180 deg from the tube bottom) to investigate variations in local heat transfer coefficients along the tube periphery. The local coefficient changes much along the tube periphery and the minimum was observed at the tube bottom. It is found that heat transfer on the inside surface is strongly dependent on the intensity of the liquid agitation and the evaporative mechanism. [DOI: 10.1115/1.1778190]

Keywords: Boiling, Convection, Heat Transfer, Heat Exchangers, Nuclear

Introduction

As a way of improving heat transfer on a heated surface, mechanisms of pool boiling have been studied for several decades. Pool boiling is closely related with the design of passive type heat exchangers in advanced nuclear reactors [1]. Since the space for the installation of the heat exchanger is usually limited, to develop more efficient heat exchangers is inevitable. One of the possible orientations to install a tubular type heat exchanger is its horizontal direction. Pool boiling can be created on the inside or outside surfaces according to the location of heat sources. Although some results of pool boiling on the outside surface have been published [2–4], to the author's knowledge, the study for the inside surface of a tube is almost nothing.

Jung et al. [5] experimented boiling heat transfer in R-11 to investigate heat transfer mechanisms on the inside surface of a circular cylindrical tank. They simulated the surface by a flat plate. That is, the plate facing downward simulated the uppermost region of the surface. Somewhat detailed study on the inclination angle itself was previously done by Nishikawa et al. [6] by using the combination of a plate and water. To simulate a circular tank by a flat plate might be reasonable as the diameter of the tank was large enough. However, it is doubtable to use the results for the design of tubular heat exchangers. Jabardo and Filho [7] performed an experimental study of forced convective boiling of refrigerants in a 12.7 mm internal diameter copper tube. They investigated effects of physical parameters over the variations in local surface temperature as a function of the fluid quality. However, mechanisms of pool boiling are different from those of the forced convective boiling.

Summarizing the previous works, both results of the flat plate or forced convective boiling cannot be applied directly to the analysis of pool boiling heat transfer in a small size tube. Therefore, the present study is aimed at the determination of heat transfer characteristics on the inside surface of a small size horizontal tube. Through the study variations in local heat transfer coefficients along the tube periphery will be investigated.

Contributed by the Heat Transfer Division for publication in the JOURNAL OF HEAT TRANSFER. Manuscript received by the Heat Transfer Division November 10, 2003; revision received May 4, 2004. Associate Editor: M. K. Jensen.

Experiments

A schematic view of the present experimental apparatus is shown in Fig. 1(a). The water storage tank is made of stainless steel and has a rectangular cross section (950×1300 mm) and a height of 1400 mm. This tank has a glass view port (1000×1000 mm) which permits viewing of the tubes and photographing. The tank has a double container system. The inside tank has several flow holes to allow fluid inflow from the outer tank. To reduce heat loss to the environment, the left, right, and rear sides of the tank were insulated by glass wool of 50 mm thickness.

Figures 1(b) and 1(c) represent a supporter and a test section, respectively. Several rows of resistance wires are arrayed uniformly around the outside surface of the heated tube ($L=300$ mm and $D_i=51$ mm), which is made of stainless steel. Then, the heating wires were covered with insulating material. Some powder was packed into the space of the heating wires to heat the tube uniformly. The inside surface was lathed to have smooth surface. The test section and the supporter were assembled with bolts.

Temperatures of the heated tube were measured on the outside surface of the heated tube with two T-type sheathed thermocouples (diameter is 1 mm) located at 100 mm distance from both ends of the heated tube, respectively. The temperatures of the inside tube surface were calculated by the one dimensional conduction equation. To install the thermocouples on the surface two grooves (width×depth=1 mm×1 mm) of 105 mm length were manufactured on the surface. The water temperatures were measured with six sheathed T-type thermocouples placed at the tank wall vertically from the bottom of the inside tank with equal spacing (i.e., 180 mm). All thermocouples were calibrated at the boiling point of water.

For the tests, the assembled part is placed at the bottom of the tank (Fig. 1(a)). After the tank is filled with water until the initial water level is at 750 mm from the outer tank bottom, the water is heated using four pre-heaters at constant power (5 kW/heater). When the water temperature reaches the saturation value (100°C since all the tests are run at atmospheric pressure), the water is then boiled for 30 minutes at saturation temperature to remove the dissolved gases. The temperatures of the heated tube are measured when they are at steady state while controlling the heat flux on the tube surface with input power. To make the azimuthal angle, both sides of the test section have flanges. The peripheral variation in heat transfer was determined by rotating the tube following each set of readings.

The error bound of the voltage and current meters used for the test are ±0.5 percent of the measured value. Therefore, the calculated power (voltage×current) has ±1.0 percent error bound. Since the heat flux has the same error bound as the power, the uncertainty in the heat flux is estimated to be ±1.0 percent.

The measured temperature has uncertainties originated from the thermocouple probe itself and the instrument. To evaluate the error bound of the thermocouple probe, three thermocouples brazed on tube surface were submerged in an isothermal bath of ±0.01 K accuracy. The measured temperatures were compared with the set temperature. The deviation between the values is within ±0.1 K inclusive of the bath accuracy. The error bound of the data acquisition system is ±0.05 K. Therefore, the total uncertainty of the measured temperatures is defined by adding the above errors and its value is ±0.15 K.

The heat flux along the tube periphery has been evaluated by using one-dimensional conduction equation. The maximum possible heat flux is 2.3 kW/m^2 as the tube wall superheat (ΔT_{sat}) is 4 K. The value is about 11 percent of the averaged radial heat flux (40 kW/m^2). This can results in additional ±10 percent uncertainty in the heat flux. The axial heat loss from the ends of the test section is also calculated and is less than 30 W (e.g., 24 W at $q''=91$ kW/m^2 and $\theta=0$ deg). Since this is very small comparing with the radial heat transfer (e.g., 4.4 kW at $q''=91$ kW/m^2), its effect on the heat transfer coefficient is neglected.

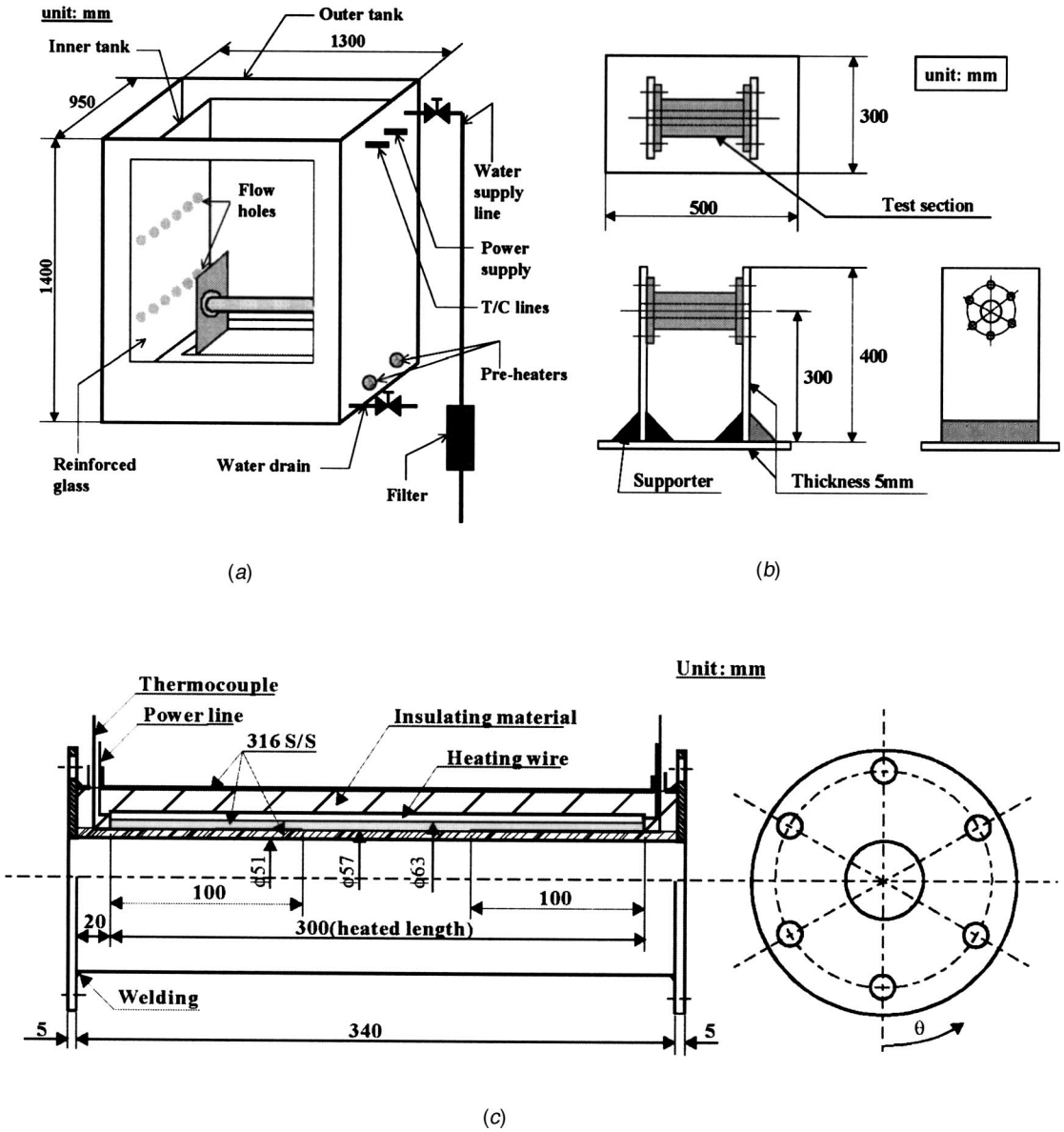

Fig. 1 Schematic of the experimental apparatus: (a) water storage tank; (b) test section supporter; and (c) test section

The heat flux (q'') from the electrically heated tube surface is calculated from the measured values of the AC power input as follows:

$$q'' = \frac{VI}{\pi D_i L} = h_b(T_W - T_{sat}) = h_b \Delta T_{sat} \quad (1)$$

where V and I are the supplied voltage (in volt) and current (in ampere), and D_i and L are the inside diameter and the length of the heated tube, respectively. T_W and T_{sat} represent the temperatures of the inside surface and the saturated water, respectively.

Results and Discussion

Figure 2 shows variations in local heat transfer on the inside surface of a horizontal tube. At $\theta=0$ deg changes in the local coefficient is proportional to the change in the heat flux as $q'' \leqslant 30\ \text{kW/m}^2$. The slope ($\Delta h_b/\Delta q''$) is suddenly decreased and, then, increased as $30 < q'' \leqslant 75\ \text{kW/m}^2$. At $\theta=45$ deg the slope of h_b versus q'' curve decreases gradually as q'' gets 60 kW/m^2. The slope is then increases suddenly and maintains a constant value as the heat flux increases. At $\theta=120$ deg the slope is about 1.2 until q'' gets 18 kW/m^2, and then suddenly changes to around 0 and maintains the value as the heat flux increases. At $\theta=180$ deg the slope of the curve is nearby 0 as $q'' \leqslant 30\ \text{kW/m}^2$. As the heat flux increases larger than 30 kW/m^2 the slope changes to 0.03 and maintains the same value. As q'' is more than 70 kW/m^2 the value of ΔT_{sat} is almost same as shown in Fig. 2(a).

At $\theta=0$ deg and 45 deg the intensity of the liquid agitation is very weak at lower heat fluxes. Regions at $\theta=0$ deg and 45 deg are relatively free from the liquid agitation at low and medium heat fluxes since bubbles are just moving upward. Therefore, the major mechanism affecting on heat transfer is the density of nucleation sites. At $\theta=120$ deg the intensity of the liquid agitation is strongly affecting on heat transfer at lower heat fluxes less than 18 kW/m^2. The source of the liquid agitation is bubbles coming from the bottom of the tube. As the heat flux increases more than 18 kW/m^2 this region is nearby the boundary of an elongated bubble. The intensity of the liquid agitation decreases suddenly and bubbles become coalescing around this angle. At $\theta=180$ deg, the higher coefficient was observed at a very low heat flux nearby

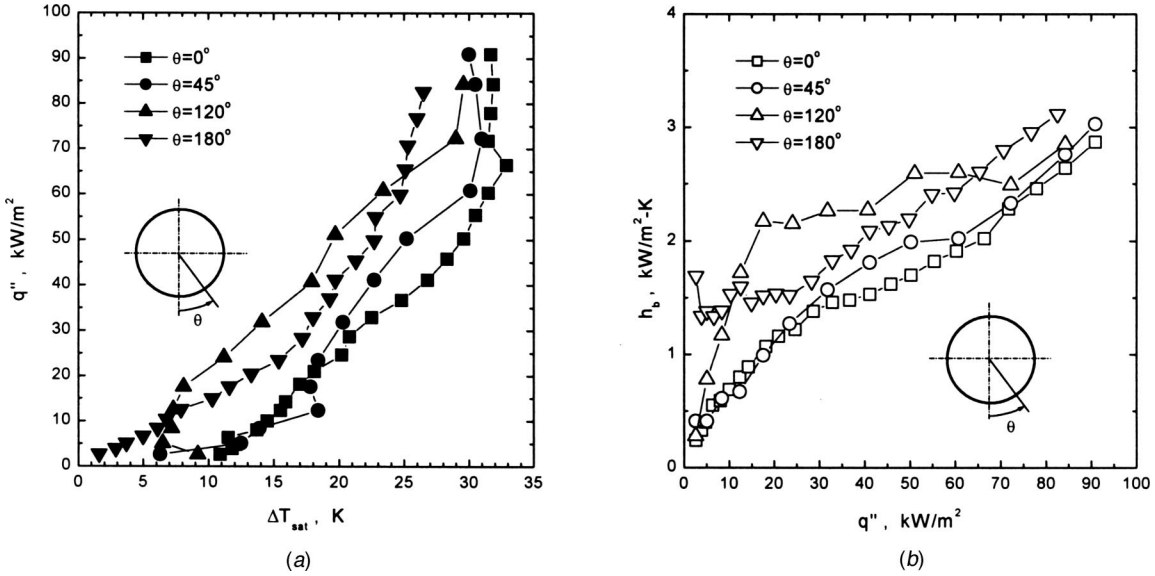

Fig. 2 Changes in local values along the tube periphery: (a) q'' versus ΔT_{sat}; and (b) h_b versus q''

0. This is very unusual regarding the previously published results for the several geometries. The departed bubbles from the tube bottom and side regions move upward and coalesce at the uppermost regions of the tube inside to generate a very large elongated bubble underneath the surface. The existence of a micro liquid layer might be suggested between the elongated bubble and the surface. As the bubble flows out from the ends of the tube, environmental liquid rushes into the space and, accordingly, the active liquid agitation is generated inside the tube. Therefore, the higher heat transfer coefficient at low heat fluxes can be explained by both of the evaporative mechanism underneath the elongated bubble and the active liquid agitation. As $5 < q'' \leqslant 25\ \mathrm{kW/m^2}$ the local coefficient is almost constant. This means that the evaporative mechanism and the liquid agitation is not enough to remove heat from the surface. As q'' increases more than 25 $\mathrm{kW/m^2}$ upcoming bubbles from the bottom destroy the lower side boundary of the elongated bubble and generates a kind of active mixing movement in the elongated bubble. Thereafter, gradual increase in the local coefficient is obtained. The intensity of the liquid agitation increases much and this regards as the major cause of the increase in heat transfer at higher heat fluxes larger than 70 $\mathrm{kW/m^2}$.

Through the heat flux regions clear boundaries in pool boiling (see Fig. 3) were observed and those could be categorized as following four stages. These four stages are inferred from both experimental data and visual observation. The drawings in Fig. 3 represent not direct observations of the boiling process inside the tube but observations from the end of the tube, and that the bubble masses are flowing out of the tube at its top.

Stage 1. Small size bubbles move toward the upper regions and create an elongated bubble underneath the tube surface. Although this kind of elongated bubble was also observed on the surface of a flat plate facing downward [6], the mechanism of bubble growth is different from each other. Bubbles generated on the surface of a flat plate coalesce with nearby bubbles as the density of nucleation increases. For the present case, coalescence of bubbles as well as upcoming bubbles from the bottom and sides of the tube contribute to the growing of the elongated bubble. This stage is very important in heat transfer at heat fluxes less than 5 $\mathrm{kW/m^2}$. One of the major heat transfer mechanisms for the stage is the micro layer evaporation underneath the elongated bubble [8]. Other one mechanism is the liquid agitation. If a big bubble were departed from the tube surface, there would be sudden liquid movement into the space.

Stage 2. As the heat flux increases the sizes of bubbles increase larger comparing with the bubbles in the stage 1. This stage is raging from 5 $\mathrm{kW/m^2}$ to 15 $\mathrm{kW/m^2}$. At this stage upward movement of bubbles from the tube bottom is clearly observed. Outflow of the elongated bubble from the tube is more frequently observed than the stage 1. Therefore, the intensity of the liquid agitation gets stronger.

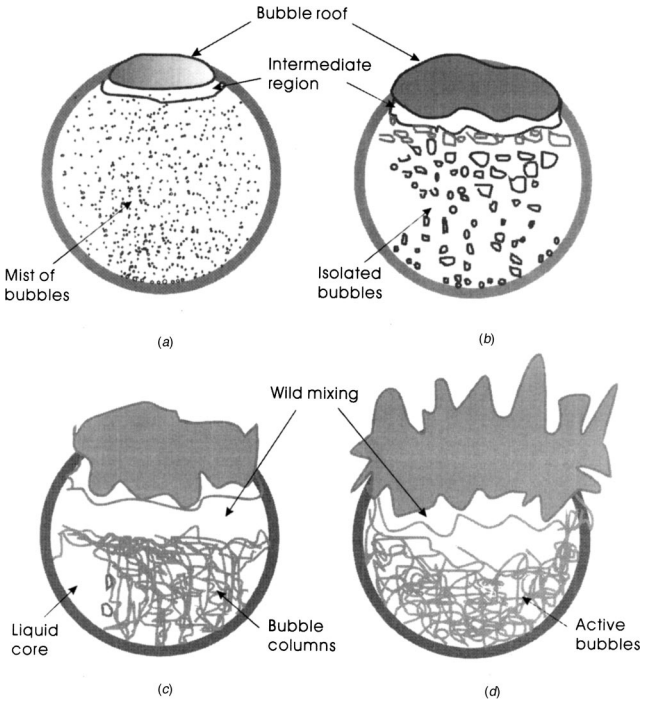

Fig. 3 Boiling mechanisms on the inside surface of a horizontal tube: (a) stage 1; (b) stage 2; (c) stage 3; and (d) stage 4

Stage 3. As the value of the heat flux increases gradually, bubbles generated at the tube bottom regions coalesce together and get bigger buoyancy. The bunch of coalesced bubbles breaches the boundary of the elongated bubble. A region of wild mixing between the bubble slug from the tube bottom and the elongated bubble is observed abound the mid-regions of the tube. The region of wild mixing expands toward up and downward as the heat flux increases. At this stage, a liquid core was generated near the sidewall and swirling bubble columns around the liquid core were observed. This continues up to 60 kW/m^2. At this stage the major mechanism to increase heat transfer is regarded as the active liquid agitation.

Stage 4. The shape of the elongated bubble is almost disappeared and no clear boundary is observed as the heat flux increases more than 60 kW/m^2. Very frequent outflow of bubbles from the tube sides is observed. This is somewhat similar to the heat transfer in the vertical tube annuli with closed bottom [9]. However, the slope of h_b versus q'' is increasing for the present case while the values for the tube annuli with closed bottom is decreasing abruptly. The major reason for the difference is due to the restriction of the flow inflow to the heated surface and the narrower flow area at the tube annuli.

Conclusions

An experimental study of pool boiling heat transfer in a horizontal tube at atmospheric pressure has been performed and the major conclusions are as followings:

1. Local heat transfer coefficients change much along the tube periphery and the minimum was observed at the tube bottom.
2. The major pool boiling mechanisms affecting the heat transfer in a tube are the micro layer evaporation and the liquid agitation. The mechanism of micro layer evaporation is most effective at heat fluxes regions less than 5 kW/m^2. As the value of the heat flux increases the mechanism of the liquid agitation gets effective.

Acknowledgment

This work was supported by grant No. 2000-1-304-012-3 from the Basic Research Program of the Korea Science and Engineering Foundation.

Nomenclature

D_i = tube inside diameter
h_b = boiling heat transfer coefficient
I = supplied current
L = tube length
q'' = heat flux
T_{sat} = saturated water temperature
T_W = tube wall temperature
V = supplied voltage
θ = azimuthal angle along the tube periphery

References

[1] Chun, M. H., and Kang, M. G., 1998, ''Effects of Heat Exchanger Tube Parameters on Nucleate Pool Boiling Heat Transfer,'' ASME J. Heat Transfer, **120**, pp. 468–476.
[2] Lance, R. P., and Myers, J. E., 1958, ''Local Boiling Coefficients on a Horizontal Tube,'' AIChE J., **4**(1), pp. 75–80.
[3] Cornwell, K., and Houston, S. D., 1994, ''Nucleate Pool Boiling on Horizontal Tubes: A Convection-Based Correlation,'' Int. J. Heat Mass Transfer, **37**, Suppl. 1, pp. 303–309.
[4] Kang, M. G., 2000, ''Effect of Tube Inclination on Pool Boiling Heat Transfer,'' ASME J. Heat Transfer, **122**, pp. 188–192.
[5] Jung, D. S., Venant, J. E. S., and Sousa, A. C. M., 1987, ''Effects of Enhanced Surfaces and Surface Orientations on Nucleate and Film Boiling Heat Transfer in R-11,'' Int. J. Heat Mass Transfer, **30**(12), pp. 2627–2639.
[6] Nishikawa, K., Fujita, Y., Uchida, S., and Ohta, H., 1984, ''Effect of Surface Configuration on Nucleate Boiling Heat Transfer,'' Int. J. Heat Mass Transfer, **27**(9), pp. 1559–1571.
[7] Jabardo, J. M. S., and Filho, E. P. B., 2000, ''Convective Boiling of Halocarbon Refrigerants Flowing in a Horizontal Copper Tube—An Experimental Study,'' Exp. Therm. Fluid Sci., **23**, pp. 93–104.
[8] Hewitt, G. F., 1978, *Nucleate Boiling Heat Transfer, Two-Phase Flows and Heat Transfer With Application to Nuclear Reactor Design Problems*, J. J. Ginoux, ed., Hemisphere Publishing Corporation, pp. 89–109.
[9] Kang, M. G., 2002, ''Pool Boiling Heat Transfer in Vertical Annular Crevices,'' Int. J. Heat Mass Transfer, **45**, pp. 3245–3249.

Three-Dimensional Conjugate Heat Transfer in a Horizontal Channel With Discrete Heating

Qinghua Wang and Yogesh Jaluria
Department of Mechanical and Aerospace Engineering,
Rutgers, The State University of New Jersey,
Piscataway, NJ 08854-8058

Three-dimensional conjugate heat transfer in a rectangular duct with two discrete flush-mounted heat sources has been studied numerically in the context of cooling of electronic equipments. The Grashof number is fixed as 10^6 and the working fluid is taken as air. The effects of the spatial arrangement of heat sources, the thermal conductivity ratio of the bottom plate material to air, and the Reynolds numbers on the overall and local heat transfer in the duct are evaluated. The magnitudes of the conduction and the convection transport are compared for different parametric combinations. Of particular interest are the transverse variation in the flow, temperature and heat transfer, the interaction between the heat sources, and the effects of conjugate transport.
[DOI: 10.1115/1.1773195]

Keywords: Channel Flow, Conjugate, Heat Transfer, Mixed Convection

Introduction

Flow instability and heat transfer in three-dimensional mixed convection flow in a horizontal duct were investigated in an earlier study [1]. In the present work, conduction heat transfer in the bottom plate is also considered, since it can be important for three-dimensional flow in a duct with a moderate Reynolds number and compact size. The heat generated in the heat sources is not only dissipated directly into the ambient fluid by convection, but also lost to the substrate and then eventually convected into the fluid. The interaction between the heat sources becomes more complicated. In the streamwise direction, the heat source at a downstream location has a stronger influence on the upstream source than that in pure convection, because, although the downstream heat source is in the wake of the upstream one, the latter is also affected by heat transfer due to conduction in the board.

Nakayama [2] reviewed the studies addressing the convective/conductive conjugate heat transfer in electronic systems, and pointed out that it was the dominant mode of heat transfer in compact systems, particularly in air-cooling systems. His reviews mainly concentrated on the two-dimensional heat transfer and flow between plates with flush or protruding heat blocks, and a composite approach, consisting of both experiment and numerical analysis, was proposed for the three-dimensional complex flow in channels with a single protruding heat source. Many papers have been published on conjugate heat transfer in two dimensional channels. Sugavanam et al. [3] studied the coupled forced convection and conduction in a channel with a strip flush-mounted heat source. They evaluated the effects of board conduction on the overall heat transfer, and obtained correlations between the Nusselt number and the ratio of thermal conductivities. They also validated the superposition principle for the prediction of the board temperature distribution with multiple heat sources based on the simulation for a single heat source. Kim et al. [4] simulated two-dimensional conjugate mixed convection in a wide channel with protruding heat blocks, with the conductivity ratio fixed at 10. As expected, the vertical-oriented channel was found to have a better cooling effect than the horizontal-oriented channel. Ramadhyani et al. [5] investigated the interaction between two discrete heat sources mounted flush on the bottom wall of a channel. The flow in the channel was assumed to be a fully developed laminar flow. They found that conductive heat transfer in the substrate could be greater than the direct convective heat transfer, and the upstream heat source imposed a much stronger influence on the downstream heat source than the latter on the former. Nigen and Amon [6] investigated the self-sustained oscillatory flows in a grooved channel, and the conjugate conduction/convection formation was found to show different thermal characteristics from the uniform heat flux representation.

In most of the previous work, the three-dimensional convective transport in a duct was analyzed as a nonconjugate problem, and the bottom surface was assumed to be either isothermal or at a uniform heat flux [7–10]. Nicolas et al. [7] presented the stability analysis of mixed convection flow in a horizontal duct, and the critical values for Reynolds and Rayleigh numbers, corresponding to different flow patterns, were obtained. Lin and his colleagues [8–10] investigated the thermal transport and flow patterns in a duct with the top and bottom kept at constant temperatures. Several different flow patterns were found, and the stability diagram was presented.

In contrast, much less attention has been paid to the three-dimensional conjugate convection/conduction flow in a channel. Lin et al. [11] conducted a combined experimental and numerical study on the flow structure in a horizontal duct with thermally conducting side walls, and uniform heat flux applied at the bottom. The conduction into the side wall was found to influence the vortex structure significantly. Choi and Kim [12] investigated the mixed convection flow in a duct with a horizontal thermally conducting board. The convective flow was divided into three regimes based on 5% deviation between regimes. Correlations for the average Nusselt number and the maximum temperature were obtained.

The main objectives of the present research are the following. First, the effects of thermal properties of the bottom board and the spatial arrangement of the heat sources on the overall thermal performance of the duct are studied. Much of the previous work done in this area has been with two-dimensional simulations. In the three-dimensional case, greater heat is dissipated via the conduction mode since the heat transport is spread out in the lateral direction as well. Second, for a set of thermal properties, the spatial arrangement, particularly the transverse separation, of the heat sources on the board is optimized to obtain the best overall heat transfer rate at given Reynolds and Grashof numbers. The results obtained could form the basis for the design and optimization of the cooling arrangement for a typical electronic system.

Governing Equations

The system under consideration in the present study is a horizontal duct with discrete heat sources mounted flush on the bottom, as shown in Fig. 1. A uniform flux q'' is assumed to be dissipated by each heat source. Several heat sources are deployed on the bottom plate in the streamwise direction or in the spanwise direction, and the leading edge of the upstream heat source is located at $L_e = 4.0$. The heat sources are not necessarily aligned along the center axis. Thus, different three-dimensional geometrical configurations are of interest. With the Boussinesq approximations, the dimensionless governing equations for the fluid and solid regions can be expressed as follows:

The Fluid Region.

$$\nabla \cdot \vec{V} = 0 \tag{1}$$

$$\frac{\partial \vec{V}}{\partial \tau} + \vec{V} \cdot \nabla \vec{V} = -\nabla P + \frac{1}{\mathrm{Re}} \nabla^2 \vec{V} - \frac{\mathrm{Gr}}{\mathrm{Re}^2} \theta \vec{g} \tag{2}$$

Contributed by the Heat Transfer Division for publication in the JOURNAL OF HEAT TRANSFER. Manuscript received by the Heat Transfer Division May 22, 2003; revision received March 24, 2004. Associate Editor: K. S. Ball.

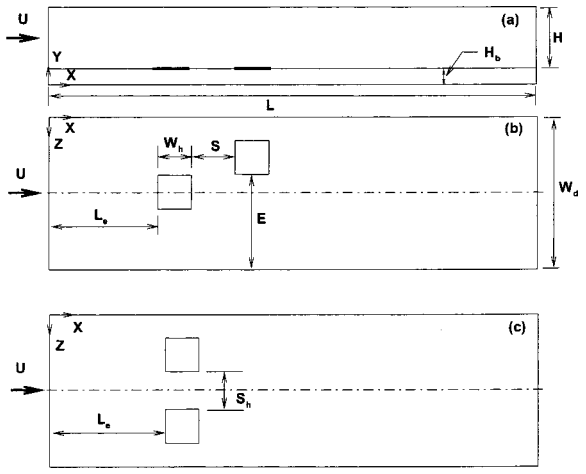

Fig. 1 (*a*) Geometrical configuration for three-dimensional flow in a duct with flush-mounted discrete heat sources; (*b*) stream-wise arrangement of sources; (*c*) spanwise arrangement of sources

$$\frac{\partial\theta}{\partial\tau}+\vec{V}\cdot\nabla\theta=\frac{1}{\mathrm{Re\,Pr}}\nabla^2\theta \tag{3}$$

The Solid Region.

$$\vec{V}=0 \tag{4}$$

$$\frac{\partial\theta}{\partial\tau}+\vec{V}\cdot\nabla\theta=\frac{r_a}{\mathrm{Re\,Pr}}\nabla^2\theta \tag{5}$$

Here, r_a is the ratio of the thermal diffusivities, i.e., a_s/a_f, and $\vec{g}$ is the unit vector in the direction of gravity.

The flow is initially assumed to be a three-dimensional developed flow in the fluid region with zero temperature everywhere, i.e.,

$$V=W=0,\quad U=U_{\mathrm{dev}},\quad \theta=0,\quad \text{for } \tau<0 \tag{6}$$

Here, U_{dev} is the velocity of a fully developed flow, and the distribution can be obtained using the following expression given by Shah and London [13],

$$U_{\mathrm{dev}}=\left(\frac{m+1}{m}\right)\left(\frac{n+1}{n}\right)(1-|2Y-1|^n)\left(1-\left|\frac{2Z}{Ar}-1\right|^m\right)$$

where m and n are constants dependent on the lateral aspect ratio, W_d/H, of the duct. No-slip conditions are applied at all solid surfaces. The side walls and the outer surface of the bottom plate are taken as adiabatic, and the top plate is cooled and assumed to be at a lower temperature T_0, the ambient temperature. Therefore, the boundary conditions can be summarized as follows:

$$U=V=W=\frac{\partial\theta}{\partial Z}=0,\quad Z=0,Ar \tag{7}$$

$$U=V=W=\frac{\partial\theta}{\partial Y}=0,\quad Y=0 \tag{8}$$

$$U=V=W=\theta=0,\quad Y=1+H_b \tag{9}$$

$$U=U_{\mathrm{dev}},\quad V=W=\theta=0,\quad X=0 \tag{10}$$

$$\frac{\partial U}{\partial X}=\frac{\partial V}{\partial X}=\frac{\partial W}{\partial X}=\frac{\partial\theta}{\partial X}=0,\quad X=L \tag{11}$$

Particular attention is directed at the solid-fluid interface when considering the energy equation. In order to maintain the consistency of heat flux at the interface, the harmonic mean formulation for thermal conductivities, described in [14], is employed.

Numerical Model and Code Validation

In an earlier paper [1], a finite volume method (FVM), with an approach similar to the SIMPLER algorithm, was developed to solve the preceding partial differential equations. The diffusion and the convective terms were discretized using the center difference scheme (CD) and the second-order upwind scheme (SOU), respectively. However, the code has to be validated for conjugate heat transfer. The code was used to simulate the three-dimensional conjugate heat transfer in a duct with the outer surface of the bottom wall insulated. The lateral aspect ratio of the duct was taken as 10, in order to make the flow similar to the two-dimensional channel flow described by Sugavanam et al. [3]. The present calculations agree with those of Sugavanam et al. qualitatively, except that the predicted temperatures along the axis on the solid-fluid interface are slightly lower than theirs. This is because conduction in the spanwise direction is involved in the present three-dimensional simulation. A grid dependence test was also carried out to determine the appropriate grid. Three different grid sizes were chosen to simulate the flow at $\mathrm{Re}=500$ and $\mathrm{Gr}=10^6$. It's found that all solutions for the chosen dependent variables are quite close for the different grid systems, and the maximum difference is within 5.0%, and thus the nonuniform grid system with size of $131\times31\times51$, is chosen for the following calculations.

Results and Discussion

Multiple Streamwise-Deployed Heat Sources. As shown in Fig. 1(*b*), two heat sources are deployed on the board in the streamwise direction, and the entry portion length L_e is taken as 4. The normalized temperature and the local Nusselt number results are presented as three-dimensional distributions in Fig. 2. The second heat source has higher temperatures and lower Nusselt numbers than the upstream heat source. The temperatures far downstream are essentially uniform. The Nusselt number downstream of the second heat source takes the flat "*M*" form, and negative values appear along the axis. The appearance of negative Nusselt numbers in the wake implies that the substrate is heated by the fluid.

In order to study the interaction between the heat sources, the approach described in [5] is employed here. The average temperature and the ratio of heat conduction to the total heat transfer are normalized by the corresponding values for the case of a single heat source. The normalized variables are represented by an asterisk. Figure 3 presents the variation of the average temperature, the normalized average temperature and the normalized ratio of heat conduction to total heat transfer, with the spacing S between the heat sources. In the top figure, the temperatures for both the heat sources drop with an increase in spacing S, but as S becomes large, $S\geqslant4$, the temperature of the first heat source attains an essentially constant value. This means that the second heat source does not affect the first heat source at larger spacings, which is an expected behavior. More evident interaction between the heat sources can be seen in the middle figure. First, the normalized average temperature is not less than 1, which implies that the presence of another heat source always increases the average temperature except at very large spacings. Second, when $S\leqslant4$, the second heat source has a significant effect on the first one. The effect becomes weaker with an increase in the spacing S. Third, the first heat source has a pronounced effect on the second heat source, even for large spacings, $S\geqslant5$. It is found that, even at $S=5.0$, the average temperature of the second heat source increases by 15% due to the presence of the first heat source. In the bottom figure, the normalized ratio of conduction heat transfer to the total heat transfer from the first heat source is asymptotic to 1, since the effect of the second heat source is weakened with S increasing. However, the profile for the second heat source is fairly constant, and is at around 1.005. The normalized ratio is greater than unity, so that conduction heat transfer over the second heat source is slightly more important than that in the case of a single heat

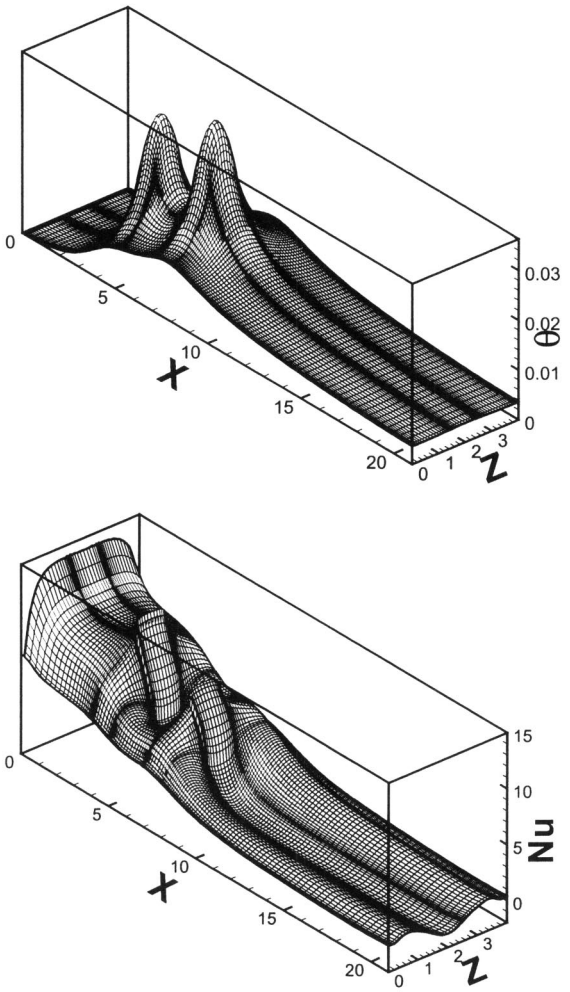

Fig. 2 The distributions of temperature (top figure) and the local Nusselt number (bottom figure) on the fluid-solid interface, in the case of two streamwise-deployed heat sources, with Re=500, Gr=10^6, r_k=50, W_h=1, and S=2

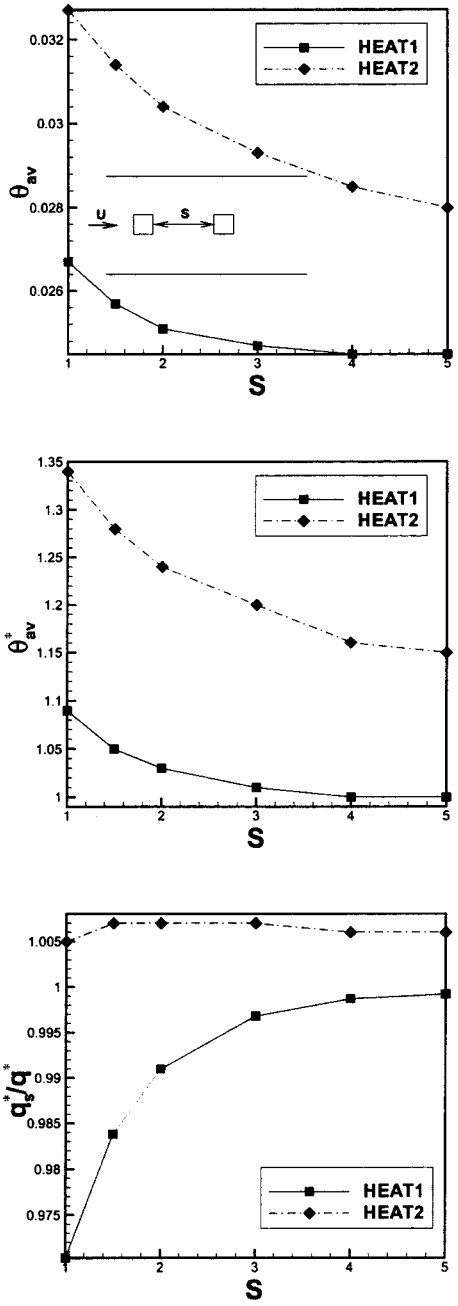

Fig. 3 The effect of axial spacing S between heat sources on the average temperature (top figure), the normalized average temperature (middle figure), and the normalized ratio of conductive heat transfer to total heat input (bottom figure) from the heat sources, in the case of two streamwise-deployed sources, for Re=500, Gr=10^6, and r_k=50

source. In other words, the convection heat transfer component decreases, since the total heat transfer rate remains constant.

The effect of thermal properties of the substrate material is further illustrated in Fig. 4. The higher the thermal conductivity ratio, the lower the average temperature for both the heat sources, and more important the conductive heat transfer. It is noted that the difference between the average temperatures of the two heat source decreases as r_k is increased. A high thermal conductivity in the substrate makes the temperature distribution on the fluid-solid interface more uniform. The ratio of conduction heat transfer rate increases with r_k, and the values for the second heat source remain greater than those for the first heat source. Conduction plays a more important role for the second heat source than for the first heat source, except when r_k is very small, say 0.1, for which conduction heat transfer is less than 1% of the total heat transfer rate.

Figure 5 shows the variation of the average temperature and the ratio of convective heat transfer to total heat transfer over the heat sources with the Reynolds number. At large Reynolds numbers, convection is expected to prevail over conduction, and the average temperature decreases. The difference between the average temperatures of the two heat sources is almost the same except at Re=100. The buoyancy effects become stronger as the Reynolds number decreases, and longitudinal vortices may occur after the flow is heated, as described in [1]. This secondary flow pumps the hot fluid upwards to the cold top plate and, therefore, improves the local heat transfer. Such vortices do not occur at higher Reynolds numbers, say at Re=500. With an increase in the Reynolds number, the forced convection transport is enhanced, and more heat is dissipated directly into the fluid, as shown in the bottom figure. Convection heat transfer from the upstream heat source is greater than that from the second heat source, which results from the fact that the fluid temperature in the wake of the first heat source is higher than that in the entry portion of the duct. As seen for the temperature difference, the difference in convection heat transfer, between the two heat sources, does not change signifi-

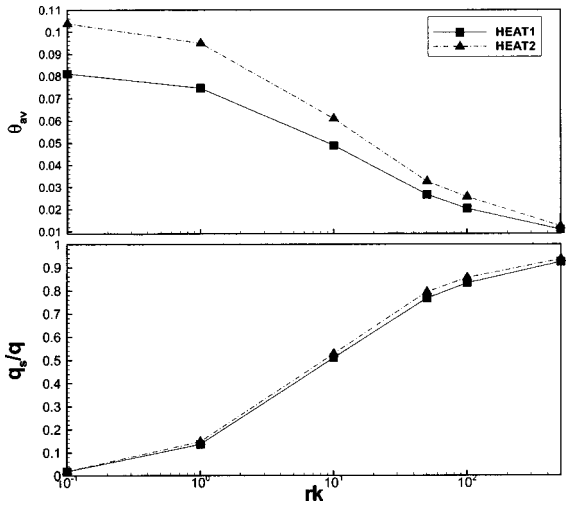

Fig. 4 The effect of conductivity ratio r_k on the average temperature (top figure) and ratio of conduction to total heat transfer of heat sources (bottom figure), in the case of two streamwise-deployed sources, at Re=500, Gr=10^6, and $S=1$. HEAT1 and HEAT2 represent the first and the second heat sources in the streamwise direction, respectively.

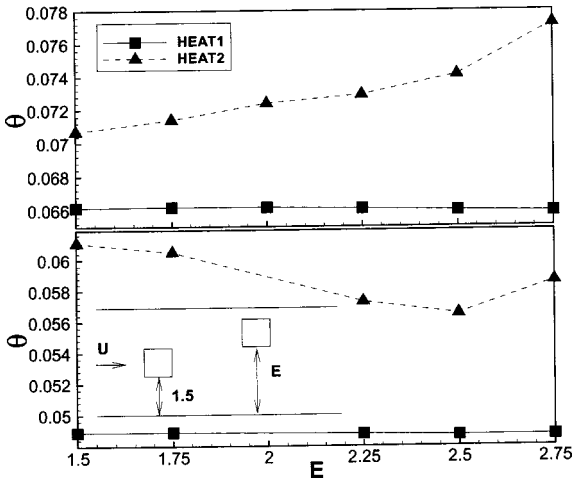

Fig. 6 Variation of the average temperature with the spatial arrangement of the second heat source on the bottom, in the case of two streamwise-deployed sources, for Gr=10^6, $r_k=10$, $S=1$, Re=100 (top figure), and Re=500 (bottom figure)

cantly with Re. This implies that the interaction between the two heat sources does not change very much with the Reynolds number in the forced convection region. In view of the bottom figures in Figs. 4 and 5, one may conclude that convective heat transfer from the first heat source is always greater than that from the second heat source, while conductive heat transfer is less than that from the second heat source.

It is also of interest to find the effects of the spatial arrangement of the heat sources. Figure 6 indicates how the location of the second heat source affects the average temperatures of both the heat sources. First, the change of location for the second heat source does not have a significant influence on the first heat source. Second, at lower Reynolds numbers, it may be wise to put the second heat source in the center of the wake of the first heat source, since it can benefit from the secondary flow induced by the first heat source. For large Reynolds numbers, there must exist a trade-off location for the second heat source. At the axis of the duct, the axial velocity u is at its maximum value, and a higher velocity results in higher heat transfer, but it is also in the wake of the first heat source, which worsens the heat transfer. It can be seen that the trade-off location at Re=500 is $E=2.5$. This optimal location is dependent on the flow condition and the thermal conductivity of the substrate.

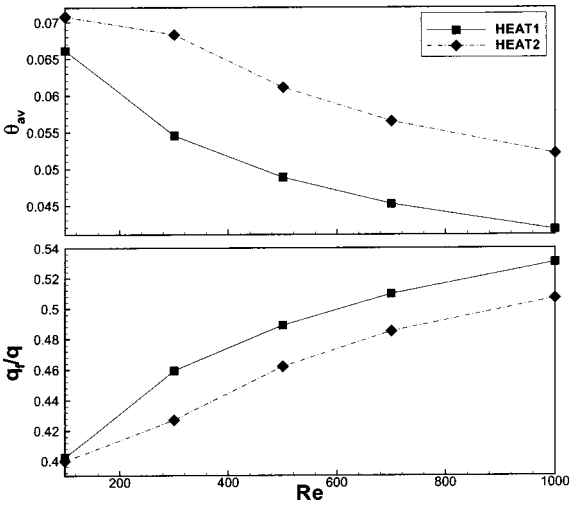

Fig. 5 Variations of the average temperature (top figure) and ratio of convection to total heat transfer (bottom figure) over heat sources, with Reynolds numbers, in the case of two streamwise-deployed sources, at Gr=10^6 and $r_k=10$. HEAT1 and HEAT2 represent the first and the second heat sources in the streamwise direction, respectively.

Multiple Spanwise-Deployed Heat Sources. In the preceding calculations, it was found that the second heat source always has a higher average temperature due to the wake of the first heat source. Now we consider the case in which the heat sources are deployed in the spanwise direction, as sketched in Fig. 1(*c*). The spanwise width of the duct is kept unchanged, i.e., $W_d=4$. As shown in Fig. 7, two heat sources are deployed symmetrically about the axis. The distributions of temperature and the local Nusselt number show the symmetry. Let us consider the differences between the spanwise and the streamwise arrangements of the heat sources. Two cases with the same spacing, $S=S_h=1$, between the heat sources, and the same thermal conductivity ratio $r_k=10$, and same Reynolds and Grashof numbers, are chosen for the comparison. For the streamwise arrangement, the average temperatures of the first and the second heat sources can be found in Fig. 4, and they are 0.048 and 0.062, respectively. For the case with the spanwise arrangement, the average temperatures of both heat sources are 0.0514, which is much closer to the temperature of the first heat source in the streamwise arrangement.

Figure 8 shows the variation of the average temperature and convective heat transfer rate with the spanwise spacing. The minimum temperature occurs at $S_h=0.8$. There are two competing factors to determine the average temperature. One is the negative effect from the neighboring heat source. The thermal boundary layer develops in the spanwise direction as well. It is apparent that the influence from neighboring heat sources weakens as the spacing between them increases. The ratio of convective heat transfer decreases from the very close arrangement until $S_h=1.0$, where it hits the minimum value. Because the influence of the neighboring heat source weakens, a higher conductive heat transfer is obtained. However, when the heat source moves very close to the side walls, conduction in the direction toward the side wall is weakened, since the side walls are insulated, and convection heat source is also decreased because of a lower axial velocity. This can be seen very clearly in the bottom figure. The conduction in the streamwise direction, including both upstream and down-

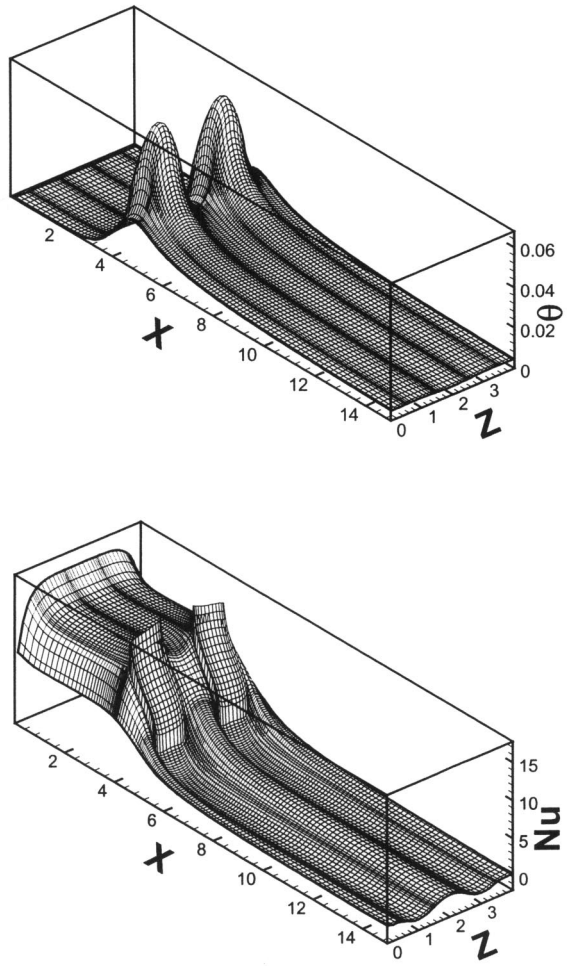

Fig. 7 The temperature distribution (top figure) and the local Nusselt number (bottom figure) on the fluidsolid interface, in the case of two spanwise-deployed sources, for Re=500, Gr $=10^6$, $r_k=10$, $W_h=1$, and $S_h=1$

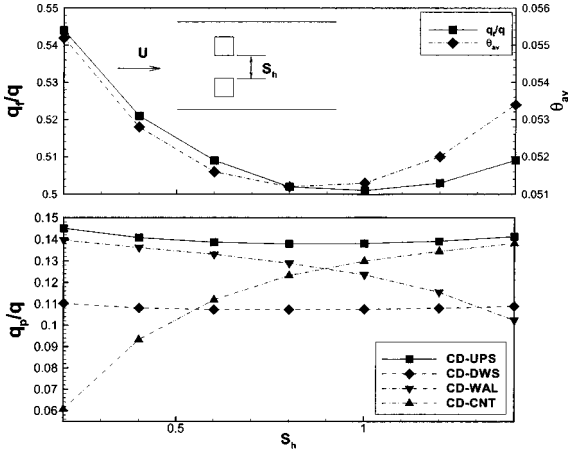

Fig. 8 The average temperature and the ratio of direct convection to total heat transfer (top figure), and the ratios of heat transfer in each direction to total heat transfer (bottom figure) from the heat sources at different spanwise spacings S_h, in the case of two spanwise-deployed sources, for Re=500, Gr=10^6, $W_h=1$, and $r_k=10$. CD-UPS, DWS, WAL, and CNT represent heat conduction in the directions to the upstream, to the downstream, to the side-wall, and to the axis, respectively.

stream directions, remains almost unchanged. However, conduction toward the axis in the spanwise direction increases very quickly, and conduction toward the side wall drops when the heat source is moved close to the side wall. But the decrease in convection is not as much as the decrease in conduction. This is why the ratio of convection to the total heat transfer increases when the heat source is moved closer to the side wall.

Conclusions

Three dimensional conjugate heat transfer in a duct with discrete flush-mounted heat sources has been investigated numerically. Interest lies in both streamwise and spanwise separation of sources. When the heat sources are mounted in the streamwise direction, the upstream heat source is found to affect the downstream heat source significantly, while the latter has a negligible effect on the former when the spacing is large. The ratio of convection to the total heat transfer from the upstream heat source is larger than that from the downstream one, but the ratio of conduction to the total heat transfer is less than that from the downstream heat source. The spanwise arrangement of heat sources may result in a lower global average temperature for the two heat sources. The possibility of optimizing the location for maximum heat transfer is evident from these results.

Acknowledgment

Support of this work by the National Science Foundation under Grant No. CTS-0121058 is gratefully acknowledged.

Nomenclature

Ar = lateral aspect ratio, Ar$=W_d/H$
E = distance to the side wall
Gr = Grashof number, Gr$=(g\beta H^2 q)/k_f\nu^2$
H = duct height
H_b = thickness of the bottom plate
k = thermal conductivity
L = dimensionless duct length scaled by H
L_e = dimensionless entry duct length scaled by H
Nu = Nusselt number
p = pressure
P = dimensionless pressure, $P=p/\rho u_m^2$
Pr = Prandtl number
q = heat transfer rate from heat sources
q'' = heat flux from heat sources
r_k = ratio of thermal conductivities, $r_k=k_s/k_f$
r_α = ratio of thermal diffusivities, $r_\alpha=\alpha_s/\alpha_f$
Ra = Rayleigh number, Ra=GrPr
Re = Reynolds number, Re$=u_m H/\nu$
S = streamwise spacing between sources
S_h = spanwise spacing between sources
t = time
T = temperature
T_0 = the temperature of the inflow fluid
u_m = average inflow velocity
U, V, W = dimensionless velocity components in the x, y, and z direction scaled by u_m
U_{dev} = velocity of the fully developed flow
W_b = width of the square heat source
W_d = width of the duct
X, Y, Z = Cartesian coordinates

Greek Letters

α = thermal diffusivity
β = volumetric thermal expansion coefficient
θ = dimensionless temperature, $\theta=(T-T_0)Hk_f/q$
ν = kinematic viscosity
τ = dimensionless time, $\tau=(tu_m/H)$

Subscripts

f = fluid properties
s = solid properties

References

[1] Wang, Q., and Jaluria, Y., 2002, ''Instability and Heat Transfer in Mixed Convection Flow in a Horizontal Duct With Discrete Heat Sources,'' Numer. Heat Transfer, **42**, pp. 445–463.

[2] Nakayama, W., 1997, ''Forced Convective/Conductive Conjugate Heat Transfer in Microelectronic Equipment,'' Annu. Rev. Heat Transfer, **8**, pp. 1–45.

[3] Sugavanam, R., Ortega, A., and Choi, C. Y., 1995, ''A Numerical Investigation of Conjugate Heat Transfer From a Flush Heat Source on a Conductive Board in Laminar Channel Flow,'' Int. J. Heat Mass Transfer, **38**, pp. 2969–2984.

[4] Kim, S. Y., Sung, H. J., and Hyun, J. M., 1992, ''Mixed Convection From Multiple-Layered Board With Cross-Streamwise Periodic Boundary Conditions,'' Int. J. Heat Mass Transfer, **35**(11), pp. 2941–2952.

[5] Ramadhyani, S., Moffatt, D. F., and Incropera, F. P., 1985, ''Conjugate Heat Transfer From Small Isothermal Heat Sources Embedded in a Large Substrate,'' Int. J. Heat Mass Transfer, **28**(10), pp. 1945–1952.

[6] Nigen, J. S., and Amon, C. H., 1994, ''Time-Dependent Conjugate Heat Transfer Characteristics of Self-Sustained Oscillatory Flows in a Grooved Channel,'' J. Fluids Eng., **116**, pp. 449–507.

[7] Nicolas, X., Luijkx, J. M., and Platten, J. K., 2000, ''Linear Stability of Mixed Convection Flows in Horizontal Rectangular Channels of Finite Transversal Extension Heated From Below,'' Int. J. Heat Mass Transfer, **43**, pp. 589–610.

[8] Yu, C. H., Chang, M. Y., Huang, C. C., and Lin, T. F., 1997, ''Unsteady Vortex Rolls Structures in a Mixed Convection Air Flow Through a Horizontal Plane Channel: A Numerical Study,'' Int. J. Heat Mass Transfer, **40**, pp. 505–518.

[9] Chang, M. Y., Yu, C. H., and Lin, T. F., 1997, ''Flow Visualization and Numerical Simulation of Transverse and Mixed Vortex Roll Formation in Mixed Convection of Air in a Horizontal Flat Duct,'' Int. J. Heat Mass Transfer, **40**, pp. 1907–1922.

[10] Lir, J. T., Chang, M. Y., and Lin, T. F., 2001, ''Vortex Flow Patterns Near Critical State for Onset of Convection in Air Flow Through a Bottom Heated Horizontal Flat Duct,'' Int. J. Heat Mass Transfer, **44**, pp. 705–719.

[11] Lin, W. L., Ker, Y. T., and Lin, T. F., 1996, ''Experimental Observation and Conjugate Heat Transfer Analysis of Vortex Flow Development in Mixed Convection of Air in a Horizontal Rectangular Duct,'' Int. J. Heat Mass Transfer, **39**, pp. 3667–3683.

[12] Choi, C. Y., and Kim, S. J., 1996, ''Conjugate Mixed Convection in a Channel: Modified Five Percent Deviation Rule,'' Int. J. Heat Mass Transfer, **39**, pp. 1223–1234.

[13] Shah, R. K., and London, A. L., 1978, *Laminar Flow Forced Convection in Ducts*, Academic Press, Inc., New York, NY.

[14] Patankar, S. V., 1980, *Numerical Heat Transfer and Fluid Flow*, Hemisphere, Washington, DC.

Use of Wavelets for Analyzing Transient Radiative Heat Transfer in an Inhomogeneous Medium

Oguzhan Guven and Yildiz Bayazitoglu
e-mail: bayaz@rice.edu
Department of Mechanical Engineering and Materials Science, Rice University, 6100 South Main Street, Houston, Texas 77005

Transient radiative heat transfer in a two-dimensional inhomogeneous rectangular medium is considered. The medium is gray, absorbing, emitting and strongly scattering, and bounded by cold, black walls. Inhomogeneous zones of various sizes are placed at different locations within the medium. The incident radiant energy due to a short laser pulse produces a highly transient and unique transmittance, which is investigated. The discrete wavelets method is used to solve the corresponding equation of transient radiative transfer. The time dependent transmittance for various inhomogeneous areas and the significance of the size and location of the inhomogeneous zones are computed. [DOI: 10.1115/1.1773193]

Keywords: Heat Transfer, Laser, Radiation, Scattering, Transient

Introduction

This paper deals with transient radiative heat transfer in a two-dimensional medium, containing an inhomogeneous zone of varying size, location and optical parameters. Guo and Kumar [1] used the discrete ordinates method to solve the radiation transfer equation (RTE) in a similar case to the one considered in this work, namely a laser beam impinging on one of the boundaries. They considered an inhomogeneous zone at the center of the host medium and examined the transmittance results. In the present work, the discrete wavelet analysis [2] is applied, because of its capability of modeling the localized variations in the intensity field. In this paper first the discrete wavelet method is applied and then the transmittance results are presented.

Formulation

For two-dimensional Cartesian coordinates, the transient RTE can be written as

$$\frac{1}{c}\frac{\partial I}{\partial t}+\xi\sqrt{1-\mu^2}\frac{\partial I}{\partial y}+\mu\frac{\partial I}{\partial z}+\beta I=S \tag{1}$$

where $I=I(t,y,z,\mu,\xi)$ is the radiative intensity and the angular parameters are $\mu=\cos\theta$ and $\xi=\sin\phi$. The system geometry for a rectangular enclosure containing an absorbing, emitting and highly scattering host medium is sketched in Fig. 1. A collimated laser pulse impinges on the medium at the center of the bottom wall. The radiative heat transfer problem is treated by separating the intensity into its diffuse I_d and collimated I_c parts [3].

The solution to the collimated portion of the problem is

$$I_c(t,z,\mu)=I_0e^{-\beta z}\{H[t-(z/c)]-H[t-t_p-(z/c)]\}\delta_{\mu,1} \tag{2}$$

where I_0 is the incident laser intensity; t_p is the duration of the laser pulse, and δ is the Kronecker δ-function. H is Heaviside's unit step function

$$H(t)=\begin{cases}0, & t<0,\\ 1, & t>0.\end{cases} \tag{3}$$

When the collimated laser beam enters the medium, it is absorbed, reemitted and scattered by the medium. This results in a radiative transfer problem of diffuse intensities. The transfer equation for the diffuse intensity, I_d, can be written as

$$\frac{1}{c}\frac{\partial I_d}{\partial t}+\xi\sqrt{1-\mu^2}\frac{\partial I_d}{\partial y}+\mu\frac{\partial I_d}{\partial z}+\beta I_d=S \tag{4}$$

with a source function S

$$S(t,y,z,\Omega)=\kappa I_b(y,z)+\frac{\sigma}{4\pi}\int_{4\pi}I_d(t,y,z,\Omega')\Phi(\Omega',\Omega)\mathrm{d}\Omega'+S_c. \tag{5}$$

S_c is the contribution of collimated intensity to the source function and is defined as

$$S_c(t,z,\mu)=\frac{\sigma}{2}I_0e^{-\beta z}\{H[t-(z/c)]-H[t-t_p-(z/c)]\}\Phi(\mu,1). \tag{6}$$

In this work, the wavelet method is used to solve the transport equation given in Eq. (4). The Daubechies' wavelets are chosen as the basis functions. These basis functions have only applicability in [0,1]. However, μ and ξ have values from negative one to positive one. To overcome this limitation, we divide the angular domain into four subdomains, and denote the diffuse intensity I_d with i, j, k, l in these subdomains [2]. Then we expand the intensity into its wavelet basis in each subdomain:

$$i=\sum_m\sum_n a_{m,n}(t,y,z)\cdot W_{m,n}(\mu,\xi)$$

$$\text{where } 0\leqslant\mu<1 \quad \text{and} \quad 0\leqslant\xi<1 \tag{7a}$$

$$j=\sum_m\sum_n b_{m,n}(t,y,z)\cdot W_{m,n}(\mu,\xi)$$

$$\text{where } -1\leqslant\mu<0 \quad \text{and} \quad 0\leqslant\xi<1 \tag{7b}$$

$$k=\sum_m\sum_n c_{m,n}(t,y,z)\cdot W_{m,n}(\mu,\xi)$$

$$\text{where } 0\leqslant\mu<1 \quad \text{and} \quad -1\leqslant\xi<0 \tag{7c}$$

$$l=\sum_m\sum_n d_{m,n}(t,y,z)\cdot W_{m,n}(\mu,\xi)$$

$$\text{where } -1\leqslant\mu<0 \quad \text{and} \quad -1\leqslant\xi<0 \tag{7d}$$

where $a_{m,n}$, $b_{m,n}$, $c_{m,n}$, and $d_{m,n}$ are wavelet expansion coefficients, and $W_{m,n}$ are the two dimensional wavelets. Substitution of Eqs. (7) into Eq. (4) and application of Galerkin's method yield the following set of hyperbolic partial differential equations:

$$\frac{1}{c}\frac{\partial a_{m,n}}{\partial t}+\sum_m\sum_n\left[A_{mm',nn'}\frac{\partial a_{m,n}}{\partial y}+B_{mm',nn'}\frac{\partial a_{m,n}}{\partial z}\right]+\beta a_{m',n'}=S\cdot\delta_{m',1}\cdot\delta_{n',1} \tag{8a}$$

$$\frac{1}{c}\frac{\partial b_{m,n}}{\partial t}+\sum_m\sum_n\left[A_{mm',nn'}\frac{\partial b_{m,n}}{\partial y}-B_{mm',nn'}\frac{\partial b_{m,n}}{\partial z}\right]+\beta b_{m',n'}=S\cdot\delta_{m',1}\cdot\delta_{n',1} \tag{8b}$$

$$\frac{1}{c}\frac{\partial c_{m,n}}{\partial t}+\sum_m\sum_n\left[-A_{mm',nn'}\frac{\partial c_{m,n}}{\partial y}+B_{mm',nn'}\frac{\partial c_{m,n}}{\partial z}\right]+\beta c_{m',n'}=S\cdot\delta_{m',1}\cdot\delta_{n',1} \tag{8c}$$

Contributed by the Heat Transfer Division for publication in the JOURNAL OF HEAT TRANSFER. Manuscript received by the Heat Transfer Division January 30, 2003; revision received February 27, 2004. Associate Editor: S. T. Thynell.

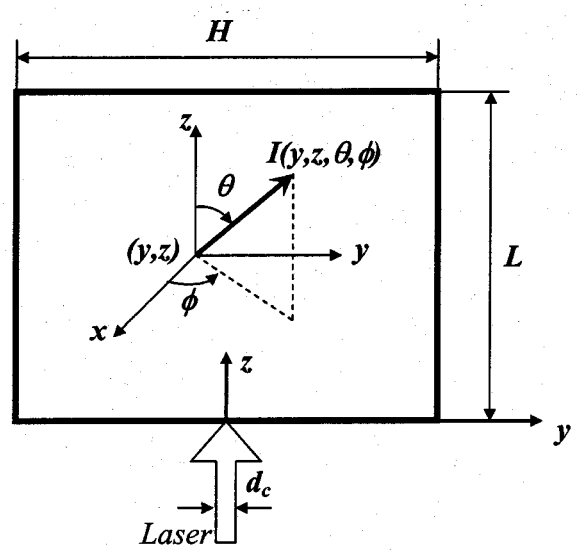

Fig. 1 Sketch of the two dimensional system

$$\frac{1}{c}\frac{\partial d_{m,n}}{\partial t}+\sum_m\sum_n\left[-A_{mm',nn'}\frac{\partial d_{m,n}}{\partial y}-B_{mm',nn'}\frac{\partial d_{m,n}}{\partial z}\right]+\beta d_{m',n'}=S\cdot\delta_{m',1}\cdot\delta_{n',1} \tag{8d}$$

where $m, m', n, n'=1,\ldots,N$. N indicates the level of the wavelet expansion, and variables $a_{m,n}=a_{m,n}(t,y,z)$, $b_{m,n}=b_{m,n}(t,y,z)$, $c_{m,n}=c_{m,n}(t,y,z)$ and $d_{m,n}=d_{m,n}(t,y,z)$ are wavelet expansion coefficients. $A_{mm',nn'}$ and $B_{mm',nn'}$ are defined as

$$A_{mm',nn'}=\int_{\mu=0}^{1}\int_{\xi=0}^{1}(\xi\sqrt{1-\mu^2})W_{m,n}(\mu,\xi)\cdot W_{m',n'}(\mu,\xi)d\xi d\mu \tag{9a}$$

$$B_{mm',nn'}=\int_{\mu=0}^{1}\int_{\xi=0}^{1}\mu\cdot W_{m,n}(\mu,\xi)\cdot W_{m',n'}(\mu,\xi)d\xi d\mu \tag{9b}$$

The boundary conditions for Eq. (8*a*) in its most general form are [2]

$$a_{m',n'}(t,y=-H/2,z)=\left\{\varepsilon_1\cdot I_b(y=-H/2,z)+\frac{\rho_1}{\pi}\sum_m\sum_n\left[c_{m,n}(t,y=-H/2,z)+d_{m,n}(t,y=-H/2,z)\right]\int_0^1\int_0^1 W_{m,n}(\mu,\xi)\frac{\mu}{\sqrt{1-\xi^2}}d\mu d\xi\right\}\cdot\delta_{m',1}\delta_{n',1} \tag{10a}$$

$$a_{m',n'}(t,y,z=0)=\left\{\varepsilon_1\cdot I_b(y,z=0)+\frac{\rho_1}{\pi}\sum_m\sum_n\left[b_{m,n}(t,y,z=0)+d_{m,n}(t,y,z=0)\right]\times\int_0^1\int_0^1 W_{m,n}(\mu,\xi)\frac{\mu}{\sqrt{1-\xi^2}}d\mu d\xi\right\}\cdot\delta_{m',1}\delta_{n',1} \tag{10b}$$

Similar expressions can be written for Eqs. (8*b*), (8*c*), and (8*d*). The set of hyperbolic partial differential, given by Eqs. (10), can be solved by applying an upwind finite difference scheme, provided that proper initial conditions for the intensity are implemented.

Special attention needs to be paid to the choice of the time step, Δt, to assure the solution method is stable, physically realistic, and that the numerical diffusion is minimal. The distance that light travels in the time step, $c\Delta t$, should not exceed spatial mesh size, i.e., $c\Delta t<\min(\Delta y,\Delta z)$. To reduce the numerical diffusion, the time step should be chosen in such a way that value of the Courant number be close to one.

Table 1 Shapes, dimensions and locations of the inhomogeneous zones

Sketch	Label	Dimensions H_1XL_1	Center Coordinates (y_1/H, z_1/L)
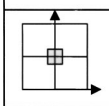	A	1mmX1mm	(0 , 0.5)
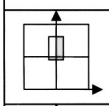	B	1mmX3mm	(0 , 0.6)
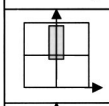	C	1mmX5mm	(0 , 0.7)
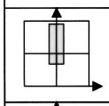	D	1mmX6mm	(0 , 0.65)
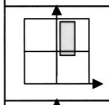	E	1mmX5mm	(0.06 , 0.7)
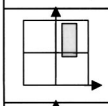	F	1mmX5mm	(0.1 , 0.7)
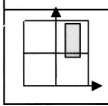	G	1mmX5mm	(0.2 , 0.7)

Results

In this section, the transient transmittance characteristics due to a short laser pulse interacting with an inhomogeneous medium in a square enclosure are investigated. The medium absorbs and scatters the radiation. Emission from the medium, however, is negligible compared to the intensity due to the laser beam (both the laser beam itself and the intensity scattered away). The optical and geometrical parameters of the host medium are as follows: $L=H=10$ mm, $\sigma=1$ mm^{-1}, $\kappa=0.01$ mm^{-1}, and $n_s=1.4$ (Fig. 1). The ultra-short laser beam is incident on the bottom wall at the position ($y=0$, $z=0$). The duration of the pulse is $t_p=1$ ps and the width of the laser beam is $d_c=0.1$ mm (Fig. 1). Initially, the intensity is zero; that is, no radiative transfer is present. Radiative transfer within the medium is triggered by the laser pulse incident on the medium at the bottom wall.

Various rectangular inhomogeneous zones with different dimensions are placed at different locations in the medium (Table 1). The optical properties of the inhomogeneous zones are chosen as $\sigma_1=1.2$ mm^{-1}, $\kappa_1=0.2$ mm^{-1}, and $n_{s1}=1.4$. The refractive indexes of the medium and inhomogeneous zone are chosen to be the same; therefore the light beam does not change direction after entering the inhomogeneous zone.

We group the inhomogeneties in Table 1 as follows: (i) *A*, *B*, *C*, and *D* are all located at the centerline of the enclosure but they

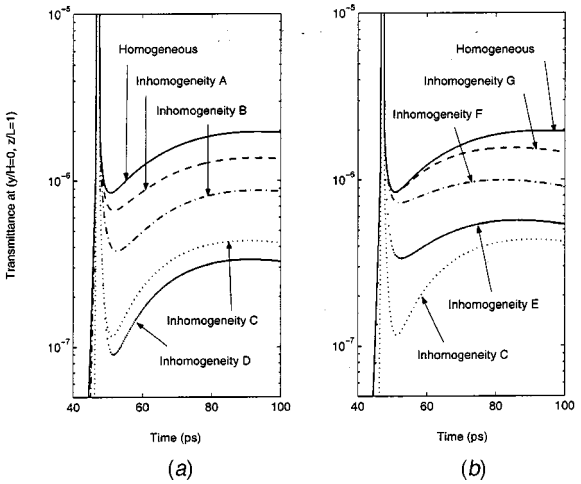

Fig. 2 Comparison of logarithmically varied temporal transmittance results of the homogeneous medium (σ=1 mm^{-1}, κ=0.01 mm^{-1}), (*a*) inhomogeneous media A, B, C, D and (*b*) inhomogeneous media C, E, F, G

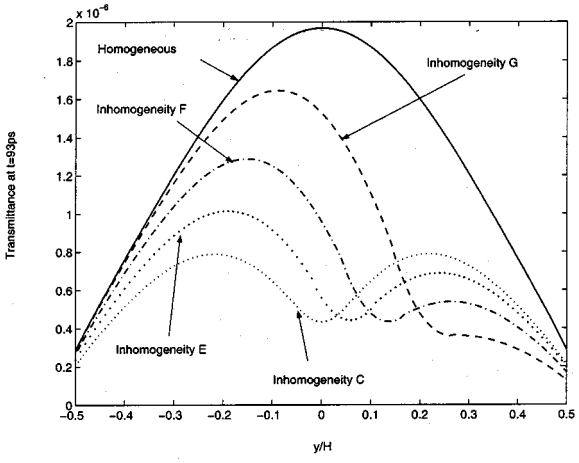

Fig. 4 Comparison of the transmittance distributions of homogeneous medium and inhomogeneous media C, E, F and G at time t=93 ps. Optical parameters of inhomogeneties are σ_1 =1 mm^{-1}, κ_1=0.01 mm^{-1}.

differ in size. (ii) *E*, *F*, and *G* have the same size as *C*; however, they are positioned away from the centerline. Temporal transmittance results at the center of the top wall for these two groups are compared with those of the homogeneous medium in Fig. 2. After the laser pulse completely passes through the top wall (after the sharp initial rise in the transmittance profiles), each inhomogeneity exhibits distinct profiles. For the first group of inhomogeneties, it is apparent from Fig. 2(*a*) that as the size of the inhomogeneous zones increases, the magnitude of the radiative heat fluxes leaving the top wall decreases, but the temporal profiles remain similar. However, for the second group, the profile is less affected as the inhomogeneity is placed farther away from the centerline. From these results, it is evident that a size change has a pronounced effect on the transmittance values. Overall, a size change size is more distinguishable than that of a location change of the inhomogeneity, in terms of the temporal transmittance results at the top wall.

The same observations are more apparent from the spatial transmittance distribution on the top wall (Figs. 3 and 4). These results are shown for time $t=93$ ps, which means that the collimated portion of the laser pulse has already passed through the top wall and the profiles seen in the figures are solely due to diffuse (scattered) intensities. The heat flux is at its maximum value at the center of the top wall since the largest concentration of the scattering occurs along the centerline where the initial, collimated laser pulse travels. When an obstacle is placed at centerline, a significant reduction in this value must occur. As the size of the zone increases, the spatial transmittance profile flattens and a dip is created. Placing the inhomogeneous zone at different locations within the medium also greatly alters the spatial transmittance profile (Fig. 4). As the inhomogeneity moves to the right (inhomogeneties *E*, *F*, *G*), spatial transmittance profiles slant to the left and the minimal point of the profiles shift to the right. These minimal points coincide with the centerlines of the inhomogeneties. It is also noteworthy that the path of laser does not go through any of the off-centered inhomogeneties (*E*, *F*, and *C*). Since the inhomogeneties considered here have higher scattering coefficients, they create a blocking effect by scattering of photons. As an inhomogeneity moves away from the laser beam, the blocking effect is reduced.

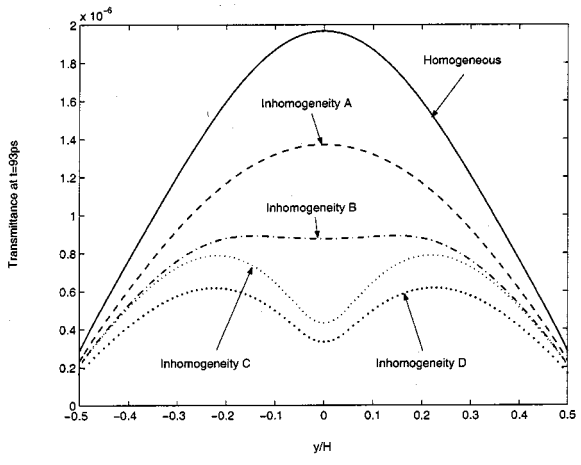

Fig. 3 Comparison of transmittance distributions over the top wall at time t=93 ps for inhomogeneties with different sizes (A,B,C,D). Optical parameters of inhomogeneties are σ_1 =1 mm^{-1}, κ_1=0.01 mm^{-1}.

Discussions and Conclusions

Formulation of the transient radiative transfer within a highly scattering medium with a laser beam impinging on one of the boundaries is given in the first section. To verify the accuracy of the method, the reflectance results for a homogeneous medium with the system parameters $L=H=10$ mm, $\sigma=0.997$ mm^{-1}, $\kappa=0.003$ mm^{-1}, $n_s=1.33$, $t_p=10$ ps, and $d_c=1$ mm are compared with those calculated by the Monte Carlo method [4]. The reflectance values at the center of the bottom wall display less than 1% deviation up to 10 ps. The difference in the results increases to 5% in the time interval 10 ps–40 ps, and again reduces to less than 1% after 40 ps. The heat balance within the same system is also calculated as a means of verifying the accuracy of the method. The heat gain to the system is only due to the incident laser beam. The heat losses from the medium consist of the heat losses through the boundaries and the absorbed energy by the medium (assuming that the absorbed energy is not reemitted to the medium). However, the contribution of the absorption to the heat loss is very small ($\kappa=0.003$ mm^{-1}) compared to the scattered intensity ($\sigma=0.997$ mm^{-1}) and can be neglected. The heat balance as the ratio of the heat loss over the heat gain is calculated as to be 0.998 after 200 ps.

The method is applied to a system with various inhomogeneties. The geometry and the locations of the inhomogeneties are altered, and temporal and spatial transmittance results at the top wall are plotted in Figs. 2–4. These results are compared both

with those of the homogeneous medium and with each other. As it can be seen from the figures, valuable information about the locations, shapes and optical properties of the inhomogeneous zones can be obtained from the transmittance profiles.

The current work shows that the wavelet method is applicable to transient radiation problems with inhomogeneous medium and produces fairly accurate results. The prospects of increasing its accuracy and stability should be investigated by reformulating it using different wavelet basis and higher-order numerical difference schemes in the spatial domain.

Nomenclature

$a_{m,n}$, $b_{m,n}$, $c_{m,n}$, $d_{m,n}$ = wavelet expansion coefficients
c = speed of light
$H(t)$ = Heaviside's unit function
H = width of two-dimensional enclosure
H_1 = width of inhomogeneous zone
I = radiative intensity
I_0 = intensity of laser
L = height of two-dimensional enclosure
n_s = refractive index
S = source function
t = time
W = wavelet functions
x, y, z = Cartesian coordinates

Greek Symbols

β = extinction coefficient
δ = Kronecker's δ function
ε = emissivity of surface
ϕ = azimuthal angle
κ = absorption coefficient
μ, ξ = angular parameters
θ = polar angle
ρ = reflectivity of surface
σ = scattering coefficient
τ = optical thickness
ω = single scattering albedo
Φ = scattering phase function
Ω = solid angle

Subscripts

1 = inhomogeneity
c = collimated
d = diffuse

Superscripts

$'$ = incoming directions

References

[1] Guo, Z., and Kumar, S., 2001, "Discrete-Ordinates Solution of Short-Pulsed Laser Transport in Two-Dimensional Turbid Media," Appl. Opt., **40**, pp. 3156–3163.
[2] Guven, O., and Bayazitoglu, Y., 2003, "The Radiative Transfer Solution of a Rectangular Enclosure Using Angular Domain Discrete Wavelets," Int. J. Heat Mass Transfer, **46**, pp. 687–694.
[3] Modest, M. F., 1993, *Radiative Heat Transfer*, McGraw-Hill, New York.
[4] Guo, Z., Kumar, S., and San, K. C., 2000, "Multidimensional Monte Carlo Simulation of Short-Pulse Laser Transport in Scattering Media," J. Thermophys. Heat Transfer, **14**, pp. 504–511.

The Thermal Constriction Resistance for an Eccentric Spot on a Circular Heat Flux Tube

A. Baïri
e-mail: abairi@u-paris10.fr

N. Laraqi
Department of Heat Transfer,
University of Paris 10, LEEE, EA. 387,
1, Chemin Desvallières, 92410 Ville d'Avray,
France

An analytical solution is proposed to calculate the thermal constriction resistance for an eccentric circular spot with uniform flux on a semi-infinite circular heat flux tube. This solution is developed using the finite cosine Fourier transform and the finite Hankel transform. It allows to calculate the stationary three-dimensional temperature distribution and the thermal constriction resistance. The results of proposed solution are in agreement with available theoretical and experimental studies. We show that the thermal constriction resistance for an eccentric contact is greater than the one of a centered contact (few tens percent), which is consistent with recent studies on random contacts. A simple correlation is also proposed to calculate the thermal constriction resistance as a function of the eccentricity and the relative contact size. [DOI: 10.1115/1.1778189]

Keywords: Conduction, Contact Resistance, Interface, Roughness, Tribology

1 Introduction

Thermal constriction is an important phenomenon which occurs at the interface of two solids due to surface defects (flatness, roughness of first, second order . . .). This phenomenon is modeled by a thermal constriction resistance R_c which is an intrinsic parameter. Several analytical solutions have been developed in the literature in order to calculate R_c according to contact shape and boundary conditions (e.g., Bardon [1], Cooper et al. [2], Yovanovich [3], Beck [4], Degiovanni et al. [5], Tio and Sadhal [6]).

The models proposed in the literature are generally based on idealized contact areas, where the asperities are assumed identical and regularly distributed over the contact plane. In practice, the real contact areas are different, and their distribution is random. Experimental studies based on the use of the electric analogy has been performed by Bardon [1] and Cooper [7] to examine the effect of the eccentricity of a unique contact on the evolution of the thermal constriction resistance. The authors have shown that the constriction resistance increases with the increase of the eccentricity. Theoretical studies have also carried out the analysis of the effect of random contacts on the evolution of thermal contact resistance [8,9].

In this paper, an analytical solution for an eccentric spot on the surface of a semi-infinite circular heat flux tube is presented. The cosine Fourier and finite Hankel transforms are used to solve the heat conduction equation for this configuration. The details of calculation, comparison with available experiments and a simple correlation are presented and discussed.

Contributed by the Heat Transfer Division for publication in the JOURNAL OF HEAT TRANSFER. Manuscript received by the Heat Transfer Division October 24, 2003; revision received May 14, 2004. Associate Editor: B. Farouk.

2 Problem Formulation

We consider a laterally insulated semi-infinite cylinder, with thermal conductivity k, radius b, and zero reference temperature (Fig. 1). The face, $z=0$, is subjected to a uniform circular heat source q, with radius a, for which the axes is at a distance e, from the center of cylinder. The remainer of this face is insulted. The heat conduction into the cylinder is three-dimensional, except for the case when $e=0$ (for which the problem becomes axisymmetric).

The governing equations of steady thermal regime can be written as follows:

Equation of Heat.

$$\nabla^2 T(r,\theta,z)=0 \tag{1}$$

Symmetry Conditions With Respect to θ-Direction.

$$\left(\frac{\partial T}{\partial \theta}\right)_{r,0,z}=0 \tag{2}$$

$$\left(\frac{\partial T}{\partial \theta}\right)_{r,\pi,z}=0 \tag{3}$$

Boundary Conditions With Respect to r-Direction.

$$(T)_{0,\theta,z} \text{ is finite} \tag{4}$$

$$\left(\frac{\partial T}{\partial r}\right)_{b,\theta,z}=0 \tag{5}$$

Boundary Conditions With Respect to z-Direction.

$$-k\left(\frac{\partial T}{\partial z}\right)_{r,\theta,0}=\begin{cases} q & \text{(at contact)} \\ 0 & \text{(elsewhere)} \end{cases} \tag{6}$$

$$T_{r,\theta,z\to\infty}=0 \tag{7}$$

3 The Solution

3.1 Temperature Distribution. Taking into account of the symmetry with respect to θ-direction, we first apply the cosine Fourier transform to Eqs. (1) to (7) as

$$\tilde{T}=\frac{1}{\pi}\int_0^{\pi} T\cos(m\theta)\,d\theta \tag{8}$$

Then, Eqs. (1) to (7) become

$$\frac{\partial^2 \tilde{T}}{\partial z^2}+\frac{1}{r}\frac{\partial}{\partial r}\left(r\frac{\partial \tilde{T}}{\partial r}\right)-m^2\tilde{T}=0 \tag{9}$$

$$(\tilde{T})_{0,z} \text{ is finite} \tag{10}$$

$$\left(\frac{\partial \tilde{T}}{\partial r}\right)_{b,z}=0 \tag{11}$$

$$-k\left(\frac{\partial \tilde{T}}{\partial z}\right)_{r,0}=\begin{cases} \tilde{q} & \text{(at contact)} \\ 0 & \text{(elsewhere)} \end{cases} \tag{12}$$

$$\tilde{T}_{r,z\to\infty}=0 \tag{13}$$

As a second step, we apply to Eqs. (9) to (13) the finite Hankel transform with respect to r-direction as

$$\tilde{\tilde{T}}=\int_0^b r\tilde{T}J_m(\beta_n r)\,dr \tag{14}$$

where J_m is the Bessel function of first kind of order m, and β_n are the roots of the following transcendental equation

$$J'_m(\beta_n b)=0 \tag{15}$$

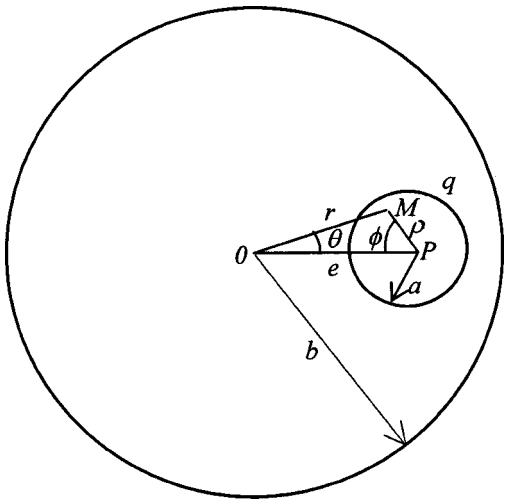

Fig. 1 An eccentric spot on circular heat flux tube

Then, Eqs. (9) to (13) become

$$\frac{d^2\tilde{\tilde{T}}}{dz^2}-\beta_n^2\tilde{\tilde{T}}=0 \tag{16}$$

$$-k\left(\frac{d\tilde{\tilde{T}}}{dz}\right)_{z=0}=\tilde{\tilde{q}} \tag{17}$$

$$\tilde{\tilde{T}}_{z\to\infty}=0 \tag{18}$$

The solution of the transformed temperature $\tilde{\tilde{T}}$ can be written as

$$\tilde{\tilde{T}}=\frac{\tilde{\tilde{q}}\exp(-\beta_n z)}{k\beta_n} \tag{19}$$

In order to determine $\tilde{\tilde{q}}$ we apply the above integral transforms (8) and (14) to the eccentric contact region as

$$\tilde{\tilde{q}}=q\int\int_{(A_c)}\cos(m\theta)rJ_m(\beta_n r)dr\,d\theta \tag{20}$$

where A_c is the contact area, with $A_c=\pi a^2$. The double integral (20) is difficult to solve because the limits of integration with respect to r-direction and θ-direction are dependent. In order to perform these integrations we apply a coordinates transformation. For that, we consider the scheme of Fig. 1 and the triangle $(0MP)$ for which we can write the relationship

$$r^2=e^2+\rho^2-2e\rho\cos(\phi) \tag{21}$$

The terms $J_m(\beta_n r)\cos(m\xi)$ in Eq. (20) can be expressed in the referential (ρ,ϕ) by using the following relationship [[10], p. 363]

$$J_m(\beta_n r)\cos(m\xi)=\sum_{k=-\infty}^{\infty}J_k(\beta_n\rho)J_{k+m}(\beta_n e)\cos(k\phi) \tag{22}$$

The double integration in this referential is easy to calculate and allows to write $\tilde{\tilde{q}}$ in the following form:

$$\tilde{\tilde{q}}=q\sum_{k=-\infty}^{\infty}\left[\int_{\phi=0}^{2\pi}\cos(k\phi)d\phi\int_{\rho=0}^{a}\rho J_k(\beta_n\rho)J_{k+m}(\beta_n e)d\rho\right] \tag{23}$$

where

$$\int_{\phi=0}^{2\pi}\cos(k\phi)d\phi=\begin{cases}2\pi & (k=0)\\ 0 & (k\neq 0)\end{cases} \tag{24}$$

Only the case when $(k=0)$ in the term in $\cos(k\phi)$ has non zero integral. Then, Eq. (23) becomes

$$\tilde{\tilde{q}}=qJ_m(\beta_n e)\int_{\rho=0}^{a}\rho J_0(\beta_n\rho)d\rho \tag{25}$$

Let

$$\tilde{\tilde{q}}=qa\,\frac{J_1(\beta_n a)J_m(\beta_n e)}{\beta_n} \tag{26}$$

To determine the temperature, we apply the inverse transforms as

$$\tilde{T}=2\sum_{n=0}^{\infty}\frac{\beta_n^2 J_m(\beta_n r)}{[(\beta_n b)^2-m^2]J_m^2(\beta_n b)}\tilde{\tilde{T}} \tag{27}$$

for the finite Hankel transform, and

$$T=\sum_{m=0}^{\infty}\epsilon_m\cos(m\theta)\tilde{T}\begin{cases}\epsilon_m=1:m=0\\ \epsilon_m=2:m\neq 0\end{cases} \tag{28}$$

for the finite cosine Fourier transform.

The temperature T, can be written as follows:

$$T=\frac{2qa}{k}\left\{\sum_{n=1}^{\infty}\frac{J_0(\beta_n r)J_1(\beta_n a)J_0(\beta_n e)e^{-\beta_n z}}{(\beta_n b)^2J_0^2(\beta_n b)}+2\sum_{m=1}^{\infty}\sum_{n=1}^{\infty}\frac{J_m(\beta_n r)J_1(\beta_n a)J_m(\beta_n e)\cos(m\theta)e^{-\beta_n z}}{[(\beta_n b)^2-m^2]J_m^2(\beta_n b)}\right\} \tag{29}$$

3.2 Thermal Constriction Resistance. The thermal constriction resistance due to a spot is defined as

$$R_c=\frac{\Delta T_c}{q\pi a^2}=\frac{T_c-T_a}{q\pi a^2} \tag{30}$$

where T_c and T_a are the average temperatures of the real contact area and the apparent contact area respectively. Here, $T_a=0$ (because $T_{z\to\infty}=0$). The expression of T_c is obtained by integration of Eq. (29) over the spot area as follows:

$$T_c=\frac{4qb}{\pi k}\left\{\sum_{n=1}^{\infty}\frac{J_1^2(\beta_n a)J_0^2(\beta_n e)}{(\beta_n b)^3J_0^2(\beta_n b)}+2\sum_{m=1}^{\infty}\sum_{n=1}^{\infty}\frac{J_1^2(\beta_n a)J_m^2(\beta_n e)}{(\beta_n b)[(\beta_n b)^2-m^2]J_m^2(\beta_n b)}\right\} \tag{31}$$

Then, the thermal constriction resistance can be written as

$$R_c=\frac{4b}{\pi^2 ka^2}\left\{\sum_{n=1}^{\infty}\frac{J_1^2(\beta_n a)J_0^2(\beta_n e)}{(\beta_n b)^3J_0^2(\beta_n b)}+2\sum_{m=1}^{\infty}\sum_{n=1}^{\infty}\frac{\epsilon_m J_1^2(\beta_n a)J_m^2(\beta_n e)}{(\beta_n b)[(\beta_n b)^2-m^2]J_m^2(\beta_n b)}\right\} \tag{32}$$

4 Results and Discussion

4.1 The Particular Case $(e=0)$. To validate this model, we consider the particular case of a unique circular contact, with radius a, centered on a circular flux tube [3–6], with radius b, and receiving a uniform heat flux q. For this configuration, we have $(e=0)$ and $J_m(\beta_n e)=0$ in Eq. (32) except the particular value $(m=0)$ for which $J_0(\beta_n e)=1$. Using the dimensionless expression of the thermal constriction resistance, $\psi=R_c k\sqrt{A_c}$ (with $A_c=\pi a^2$) we deduce ψ as follows:

$$\psi_0=\psi(e=0)=\frac{4b}{\sqrt{\pi}a}\sum_{n=1}^{\infty}\frac{J_1^2(\beta_n a)}{(\beta_n b)^3J_0^2(\beta_n b)} \tag{33}$$

Table 1 Number of terms for the convergence of series in Eq. (32)

ε	0.02	0.05	0.1	0.3	0.5	0.7	0.9
single summation	200	180	100	50	40	30	20
double summation	2000	1600	600	200	100	80	50

This expression is consistent with that predicted by the authors of references [3–6].

4.2 Comparison With Available Experimental Results The second validation of the proposed solution is about the comparison with experimental works [1,7]. The authors have studied the evolution of the constriction resistance by electrical analogy for a unique contact with circular shape (radius a) on a circular flux tube (radius b) varying the ecentricity e and the relative contact size $\varepsilon = a/b$. To perform the calculation of R_c from Eq. (32) the upper limits of series summation are adjusted as a function of ε value (see Table 1). Figure 2 shows a comparison between the present model and Bardon [1] and Cooper [7] experiments, for several values of ε. The results are in agreement. They show that the constriction resistance increases with the increase in the eccentricity of the spot and that this effect is more pronouced when the ε value is high. The increase of the constriction resistance with the increase of the eccentricity is very small for the small eccentricity (lower to 10 percent until $e/b \approx 70$ percent) and becomes important beyond this threshold. This phenomenon is due to the edge effect that becomes more pronounced when the spot approaches the contour of flux tube. Otherwise, the maximum relative difference between an eccentred and a centred contact varies from 35 percent to 58 percent when ε varies from 0.05 to 0.9. This result is consistent with recent works for random contacts [8,9].

5 Proposed Correlation

The use of solution (32) requires the determination of roots of the transcendental equation (15) and the convergence of double series. In order to facilitate the calculation of the thermal constriction resistance due to an eccentric spot, we propose a simple correlation. To perform this correlation we first establish a correlation given the maximum value of constriction resistance, denoted $\psi_{\max}$, which corresponds to the maximum eccentricity, i.e., $e^*_{\max} = 1-\varepsilon$, as a function of ε and ψ_0. This correlation can be written as

$$\psi_{\max} = \psi(e^*_{\max}) = 1.5816\varepsilon^{0.0528}\psi_0 \tag{34}$$

with an accuracy greater than 98.98% for ε between 0.05 and 0.9.

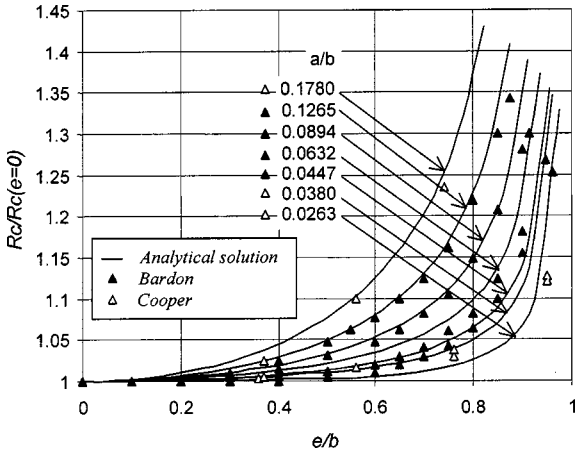

Fig. 2 Comparison between the proposed model and Bardon [1] and Cooper [7] experiments

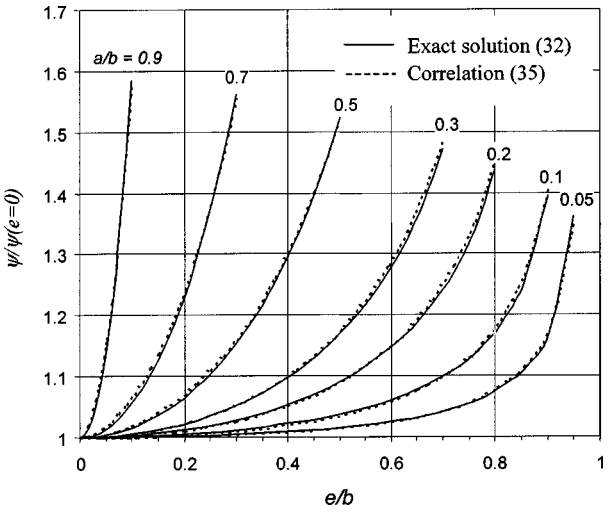

Fig. 3 Comparison between the exact solution (32) and correlation (35)

The constriction resistance varies between $\psi_0 = \psi(e^* = 0)$, which is the minimum value of ψ, and $\psi_{\max}$, which is the maximum value of ψ. We propose the following dimensionless correlation to calculate ψ as a function of ε and e:

$$\psi^* = \frac{\psi}{\psi_0} = 1 + [1.5816(a/b)^{0.0528} - 1]\left(\frac{e}{b-a}\right)^{1.76}\left(\frac{a}{b-e}\right)^{0.88} \tag{35}$$

where ψ_0 is given by the following correlation [11]:

$$\psi_0 = 0.47890 - 0.62076(a/b) + 0.114412(a/b)^3 + 0.01924(a/b)^5 + 0.00776(a/b)^7 \tag{36}$$

Figure 3 compares the evolutions of ψ/ψ_0 between the exact solution (32) and the proposed correlation (35) as a function of the dimensionless eccentricity e^* for several values of the relative contact size ε. The range of ε is between 0.05 and 0.9. For the all plotted points, the relative difference is between -2 percent and 4 percent.

6 Conclusions

In this paper, an exact analytical solution was developed in order to calculate the thermal constriction resistance R_c for an eccentric contact on a circular heat flux tube. The evolution of R_c is given as a function of two parameters: (*i*) the relative contact size ε and (*ii*) the eccentricity of spot e. It is shown that R_c increases with the increase in the eccentricity and this effect is more pronounced when the ε value is high. The relative difference is between 35 percent (for $\varepsilon = 0.05$) and 58 percent (for $\varepsilon = 0.9$). These values are consitents with that obtained for random contacts. The theoretical results are in agreement with available experimental studies. Taking into account the difficulty to determine the eigenvalues of the transcendental equation and to ensure the convergence of series we have performed a simple correlation, which is accurate for a large range of ε values.

Nomenclature

a = radius of contact
A = area
b = radius of heat flux tube
e = eccentricity of contact
k = thermal conductivity
q = heat flux density
r, θ, z = polar coordinates
R_c = thermal constriction resistance

T = temperature

Greek Symbols

ε = relative contact size, $=a/b$

ψ = dimensionless constriction resistance, $=R_c k\sqrt{\pi a^2}$

Subscript

0 = for zero eccentricity ($e=0$)

a = apparent contact

c = real contact or constriction

max = maximum

Superscript

$*$ = dimensionless quantity

References

[1] Bardon, J. P., 1965, ''Contribution to the Study of Thermal Contact Resistance,'' (in French), thesis, University of Poitiers, France.

[2] Cooper, M. G., Mikic, B. B., and Yovanovich, M. M., 1969, ''Thermal Contact Conductance,'' Int. J. Heat Mass Transfer, **17**, pp. 205–214.

[3] Yovanovich, M. M., 1976, ''General Expression for Circular Constriction Resistances for Arbitrary Flux Distribution,'' AIAA 13th Aerospace Sciences Meeting, Pasadena, California, pp. 381–396.

[4] Beck, J. V., 1979, ''Effects of Multiple Sources in the Contact Conductance Theory,'' ASME J. Heat Transfer, **101**, pp. 132–136.

[5] Degiovanni, A., and Moyne, C., 1989, ''Thermal Contact Resistance in Steady Regime. Influence of Contact Shape,'' (in French), Revue Générale de Thermique Fr., **334**, pp. 557–563.

[6] Tio, K. K., and Sadhal, S. S., 1992, ''Thermal Constriction Resistance: Effects of Boundary Conditions and Contact Geometries,'' Int. J. Heat Mass Transfer, **35**(6), pp. 1533–1544.

[7] Cooper, M. G., 1969, ''A Note on Electrolytic Analogue Experiments for Thermal Contact Resistance,'' Int. J. Heat Mass Transfer, **12**, pp. 1715–1718.

[8] Das, A. K., and Sadhal, S. S., 1999, ''Thermal Constriction Resistance Between Two Solids for Random Distribution of Contacts,'' Heat Mass Transfer, **35**, pp. 101–111.

[9] Laraqi, N., and Baïri, A., 2002, ''Theory of Thermal Resistance at the Interface of Solids With Randomly Sized and Located Contacts,'' Int. J. Heat Mass Transfer, **45**(20), pp. 4175–4180.

[10] Abramowitz, M., and Stegun, I. A., 1964, *Handbook of Mathematical Functions*, Dover Publications.

[11] Negus, K. J., Yovanovich, M. M., and Beck, J. V., 1989, ''On the Nondimensionalization of Constriction Resistance for Semi-Infinite Heat Flux Tubes,'' ASME J. Heat Transfer, **111**, pp. 804–807.

Entropy Generation Minimization of Fully Developed Internal Flow With Constant Heat Flux

Eric B. Ratts
University of Michigan, Dearborn, Dept. Mechanical Engineering, 4901 Evergreen Road, Dearborn, MI 48128-1491

Atul G. Raut
University of Michigan, Dearborn, Dept. Mechanical Engineering, 4901 Evergreen Road, Dearborn, MI 48128-1491

This paper uses the entropy generation minimization (EGM) method to optimize a single-phase, convective, fully developed flow with uniform and constant heat flux. For fixed mass flow rate and fixed total heat transfer rate, and the assumption of uniform and constant heat flux, an optimal Reynolds number for laminar and turbulent flow is obtained. The study also compares optimal Reynolds number and minimum entropy generation for cross sections: square, equilateral triangle, and rectangle with aspect ratios of two and eight. The rectangle with aspect ratio of eight had the smallest optimal Reynolds number, the smallest entropy generation number, and the smallest flow length. [DOI: 10.1115/1.1777585]

Introduction

This paper presents the thermodynamic optimum for fully developed internal convective flow, i.e., flow through a tube with constant and uniform heat flux. The optimum is obtained by minimizing the sum of viscous momentum transfer losses and heat transfer losses. The viscous momentum transfer losses are due to fluid friction between the wall and the fluid and within the fluid. Heat transfer losses are due to heat transfer across finite temperature differences between the wall and the fluid. The losses must be quantified in equal units in order to compare them and to minimize the sum of losses. One method of comparing losses is based on the second law of thermodynamics, entropy generation minimization (EGM).

Bejan [1–6] presents analyses of a tube flow using EGM. He has found thermodynamic optimums of the ratio of film coefficient to pumping power and the dimensionless temperature difference with constant mass flow rate and heat transfer rate per unit length. Note constant heat transfer rate per unit length is different from uniform and constant heat flux. Reference [5] presents laminar and turbulent flow through a tube with circular cross-section. Entropy generation rate per unit length was minimized at a fixed heat transfer rate per unit length and mass flow rate, and the optimal Reynolds number (optimal tube diameter) was obtained. For laminar flow, the optimal Reynolds number is zero. For turbulent flow, the optimal Reynolds number is a function of Prandtl number and duty parameter. The duty parameter is a function of fluid properties, heat transfer rate per unit length, and mass flow rate.

Sahin [7–9] investigated laminar and turbulent flow through a tube with uniform and constant heat flux. He investigated the effect of temperature-dependent viscosity on the entropy generation rate as well as the ratio of pumping power to heat transfer [7,8]. He presented the optimum cross-section shape for laminar flow and constant heat flux while comparing ducts of the same cross-sectional area and length [9]. He determined that the circular cross-section was superior and the equilateral triangular and rectangular cross-sections were inferior.

Nag and Mukherjee [10] investigated the tradeoff losses within a heat exchanger's fluid passage minimizing entropy generation rate for fixed wall temperature and mass flow rate. They obtained the optimal wall-fluid temperature difference and the optimal ratio of film coefficient to pumping power. Sahin [11] also investigated the entropy generation at fixed wall temperature. He presented particularly the effect of temperature-dependent viscosity on entropy generation and pumping power.

The rationale for this study is to complement the work by others in regards to convective flow through a tube. This paper is different by considering a different boundary condition, uniform and constant heat flux without fixing the duct geometry. This paper describes the optimal passage geometry (cross-section shape, tube length, and tube hydraulic diameter) for fully-developed laminar and turbulent flows with fixed total heat transfer rate, fixed mass flow rate, and uniform and constant heat flux. Also the paper presents the solution's dependence on the heat transfer and friction factor correlations.

Model Development

Figure 1 is a description of single-phase, steady, and fully developed flow through a tube subjected to heat transfer as well as wall shear forces. A small differential section of the flow is shown, where its properties change across dx due to the interactions. Bejan [6] developed the entropy generation equation per unit length of tube.

$$\dot{S}'_{\text{gen}}=\frac{\dot{q}''\mathscr{P}(T_w-T)}{T^2}+\frac{\dot{m}^3 f}{2\rho T D_h A_c^2} \tag{1}$$

where $\dot{q}''$, $\mathscr{P}$, T_w, T, $\dot{m}$, f, ρ, D_h, and A_c are the heat flux, tube perimeter, wall temperature, bulk fluid temperature, mass flow rate, Darcy friction factor, fluid density, hydraulic diameter, and cross-sectional area, respectively.

Ratts and Atul [12] integrated the equation over the tube length L. They assumed that fluid properties were constant. Their result was

$$\dot{S}_{\text{gen}}\cong\frac{(\dot{q}'')^2\mathscr{P}D_h L}{\text{Nu}\cdot k T_1 T_2}+\frac{8\dot{m}^3 f L}{\rho^2 T_{\text{ave}} D_h^3 \mathscr{P}^2} \tag{2}$$

where Nu is the Nusselt number, k is the thermal conductivity, T_1 and T_2 are the inlet and outlet fluid temperatures, and

$$T_{\text{ave}}\equiv\frac{(T_1-T_2)}{\ln(T_1/T_2)} \tag{3}$$

Integration was based on the boundary condition of uniform and constant heat flux. The first term on the right hand side of Eq. (2) is the entropy generation rate due to heat transfer dissipation and the second term is the entropy generation rate due to viscous dissipation.

The entropy generation rate in it its final form is

$$N_S=N_{S,\Delta T}\left(1+\frac{1}{\phi}\text{Re}^{7-\gamma+\alpha}\,\text{Pr}^{\beta}\right) \tag{4}$$

where the variables are: the entropy generation number

$$N_S\equiv\frac{\dot{S}_{\text{gen}}}{\dot{Q}/T_{\text{ave}}} \tag{5}$$

the entropy generation due to heat transfer dissipation

$$N_{S,\Delta T}=\frac{4}{\chi C_h}\left[\frac{\dot{q}''\dot{m}}{\mu k T_m}\right]\text{Re}^{\alpha+1}\,\text{Pr}^{-\beta} \tag{6}$$

Contributed by the Heat Transfer Division for publication in the JOURNAL OF HEAT TRANSFER. Manuscript received by the Heat Transfer Division October 9, 2003; revision received January 16, 2004. Associate Editor: K. S. Ball.

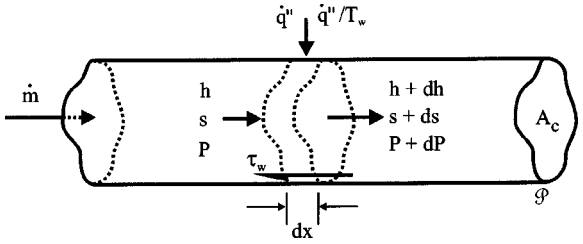

Fig. 1 Fully developed internal flow

the mean fluid temperature

$$T_m \equiv \frac{T_1 T_2}{T_{\text{ave}}} \tag{7}$$

the ratio of cross-section perimeter to hydraulic diameter (a constant for a given cross-section shape and referred to as the shape ratio)

$$\chi = \frac{\mathcal{P}}{D_h} \tag{8}$$

and

$$\phi = \left[\frac{(4)^7}{8\chi^4 C_h C_f}\right]\left[\frac{\dot{q}''\rho\dot{m}^2}{\mu^{3.5}\sqrt{kT_m}}\right]^2 \tag{9}$$

The second term in brackets in Eq. (9) is the design criteria and is referred to as the duty parameter [5]. The constants C_h, C_f, and exponents α, β, and γ are from the Nusselt correlation

$$\text{Nu} = C_h \,\text{Re}^{\alpha}\,\text{Pr}^{\beta} \tag{10}$$

and the friction factor correlation

$$f = C_f \,\text{Re}^{-\gamma} \tag{11}$$

There is an optimal Reynolds number that minimizes the entropy generation. The minimum is found by taking the derivative of Eq. (4) with respect to Reynolds number, setting the derivative equal to zero, and solving for the Reynolds number. The optimal Reynolds number is

$$\text{Re}_{\text{opt}} = \left[\phi\left(\frac{\alpha+1}{6-\gamma}\right)\text{Pr}^{-\beta}\right]^{1/(7-\gamma+\alpha)} \tag{12}$$

Note the optimal Reynolds number scales inversely to the shape ratio, the heat transfer correlation coefficient, and the friction factor correlation coefficient. Substituting the optimal Reynolds number into Eq. (4) results in the minimum entropy generation number.

$$N_{S,\min} = \frac{4}{\chi C_h}\left[\frac{\dot{q}''\dot{m}}{\mu k T_m}\right]\left[1+\frac{(\alpha+1)}{(6-\gamma)}\right]\text{Re}_{\text{opt}}^{-(\alpha+1)}\,\text{Pr}^{-\beta} \tag{13}$$

The ratio of Eq. (4) to Eq. (11) is

$$\frac{N_S}{N_{S,\min}} = \left(\frac{6-\gamma}{7-\gamma+\alpha}\right)\left(\frac{\text{Re}}{\text{Re}_{\text{opt}}}\right)^{-(\alpha+1)} + \left(\frac{\alpha+1}{7-\gamma+\alpha}\right)\left(\frac{\text{Re}}{\text{Re}_{\text{opt}}}\right)^{6-\gamma} \tag{14}$$

Note that this equation is independent of the Prandtl exponent, and therefore the solution is the same for heating and cooling.

Circular Cross-Section Tubes

The model was applied to a circular cross-section tube. For laminar flow, the heat transfer and friction factor correlations are given in Table 1. The constants for Eq. (10) are $C_h = 4.36$ and $\alpha = \beta = 0$. The constants for Eq. (11) are $C_f = 64$ and $\gamma = 1$. Substituting the constants into Eq. (12) provides the optimal Reynolds number as a function of the duty parameter. Figure 2 presents Eq. (12) for laminar flow. As the duty parameter increases, the optimal Reynolds number increases. Substituting the constants into Eq. (14) results in the entropy number ratio as a function of the Reynolds number ratio. Figure 3 presents Eq. (14) for laminar flow.

Table 1 Different Cross Section Tubes

Cross section	Diagram	Perimeter	Area	Hydraulic Diameter	Nu†	fRe†
Circular	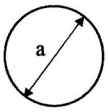	πa	$\frac{\pi a^2}{4}$	a	4.36	64
Square	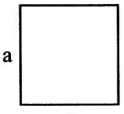	$4a$	a^2	a	3.61	57
Rectangle	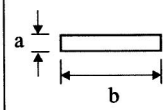	$2a\left(1+\frac{b}{a}\right)$	$a^2\left(\frac{b}{a}\right)$	$\frac{2a}{\left(\frac{a}{b}+1\right)}$	$b/a=2$: 4.12 $b/a=8$: 6.49	$b/a=2$: 62 $b/a=8$: 82
Equilateral Triangle	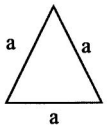	$3a$	$\frac{\sqrt{3}}{4}a^2$	$\frac{\sqrt{3}}{3}a$	3.11	53

†Cengel [13]

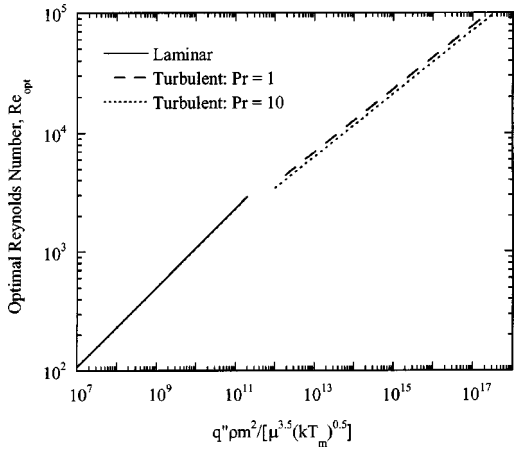

Fig. 2 Optimal Reynolds number for circular cross-section

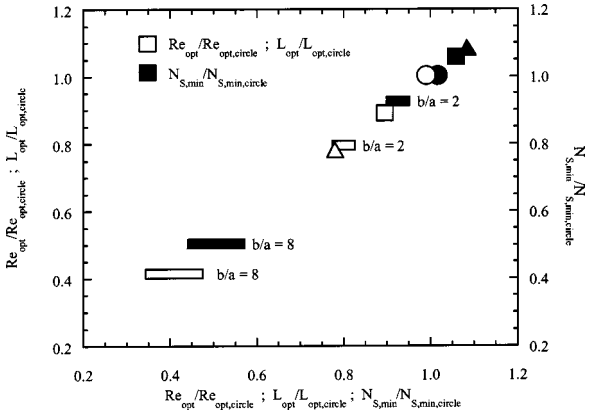

Fig. 4 Optimal solutions for laminar flow

For an incremental change in the Reynolds number from the optimal condition, more entropy is generated in the direction of viscous dissipation than heat transfer dissipation.

For turbulent flow, the Dittus-Boelter equation [14] constants for Eq. (10) are $C_h=0.023$, $\alpha=4/5$, $\beta=0.4$ (heating) and 0.3 (cooling). The constants [14] for Eq. (11) are $C_f=0.316$ and $\gamma=1/4$ for $\mathrm{Re}_D<2\times10^4$, and $C_f=0.184$ and $\gamma=1/5$ for $2\times10^4<\mathrm{Re}_D<3\times10^5$. Substituting the constants into Eq. (12) provides the optimal Reynolds number for turbulent flow and is presented in Fig. 2 (dashed lines). The optimum is plotted for two Prandtl numbers. As the Prandtl number increases, the optimal Reynolds number decreases. Equation (14) for turbulent flow is plotted in Fig. 3. Note that the turbulent solution is more symmetric around the optimum in comparison to the laminar solution. With an incremental change in Reynolds number from the optimal condition, the increase in heat transfer loss is closer in value to the increase in viscous loss. Both the heat dissipation and viscous dissipation losses are larger than for the laminar case. In addition the solution by Bejan [6] is also plotted for comparison.

Noncircular Cross-Section Tubes

The model is applicable to noncircular cross-section tubes. Table 1 presents the different cross-sections to be considered. The table provides the geometric parameters: perimeter, cross-sectional area, and hydraulic diameter. The noncircular solutions were compared to the circular solution. The optimal Reynolds number for the noncircular cross-sections with respect to the optimal Reynolds number for the circular cross-section is

$$\frac{\mathrm{Re}_{\mathrm{opt}}}{\mathrm{Re}_{\mathrm{opt,circle}}}=\left[\frac{(\chi^4 C_h C_f)_{\mathrm{circle}}}{(\chi^4 C_h C_f)}\right]^{1/(7-\gamma+\alpha)} \tag{15}$$

The minimum entropy generation for the noncircular cross-section with respect to the minimum entropy generation for the circular cross-section is

$$\frac{N_{S,\min}}{N_{S,\min,\mathrm{circle}}}=\frac{(\chi C_h)_{\mathrm{circle}}}{(\chi C_h)}\left[\frac{\mathrm{Re}_{\mathrm{opt,circle}}}{\mathrm{Re}_{\mathrm{opt}}}\right]^{\alpha+1} \tag{16}$$

The solution for Eq. (15) is shown in Fig. 4 for laminar flow. For the optimal Reynolds number, the shape order from highest to lowest is the circle, square (90 percent), rectangle ($b/a=2$) (80 percent), triangle (78 percent), and rectangle ($b/a=8$) (41 percent). The optimal Reynolds number is a strong function of the shape ratio, χ. The larger its value, the smaller the Reynolds number. Shapes with a larger value of χ can reduce the hydraulic diameter to increase heat transfer without excessive viscous dissipation losses.

The optimal Reynolds number fixes the tube diameter and it also fixes the tube length. It can be shown that the ratio of the noncircular tube length to the circular tube length is equal to the ratio of the Reynolds number of the noncircular tube to the Reynolds number of the circular tube. The optimal length ratio is plotted in Fig. 4. The rectangle ($b/a=8$) is the shortest and the circle is the longest.

For the minimum entropy generation, the shape order from most irreversible to least irreversible is the triangle (109 percent), square (105 percent), circle, rectangle ($b/a=2$) (93 percent), and rectangle ($b/a=8$) (51 percent). The triangle and square generate more entropy than the circle. Equation (16) is strongly dependent on the product of the heat transfer correlation coefficient and the shape ratio. All of the cross-sections accept for the rectangle ($b/a=2$) are ordered with respect to the value of the correlation coefficient. For higher values of the coefficient, less entropy is generated. The rectangle ($b/a=2$) has a high enough perimeter-to-diameter ratio to reduce the entropy generation below the circle.

The solution for Eq. (15) is shown in Fig. 5 for turbulent flow. For the optimal Reynolds number, the shape order from highest to lowest is the circle, square (88 percent), rectangle ($b/a=2$) (83 percent), triangle (77 percent), and rectangle ($b/a=8$) (54 percent). The optimal Reynolds number is solely a function of the shape ratio. The heat transfer and friction factor coefficients are the same for all cross-sections. The optimal length ratio is plotted in Fig. 5. The rectangle ($b/a=8$) is the shortest and the circle is the longest.

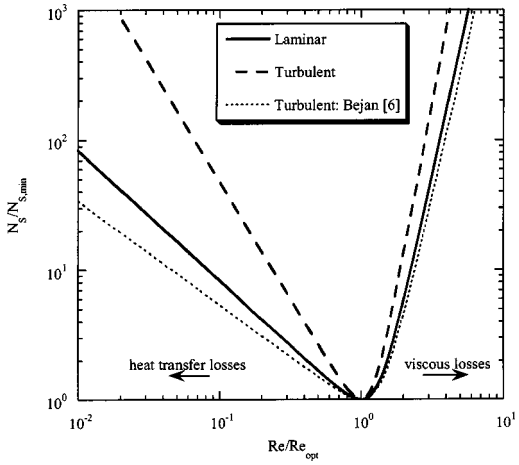

Fig. 3 Entropy generation for circular cross-section

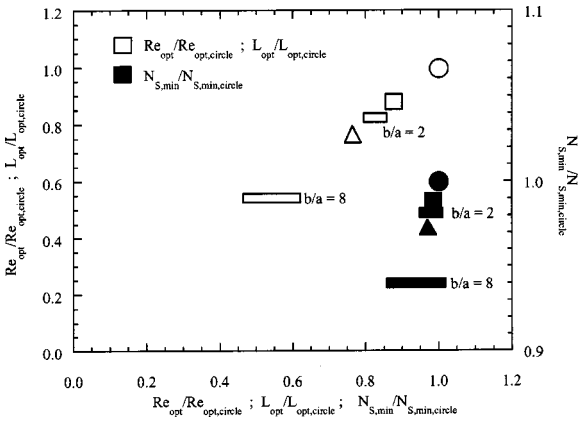

Fig. 5 Optimal solutions for turbulent flow

For the minimum entropy generation, the shape order from most irreversible to least irreversible is the circle, square (98.8 percent), rectangle ($b/a=2$) (98.3 percent), triangle (97.5 percent), and rectangle ($b/a=8$) (94.1 percent). The entropy ratio is only dependent on the shape ratio, but not as strong with respect to the optimal Reynolds number ratio.

Conclusions

The paper presented the optimal configuration for laminar and turbulent flow in a tube with a constant and uniform heat flux for a given total heat transfer rate and mass flow rate using the EGM method. Considering the heat transfer and viscous momentum transfer entropy generation, the total entropy generation was minimized providing the optimal Reynolds number, hydraulic diameter, and tube length. By the EGM method, the following conclusions were made:

- For fixed heat transfer rate and mass flow rate with a constant heat flux, there is an optimal Reynolds number for laminar and turbulent flow.
- For the same deviation from optimal Reynolds number in laminar flow, the increase in entropy generation is smaller for heat dissipation than for viscous dissipation. The same is true for turbulent flow, but not as pronounced.
- In turbulent flow, the optimal Reynolds number is larger for smaller Prandtl numbers.
- The optimal Reynolds number in laminar and turbulent flow scales inversely with the shape ratio. The shape order from highest to lowest is the circle, square, rectangle ($b/a=2$), triangle, and rectangle ($b/a=8$).
- The minimum entropy generation in laminar flow is strongly dependent on the inverse of the product of heat transfer correlation coefficient and shape ratio. The shape order from most irreversible to least irreversible is the triangle, square, circle, rectangle ($b/a=2$), and rectangle ($b/a=8$).
- The minimum entropy generation in turbulent flow is dependent solely on the inverse of the shape ratio. The shape order from most irreversible to least irreversible is the circle, square, rectangle ($b/a=2$), triangle, and rectangle ($b/a=8$).
- The optimal tube length scales with the optimal Reynolds number. The longest to shortest length is the same order as the optimal Reynolds number. For the cross-sections considered, the rectangle ($b/a=8$) is the shortest length and the circle is the longest length.

Nomenclature

A_c = cross-section area, m^2
D = diameter, m
D_h = hydraulic diameter, m
C_h = correlation coefficient
C_f = correlation coefficient
f = friction factor
h = enthalpy, $J\,kg^{-1}$
k = thermal conductivity, $W\,m^{-1}\,K^{-1}$
L = tube length, m
N_S = entropy generation number
$N_{S,\min}$ = entropy generation number
$N_{S,\Delta T}$ = entropy generation number
Nu = Nusselt number
$\dot{m}$ = mass flow rate, $kg\,s^{-1}$
p = perimeter, m
P = Pressure, $N\,m^{-2}$
Pr = Prandtl number
Re = Reynolds number
$\mathrm{Re}_{\mathrm{opt}}$ = Reynolds number, optimum
$\dot{q}''$ = heat transfer flux, $W\,m^{-2}$
s = entropy, $J\,kg^{-1}\,K^{-1}$
$\dot{S}'_{\mathrm{gen}}$ = entropy generation gradient, $W\,K^{-1}\,m^{-1}$
$\dot{S}_{\mathrm{gen}}$ = entropy generation rate, $W\,K^{-1}$
T = temperature, K
T_w = wall temperature, K
$\dot{Q}$ = heat transfer rate, W
x = coordinate, m
α = correlation exponent
β = correlation exponent
γ = correlation exponent
μ = dynamic viscosity, $N\,s\,m^{-2}$
ρ = density, $kg\,m^{-3}$
τ_w = wall shear stress, $N\,m^{-2}$
ϕ = Eq. (7)
χ = shape ratio: ratio of perimeter to hydraulic diameter

References

[1] Bejan, A., 1982, "Second-Law Analysis in Heat Transfer and Thermal Design," Adv. Heat Transfer, **15**, pp. 1–58.
[2] Bejan, A., 1982, *Entropy Generation Through Heat and Fluid Flow*, Wiley, New York.
[3] Bejan, A., 1980, "Second Law Analysis in Heat Transfer," Energy, **5**, pp. 721–732.
[4] Bejan, A., 1978, "General Criterion for Rating Heat-Exchanger Performance," Int. J. Heat Mass Transfer, **21**, pp. 655–658.
[5] Bejan, A., 1979, "A Study of Entropy Generation in Fundamental Convective Heat Transfer," ASME J. Heat Transfer, **101**(4), pp. 718–725.
[6] Bejan, A., 1988, *Advanced Engineering Thermodynamics*, Wiley, New York, pp. 594–598.
[7] Sahin, A. Z., 1996, "Thermodynamics of Laminar Viscous Flow Through a Duct Subjected to Constant Heat Flux," Energy, **21**(12), pp. 1179–1187.
[8] Sahin, A. Z., 2002, "Entropy Generation and Pumping Power in a Turbulent Fluid Flow Through a Smooth Pipe Subjected to Constant Heat Flux," Exergy-an International Journal, **2**, pp. 314–321.
[9] Sahin, A. Z., 1998, "Irreversibilities in Various Duct Geometries With Constant Wall Heat Flux and Laminar Flow," Energy, **23**(6), pp. 465–473.
[10] Nag, P. K., and Mukherjee, P., 1987, "Thermodynamic Optimization of Convective Heat Transfer Through a Duct With Constant Wall Temperature," Int. J. Heat Mass Transfer, **30**, pp. 401–405.
[11] Sahin, A. Z., 2000, "Entropy Generation in Turbulent Liquid Flow Through a Smooth Duct Subjected to Constant Wall Temperature," Int. J. Heat Mass Transfer, **43**, pp. 1469–1478.
[12] Ratts, E. B., and Raut, A., 2003, "Entropy Generation Minimization of Fully-Developed Internal Convective Flows With Constant Heat Flux," *Proceedings of 2003 ASME Summer Heat Transfer Conference*, ASME, New York.
[13] Cengel, Y. A., 2003, *Heat Transfer: A Practical Approach*, 2nd Ed., McGraw-Hill, New York, p. 437.
[14] Ozisik, M. N., 1985, *Heat Transfer: A Basic Approach*, 1st Ed., McGraw-Hill, New York.

Journal of Heat Transfer

Discussion

Discussion: "Self-Organization and Self-Similarity in Boiling Systems" [L. H. Chai and M. Shoji, ASME J. Heat Transfer, 124(3), pp. 507–515 (2002)]

E. Yantovski
Viktoriastr. 81, D-52066, Aachen, Germany

[DOI: 10.1115/1.1771713]

A general law, as formulated by the authors [1], should be accompanied by the necessary references [2–4]. The particular observations were quite different, namely, boiling bubbles formation in [1] and heat conduction in electronic packages in [2], whereas the formulation of the general law is almost identical, e.g.,

"There is no difference between living and not living systems when facing the competition for obtaining flux from environment. The stronger and more efficient subsystems can get more flux from environment and then survive...[1]."

"For a finite-size system to persist in time (to live), it must evolve in such a way that it provides easier access to the imposed (global) currents that flow through it [2]."

Figure 8 [1] is very similar to Fig. 6(b) [2].

All the selected examples in the section "Industrial Implications" of [1], rivers, cities, blood vessels, and Bénard flow system, coincide with [4], with the same division of flows by slow and fast and explanation of tree-like structures. In [1], references [15,16] are associated with Bénard flow only, attributing all the other findings to the authors [1].

I think the authors [1] would be thanked by the readership if they would confirm or reject the statements and pictures of [2–4], clearly indicating the difference of their approach. To ignore these references is incorrect.

References

[1] Chai, L. H., and Shoji, M., 2002 "Self-Organization and Self-Similarity in Boiling Systems," J. Heat Trans., **124**, pp. 507-515.
[2] Bejan, A. 1997, "Constructal Theory Network of Conducting Paths for Cooling a Heat Generating Volume," Int. J. Heat. Mass. Trans., **40**(4), pp. 799-816.
[3] Bejan, A. 1999, "How Nature Takes Shape: Extension of Constructal Theory to Ducts, Rivers, Turbulence, Cracks, Dendrite Crystals, and Special Economics," Int. J. Therm. Sci., **38**, pp. 653-663.
[4] Bejan, A., 2000, *Shape and Struture: From Engineering to Nature*, Cambridge University Press.

Allan D. Kraus
Beachwood, OH, 44122

The subject paper provides yet another interesting application of what has come to be known as constructal theory. However, the paper presents only an application and not a general theory. This is because, constructal theory or the maximum access principle deals with self organization in nature in general and the generation of architecture in flow systems in particular. Moreover, the authors cannot claim this theory as their own since the entire foundation for constructal theory has been laid down in at least seven papers or books by Bejan and his coworkers [1–7].

Indeed, the application of constructal theory to the boiling phenomenon was considered by Nelson and Bejan [4] on pp. 151–156 and by Nelson and Bejan [5]. In addition, Bejan [7] on pp. 169, 174, and 175 also comments on constructal theory with photographic applications.

There is a great deal of similarity between the subject paper and Bejan's work and I feel that Bejan and his coworkers should have had the benefit of an acknowledgment and a listing of their work in the bibliography.

References

[1] Bejan, A., 1996, "Street Network Theory of Organization in Nature," J. Adv. Transp., **30**, pp. 85–107.
[2] Bejan, A., 1997, *Advanced Engineering Thermodynamics*, 2ed, John Wiley and Sons, New York, NY.
[3] Bejan, A., 1997, "Constructal-Theory Network of Conducting Paths for Cooling a Heat Generating Volume," Int. J. Heat Mass Transfer, **40**, pp. 799–816.
[4] Nelson, Jr., R. A., and Bejan, A., 1998, "Self-Organization of the Internal Flow Geometry in Convective Heat Transfer," ASME HTD-Vol 356-3, pp. 149–161.
[5] Nelson, Jr., R. A., and Bejan, A., 1998, "Constructal Optimization of Internal Flow Geometry in Convection," ASME J. Heat Transfer, **120**, pp. 357–364.
[6] Bejan, A., and Tondeur, D., 1998, "Equipartition, Optimal Allocation, and the Constructal Approach to Predicting Optimization in Nature," Rev. Gen. Therm., **37**, pp. 165–180.
[7] Bejan, A., 2000, *Shape and Structure From Engineering to Nature*, Cambridge University Press, Cambridge, UK.

José Viriato Coelho Vargas
Universidade Federal do Parana, Departamento de Engenharia Mecânica, Setor de Tecnologia—Caixa Postal 19011, Curitiba, PR 81531-990, Brazil

Chai and Shoji [1] claim to themselves the credit for introducing a new theory of "self-organized growth processes from small to large caused by interactions among sub-systems", as they point out in the Concluding Remarks section of their paper. In the same section they also write: "In reality, the present investigation introduced new ideas of exploring the theories of complex systems. The present investigation not only provide clear physical picture, but also are based on firm theoretical foundation. The new theory of complex system presented here significantly wins the advantage over the traditional theory". Although the authors have cited

on the last page of their paper two references from Bejan [2,3], they did not state that the theory comes from Bejan, and that it is called constructal theory.

The authors deserve credit for using an existing theory for approaching a problem on boiling (not for the first time, since this has been done before by Nelson and Bejan [2,4], and Bejan [5]) and for developing their own mathematical understanding of it. This work is in fact a contribution to the spreading of the new theoretical concept introduced originally by Adrian Bejan. However, they should not have claimed that they are introducing a new theory.

References

[1] Chai, L. H., and Shoji, M., 2002, ''Self-Organization and Self-Similarity in Boiling Systems,'' ASME J. Heat Transfer, **124**(3), pp. 507–515.
[2] Nelson, Jr., A., and Bejan, A., 1998, ''Constructal Optimization of Internal Flow Geometry in Convection,'' ASME J. Heat Transfer, **120**(2), pp. 357–364.
[3] Bejan, A., 1997, *Advanced Engineering Thermodynamics*, Wiley, New York, Chap. 13.
[4] Nelson, Jr., A., and Bejan, A., 1998, ''Self-Organization of the Internal Flow Geometry in Convective Heat Transfer,'' ASME HTD, **357**(3), pp. 149–161.
[5] Bejan, A., 2000, *Shape and Structure, from Engineering to Nature*, Cambridge University Press, Cambridge, UK.

Gianfranco Guerreri

Dipartimento di Chimica Industriale e Ingegneria Chimica, Giulio Natta, Politecnico di Milano, Piazza Leonardo da Vinci 32, 20133 Milano, Italy

I refer to the article ''Self Organization and Self Similarity in Boiling Systems'' by L. H. Chai and M. Shoji published on Journal of Heat Transfer, June 2002, pp. 515–507.

Constructal theory is repeatedly discussed in many previous works by Adrian Bejan; take, for example, ''Constructal theory network of conducting paths for cooling a heat generating volume'' by A. Bejan, *Int. J. Heat Mass Transfer*, Vol. 40, No. 4, pp. 799–816, 1997. Chai and Shoji remind in the references of their article only one book of A. Bejan: ''Advanced Engineering Thermodynamics,'' Wiley, New York, 1997.

Tanmay Basak

Assistant Professor, Department of Chemical Engineering, Indian Institute of Technology, Madras, Chennai 600036, India. e-mail: tanmay@iitm.ac.in

Chai and Shoji [1] tried to analyze the boiling systems at a microscopic level. Their analysis on microscopic scale attempted to explain the boiling phenomena in presence of nonlinear effects such as nonuniform site characteristics, bubble generation, growth and coalescence, nonuniform temperature distribution near the heater surface and nonlinear interactions. They obtained the relationship between the heat flux ''J'' and instability parameter ''α'', but they failed to establish theoretically the evolution of tree structures (Figs. 5–8 [1]) in the second part of the article.

The evolution of self-similar tree structure was first derived by Bejan [2] based on a constructal theory, which was developed to explain optimal geometric configuration in natural systems. It is surprising to see that based on mere qualitative arguments, the current authors [1] simply obtained the tree structures (Figs. 5–8 [1]) which are exactly similar to the figures based on first, second, and third constructs as obtained by Bejan [2]. The following discussions highlight some critical issues on the article by Chai and Shoji [1].

Chai and Shoji [1] cannot claim that their statistical theory on open and nonequilibrium system is new. The paradigm on evolution of optimal geometric configurations was established by Bejan [2] based on macroscopic length scales. The principle that Chai and Shoji [1] invokes is a macroscopic law of flow access maximization which Bejan [2] defined as ''constructal law'' or the fourth law, a principle of global performance, global objective under finite space and time constraints. This is why the principle works, why it is new, why it is overlooked in physics even though it is known in Darwin's continuously changing biosphere model: there is a global tendency for macro flows to flow more easily if possible, i.e., if the flow geometry is malleable, changing, morphing.

In order to derive the statistical theory, the authors [1] stated an assumption: ''An open system far from equilibrium always seeks an optimization process so that the obtained flux J from outside is maximal under given prices or constraints''. This, I believe, is not an assumption, but rather a generic optimization concept if one looks into many transport processes occurring in any open and nonequilibrium system. Natural flow systems are classic examples for open systems. For example, several thousand honey bees form swarms in order to regulate the ''core'' or central temperature, which does not exceed 35°C irrespective of cold/hot ambient temperature [3,4]. Heinrich [3] investigated a series of swarms consisting of several thousand of bees which control the internal configuration and optimal shape of the swarm such that they have suitable environment to live. Basak et al. [4] proposed a mathematical model based on both thermal and biological sciences where the heat transport process was coupled with the rate of metabolism within a realistically shaped swarm and their predicted temperature profiles are in well agreement with Heinrich's [3] observations. At higher ambient temperature, the swarm consists of several vertical channel connected with each other like tree-branches which are in accord with constructal tree network as proposed by Bejan [2,5]. Historically, Bejan [2] proposed the ''constructal theory'' for devising an efficient cooling system based on optimal configuration for electronic packaging.

No matter whether the transport length scale is macro or micro, the natural phenomena based on constructal concept [2] is invariant. As seen in the swarm of bees which can be treated as dynamic system to persist in time (to live), it evolves in such a way that it provides easier access to the imposed (global) currents that flow through it. The fourth or ''constructal law'' brings life and time explicitly into thermodynamics and creates a new bridge between physics and biology.

Chai and Shoji [1] established the conditions for bifurcation phenomena and formation of new bubbles which denote new boiling modes. The nonideality due to interaction of bubbles was illustrated via probability distribution function using Gibbs statistical mechanics. Based on potential functions (Eqs. 20 and 23 [1]), the conditions for unstable modes during nonideal phase transition was derived. The presence of unstable mode corresponds to the formation of bubble or new boiling mode. During the phase transition, an expression of the change in flux is obtained as [1]

$$\overline{J}(\alpha_1)-\overline{J}(\alpha_2)\approx J_u(\alpha_1)-J_u(\alpha_2) \tag{1}$$

A few bubbles corresponding to unstable mode can destabilize and grow to visible bubbles while other bubbles remain damped. However, their mathematical theory [1] cannot explain the natural structures. In order to obtain the tree network, the bubbles are assumed to be rectangular as illustrated in Figs. 4–8 [1]. Although Fig. 4 [1] can be explained using symmetry of unstable modes in $m1$ subsystems, the two perpendicular subsections Ω_1 and Ω_2 in Fig. 5 [1] cannot be obtained from their mathematical theory [1]. The authors [1] use the flux relationship (Eq. 1) which cannot provide the topological dynamics on optimal system evolution and subsequent tree-branching. Their mathematical theory [1] even fails to answer the fundamental questions on evolution of natural tree structure: What is the optimal concept of the evolution of the first construct (Fig. 5 [1])? Why are the successive branches in the

tree network perpendicular? What will be the width of consecutive tree paths? (Figs. 5–8 [1])? How many constructal assemblies are optimally sufficient to maximize the flux (Eq. 1)?

The state-of-the art concept of ''constructal theory'' [2] answers all the above questions based on evolution of the bigger tree-network from a smallest tree, a basic construct. Bejan [2] established the tree network based on maximization of heat flux within highly conductive paths in a volumetric domain and these conductive paths form the tree where the geometric detail for each tree was derived theoretically. To develop a first construct, Bejan [2] mathematically established the ''rectangular bend'' in the first construct where the bend in the high conductivity path divides equally the maximum temperature difference thereby minimizing the maximum temperature within a body. In perspective, constructal theory [2] is a thermodynamically consistent approach which governs the dynamics on system topology via minimizing the resistance along the constructal paths and minimization of entropy generation. Evolution of subsequent ''tree-shaped self-similar structure'' is viewed as the response of natural system (living/nonliving) based on feed-back from physical principles (thermodynamic laws).

Unlike the ''constructal theory'' [2], the ''statistical theory'' [1] proposed by Chai and Shoji failed to prove the evolution on ''tree-network'' and ''self-similar structures'' during boiling and therefore discussions on Figs. 5–8 [1] should be disregarded. The originality of their work [2] is the ''statistical theory,'' neither the ''self-organization'' nor the ''self-similar structure'' and therefore, the article [1] cannot justify the ''title.''

Before concluding this discussion, I would like to focus on authors' ''concluding remarks'' [1] which are not mathematically established, and, hence, should be disregarded. In ''academic implications'' section on item 2 (pp. 513 [1]) the authors' comments: ''In other word, we mathematically demonstrated that the complex natural occurrence of self-similar structures is realized by fluctuations and continuous bifurcations'', should be ignored. In addition, the statement in item 3: ''In other word, the present theory brings the time into natural science and provides a bridge between physics or chemistry and biology'', completely lacks originality. This is neither established by the authors [1] nor is this a new theory proposed by them. As I mentioned earlier, Heinrich [3] and Basak et al. [4] already investigated the natural evolution on optimal geometric configurations and subsequently Bejan [2] established the foundation of the optimal natural evolution by ''constructal concept'' where dynamics (living/nonliving) are correlated with time. Similarly items 4 and 6 (academic implications, pp. 513 [1]) were already proposed by Bejan [2] and item 5 lacks any theoretical perception.

The unproven facts on ''self-similarity'' or ''self-organization'' in a microscopic scale by Chai and Shoji [1] are also highlighted in the section: ''industrial implication,'' which also lack originality (see Bejan [2]). Therefore items 1–4 (pp. 514 [1]) are merely repetitions of statements from Bejan [2]. Lastly, the generalized concluding remarks on ''formation of fractal structure and self-organization etc.'' should also be disregarded. Authors' philosophical comments on ''self-organization'' or ''self-similarity'' are not the theme of the article [1].

References

[1] Chai, L. H., and Shoji, M., 2002, ''Self-Organization and Self-Similarity in Boiling Systems,'' ASME J. Heat Transfer, **124**, pp. 507–515.
[2] Bejan, A., 1997, ''Constructal-Theory Network of Conducting Paths for Cooling a Heat Generating Volume,'' Int. J. Heat Mass Transfer, **40**, pp. 799–816.
[3] Heinrich, B., 1981, ''The Mechanism and Energetics of Honeybee Swarm Temperature Regulation,'' J. Exp. Biol., **91**, pp. 25–55.
[4] Basak, T., Rao, K. K., and Bejan, A., 1996, ''A Model for Heat Transfer in a Honey Bee Swarm,'' Chem. Eng. Sci., **51**, pp. 387–400.
[5] Bejan, A., 2000, ''From Heat Transfer Principles to Shape and Structure in Nature: Constructal Theory,'' ASME J. Heat Transfer, **122**, pp. 430–449.

Signe Kjelstrup
Department of Chemistry, Norwegian University of Science and Technology, Trondheim, Norway

Dick Bedeaux
Leiden Institute of Chemistry, Gorlaeus Laboratories, Leiden University, Leiden, The Netherlands

The article by Chai and Shoji [1] appears to claim an original non-equilibrium statistical theory for self-organized boiling. We question both their claims, and also whether the non-equilibrium statistical basis of the article is sound.

The authors are citing Bejan, but not the work that is central for their paper, namely his article of 1997 [2] or his book [3]. In the article of 1997, Bejan proposes as a new law of nature ''That a finite-size system, in order to persist, must evolve in such a way that it provides easier access to the imposed global currents that flow through it''. Bejan proves that a confined system chooses a tree-like network to channel the heat that is produced at a constant rate everywhere inside.

Chai and Shoji [1] take as premise for their work that ''an open system far from equilibrium always seeks an optimization process, so that the obtained flux from the outside is maximal under given constraints''. They say, as Bejan does, that ''the assumption may be considered as a kind of thermodynamic law''. They do not prove a resulting geometric structure, they deduce it by qualitative arguments. The main point we want to make is thus, that the authors should properly have pointed out that their basic assumption has been formulated by Bejan already.

The next issue is whether a nonequilibrium statistical thermodynamic basis has been given for self-organized boiling. Our answer is no. The state of the system is characterized by the forces x_i. Given these forces, one obtains a certain flux, J. But, according to the authors, the flux does not just depend on the forces, x_i, it depends also on the probability distribution of the forces $\rho(x_i)$. This is an assumption without physical justification. There is no reason why the flux shall, given all the forces, depend on the probability to have other values of the forces realized. Without this assumption, there is no foundation for Eq. 16, upon which all other results rest.

References

[1] Chai, L. H., and Shoji, M., 2002, ''Self-Organization and Self-Similarity in Boiling Systems,'' ASME J. Heat Transfer, **124**, pp. 507–515.
[2] Bejan, A., 1997, ''Constructal-Theory Network of Conducting Paths for Cooling a Heat Generating Volume,'' Int. J. Heat Mass Transfer, **40**, pp. 799–816.
[3] Bejan, A., 2000, *Shape and Structure, From Engineering to Nature*, Cambridge University Press, Cambridge, UK.

Jaime Cervantes de Gortari
UNAM Chair Distinguished Professor, National University of Mexico

In the section of the paper titled ''The Formation of Self-Similar Structures,'' the authors describe the essential aspects of Constructal Theory. However, Professor Adrian Bejan from Duke University has been working for a long time in putting together the ideas and the formalism of this theory—he actually gave it the appropriate name of ''Constructal'' [1], and has analyzed many examples in nature and engineering within the framework of this theory, extending it to a variety of situations, with his original contributions, most of them nicely described in his book [2].

After having reviewed the book written by Professor Bejan [3] and having closely followed his publications during the last decade, I found that the core analysis and synthesis methods of Constructal Theory are totally based on the author's own research experience during many years, previously published in specialized

journals and books, and supported by many observed facts and results, fully documented in the open literature. The Constructal Theory, established by Bejan, explains how certain basic elements, individually and collectively optimized to form an arrangement, are employed to construct more complex natural systems, within the specific constrains imposed by the physics in every case.

The paper by Chai and Shoji is full of ideas and expressions of Constructal Theory that were first contributed and published by Professor Bejan, especially the discussion about academic and industrial implications, in the ''Concluding Remarks.''

References

[1] Bejan, A., 1997, ''Constructal-Theory Network of Conducting Paths for Cooling a Heat Generating Volume,'' Int. J. Heat Mass Transfer, **40**(4), pp. 799–816.

[2] Bejan, A., 2000, *Shape and Structure, From Engineering to Nature*, Cambridge University Press, Cambridge.

[3] Cervantes-de Gortari, J., 2002, ''Shape and Structure, from Engineering to Nature,'' by A. Bejan, book review, Int. J. Heat Mass Transfer, **45**(7), p. 1583.

Closure to ''Discussion of 'Self-Organization and Self-Similarity in Boiling Systems' [ASME J. Heat Transfer, 124(3), pp. 507–515 (2002)]''

L. H. Chai[1] and M. Shoji[2]

In reference to discussions received on our paper, ''Self-Organization and Self-Similarity in Boiling Systems,'' published in the February issue of the *Journal of Heat Transfer* [1], here, we would like to summarize our responses to these comments as well as our own understanding of them so that some key differences can be understood more explicitly.

During the process of studying boiling heat transfer over the past few years, we discovered self-organized and cooperative or competitive phenomena among sites or bubbles in boiling systems [2,3]. Based on this discovery, we further developed and formulated the present analyses [1]. In whole, the paper [1] deals with self-organized and self-similar phenomena in boiling systems and other open dissipative systems, which are based mainly on statistical thermodynamics analyses, and, to our best knowledge, not Constructal Theory originated by Professor Bejan. With this in mind, there is no point to debate whether or not we have inexplicably misrepresented Constructal Theory as our own. Since the beginning of 1995, we have shown an interest in self-organization theory and nonlinear sciences theory [2]. However, many excellent literatures in this field [4–14], including Professor Bejan's textbook [15], played an important role on the primary ideas of this paper [1]. In fact, in August 2000, when we began to write our paper [1], we developed a good understanding of Professor Bejan's Constructal Theory. Surprisingly, we found that our final results and conclusions were in good agreement with results from Professor Bejan's Constructal Theory. Even though our method was different from Constructal Theory, some similar industrial examples were surely inevitable. Most of the comments that we received have paid much attention to the language and not the content of our paper [1], however, the content is surely more important. As non-native English speakers, we learned English from different literature and excellent English textbooks. Because of this, we used very common language in our paper [1], which may be found in many books on self-organization theories and nonlinear science theories. These theories were created and gradually formulated by the contributions of many scientists, such as those of Professor Bejan.

In response to the comments that we have received, the following sections give our detailed explanations on a few primary features in our paper that distinguish it from those found in Professor Bejan's Constructal Theory [15].

Nonlinear Non-Equilibrium Statistical Thermodynamics Perspective

Let us begin with the ''assumption'' that appeared in the paper [1] in which the authors' propose from the view of statistical mechanics [1]. In fact, statistical mechanics shows that the same kind of hypothesis as equilibrium systems is required for describing open non-equilibrium complex systems. More importantly, we obtained probability distribution functions by giving constraints ranging from one-order driving forces to four-order driving forces, which was a way of statistical thinking. This assumption is very common. A similar description can be found in Professor Bejan's Constructal Theory [15]. Of course, we can also find similar statements in much earlier literature [16]. In many books, this idea has been proposed as common sense, however, general law or mathematical formulations has not been available.

Though thermodynamics is a rather old discipline of physics, it is surely not old-fashioned. For the universality of thermodynamics, such modern topics as the big bang model, the theory of black holes, and the theory of biological or information systems show that thermodynamics is going through a renaissance. Currently, many scientists are looking for the fourth law of thermodynamics. At present, there are many similar and different descriptions on possible fourth law. For example, according to [17] many scientists at the Santa Fe Institute are eager for the appearance of fourth law or new second law. In our paper [1], we started our discussion from driving forces and generalized fluxes borrowed from classical irreversible processes where thermodynamics impression was evident. Furthermore, by assuming the nonlinear relation between driving forces and generalized fluxes

$$J = \eta + \sum_i \gamma_i x_i + \sum_{ij} \gamma_{ij} x_i x_j + \sum_{ijk} \gamma_{ijk} x_i x_j x_k + \sum_{ijkl} \gamma_{ijkl} x_i x_j x_k x_l + \Lambda \quad (1)$$

We could deduce that our analysis was a kind of nonlinear non-equilibrium thermodynamics.

Perspective of Renormalization Group Transformation (RGT)

With the constant victories of exploring the ultimate structure of matter from the process of molecules to atoms, atoms to electrons and nuclei, to nucleons, to elementary particles, and to quarks, another mainstream of modern physics has been concentrated on the understanding of structural organization of complex systems, which are more often encountered in our common experience.

Complex systems represent hierarchies, i.e., increasing complexity. This means that they can be divided into different levels, each representing a subsystem, which consists of relatively uniform elements that interact in some way with each other. These interactions may be responsible for autonomous pattern formation at any given hierarchical level. The higher subsystems in the hierarchy provide control over the processes of pattern formation at the lower sub-ordinary levels. The curiosity on the nature of increasing complexity has provided an incentive for numerous investigations over past decades. A substantial number of such efforts have been devoted to understanding and modeling it. A plethora of investigations are available in the literature. For ex-

[1] School of Environmental Science and Engineering, Tianjin University, Tianjin 300072, China; e-mail: shoji@photon.t.u-tokyo.ac.jp

[2] Department of Mechanical Engineering, The University of Tokyo, Hongo 7-3-1, Bunkyo-ku, Tokyo 113-8656, Japan; e-mail: shoji@photon.t.u-tokyo.ac.jp

ample, in chemistry, we may find a lot of these investigations [10]. Renormalization Group theory, as a typical method of analyzing increasing complexity, was originated by K. Wilson and has been developed gradually over past decades [12].

Our paper [1] deals with more general problems, mainly constructing the fractal networks from Scale Transformation theory in statistical mechanics, especially Renormalization Group theory [12], and is not based on any specific example. It is our logical conclusion that the present method is very general. By the factors group or parameters group transformations at different hierarchies or scales:

$$K_n = \mathrm{RTG}(K_{n-1}) \tag{2}$$

This method is a kind of typical geometric analysis in statistical perspective.

According to Renormalization Group theory [12], there are two directions for analyzing complex systems: zoom-in and zoom-out. Considering the growth processes, the present analysis [1] was based on zoom-out, that is, from small scale to large scale. We can derive the fractal structure in following way for two-dimensional problems,

$$\frac{\Omega_n}{\Omega_{(n-1)}} \approx \frac{J_{un}(\alpha_1) - J_{un}(\alpha_2)}{J_{u(n-1)}(\alpha_1) - J_{u(n-1)}(\alpha_2)} = \frac{h_n l_n^2}{h_{(n-1)} l_{(n-1)}^2} = \left[\frac{l_n}{l_{(n-1)}}\right]^{(2-p)} \tag{3a}$$

Or for three-dimensional problems,

$$\frac{\Omega_n}{\Omega_{(n-1)}} \approx \frac{J_{un}(\alpha_1) - J_{un}(\alpha_2)}{J_{u(n-1)}(\alpha_1) - J_{u(n-1)}(\alpha_2)} = \frac{h_n l_n^3}{h_{(n-1)} l_{(n-1)}^3} = \left[\frac{l_n}{l_{(n-1)}}\right]^{(3-p)} \tag{3b}$$

Depending on actual conditions, p, as a specific parameter ranging from 0 to 1, reflects the effects of the system's internal configurations and environment on dynamics fractal structure of evolutional complex system. System adaptation to environment is highly exhibited.

Other Related Problems

Open systems must optimize to live, which is generally common sense [18]. Modern sciences are trying to repair the gap between living science and non-living science [6]. Indeed, the present analysis [1] shows that same principle could be applied for any open dissipative systems, whether they are living or non-living.

Time direction arouses many interests, though it is still a puzzling problem [6]. As for present authors' viewpoints, though affected by literature [15], often other researchers state it similarly too [6,10,18]. In some cases, they even express it as common sense.

Compared to available theories and to our best knowledge, in our present paper [1], we indeed derived detailed dissipative structure from a general viewpoint, which is always our objective in studying dissipative structure theory of Nicolis and Prigogine [7]. In addition, our paper [1] derived detailed fractal structure from a general viewpoint. From the beginning of knowing fractal theory, we have realized that available fractal theory can only describe fractal structures, but not explain the physics of the formation of fractal structures.

From 1970s, urban evolution was a typical dissipative example even. We can find it in many books on self-organization; especially the self-organization of social problems. Professor Bejan's theory [15] is a typical description on urban evolution.

In our paper, the term ''Equilibrate means death'' [1] means that it is impossible for energy or flow to be equally distributed in open systems. The present theory stresses the feedback effect [1], and it is by feedback effect that the ordered network can be constructed. The dominant subsystems must satisfy two conditions. Firstly, they need to get enough flux from the environment to destabilize them. In this case, new modes will be formed and more flux will be consumed. Secondly, the maintaining of this new mode, i.e., the maintaining of the ordered structure, will need more flux from environment. Actually, according to the above theory, tree-like network means that by competition and natural selection this new mode will indeed get most of the flux from the environment.

As for Figs. 4–8 in paper [1], we can only say that it is possible that we received some hints from Bejan's book [15]. The senior author has developed the idea of describing dynamics processes by using this type of figure over a period of time, and it cannot be attributed to a single source. It seems very natural to keep in mind the processes of Renormalization Group Transformation (RGT). More importantly, our figures differ greatly from Professor Bejan's figures [15]: For instance, in Professor Bejan's figures [15], there are only two or three types of lattices dealing with only two or three types of sub-systems or factors. However, in our figures, we deal with real complex systems, which include amounts of sub-systems. So, in our figures, we draw many lattices indicated by many specific symbols dealing with enormous factors. Even though at first glance our figures are similar to Professor Bejan's figures [15], they reflect completely different physical means. Professor Bejan's figures [15] deal with solid geometry, whereas our figures stand for geometry in a statistical view, which were indicated by lots of symbols in our figures. Moreover, these symbols have specific statistical representing means. In conclusion, our figures differ from Professor Bejan's figures [15] both in much-detailed configurations and in physical means.

Conclusions

In conclusion, our paper [1] is making a renewed effort to develop the theories of complex systems from statistical mechanics. By paying more attention to understanding the processes of non-equilibrium phase change, the present investigations analyzed the physics of fractal structure and the mechanism of dissipative structure from statistical mechanics and renormalization perspectives. Of course, many results in our paper [1] agree well with the results derived by using Professor Bejan's Constructal Theory [15], which demonstrated the unifications of natural laws. According to the history of any scientific developments, whether our paper lives in the large umbrella of Constructal Theory, or whether it is only a supplement to Constructal Theory will have to wait the test of time.

Acknowledgment

The Project is Currently Sponsored by the Scientific Research Foundation for the Returned Overseas Chinese Scholars, State Education Ministry.

Nomenclature

h = generalized flux transfer rate
l = scale, m

References

[1] Chai, L. H., and Shoji, M., 2002, ''Self-Organization and Self-Similarity in Boiling Systems,'' ASME J. Heat Transfer, **124**, pp. 507–515.
[2] Chai, L. H., 1999, ''Binary Mixtures Boiling Under Microgravity and Nonlinear Features of Boiling,'' Ph.D. thesis, Tsinghua University, China.
[3] Chai, L. H., Peng, X. F., and Wang, B. X., 2000, ''Nucleation Site Interaction During Boiling,'' Int. J. Heat Mass Transfer, **43**, pp. 4249–4258.
[4] Klimontovich, Y. L., 1991, *Turbulent Motion and the Structure of Chaos. A New Approach to the Statistical Theory of Open Systems*, Kluwer Academic Publishers, Boston, London.
[5] Haken, H., 1977, *Synergetics*, Springer, Berlin.
[6] Prigogine, I., 1980, *From Being to Becoming*, W. H. Freeman, San Francisco.
[7] Nicolis, G., and Prigogine, I., 1977, *Self-Organization in Nonequilibrium Systems*, Wiley, New York.

[8] Stratonovich, R. L., 1992, *Nonlinear Non-Equilibrium Thermodynamics I*, Springer Verlag, Berlin.
[9] Lavenda, B. H., 1993, *Thermodynamics of Irreversible Processes*, Dover ed., Dover, New York.
[10] Gallagher, R., and Appenzeller, T., 1999, "Beyond Reductionism," Science, **284**, pp. 87–109.
[11] Haken, H., 1983, *Advanced Synergetics*, Springer, Berlin.
[12] Toda, M., Kubo, R., and Saito, N., 1992, *Statistical Physics 1*, Springer, Berlin.
[13] Haken, H., 2000, *Information and Self-Organization*, Springer, Berlin.
[14] Mandelbrot, B., 1982, *The Fractal Geometry of Nature*, W. H. Freeman, San Francisco, CA.
[15] Bejan, A., 1997, *Advanced Engineering Thermodynamics*, Wiley, New York, Chpt. 13.
[16] Takayasu, H., 1992, *Fractals in the Physical Sciences*, John Wiley & Sons.
[17] Waldrop, M. M., 1992, *Complexity: The Emerging Science at the Edge of Order and Chaos*, Simon & Schuster, New York.
[18] Davies, K. G., 2000, "Creative Tension—What Links Aristotle, William Blake, Darwin and GM Corps?" Nature (London), **407**(6807), p. 135.

Journal of Heat Transfer

Erratum

Erratum: "Investigation of Steady-State Drawing Force and Heat Transfer in Polymer Optical Fiber Manufacturing" [Journal of Heat Transfer, 2004, 126(2), pp. 236–243]

H. M. Reeve, A. M. Mescher, and A. F. Emery

[DOI: 10.1115/1.1765115]

The following captions should read:

Fig. 2 Numerically predicted contour plots of temperature (at left in °C) and stream function (right) for (a) case E1 and (b) case E2

Fig. 3 Axial variation of the predicted polymer temperature (at $r=0$) and the furnace wall temperature for cases E1 ($V_f=10$ cm/s) and E2 ($V_f=20$ cm/s)

Fig. 4 Axial variation of the radiative and convective heat flux experienced at the polymer's surface for case E1

Fig. 5 Numerically predicted and experimentally measured free surface shapes for case E1. (The initial guess is shown for comparison.)

Fig. 6 Effect of preform feed speed on the predicted (solid line) and measured (symbols) free surface shapes

Fig. 8 Effect of the furnace wall temperature on the predicted and measured draw force ($D=25.4$ mm, $V_f=10$ cm/s, $V_p=25$ μm/s)

Fig. 9 Effect of upstream heating (U_t) on the predicted free surface shape. A comparison between the results for $U_t=0$ W/m^2 K (solid line) and $U_t=30$ W/m^2 K (dashed line) is shown.

